THE FIBER SOCIETY

Advancing Scientific Knowledge
Pertaining to Fibers and Fibrous Materials

The Fiber Society Spring 2013
Technical Conference

May 22–24, 2013

Conference Chair

Professor Xungai Wang
Deakin University

Venue

Mercure Hotel
Geelong, Victoria, Australia

Program

Wednesday, May 22

8:00 Registration; Coffee and Tea Service
9:00 Welcoming Remarks, Business, and Announcements *Xungai Wang, Conference Chair*
Rudolf Hufenus, President, Fiber Society
Professor Lee Astheimer, DVC(R), Deakin University

Morning Session

9:20–10:00	**Keynote Speaker: Professor Gordon Wallace, University of Wollongong** ***Highly Functional Fibres for Bionics*** **(Room 1)**

	Room 1	**Room 2**
	Session: Functional Fibrous Materials ***Laurence Schacher, Chair***	**Session: High-Performance Fibres and Composites** ***Greg Rutledge, Chair***
10:00	*Self-Healing Superamphiphobic Fabrics with Directional Fluid-Transport Function* Tong Lin, Hua Zhou, and Hongxia Wang, Deakin University	*Biodegradable Fibers from Renewable Sources: Melt Spinning of Polyhydroxyalkanoates (PHAs)* Rudolf Hufenus[1], Felix A. Reifler[1], Katharina Maniura-Weber[1], Manfred Zinn[2], Adriaan Spierings[3], and Urs J. Hänggi[4], [1]Empa, [2]University of Applied Sciences Western Switzerland, [3]irpd, institute for rapid product development, [4]Biomer
10:20	*Instrumented Manikin Evaluation System for Optimizing Protective Clothing Performance* Guowen Song[1,2], Mei Zhang[2], Yehu Lu[3], and Chunyan Wu[2], [1]University of Alberta, [2]Jilin University, [3]Donghua University	*Structure/Properties Relationship in a Single Para-Aramid Fibre* Judith Wollbrett-Blitz[1,2], Alba Marcellan[1], Sébastien Joannès[2], and Anthony Bunsell[2], [1]PPMD, ESPCI, UPMC, [2]Centre des Matériaux P-M Fourt, ENSMP
10:40	***Break***	
11:00	*Functional Fabric Design for Improvement of Garment Ventilation* Chao Sun[1], Joe Sau-chuen Au[1], Jintu Fan[1, 2], and Rong Zheng[3], [1]Hong Kong Polytechnic University, [2]Cornell University, [3]Beijing Institute of Fashion Technology	*Toward the Development of a High Strain Rate Testing Standard for Advanced Fibers* Gale A. Holmes, Jae-Hyun Kim, N. Alan Heckert, Walter G. McDonough, Stefan D. Leigh, and Kirk D. Rice, National Institute of Standards and Technology
11:20	*Biomechanically Compliant Polymeric Structures for Cardiovascular Implant Applications* Charanpreet Singh[1], Yosry Morsi[2], and Xungai Wang[1], [1]Deakin University, [2]Swinburne University of Technology	*Surface and Bulk Crystallinity of Polypropylene Filaments* Ali Kilic[1], Eunkyoung Shim[2], and Behnam Pourdeyhimi[2], [1]İstanbul Technical University, [2]North Carolina State University
11:40	*Thermal Insulation Properties of Silkworm Cocoons* Jin Zhang[1], Rangam Rajkhowa[2], Jingliang Li[1], Ziangyang Liu[2], Xungai Wang[1,3], [1]Deakin University, [2] National University of Singapore, [3]Wuhan Textile University	*Effect of Electrolytic Oxidation and Sizing on the Mechanical Performance of Carbon Fibre Composites* Claudia Creighton, Abdullah Kafi, and Bronwyn Fox, Deakin University

12:00	*The Mechanism of Needle Penetration Through a Woven Aramid Fabric* Christopher Hurren, Qing Li, Alessandra Sutti, and Xungai Wang, Deakin University	*Multifunctional Carbon Nanotube Yarns — Production, Properties, and Applications* Menghe Miao, CSIRO Materials Science and Engineering Division
12:20	*Vibration Isolation Properties of Weft-Knitted Spacer Fabrics* Hong Hu, Fuxing Chen, and Lai Xu, Hong Kong Polytechnic University	*Transverse Modulus of Carbon Fibres* Linda Hillbrick, Jamieson Kaiser, Mickey Huson, and Geoff Naylor, CSIRO Materials Science and Engineering
12:40	***Lunch at Mercure Hotel***	

Afternoon Session

2:00–2:40	**Keynote Speaker: Professor Lei Jiang, Chinese Academy of Sciences** ***Bioinspired, Smart, Multiscale Interfacial Materials*** **(Room 1, via Skype)**	
	Room 1	**Room 2**
	Session: Functional Fibrous Materials *cont'd* ***Stephen Michielsen, Chair***	**Session: Natural Fibres** ***Janice R. Gerde, Chair***
2:40	*Detecting Free Radicals in Fibrous Materials Exposed to Light* Keith R Millington[1] and Siti Farhana Zakaria[2], [1]CSIRO Materials Science and Engineering, [2]Universiti Teknologi MARA	*Biomimetic Melanin Dyestuffs for Wool Fabric In Situ Coloration* John H. Xin, Vicky L. L. So, and Liang He, Hong Kong Polytechnic University
3:00	*A Novel Conducting Polymer-Carbon Nanotube Composite Yarn* J. Foroughi[1], G. M. Spinks[1], G. G. Wallace[1], and R. H. Baughman[2], [1]University of Wollongong, [2]University of Texas at Dallas	*Mohair Fibre Quality and Production as Related to Animal Size* Bruce A. McGregor[1] and Kym Butler[2], [1]Deakin University, [2]Department of Primary Industries
3:20	*Photoreduction of Graphene / Photocatalyst Nanostructured Fabric for Recycled Pollutant Removal* Jinfeng Wang[1], Takuya Tsuzuki[1,3], Lu Sun[1], and Xungai Wang[1,2], [1]Deakin University, [2]Wuhan Textile University, [3]Australian National University	*Chemical Treatments on Hemp Fibre Composites* Hao Wang[1], Mazed Kabir[1], and K. T. Lau[2], [1]University of Southern Queensland, [2]Hong Kong Polytechnic University
3:40	***Break***	
4:00	*Effect of Softener on Flame Retardant Finish of Cotton Fabrics* K. P. Tang[1], C. W. Kan[1], J. T. Fan[1,2], S .L. Tso[1], [1]Hong Kong Polytechnic University, [2]Cornell University	*Water and Soil Resistant Bamboo Fabric by Sol-Gel Nano-Coating* Awais Khatri, Zahir Ahmed, Saiqa Agha, Saqib Munawar, Shahwaiz Khanzada, and Saif-ur-Rehman, Mehran University of Engineering and Technology
4:20	*Robust, Electro-Conductive, Self-Healable, Superamphiphobic Fabrics from PEDOT/FD-POSS/FAS Coating* Hongxia Wang, Hua Zhou, and Tong Lin, Deakin University	*Silk Cocoon Structure and Its Protective Roles* Jasjeet Kaur[1], Rangam Rajkhowa[1], Takuya Tsuzuki[1], Keith Millington[2], and Xungai Wang[1], [1]Deakin University, [2]CSIRO Materials Science and Engineering

4:40	*In Situ Electrochemical Polymerization of Pyrrole onto Textiles: Influence of Add-On and Surface Roughness* Kushal Sen, Dipayan Das, and Syamal Maiti, Indian Institute of Technology	*Wrinkle Resistant Finishing of Cotton Fabric Using HDAS on the Crosslinking Agent* Jianwei Xing, Chengshu Xu, Yan Ren, Wenzhao Shi, and Jinshu Liu, Xi'an Polytechnic University
5:00	*Design of Smart Functional Apparel Products for Moxa Moxibustion* Li Li, Wai-man Au, Feng Ding, and Kwok-shing Wong, Hong Kong Polytechnic University	*Cottonscope Determination of Cotton Fiber Maturity and Fineness Using Small Samples* G. R .S. Naylor[1] and J.E. Rodgers[2], [1]CSIRO Materials Science and Engineering, [2]USDA-ARS-Southern Regional Research Center
5:20	*Dynamic Plantar Pressure Monitoring of Diabetic Patients Using Intelligent Footwear System Based on Fabric Sensor During Daily Activities* Kaiyang Mai[1], Lin Shu[1], Xiaoming Tao[1], Wingcheung Wong[2], Kafai Lee[2], Siuleung Yip[2], Anthony Waihung Shum[2], Wailam Chan[2], Chipang Yuen[2], Ying Li[1], [1]Hong Kong Polytechnic University, [2]Kwong Wah Hospital	*Ionic Liquids: Solvents for Protein Polymer Processing* Nolene Byrne and Xungai Wang, Deakin University
5:40	*Wearable Sensors for the Prophylaxis of Lower Limb Pathologies* M. J. Abreu[1], A. Catarino[1], A. M. Rocha[1], F. Derogarian[2,3], R. Dias[2], J. M. da Silva[2,3], J. C. Ferreira[2,3], V. G. Tavares[2,3], and M. V. Correia[2,3], [1]Universidade do Minho, [2]Inesc Tec, [3]Universidade do Porto	*Eri Silk: Cocoon, Fibre, and Proteins* Rangam Rajkhowa[1], Ravindeer Rawat[2], Suradip Das[2], Jasjeet Kaur[1], Ben J. Allardyce[1], Utpal Bora[2], and Xungai Wang[1], [1]Deakin University, [2]Indian Institute of Technology

6:30 p.m. Dinner at Wharf Shed Café (walking distance; shuttles available)

Thursday, May 23

8:00 Coffee and Tea Service

Morning Session

9:00–9:40	**Keynote Speaker: Dr. Gregory Rutledge, MIT** ***Applications of Electrospun Nonwoven Fiber Membranes for Sensing and Separations*** **(Room 1)**

	Room 1	Room 2
	Session: Nanofibres ***Tong Lin, Chair***	**Session: Functional Fibrous Materials** ***John Xin and Rangam Rajkhowa, Chairs***
9:40	*Super-Crystalline Cellulose Nanofibers by Self-Assembling* You-Lo Hsieh, University of California at Davis	*Characterization of Thermal Comfort of Weft-Knit Ballistic Nylon/Wool Fabric* Rana Mahbub, Lyndon Arnold, and Lijing Wang, RMIT University
10:00	*Mechanical-to-Electrical Energy Conversion of Needleless Electrospun Poly(vinylidene fluoride) Nanofiber Webs* Jian Fang, Haitao Niu, Hongxia Wang, Xungai Wang, and Tong Lin, Deakin University	*Optimization of Fibre Composition in Nonwoven Air Filter Media* R. Chattopadhyay, Dipayan Das, and Arun Kumar Pradhan, Indian Institute of Technology

10:20	*Electrospun Nanofiber Mats with Controlled Microstructures for Nanoparticle Filtration* Negar Ghochaghi, Adetoun Tawio, and Gary Tepper, Virginia Commonwealth University	*Graft Co-Polymerization of Acrylic Acid on Nylon 6 Knitted Fabric Using Redox Systems* Farzad Mohaddes, Stanley Fergusson, and Lijing Wang, RMIT
10:40	***Break***	
11:00	*Induced Negative Viscosity as a Degree of Freedom in the Electrospinning of Polymeric Solutions* Juan P. Hinestroza, Lina M. Sanchez-Botero, and Alejandro Garcia, Cornell University	*Multifunctional Cotton Fabric Using* TiO_2/SiO_2 *Nanocomposite* Esfandiar Pakdel[1], Walid A. Daoud[2], and Xungai Wang[1], [1]Deakin University, [2]City University of Hong Kong
11:20	*Characterization of Electrospun Mat Composed of Polymer and Mesoporous Silica Nanoparticles* Laurence Schacher[1], Slimane Almuhamed[1], Nabyl Khenoussi[1], Magali Bonne[2], Bénédicte Lebeau[2], Dominique C. Adolphe[1], and Jocelyne Brendle[2], [1]ENSISA, [2]Institut de Science des Matériaux de Mulhouse	*Measurement and Evaluation of Magnetic Fabric* Yan Chen, Gao Jie Yu, and Fei Fei Wu, Soochow University
11:40	*Encapsulation of Active Agents in Electrospun Nanofibers/Nanowebs* Tamer Uyar, Fatma Kayaci, Zeynep Aytac, and Asli Celebioglu, Bilkent University	*A Novel Super Absorbent Polyester Fabric Functionalized by a Biodegradable Poly (γ-glutamic acid) Hydrogel* Zheng Li, JianFei Zhang, JianJun Yan, JiXian Gong, and JingXin Wang, Tianjin Polytechnic University
12:00	*ZnO Nanorod-Based Solar Textiles for Smart Clothing* Youngjin Chae and Eunae Kim, Yonsei University	*Enhancing Thermal Conductivity of Cotton Fabrics with Nanocomposite Coatings* Yan Zhao, Amir Abbas, Xungai Wang, and Tong Lin, Deakin University
12:20	*Nanocrystal* TiO_2 *as Scattering Layer for Dye-Sensitized Solar Cells* Xueyang Liu[1], Jian Fang[1], Mei Gao[2], and Tong Lin[1], [1]Deakin University, [2]CSIRO	*Study on Parameters Affecting the Performance of Piezo-Resistive Conductive Fabric* Weijing Yi[1,2], Xiaoming Tao[2], Yangyon Wang[3], Guangfeng Wang[3], and Rong Zheng[1], [1]Beijing Institute of Fashion Technology, [2]Hong Kong Polytechnic University, [3]AdvanPro Limited

12:40	***Lunch at Mercure Hotel***

Afternoon Session

2:00–2:40	**Keynote Speaker: Professor Zhengzhong Shao, Fudan University** ***Structure and Property Relationships of Animal Silks*** **(Room 1)**

	Room 1	**Room 2**
	Session: Natural Fibres *cont'd* ***Cheryl Gomes, Chair***	**Session: High-Performance Fibres and Composites** ***Bronwyn Fox, Chair***

2:40	*An Assessment of Alternative Cotton Fiber Quality Attributes and Their Influence on Yarn Strength* Robert L. Long[1], Michael P. Bange[2], Christopher D. Delhom[3], Jeffrey S. Church[1], and Greg A. Constable[2], [1]CSIRO Materials Science and Engineering, [2]CSIRO Plant Industry, [3]USDA-ARS Southern Regional Research Center	*Water Effects on Natural Fibers and Its Implications to Shape Memory Polymer Composite Fiber* Jinlian Hu, Jing Lu, and Jianping Han, Hong Kong Polytechnic University
3:00	*Photostability of Chemically Modified Silk* Weiguo Chen[1,3], Zongqian Wang[1], Donghui Pan[1], Zhihua Cui[1], Keith Millington[2], and Xungai Wang[3], [1]Zhejiang Sci-Tech University, [2]CSIRO Materials Science and Engineering, [3]Deakin University	*Open*
3:20	*Open*	*Deformation of Dispersed Phase During PS/PP Melt Spinning* Long Chen, Houkang He, Shanshan Sun, Yu Zhang, and Zongyi Qin, Donghua University
3:40	***Break***	
4:00	*Assessing Yarns to Predict the Comfort Properties of Fabrics* Maryam Naebe[1], Bruce A. McGregor[1], David Tester[2], and Xungai Wang[1], [1]Deakin University, [2]CRC for Sheep Industry Innovation Ltd.	*Characterisation of Composite Honeycomb Sandwich Structures Cured Using the Quickstep Process* M. Jennings[1], M. de Souza[1], C. Creighton[1], S. Agius[1], T. Pierlot[2], and B. Fox[1], [1]Deakin University, [2]CSIRO Materials Science and Engineering
4:20	*Sock Fabrics: Measuring the Coefficient of Static and Dynamic Friction to Prevent Blisters* Rebecca Van Amber, Raechel Laing, Cheryl Wilson, Bronwyn Lowe, and Brian Niven, University of Otago	*Interfacial Improvement of Carbon Fiber/Epoxy Composites by Using Electrospray Carbon Nanotube Deposition* Quanxiang Li[1], Jeffrey Church[2], Abdullah Kafi[1], Minoo Naebe[1], and Bronwyn Fox[1], [1]Deakin University, [2]CSIRO Materials Science and Engineering
4:40	*Comparative Study of Wool, Cotton, and Ramie Bundle Fibers' Dynamic Mechanical Properties* Zhigang Xia, Weilu Xu, Weigang Cui, JingJing Huang, Wuhan Textile University	*Force Shield Textile Composite with Microcapsule System* Xing Liu[1,2], Rui Wang[1,2], Fangli Pang[1,2], Mengxuan Li[1,2], Jiao Huang[1,2], and Zhili Zhong[1,2], [1]Tianjin Polytechnic University, [2]Key Laboratory of Advanced Textile Composite Materials
5:00	*The Weft-Knitted Plant-Structured Fabric for Polo Shirt* Qing Chen[1] and Jintu Fan[2], [1]Hong Kong Polytechnic University, [2]Cornell University	*Study on Preparation and Properties of Modified Polypropylene Fibers Used in Engineering* Yiren Chen[1], Li He[1], and Zhiqiang Fan[2], [1]Wuhan Textile University, [2]Changjiang Water Resources Commission

5:20	*Silk Films as Promising Materials for the Repair of Chronic Perforations of the Tympanic Membrane* Ben Allardyce[1], Bing Mei Teh[2,3], Rangam Rajkhowa[1], Robert Marano[2,3], Sharon Redmond[2,3], Yi Shen[2,3,4], Marcus Atlas[2,3], Rodney Dilley[2,3], and Xungai Wang[1], [1]Deakin University; [2]Ear Science Institute Australia, [3]University of Western Australia, [4]Ningbo Medical Centre	*Methacrylate/Hydroxyethyl Methacrylate Fiber for Organic Compounds Absorbents* Yan Feng[1,2], Xiuyang Hao[1], and Jian Chen[1], [1]Tianjin Polytechnic University, [2]Key Laboratory of Advanced Textile Composite Materials of Ministry of Education
5:40	*Enhanced Moisture Management Properties of Denim Fabrics* Sung Hoon Jeong[1], Muhammad Bilal Qadir[1], Uzair Hussain[2], [1]Hanyang University, [2]National Textile University	*Characterization and Preparation of Polyamide 66/OV-POSS Nanocomposite Fibre* Yimin Wang, Lin Xiaoxia, Shao Qun, and Kiptanui Koech Jacob, Donghua University

6:00 p.m. Reception at Mercure
7:00 p.m. Banquet
David Tournier, Wathaurong Aboriginal Co-operative, *Plants for Weaving*
Norm Stanley, Wathaurong Aboriginal Co-operative, Didgeridoo Player

Friday, May 24

9:00 Coffee and Tea Service

10:00–10:40	**Keynote Speaker: Associate Prof. Bronwyn Fox, Deakin University** **Developments in Carbon Fibre Research in Australia** **(Room 1)**

	Room 1	**Room 2**
	Session: High-Performance Fibres and Composites ***Stuart Lucas, Chair***	**Session: Nanofibres** ***Rudolf Hufenus, Chair***
10:40	*Graphene Fibers: A Promising Multifunctional Material* Chao Gao, Zhen Xu, and Xiaozhen Hu, Zhejiang University	*Process Control of High-Throughput Core-Sheath Electrospinning from a Slit Surface* Toby Freyman, Xuri Yan, Quynh Pham, John Marini, and Robert Mulligan, Arsenal Medical, Inc.
11:00	*Structure and Property Change of Pre-Drawn Aromatic Copolysulfonamide Fiber During Heat-Drawing Process* Yumei Zhang[1], Jinchao Yu[1], Rui Wang[1], Shenghui Chen[2], Xiaofeng Wang[2], and Huaping Wang[1], [1]Donghua University, [2]Shanghai Tanlon Fiber Co.	*Structure and Properties of Melt Blown Submicron Fiber Nonwoven* Gajanan Bhat[1] and Wanli Han[2], [1]University of Tennessee at Knoxville, [2]Donghua University
11:20	*Thermal Properties of Poly(ethylene terephthalate) / Nanoclay Nanocomposites Fibers* Yusuf Ulcay and Rustam, Uludağ University	*Electrospun Nanofibers for Blood Vessel Tissue Engineering* Xiumei Mo, Anlin Yin, and Chen Huang, Donghua University

11:40	*Molecular Orientation Development in Highly Uni- and Bi-axially Stretched ePTFE Filaments* Kyung-Ju Choi, Clean & Science Co.	*Discretized Modeling of Whipping Motion During Electrospinning Process* Yong Lak Joo and An-Cheng Ruo, Cornell University

12:00–2:00	**Excursion to Deakin University, Waurn Ponds Campus, for Lunch, Poster Setup, and Lab Tour**

2:00–4:00	**Poster Presentations** **Tour (in separate groups) of Australian Future Fibres Research & Innovation Centre (AFFRIC), Institute for Frontier Materials (IFM), Deakin University**

4:00–4:30	**Poster Awards** **Close of Conference**

****

Poster Presentations

Session Chair: You-Lo Hsieh

Guoqiang Chen	*Performance of Flame Retardancy Silk Modified with Water Soluble Vinyl Phosphoamide*
Ai Xin	*The Preparation of Semi-Aromatic Polyamide Fibers*
Linden Servinis	*Functionalisation of Carbon Fiber Toward Enhanced Fiber-Matric Adhesion*
Pengfei Li	*Defect Detection Method on Printed Fabrics*
Na Han	*Effects of Feeding Modes on the Melt Processability of Acrylonitrile-Methyl Acrylate Copolymers and Fibers*
Xiangrong Wang	*Dyeing and UV Protection Properties of Chrysophanol on Polylactic Acid Fiber*
Youngjoo Chae	*Verification of Color Prediction Models for Yarn-Dyed Woven Fabrics*
Lin Xiaoxia	*Rheological of OV-POSS / PA66 Nanocomposites*
Chuanxiang Qin	*Preparation and Photoluminescence of* $LaBO_3$*:* Eu^{3+}*Nanofibres*
Baijun Xi	*The Study of Compatible Performance Between β-Cyclodextrin / Lavender Spices and regenerated Cellulose*
Wenbin Li	*Preparation and Mechanical Properties of Thermoplastic Films from Superfine Down Powder*
Xin Liu	*Mechanical Properties of Polypropylene Composites Reinforced with Down Feather Whisker*
Haihua Zhan	*Study of a New Type of Hot-Melting Polyester Sea-Island*
Yunli Wang	*Research on Mechanical Properties of 100% Cotton Anti-Creasing Yarns*
Bin Tang	*Coloration of Silk Fibers with Gold Nanoparticles*
Xiangling Chen	*Hydrophilicity of the Hydrophilic Copolyester*
Huaping Wang	*Understanding the Interactions in Acrylic Copolymer / 1-Butyl-3-Methylimidazolium Chloride from Solution Rheology*

Yusuf Ulcay	*Reducing Noise Level in Vehicles by Spunbonded Nonwovens Made from Bicomponent Filaments*
Sung Hoon Jeong	*Optimizing Spindle Speed of Ring Spun Yarn*
Maria José Abreu	*Thermal Properties of Mattress Protectors for the Prevention of Pressure Ulcers*
Yao Yu	*Factors Affecting UV Protection of Textiles at the Fiber Level*
Mingwen Zhang	*Preparation of* SiO_2 */* TiO_2 *with Eliminated Photocatalytic Activity*
Xuming Li	*Influence of He /* O_2 *Atmospheric Pressure Plasma Jet Treatment on Desizing of Starch Phosphate and Poly(vinyl alcohol)*
Eunae Kim	*Heat and Moisture TransferThrough Hydrophilic and Hydrophobic Multilayered Fabric System*
Yumin Xia	*Intuitional and Quantitative Evaluation Technique of Polyvinyl Alcohol(PVA) Fiber Dispersion in Concrete via X-ray Imaging*
Yurong Yan	*Emulsion Electrospinning of Sodium Alginate and Polylactic Acid Fiber with Skin-Core Structure*
John Xin	*Smart Fibrous Materials for Water Harvesting*
Li-Chu Wang	*Evaluation of Two Cooling Systems Under a Fire Fighter Coverall*
Jianwu Li	*Preparation of a Novel Hydrophilic Copolyester*
Daniela Agnello	*Ambulatory Monitoring of ECG Signals Using Textile Electrodes*
Chaosheng Wang	*Non-Isothermal Crystallization Kinetic of Bio-Based Polyester*
Kiran Patil	*Biosorption of Phenol by Cashmere Guard Hair Powder*
Rasike De Silva	*Tri-Component Bio-Composite Materials from 'Green Processing'*
Ken Ri Kim	*Creative Shading Effect in Digital Jacquard Textiles*
Genyang Cao	*Structure and Composition Research of Lotus Petiole Fiber and Ramie Fiber*
Hu Zhang	*A Comparative Study on UV-Absorbing Titanium Dioxide Sol Gel Treatments for Wool*
Shangmei Wu	*Study on the Clothing Pressure of Elastic Weft Knitted Fabrics*
Zhiqiang Chen	*Coating of Carbon Fibres Using a Novel Three-Step Plasma Treatment*
Hongjie Zhang	*The Feasibility Study on the Grill Application of Basalt Continuous Filament*
Abdullah Kafi	*A Multiscale Approach to Quantify Friction Properties of Carbon Fibres*
Jixian Gong	*Evolutionary Engineering of Bacillus Strain for Biofunctionalization of PET Fabric*
Muhammad Shuakat	*Electrospinning of Nanofibre Yarns Using a Novel Ring Collector*
Jing Wang	*Thermo-Responsive PNIPAM Hydrogel Nanofibres Photocrosslinked by Azido-POSS*
Wai Ting Lo	*The Effect of Composites Thickness on the Performance of FootwearInsole Used for Diabetic Patients*
Simon Moulton	*Multifunctional Conducting Polymer Fibres for Drug Delivery Applications*

Rhys Cornock	*Precision Wet-Spinning of Cell-Impregnated Alginate Fibres for Tissue Engineering*
Rouhollah Jalili	*Wet-Spinning of Multifunctional Graphene Fibers Using Graphene Oxide Liquid Crystals*
Dorna Esrafilzadeh	*Combined Wet-Spinning and Electrospinning: Novel and Facile Method to Fabricate Micro-Nano Scale Conducting Fibres*
Anita Quigley	*Living Fibres: 3D Hydrogel Fibres for Tissue Engineering*
Mehdi Kazemimostaghim	*Production of Silk Nanoparticles*

Functional Fibrous Materials

Self-Healing Superamphiphobic Fabrics with Directional Fluid-Transport Function

Hua Zhou, Hongxia Wang, Tong Lin
tong.lin@deakin.edu.au
Institute for Frontier Materials, Deakin University, Geelong, VIC 3217, Australia

INTRODUCTION

Superamphiphobic fabrics, not only having a dual superhydrophobic and superoleophobic surface [1] but also being breathable, are useful for development of protective clothing to withstand liquid chemicals and biological contaminations. However, the main issue related to the existing superamphiphobic fabrics is low durability. Recently, Wang et al [2] introduced 'bio-inspired' self-healing ability into superamphiphobic fabrics, which represents an important development in the area.

When hydrophobicity is regionally combined with hydrophilicity, the surface shows remarkable ability to direct the motion of water drops towards hydrophilic areas.[3, 4] This phenomenon has been utilized to prepare directional water transport function on single layer fabrics. [5]

In our recent study, we have found that a fabric, after being treated by a wet-chemistry coating technique, can have a durable, self-healing, superamphiphobic surface. When the coated fabric was irradiated with strong UV light, it showed a directional fluid-transport function.

APPROACH

Silica nanoparticles, prepared by co-hydrolysis of tetraethylorthosilicate and fluorinated alkyl silane (FAS) in ethanol under an alkaline condition, and poly(vinylidene fluoride-hexafluoropropylene) (PVDF-HFP) in dimethylformamide (DMF) containing FAS, were applied in sequence onto a polyester fabric using a dip-coating method. After coating, the fabric was dried at 130 °C for 1 hour.

RESULTS AND DISCUSSION

Fig. 1a shows the coating procedure to the prepare superamphiphobic fabric. Two coating solutions were applied in sequence onto the fabric using a dip-coating method. Fig. 1b shows the super-repellency of the coated polyester fabric to liquid droplets (10 µL). Sphere-like droplets of blue-colored water, red-colored hexadecane and clear soybean oil were formed stably on the coated fabric. The coated fabric showed a contact angle (CA) of 172°, 165° and 160° to water, soybean oil and hexadecane, respectively.

A plasma treatment was employed to deliberately degrade the surface. After plasma treatment, the coated fabric became both hydrophilic and oleophilic with a contact angle of 0° to water, soybean oil and hexadecane (Fig. 1c). However, when the plasma treated fabric was heated at 130 °C for 5 minutes, it restored the superamphiphobicity. The contact angle after the heating treatment changed to 171°, 165° and 160° to water, soybean oil and hexadecane, respectively. The self-healing is repeatable. After 100 cycles of plasma & heating treatment, the fabric was still highly resistant to both water and oil fluids (Fig. 1d).

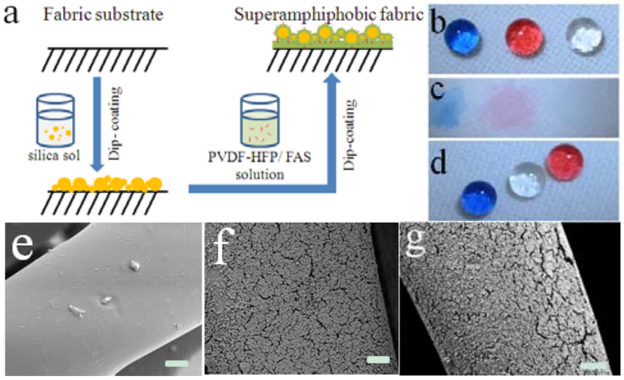

FIG. 1 a) Coating procedure for preparing superamphiphobic fabrics, b) photo of blue-colored water, red-colored hexadecane and clear soybean oil (10 µL) on the coated fabric, c) photo of liquids on the coated fabric after plasma treatment, d) photo of liquids placed on the coated fabric after 100 cycles of plasma & heat treatments, e) & f) SEM images of polyester fiber e) before, f) after coating treatment without plasma, and g) after coating treatment and 100 cycles of plasma & heating treatment (scale bar = 2µm).

Fig. 1e ~ g show the SEM images of the un-coated polyester fiber, the fiber after coating treatment and the coated fiber after 100 cycles of plasma and heating treatment. A nano-scale hierarchical structure was formed on the fiber after the coating treatment, which was maintained after 100 cycles of plasma and heating treatment.

Upon irradiation of the coated fabric with a strong UV lamp for 24 hours, the contact angle of the irradiated surface reduced to 0° to water, soybean oil and hexadecane. Although water spread on the front surface of the fabric, no liquid penetrated through the fabric and wick to the other side.

When water was dropped onto the back side which did not receive the UV irradiation directly, it moved immediately through the fabric and spread on the front side. This suggests that the 24-hour UV irradiation makes the coated fabric have a unidirectional water-transport effect.

More interestingly, the coated fabric also showed directional liquid transport effect to soybean oil, when it was UV irradiated for 14 hours under the same condition. Fig. 2a & b show series of frames taken from videos of soybean oil transport on either side of the coated fabric after UV irradiation. A shorter UV irradiation period, i.e. 10 hours, resulted in directional transport of hexadecane.

These results clearly demonstrate that the coated fabric develops a unique directional fluid-transport function after an asymmetric UV irradiation treatment.

To test the CA on the back side of the UV-irradiated fabric, an indirect method was employed by irradiating two layers of the same fabric, which were closely in contact with each other, and testing the front surface of second fabric layer [5]. As shown in Fig. 2c, after 10 hours of UV irradiation, the CA changes to 166°, 158° and 151° to water, soybean oil and hexadecane, while after 24 hours of UV treatment, the CA decreases to 160°, 130° and 80° for these liquids. Such a CA change was greatly different to that on the front surface of the first layer which reduced to 0° in a much shorter irradiation period (Fig. 2c).

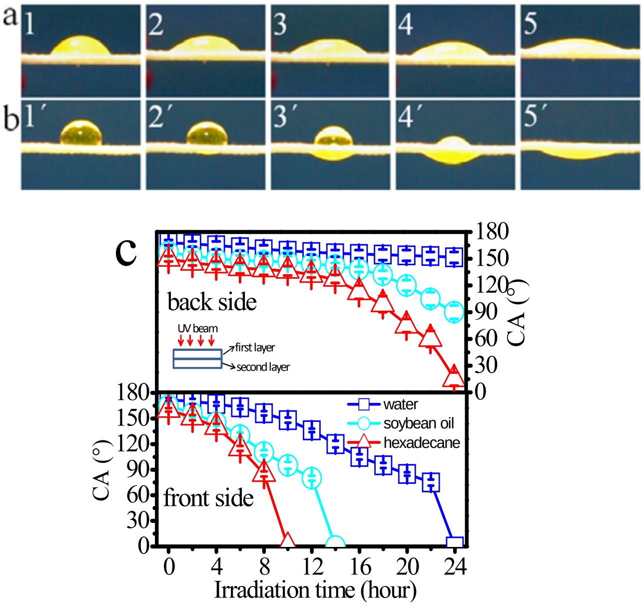

FIG. 2 a & b) Still frames taken from videos showing soybean oil (45 μL) on the coated fabric after 14 hours of UV irradiation, a) on the front side (time interval 0.1s) and b) on the back side (time interval 0.55s), c) CAs of UV irradiated fabrics changing with the UV irradiation time.

To further characterize the directional fluid-transport effect, the initial pressure required for the fluids to break through the fabric was measured. At least 1.96 kPa of pressure was needed for water to break through the coated fabric from the UV irradiated side when the fabric was subjected to 24-hour UV irradiation, whereas the breakthrough pressure on the back side was only 0.29 kPa. Lower pressure of 1.76 kPa and 1.57 kPa were measured for soybean oil and hexadecane to break through the front side of the coated fabric after it was UV irradiated respectively for 14 and 10 hours. However, the corresponding pressure on the back side was still very small, less than 0.29 kPa. For comparison, the breakthrough pressure of the un-coated pristine polyester fabric was measured to be 0.29 kPa, 0.26 kPa and 0.24 kPa for water, soybean oil and hexadecane, respectively. The fabric showed no difference on the two sides.

Washing and abrasion durability of the coated fabrics were evaluated. After 600 cycles of standard machine laundry, the coated fabric still maintained its superamphiphobicity (Fig. 3a). The abrasion durability was tested by the Martindale method using untreated fabric to simulate actual damage. A load pressure of 12 kPa was employed, which is often used for evaluating heavy duty upholstery usages. As shown in Fig. 3b, a decrease in the oleophobicity is observed after 8,000 abrasion cycles. However, the coated fabric still retained its superhydrophobicity after 25,000 abrasion cycles.

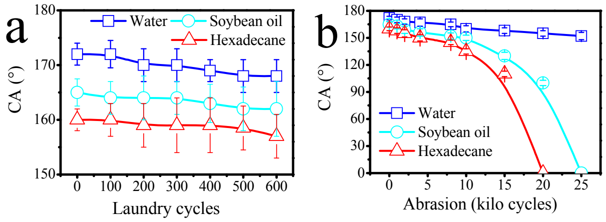

FIG. 3 CA change with a) laundry and b) abrasion cycles.

In addition, the coated fabric showed excellent durability against strong acid and base etching, ozone oxidation and even boiling in coffee. When the coated fabric was boiled in a coffee solution for 1 hour, and then left at room temperature for 24 hours, followed by rinsing with water and finally drying at room temperature, the coated fabric was not stained at all and it still maintained the superamphiphobicity.

CONCLUSION

This novel fabric may be useful for development of innovative "smart" clothing and functional membranes for various applications.

KEYWORDS: Superamphiphobic, self-healing, durability, directional fluid-transport, fabric, coating

ACKNOWLEDGMENT

Funding support from Australia Research Council through a Discovery project and Deakin University under its Central Research Grant scheme is acknowledged.

REFERENCES

[1] X. Deng, L. Mammen, H. J. Butt, D. Vollmer, *Science* 2011, *335*, 67.
[2] H. Wang, Y. Xue, J. Ding, L. Feng, X. Wang, T. Lin, *Angewandte Chemie International Edition* 2011, *50*, 11433.
[3] A. R. Parker, C. R. Lawrence, *Nature* 2001, *414*, 33.
[4] Y. Zheng, H. Bai, Z. Huang, X. Tian, F. Q. Nie, Y. Zhao, J. Zhai, L. Jiang, *Nature* 2010, *463*, 640.
[5] H. Wang, J. Ding, L. Dai, X. Wang, T. Lin, *Journal of Materials Chemistry* 2010, *20*, 7938.

Instrumented Manikin Evaluation System for Optimizing Protective Clothing Performance

Guowen Song[1,2], Mei Zhang[2], Yehu Lu[3], and Chunyan Wu[2]
[1]Department of Human Ecology, University of Alberta, Canada
[2]Department of Fashion Design and Engineering, Jilin University, China
[3]Fashion Institute, Donghua University, China
gwsongsgs@gmail.com

INTRODUCTION

The application of full scale manikin system to evaluate both clothing flammability and the effectiveness of thermal protective performance started in the late 1960's by the military. Later, the flash fire manikin evaluation system was fully developed by several groups [1-4]. The system is aimed at improving the textile materials used, the design of the garments and garment systems. Several systems [3-4] have been built and relevant standards have been developed. Standard test methods include ASTM F1930 (2000) and ISO 13506 (2008). The manikin system includes three key components: simulated flash fire, manikin body, and system control. In fire simulations, an instrumented manikin dressed in a thermal protective garment is exposed to an average incident heat flux of approximately 84kW/m^2, usually between 3 to 10 seconds, intended to mimic a real-life flash fire. Most manikins have a minimum of 100 sensors evenly distributed over the body that respond to heat in a way similar to that of human skin. Upon exposure to flames and radiation from gas burners, the sensors measure the surface temperature and heat flux, from which computer software converts the data into corresponding skin temperature changes. The degree of burn damage, expressed numerically and graphically as a body burn percentage; the time it takes to reach these burns; and the total energy absorbed by each sensor are then calculated. Results indicate how well a garment resists the transfer of energy to the skin. The development of the full scale instrumented manikin evaluation system is a significant step toward the clothing performance evaluation and provides predictions of the final performance of the system in an actual field exposure. With the system, a numerical model was developed [2] and an in-depth understanding of heat and mass transfer among simulated fire, clothing and human skin can be obtained.

PREDICTED PERFORMANCE FOR SINGLE LAYER COVERALL

Two types of coverall made of single layer Kevlar/PBI (153g/m^2) and Nomex®IIIA (203g/m^2) were tested using flash fire manikin system under exposure of three and four seconds. The overall predicted results are listed in Table 1 for both 3 second and 4 second exposure. These results suggest that the for single layer clothing a range of 20 - 50% total burns were predicted under three and four seconds exposure, and most burn areas occurred at locations with small air gap sizes, such as shoulders and chest area. The study demonstrated the fabric thermally induced shrinkage during 4 second exposure tremendously reduced the predicted clothing protective performance. Based on a numerical model [2], the average temperature predicted from the front and back of the fabric in 4 second exposure shows a difference about 300°C and the temperature distribution in the clothing fabric is not linear because of the fabric transient thermal conductivity and volumetric heat capacity, as well as the in-depth radiation. About 250°C temperature drop in the air gap is also demonstrated in these two exposures.

Table 1. Predicted Burn Injury for selected coveralls

	Kevlar®/PBI (SD*)		Nomex®IIIA (SD*)	
	3 sec	4 sec	3 sec	4 sec
2nd %	17.7 (2.0)	50.8 (2.2)	24.0(1.9)	48.4(3.6)
3rd %	6.6 (0)	7.9 (0.5)	6.6 (0)	13.1(2.5)
Total	24.3	58.8	30.6	61.5

*represents standard deviation

FEMALE MANIKIN AND PREDICTIONS

Most full scale studies have only been conducted on male manikins. As well, most standard test methods, such as ASTM F1930, specify the use of a male manikin. Because body geometry affects garment fit and size, therefore garments that have sometimes been burned on male manikins in flammability and performance tests may result in garment burning behavior and predicted injury unlike that on a female form. As well, because the proportion, size, and local body geometry define the thickness and distribution of air spaces beneath garments, differences in body shapes could result in differences in burn predictions.

Several female manikins have been developed by several groups [3, 4]. In 2006, a female instrumented manikin was constructed based on an existing male manikin system. This size 6 manikin is slimmer than the average woman. Other than the size and shape, other aspects of the manikin are the same as the male one. The 110 sensors, uniformly distributed over the surface of the manikin, are cylinders (1.9 cm diameter x 3.2 cm height) made from Colorceran (skin stimulant sensor). The heat flux at the surface of the manikin and its variation with location and time are determined by a computer-controlled data acquisition system.

Clothing designed for women and men were compared using the female manikin system. Data on air gaps between a female-form manikin and a garment were used to investigate the effect of garment style and fit on thermal performance. Three-dimensional scanning was used to measure the size and distribution of air gaps, and simulated flash fire testing was used to determine predicted burn injury and energy absorbed by the mannequin. Findings demonstrated that garment style and fit influenced protection (Table 2), as the improper fit of the women's style compared to the men's made areas of the female mannequin more susceptible to burns than others. Air gap size had a positive correlation with time to burn injury and a negative correlation with energy absorbed.

Table 2. Burn injury predicted by female manikin

	2nd degree burn	3rd degree burn	Total burn
Women's	8.2 (0.8)	4.0 (0)	12.2
Men's	7.3 (0.6)	4.0 (0)	11.3

The greatest differences in style between the women's and men's garments were in the mid-back region. Despite the larger air gap in the women's style, greater thermal protection was not provided. Convection may have initiated within this space, negating any added benefit of the larger air gap. Excess fabric above the waistband in the back of the women's style caused flames to accumulate beneath, causing burns in the seat region. The extra material also created an uneven garment surface and fabric folds, resulting in charring and subsequent breaking open of the garment in these areas. Burns occurred in the lower back when wearing the men's style, which is likely to be due to the absence of the multi-layered waistband in this area.

HOT LIQUID SPRAY MANIKIN

Hot liquid hazards existing in work environments present a common risk in workplace safety in numerous industries. A newly developed instrumented manikin system was used to assess the protective performance provided by protective clothing against hot liquid splash. The major components for this system are the same as above mentioned manikin system. Four groups of cylinder spray jets that are automatically controlled replaced the fire simulation system and spray hot liquid to manikin. The skin burn injury and its distribution caused by the hot liquid can be predicted and the performance of clothing system and its design features (fabric properties and garment size) can be investigated. Several garments with different properties were selected and tested using the hot liquid spray manikin system. As illustrated in Table 3, the second degree burn ranged from 0 to 50% and total absorbed energy for the G4 with no predicted burn is 0.5 cal/cm^2. Given the fabric properties, this is mainly associated with minimal mass transfer. Figure 1 shows an example of burn injury prediction of G1, as this permeable fabric, the mass transfer contributed huge amount of energy to skin.

Table 3. Burn injury and absorbed energy of tested garments

Garment code	2nd degree burn (%)	3rd degree burn (%)	Total absorbed energy (cal/cm^2)
Nude	77.3	0.53	4.6
G1	48.1	8.17	4.1
G2	8.9	0	1.3
G3	16.8	0	2.2
G4	0	0	0.5

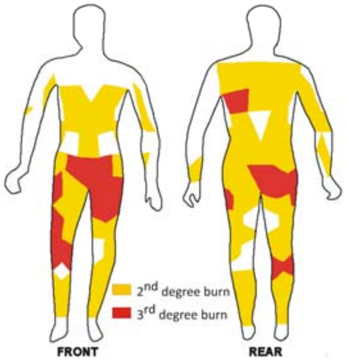

Figure 1. Predicted burn injury distribution

Minimizing mass transfer is recognized as the critical factor for protection from hot water. The thickness of fabric and design features showed effects on the performance of impermeable and semipermeable clothing. The effect of fabric weight on heat transfer through protective clothing system seems to be minimal. Maintaining a proper air gap between the garment and human body was a critical factor in improving thermal performance. Burn injury mainly occurred at the areas of compression upon water spray, heavy water flow and small air gap. Reflective tape could provide extra protection. These findings could be helpful to provide a technical basis to fabric engineering and garment design.

REFERENCES

1. Crown, E. M., Ackerman, M. Y., Dale, J. D., & Tan, Y. (1998). Design and Evaluation of Thermal Protective Flightsuits: Part II: Instrumented Mannequin Evaluation. Clothing and Textile Research Journal, 16(2), 79-87.
2. Song, G., Barker, R., Hamouda, H., Kuznetsov, A., Chitrphiromsri, P., and Grimes, R. (2004). Modeling the thermal protective performance of heat resistant garments in flash fire exposures. Textile Res. J., Vol. 74 (12), 1033-1040.
3. Norton, M. J. T., Kadolph, S. J., Johnson, R. F., & Jordan, K. A. (1985). Design, construction, and use of Minnesota Woman, a thermally instrumented mannequin. Textile Research Journal, 55(1), 5-12.
4. Eaton, P., & Healey, M. (2006). The development of a 'female' form manikin as part of a test facility to assess the fire protection afforded by personal protective equipment (Research Report 475). Colgate, Norwich: Health and Safety Executive.

Functional Fabric Design for Improvement of Garment Ventilation

Chao Sun[1], Joe Sau-chuen Au[1], Jintu Fan[1, 2], Rong Zheng[3]
[1]Institute of Textiles and Clothing, The Hong Kong Polytechnic University, Hung Hom, Kowloon, Hong Kong
[2]Department of Fiber Science & Apparel Design, College of Human Ecology, Cornell University, Ithaca, NY,USA
[3]Aimer Human Engineering Research Centre, Beijing Institute of Fashion Technology, Beijing, China
Contact: Prof. JT Fan, jf456@cornell.edu; Speaker: 10902992r@connect.polyu.hk

INTRODUCTION

Thermal comfort is an important factor in sportswear design. Many works have been conducted to improve thermal performance and moisture permeability of garments by employing a variety of approaches [1-3]. However, the fabric tends to stick to human skin during sweating, which creates “clingy” discomfort and hinders the convection around the body.

The "bumpy" surface on fabrics arising from functional fibers has been designed to increase airflow across the skin and reduce cling [4]. However the surface is only raised a small amount by yarn factor, which is not strong enough to make the air access freely and to reduce the heat accumulation. Ho and Fan [5] developed a ventilation garment with open mesh and numbers of spacers. The spacers are arch-shaped and 0.5 – 2.5cm in height, making a big distance from the body of a wearer to improve the ventilation. However, the spacer is too big and heavy to do exercises. Hence, the method of prop up the garment away from the body with ventilation openings should be further investigated to keep comfort.

In this study, knitted fabrics with spacers and ventilation panels were developed simultaneously and the properties were examined.

APPROACH

Materials

Four kinds of fabric with same yarn but different structures were knitted by circular knitting machine. Fabric A is a control fabric without spacers and openings, fabric B has openings but no spacers, fabric C has spacers but no openings while fabric D with both spacers and openings. Jersey was selected for comparison. The appearance of fabrics on face and back sides are shown in Figure 1. The dimension of all fabrics was 20cm*20cm and they were conditioned according to ASTM D1776.

Experiments

The air permeability of the four fabrics was examined by a KES-F8-AP-1 air permeability tester. The result of air permeability expressed as air resistance (R) was recorded in terms of kpa s/m in which a larger value of R indicated poorer air permeability. The experiment was repeated for five times and the average data was recorded.

The Kawabata Evaluation System Fabric (KES-F) was used for measuring the necessary information for wearability and design specification of the developed fabrics, including tensile, shearing, bending, compression and surface properties. The tensile properties were the tensile energy (WT), tensile resilience (RT), and extensibility (EMT). The bending properties were the bending rigidity (B). The shear stiffness (G) reflects the ability of the fabric to resist a shear stress, i.e. the rigidity to shear. The surface properties of the samples were evaluated using the coefficient of friction (MIU), which reflects the fabric smoothness, roughness, crispness and geometrical roughness (SMD). The compression properties were evaluated the fabric thickness at 0.5(T_o) and 50($T_{m)}$) gf/cm^2 pressure.

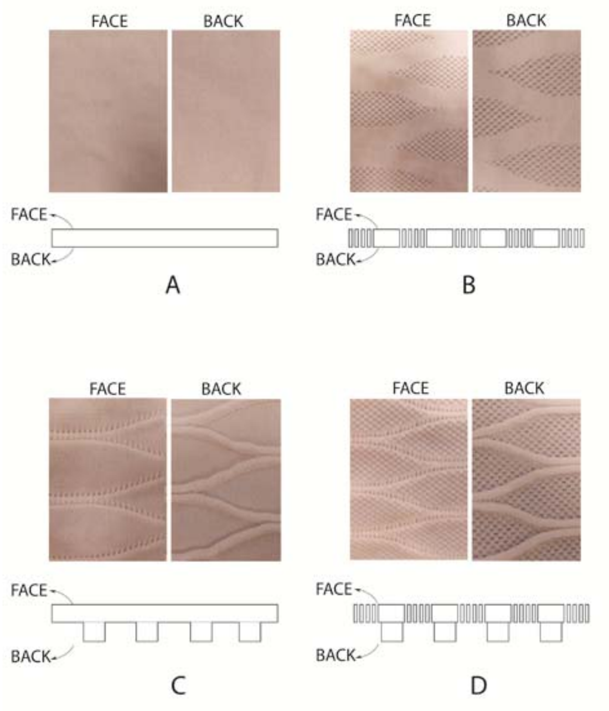

Figure 1 Appearance of fabric A, B, C and D

RESULTS AND DISCUSSION

The air permeability of the four kinds of fabric is shown in Figure 2. As a control fabric, fabric A shows a small R value of 0.184 kPa s/m. But the value of fabric D is only 25% of fabric A. Compared to fabric A; the addition of spacer structure on fabric C slightly increased ventilation. The air resistance of fabric D is about half of fabric B. It means that the fabric with both openings and spacer structure increased the air permeability significantly. The weight of the four fabrics is summarized in Table I. Compared to fabric A, the weight of fabric D increased by 15.32%, but the air resistance reduced by 75.54%.

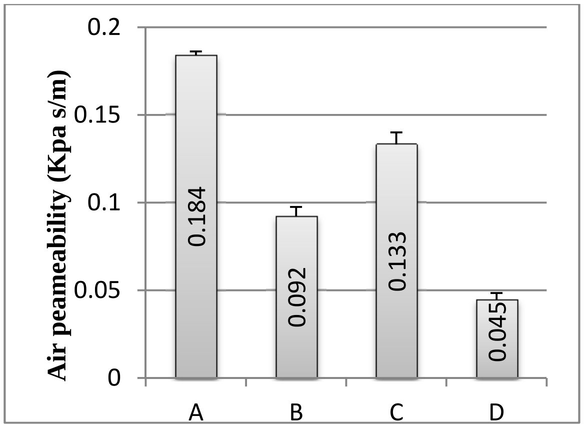

Figure 2 Air permeability of four fabrics

The compression property of the fabrics is shown in Table I. It can be found that the thickness of fabric C and D is similar, which is approximately two times higher than that of fabric A and B at T_m and T_o, which means that the developed knitted structure can prop up a big space between the garment and human body.

The coefficient of friction (MIU) of the fabrics is summarized in Table I. The value of MIU increased after the addition of spacer structure, which indicates that the fabric surface became less smooth.

The tensile property of the four fabrics was measured by the KES-F system and is shown in Table I. The fabric D shows a higher tensile strength (WT) but a lower recover ability (RT) than fabric A. But the extensibility (EMT) of fabric B is better than fabric A. It means that fabric D needs a lower tensile stress in the same extended length.

The shear rigidity (G) reflects the ability of fabric to resist shear stress as well as the subjective handle of fabrics. The G value of fabric D is slightly lower than the other three fabrics and it indicates that the handle of fabric D is relatively soft.

The bending rigidity (B) reflects the flexibility of fabrics. The increase in the value of B for fabric C and D demonstrates that the spacer structure decreased the flexibility of the fabrics and it also influences the fabric's drapability and wearability. But the result is still acceptable in sportswear design [6].

As discussed before, compared to jersey, knitted fabrics with opening and spacer structure show a much higher air permeability without losing the characteristic of being light, soft and elastic. The spacer structure makes the fabric surface slightly rough, but it also reduces the contact area and contributes to the improvement of clingy discomfort during sweating.

CONCLUSIONS

The opening knitting structure demonstrates a lower air resistance; while the spacer knitted structure contributes to the improvement of ventilation. The fabric with both spacer and opening knitted structures shows higher air permeability without losing the superiority in weight, softness and elasticity. The developed fabric can be applied to develop new active sportswear, casual wear, work clothes with better thermal comfort.

REFERENCES

[1] Duenser, E. (2003) Circular knits of modal /elastane and lyocell /elastane. Lenzinger Berichte, 82, pp.76-78.
[2] Elena, O., Ana, M. R. and André, C. (2011) The influence of knitted fabrics' structure on the thermal and moisture management properties. Journal of Engineered Fibers and Fabrics, 6(4), pp.10-22.
[3] Chen, Q. (2011) Development of plant structured knitted fabrics. Ph.D. Thesis, The Hong Kong Polytechnic University.
[4] HC International Inc. (2006) The jersey fabric of world Cup：Sphere React Dry, Available at: <http://info.textile.hc360.com/2006/06/08220146012.shtml>. Accessed on 04/06/ 2012.
[5] Ho, C.P. and Fan, J.T., inventors; The Hong Kong Polytechnic University. Ventilated Garment. US 2011/0239350 A1.
[6]Postle, R. and Gibson, V.L. (1978) An Analysis of the Bending and Shear Properties of Woven, Double-Knitted, and Warp-Knitted Outerwear Fabrics. Textile Research Journal, 48(1), pp. 114-27.

Table I Tensile, shearing, bending, surface, compression properties measured using the KES-F system

KES-F properties		Fabric A	Fabric B	Fabric C	Fabric D
Tensile	WT (gf.cm/cm^2)	8.52	10.52	7.83	9.42
	RT (%)	58.6	56.45	57.86	55.53
	EMT (%)	48.23	59.12	45.2	53.83
Shearing	G (gf/cm.deg)	0.33	0.29	0.31	0.27
Bending	B (gf.cm^2/cm)	0.0057	0.006	0.023	0.027
Surface	MIU	0.29	0.31	0.37	0.37
Compression	T_o (mm)	0.81	0.93	2.04	2.07
	T_m (mm)	0.63	0.64	1.26	1.21
Weight	g/m^2	117.5	100.5	154.75	135.5

Biomechanically Compliant Polymeric Structures for Cardiovascular Implant Applications

Charanpreet Singh[1], Yosry Morsi[2], Xungai Wang[1]
[1]Institute for Frontier Materials, Deakin University, Australia
[2]Faculty of Engineering & Industrial Sciences, Swinburne University of Technology, Australia
xwang@deakin.edu.au; csingh@deakin.edu.au

KEYWORDS
Cardiovascular disease, Stent-graft, Compliance

INTRODUCTION

Increased incidences of abdominal aortic aneurysms and extensive efforts to achieve their successful repair have led to many experimental investigations in developing advanced stent-graft (SG) designs. However, SG related complications are still a major reason for poor long-term outcomes of the treatment viz. endoleaks, migration and eventual aneurysm rupture [1]. The primary factor behind the implant failure is the sophisticated biomechanical nature of human cardiovascular system, which presents technical challenges in designing an ideal blood vessel substitute [2]. Cardiovascular system relies on the elastic buffering properties of proximal large vessels (aorta) for efficiently pumping the blood to the peripheral extremities of vascular network [3]. However, commercially used SGs are stiff metallic structures (stainless steel or nitinol) covered with an inelastic graft (woven Dacron® or ePTFE) and unable to exhibit optimum distensibility property. A stiff SG acts as a highly non-compliant segment within the vascular network which alters local hemodynamics of the implant site and triggers pathophysiological events leading to hypertension, coronary artery disease, and left ventricle hypertrophy [4]. Apparently, the biomechanical property criterion of natural blood vessels appears too stringent for the conventional metallic structures to satisfy. Therefore, the transformation of SG research into novel polymeric design concepts is imminent.

APPROACH

The design approach adopted in current work involves the use of multi-component knitting technique to achieve optimum balance between structural flexibility and robustness of SG structures by replacing metallic stents with polymeric (polyester) filaments. The polymeric SG structures are designed in a composite tubular fashion with intermittent compliant components (elastic fibre knit) in series with relatively stiff components (monofilament knit).

RESULTS AND DISCUSSION

The experimental analysis involved biomechanical characterisation (compliance, viscoelasticity, and flexibility) of polymeric SGs in comparison with a commercial metallic SG (Zenith Flex®, Cook Medical Inc.) in physiological pressure range (120/80 mmHg) using an *in-vitro* vascular model. The polymeric SGs displayed significantly better distensibility property than metallic SGs. The volumetric compliance, C_v was improved by four fold relative to metallic structures (Fig. 1).

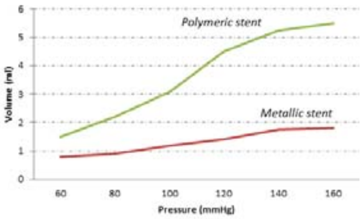

Figure 1: Pressure-volume curves showing distensibility of SGs

Also, the stiffness parameters (E_p, β) of polymeric SGs were comparable with human aortic vessels while metallic structures exhibited their inherent stiffened response to intraluminal hoop stresses (Table I).

Sample	Stiffness parameter	
	E_p (N/cm^2)	β
Polymeric SG	20.5	15.6
Zenith Flex®	53.3	40.5
Human aorta [5]	10 - 20	8 - 12

Table I: Stiffness property of SGs in comparison to human aortic vessel parameters

In relation to aortic SGs, viscoelasticity is an important property for improving systolic wave energy storage and its release in diastolic cycle. Stress relaxation experiments (30% strain, 20 mins) were conducted to compare viscoelastic component in SGs. The relaxation curves exhibited relaxation strength of 13.8 % for knitted structures owing to delayed response of elastic knitted loop sections (Fig. 2). On the contrary, metallic SGs displayed relatively lower relaxation potential (9.1 %) where inelastic woven Dacron graft did not allow for accommodation of induced stresses within the structure itself. In long-term implantation, poor viscoelastic behaviour leads to rupture of graft segments under constant stress.

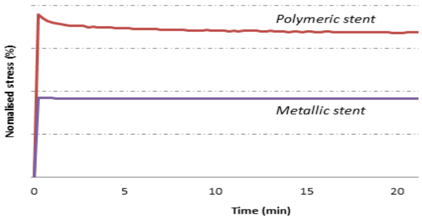

Figure 2: Normalised stress relaxation curves of polymeric and metallic SGs

The longitudinal and bending flexibility of a SG device is important in assessing migration tendency under pulsatile conditions. A longitudinally rigid graft undergoes kinking at tortuous aortic curvatures and is prone to terminal end migration at fixation sites. Zenith Flex® SG exhibited very low axial elongation (10 %) while the tension force increased to 28 N. On the contrary, knitted SG was observed to be highly flexible under axial elongation and compression forces at similar strains (Table II).

Stent-graft	Flexibility behaviour			
	Axial force (N)	Axial comp. ratio	Bending moment (Nmm)	Kinking curvature (angle ^{o})
Zenith Flex®	28	0.94	48	55^{0}
Polymeric	0.72	0.86	8	180^{0}

Table II: Flexibility behaviour of SG structures

The compression ratio was defined as ratio of maximum compressed length (reached just before kinking or buckling) to normal stent length (10 cm). Bending behaviour was evaluated by calculating bending moment required to bend a 10 cm length of stent and subjective measurement of kinking angle. Bending resistance improved remarkably in sectional design of polymeric stent owing to absence of local compressive stresses on the inner curvature (Fig. 3). Kinking curvature for metallic stents was relatively lower with higher bending moments (55^{o}, 48 Nmm) than polymeric stents (180^{o}, 8 Nmm).

Figure 3: Bending behaviour comparison of stent-grafts. (a) Polymeric and (b) Zenith Flex® stent-graft subjected to 180^{o} bending

CONCLUSION

The study confirms that use of polymeric fibre based structures can remarkably improve biomechanical property of SG devices. The fundamental sectional design concept provided multi-dimensional distensibility feature to the SG while maintaining optimum structural toughness. Thus, the proposed polymeric knitted design may provide a robust structure for achieving optimum performance with an implant post aneurysm treatment.

FUTURE WORK

Apart from static biomechanical behaviour, SGs need to comply with long-term fatigue endurance and minimum degree of physical property deterioration. Therefore, we plan to further test the dynamic behaviour of SGs under long-term (3-5 months *in-vitro*) pulsatile conditions and evaluate hemodynamic variations induced by the new implant in vascular model and any potential deviation from ideal behaviour.

REFERENCES

1. Arko Iii, F.R., et al. Current Status of Endovascular Aneurysm Repair: 20 Years of Learning. *Seminars in Vascular Surgery*, 2012. 25(3): p. 131-135.
2. Moore Jr, J.E. Biomechanical issues in endovascular device design. *Journal of Endovascular Therapy: An Official Journal of the International Society of Endovascular Specialists*, 2009. 16 Suppl 1: p. I1-11.
3. Belz, G.G. Elastic properties and Windkessel function of the human aorta. *Cardiovascular Drugs and Therapy*, 1995. 9(1): p. 73-83.
4. Weber, T., et al. Arterial Stiffness, Wave Reflections, and the Risk of Coronary Artery Disease. *Circulation*, 2004. 109(2): p. 184-189.
5. Lanne, T., et al. Diameter and compliance in the male human abdominal aorta: Influence of age and aortic aneurysm. *European Journal of Vascular Surgery*, 1992. 6(2): p. 178-184.

Thermal Insulation Properties of Silkworm Cocoons

Jin Zhang[1], Rangam Rajkhowa[1], Jingliang Li[1], Xiangyang Liu[2], Xungai Wang[1,3]

[1]Australian Future Fibres Research and Innovation Centre, Institute for Frontier Materials, Deakin University, VIC 3217, Australia; [2]Biophysics and Micro/Nanostructures Lab, Department of Physics, Faculty of Science, National University of Singapore, 117542, Singapore; [3]School of Textile Science and Engineering, Wuhan Textile University, Wuhan 430073, People's Republic of China
xwamg@deakin.edu.au

INTRODUCTION

The silkworm cocoon is a multilayer composite material formed by continuous twin silk filaments bonded by silk gum. The process of silk spinning and cocoon building has evolved over thousands of years through natural selection. As a fine product of these fully developed processes, silkworm cocoon provides strong protection against both natural predators, environmental and physical adversaries, including extreme environmental temperature, during the immobile phase of life cycle when the silkworm enters diapause and metamorphosis.

Understanding the relations between structure, property and function of this important biological material will provide a conceptual platform to design and develop novel bio-inspired textiles for thermal regulation applications. In this study, we examined the thermal properties of four silkworm cocoon types: the mulberry (from domestic *Bombyx mori*, *B. mori*), eri (from domestic *Samia Cynthia, S. cynthia*) and tasar (from wild *Antheraea pernyi*, *A. pernyi* and *Antheraea mylitta, A. mylitta*) silkworm cocoons.

KEYWORDS

Thermal function, Silk cocoon, Protection, Biological composite.

APPROACH

Temperature was measured both inside and outside of the cocoons (3~5 mm close to the outer surface) using two needle-type temperature probes (ICT SFM) (Figure 1). Four thermal conditions (I~IV) were tested. For condition I, a gradual rise of temperature was introduced by placing the cocoons into an oven (Binder) with isothermal temperature setting (at 37 ºC, 45 ºC and 50 ºC, respectively); for condition II, a sudden drop of temperature was introduced by transferring the warmed cocoons that have reached temperature equilibrium from the oven to air.

The other two thermal conditions were applied by heating a tube furnace (Lindberg/BlueM) with two different ramp rates (2 ºC/min for thermal condition III and 4 ºC/min for thermal condition IV) from ambient temperature to 50 ºC, respectively, while the cocoons were located inside. The thermal conductivity of four types of cocoon walls was obtained using TA Q200 DSC through the modulated DSC method.

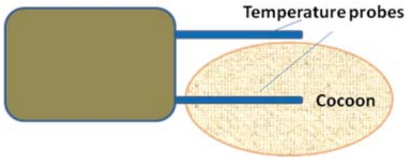

Figure 1. Temperature measurements of both inside and outside of cocoons.

RESULTS AND DISCUSSION

Silkworm cocoon has a non-woven structure with twin silk fibroin fibres coated with sericin. The cocoon outer surface (the outmost layer) and inner surface (the inner most layer) are remarkably different in terms of the silk fibre morphology, fibre width and the porous structure created by silk fibres. The fibre width is generally smaller for the cocoon inner surfaces than the outer surfaces. The nominal density is 711 kg/m^3 for the *A. pernyi* cocoon walls and 693 kg/m^3 for the *A. mylitta* cocoon walls, which are also much higher than the 377 kg/m^3 for the *B. mori* cocoon walls and 450 kg/m^3 for the *S. cynthia* cocoon walls [1].

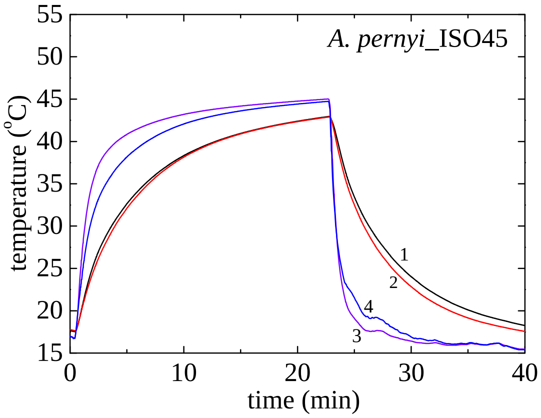

Figure 2. Temperature profiles of locations both inside and outside of the *A. pernyi* cocoon. 1, 2-inside; 3,4-outside.

Figure 2 shows the temperature profiles of the *A. pernyi* cocoon when it was moved into an isothermal oven from atmosphere and then moved out from the oven. The temperature change inside the cocoon was slower than the outside when a sudden temperature change occurred in the environment, which indicates a certain degree of temperature buffer from the cocoon. The wild cocoons (*A. pernyi* and *A. mylitta*) exhibited stronger thermal damping than the domestic ones (*B. mori* and *S. cynthia*).

For example, the temperature lag of the *A. mylitta* cocoon was 400 % higher than the *B. mori* cocoon for the case when cocoons were heated in the oven with an isothermal setting of 45 ºC. The inside temperature of the *A. pernyi* and *A. mylitta* cocoons reached 10 ºC and 12 ºC lower than the outside during heating, and 15 ºC and 17 ºC higher than the outside during cooling, respectively. It also took a considerably longer time for the wild cocoons to reach an equilibrium temperature than the domestic cocoons. For example, after 23 mins, the temperature inside of the *A. pernyi* cocoon remained 2 ºC lower than the outside in a 45 ºC oven, in contrast to the equal temperature between inside and outside of the *B. mori* cocoon after 14 mins' heating.

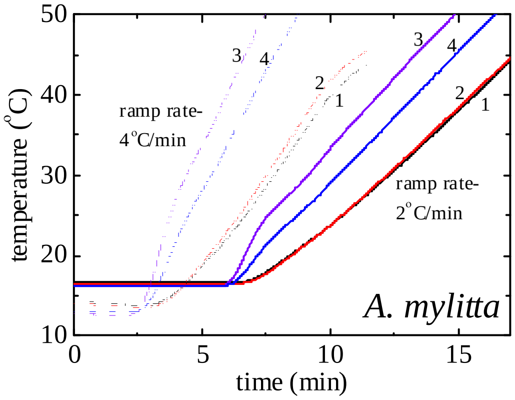

Figure 3. Temperature profiles for locations both inside and outside of the *A. mylitta* cocoon under heating ramp rates of 2°C/min and 4°C/min. 1, 2-inside; 3, 4-outside.

The non-steady state thermal conditions were tested by applying two different heating rates, i.e. 2 ºC/min and 4 ºC/min. At the furnace heating rate of 2 ºC/min, the ramp rate difference was 0.22 ºC/min, 0.22 ºC/min, 0.78 ºC/min and 0.99 ºC/min for the *B. mori*, *S. cynthia*, *A. pernyi* and *A. mylitta* cocoons, respectively. A remarkable case was that the *A. mylitta* cocoon demonstrated the highest thermal damping. While the outside temperature of cocoon increased at a ramp rate of 6.8 ºC/min, the temperature of its inner space merely increased at a ramp rate of 4.0 ºC/min, which was 40 % slower than the temperature change of the outside environment. At the slower furnace heating rate (2 °C/min), the *A. pernyi* and *A. mylitta* cocoons exhibited relatively greater thermal buffer capacity over the domestic cocoons. However, at the faster furnace heating rate (4 °C/min), the advantage was only maintained by the *A. mylitta* cocoon, which has the largest volume of inner space (27 cm^3).

Silkworm cocoon walls contribute to the thermal insulation of cocoons. To further understand the thermal properties of cocoon walls, temperature modulated differential scanning calorimetry (DSC) was used to measure the thermal conductivity. The thermal resistance, thermal diffusivity and thermal absorptivity were also indirectly calculated from the conductivity values.

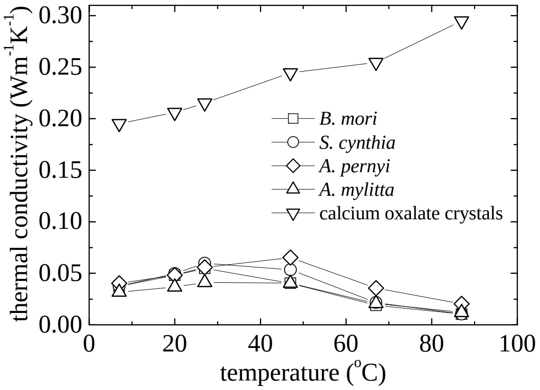

Figure 4. Thermal conductivity of silkworm cocoon walls.

As shown in Figure 4, the thermal conductivity values of cocoon walls are within the range from 0.0106 Wm^{-1}K^{-1} to 0.0653 Wm^{-1}K^{-1}. On the outer surfaces of wild cocoons, there exist many cubic crystals, which were verified to be calcium oxalate crystals [2] . A calcium oxalate crystal pellet (prepared from purchased calcium oxalate powder from Aldrich) was also measured and its thermal conductivity is higher than 0.2 Wm^{-1}K^{-1}, which can be as high as 27 times of that of the cocoon walls.

The *A. pernyi* and *A. mylitta* cocoon walls had much lower thermal diffusivity than the *B. mori* and *S. cynthia* cocoon walls before the temperature increased to 47 ºC, mainly due to the higher density of their cocoon walls. This partially contributes to the lower temperature changing rate and the longer equilibrium time experienced by the wild cocoons.

CONCLUSION

Under both steady and non-steady state thermal conditions, the inner temperature of silkworm cocoons showed significant thermal damping characteristics against sudden changes in outside temperature. However, the wild cocoons exhibited a higher level of thermal buffer than the domestic ones.

REFERENCES

1. J. Zhang, J. Kaur, R. Rajkhowa, J.L. Li, X.Y. Liu, X.G. Wang. Mechanical properties and structure of silkworm cocoons: A comparative study of Bombyx mori, Antheraea assamensis, Antheraea pernyi and Antheraea mylitta silkworm cocoons. *Mater Sci Eng C*, 2013, http://dx.doi.org/10.1016/j.msec. 2013.03.051.

2. J. Zhang, R. Rajkhowa, J.L. Li, X.Y. Liu, X.G. Wang. Silkworm cocoon as natural material and structure for thermal insulation. *Mater Des*, 2013: 49, pp. 842-9.

The Mechanism of Needle Penetration Through a Woven Aramid Fabric

Christopher J. Hurren, Qing Li, Alessandra Sutti, and Xungai Wang
Australian Future Fibres Research & Innovation Centre, Institute for Frontier Materials, Deakin University, Geelong, Australia
christopher.hurren@deakin.edu.au

ABSTRACT

Fabrics that resist needle penetration are important for the manufacture of protective gloves and clothing. Understanding the mechanism of needle penetration through a fibrous structure enables optimisation of protective fabric design. This work investigated the process of low speed penetration of a needle through a woven aramid fabric. Motion image capture of the needle enabled needle position correlation with the needle penetration force profile. The needle penetration force curve had three characteristic peaks and more than 70% of the needle tip was already exposed at maximum penetration force.

INTRODUCTION

Puncture resistant fabrics are widely used to protect workers from needle stick injuries. Needle stick injuries can occur in a wide range of occupations, including the medical industry, law enforcement, corrections, gardeners, cleaners and maintenance[1].

The standard method for determining puncture resistance to a hypodermic needle is ASTM F2878-10 [2]. Although several studies have looked at the hypodermic puncture mechanism in elastomer materials [3, 4], the puncture mechanism of woven aramid fabrics has not been investigated.

The current test method identifies penetration via electrical responses [5], however optical methods, which provide further insight into the penetration process, have not been investigated. This work will investigate the mechanism of puncture and the point of needle penetration with respect to penetration force for a woven aramid fabric using motion video capture.

EXPERIMENTAL

The woven fabric used in these experiments was obtained from a Turtleskin Insider glove (Warwick Mills, USA) and was a plain weave fabric (240end/10cm warp, 480ends/10cm weft).

The needles were a 21 guage (0.80 mm) needle (Terumo Corporation, USA) with a triple lancet design. Five of the needles had their cutting edge rounded from their lancet using a WS Flex 18C P1200 grit paper (Hermes Abrasives, Australia). Both sharp and blunt needle types were tested five times.

Fabrics samples (15 mm x 30 mm) were clamped on either side 20 mm apart under tension using a specially designed rig shown in figure 1. The tension force was 2.3 N applied by a spring between the two mounting blocks. The needle penetration force was measured at 10 mm/min using a 100 N load cell with a 5967 Materials Testing System (Instron Corporation, USA).

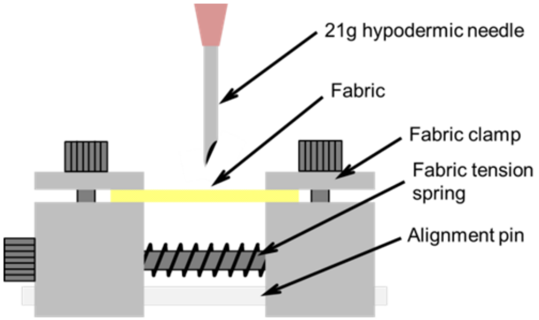

Figure 1 Diagram of needle penetration rig.

Motion image capture was undertaken using a QC3247 USB camera (Digitech Industries, Hong Kong). Images were removed from the captured video using Windows Live™ Movie Maker (Microsoft Corporation, USA)

RESULTS AND DISCUSSION

The applied needle force versus needle displacement measured for each of the needle types tested was plotted (Figure 2). Three distinct force peaks were observed during fabric penetration by a needle. Each peak represents a significant point in the needle penetration sequence as exemplified in Figures 3 and 4, which show the key penetration points. Peak 1 coincided with the needle tip penetration, exposing the tip to the underside of the fabric. Peak 2 coincided with the end of the cutting induced by the needle lancet. Peak 3 could appear as a single peak or a double peak. The single peak represented ejection of the bevel heal from the cut hole. The double peak represented the ejection of the fabric flap from the needle heal liquid tube followed by the ejection of the bevel heal from the cutting hole.

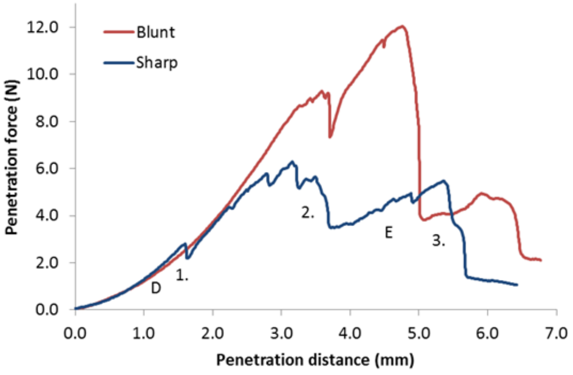

Figure 2 Applied needle force with respect to penetration distance.

The force measured in peak 1 results from the contribution of extension and bending of the fibres during the initial displacement of the fabric (D). Once the needle tip has penetrated the fabric, the remaining force resisting the needle is believed to be from the energy required to move away and cut the fibres to allow a path for the needle to penetrate. There may also be a contribution from the displacement of fibres within the fabric, resulting from the increase in effective size of the needle section as this progresses through the fabric. The peak arising from the end of the lancet entering the top layer of the fabric occurred due to the sudden shape change in the needle from lancet grinding to needle bevel caused by the lancet grinding process. Force/displacement curve comparison for the blunt and the sharp needles revealed the lower load in the lancet cutting stage for the sharp needle, suggesting that the presence of a cutting-efficient edge reduced the force required for the needle to pass through the fabric, substantiating the hypothesis of a fibre-cutting mechanism during needle penetration. The lower cutting efficiency of the blunt needle resulted in a higher force required for penetration through the same fabric.

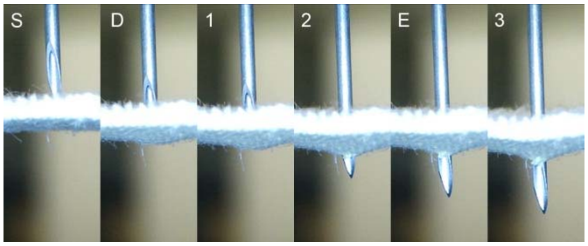

Figure 3 Sharp needle cutting sequence.

Peak 3 was due to the displacement force required to open the penetration hole to allow for the bevel to pass. Once the bevel heal had passed, the surface resistance of the fibres contacting the shank surface still imparted some resistance on it.

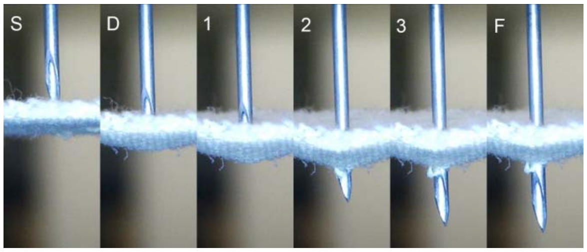

Figure 4 Blunt needle penetration sequence.

For both the sharp and blunt needle tests conducted, needle tip penetration had occurred at under 4 N of force (figures 3 and 4, image 1). By the time of maximum force of penetration at least 70% of the needle bevel was already protruding through the fabric (Figures 3 and 4, image 3). This was similar to that observed by Gauvin *et al* [5] however the penetration distances at the slower test speeds measured visually in this work were higher than those measured electrically by Gauvin *et al*.

CONCLUSION

The penetration of a sharp hypodermic needle through a tightly woven textile fabric normally produces three force peaks associated with tip, lancet top and bevel heal penetration of the fabric. The maximum force of penetration is reached with at least 70% of needle bevel already protruding through the fabric. Test methods should consider exit of the needle tip as an end point for testing, rather than the maximum force recorded during fabric penetration.

REFERENCES

1. O'Leary, F.M. and T.C. Green, *Community Acquired Needlestick Injuries in Non-health Care Workers Presenting to an Urban Emergency Department.* Emergency Medicine, 2003. 15(5-6): p. 434-440.
2. ASTM International, *ASTM F2878-10 Standard test method for protective clothing material resistance to hypodermic needle puncture.* 2010: West Conshohocken, PA.
3. Nguyen, C.T. and T. Vu-Khanh, *Mechanics and mechanisms of puncture by medical needles.* Procedia Engineering, 2009. 1(1): p. 139-142.
4. Dolez, P., T. Vu-Khanh, C.T. Nguyen, G. Guero, C. Gauvin, and J. Lara, *Influence of medical needle characteristics on the resistance to puncture of protective glove material.* Journal of ASTM International, 2008. 5(1).
5. Gauvin, C., O. Darveau, C. Robin, and J. Lara, *Analysis of test paramteres and criteria for charcaterizing and comparing puncture resistance of protective gloves to needles.* ASTM - Performance of Protective Clothing and Equipment: Emerging Issues and Technologies, 2012. STP1544: p. 1-14.

Vibration Isolation Properties of Weft-Knitted Spacer Fabrics

Fuxing Chen, Hong Hu, Lai Xu
Institute of Textiles and Clothing, The Hong Kong Polytechnic University, Hong Kong
tchuhong@polyu.edu.hk; fuxing.chen@connect.polyu.hk

OBJECTIVE

This study investigates how the knit pattern, material property and load weight affect the vibration isolation performance of weft-knitted spacer fabric as potential cushion material.

INTRODUCTION

Regular passive vibration isolation materials include rubber, springs, air isolators, resilient materials such as cushion pads and PU foams, and etc. [1] Their typical natural frequencies and isolation performance are limited by both material properties and applicable environments.

Weft-knitted spacer fabric could be potentially used to prevent chronic leg ulcers, buffer sports or occupational vibrations as knee braces, shoes materials, vehicle seats and anti-vibration gloves. As one benefit, spacer fabric provides excellent thermo-physiological wear comfort due to its regulating capacity in air, moisture and perspiration. Although Liu and Hu reported a study on the vibration isolation performance of warp-knitted spacer fabric [2], the same study on weft-knitted spacer fabric is still lacked. This paper presents a comparative study of the vibration transmissibility of different weft-knitted fabric samples under laboratory conditions. At the same time, the associated quasi-static transversal compression curves are used to locate the local compressive modulus of these samples and predict the resonant frequencies.

APPROACH

Weft-knitted spacer fabrics of different knit patterns and materials were knitted on a computerized flat knitting machine STOLL CMS822 of gauge 14. Face sheets are all knitted from the same elastic yarn formed with both nylon and spandex components. Three samples with different thickness were produced. The difference in S1 and S2 is on the knit pattern, i.e., the floating distance of loop pillar between two adjacent tucking stitches for spacer monofilaments (FIGURE 1); the difference in S2 and S3 is on the diameter of spacer monofilaments (TABLE I).

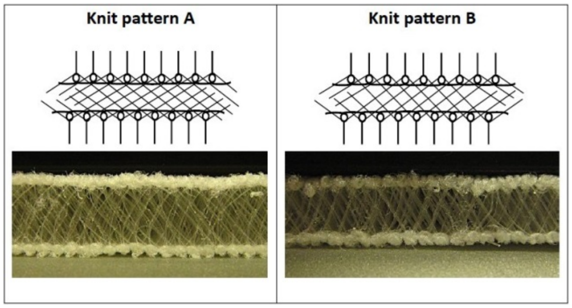

FIGURE 1. Two knit patterns obtained by controlling the distance of loop pillars between two adjacent tuck stitches for spacer monofilament.

TABLE I. Parameters of three weft-knitted spacer fabrics

Sample code	Knit pattern	PET monofilament diameter (mm)	Fabric thickness (mm)
S1	A	0.08	6.78
S2	B	0.08	5.56
S3	B	0.12	5.60

To measure the vibration transmissibility, weft-knitted spacer fabric was put on a shaker platform and compressed using a cylindrical steel mass with a 150mm areal diameter (FIGURE 2). Two options of load mass *m* (5.5kg and 15.5kg) were selected. An electromechanical shaker was used to supply vibration excitations of sinusoidal sweep signals from 1-200Hz to the shaker platform (FIGURE 3). Two accelerometers were rigidly mounted on the shaker platform and mass m to record the acceleration signals $\ddot{x}_1$ and $\ddot{x}_2$, respectively.

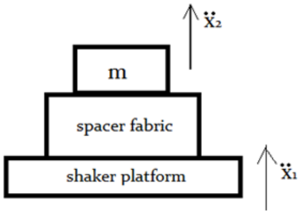

FIGURE 2. Setup for the measurement of vibration transmissibility of weft-knitted spacer fabric loaded with a mass *m*

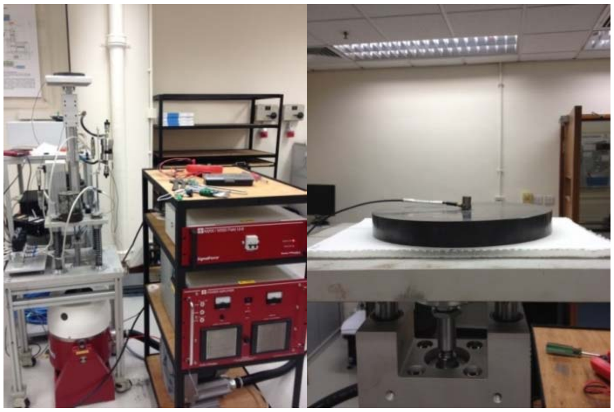

FIGURE 3. Vibration measurement system and sample placement.

RESULTS AND DISCUSSION

FIGURES 4-6 illustrates the influence of three variables, knit pattern, monofilament diameter and load mass, on the vibration transmissibility curves for samples S1, S2 and S3, where multiple resonant peaks take place. Additionally, intermittent vibration isolation intervals where the logarithmic transmissibility is below zero dB are all larger than 40Hz. FIGURE 7 exhibits the quasi-static compression curves of the identical samples.

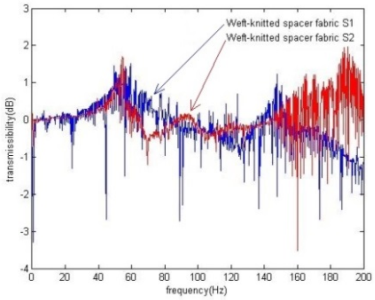

FIGURE 4. Transmissibility curves for sample S1 and S2 having different knit patterns A and B under 5.5kg load mass.

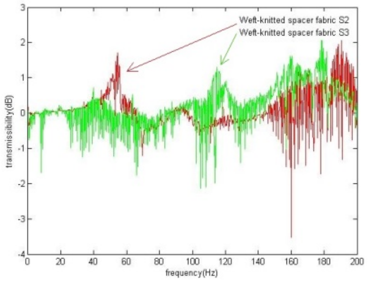

FIGURE 5. Transmissibility curves for sample S2 and S3 having monofilament diameters of 0.08mm and 0.12mm under 5.5kg load mass.

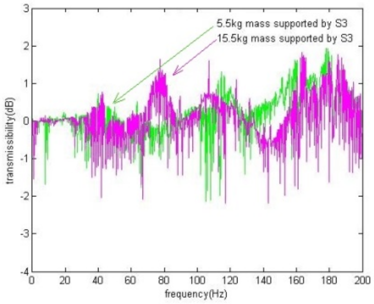

FIGURE 6. Transmissibility curves for sample S3 under load mass of 5.5kg and 15.5kg.

Based on the quasi-static compression curves in FIGURE 7, the local compressive modulus for samples S1, S2 and S3 under two different loading conditions can be calculated (TABLE II). Assuming the spacer fabric and load mass as a one-piece single-degree-of-freedom spring-mass system, and ignoring material damping effect, the natural frequencies of three fabrics are predicted using Eq. (1).

$$f_n = \frac{1}{2\pi}\sqrt{\frac{k}{m}} = \frac{1}{2\pi}\sqrt{\frac{Y \cdot A}{t \cdot m}} \tag{1}$$

where f_n is the natural frequency, k is material stiffness, m is the load mass, Y is the compressive modulus, A is the cross-sectional area of the load mass, and t is the original fabric thickness. The predicted resonant frequencies are listed in TABLE II, in comparison with the measured resonant frequencies obtained from the transmissibility curves.

In TABLE II, with 5.5kg load mass, the predicted resonant frequencies are underestimated for samples S1 and S2, though ignoring material damping should have elevated the resonant frequencies, which could be caused by the ideal one-piece system assumption; besides, to compare their transmissibility curves, we learn that knit pattern A outperforms B when excitation frequency is above 150Hz, indicated from FIGURE 4, so that sample S1 would exhibit better isolation under similar working conditions. Compare the results between sample S2 and S3 in FIGURE 5, we see larger monofilament diameter results in reduced resonant frequencies. As indicated in FIGURE 6, vibration experiments for sample S3 under load mass of 5.5kg and 15.5kg result in approximately equal resonant frequencies; besides, the transmissibility at the first resonance peak is less than 1dB for sample S3, which performs best among three samples.

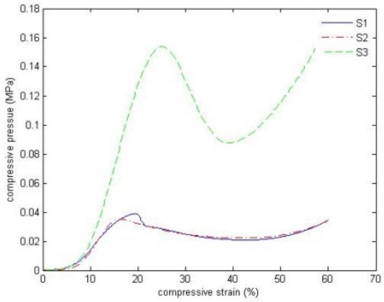

FIGURE 7. The quasi-static compression curves of three samples.

TABLE II. Comparison between predicted and experimental resonance

Sam. code	Compressive modulus Y (MPa) (m=5.5kg)	Resonant frequency (Hz) (m=5.5kg)		Compressive modulus Y (MPa) (m=15.5kg)	Resonant frequency (Hz) (m=15.5kg)	
		predicted	measured		predicted	measured
S1	0.14	41.57	48	0.27	34.00	n/a
S2	0.19	52.91	56	0.34	42.09	n/a
S3	0.16	48.53	42	0.31	39.82	42

CONCLUSIONS

Frequency intervals exhibiting vibration isolation effect are intermittent and larger than 40Hz for all samples. The calculations based on a single d.o.f. spring-mass system gave a good prediction on resonant frequencies.

FUTURE WORK

The causes for the higher resonance modes need to be investigated and optimum weft-knitted spacer fabric should be designed based on further comparative studies in a systematic manner.

ACKNOWLEDGMENT

The authors would like to acknowledge the funding support from the Research Grants Council of HK Special Administrative Region Government (Grant No. 516011)

REFERENCES

[1] Harris, Cyril M., and Allan G. Piersol, *Harris' shock and vibration handbook*, Vol. 5, McGraw-Hill, 2002.

[2] YP Liu, H Hu, Vibration Isolation Performance of Warp-knitted Spacer Fabrics, The Fiber Society 2011 Spring Conference, Hong Kong 23-25 May, pp 63-64.

Detecting Free Radicals in Fibrous Materials Exposed to Light

Keith R Millington[1], Siti Farhana Zakaria[2]
[1]CSIRO Materials Science & Engineering, Geelong Technology Precinct, Waurn Ponds, VIC 3216, Australia
[2]Faculty of Art & Design, Universiti Teknologi MARA, Shah Alam 40000, Malaysia
keith.millington@csiro.au

OBJECTIVE

The photostability of fibrous and organic materials is normally assessed by exposing samples to sunlight for extended periods and measuring changes in properties, such as mechanical strength, flexibility or colour. Whilst such empirical information is useful, it cannot relate the performance of different materials to their chemistry and structure, predict working lifetimes from studies on unexposed samples or explain the photochemical degradation mechanisms that occur. Photodegradation occurs via free radical oxidation and a simple means of reproducibly quantifying the number of free radicals formed in materials briefly exposed to ultraviolet (UV) light is described. Such studies can be carried out on virgin materials well before any visible changes become apparent.

INTRODUCTION

Most organic materials, including natural and synthetic fibres, undergo degradation by free radical oxidation. Free radical reactions are commonly initiated by heat, light, and in particular energetic ultraviolet wavelengths, and by ionizing radiation. The standard method for studying organic free radicals is electron spin resonance (ESR) spectrometry. Free radicals always contain at least one unpaired electron and are therefore paramagnetic. However ESR has low sensitivity, requiring low temperature cryogenics or spin trapping to maintain a high concentration of free radicals in the sample, so that a reasonable signal intensity can be obtained.

A simpler means of quantifying free radical populations in organic materials, which is particularly suited to studies on fabrics and films, is by measuring chemiluminescence (CL) emission. It is well known that the key stage in the autoxidation of organic materials, expounded by Bolland and Gee [1] in 1946, is the rapid addition of oxygen to carbon-centred free radicals, the first propagation reaction shown in Scheme 1. Organic macroperoxy radicals $POO^{\cdot}$ react to form a unstable dimer [POOOOP], which decomposes to produce a ketone in an excited state $P'_2C{=}O^*$. These macroperoxy radicals, and also hydroperoxides POOH, produce CL emission in polymers [2, 3]. Although bimolecular reaction of macroperoxy radicals has a very low quantum yield (10^{-8}–10^{-5}), use of photon counting makes the technique extremely sensitive.

$$
\begin{array}{lrcl}
 & I & \xrightarrow{h\nu} & I^* \\
\text{Initiation} & I^* & \longrightarrow & A^{\cdot} + B^{\cdot} \\
 & A^{\cdot} + PH & \longrightarrow & P^{\cdot} + AH \\
\hline
\text{Propagation} & P^{\cdot} + O_2 & \xrightarrow{\text{fast}} & POO^{\cdot} \\
 & POO^{\cdot} + PH & \longrightarrow & POOH + P^{\cdot} \\
\hline
 & POO^{\cdot} + POO^{\cdot} & \longrightarrow & \{POOOOP\} \\
\text{CL emission} & \{POOOOP\} & \longrightarrow & P'_2C{=}O^* + P''OH + O_2 \\
 & P'_2C{=}O^* & \longrightarrow & P'_2C{=}O + h\nu_{CL}
\end{array}
$$

I = primary light absorber (radical initiator)
$A^{\cdot}$ and $B^{\cdot}$ = radical products from excited state of initiator
PH = polymer

Scheme 1 Mechanism for PICL emission from macroperoxy radicals

EXPERIMENTAL

We modified a commercial CL instrument (Lumipol 3, Slovak Academy of Sciences, Bratislava) that allows samples (8 mm discs of fabric or polymer film) to be irradiated in an inert N_2 atmosphere [4]. The instrument is shown in Figure 1. Immediately after irradiation of the sample with UV light, photophysical light emission processes such as fluorescence, phosphorescence and charge recombination luminescence occur.

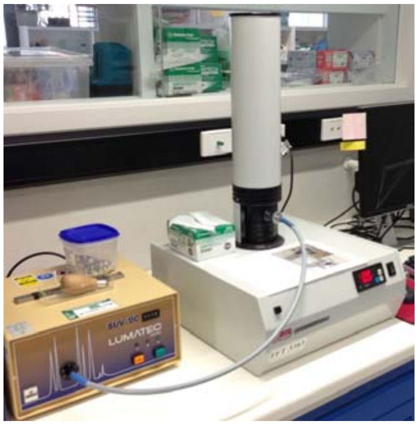

Figure 1 Lumipol 3 CL instrument modified to carry out PICL studies

However the free radicals that form in solid materials are more stable under an inert atmosphere and tend to be long lived. After photophysical light emission has decayed and a baseline has been reestablished, oxygen is admitted to the sample. Oxygen immediately reacts with accessible carbon-based free radicals and a burst of photo-induced chemiluminescence (PICL) is released from the sample. This protocol for separating photophysical light emission from PICL was described in the 1980s by George et al [5].

RESULTS AND DISCUSSION

A typical PICL decay profile is shown in Figure 2 for nylon 6 fabric. The sample was irradiated with UVA wavelengths from a medium pressure Hg arc (320–400 nm) in N_2 for two minutes and the photophysical light emission was allowed to decay back to the baseline for a further 2 minutes. Then O_2 was admitted and burst of PICL was immediately observed that gradually decayed. It is clear that photophysical light emission is far more intense than the PICL emission from free radicals observed as O_2 is admitted to the sample cavity. This clearly demonstrates the need to separate the PICL associated with free radical reactions from other emission processes. The intensity of the PICL peak is proportional to the population of reactive free radicals formed in the sample during irradiation, and the rate of PICL decay depends on the oxygen permeability of the sample material and the mobility of the macroperoxy radicals.

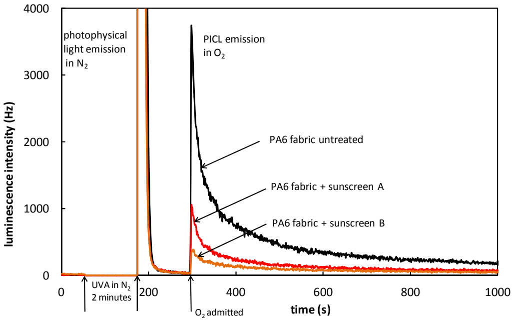

Figure 2 PICL decay profile for nylon 6 fabric exposed to UVB for 2 minutes and the same fabric treated with two commercial sunscreens at 35°C.

Also shown in Figure 2 are PICL profiles from samples of the same fabric to which small amount (2–3 mg) of two commercial broad spectrum sunscreens was applied. Since these sunscreens attenuate the dose of UVA radiation reaching the fabric surface, fewer free radicals are formed in the nylon 6 and the PICL emission intensity is significantly lower in both cases. This demonstrates how PICL can be used to study the effects of UV absorbers on radical formation in fibrous materials. The technique has also recently been applied to studies on free radical photogeneration in skin [6].

The decay kinetics of PICL profiles from wool, nylon 6 and polypropylene have been studied [7]. The decay does not follow simple first or second order kinetics, but does fit a second order decay model assuming the presence of an unreactive fraction of free radicals is present [7]. These unreactive radicals may be trapped in crystalline regions of the polymer that are not accessible to O_2. Second order kinetics is consistent with a bimolecular reaction of macroperoxy radicals.

The natural fibres wool, silk and cotton also produce PICL emission, as shown in Figure 3. Dyed fabrics usually have much lower PICL emission than undyed material, except where the dyes are known photosensitizers, including xanthenes [8]. A potential application of PICL could be to determine the free radical population formed in different materials under the filtered lighting conditions used in museums and galleries, to manage the conservation of cultural artifacts.

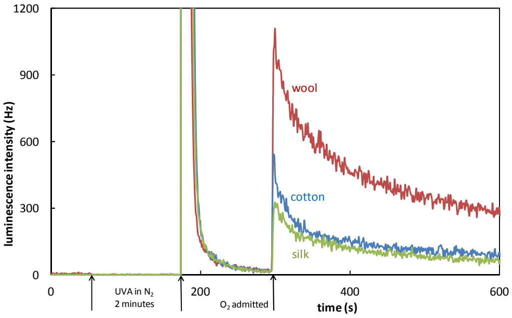

Figure 3 PICL decay profiles for wool, cotton and silk fabrics exposed to UVB for 2 minutes at 40°C

CONCLUSIONS

PICL can be used as a simple alternative to ESR for studying free radical reactions involved in the photodegradation of fibrous materials.

REFERENCES

1. Bolland JL and Gee G. *T Faraday Soc*. 1946; 42: 236-43.
2. Jacobson K, Eriksson P, Reitberger T and Stenberg B. *Adv Polym Sci*. 2004; 169: 151-76.
3. Blakey I, Goss B and George G. *Aust J Chem*. 2006; 59: 485-98.
4. Millington KR, Deledicque C, Jones MJ and Maurdev G. *Polym Degrad Stabil*. 2008; 93: 640-7.
5. George GA, Egglestone GT and Riddell SZ. *Polym Eng Sci*. 1983; 23: 412-8.
6. Millington KR, Jones LN and Sinclair RD. *J Photoch Photobio B*. 2012; 114: 140-6.
7. Millington KR and Maurdev G. *Polym J*. 2009; 41: 1085-91.
8. Millington KR, Zhang H, Jones MJ and Wang XG. *Polym Degrad Stabil*. 2010; 95: 34-42.

A Novel Conducting Polymer-Carbon Nanotube Composite Yarn

J. Foroughi[1], G.M. Spinks[1], G.G. Wallace[1], R. H. Baughman[2]

[1]ARC Centre of Excellence for Electromaterials Science, Intelligent Polymer Research Institute, University of Wollongong, Wollongong NSW 2519, Australia; [2]Alan G MacDiarmid NanoTech Institute, University of Texas at Dallas, Richardson, TX 75083, USA
foroughi@uow.edu.au

Keywords: Carbon nanotube, conducting polymer, polypyrrole

Abstract

Hybrid polypyrrole (PPy)–multi walled carbon nanotube (MWNT) yarns were obtained by chemical and electrochemical polymerization of pyrrole on the yarn surface. The material was characterized by SEM imaging, electrochemical, mechanical and electrical measurements. It was found that the hybrid PPy-MWNT yarns possess significantly higher mechanical strength (over 740 MPa) and Young's modulus (over 54 GPa) and than the pristine MWNT yarn. The material also exhibited substantially higher electrical conductivity (over 23500 S/m). Specific capacitance for PPy-MWNT yarn was found over 60 F/g. Measurements of temperature dependences of electrical conductivity revealed metallic behaviour at high temperature and semiconducting behaviour at low temperature with the metal-to- insulator transition near 100 K. The collected low temperature data are in the good agreement with variable range hopping model (3D-VRH). The improved durability of the yarns is important for electrical applications. The composite yarns can be produced in commercial quantities and used for the applications where the electrical conductivity is of primary importance.

Introduction

Recently developed carbon nanotubes (CNT) assemblies in the form of fibers, yarns and sheets [1-2] are expected to be produced in commercially viable quantities. Their uncommon electrical, mechanical and thermal properties can benefit various products that relay on conductive nanostructures. The range of properties available from the nanotube assemblies can be substantially extended by incorporating particles of diverse functional materials in their structure [3]. The developed "bi-scrolling" technology facilitates applications of the assemblies for catalysis, batteries etc. The infiltration of three-dimensional MWNT forests with an elastomeric polymer binder resulted in formation of highly conductive and very stretchable accordion-like composites [3, 4]. The later can be used for high performance strain sensors, touch-sensitive robotic skin, stretchable electrodes for artificial muscles. In this paper we explore one more type of conductive composites prepared by the polymerization of a conductive polymer on the surface of the MWNT yarns. The developed preparation procedure is substantially different from the conventional composite fabrication process consisting in mixing of the polymer and the carbon nanotube filler that can be shaped in the form of fiber or film. In our case the polypyrrole (PPy) binder was incorporated into the MWNT yarn from solution using both electrochemical and chemical polymerization methods. The composite yarn obtained as a result exhibited improved mechanical, electrical and electrochemical properties as compared with the pristine material. The improved durability of the yarns is important for electrical applications. The composite yarns exceed performance of polypyrrole (PPy) fibres reported previously [5-6] and those improved by the incorporation of small (<2%) amounts of carbon nanotubes. The hybrid PPy-MWNT yarns prepared by our method have much higher CNT loading (over 50 wt %) and possess much higher Young's modulus, electrical conductivity than the host conducting polymer. Our strategy for the preparation of the high-performance CNT-PPy composite yarn can be beneficial to both CNT and PPy fibres. It also helps to retain and improve the performance of the pristine carbon nanotube matrix. The composite yarns can be produced in commercial quantities and used for the applications where the electrical conductivity is of primary importance.

Experimental

The MWNT forest was synthesized by catalytic CVD (chemical vapour deposition) using acetylene gas as the carbon source [1]. Carbon nanotubes in the forest typically had diameter of about 10 nm. The yarn was drawn from the forest by pooling and twisting as described in [2]. The two-ply yarns were obtained by overtwisting the single ply yarn then allowing it to relax until it reached a torque-balanced state. The samples used in this work are single ply MWNT yarn with 6 – 10 μm diameter and 20000 turns per meter (TPM) inserted twist and two-ply MWNT yarns with 15 - 20 μm diameter and 16000 TPM inserted twist. The hybrid PPy-MWNT yarn was prepared by electrochemical (Fig. 1) and chemical polymerization of pyrrole on the surface of the MWNT yarn. CNT-PPy yarns were produced by chemical polymerization of pyrrole through vapour phase polymerization. A comparison of the weight of sample before and after polymerization indicated that the weight fraction of the PPy in the CNT-PPy yarn was ~ 8 wt%. In addition, polypyrrole was incorporated into the CNT yarn successfully by anodic oxidation of pyrrole monomer. A comparison of the weight of sample before and after polymerization indicated that the weight fraction of PPy in CNT-PPy yarn has ~ 74 wt%. Electrical transport of the carbon nanotubes and PPy-CNT yarns has been characterized by standard four probe technique (Quantum Design PPMS).

Conclusions

Development and characterization of the CNT-PPy yarn has been successfully achieved using chemically and electrochemically polymerization of pyrrole. Single and two-ply multi walled carbon nanotube yarns (MWNT) were used to develop the CNT-PPy yarn. SEM micrographs of the pristine CNT and CNT-PPy yarns were carried out to reveal a core-sheath structure for the electrochemically prepared CNT-PPy yarn. However, chemically developed CNT-PPy yarn had a heterogeneous morphology consisting of dense regions of PPy-infiltrated CNT and more porous areas having less PPy. Raman spectra of the MWNT yarn and CNT-PPy yarn showed that pyrrole was successfully polymerized on to the CNTs. The chemically prepared CNT-PPy yarn exhibited much higher stress at break (740 MPa) and Young's modulus (54 GPa). Electrical properties of pristine CNT yarn and CNT-PPy yarns were obtained. The effective energy separations between localized states of the pristine CNT yarn (2.14 K) is larger than that for both the electrochemically and chemically prepared CNT-PPy yarn (1.1 K) show different electrical properties. They show metallic behaviour at high temperature but insulator behaviour at high temperature. It was found that a metallic- insulator transition occur at T ≈ 100 K. The conductivity results are in good agreement with the conductivity analyses in the frame of the 3D-VRH model at low temperatures.

These results suggest that novel developed CNT-PPy yarns may useful for some application such as actuators, sensors, and batteries.

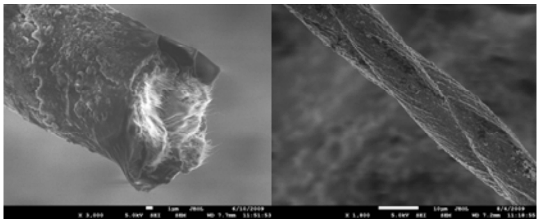

Fig. 1. SEM micrographs of electrochemically prepared CNT-PPy yarn (L) and surface morphology two-ply CNT-PPy yarn(R)

References

[1] Zhang, M., S. Fang, A.A. Zakhidov, S.B. Lee, A.E. Aliev, C.D. Williams, K.R. Atkinson, R.H. Baughman. Strong, Transparent, Multifunctional, Carbon Nanotube Sheets. *Science*, 309 (2005): pp. 1215-1219.

[2] Zhang, M., K.R. Atkinson, and R.H. Baughman, Multifunctional Carbon Nanotube Yarns by Downsizing an Ancient Technology. *Science*, 2004, 306(5700): pp. 1358-1361.

[3] Lima, M.r.D., et al. Biscrolling Nanotube Sheets and Functional Guests into Yarns. *Science*, 331(6013): pp. 51-55.

[4] Shin, M.K., et al. Elastomeric Conductive Composites Based on Carbon Nanotube Forests. *Advanced Materials*, 22(24): pp. 2663-2667.

[5] Foroughi, J., G.M. Spinks, and G.G. Wallace, Effect of synthesis conditions on the properties of wet spun polypyrrole fibres. *Synthetic Metals*, 2009, 159(17-18): pp. 1837-1843.

[6] Foroughi, J. Development of Novel Nanostructured Conducting Polypyrrole Fibres. *Engineering*, 2009, University of Wollongong.

Photoreduction of Graphene/Photocatalyst Nanostructured Fabric for Recycled Pollutant Removal

Jinfeng Wang[1], Takuya Tsuzuki[1,3], Lu Sun[1] and Xungai Wang[1,2]
[1]Institute for Frontier Materials, Deakin University, 75 Pigdons Road, Waurn Ponds, VIC 3216, Australia
[2]Ministry of Education Key Laboratory for Textile Fibers and Products, Wuhan Textile University, Wuhan, China
[3]Research School of Engineering, College of Engineering and Computer Science, Australian National University, Ian Ross Building 31, North Road, Canberra ACT 0200 Australia

Contact: xungai.wang@deakin.edu.au; Speaker: jinfeng.wang@deakin.edu.au

INTRODUCTION

Aromatic pollutants are widely found in many industrial effluents. Because of their high solubility in water, they can be easily spread in the environment and may cause serious problems to our health. In the past, many studies have been conducted on the use of adsorbents for the efficient elimination of organic pollutants. However, for most of the conventional adsorbents, the adsorption properties are not recoverable after use. Therefore, it is important to develop new reusable adsorbents with high adsorption capacities for the management of aromatic pollutant. In this study, a novel type of reusable pollutant-scavenging composite was developed from reduced graphene oxide (RGO) and ZnO nanoparticle photocatalyst. The dye adsorbed on RGO@ZnO composites can be further degraded by the photocatalytic activity of ZnO, thus re-generating the adsorption sites on RGO to provide recyclability/reusability to the composite adsorbent. RGO@ZnO composite was also assembled on polyester fabric by a layer-by-layer (LbL) technique. This new type of adsorbent, fabric functionalized with RGO@ZnO, is highly efficient, flexible and recyclable for the removal of oil spills and organic dye pollutants from water.

RESULTS AND DISCUSSION

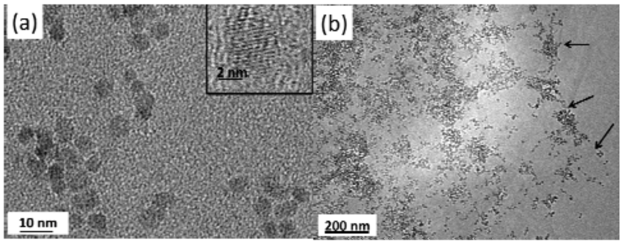

Figure 1. TEM images of PVP-capped ZnO (a) and RGO@ZnO (b).

The composite RGO@ZnO was synthesized using a combination of a self-assembly method and an in-situ photo-reduction technique. First, ZnO nanoparticles and graphene oxide sheets were assembled by using PVP as an intermediate to improve the adhesion between RGO and ZnO nanoparticles. Then, graphene oxide was reduced to RGO, by utilizing the photocatalytic activity of ZnO nanoparticles. Using this synthesis approach, a dense and stable loading of ZnO nanoparticles on RGO surface was achieved as shown in Figure 1b, thus enabling the integrity of the composite structure and pollutant-removal function during a number of reusing cycles.

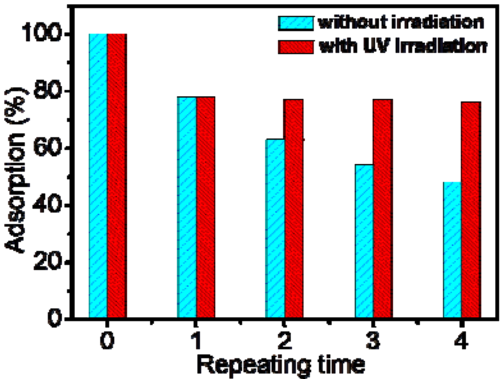

Figure 2. Dye adsorption efficiency of RGO@ZnO with and without sunlight irradiation after several sequential cycles (RhB, 6 ppm; RGO@ZnO, 4 mg/mL).

Compared to neat ZnO nanoparticles, the composite exhibited improved efficacy in the adsorption/decomposition of organic dye molecules. In comparison, the degradation of RhB can be observed in the presence of ZnO and was completed within 75 min. In the presence of RGO@ZnO, the degradation of RhB was completed within a shorter time of 60 min. This is due to the high surface area of RGO and the charge separation caused by the RGO/ZnO heterojunction. The efficiency to adsorb organic dyes showed 99% recovery upon simulated-sunlight irradiation as shown in Figure 2. The photocatalytic activity of ZnO nanoparticles decomposed the organic dye molecules adsorbed on RGO. In this manner, the reusability of the composite adsorbent was maintained over many adsorption/light-irradiation cycles.

The RGO@ZnO composite was also assembled onto polyester fabric by a LbL technique. RGO@ZnO delivers excellent dye adsorption property and recyclability, while fabric membranes offer bulk-handling capability, high surface areas, capillary adsorption property and structural flexibility. As shown in Figure 3, functionalized polyester fabric turns from brown to dark after UV irradiation, which indicates the reduction of GO to be RGO. Figure 4 shows the appearance of a RhB solution at different removal stages, i.e., adsorption and subsequent photocatalytic degradation. (RGO@ZnO)/fabric exhibited a high efficiency for RhB adsorption compared to uncoated polyester fabric even before the photocatalytic degradation. This fabric functionalized with RGO@ZnO removed 98% of RhB dye from water within 30 min under the irradiation of simulated sunlight.

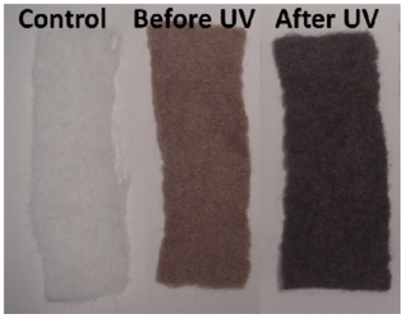

Figure 3. Optical images of polyester fabric, GO@ZnO functionalized polyester fabric before and after UV irradiation for 3 hours.

The recycling performance of (RGO@ZnO)/polyester was investigated by performing several cycles of dye adsorption and sunlight irradiation. In the first cycle, 98% of RhB was removed by (RGO@ZnO)/polyester within 30 min. After 5 cycles of dye adsorption and sunlight irradiation, the (RGO@ZnO)/polyester maintained the removal efficiency of 97% for RhB.

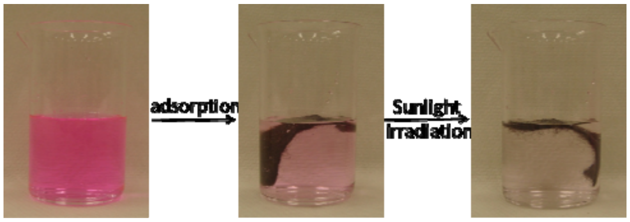

Figure 4. Optical images of (RGO@ZnO)/polyester adsorbing dye from water and degrading dye under simulated sunlight.

CONCLUSIONS

RGO@ZnO composite has been successfully fabricated as a pollutant adsorbent and photocatalyst, which combines a self-assembly deposition and in situ photo-reduction procedure. The RGO in the RGO@ZnO possessed great adsorptivity of RhB dye molecules and ZnO in the RGO@ZnO can degrade RhB under simulated sunlight irradiation. Therefore, the adsorption property of RGO@ZnO can be recovered using the photocatalytic activity of ZnO under simulated sunlight irradiation. The cycling performance of RGO@ZnO for dye adsorption was achieved up to 99% over 4 cycles. RGO@ZnO has also been assembled onto polyester fabric. The (RGO@ZnO)/polyester membrane also showed excellent adsorption efficiency (due to graphene) and cycling performance (due to photoactivity of ZnO) for dye removal from water. Our results indicate that this novel membrane overcomes the major limitation of the traditional adsorbents in recyclability and water-adsorbent separation.

REFERENCE

[1] J. Wang et al., ACS Applied Materials & interfaces, 4 (2012) 3084-3090.

Effect of Softener on Flame Retardant Finish of Cotton Fabrics

K.P. Tang[1], C.W. Kan[1], J.T. Fan[1,2], S.L. Tso[1]
[1]Institute of Textiles and Clothing, The Hong Kong Polytechnic University, Hung Hom, Hong Kong
[2]Dept of Fiber Science & Apparel Design, Cornell University, Ithaca, United States
10900624r@connect.polyu.hk

ABSTRACT

Untreated cotton fabrics burn vigorously under ignition. The ignition temperature for cotton is around 400 ˚C while for wool and nylon is 600 and 530 ˚C, respectively [1]. Due to government regulations and general safety awareness, the demand for flame resistant fabrics is increasing. Generally, flame retardant fabrics can be used for children's sleepwear, home furnishing or work wears. These fabrics are designed to preserve the spreading speed of flames, increase the time available for the wearer to escape from a hazardous situation and avoid burn injury. Researchers have attempted to improve the flammability by optimizing the types of flame retardant agent or the finishing conditions. Despite the much research work carried out on flame-retardant cotton fabric, majority of the studies concentrated on the mechanical properties and the comfort aspect is largely neglected. To deal with these problems, here Pyrovatex CP New and modified DMDHEU (low formaldehyde) were used with various softeners under Pad-Dry-Curing process and these finishes were applied onto fabrics with conventional structure as well as the plant-structured design of similar weight. The water absorbency, comfort-related and mechanical properties were measured. The result demonstrated that the addition of softener could remarkably improve the handle and fabric strength while no adverse effect was brought on flame retardant property in which softener "Turpex ACN New" is the optimum choice for both plain and plant-structured design. It also reveals that plant-structured fabrics got superior performance than the plain.

EXPERIMENTAL DETAILS

The plain and plant-structured fabrics were treated by the commercial products. Fabric samples were dipped and nipped twice in a laboratory scale padding machine at 5 kg/cm^2 pressure and 5 rpm to achieve 80 % wet pickup. The formulations of the five recipes are listed in TABLE I. After padding, the padded fabrics were dried at 110 ˚C for 5 min, cured at 150 ˚C for 1 min, washed with 30g/L sodium carbonate at 50˚C for 30 min and then rinsed with 50˚C water for 30 min.

TABLE I. Formulation of each recipe (in mL/L, by volume)

Recipe		1	2	3	4	5
Flame retardant agent	Pyrovatex CP New	400	400	400	400	400
Crosslinking agent	Knittex CHN	50	50	50	50	50
Catalyst	Phosphoric Acid (25%)	85	85	85	85	85
Softener	Ultratex FSA New		30			
	Turpex ACN New			30		
	Ultratex FH New				30	
	Ultraphil DCW New					30

TESTING OF FABRIC SAMPLES

The flammability of fabrics was measured in accordance with ASTM D1230 where the specimen was burnt at an angle of 45˚ for 15 seconds (the original setting was 1 s). The shorter the char length, the better the flame retardant property is. With regard to the comfort features, the absorption property of fabrics was measured by the wettability test (AATCC 79). The longer the absorption time, the poorer the absorption it is. The air resistance was measured by the KES-F air-resistance tester (KES-F8-AP1) and it is the inverse of air permeability. In addition, the low stress mechanical properties of fabrics including shearing, tensile and surface friction properties were measured using KES-F. Referring to the strength of the fabrics, tearing strength testing was performed in line with ASTM D1424 while the tensile strain measurement was conducted according to ASTM D5034.

RESULTS AND DISCUSSION

Studying the effect of softener on the plain structure

The fingerprint of different recipes on various fabric properties is summarized in FIGURE 1. All the raw data was normalised based on the minimum and maximum value obtained. In order to standardise the polarity of scale for each property, factors representing negative meaning (i.e. char length, water absorption time, shear stiffness and surface friction) will be converted so that 1 is equal to good performance and vice versa for 0. This figure could give the general picture about the ranking of recipes on each property. In general, it can be seen that softener "Turpex ACN New" (i.e. recipe 3) got the most outstanding performance in terms of flammability, tensile and shearing.

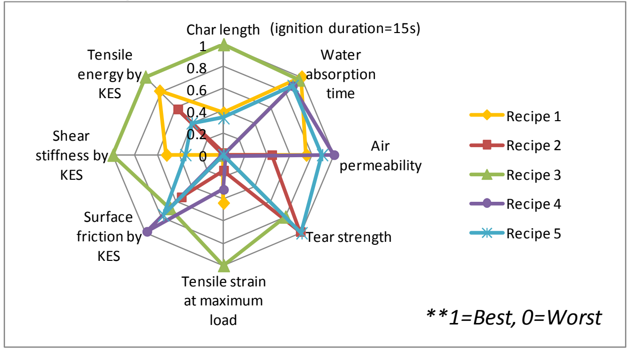

FIGURE 1. Fingerprint of different recipes

To determine the significance of the effect of softener on the dependent variables, ANOVA test was performed. The result indicated that the mean score of different recipes differ significantly in wettability test (p=.000<.05), air permeability ($p=.007<.05$), tensile strain ($p=.019<.05$), tear strength ($p=.000<.05$), surface friction ($p=000<.05$) shear stiffness ($p=.008<.05$) and tensile energy ($p=.007<.05$). However, the char length for various recipes does not show significant difference (warp: $p=.242>.05$; weft: $p=.728>.05$). In other words, we could say that the addition of softener does not bring remarkable adverse effect on the flame retardant property. Chen et al. [2] found that the rinse-type softener would increase the flammability of cotton fabrics. In contrast to an early study, this study found that by incorporating various softeners into the optimum recipe developed by Lam et al. [3] does not deteriorate its flame retardant ability.

Here, recipe 1 is the one without softener while the rest were treated with various types of softener. Independent t-test was used to check the significance of difference between recipes and the result indicates that the addition of softeners (i.e. recipe 2,3,4,5) does not affect its flame retardant property significantly. Independent t-test also suggested that the surface friction of all the softener-treated fabrics is significantly lower than the one without softener ($p<.05$), suggesting better handle for the softener-treated fabrics. The tear strength for the softener-treated fabrics is also higher than recipe 1 in which recipe 2 and 5 is significantly higher than it ($p<.05$). The incorporation of softener reduces the friction of yarns which allows yarn movement. Yarns can then grouped together improving the tear resistance as more than one thread has to be broken at a time. Once again, it demonstrates the benefit brought by the softener.

Comparison of plain against plant-structured design

All these finishes have also been applied onto the plant-structured fabrics in which the char length, water absorption time and air permeability were measured and the result is summarized in TABLE II. For the char length, the flame retardant effect of the treated fabrics improves significantly as compared with the control no matter what structure it is. The control fabrics burn immediately while only a brownish spot was observed in the treated fabrics. Paired t-test was performed to see the significant of difference between plain and plant-structured fabrics among the five recipes. The result indicated that plant-structured fabrics have significantly shorter char length than the corresponding plain fabrics ($p<.05$). Plant-structured fabrics are woven with finer yarns which facilitate chemical penetration deeply into the fibers and this might be one of the possibilities for better flame retardant effect. Also, the superiority of plant-structured design might attribute to the lower surface area (lower pore volume) of its fabric face. Indeed, the total pore volume in plant-structured and plain fabrics is of similar level (84% and 82% respectively). However, the pores in the plant-structured fabrics can be differentiated into open and closed pores. The pores in-between the top and bottom layer could be termed as closed pores which are believed to bring little contribution to combustion. Plant-structured fabrics with rougher surface (2/2 matt) at the back side and smoother surface (plain) at the face side and so the open pore volume at its face is comparatively less than its back. Excluding the closed pores and considering the asymmetrical pore distribution in the plant-structured fabric, the lower open pore volume (smaller surface area) on the face side of plant-structured fabric might contribute to better flame retardant effect.

The water absorption property and air permeability of plant-structured fabrics is also significantly better than the corresponding plain fabrics, suggesting better comfort. Plant-structured fabric absorbs water readily; the moisture content might be higher when wears (sweating) and so the propensity for it to burn is lower.

TABLE II. Comparison of plain and plant structure

Recipe		Char length (ignition duration =15s) (mm)	Water absorption time in wettability test (s)	Air resistance, R (kPa s/m)
Control	Plain	150.00	10.417	1.544
	Plant	150.00	2.038	0.231
1	Plain	35.46	6.773	2.205
	Plant	30.36	1.949	0.325
2	Plain	36.40	21.239	2.222
	Plant	30.47	2.079	0.340
3	Plain	33.86	7.336	2.245
	Plant	28.47	1.916	0.317
4	Plain	36.45	8.472	2.192
	Plant	31.67	2.252	0.329
5	Plain	35.58	8.424	2.198
	Plant	31.31	2.022	0.352

In general, the char length, water absorption time and air resistance of recipe 3 (with Turpex ACN New) is the least. Similar to the plain fabrics, softener “Turpex ACN New” is, therefore, the recommended additives for the flame retardant finish in the plant-structured fabric.

CONCLUSIONS

This study demonstrates that the addition of “Turpex ACN New” softener in the flame retardant finish could significantly improve the strength and handle of the fabric while the flame retardant effect, water absorbency and air permeability is unaffected. The flame retardant effect and other comfort features are further enhanced for plant-structured design. Thus, it can potentially become a safe and comfortable shirting material or uniform.

ACKNOWLEDGMENT

This work is supported by the studentship of the Hong Kong Polytechnic University and thanks were given to HUNTSMAN™ for the sponsor of chemical.

REFERENCES

1. Flame resistant fibres and fabrics. *Technical Textile Markets*, Textiles Intelligence Limited. 85, 2011, 50-84.
2. J.H. Chen-Yu, J.M. Guo and B.K. Gatterson, *AATCC Rev.*, 9, 2009, p. 43-47.
3. Y. Lam, C. Kan and C. Yuen, *J. Appl. Polym. Sci.*, 121, 2011, p. 612-621.

Robust, Electro-Conductive, Self-Healable, Superamphiphobic Fabrics from PEDOT/FD-POSS/FAS Coating

Hongxia Wang, Hua Zhou, Tong Lin
Australian Future Fibers Research and Innovation Centre, Deakin University, Geelong, VIC, 3217, Australia
tong.lin@deakin.edu.au

INTRODUCTION

Smart or intelligent textiles are being widely developed as a new generation of textiles with advanced enforcement of wearers' physiology, health and safety[1]. As such, electrically conductive textiles are prerequisite to functioning smart textiles[2], and their quality also determines the durability, launderability, reusability and fibrous performances of smart textiles.

Recently, superhydrophobicity or superoleophobicity has been added to conducting polymers with the purpose of creating multifunctional materials. Superamphiphobic surface has a contact angle greater than 150° to oil fluids. They have great potential in antifouling from hazardous chemicals and biological contaminants[3], which are useful for development of smart textiles. However, all these techniques are based on hard conductive substrates. Conductive superhydrophobic/superoleophobic fabrics have received little attention until very recently[4].

In our recent study, we found that when poly(3,4-ethylenedioxythiophene) (PEDOT) was vapor phase polymerized onto fabrics, the incorporation of a fluorinated decyl polyhedral oligomeric silsesquioxane (FD-POSS) and a fluorinated alkyl silane (FAS) into the coating layer during the polymerization process endowed the conductive coating with a durable superamphiphobic surface. More interestingly, the coating had a self-healing ability to auto-repair from chemical damages.

APPROACH

Fabric substrates were dip-coated with a $FeCl_3 \cdot 6H_2O$ solution containing FD-POSS and FAS. After drying at room temperature, the coated fabric was placed into a small chamber filled with saturated EDOT vapor at 60 °C for 30 minutes to carry out the polymerization reaction. The fabric was finally rinsed with ethanol and water to remove any side products. For comparison, a coating containing FAS without FD-POSS was also prepared in a similar way. FD-POSS without FAS was not soluble in the $FeCl_3$ solution, which prevented the formation of a PEDOT/FD-POSS coating.

RESULTS AND DISCUSSION

The chemical structures of FD-POSS, FAS and EDOT are presented in Fig. 1a. After coating treatment, the fabric turned black (Fig. 1b), indicating the successful polymerization of PEDOT[3]. Fig. 1c shows the SEM image of the PEDOT/FDPOSS/FAS coated fibres, which looks similar to the uncoated ones. The TEM image shown in the inset of Fig. 1c indicates the formation of a thin conformal coating with a thickness around 100 nm after the coating treatment. Fig.1d showed water and hexadecane drops on the coated fabric surface. The contact angle (CA) measurement indicated that the coated fabric had a CA of 169° and 156° to water and hexadecane, respectively.

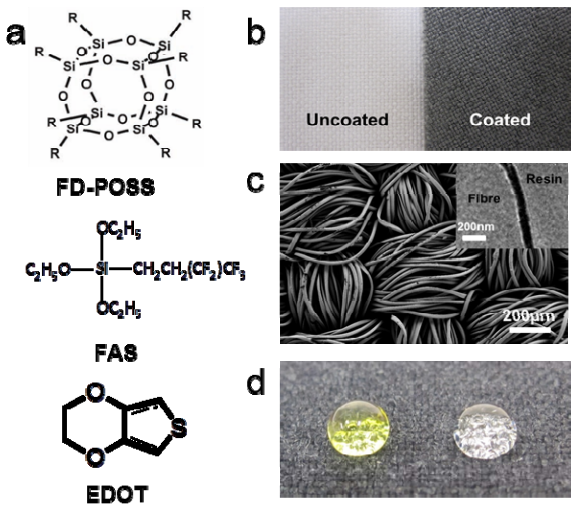

FIGURE 1. (a) Chemical structures of FD-POSS, FAS and EDOT, (b) photo of polyester fabric before (left) and after (right) coating treatment, (c) SEM image of the polyester fabric after coating with PEDOT/FD-POSS/FAS (inset is a cross-sectional TEM image of a PEDOT/FD-POSS/FAS coated fibre), (d) colored water (yellow) and clear hexadecane drops on the PEDOT/FD-POSS/FAS coated fabric.

The surface conductivity of fabrics was measured using a standard method (AATCC 76-1995). Before coating treatment, the polyester fabric had a very large surface resistance due to its non-conductive nature. When the fabric was coated with PEDOT/FD-POSS/FAS, the surface resistance became 1.0 ± 0.2 KΩ/□ (KΩ/centermeter squar). In comparison, the fabrics coated with PEDOT alone or PEDOT/FAS showed a surface resistance of 0.6 ± 0.15 KΩ/□. The slightly decreased conductivity suggests that FD-POSS has a very small influence on the conductivity of the PEDOT coating. Previous studies using polypyrrole as the conducting polymer in a fabric coating also showed little change in surface resistance upon addition of FAS to the coating[4].

The abrasion durability was measured using the Martindale method (ASTM D4966). As expected, the contact angle decreased with increasing abrasion cycles for both PEDOT/FD-POSS/FAS and PEDOT/FAS coated fabrics (Fig. 2a). The PEDOT/FD-POSS/FAS coating showed enhanced abrasion durability over the PEDOT/FAS coating. After 10,000 cycles of abrasion, the PEDOT/FD-POSS/FAS coated fabric still retained its liquid repellency. For the PEDOT/FAS coated fabric, the contact angle to hexadecane became 0° after 8,000 abrasion cycles, and the water contact angle dropped to only 137°.

The effect of abrasion cycles on the surface conductivity was similar to their effect on the contact angle. As shown in Fig. 2b, the surface resistance (R) increases with increasing the abrasion cycles for all PEDOT coated fabrics regardless of whether the coating contains FD-POSS or FAS additive. The surface resistance of the PEDOT/FD-POSS/FAS coated fabric changed at a lower rate compared to the PEDOT/FAS fabric. After 10000 abrasion cycles, the average surface resistance of the PEDOT/FD-POSS/FAS coated fabric increased only from 1.0 to 1.5 KΩ/□, while a larger resistance increase was observed for the PEDOT/FAS coated fabric, from 0.6 to 1.9 KΩ/□.

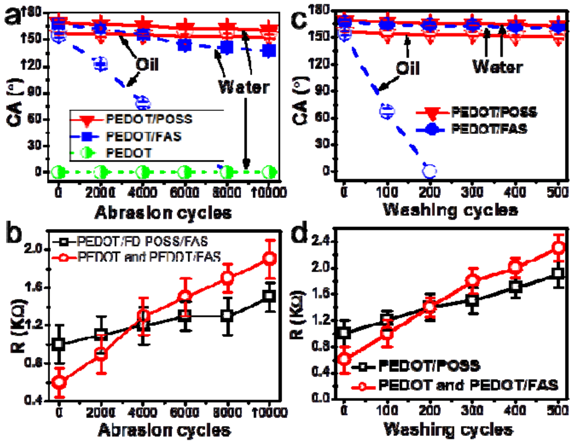

FIGURE 2. (a) Effect of abrasion cycles on the liquid contact angle of coated fabrics, and (b) surface resistance of coated fabrics, (c) effect of washing cycles on contact angle and (d) surface resistance of coated fabrics.

Fig. 2c and d show the effect of repeated washing on the contact angle and surface resistance. With increasing laundry cycles, the PEDOT/FD-POSS/FAS coated fabric had a small decrease in both water and hexadecane contact angles. After 500 cycles of washing, the superamphiphobic property was retained. However, for the PEDOT/FAS coated fabric, although superhydrophobicity was retained throughout the whole 500 laundry cycles, the superoleophobicity was lost after just a few cycles of washing, and the fabric became completely oleophilic to hexadecane (contact angle 0°) after only 200 washing cycles. This was presumably due to the removal of FAS molecules from the coating layer during washing. The detergent in water may facilitate the leaching FAS molecules off the coating layer. Since the FD-POSS molecule has a large size, it is relatively hard to diffuse into water from the polymer layer.

It was also noted that the surface resistance increased with increasing washing cycles. After 500 washing cycles, the average surface resistance of the PEDOT/FD-POSS/FAS coated fabric increased from 1.0 KΩ/□ to 1.9 KΩ/□. A larger resistance increase was found on the PEDOT/FAS coated fabric which increased from 0.6 KΩ/□ to 2.3 KΩ/□.

More interestingly, we found that the coated fabric showed a self-healing property that can auto-repair from chemical damages and restore the surface liquid repellency. Here, the surface of the coated fabric was deliberately damaged by a vacuum plasma treatment using air as the gas source. After plasma treatment for a few minutes, both PEDOT/FD-POSS/FAS and PEDOT/FAS coated fabrics became hydrophilic and oleophilic with a contact angle of 0° to both water and hexadecane (Fig. 3). When the plasma-treated fabrics were then heated to 135 °C for 5 minutes, the fabrics completely restored their superamphiphobic property (Fig. 3). The self-healing also took place at room temperature but took considerably longer, on a scale of 24 hours. However, the plasma treatment showed no influence on the surface resistance.

FIGURE 3. Photos to show water and hexadecane drops on the coated fabric before and after plasma treatment and self-healing.

This self-healing was repeatable. After the first 10 cycles of plasma and heat treatment, the water contact angle of the PEDOT/FD-POSS/FAS coated fabric changed from 169° to 165°.

CONCLUSIONS

Adurable liquid-repellent conductive fabrics have been prepared by one-step vapor-phase polymerization of EDOT with the presence of FD-POSS and FAS. The addition of FD-POSS and FAS to the PEDOT showed little influence on the surface resistance, but it can impart the PEDOT coating with not only durable liquid repellency but also self-healing ability to auto-repair from chemical damages. This novel, electrically conductive superamphiphobic coating may be useful for development of durable smart fabrics for various applications.

ACKNOWLEDGMENT

Funding support from the Australia Research Council under the Discovery Project scheme and Deakin University under the Central Research Grant scheme is acknowledged.

REFERENCES

[1] P. Gould, Mater. *Today*, 2003, 6, 38–43.
[2] L. Wang, X. Wang and T. Lin. in *Smart Textile Coatings and Laminates*, ed. W. C. Smith, Woodhead Publishing, 2010, pp. 155–188.
[3] J. Kim, E. Kim, Y. Won, H. Lee and K. Suh. *Synth. Met.*, 2003, 139, 485–489.
[4] H. Wang, Y. Xue and T. Lin, *Soft Matter*, 2011, 7, 8158–8161.

In Situ Electrochemical Polymerization of Pyrrole onto Textiles: Influence of Add-On and Surface Roughness

Kushal Sen, Dipayan Das, Syamal Maiti
Department of Textile Technology, Indian Institute of Technology Delhi, Hauz Khas, New Delhi-110016
kushal@textile.iitd.ac.in

INTRODUCTION

Polypyrrole is one of the very promising electro-conductive polymers that has received considerable interest due to its high conductivity, environmental stability, and easy polymerization. Pyrrole can be polymerized onto textile substrates via *in situ* chemical and electrochemical polymerization to obtain flexible and non-metallic electro-conductive textiles. Such textile materials can be used as electromagnetic shields, heating pads, and gas sensors [1-3].

A few attempts were made to understand the electrochemical polymerization process and establish the role of process parameters on electrical conductivity of the resulting fabrics. The results were however found to be contradictory. Kim et al. [4] prepared a stretchable electro-conductive fabric by electrochemical polymerization of pyrrole onto nylon/spandex stretchable fabric. They observed that the electro-conductivity of the fabric first increased and then decreased with an increase in the concentrations of monomer and dopant. Babu et al. [5] produced an electro-conductive cotton fabric by the combination of chemical and electrochemical polymerization at constant current density (2 mA/cm^2) at room temperature for 4 h. They reported that the conductivity and weight gain were directly proportional to monomer concentration as well as polymerization time. It is clear that the influence of add-on on electrical conductivity is not yet understood clearly.

In this work, an attempt has been made to establish the roles of add-on and surface roughness on surface resistivity of electro-conductive textiles prepared by *in situ* chemical and electrochemical polymerization of pyrrole.

EXPERIMENTAL

Materials and chemicals

A polyester fabric of 58 g/m^2 weight, 0.19 mm thickness, 96 ends per inch, and 80 picks per inch was chosen as a substrate. The chemicals used were sodium carbonate, sodium hydroxide, non-ionic detergent Lissapol N (HR Chemical, India), pyrrole (Spectrochem, India), ferric chloride, and p-toluenesulfonic acid (Lobal Chemie, India). All the chemicals used were of laboratory grade and they were used as received.

Preparation of electro-conductive fabric

The electro-conductive fabric was prepared by a combined *in situ* chemical and electrochemical polymerization of pyrrole. The chemical polymerization was carried out prior to the electrochemical polymerization in order to achieve more uniform deposition of polypyrrole on the surface of the fabric during electrochemical polymerization.

The fabric was first hydrolyzed with 100 gpl sodium hydroxide at 90°C for 20 min, keeping the material-to-liquor ratio as 1:30. Then a two-step *in situ* chemical polymerization of pyrrole was carried out onto the hydrolyzed fabric. In the first step, the hydrolyzed fabric was immersed into pyrrole solution containing 0.5 M pyrrole at 25°C for 20 min. In the second step, the pyrrole-enriched fabric was immersed into 0.75 M ferric chloride solution so as to initiate polymerization onto the fabric at 5°C for 10 min. Afterwards, the fabric was washed thoroughly with deionized water and dried in an oven at 60°C for 40 min.

The electrochemical polymerization of pyrrole was carried out onto the chemically polymerized fabric in a potentiostat using a regulated DC power supply (ESCORP). The stainless steel electrodes were kept vertically parallel to each other. The electrolyte solution was prepared in aqueous medium with different concentrations of pyrrole and p-toluenesulfonic acid. The chemically polymerized fabric was fixed on the anode surface to enable *in situ* electrochemical polymerization.

The surface resistivity of the fabric was determined using ASTM standard D-257. The surface characteristics of the fabric were examined by scanning electron microscopy (Zeiss EVO 50 scanning electron microscopy system). The SEM micrographs were taken without any coating applied onto the fabric for scanning. The surface roughness of the fabric was measured on an instrument named Form Talysurf Intra supplied by Taylor Hobson Precision, UK.

RESULTS AND DISCUSSION

Effect of polymer deposition on surface resistivity

The generalized effect of deposition of electrically conducting polymer, irrespective of process parameters, on the surface resistivity of the electro-conductive fabric is shown in Figure 1a. It can be seen that the surface resistivity of the fabric decreased rapidly with an increase in add-on, but leveled off after about 10 g/m^2. It may be hypothesized that the polymer covered the entire available surface of the fabric at this level of deposition; therefore, any additional deposition of polymer did not bring to lower the resistivity significantly. A closer look on the stabilized region revealed however that there is an irregular trend between surface resistivity and add-on within a band of resistivity of 0-200 Ω (Figure 1b). Some fabrics with a higher add-on showed more resistivity, while some other fabrics with higher add-on showed less resistivity as depicted in the scanning electron micrographs (Figure 2), i.e. below a value of about 200 Ω the resistivity and add-on were not correlated well. In order to understand this behavior, the surface roughness of the fabrics was measured.

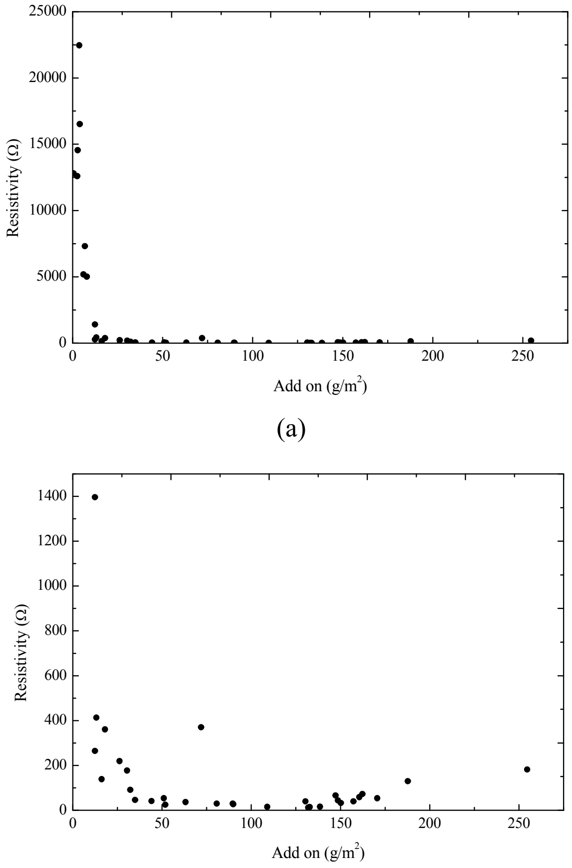

(a)

(b)

Figure 1. Effect of add-on on surface resistivity of electro-conductive fabric (a) generalized effect (b) in a specific band of resistivity

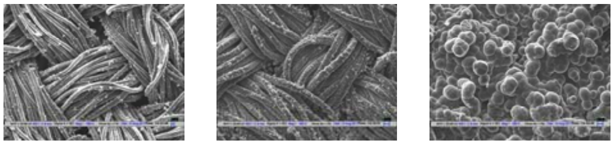

Add-on (g/m²): 51.03
Resistivity (Ω): 53.05

Add-on (g/m²): 80.65
Resistivity (Ω): 29.95

Add-on (g/m²): 170.54
Resistivity (Ω): 53.66

Figure 2. Scanning electron microscopic images of electro-conductive fabrics

Effect of add-on and surface roughness on electrical resistivity

Table 1 reports on the effect of add-on and surface roughness on electrical resistivity. It can be observed in case of fabric that has higher add-on but a lower surface roughness resulted in lower surface resistivity. A similar behavior was found in case of film not facing the electrode surface where the roughness varied constantly. But, the film facing the electrode surface registered almost no significant change in the electrical resistivity. This might be attributed to relatively smoother surfaces of the films facing the electrode. It may be hypothesized that the electron had to travel a longer path with an increase in surface roughness, thus leading to higher surface resistivity. The other reason might be associated with the measurement of surface resistivity. Under the application of same pressure onto the fabric samples by electrode weight, the fabric with higher roughness would have less contact points, hence registered higher resistivity.

Table 1. Effect of add-on and surface roughness on surface resistivity

Material	Add-on/ Weight per unit area (g/m²)	Surface roughness (µm)	Surface resistivity (Ω)
Fabric	34.90	14.5	46.26
	132.73	12.4	14.19
	254.63	31.0	181.21
Film surface not facing electrode	83	6.0	4.72
	135	24.6	6.57
	164	37.5	9.25
Film surface facing electrode	83	0.70	2.88
	135	0.42	2.69
	164	1.30	2.46

CONCLUSION

The surface resistivity of the fabrics was decreased rapidly with an increase in add-on. But, after a certain level of add-on, the surface resistivity of the fabrics was stabilized more or less. Below a resistivity value of about 200 Ω the add-on and resistivity were not correlated. This behavior can be explained in terms of surface roughness of the fabrics. It was observed that higher add-on but lower surface roughness resulted in lower surface resistivity. A similar behavior was found in case of films as well.

REFERENCES

[1] Y Li. *Journal of Electroanalytical Chemistry* 1997, 433, 181.
[2] S Maiti, D Das, K Sen. *Journal of Electrochemical Society*. 2012, 159, E154.
[3] S Maiti, D Das, K Sen. *Journal of Applied Polymer Science*. 2012, 123, 455.
[4] SH Kim, KH Oh, JH Bahk. *Journal of Applied Polymer Science*. 2004, 91, 4064.
[5] KF Babu, R Senthilkumar, M Noel, MA Kulandainathan. *Synthetic Metals*. 2009, 159, 1353.

Design of Smart Functional Apparel Products for Moxa Moxibustion

Li Li, Wai-man Au, Feng Ding, Kwok-shing Wong
li.lilly@polyu.edu.hk

ABSTRACT

Moxa Moxibustion is a common traditional Chinese therapy in which burning Moxa is applied to affected body areas. This method has been employed for thousands of years to achieve certain medical objectives, such as pain relief or anti-bacterial and anti-inflammatory effects. Its therapeutic effectiveness has been demonstrated successfully both in research and clinical studies. However, this traditional approach may cause undesirable side effects, for example: 1) burning of Moxa produces by-products such as smoke and ash; 2) patients are at risk of being burnt; 3) the active ingredients of the Moxa leaf oil are volatile, odorous, unstable in air and easy to dissipate, and difficult to store and transport; 4) it is inconvenient to operate. These side effects limit its further high-potential and high-value applications.

This study is aimed at developing a multi-functional smart textile system that will adopt smart fabrics containing encapsulated Moxa oil integrated with thermally conductive materials to replace the conventional Moxa products. This will efficiently deliver the active ingredients of Moxa to a human body at optimum conditions, i.e., in a precise and controllable way, with maximum convenience and a high level of comfort. Doing so would solve the existing problems mentioned above. Both garment design skill and textile technology will be applied to Moxa Moxibustion textile to enhance the aesthetics and functionality. The smart garment performance will be assessed subjectively in a clinical trial and objectively by a number of instrumental methods.

INTRODUCTION

Moxa Moxibustion is a traditional Chinese method and common modality to apply burning Moxa leaf to affected body areas to achieve certain medical effects (Figure 1) [1]. In Chinese history, the earliest record of Moxa Moxibustion is from《左传》(Zuo Zhuan) [2]. China's famous medical books《皇帝内经》(Huang Di Nei Jing) and《伤寒杂病论》(Shang Han Za Bing Lun) have the records about the clinical theory of Moxa Moxibustion. Furthermore, a large amount of clinical evidence and research has demonstrated the effectiveness of Moxa Moxibustion on the human body. The principle of Moxa Moxibustion is that the main active substances—volatile Moxa oil—is released during burning Moxa leaves. In the meantime, the generated heat uses the expansion of skin pores to facilitate the absorption of the oil substances and promote blood circulation. However, the traditional approach may cause undesirable side effects, such as, conventional Moxa Moxibustion methods involve the burning of Moxa, which produces such by-products as smoke and ash and the risk of burning the patient. This may cause suffering and unpleasant experiences for patients. Some books even provide specific guidance on how to treat burns by Moxa Moxibustion. In addition, the active ingredients of the Moxa leaf oil are volatile, odorous, unstable in air and easy to dissipate, and it is difficult to facilitate their storage and transportation. Moreover, current commercial products of Moxa Moxibustion are inconvenient to mount, especially for positions at the back of the body, which require turning to assistants or specialists, and they are unable to either focus on acupuncture points or do multiple treatments at the same time (Figure 1a). A possible solution to this problem is to apply a Moxa oil ointment. Nevertheless, it is rarely used in practice due to its lack of thermal assistance. An elevated skin temperature could increase the effect of Moxa oil since the heating could expand particular blood vessels, increase the speed of blood flowing, enhance the recovery from inflammation, relax the muscles. These limit this method's further applications .

To address the above challenges, the proposed project intends to develop a smart garment system for Moxa Moxibustion treatment. This project will create a fabric with microcapsules containing Moxa oil with integrated conductive thermal materials to replace the conventional Moxa products and to solve the existing problems mentioned above.

APPROACH

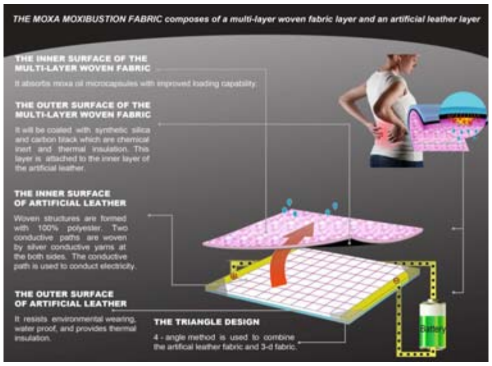

Figure 1: Architecture of Moxa moxibustion functional fabric

RESULTS AND DISCUSSION

The Moxa microcapsule emulsifiers that were characterized according to the stirring speeds, dosages, Tween80/Span80, microcapsule wall materials are shown in Figure 2a-2d. The SEM micrographs of the selected Moxa oil microcapsules are illustrated in Figure 2e. The developed Moxa oil fabric has demonstrated a competitive performance and feasibility in feature of Chinese medicine innovation and textile technology.

Gelatin-arabic gum microcapsules containing Moxa oil was prepared by complex coacervation firstly, along with its application to textile finishing using 2D resin and BTCA as crosslinking reagents were investigated with 100% cotton fabric, respectively. An optimized constitution of Moxa oil emulsion is very important since Moxa oil will aggregate into unstable flakes in aqueous solutions. With systematic experimentation, the optimized constitution of the emulsion is: 1) Highest concentration of the microcapsules with satisfying particle sizes were achieved with stirring speed of 1500 rpm during emulsification; 2) Emulsion with uniform particle sizes was achieved by using an optimized emulsifier dosage of 2%; 3) Better distribution of microcapsules resulted with HLB value of 9-10; 4) It was found that the microcapsules can be easily formed in large quantities when the concentration of the glutin-acacia based wall materials falls in the range of 0.5%-1.0%. The as-prepared microcapsules, with diameters of less than 10μm, have smooth surfaces and better uniformities, which render them suitable to attach to fabrics. The adhesion status provides the necessary chemical reaction environment for the microcapsules and the cross linkers. It can be seen from Figure 2f that few of the lost microcapsules were found after the laundering testing, indicating the microcapsules are anchored onto the fibers by the cross linkers. Further, improved performance was also observed in the anti-bacterial colibacillus and staphylococcus aureus experiment. Figure 2h shows the FTIR of the fabrics before and after the microcapsules treatments. The controlled-release effects were also studied and optimized for different wall materials and core materials, while the released amount of Moxa oil was less than 50% after 9 days. The controlled-release experiment proves that after immersing in normal saline for 24 hours under the constant temperature of 37°C, releasing amount of the microcapsules is less than 80%, thus the active compositions of Moxa still exist in the granules. In addition, the treated fabric demonstrated good anti-wrinkle properties. The wrinkle recovery angle of the microcapsules fabrics treated with 2-D resin and BTCA achieve 270° - 287° and fabric strength keeps 64% ~ 67%.

In the electric-heating fabric aspect, a formation thermal electric knitwear with proper combinations of different densities and different stitches of conductive stitches has been developed. This work is to investigate the knitwear with thermal function from a knitting technology perspective. The knitwear can provide heat to the multi-target locations. The advantages of the garment are flexible, ready to target, light-weight, washable, and suitable for repeatedly uses, etc. Analytical and empirical equations were developed to compute the resulted resistance of the conductive fabrics.

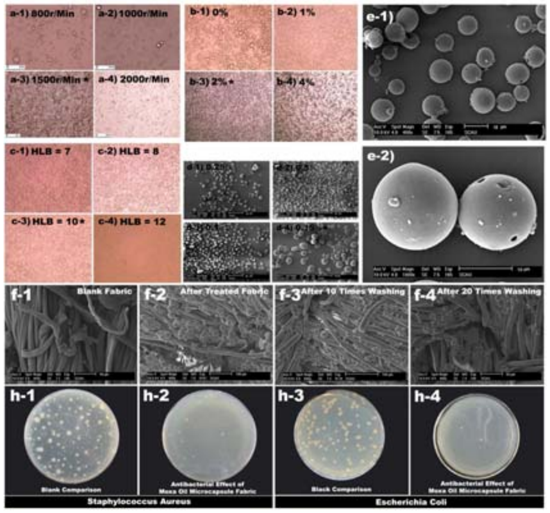

Figure 2: Moxa oil microcapsule

Analytical and empirical equations were developed to compute the resulted resistance of the conductive fabrics. The temperature of different heating pads can be set independently. Also, the conductive paths and the heating fabric pads can be made in fabric formation without external modification such as sewing. Figure 3 shows wearable electric heating knitwear (Right), the corresponding infrared image of the back of a nude human subject: (1) The temperature rise after the knitwear was applied to the human subject after 3 minutes; (2) and 20 minutes; (3) where the red and green indicates the high and low temperatures, respectively, the knitwear was removed; (4) the high temperature regions show that more blood flows to the skin surface of the body so as to alleviate the symptoms of the pains. A resistive network model for conductive knitting stitches is also shown (Left).

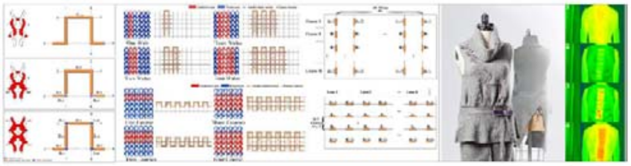

Figure 3: A resistive network model for conductive knitting stitches & wearable electric heating knitwear

CONCLUSIONS

The proposed project will result in potentially significant effects described by the following topical issues: textile in healthcare development, Chinese medicine innovation, and caring possibilities for a patient.

REFERENCES

[1] Lu, G. D. 1980. Celestial Lancets: A History and Rationale of Acupuncture and Moxa. Cambridge: Cambridge University Press.
[2] Zuo, M. Q. 2003. Chun Qiu Zuo Zhuan. Shangdong, Shandong Friendship Press.

ACKNOWLEDGMENT

Financial support for this study was provided by a grant from RGC Competitive Research Grant Hong Kong.

Dynamic Plantar Pressure Monitoring of Diabetic Patients Using Intelligent Footwear System Based on Fabric Sensor During Daily Activities

Kaiyang Mai[1], Lin Shu[1], Xiaoming Tao[1], Wingcheung Wong[2], Kafai Lee[3], Siuleung Yip[2], Anthony Waihung Shum[4], Wailam Chan[2], Chipang Yuen[2], Ying Li[1]
[1]Institute of Textile & Clothing, The Hong Kong Polytechnic University; [2]Department of Orthopaedics & Traumatology, Kwong Wah Hospital; [3]Diabetic centre, Department of Medicine and Geriatrics, Kwong Wah Hospital; [4]Department of Prosthetics & Orthotics, Kwong Wah Hospital
Contact: tctaoxm@inet.polyu.edu.hk Speaker: 11900738r@connect.polyu.hk

INTRODUCTION

Diabetes mellitus is a major issue in public health [1]. Diabetic peripheral neuropathy and foot ulceration in particular are major complications that can cause significant morbidity and mortality [2]. Prevention of foot ulceration development is better than cure. Therefore, it is highly desirable for the patients to have added artificial senses of pressure and signal them to protect the foot when abnormal high plantar pressure conditions occur. Intelligent Footwear System [3,4], developed and patented by the Hong Kong Polytechnic University, can fulfill this by providing both long-term monitoring and alarming function to the diabetic patient. Intelligent Footwear System is real-time, dynamic and specific that can be used during activities in daily. This “In-Shoe Intelligent Footwear System”, based on patented textile pressure sensing arrays developed by PolyU, measures, records and wirelessly transmits data of spatial and temporal plantar pressure distributions, in-shoe temperature and humidity, and 3-axis accelerations to a portable Smart-phone.

In this paper, two clinical trials were conducted in a regional hospital with specific multi-disciplinary care to diabetic foot problems in Hong Kong. Differences of peak plantar pressure were identified between ten healthy subjects and ten diabetic subjects in the first clinical trial. Peak plantar pressures of high risk diabetic patient with neuropathy were discussed in the second clinical trial. The main objectives of this research are to assess wearing comfort of Intelligent Footwear System and explore the differences of plantar pressure between healthy subjects and diabetic subjects during various daily-life activities.

APPROACH

10 healthy subjects (male, 56±9.5yrs, 167.4±5.0cm, 67.6±9.2kg) and a DM group of 10 diabetic patients without neuropathy (male, 55.8±10.3yrs, 165.2±4.4cm, and 71.2±10.0kg) were recruited in the first clinical trial. A diabetic patient with neuropathy (male, 59 years, 167cm, 64kg) participated in the second clinical trial. The foot size of each subject was measured by Chinese Adult Brannock Device. Sensory testing using 5.07 Semmes-Weinstein monofilaments (SWM) was performed on each subject to check whether there was neuropathy in diabetic subjects. Plantar pressures of eight plantar positions were recorded during walking using Intelligent Footwear System. The sensor positions [3] were shown in Fig.1: 1:Lateral heel; 2:Medial heel; 3:Lateral midfoot; 4:Medial midfoot; 5:4th and 5th metatarsal head; 6:2nd metatarsal head; 7:1st metatarsal head; 8:Hallux. Then the subjects were required to perform three activities: corridor walking (Fig.2), climbing up and going down a slope and stairs walking. All the pressure data were analyzed by statistical methods. Statistical analysis was carried out with SPSS 19.01® software (SPSS Inc.) An alpha level of 0.05 was chosen to assess statistical significance.

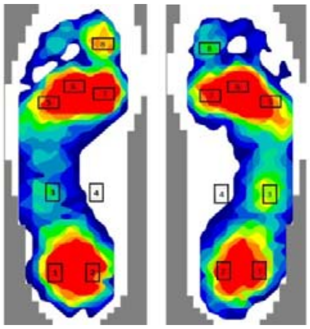

Fig. 1 Sensor Positions [3]; Fig. 2 Slope walking with Intelligent Footwear System.

RESULTS AND DISCUSSIONS

As can be seen in Fige.3, comparing plantar pressure over the same regions between two groups in the first clinical trial, the result of t-test showed the peak pressure on metatarsal 4-5 of left foot (Ls5) in going down slope were significantly higher (p=0.002) in

DM group (361.3±101.3 kPa) than H group (224.3±47.6 kPa).

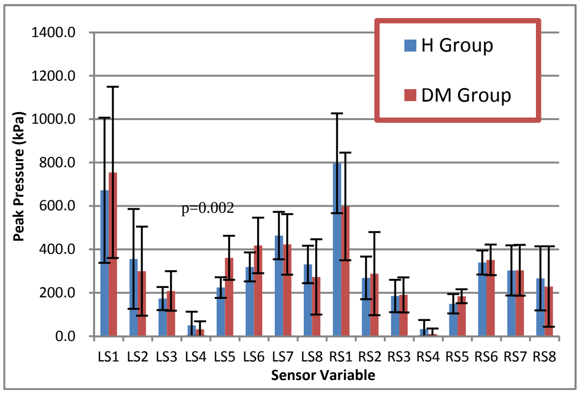

Fig. 3 Distribution of peak pressure in climbing down slope.

The regions with statistically significant high measured peak pressure coincided with the places where the patients may develop ulcers (LS5, left lateral forefoot). Data obtained from the Intelligent Footwear System were promising because the regions showing significant difference were the common sites of ulcerations in clinical cases.

Fig. 4 and Fig. 5 shows the foot photos of a high risk patient with neuropathy in the second clinical trial.


Fig.4 Dorsal foot of the patient; Fig. 5 Plantar foot of the patient.

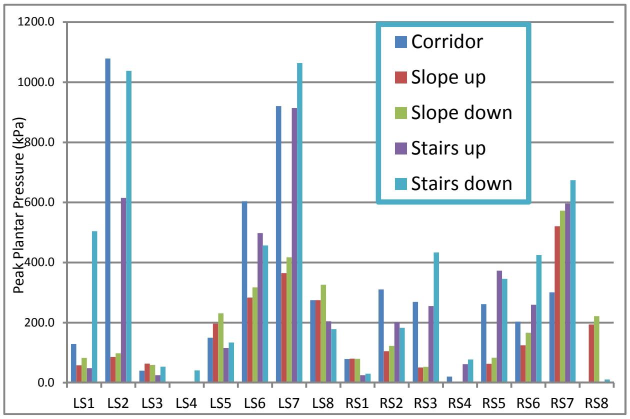

Fig. 6 Peak pressure distribution of the high risk patient.

As seen in Fig.6, peak pressure of his left foot was much higher than that of right foot in corridor walking, even larger than 900kPa, which was potentially dangerous for his left foot especially his medial side of left forefoot. In slope and stairs activities, the peak pressure was larger than 900kPa in medial side of left forefoot and larger than 700kPa in his medial side of right forefoot. It indicates that his left forefoot was in an unhealthy condition which needs protection, and right forefoot was dangerous which may affect the wounds. The recovery of normal pressure distribution may indicate the appropriateness of the amputation of toe instead of the metatarsal head so as to preserve the function. High risk patients should monitor and protect their normal foot and the other foot recovered from ulcers.

CONCLUSIONS

In this study, the regions with statistically significant high peak plantar pressure were compatible with the places where the patients may develop ulcers (lateral forefoot). Data obtained from the Intelligent Footwear System were promising as the regions showing significant difference were the common sites of ulcerations in clinical cases. For high risk diabetic patients, Intelligent Footwear System can monitor their plantar pressure during walking in activities of daily living in order to protect their foot.

ACKNOWLEDGMENT

The authors thank Hong Kong Research Grants Council (PolyU5272/11E), Innovation and Technology Commission (ITT/002/11TT) for funding as well as AdvanPro Ltd for assistance in fabrication of the intelligent footwear system.

REFERENCES

[1] Wild S, Roglic G, Green A, Sicree R, King H (2004). “Global prevalence of diabetes: estimates for 2000 and projections for 2030.” *Diabetes Care* 27 (5): 1047-53.

[2] JJ Duby, RK Campbell, SM Setter, White JR and KA Rasmussen (2004). “Diabetic neuropathy: an intensive review.” *American Journal of Health-System Pharmacy*. 61(2): 160-173

[3] L Shu, T Hua, YY Wang, Q Li, DD Feng, XM Tao (2010). “In-Shoe Plantar Pressure Measurement and Analysis System Based on Fabric Pressure Sensing Array.” *IEEE Transactions on Information Technology in Biomedicine*, 14(3): 767-775.

[4] L Shu, DD Feng, XM Tao (2010). “A wearable wireless electronic interface for textile sensors.” *Proceedings of IEEE International Symposium on Circuits and Systems (ISCAS)*: 3104-3107.

Wearable Sensors for the Prophylaxis of Lower Limb Pathologies

M. J. Abreu[1], A. Catarino[1], A. M. Rocha[1], F. Derogarian[2,3], R. Dias[2], J. M. da Silva[2,3], J. C. Ferreira[2,3], V. G. Tavares[2,3], M. V. Correia[2,3]

[1]Centro de Ciência e Tecnologia Têxtil, Departamento de Engenharia Têxtil, Universidade do Minho, Portugal; [2]Inesc Tec (formely INESC Porto); [3]FEUP, Rua Dr Roberto Frias, 4200-465 Porto, Universidade do Porto, Portugal
whiteman@det.uminho.pt

OBJECTIVE

In this paper a new wearable locomotion data capture system for gait analysis is presented. The system under development intends to help clinicians to detect and identify mobility impairments as well as to evaluate the effectiveness of surgical or rehabilitation intervention. The proposed system allows the measurement of kinematic and biomechanical parameters in a practical and comfortable weft knitted legging, in which the sensors are incorporated.

INTRODUCTION

Several techniques were proposed to capture and analyze human movement. The approach that is more popular is based on Vision. Cameras capture specific markers placed in predefined places on the human body in order to determine the spatial location [1]. Recent developments involve the measurement of human movement using inertial units equipped with accelerometers and gyroscopes which record kinematic variables [2]. These solutions are normally very expensive and complex, difficult to apply by the health care staff and also uncomfortable for the patient [1].

Figure 1 – Conventional sensors used for EMG and data recording.

RESULTS AND DISCUSSION

With the purpose of proposing a more comfortable solution for the wearer a new autonomous, real time monitoring wearable body sensor network for human locomotion data capture is under development. With this solution the patient will be able to dress it without help, or in the cases where it is not possible, the effort and complexity for dressing a patient will be dramatically reduced.

Figure 2 – Legging prototype made with a polyamide base yarn and silver yarn for communication and power lines.

The system is able to record inertial and surface electromyographic (sEMG) signals of the lower limbs for long time periods involving typical movement activities under everyday living conditions.

The recording is accomplished through a body sensor network where sensor nodes communicate with a central unit by wireless technology or using conductive embedded paths in the knitted fabric (Figure 2) [3,4]. The sensors and actuators are also incorporated in a specially designed legging produced in a full jacquard seamless weft circular knitting machine.

Regarding the sensors to be embedded in the legging, the biopotential parameters are the ones that are more successful in terms of reliability.

For that reason sEMG electrodes for measuring muscles essential for locomotion (*quadriceps femoris*, *biceps femoris*, *tibialis anterior* and *gastrocnemius medialis*) [6] were embedded in the knitted fabric, making use of the jacquard technology available on weft knitting machine (Figure 3, top).

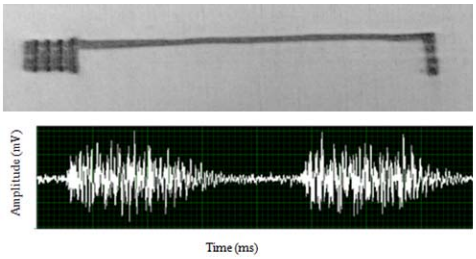

Figure 3 – Example of an sEMG electrode and path made with silver coated yarns and corresponding EMG signal for two voluntary contractions of *biceps brachii* muscle.

Two types presenting relatively good electrical properties have been used [7]: A) spun yarns with a mixture of polyester, and stainless steel fibres with linear resistances of 350 Ohm/m; B) and yarns made with twisted filaments, each one a polymeric filament covered with silver with linear resistances of about 30-40 Ohm/m. Tests made with conventional electrodes and textile based electrodes produced according to SENIAM recommendations in simultaneous measurements revealed an excellent correlation between them (Figure 3, bottom right) [6].

CONCLUSIONS

This paper presented a new solution that is under development with the objective of proposing an e-garment for monitoring lower limb movements and thus aid the health staff to assess disease or accident severity on human gait. A brief presentation was made regarding the body network, the textile based sensors embedded in the knitted fabric and the paths through which the communication and power is transferred to the sensor nodes. Several improvements are currently under development in order to achieve the most flexible and reliable system, namely power and data transfer using a single path, new textile based sensors and an efficient production process.

KEYWORDS: wearable sensors, e-textiles, weft knitted fabrics, conductive textiles, lower limb pathologies

ACKNOWLEDGMENTS

This work is financed by FEDER funds through the Competitive Factors Operational Program (COMPETE) and by national funds through FCT (Portuguese Foundation for Science and Technology) with the grant SFRH/BD/79762/2011 and the project PEst-C/CTM/U10264/2011.

REFERENCES

1. Iezzoni, L.I., O'Day, B. More than Ramps: A Guide to Improving Health Care Quality and Access for People With Disabilities. Oxford University Press (2005).
2. Yuting, Z., Markovic, S., Sapir, I., Wagenaar, R. C., Little, T. D. C. Continuous functional activity monitoring based on wearable tri-axial accelerometer and gyroscope. 5th International Conference on Pervasive Computing Technologies for Healthcare (Pervasive Health), 370–373, 2011.
3. Derogarian, F., Ferreira, J. C., Grade Tavares, V. M. A Routing Protocol for WSN Based on the Implementation of Source Routing for Minimum Cost Forwarding Method. Fifth International Conference on Sensor Technologies and Applications, Jens M. Hovem, et al. (eds), 85–90, 2011.
4. Ye, F., Chen, A., Lu, S.. Zhang, L. A scalable solution to minimum cost forwarding in large sensor networks. Proceedings of the Tenth International Conference on Computer Communications and Networks, 304–309, 2001.
5. Vila-Chã, C. Electrophysiological assessment of neuromuscular adaptations to training. PhD thesis in Biomedical Engineering, University of Porto, Faculty of Engineering, 2012.
6. Barros, L., Dias, M. J., Carvalho, H., Catarino, A. P. Aquisição de sinais electromiográficos recorrendo a eléctrodos em substratos têxteis. 4º Congresso Nacional de Biomecânica, Coimbra, 2011.
7. Zambrano, A.. Silva, J. M. Signal Integrity and Interconnections Test on Technical Fabrics, 18th IEEE Int. Mixed Signal, Sensors and Systems Testing Workshop, 2012.

Characterization of Thermal Comfort of Weft-Knit Ballistic Nylon/Wool Fabric

Rana Mahbub, Lyndon Arnold, Lijing Wang
School of Fashion and Textiles, RMIT University, Brunswick, VIC 3056, Australia
lijing.wang@rmit,edu.au; s3183907@student.rmit.edu.au

INTRODUCTION

Knitted fabric structures have been used as stab resistant material to enhance the strength and damage tolerance of body armour [1, 2]. Most ballistic body armours used today consist of multiple layers of fabric, and are made of expensive high-performance fibres such as Kevlar, Zylon, Twaron, or Spectra [1, 2]. Several knitted structures, including single jersey, plush, interlock and 1×1 rib, have been investigated to understand their stab resistant performance. Flambard [2] developed a plush and single jersey knitted fabric using an 18 gauge circular knitting machine. The fabrics were produced using spun yarns of Zylon and Kevlar®29 and tested for stab resistance using a single-bladed knife. The 2640 g/m^2 knitted fabric passed the test with 25 joules stab energy resistance. Alpyildiz [1] proposed a new style of knitted structure fabric called "double-face" and "double-faceInlay" for stab and cut resistance by using a flat knit machine. The yarns used were similar to those used by Flambard [2]. This study proved that the new "double-face" and "double-faceInlay" fabrics provided better stab resistance than the plush and jersey knitted structures. However, the thermal comfort properties of the knitted ballistic fabric were not examined. Traditional protective fabrics used in most stab protection panels are heavy, bulky, inflexible, and uncomfortable to wear, especially in hot-humid climates [3]. In this study, the knitted fabric structure was manufactured based on the Flambard knitted single jersey fabrics [2], and wool has been incorporated in the fabric to enhance the thermal comfort performance. In addition, ballistic nylon was used to reduce the fabric cost. The designed knitted fabric was evaluated for thermal comfort using sweating guarded hot-plate (SGHP) and moisture management tester (MMT). The SGHP was used to simulate the heat and moisture transfer processes that occur between the skin and the fabric. The MMT was used to measure liquid moisture transport behaviour of the fabric including the liquid absorbency, liquid spreading and transport of water through the fabric.

MATERIAL DESIGN

The weft-knitted fabric was produced using a flat knitting machine, Shima Seiki SES-S.WG®, and its CAD program. The yarns used in this study were 93 tex ballistic nylon filament and 41 tex wool yarn.

EXPERIMENT

The fabric thickness, mass per unit area, moisture management as well as thermal and vapour resistance were measured. The testing methods used were AS 2001.2.15-1989 for fabric thickness, AS 2001.2.13-1987 for mass per unit area, AATCC TM 195-2009 for moisture management properties and ISO 11092:1993 for thermal and water-vapour resistance. The fabric specimens were conditioned for 24 hours under standard conditions of 65% RH and 20°C, according to the Australian Standard AS 2001.1-1995.

MOISTURE MANAGEMENT TESTER (MMT)

The moisture management properties were tested by placing an 80mm × 80mm test specimen between two horizontal electrical sensor rings. The test solution was located in the centre of the sensor rings. The water solution was dripped freely onto the top surface of the fabric and it then transferred throughout the fabric. As the solution moved, the moisture behaviour of the test specimen was measured and recorded.

SWEATING GUARDED HOT-PLATE

The thermal resistance test measures the energy required to maintain a constant temperature of 35°C on the surface of the measuring plate [4]. The test specimens were cut as squares 350×350 mm^2 and three specimens were tested. Both thermal measurement unit temperature and the thermal guard temperature were set to 35.0°C. The air temperature was 20.0°C and the relative humidity (RH) was 65%. The air speed was 1 m/sec. The thermal resistance for the fabric was calculated by measuring the heat temperature between the plate surface and the surrounding ambient air. The value of the arithmetic mean of three reading results from each fabric was calculated according to the Standard.

The water-vapour test measured the power required to keep a constant vapour pressure between the top and the bottom surface of the fabric [4]. The test recorded the average power required to keep the measuring unit at its selected temperature based on a 15 minute integration. The test atmosphere was 35.0°C and 40% relative humidity for the water vapour test measurement unit. The thermal guard temperature was set to 35.0°C and the air speed was 1 m/sec. The water-vapour resistance results were calculated by the vapour pressure difference between the saturated plate surface and the ambient air according to the Standard.

RESULTS AND DISCUSSION

The plated nylon/wool knitted fabric was produced at 18 gauge with 30 knitted fabric quality (tightness). The fabric structure is shown in Figure 1. The ballistic nylon has been knitted on the front face and wool yarn plated on the back of the fabric.

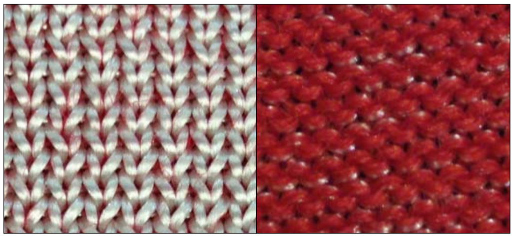

Figure 1. Fabric structure, outer and inner surfaces

The fabric results in Table I show that the nylon/wool fabric is heavy and has achieved a good thermal resistance value with 0.021 m² K/W. Data indicates that the developed fabric can transfer heat away, hence can be comfortable in moderate activity. According to the Standard, the thermal resistance for heavy-weight fabrics should be between 0.02 and 0.025 m² K/W. Likewise, the water-vapour resistance of the nylon/wool is 6.2 m² Pa/W. Therefore, the fabric can be considered as a comfortable and breathable fabric. According to Horrocks [5], if a fabric achieves a value less than 20m² Pa/W, it can be considered as breathable and comfortable at a moderate activity rate.

Table I. Fabric test results

Thickness (mm)	Mass per unit area (g/m²)	Thermal resistance (R_{ct}) m² K/W	Water vapour resistance (R_{et}) m² Pa/W
1.2	530	0.021	6.2

For MMT tests, the ballistic nylon face was on the outer-to-skin surface (B_s) and the plated wool was located on the next-to-skin surface (T_s). The moisture measurement properties for the nylon/wool are summarized in Table II. The results show that the wetting time between the two surfaces varied. The low wetting time and high absorption rate of the wool surface suggest that the wool surface can absorb water faster than the ballistic nylon surface. Hence the wool face is next-to-skin for better moisture management. In addition, the wet-out radius for T_s was lower than B_s, which means T_s has a moderate ability to transfer the absorbed water to the outer surface.

Table II. Fabric MMT Results

	T_S	**B_S**
Wetting Time (s)	15.2	30
Absorption Rate (%/s)	37.3	25.5
Wet-out Radius (mm)	15	19
Spreading Speed (mm/s)	1.3	2.5
Accumulative One-Way Transport (%)	145.8	
OMMC	0.4	

Figure 2 shows the wet-out radius difference between the two surfaces. The result reveals that the nylon/wool fabric has a relatively large spreading rate (2.5 mm/s) and large wet-out radius (19 mm) on the B_s, indicating that liquid can spread quickly, transfer easily and dry quickly on the outer surface of the fabric. The fabric accumulative one way transport capacity (OWTC) was 145.8%. Also the overall moisture management capacity (OMMC) was 0.4. Therefore, the OMMC and OWTC grade was good, indicating that the nylon/wool knitted fabric has moderate water penetration between both surfaces.

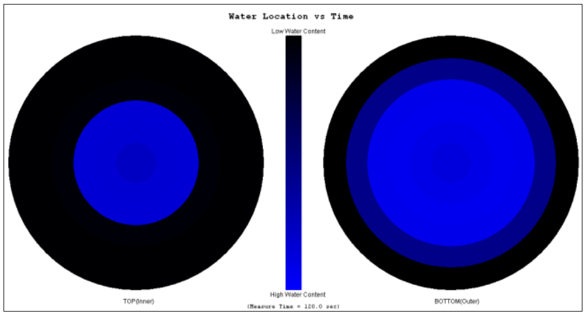

Figure 2. Fabric moisture transport

CONCLUSIONS

A new weft-knitted fabric made from ballistic nylon and wool was developed to evaluate its thermal comfort and moisture management performance. The results reveal that the new fabric has good thermal and water-vapour resistance. Furthermore, plating wool into the fabric produced good moisture absorbency and transport properties. Further research is being carried out to evaluate other properties of the fabric, including stab resistance protection.

KEYWORDS

Thermal comfort, knitted fabric, moisture management, ballistic nylon/wool blend

ACKNOWLEDGMENT

Acknowledges King Abdulaziz University for scholarship

REFERENCES

1. Alpyildiz T, Rochery M, Kurbak A and Flambard X. Stab and cut resistance of knitted structures: a comparative study. *Textile Research Journal*. 2011, 81: pp. 205-14.
2. Flambard X and POLO J. Stab resistance of multi-layers knitted structures: Comparison between para-aramid and PBO fibers. *Journal of Advanced Materials A*. 2004, 36: pp. 30-35.
3. Tavana H, Wang L, Golozar M and Ebrahimzade M. An Investigation on the Piercing Resistance of Abrasive Particle Coated Fabrics. *The 1st International and the 7th National Iranian Textile Engineering Conference*. Rasht, Iran: ACECR-Amirkabir University of Technology Branch, 2009.
4. Gibson P, Auerbach M, Giblo J, Teal W and Endrusick T. Interlaboratory Evaluation of a New Sweating Guarded Hot Plate Test Method (ISO 11092). *Journal of Building Physics*. 1994, 18: pp. 182-200.
5. Horrocks AR, Subhash A and Subhash CA. *Handbook of Technical Textiles*. CRC Press, 2000.

Optimization of Fibre Composition in Nonwoven Air Filter Media

R. Chattopadhyay, Dipayan Das, Arun Kumar Pradhan
Department of Textile Technology, Indian Institute of Technology Delhi, New Delhi-110016, India
rchat@textile.iitd.ac.in

INTRODUCTION

Nonwoven air filter media are extensively used for separation of hazardous contaminants from air streams. The products are quite diverse and range from heating, ventilation, and air-conditioning filters to automotive cabin filters to vacuum cleaner filters, dust bags, facemasks, and respirators [1]. The nonwoven air filter media are generally evaluated for filtration efficiency and pressure drop. It is always desirable for such media to exhibit high filtration efficiency as well as low pressure drop. These two requirements are however contradictory in nature. As known, a filter medium consisting of finer fibres exhibits higher filtration efficiency than that of coarser fibre, but the latter registers less pressure drop than the former [2]. The filter media composed of either finer or coarser fibres cannot therefore offer high filtration efficiency and low pressure drop simultaneously. To derive the best from the both, the nonwoven filter media should be prepared from an appropriate combination of finer and coarser fibres. However, there is no analytical expression available for designing such filter media. This is often required by the product development engineers and scientists working in the area of nonwoven air filters. In this work, an attempt has been made to optimize fibre composition in nonwoven air filter media to achieve enhanced filtration performance.

MATERIALS AND METHODS

In this work, a series of nonwoven air filter media was developed by using polypropylene fibres of three different linear densities viz. 2.5 denier, 6 denier and 15 denier following simplex lattice design principle. The lay-out of this design is displayed in Figure 1. Here $x_{2.5}$, $x_{6.0}$, and $x_{15.0}$ stand for the mass proportion of fibres of 2.5 denier, 6.0 denier, and 15.0 denier finenesses, respectively. The fibres were mixed in different proportions accordingly and processed on a laboratory based nonwoven line consisting of fibre opening, roller carding, cross-lapping and needle punching machines. All the nonwoven fabrics were produced under identical processing condition so as to maintain practically same basis weight and solid volume fraction.

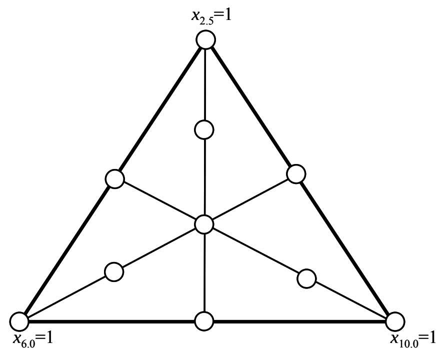

Figure 1: Lay-out of a simplex lattice design

The nonwoven fabrics were tested for filtration efficiency and pressure drop by using an air filter test rig developed in house. The samples were exposed to a known quantity of dust and the filtration efficiency was calculated by using thy following formula: E =1- ($N_{\text{down}}/N_{\text{up}}$), where E stands for filtration efficiency, N_{up} denotes concentration of dust particles at upstream side, and N_{down} indicates concentration of dust particles at downstream side. The dust particles of interest were of 10 micron diameter. The pressure drop across the test media was measured by using a digital differential manometer of 1 Pa resolution. The quality factor of the nonwoven filter media was calculated based on filtration efficiency and pressure drop as mentioned below: $q_F = -\ln(1-E)/\Delta P$, where q_F stands for quality factor and ΔP refers to pressure drop across the media. The results of experiments were analyzed by response surface methodology using Design-Expert® software version 8.

RESULTS AND DISCUSSION

The filtration efficiency of the nonwoven air filter media was determined. The experimental data were used to fit a special cubic model and the following expression was obtained

$$\begin{aligned} E = {} & 76.29\,g_{2.5} + 69.81\,g_{6.0} + 52.13\,g_{15.0} + 6.58\,g_{2.5}\,g_{6.0} + 35.22\,g_{6.0}\,g_{15.0} + \\ & + 27.93\,g_{15.0}\,g_{2.5} + 17.46\,g_{2.5}\,g_{6.0}\,g_{15.0}. \end{aligned}$$

Here, all the single as well as interaction effects were found to be positive, registering a synergy between fibre components. It means a binary or ternary blending of fibres of different finenesses resulted in higher filtration efficiency than would have expected just by averaging the filtration efficiencies of the corresponding pure blends. The fibres of 2.5 denier fineness contributed maximum to the filtration efficiency, followed by the fibres of 6 denier fineness and 15 denier fineness, respectively. The interaction effect was found to be the highest between the fibres of 6 denier & 15 denier finenesses, followed by the fibres of 15 denier & 2.5 denier finenesses and the fibres of 2.5 denier & 6 denier finenesses. It can be observed that if maximum filtration was desired alone, a pure blend of fibres of 2.5-denier fineness would have been chosen. The results of analysis of variance showed that the aforesaid model was significant at a very small level of significance (P-value<0.0001). The coefficient of determination between the predicted and measured filtration efficiencies was found as 0.9900.

The nonwoven air filter media were tested for their pressure drop. The experimental data were used to obtain the following expression

$$\begin{aligned}\Delta P = 8.58\, g_{2.5} + 4.09\, g_{6.0} + 1.83\, g_{15.0} - 0.79\, g_{2.5}\, g_{6.0} - 2.33\, g_{2.5}\, g_{15.0} \\ - 0.45\, g_{6.0}\, g_{15.0} - 1.16\, g_{2.5}\, g_{6.0}\, g_{15.0}.\end{aligned}$$

It can be observed that all the single effects were positive, whereas all the interaction effects were negative. This is an indicative of the fact that a binary or ternary blending of fibres of different finenesses resulted in lower pressure drop than would have expected just by averaging the pressure drops of the corresponding pure blends. The fibres of 2.5 denier fineness contributed maximum to increase the pressure drop across the media, followed by the fibres of 6 denier and 15 denier finenesses. With a view to reduce the pressure drop across the media, the interaction effect was found to be highest between fibres of 15 denier & 2.5 denier finenesses, followed by fibres of 2.5 denier & 6 denier finenesses and 6 denier & 15 denier finenesses. It can be observed that if minimum pressure drop was desired alone, a pure blend of 15-denier fibres would have been chosen. The results of analysis of variance showed that the model was significant at a very small level of significance (P-value < 0.0001). The coefficient of determination between the predicted and experimental pressure drops was found as 0.997.

The quality factor of the nonwoven filter media was determined and the experimental data were used to fit the following expression

$$\begin{aligned}q_F = 0.1674\, g_{2.5} + 0.2932\, g_{6.0} + 0.4064\, g_{15.0} - 0.0238\, g_{2.5}\, g_{6.0} - 0.0793\, g_{2.5}\, g_{15.0} \\ + 0.2889\, g_{6.0}\, g_{15.0} + 0.7645\, g_{2.5}\, g_{6.0}\, g_{15.0}\end{aligned}$$

It can be observed that all single effects were positive. Also, the interactions effect between fibres of 6 denier & 15 denier finenesses and the interaction effect accounting for the ternary blending of three components were positive. This means a binary blending of 6-denier and 15-denier fibres or a ternary blending of fibres of three different finenesses resulted in higher quality factor than would have expected just by averaging the quality factors of the corresponding pure blends. But, the interaction effects between the fibres of 2.5 denier& 6 denier finenesses and between the fibres of 2.5 denier & 15 denier finenesses were negative. This is an indicative of the fact that a binary blending of 2.5-denier fibres and 6-denier or 15-denier fibres produced lower quality factor than would have expected just by averaging the quality factors of the corresponding pure blends. The fibres of 15 denier fineness contributed maximum to the quality factor, followed by the fibres of 6 denier and 2.5 denier finenesses. The results of analysis of variance showed that the model was found to be significant at a very small level of significance (P-value < 0.0001). The coefficient of determination between the predicted and experimental quality factors was found as 0.990. Figure 4 plots the contours of quality factor. It can be observed that a higher quality factor could be achieved with higher proportion of coarser fibres in a blend of 6-denier & 15-denier fibres. It thus leaves a scope for further enhancement of quality factor by selecting an appropriate blend of fibres of 6 denier & 15 denier finenesses.

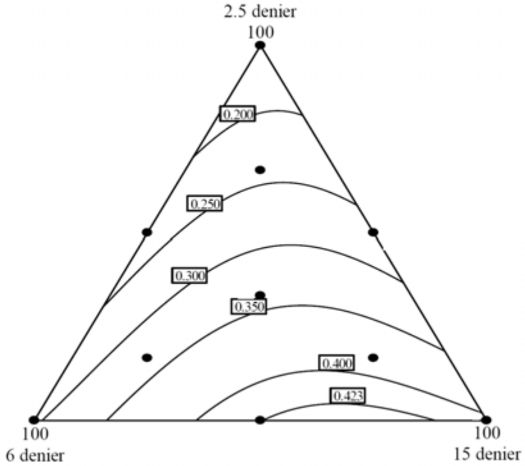

Figure 2: Contour plot of quality factor

The response surface equation of quality factor was used to determine an optimum blend of fibres that would enhance the filtration performance of nonwoven filter media. It was predicted that a binary blend (70/30) of 15-denier & 6-denier fibres would lead to highest quality factor of 0.433 Pa^{-1}. In order to verify this, a real nonwoven material was prepared from the same fibre composition and evaluated for filtration performance. The quality factor of this nonwoven material was determined as 0.425 Pa^{-1}.

CONCLUSION

A simplex lattice design along with response surface analysis was employed for determining optimum fibre composition for nonwoven air filter media. A set of expressions was obtained for predicting the filtration efficiency, pressure drop, and quality factor as a function of proportion of fibres of different finenesses. The predicted results were found to correlate well with the experimental results. The fibres of different finenesses registered a synergistic effect on the filtration efficiency of nonwoven filter media. Also, a binary or ternary blending of fibres of different finenesses resulted in lower pressure drop than would have expected just by averaging the pressure drops of the corresponding media made from 100% single component fibre. The optimal design of nonwoven filter media corresponded to a binary (70/30) blend of 15-denier & 6-denier fibres. Nonwoven material prepared from this composition registered highest quality factor of 0.425 Pa^{-1}.

REFERENCES

[1] Hutten, I. M. *Handbook of Nonwoven Filter Media*, Elsevier Ltd., 2007.
[2] Payen, J., Vroman, P., Lewandowski, M., Perwuelz, A., Callé-Chazelet, S., and Thomas, D. *Textile Research Journal*, 80, 1948-1959, 2012.

Graft Co-Polymerization of Acrylic Acid on Nylon 6 Knitted Fabric Using Redox Systems

Farzad Mohaddes, Stanley MacArthur Fergusson, Lijing Wang
School of Fashion and Textiles, RMIT University, Brunswick, VIC 3056, Australia
s3266821@student.rmit.edu.au

SYNOPSIS

Vinyl containing monomers have been recognized as potential grafting agents on polyamides through radical co-polymerization. Potassium persulphate/ copper sulphate pentahydrate ($K_2S_2O_8/CuSO_4.5H_2O$) redox system was used to form acrylic acid free radicals capable of making new covalent bonds with nylon 6 backbone. In this paper, the influences of effective factors on the rate of acrylic acid grafting on nylon 6 fabrics were investigated.

INTRODUCTION

Graft co-polymerization of vinyl containing monomers onto nylon 6 was previously investigated for different purposes such as enhancing dyeability and hydrophobicity, and intensifying thermal resistance as well as moisture regain [1-3]. Mosleh grafted 2-ethyl methacrylate phosphoric acid onto nylon 6 fabric using the $K_2S_2O_8/CuSO_4$ system as reaction initiators [3]. Bhattacharya et al. reviewed different means of grafting, including grafting initiated by chemicals and by radiation technique, photochemical grafting, plasma radiation induced grafting, and enzymatic grafting [4].

In the current work the basic vinyl containing monomer, acrylic acid, was chemically grafted onto nylon 6 knitted fabric using a reaction initiator system, $K_2S_2O_8/CuSO_4$. It was assumed that successful grafting of such vinyl containing monomer can be considered as a reference procedure for grafting more complex vinyl containing structures with different physical and chemical properties to nylon polymeric structure, including flame retardant effect, higher moisture regain, and increased fastness to wash.

EXPERIMENTAL

Pretreatment

Nylon fabric samples (0.5 g) were first pretreated with 20% w/w formic acid solution for different periods between 0.5 and 4 hours, then washed, and dried in the conditioning room (20^{o}C and RH 65%) for 2 days.

Graft copolymerization

The pretreated samples were immersed in hermetically closed Pyrex containers containing different monomer concentrations between 1.16 and 2.89 (mol/L), $K_2S_2O_8$ concentrations between 0 and 2.77×10^{-2} mol/L, and $CuSO_4.5H_2O$ concentrations between 0 to 2.67×10^{-2} mol/L. Containers containing the materials were heated in a thermostatically controlled bath at different temperatures (55, 65, 75°C) for a specific period. The grafted samples were thoroughly washed with 2 g/l nonionic detergent solution at 55°C for 30 minutes. Washed fabrics were rinsed using warm and then cold water, and finally extracted with acetone to remove any residual homopolymer. The samples were dried and conditioned for 4 days, and the graft yield was calculated as follows:

$$G0 = \frac{(Wg - W0)\times 100}{W0}$$

Where, G0 is the graft yield referred to the untreated sample; W_0 is the initial sample weight; and Wg is the grafted sample weight [3].

RESULTS AND DISCUSSION

Effect of time of pretreatment with formic acid solution

The highest yield of grafting, 46%, was achieved for the fabric pretreated with formic acid solution 20% w/w after 3 hours, and no further increase in graft yield was observed after 3 hours.

Effect of cupric ion concentration

The effect of incorporating different concentrations of copper sulphate (0, 0.0667, 0.0133, 0.02, 0.0267 mol/L) as an anti homo-polymerization agent upon grafting acrylic acid monomer onto pretreated fabric was investigated and the highest graft yield of 46% was also attained in the presence of 1.33×10^{-2} mol/L.

Effect of monomer concentration

The yield of grafting acrylic acid onto nylon 6 knitted fabric was studied using different concentrations of monomer, and the results are shown in Fig. 1.

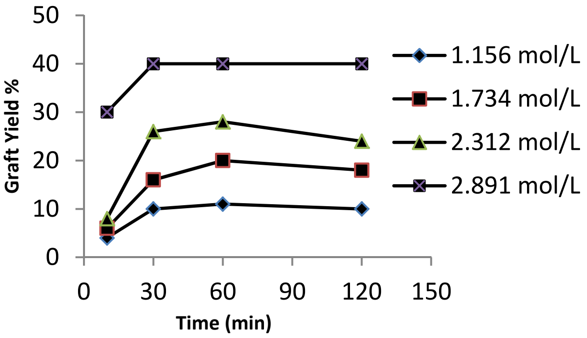

Fig. 1. The effect of acrylic acid concentration ranged between 1.156 to 2.891 mol/L on the rate of grafting at 65°C; $K_2S_2O_8$ concentration: 6.16×10^{-3} mol/L; $CuSO_4.5H_2O$ concentration: 6.67×10^{-3} mol/L; Liquor ratio: 1:100

Effect of potassium persulphate concentration

The rate of grafting is also subject to the oxidizing agent, potassium persulphate, concentration. The highest yield of grafting, 44%, was achieved at $K_2S_2O_8$ concentration 1.85×10^{-2} mol/L at 65°C after 1 hour; monomer concentration: 2.312 mol/L; $CuSO_4.H_2O$ concentration: 1.33×10^{-2} mol/L; and Liquor ratio: 1:100.

Effect of time and temperature

The graft copolymerization reaction of acrylic acid onto nylon 6 knitted fabrics was carried out at different temperatures (55, 65, and 75°C) within different periods 30–120 min; monomer concentration: 2.312 mol/L; $k_2S_2O_8$: 9.24×10^{-3} mol/L; $CuSO_4.5H_2O$ concentration: 6.67×10^{-3} mol/L. It was observed that the physical properties of treated fabrics were drastically affected at the temperatures above 65°C.

FTIR analysis

Graft co-polymerization of acrylic monomer on nylon 6 backbone was confirmed using Fourier transform infra-red spectroscopy (FTIR) in the range between 650 and 4000 cm^{-1}, as shown in Fig. 2. In the spectrum of grafted nylon 6, the peak at 1730 cm^{-1} is attributed to C=O str, and the existence of a broad acidic peak, between 2400-3500cm^{-1}, confirms the addition of acrylic acid OH group to the nylon 6 chemical structure. Moreover, the disappearance of one of the acrylic acid peaks present at 984 cm^{-1} from the grafted nylon 6 spectrum is attributed to the replacement of vinyl structure with free radicals formed during the graft process [5].

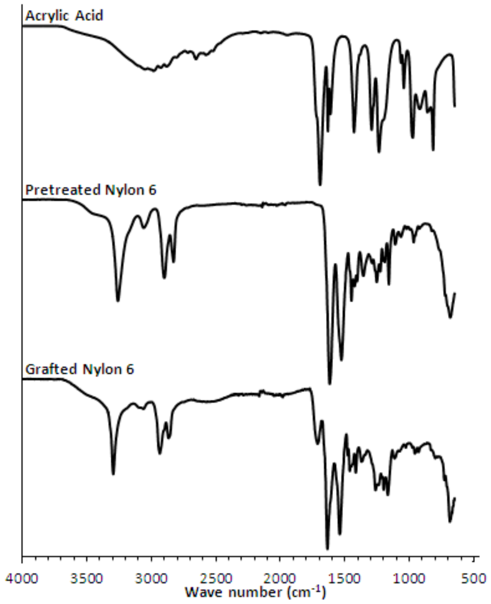

Fig. 2. FTIR spectra of nylon 6 fabrics (pretreated with formic acid solution, acrylic acid, and grafted nylon 6)

CONCLUSIONS

The factors influencing acrylic acid co-polymerization on nylon 6 fabric were investigated and the highest rate of grafting, 46%, was achieved. The most desirable experimental results were obtained at: monomer concentration: 2.312 mol/L; $k_2S_2O_8$ concentration: 1.85×10^{-2} mol/L; $CuSO_4$. $5H_2O$ concentration: 1.33×10^{-2} mol/L; grafting temperature: 65°C, and time of grafting: 1 hour. The highest yield of grafting was obtained after a pretreatment process on nylon 6 fabric using formic acid 20% (v/v) for 3 hours at 55°C. In addition to graft yield values obtained from the weight difference between the ungrafted and grafted substrates, successful graft co-polymerization of acrylic acid onto nylon 6 was also verified through FTIR analysis.

KEYWORDS

Grafting, co-polymerization, acrylic acid, nylon 6

REFERENCES

[1] Yang, H.; Yang, C. Q.; He, Q., Polymer Degradation and Stability, (2009) 94, 1023.
[2] Kolhe, S. M.; Kumar, A., Radiation Physics and Chemistry, (2007) 76, 901.
[3] Mosleh, S., Journal of Applied Polymer Science, (2000) 77, 1357.
[4] Bhattacharya, A.; Misra, B. N., Progress in Polymer Science, (2004) 29, 767.
[5] Pavia, D. L.; Lampman, G. M., Introduction to spectroscopy: a guide for students of organic chemistry, Harcourt Brace College Publishers: (1996).

Multifunctional Cotton Fabric Using TiO_2/SiO_2 Nanocomposite

Esfandiar Pakdel[1], Walid A. Daoud[2], Xungai Wang[1]

[1]Australian Future Fibres Research and Innovation Centre, Institute for Frontier Materials,
Deakin University, Geelong, 3220, Victoria, Australia
e.pakdel@research.deakin.edu.au, xungai.wang@deakin.edu.au
[2]School of Energy and Environment, City University of Hong Kong, Tat Chee Avenue,
Kowloon, Hong Kong, wdaoud@cityu.edu.hk

ABSTRACT

Cotton fabrics were treated with TiO_2/SiO_2 nanocomposite sols at ambient temperature. Three molar ratios of Ti/Si including 1:0.4, 1:1 and 1:2.3 were employed to prepare the sols. Tetra ethylorthosilicate (TEOS) and titanium tetraisopropoxide (TTIP) were used as the precursors of Si and Ti, respectively. The finishing step of samples was carried out based on the dip-pad-dry-cure process. UV-protection and self-cleaning were evaluated based on the Ultraviolet Protection Factor (UPF) and coffee stain removal under UV. The surface morphology of coated samples was analyzed by SEM images. It was observed that TiO_2/SiO_2 coated fabrics showed higher performance in UV-absorption and self-cleaning in comparison with TiO_2 coated samples.

KEYWORDS: Cotton, TiO_2, self-cleaning, UPF, sol-gel

INTRODUCTION

The role of nanoscience in the human's daily life is increasing. Textile as one of the longest-standing industries has a lot of potential to employ the advantages of new sciences [1]. Self-cleaning, UV protection, antimicrobial activities, and changing the wettability are among the most important features which can be imparted to textiles using nanoscience [1, 2]. Titanium dioxide (TiO_2) has extensively been used to accommodate the necessity of having novel values in textiles. TiO_2 as an important semiconductor is excited under UV producing pairs of negative electrons and positive holes. These products in turn react with oxygen and water molecules forming super oxide anions and hydroxyl radicals, respectively [3].

There are several main approaches to functionalize textiles. Among them, the sol-gel process has been introduced as a versatile approach to functionalize textiles [1, 4]. Self-cleaning cotton and wool have been devised using the sol-gel method [2]. Different parameters that affect the features of functionalized wool through the sol-gel method have also been discussed [2]. Application of nano TiO_2 (Degussa-25) stabilized by cross-linking agents was reported to be effective to impart new characters to wool [1]. The synergistic impact of silica addition on the self-cleaning property of wool had already been demonstrated [5].

This research is aimed at improving the functionality of nano titanium dioxide particles on textiles through the use of TiO_2/SiO_2 nanocomposite as the finishing system. In this study, fabrics were treated with TiO_2/SiO_2 composite systems to examine the impact of SiO_2 presence and its concentration on self-cleaning and UV-protection features.

MATERIALS AND METHODS

Cotton fabric with a fabric mass of 135 g/m^2 was used as substrate. Titanium tetraisopropoxide (TTIP), nitric acid, acetic acid and water were used to devise the TiO_2 sol at 60°C. SiO_2 sol was prepared from tetraethylorthosilicate (TEOS) in acidified water (pH=3). The sols were mixed based on different molar ratios of TiO_2/SiO_2 to prepare the composite sols. Cotton samples were immersed in an impregnating bath containing TiO_2/SiO_2 sol. The additional uptake of sols from samples was removed by an automatic padding machine. The samples were dried and cured at 80° and 120°C, respectively. SEM images were taken by KYKY-EM3200 (China).

RESULTS

Coffee stain removal was used as a scale to understand the photocatalytic activities on the surface of cotton fabrics. A droplet of coffee stain with concentration of 12g/L was located on the surface of fabric. The stained samples were exposed to UV and the color change was monitored at different intervals. Figure 1 demonstrates that after 10 h of UV illumination, the coffee stain can be removed from the surface of cotton coated with TiO_2/SiO_2 1:2.3. This is while the coffee stain still remains on TiO_2 coated fabric. It can obviously be seen that through increasing the concentration of silica in the impregnating bath, the self-cleaning function on the fabrics has significantly improved.

The UV-absorption feature was also studied based on the UPF rate of fabrics (Figure 2). In this study, the UPF of fabrics was measured based on the Australian/New Zealand Standard AS/NZS 4399:1996 standard. It can be seen that after coating pristine cotton with nano titanium dioxide particles the UV-protection property has improved. The UV-protection factor increased to around 42 which is a suitable rate for daily outfits. Based on the obtained results, samples treated with TiO_2/SiO_2 1:2.3 nanocomposite showed 15.68% higher UV absorption in comparison with TiO_2 treated samples. Figure 3 shows the SEM images of coated fabrics demonstrating an even distribution of nanoparticles.

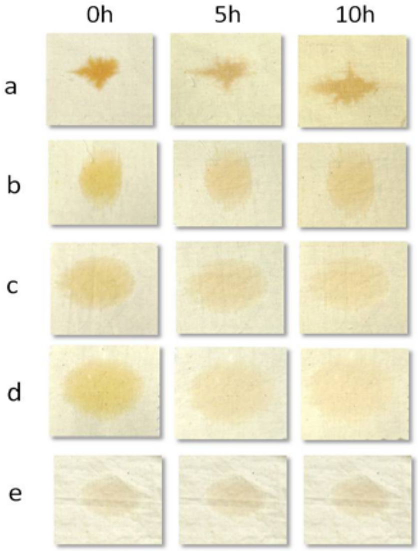

Fig 1: Coffee stain removal on cotton under UV: cotton coated with (a)TiO_2, (b)TiO_2/SiO_2 1:0.4, (c)TiO_2:SiO_2 1:1, (d) TiO_2/SiO_2 1:2.3, and (e) pristine cotton.

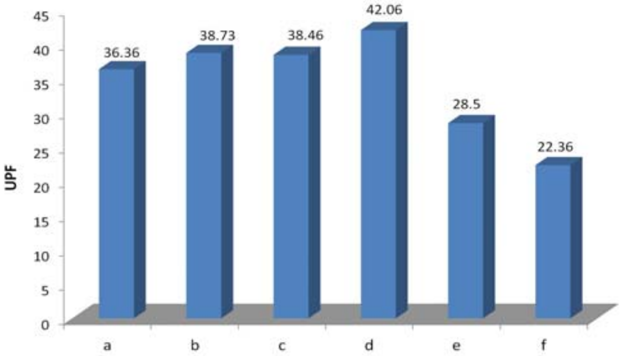

Fig 2: UPF of cotton fabrics; cotton coated with (a)TiO_2, (b)TiO_2/SiO_2 1:0.4, (c)TiO_2:SiO_2 1:1, (d) TiO_2/SiO_2 1:2.3, (e) SiO_2, and (f) pristine cotton.

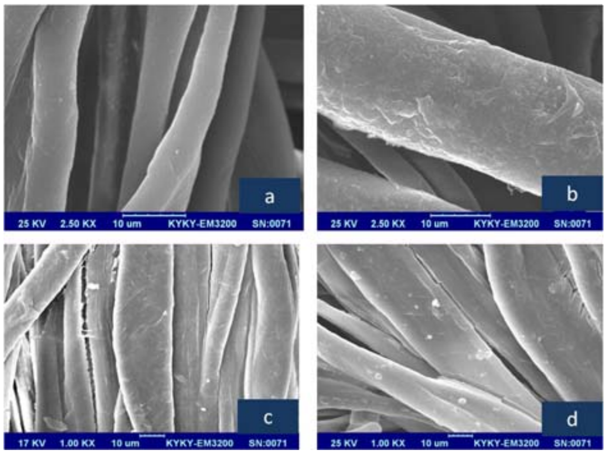

Fig 3: SEM images of cotton samples: (a) pristine cotton, cotton coated with (b)TiO_2, (c)TiO_2/SiO_2 1:1, (d) TiO_2/SiO_2 1:2.3.

CONCLUSION

TiO_2/SiO_2 nanosols based on three molar ratios of Ti/Si were devised through the sol-gel method and applied to cotton fabrics. Self-cleaning and UV-protection factors of fabrics were studied to understand the role of each component in the obtained results. It was observed that the stain-removal function and UPF both increased compared with TiO_2-coated cotton. TiO_2/SiO_2 1:2.3 followed by 1:1 showed the highest efficiency. The SEM images demonstrated an even coating on the cotton fabric.

FUTURE WORK

In the next step of this research, the main objective is to improve the sensitivity of functionalized fabrics in the visible region. To this end, noble metals such as gold, silver and platinum are incorporated into the TiO_2 sol to shift the activity threshold to visible region as well as studying the wash fastness of applied nanoparticles and the change of the physical properties of fabrics after coating.

REFERENCES

[1] Montazer M, Pakdel E. Functionality of nano titanium dioxide on textiles with future aspects: Focus on wool. *Journal of Photochemistry and Photobiology* C: Photochemistry Reviews. 2011, 12(4): 293-303.

[2] Tung WS, Daoud WA. Self-cleaning fibers via nanotechnology: a virtual reality. *Journal of Materials Chemistry*. 2011, 21(22): 7858-69.

[3] Fujishima A, Zhang X. Titanium dioxide photocatalysis: present situation and future approaches. *Comptes Rendus Chimie*. 2004, 9(5-6): 750-60.

[4] Daoud WA, Xin JH. Low Temperature Sol-Gel Processed Photocatalytic Titania Coating. *Journal of Sol-Gel Science and Technolog.* 2004, 29(1): 25-29.

[5] Pakdel E, Daoud WA, Wang X. Self-cleaning and superhydrophilic wool by TiO_2/SiO_2 nanocomposite. *Applied Surface Science.* 2012: In press.

Measurement and Evaluation of Magnetic Fabric

Yan Chen, Gao Jie Yu, Fei Fei Wu,
School of Textile and Apparel Engineering, Soochow University, China
yanchen@suda.edu.cn

INTRODUCTION

The magnetic field exists everywhere because of the convection currents in the outer liquid of Earth's core, electric currents and magnetic materials. It has been approved that the magnetic field with limited strength is favorable for human body, mussels and neural systems.

Magnetic fabric has been used as one of the innovated functional materials to provide magnetic field on the surface for the purposes of therapy and health care. In this usages, the strength and distribution of the magnetic field is critical important. The character of magnetic field on textile materials was discussed. The high accuracy apparatus was used to measure the magnetic field on the fabric surface. The methods of measurement were investigated. The fabric magnetic performance was evaluated by the strength and distribution of the magnetic field. The research in this area is requires to provide a practical base for development and evaluation of the magnetic textiles.

As the functions of magnet fields on therapy and health care have been more and more clearly recognized, the principle of magnetic therapy has been studied in medical community. The magnetic therapy equipment was developed and widely used for analgesia, antiphlogosis, apocatasis, depressurization and so on. The magnetic textiles were also been developed by upload the magnetic particles into fibers of on fabrics. The magnetic textiles for health care purposes have been used for various apparels and accessories.

The strength and distribution of magnetic field on the textile materials are great different with that of the hard and strong magnetic materials. The apparatus developed for magnetic field measurement of normal materials could not be used for textile measurement. In order to design the magnetic textiles and control the magnetic strength on the required position of the products, the measurement and evaluation of the magnetic field is the very beginning step.

APPROACH

The function of health care of the textile materials was performed by the magnetic field on the fabric surfaces. Therefore, most of magnetic materials were used for the apparels and accessories next to the skin. The surface characters of the textiles should be measured and evaluated.

The apparatus based on Hall magnetic sensor are widely used for magnetic field measurement. The influence of magnetic field in current is the basic factor of the measurement. The relation of potential difference and magnetic induction intensity U_H is given as following equation:

$$U_H = K_H \times I_H \times B \times \cos\theta$$

Where, K_H is Hall coefficient, I_H operation current, B magnetic intensity and θ the angle between magnetic field and Hall element.

The magnetic field direction on fabric surface could be divided into parallel and vertical sections. The vertical section acts on the human body. From above equation, the magnetic induction intensity will be highest at 0^o, which indicates that the Hall element should be parallel with fabric surface.

CH-1600 digital Teslameter provided by Beijing Ch-Hall Co. was used for this research. This detector of this Teslameter was specially designed for textile application, which could be moved on the fabric surface and kept the distances from detector to detect points 1±0.1mm. This Teslameter has been approved by China Standard Organization. Four knitted magnetic fabric used for health care purpose were collected for this research.

Table 1. magnetic fabric samples

No.	Magnetic fiber content (%)	Yarn thickness (tex)		Fabric thickness (mm)	Fabric weight (g/m^2)
		Magnetic fiber	cotton		
A	50	13.2	11.8	0.814	165
B	67	13.7	11.7	0.753	172
C	75	12.8	11.3	0.770	158
D	80	13.1	11.2	0.766	166

RESULTS AND DISCUSSION

The magnetic intensity is usually measured in “point”. The magnetic field intensity varies from point to point. It is necessary to measure the magnetic intensity of fabric in point but to show the characters of the fabric. The magnetic intensity of fabric is normally as low as 0.05mT, the sensitivity of the Teslameter is 1×10-4mT to ensure the accuracy of measurement.

It has been found that the magnetic field of the fabric was not uniformly distributed. 15×15cm samples were measured in 25、50、100 and 200 points. The average and the deviation of the magnetic intensity with different measurement points were used to evaluate the most practical measurement schemes. The results from different number of measurement points were given in table 2.

Table 2. effects of measurement points

Point nuber	Average at different measurement/mT 1	2	3	4	5	Av mT	CV %
25	0.037	0.049	0.043	0.032	0.052	0.042	20.80
50	0.046	0.036	0.048	0.042	0.034	0.041	15.54
100	0.046	0.045	0.043	0.040	0.051	0.045	9.06
200	0.045	0.047	0.045	0.050	0.043	0.046	5.79

It can be found from table 2 that the deviation of magnetic intensity measured tended to reduce as the increase of measurement points. There were no evident differences between the results of 100 points and 200 points.

On the basis of 100 points measurement. The descriptions of the fabric magnetic characters were also investigated. Table 3 gives out the average and maximum of magnetic field intensity measured from samples.

Table3. results of repeat measurement

	1	2	3	4	5
Max.	0.066	0.123	0.096	0.043	0.056
Ave.	0.050	0.046	0.047	0.042	0.044

It can be find that usually used maximum or average could not to give the actually intensity of the fabric magnetic field. According to the function of magnetic field on heath care of human beings, the results of measurement were divided into three groups on the basis of intensity of magnetic field. ≤0.01mT magnetic field intensity was much too weak to insert any influences on human body, the intensity between 0.01mT and 0.05mT is the dominate magnetic field, and ≥0.05mT is relative strong magnetic field for health care. Table 4 gives out the distribution of the three group magnetic field intensity.

Table 3. distribution of magnetic field intensity

samples	Percentage of magnetic field (%) ≤0.01mT	0.01mT~0.05mT	≥0.05mT
1	20	80	0
2	16	73	11
3	11	61	28
4	6	53	41

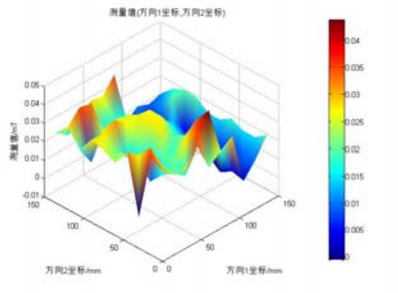

Fig. 1 distribution of magnetic field intensity (sample 1)

The magnetic field distribution can also be presented in visual forms. Fig.1 gives out the distribution of magnetic field intensity measured from samples 1 in 100 evenly distributed points.

From the figure of magnetic field intensity, it can be clearly identified that the magnetic field varies in different area. The polar of the magnetic field could also be find from the figure, which was the results of polarity of magnetic materials on fabric. The positive and negative areas were always located at adjacent position. It can be imaged that the magnetic lines webbed on the surface of the fabric which act on acupuncture points of human body. As the movement of human body, the direction and intensity of magnetic field varies and alternative function could be realized.

CONCLUSIONS

It can be concluded from this work as follows:

(1) The character of magnetic fabric should be investigated in order to apply this functional material for health care purposes.

(2) The intensity of magnetic field on the fabric could be measured by Teslameter with high accuracy and special detector designed for textile.

(3) The measurement points should be controlled to obtain the results present the fabric. In this work 100 points for 15×15cm sample gave the satisfied results.

(4) The distribution of magnetic field intensity could be described by percentage in three magnetic field intensity groups. It could also be identified in visual form.

It can be expected to design apparel and accessories for the health care purposed on the basis of researches on the intensity and distribution of fabric surface magnetic field.

REFERENCES

[1] Kuzhir, P., etal. Steady shear flow of magnetic fiber suspensions: theory and comparison with experiments. *Journal of Rheology*, 2011, 55 (1): 43-67.

[2] Shiiki, M., etal. Evaluation of characteristics of transcutaneous thin transformer utilizing amorphous magnetic fiber for implantable artificial heart. IEEE Translation *Journal on Magnetics in Japan*, 1991, 6 (7): 567-582.

[3] Hiroe, Shinnichi, etal. Evaluation of equal error rate in document authentication system using magnetic fiber. 2009 3rd International Conference on Anti-counterfeiting, Security, and Identification in Communication.

[4] Tong, Z.H, etal.An exact solution for the three-phase thermo-electro-magneto-elastic cylinder model and its application to piezoelectric-magnetic fiber composites. *International Journal of Solids and Structures*, 2008, 45 (20): 5205-5219.

[5] Kharlamova, N.S, etal. Mathematical description of 3D-magnetic field with reference to physiotherapy. *Biomedical Technologies and Radio Electronics*, 2011, (9): 72-79.

A Novel Super Absorbent Polyester Fabric Functionalized by a Biodegradable Poly(γ-glutamic acid) Hydrogel

Zheng Li, JianFei Zhang, JianJun Yan, JiXian Gong, JingXin Wang
School of Textiles, Tianjin Polytechnic University, Tianjin, 300387, China
lizheng_nx@163.com

INTRODUCTION

Hydrogels are three-dimensional hydrophilic crosslinked polymeric networks and they have potential applications in textile field. Hydrogels are grafted or finished on the surface of fibers and fabrics, which can obtain special properties. Poly(γ-glutamic acid) (γ-PGA) is an all natural, hydrophilic and biodegradable bacterium biosynthesized polymer produced from Bacillus licheniformis. γ-PGA hydrogels provide a interesting properties of high water sorption, moisture sorption, biodegradability and biocompatibility[1], which make this material suitable for applications in textile field. In this work, A novel super absorbent polyester fabric functionalized by poly (γ-glutamic acid) hydrogel.

APPROACH

γ-PGA(Mw = 3.0×10^5 Da) was dissolved in 80 ml deionized water under continuous stirring, and the concentration of γ-PGA solutions were 6%, 8%, 10%, 12%, 14% and 16% (w/w), respectively. After dissolution, the ratio of weight of the crosslinker ethylene glycol glycidyl ether to γ-PGA was 40%, which was added into solutions under intensely stirring.

Polyester fabric samples of 6 cm ×15 cm were cut and immersed for 10 min into finishing solutions. Then, the samples were passed through a laboratory padder resulting in 65%, 80%, 95%, 100% final pick-up of the fabric, respectively. Subsequently, the samples were packaged by preservative film, and were placed in the oven at 50 ℃ for 8 h. Finally, the samples get rid of preservative film and dried at 50 ℃ in oven.

Three samples of 2.5 cm × 3.0 cm were cut from the original fabrics and finished samples, respectively. The samples were immersed in a water bath for 4 h to reach swelling equilibrium. The temperatures of the water baths were 20 ℃. After 4 h, the samples were taken out from the water baths and gently blotted with filter paper to remove surface water and weighed. The water absorbency was calculated.

The samples were first conditioned at 20 ℃ and 65% relative humidity for 24 h to reach equilibrium. Then the samples were dried in oven at 105±1 ℃ until constant weight. The moisture regain was calculated.
1 g of the samples immersed in a 20 ℃ water bath. At regular intervals the samples were taken out from the water baths. Then the samples were weighed and returned to the bath. This process of weighting was continued until the samples attained a constant weight.
The surface morphology of the finished fabrics was investigated by 3D Digital Microscope with large depth of field VHX-1000 (KEYENCE, Japan). Yarns were got from the finished fabrics.

The morphology of hydrogel was observed using a scanning electron microscope (SEM) MT-1000 (HITACHI, Japan). The samples were immersed in deionized water for 4 h to reach swelling equilibrium, and then quickly put into the refrigerator for 5 h. Subsequently, the frozen samples were dried by freeze-dried method.

RESULTS AND DISCUSSION

Performance of the finished fabrics

As shown in Fig. 1. Water absorbency of finished fabrics was significantly increasing compared to that of the original fabrics, which was only 1.53 ±0.19 g/g. When the concentration of γ-PGA solution was higher than 8%, Water absorbency of finished fabrics reduced due to swelling ratios (SR) of hydrogels decreased. The SR decreased with increasing the concentration of γ-PGA solution, due to an increase in crosslinking density. The resulting network is more loosely crosslinked resulting in decreasing SR of hydrogels [2]. In addition, Water absorbency of fabrics increased with increasing pick-up owing to addition of hydrogels finished on fabric. The highest water absorbency reached 15.27±0.45 g/g, at γ-PGA 8% and pick-up 110%.

As shown in Fig. 2, the finished fabrics was significantly increasing compared to the original fabrics (moisture regain 0.4%) and showed different moisture regain. It was found that a higher concentration of γ-PGA finishing liquid or pick-up resulted in a higher moisture regain. The results were consistent to the moisture regain of the fabrics.

As shown in Fig. 3, the hydrogels finished on fabrics exhibited a three step swelling behavior when the time was increased from 0 to 180min. A significant increase in swelling ratios (SR) was observed from 0 to 15min, the SR increased slowly during 15 to 130min, the SR increased further slowly after 130min, and the hydrogels reached to equilibrium within 3 h. The samples absorbed large amounts of water quickly at the beginning, which was caused by hydrophilic properties of the carboxyl groups in hydrogel network [3].

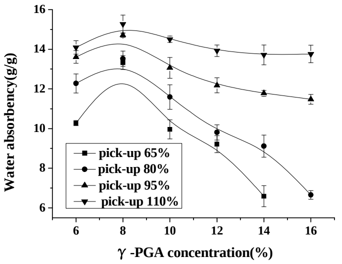

Fig. 1. Effects of the PGA concentration and pick-up on water absorbency of fabrics.

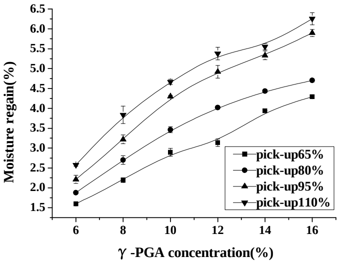

Fig. 2. Effects of the PGA concentration and pick-up on moisture regain.

As the time was increased, amounts of water permeated the hrdrogel network, resulting in the SR increasing slowly. Finally, the hydrogels gradually reached swelling equilibrium.

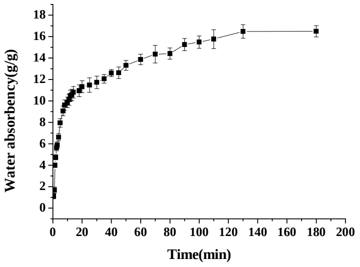

Fig. 3. Absorption curve of finished fabric (8% γ-PGA, pick-up 110%) in deionized water.

Surface Morphology of fabrics

As shown in Fig. 4, the photoes revealed that the fibers of polyester appear smooth, and the small clusters of γ-PGA hydrogels were better dispersed along the fibers. The finished fabrics were obtained high water absorbency owing to γ-PGA hydrogel.

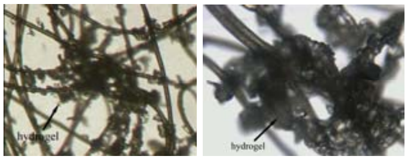

Fig. 4. Surface Morphology of fabrics (8% γ-PGA, pick-up 110%)

Morphology of swollen hydrogels

As shown in Fig. 5, the surface and interior microstructures of the γ-PGA hydrogels in swollen state was investigated by SEM. The freeze-dried hydrogels by exhibited a highly macroporous sponge-like structure, which result in the high water absorbency of finished polyester fabrics.

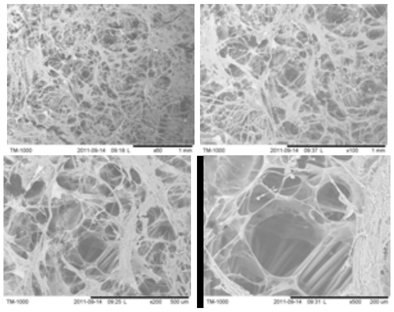

Fig. 5. SEM of swollen hydrogel (8% γ-PGA, pick-up 110%).

CONCLUSIONS

High water absorbency of polyester fabrics were finished by Poly (gamma-glutamic acid) hydrogel (γ-PGA hydrogel) using ethylene glycol glycidyl ether as a crosslinker. The fabrics displayed high water absorbency and increase in moisture regain, which were affected by the concentration of γ-PGA solution and pick-up. The finished fabrics can absorb large amount of water within short time. The highest water absorbency reached 15.27±0.45 g/g. Therefore, the γ-PGA hydrogels may hold vast potential applications in high water absorption textile.

KEYWORDS: Poly (γ-glutamic acid); Ethylene glycol glycidyl ether; Hydrogel; Polyester

ACKNOWLEDGMENTS

This work was financially supported by the National Natural Science Foundation of China (No. 31200719, 21006072)

REFERENCES

1. Kesuo Fan, Denis Gonzales, Martin Sevoian. Hydrolytic and Enzymatic Degradation of Poly(γ-Glutamic Acid) Hydrogels and Their Application in Slow-Release Systems for Proteins Characteristics. *Journal of Environmental Polymer Degradation.* 1996, 4: 253-260.

2. Oh KS, Oh JS, Choi HS, Bae YC. Effect of cross-linking density on swelling behavior of NIPA gel particles. Macromolecule. 1998, 31: 7328-35.

3. D.E. Rodríguez, J. Romero-García, E. Ramírez-Vargas, A.S. Ledezma-Pérez, E. Arías-Marín. Synthesis and swelling characteristics of semi-interpenetrating polymer network hydrogels composed of poly(acrylamide) and poly (γ-glutamic acid). *Materials Letters*. 2006, 60: 1390-1393.

Enhancing Thermal Conductivity of Cotton Fabrics with Nanocomposite Coatings

Amir Abbas, Yan Zhao, Xungai Wang, Tong Lin
Australian Future Fibres Research and Innovation Centre, Institute for Frontier Materials, Deakin University,
Victoria 3216, Australia
tong.lin@deakin.edu.au

INTRODUCTION

Heat transfer is vital for many textiles including sportswear, work uniform, shoes, bedding, and healthcare products. Such a process in fibrous materials is complex and often involves three main routes (conduction, convection and radiation), with the heat conduction being more significant than the other two. Conventionally, heat transfer in fabrics is adjusted mainly through changing fabric thickness, aerial density, porosity, or weave structure. Little attention has been paid to increasing the thermal conduction of fabrics through surface finishing with a thermally conductive material.

Carbon nanomaterials, such as carbon nanotubes (CNTs) and graphene, have been recently reported to have excellent thermal conductivity. The thermal conductivity of multi-wall carbon nanotubes (MWCNTs) has been measured to be as high as 3000 W/mK.[1] Graphene, a single layer of graphite, was recently reported to have even higher thermal conductivity. At room temperature, the thermal conductivity of a single-layer graphene was reported to be 5300 W/mK.[2] Boron nitride (BN) is another thermal conductive material widely used as filler for making thermo-conductive adhesives, pastes, and greases. Hexagonal boron nitride (h-BN) is similar to graphite having a platelet structure, thus being soft and lubricious. h-BN has a high in-plane thermal conductivity of up to 300-600 W/mK.[3]

Herein we report on the effects of the composite coatings containing these three nano fillers (MWCNT, grapheme and BN) on the thermal transfer properties of cotton fabrics.

EXPERIMENTAL

The coating solutions were prepared by dispersing the fillers in a solution containing 4 wt% Hercosett XC resin and 1.2 wt% 3-(N, N-dimethylmyristylammonio)-propanesulfonate, followed by sonication of the solution for 2 hours. After coating, the corresponding solid content of the fillers in the coating layer was controlled at 11.1, 20.0, 33.3 and 50.0 wt%.

The coating solutions were applied to the cotton fabrics simply by a dip-pad-cure technique. Sample was first dipped in the coating solution and then padded through an Atlas wringer to remove the excessive solution. A 100 % wet pickup was set by adjusting the pressure on the side of the padder. The fabric was dried and cured at 120 ºC for 10 minutes in a fan forced oven. Finally, the fabric was washed with hot and cold water separately to remove the unfixed chemicals.

For the measurement of thermal conductivity, a purpose-designed system was employed, as illustrated in Fig. 1. A circular cylinder (100 mm diameter × 160 mm length) heat source was insulated on three sides to allow only one face to contact with fabric samples for heat transfer. A thermocouple probe with temperature measurement error of ±0.05 ºC was fixed on the outer wall of the cylinder that was in contact with the fabric. During the test, the heat source was heated to 50 ºC and then left to cool down naturally. Thermal conductivity was calculated by using the Newton's law of cooling.[4]

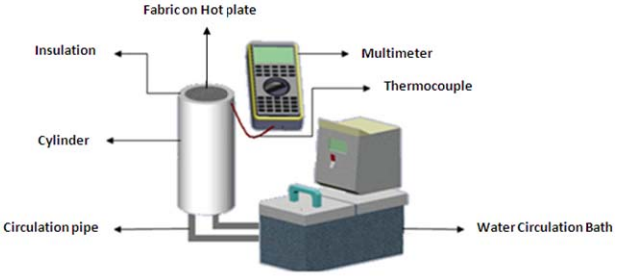

Fig. 1 Schematic illustration of the experimental setup.

The IR camera (IEC thermo tracker) was also used to record the temperature change of the whole fabric surface. The recorded thermal images were processed with ImagePro II 4.0.6 mikron infrared software. For recording the heating process, IR thermography video was taken instantly after the fabric was brought to contact with the preheated cylinder at a preset temperature of 50 ºC. For a cooling process, the fabric was first heated for 10 minutes with the heat source (50 ºC), and the IR thermography video was recorded instantly when the source was removed off the fabric.

RESTULTS AND DISCUSSION

After coating, the cotton fiber surface was covered with a uniform layer of resin containing nano fillers, which was verified by SEM (not shown here). With increasing the solid content of the fillers, the loading amount of the fillers on the fibers increased.

The thermal resistance and the thermal conductivity of the fabric samples are presented in Fig. 2. For the fabric coated with resin only without any nano fillers, the thermal conductivity was 0.047 ± 0.005 W/mK, which was 52% higher compared to the uncoated cotton fabric. When the coating layer contains 11.1 wt% fillers, the thermal conductivity was increased obviously. For graphene, BN and MWCNT, the thermal conductivity of the coated fabric changed to 0.078 ± 0.008, 0.074 ± 0.007

and 0.072 ± 0.007 W/mK, corresponding to the improvement by 152%, 139% and 132%, respectively. Among these three nano fillers, graphene showed the best improvement in the thermal conductivity. Higher content of graphene, e.g. 20.0, 33.3 and 50 wt%, in the coating layer increased the thermal conductivity of the fabric to 0.10 ± 0.001, 0.14 ± 0.001 and 0.29 ± 0.015 W/mK, corresponding to 235%, 358% and 842% improvement, respectively.

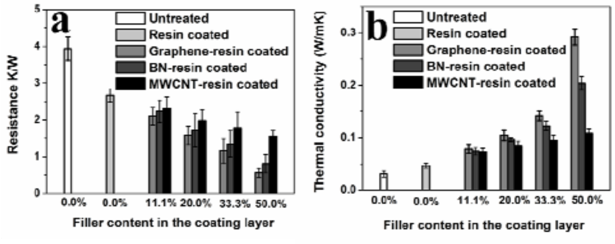

Fig. 2 Thermal resistance and conductivity of the fabric.

Fig. 3 shows the temperature vs. time curves of the cotton fabrics during heating process. Upon bringing the fabric to contact with a controlled heat source (surface temperature of 50 ºC), the untreated fabric reached a maximum temperature of 46.7 ºC in 4.5 seconds. For the fabrics coated with the three thermal conductive composites, the surface remained at lower temperature at the same testing conditions. This should come from the effective dissipation of heat through the coating layer. The maximum difference in the equilibrium surface temperature between the coated fabric and the control was 2.6 °C, which comes from the 50.0 wt% graphene coating. For the BN coated fabric, the difference in the equilibrium surface temperature was in the range of 0.9-2.4 °C, while for the MWCNT coated fabric the difference was in the range of 0.9-2.0 °C. These results suggested that graphene provided a better thermal dissipation over the other two fillers.

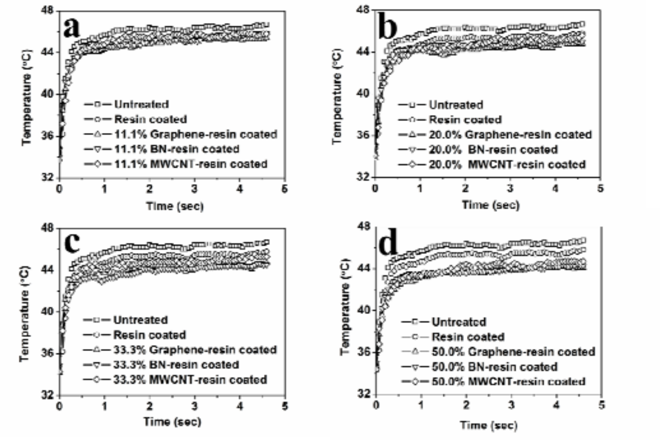

Fig. 3 Temperature vs. time curves during heating.

The equilibrium temperature of the coated fabrics during cooling was also measured (Fig. 4). During the test, all the coated samples were heated for 10 minutes so that the sample was heated to maximum equilibrium temperature, and then cooled naturally in a controlled ambient condition. After 24.5 minutes of cooling, the minimum temperature was measured. For the untreated fabric, the equilibrium temperature was 30.4 °C. The coated fabrics exhibited good cooling behavior and remained at lower equilibrium temperature than the control fabric. With increasing the filler content in the coating layer, the equilibrium cooling temperature decreased. The lowest equilibrium temperature was recorded to be 27.9 °C, which resulted from the 50.0 wt% graphene coating. However, for the BN and MWCNT coating with the same content, the equilibrium temperature was 28.4 °C and 29.4 °C, respectively.

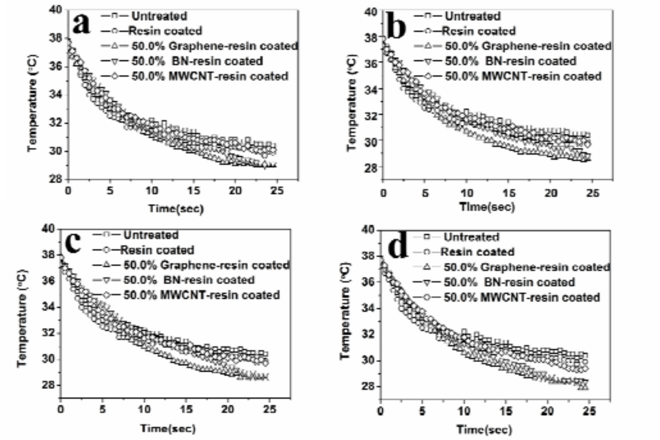

Fig. 4 Temperature vs. time curves during cooling.

CONCLUSIONS

Three thermally conductive nano fillers, graphene, MWCNT and BN, have been used to form composite coatings on cotton fabrics. Our study has indicated that they all increase the thermal conductivity of the fabric, and the graphene coated fabric showed the best improvement. BN composite coating was more effective than MWCNT.

REFERENCES

1. P. Kim, L. Shi, A. Majumdar, and P. L. McEuen, *Phys. Rev. Lett.*, 87, 215 (2001).
2. A. A. Balandin, S. Ghosh, W. Bao, I. Calizo, D. Teweldebrhan, F. Miao, and C. N. Lau, *Nano Lett.*, 8, 902 (2008).
3. M. Ishigami, S. Aloni, and A. Zettl, *AIP Conference Proceedings* 696, 94 (2003).
4. A. Abbas, Y. Zhao, X. Wang, T. Lin, *J. Text. I.*, DOI:10.1080/00405000.2012.757007 (2013).

Study on Parameters Affecting the Performance of Piezo-Resistive Conductive Fabric

Weijing Yi[1,2], Xiaoming Tao[2], Yangyon Wang[3], Guangfeng Wang[3], Rong Zheng[1]
[1]Beijing Institute of Fashion Technology, [2]The Hong Kong Polytechnic University, [3]AdvanPro Limited
tctaoxm@polyu.edu.hk; ywj1wj@gmail.com

INTRODUCTION

Carbon nano-particle (CNP) filled silicone elastomer (SE) composites with silicone oil (SO) as solvent show piezo-resistive properties when an external force is applied [1,2]. It also has a large deformation ability and low tensile modulus when the composition of the three phases is optimized, which makes it a potential material for flexible strain sensors in smart textiles [3]. However, the fatigue life of the conductive composite is not good at a high strain. Furthermore, it's difficult to make an electric connection between the conductive composite and measuring circuit with good reliability. Knitted fabrics have good fatigue resistance and high elasticity; they are also easy being connected with other textile materials by sewing or pasting methods. In this paper, a conductive fabric based on the CNP/SE/SO composite was developed and the parameters affecting the performances of the conductive fabric were discussed.

APPROACH

CNP/SE/SO mixture paste with CNP loading beyond percolation transition range was fabricated using the mechanical mixing method as described in reference [2], and it was coated on knitted fabric (83% Tactel and 17% Lycra, Sunikorn Knitters Limited, Hong Kong) using screen printing method shown in Figure 1 to form series of stripes with width of 10 mm, then the paste was cured at 100 ^{0}C for 2 hours. Three mixture pastes with CNP loadings beyond the percolation transition range were used, as shown in Table I. Conductive fabrics with stripes in both wale and course direction were fabricated. The force and displacement data were recorded by a computer connected to Universal Material Tester (Instron 5944), and resistance by the digital multi-meter (Keithley 2010) simultaneously using data acquisition system. All the measurements were conducted in a conditioned room with temperature of 20 ^{0}C and relative humidity of 65%.

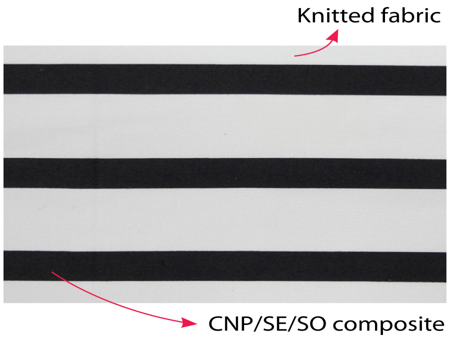

FIGURE 1 Photograph of conductive fabric

TABLE I Ingredients of mixture pastes on knitted fabric

Sample	Composition of pastes (Weight ratio)	R_0 (kΩ)	CV (%)
3.5CNP	CNP/SE/SO 3.5/96.5/50.0	115.90	5.24
4.5CNP	CNP/SE/SO 4.5/95.5/75.0	69.27	4.12
9.0CNP	CNP/SE/SO 9.0/91.0/150.0	10.29	3.50

RESULTS AND DISCUSSION

Effect of Printing Times and Conductive Composites

The electrical resistance of the conductive fabric is affected by size, thickness and CNP concentration of conductive paste coating. After curing, the size of the conductive fabric can be controlled within 1%. The thickness of the coating layer was affected by the screen printing times. Table II shows the weight changes of conductive fabric after coated with conductive composites 9.0CNP (the size of conductive fabric measured is 177 mm×126mm) for 1 time and 3 times respectively. It can be obviously observed that the weight variation of coating layer is much smaller for the conductive fabric coated for 3 times than that coated for 1 time, and the value can be controlled within 2.5%, meaning the 3 times coating process was suitable to fabricate the conductive fabric with better evenness. Table I demonstrates the average electrical resistance and coefficient of variation for conductive fabrics with different CNP concentrations. The electrical resistance decreased and the coefficient of variation of the electrical resistance also decreased, which means that the conductive fabric is getting uniform.

Effect of Fabric Structure

Due to the good elasticity of plain knitted fabric in both course and wale directions, the piezo-resistive behavior of conductive fabric can be observed on both tensile directions. Figure 2 depicts the typical electrical resistance-strain curves for the conductive fabric in two directions obtained from the electromechanical test. Electrical resistance of the conductive fabric synchronous changed with tensile strain up to 100% without yield. The linearity of the conductive fabric at wale direction is much better than that of course direction during extension. Furthermore, the hysteresis at wale direction is much smaller than that of course direction, meaning that the wale direction is more appropriate as the working direction of the conductive fabric.

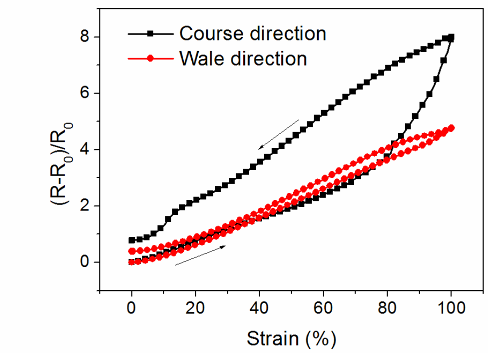

FIGURE 2 Resistance-strain curves of conductive fabric in course and wale directions

Effect of Mechanical Pretreatment

Figure 1 shows the resistance-strain curves of a virgin conductive fabric as it was stretched to various strain levels with increased sequence. Typical irreversible curves for conductive fabrics can be found, which cannot accurately reflect the strain level of the objectives. After mechanically treated with extension to 170% of its original length for 1 time, the conductive fabric shows a stable and repeatable electrical response as strains lower than the pretreated one, as shown in Figure 4. The hysteresis of resistance-strain curve significantly decreased from 17.58% to 5.55%, meaning that the mechanical pretreatment is effective to increase the stability and accuracy of the conductive fabric.

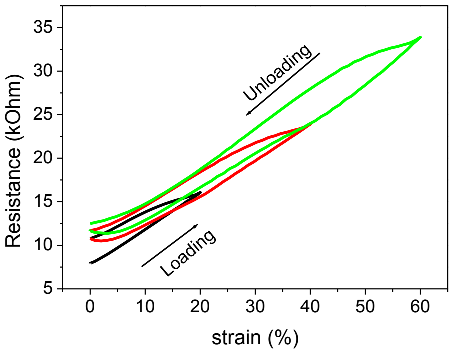

FIGURE 3 Electrical response of conductive fabric without mechanical pretreatment with sequence of increased strain levels. (The black, red and green colors stand for the maximum tensile strain is 20%, 40% and 60%, respectively)

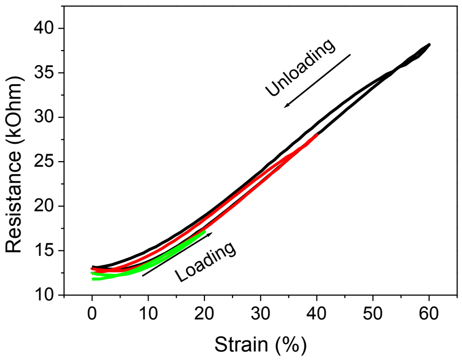

FIGURE 4 Electrical response of conductive fabric to various strains after mechanical pretreatment. (The black, red and green colors stand for the maximum tensile strain is 60%, 40% and 20%, respectively)

CONCLUSIONS

Piezo-resistive conductive fabric based on CNP/SE/SO was developed. The parameters affecting the performance of the conductive fabric were analyzed. The 9.0CNP fabric with screen printing of 3 times is preferred to achieve lower initial resistance and better evenness. The fabric has a better linearity when working in the wale direction. Mechanical pretreatment beyond the working range has an obvious effect on improving of accuracy and stability of the conductive fabric.

ACKNOWLEDGMENT

The financial support by the Postgraduate Scholarship of Hong Kong Research Grants Council (Grant No. Poly5277/07E) and the Scientific Research Project of Beijing Institute of Fashion Technology (Grant No. 2012A-01) was great appreciated by the first author.

REFERENCES

1. Mattmann, C., F. Clemens, and G. Troster, Sensor for measuring strain in textile. *Sensors*, 2008. 8(6): p. 3719-3732.

2. Kost, J., M. Narkis, and A. Foux, Resistivity Behavior of Carbon-Black-Filled Silicone-Rubber in Cyclic Loading Experiments. *Journal of Applied Polymer Science*, 1984. 29(12): p. 3937-3946.

3. W.J. Yi, Y.Y. Wang, G.F. Wang, X.M. Tao, Investigation of carbon black/silicone elastomer/ dimethyl silicone oil composites for flexible strain sensors. *Polymer Testing*, 2012. 31(5): p. 677-684.

Table II Weight of conductive composites coated on fabric

	Coated for 1 time		Coated for 3 times	
	Average weight increment (g)	CV(%)	Average weight increment (g)	CV (%)
Before curing	1.00	11.31	1.61	2.12
After curing	0.75	6.36	1.32	2.35

High-Performance Fibres and Composites

Biodegradable Fibers from Renewable Sources: Melt Spinning of Polyhydroxyalkanoates (PHAs)

Rudolf Hufenus[1], Felix A. Reifler[1], Katharina Maniura-Weber[1], Manfred Zinn[2], Adriaan Spierings[3], Urs J. Hänggi[4]
[1]Empa, Swiss Federal Laboratories for Materials Science and Technology, Switzerland, [2]University of Applied Sciences Western Switzerland, [3]irpd, institute for rapid product development, Inspire AG, Switzerland, [4]Biomer, Germany
rudolf.hufenus@empa.ch

OBJECTIVE

The goal of this work was to develop biodegradable fibers from renewable sources that show best performance with respect to mechanical properties and colonization of tissue engineered cells. Polyhydroxyalkanoates (PHAs) are polyesters that are produced by bacteria, serving as intracellular carbon storage compound. PHAs are advantageous concerning biocompatibility and biodegradability, but their complex crystallization behavior hinders the melt-processing of fibers. We propose two ways to overcome this problem, either by fundamentally modifying the draw-off procedure, or by combining PHAs with melt-spinnable biopolyesters in a core-sheath configuration.[1]

INTRODUCTION

Tailored biopolymer fibers play an important role in the medical field, e.g. as drug delivery systems, wound closure and healing products or surgical implant devices.[2] The major requirement for medical implants is that the polymers and their degradation products are biocompatible with the human body.[3] Desired properties comprise a minimal adverse effect on living tissue, i.e. the absence of inflammatory reaction or toxic response. In addition, bioresorbable fiber implants require a minimal tensile strength to fulfill their purpose in the body, and are expected to degrade after functional use[4] in order to avoid a second surgical intervention for removal.[5]

Polyhydroxyalkanoates (PHAs) are polyesters that are accumulated in bacteria as intracellular carbon and energy storage compounds.[6] Among PHAs, poly(3-hydroxybutyrate) (PHB) is the most frequently studied and the easiest to produce.[7] PHB has been proposed for several biomedical applications[4] and is of great interest because of its biotechnological generation, its thermoplastic processability, its excellent biocompatibility, and its unique combination of biodegradability and hydrophobicity.[8] Compared to the PHB homopolymer, poly(3-hydroxybutyrate-co-3-hydroxyvalerate) (PHBV) is more flexible and easier to process.[9] PHB and PHBV sutures implanted intramuscularly for up to one year did not cause any adverse effects.[10]

Regarding biocompatibility, biodegradable fibers completely based on PHAs, e.g. PHB or PHBV fibers, would be preferable. However, quality variations (molecular weight, purity) of the commercially available PHBs and PHBVs cause problems during melt-spinning.[11] In addition, rapid thermal degradation at temperatures just above the melting temperature, low melt elasticity, low crystallization rate due to a low nucleation density and brittleness of native PHB and PHBV render a rather narrow processability window.[12] Up to now, melt-spinning of PHB and PHBV could only be achieved at a small scale applying special additives,[13] uncommon procedures[14] and complex post-treatment.[15]

APPROACH

Fiber melt-spinning was carried out on Empa's custom-made pilot melt-spinning plant. This plant, with features corresponding to an industrial spinning line, enables the prototype production of mono-, bi- and tricomponent fibers with various fiber cross-sections and material combinations. To enhance the fiber properties, PHA was co-spun with polylactide (PLA). To maintain and control the polymers as long as possible at their optimal temperatures during spinning, a highly integrated spin pack allowing the separate heating or cooling of up to three polymer channels was developed (Figure 1). The influence of hydrolytic degradation on the physical properties was assessed by incubation for 4 weeks and subsequent mechanical analysis of the remaining fibers. Cytotoxicity tests were carried out according to ISO 10993-5:2009. Further, biocompatibility was assessed using normal human dermal fibroblasts (NHDF).

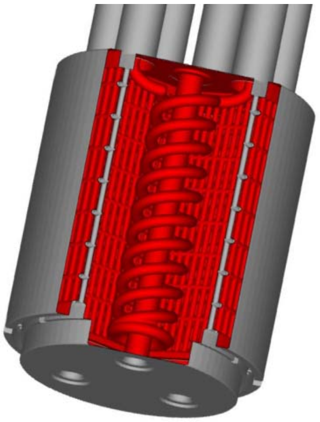

Figure 1: Schematic of the highly integrated spin pack for three different polymers with heating/cooling channels and thermal insulation grid.

RESULTS AND DISCUSSION

Since technical grade PHB starts to degrade at melting temperatures, heat stabilization is essential in order to successfully melt-spin PHB fibers. The brittleness of PHB can be overcome by adding plasticizers that improve processability and mechanical properties. Special PHB that are heat stabilized and include biodegradable plasticizers were developed. The crystalline morphology of melt-spun fibers can either be dominated by spherulitic structures, or by row nucleated lamellae, depending on the spinning parameters. We could show that, other than conventional thermoplastic polymers, PHB needs an adapted stretch-draw process that prevents the formation of spherulites and favors oriented lamellae during spinning. That way we were able to develop melt-spun PHB fibers with an ultimate tensile stress of up to 0.11 GPa and a E-modulus of up to 10 GPa.

To combine the properties of PLA and PHBV, bicomponent melt-spinning was applied. Conglutination due to secondary crystallization of native PHBV hindered the continuous melt-drawing of bicomponent fibers with PLA core and PHBV sheath, but fibers with a PHBV core and a PLA sheath were successfully spun. Higher draw ratios could be realized by applying a special spin pack that keeps the temperature of PHBV substantially lower than the PLA temperature during melt-spinning. The resulting bicomponent fibers had an ultimate tensile stress of up to 0.34 GPa and an E-modulus of up to 7.1 GPa. X-ray diffraction revealed that PLA alone was responsible for tensile strength. While the PLA component was fairly well oriented, the PHBV component developed no molecular orientation.

In vitro biocompatibility studies with human dermal fibroblasts revealed no toxicity of the fibers. Cells proliferated well along the individual fibers and spanned fiber intersections after 10 days of cultivation (Figure 2). Abiotic degradation tests showed a decrease of molecular weight and reduction in tensile strength of up to 33% after 4 weeks of incubation. The good cytocompatibility that has been found makes PHA containing fibers promising candidates for medical therapeutic approaches.

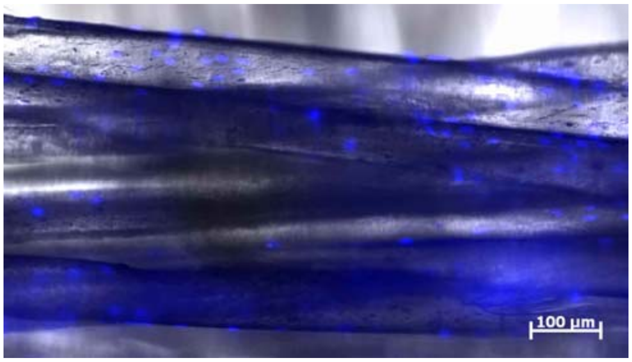

Figure 2: Overlay of light and fluorescence micrographs shows cells on PLA-PHBV core-sheath fibers which are stained for nuclei (blue).

CONCLUSIONS

PHB fibers could be melt-spun applying a specific method that in principle is upscalable. By combining PLA and PHBV in a bicomponent fiber, the known difficulties with spinning of native PHBV could be overcome. The fibers proved to be strong enough for the successful construction of a textile fabric. In vitro biocompatibility studies revealed that cells proliferate well along the individual fibers and span fiber intersections.

KEYWORDS

Biopolymers, melt-spinning, bicomponent fibers

REFERENCES

1. R. Hufenus, F.A. Reifler, K. Maniura-Weber, A. Spierings, and M. Zinn, Macromolecular Materials and Engineering 297 (1), 75 (2012).
2. K. Van de Velde and P. Kiekens, Polym Test 21 (4), 433 (2002).
3. W. He, Y. Feng, Z. Ma, and S. Ramakrishna, in *Polymers for Biomedical Applications*, edited by A. Mahapatro and A.S. Kulshrestha (American Chemical Society, Washington, DC, 2008), pp. 310; S. Ramakrishna, J. Mayer, E. Wintermantel, and K.W. Leong, Compos Sci Technol 61 (9), 1189 (2001).
4. J.C. Middleton and A.J. Tipton, Biomaterials 21 (23), 2335 (2000).
5. K.A. Athanasiou, C.M. Agrawal, F.A. Barber, and S.S. Burkhart, Arthroscopy 14 (7), 726 (1998).
6. K. Sudesh, H. Abe, and Y. Doi, Prog Polym Sci 25 (10), 1503 (2000).
7. G.Q. Chen, Chem Soc Rev 38 (8), 2434 (2009); B.M.P. Ferreira, C.A.C. Zavaglia, and E.A.R. Duek, J Appl Polym Sci 86 (11), 2898 (2002).
8. M. Zinn and R. Hany, Adv Eng Mat 7 (5), 408 (2005).
9. E. Chiellini and R. Solaro, Adv Mat 8 (4), 305 (1996).
10. E.I. Shishatskaya, T.G. Volova, A.P. Puzyr, O.A. Mogilnaya, and S.N. Efremov, J Mater Sci - Mater M 15 (6), 719 (2004).
11. R. Vogel, B. Tändler, D. Voigt, D. Jehnichen, L. Häussler, L. Peitzsch, and H. Brünig, Macromol Biosci 7 (6), 820 (2007).
12. K. Arakawa, T. Yokohara, and M. Yamaguchi, J Appl Polym Sci 107 (2), 1320 (2008); P.J. Barham and A. Keller, J Polym Sci Pt B - Pol Phys 24 (1), 69 (1986); I. Chodak and R.S. Blackburn, in *Biodegradable and sustainable fibres*, edited by R.S. Blackburn (Woodhead Publishing Limited, Cambridge, 2005), pp. 221; R. Vogel, B. Tändler, L. Häussler, D. Jehnichen, and H. Brünig, Macromol Biosci 6 (9), 730 (2006).
13. C. Hinüber, L. Häussler, R. Vogel, H. Brünig, and C. Werner, Macromol Mater Eng 295 (6), 585 (2010).
14. C. Schmack, D. Jehnichen, R. Vogel, and B. Tändler, J Polym Sci Pt B - Pol Phys 38 (21), 2841 (2000); R. Vogel, D. Voigt, B. Tändler, U. Gohs, L. Häussler, and H. Brünig, Macromol Biosci 8 (5), 426 (2008).
15. T. Iwata, Macromol Biosci 5 (8), 689 (2005); T. Iwata, Y. Aoyagi, M. Fujita, H. Yamane, Y. Doi, Y. Suzuki, A. Takeuchi, and K. Uesugi, Macromol Rapid Comm 25 (11), 1100 (2004); T. Tanaka, M. Fujita, A. Takeuchi, Y. Suzuki, K. Uesugi, K. Ito, T. Fujisawa, Y. Doi, and T. Iwata, Macromolecules 39 (8), 2940 (2006); T. Tanaka, T. Yabe, S. Teramachi, and T. Iwata, Polym Degrad Stabil 92 (6), 1016 (2007).

Structure/Properties Relationship in a Single Para-Aramid Fibre

Judith Wollbrett-Blitz[1,2], Alba Marcellan[1], Sébastien Joannès[2], Anthony Bunsell[2]
[1]PPMD, ESPCI, UPMC, Paris, France, [2]Centre des Matériaux P-M Fourt, ENSMP, Evry, France
judith.wollbrettblitz@hotmail.fr

STATEMENT OF PURPOSE

Since their introduction in the 70s, aramid fibres have been studied many times, citing for instance the early work of the first longitudinal tests on single fibre[1] or the firsts to study the transverse mechanical behaviour[2]. Their remarkable mechanical properties associated to relative low density have made them prone to some high performance application: tire reinforcement, bulletproof vest or wires. The mechanical performance of aramid fibre is due to its different scales organisation: the primary (molecular structure held by covalent bonds), the secondary (pleated sheets held by interactions) and the tertiary structure (sheets stacked together). Even though the molecular organisation is well-known, most of the in-situ mechanisms are not clear. Considering the longitudinal direction, two deformation mechanisms have been proposed[3]: (1) the elongation of the crystallites, driving the elastic deformation (2) the rotation of these crystallites, governed by H bonds, involving irreversible mechanisms, those rotations would also be the microstructural motions associate to creep[4]. Comparative to the longitudinal mechanical properties, the transverse characterizations and the micro-mechanisms involved were not so deeply investigated. In this work we propose to focus on dissipative mechanisms, both in transverse and longitudinal directions, and on the structure/property relationship.

INTRODUCTION

The main challenge of this study concerns single aramid fibres and their dissipative behaviour during cyclic mechanical loading. Coupling analysis of multiaxial mechanical dissipation (i.e. in the longitudinal and transverse directions) and temperature effects will go further in the understanding of "mechanical" properties of this high-performance fibre through the understanding of the structural parameters controlling the dissipative mechanisms. This study is based on a single fibre, taking into account the results disparities through a statistical study or the material limits whether mechanically or thermally

APPROACH

This study is based on a single fibre, taking into account the results disparities through a statistical study or the material limits whether mechanically or thermally. First of all, in order to quantify the longitudinal or transverse mechanical dissipation, two different experimental setups are used. The longitudinal dissipation is quantified by doing either a small number of load/unload cycle or for a fatigue experiment. In order to realize a transverse compression test, a new experimental protocol has been developed[5] (using a device originally used for soft adhesives, the Micro-Tack). This experiment allows to follow the experiment via an upside camera (Figure 1). The mechanical dissipation related to each experiment may not include the same molecular mechanisms, even if they may include some irreversible molecular rearrangements. Once the mechanical parameters are obtained for each direction, these experiments can be coupled in order to understand the contribution of each in the dissipative mechanism. This part of the study is used to develop a multi-scale structural characterization in order to reveal the structure/property relationship in both directions and further to understand the structural parameters controlling the dissipative mechanisms. The second part of this study deals with the effect of the temperature on the mechanical behaviour. The para-aramid fibre is very resistant to high temperature, but the dissipative mechanisms were seen to to be highly modified with temperature.

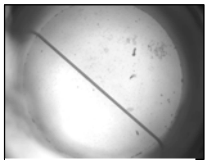

Figure 1: Upside view of the fiber.

RESULTS AND DISCUSSION

Longitudinal dissipation

The longitudinal dissipation was characterized for a small number of cycles and for a fatigue condition. After ensuring the experiment parameters such as frequency did not have any effect on the experimental results, the dissipation was quantified and the evolution of the mechanical parameters was done. At room temperature, the fibre exhibits an important dissipation which decreases with the number of cycle until it reaches a minimal limit and its Young's modulus increase of more than 20%, hence the microstructure reorganized to attain a stable state strongly correlated with the increase of its stiffness (Figure 2). The molecules rearrange which can be explained by the crystallites rotation governed by the hydrogen bonds in order to create a more dense structure and a smaller amount of energy is evacuated. This effect is seen either in the cyclic solicitation or during fatigue test at higher frequency. If a tensile test is done at high temperature (~ 150°C), the initial values of the modulus or the breaking strength are very different from the room temperature test, the former loose about 30% and the latter about 35%. But whatever the temperature is during the cycling test, the modulus or the dissipated energy

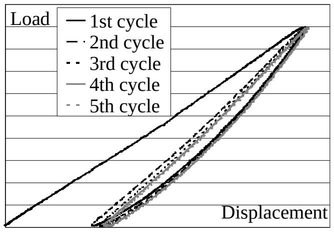

Figure 2: First five cycles of longitudinal solicitation.

stabilized at the same value, but the damage length is ten times bigger when it is done at high temperature which means the microstructure is affected by the temperature. The breaking tips (Figure. 3) are also very different because of the heat-activated molecular motions.

Transverse dissipation

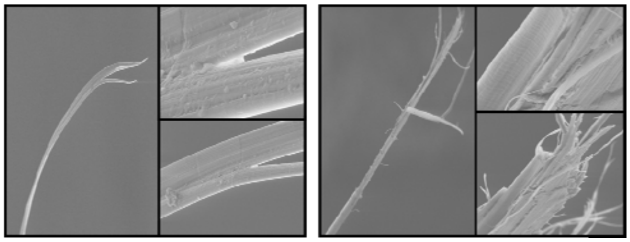

Figure 3: Breaking tips of a single fiber.
Left: 20°C and right: 150°C.

By using the Micro-tack experiment, a single para-aramid fibre can be compressed in the transverse direction for one or multiple cycles. On a three cycles experiment, the behaviour obtained shows a first cycle load/unload highly dissipative and similar response are obtained along a same fibre (Figure. 4). In the transverse direction, the elasticity limit is very low because of the high anisotropy so once the plasticity domain attained, the mechanical parameters are modified: the stiffness increases or the geometrical parameters are also modified, the fibre is not circular anymore but ellipsoidal and the surface contact increases. Because of its anisotropy, the temperature does not affect the mechanical parameters the same way than in longitudinal tests. By using the different directions solicitations, we can hypothesize the molecular motions and rearrangement related to the temperature.

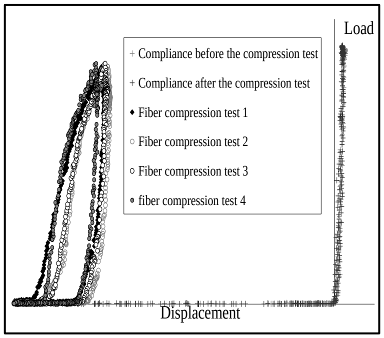

Figure 4: Response of a Micro-tack experiment: 1 cycle load/unload on four points along a fiber.

Contribution of each direction in the dissipation

As the two types of solicitation generate different types of molecular mechanisms, it is useful to link them to know if the contribution of one type of solicitation can make the fiber react a different way. By comparing a «native» fiber and an already transformed one by a longitudinal solicitation during transverse compression experiment, all the mechanical parameters during the first cycle change (figure 5). The dissipated energy increases, it could be explained by the low energy bonds broken during the longitudinal solicitation which permits more motion to the chains. The stiffness decreases because of the pleated sheets decohesion. The remaining strain is bigger due to a higher mobility of the molecules. If the experiment is done the other way around; it appears a non-negligible default is created where the compression is done, the breaking tip is different and the breaking load changes as the geometry of the fiber evolves.

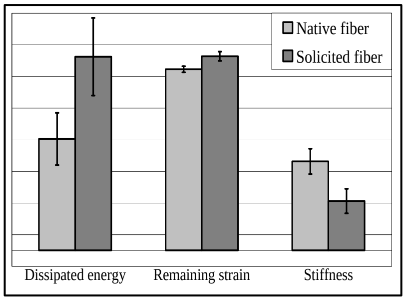

Figure 5: Comparison of mechanical parameters between a «native» fiber

CONCLUSION AND FUTURE WORK

This study has different aspects which may be strongly correlated; the mechanical behavior in each direction separately or in both directions can enhance different molecular mechanisms depending on the solicitation direction. Another parameter is taken into account; the temperature, it makes the structure change and has to be considered to understand the molecular motions. Both of the parts are necessary to understand the mechanic or the thermal contribution in the dissipation of this high performance fiber when it is in use. This experimental study is used to develop a multi-scale microstructural characterization in order to further understand the structural parameters controlling the dissipative mechanism.

To analyze those experimental results, a numerical simulation by the inverse analysis method may be helpful for the understanding of the insight mechanisms linked to the mechanical dissipation.

KEYWORDS

Aramid single fiber, molecular structure, thermo-mechanical and dissipative behaviorr, Cyclic solicitation.

ACKNOWLEDGMENT

The authors are deeply grateful to Y. Favry and A. Bunsell (Mines Paristech, France) and from J.-L. Halary and D. Martina (ESPCI Paristech, France) for providing all the technical support and the scientific advices needed for this work.

REFERENCES

[1] L. Konopasek, J. W. S. Hearle, 1976, *Bulletin of the American Physical Society*, 21, 416-417.
[2] S. L. Phoenix, J. Skelton , 1974, *Textile Research Journal*, 44, 934-940.
[3] R. J. Young, D. Lu, 1992, *Journal of Materials Science*, 27, 5431-5440
[4] M.-H. Lafitte and A.-R. Bunsell, 1985, *Polymer Engineering and Science*, 25, 182-187.
[5] G. Josse, P. Sergot, C. Creton, M. Dorget, 2004, *Journal of Adhesion, 80*, 87-100.

Toward the Development of a High Strain Rate Testing Standard for Advanced Fibers

Gale A. Holmes[1], Jae-Hyun Kim[1], N. Alan Heckert[2], Walter G. McDonough[1], Stefan D. Leigh[1], Kirk D. Rice[3]
National Institute of Standards and Technology:
[1]Materials Science and Engineering Division; [2]Statistical Engineering Division; [3]Material Measurement Science
gale.holmes@nist.gov

PURPOSE/OBJECTIVE

The use of advanced fibers in applications where they are subjected to extremely energetic events has necessitated the need to develop measurement tools that quantify their properties at high strain rates (HSR). The split Hopkinson tension bar (SHTB) has been shown to be suitable for obtaining single fiber HSR data. However, the fiber gluing approach limits the testing rate to two or less fibers per day. In this paper the SHTB is modified to permit the direct gripping of fibers, thereby increasing sample throughput. Statistical analyses of the data indicate (1) that measurement repeatability of tests using the direct grip approach is better than those using the gluing method and (2) the short fiber failure statistics of the method are consistent with the behavior expected as the gauge length decreases.

INTRODUCTION

Advanced fibers are increasingly being used in structural applications where the fibers are exposed to extremely energetic events like impacts and explosions. Two recent workshops [1,2] have emphasized the need to obtain accurate and reproducible high strain rate (HSR) test data on these fibers to evaluate and optimize their performance. Tests using a split Hopkinson tension bar (SHTB) were performed in 2005 to assess the feasibility of using this technique to overcome this deficiency [3]. Although the published HSR data were encouraging, the required testing by this method of short gauge length fibers (≈ 2mm) highlighted several issues related to sample preparation, sample throughput, and the need for an enhanced understanding of the failure statistics of short fibers that must be addressed if this technique is to become a reliable and reproducible test method.

Because fibers do not have a unique tensile strength, 40+ specimens must be typically tested to ascertain their material properties. Since the gluing approach employed in the initial investigation relied on a high-strength epoxy adhesive that required several hours of curing time, the test method could accommodate only about two specimens per day. In this paper, we discuss research efforts that have been undertaken at the National Institute of Standards and Technology laboratories to address these concerns.

EXPERIMENTAL PROCEDURE

Quasi-static test of single fibers were performed in accordance with ASTM Standard C1557-03 (Figure 1a) and using the FAVIMAT (Figure 1b) that is widely used to test single textile fibers of varying lengths using a direct clamping approach that utilizes poly(methyl methacrylate) or rubber clamping blocks to grip the fibers. This standard supersedes ASTM D3379-75 and allows for the quasi-static testing of short single fiber specimens using the mounting tab approach as long as the gauge length is reported.

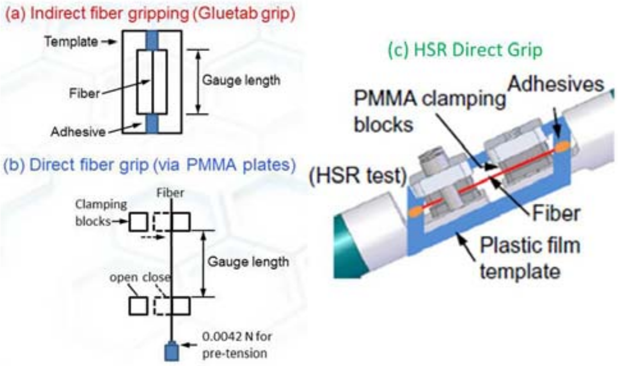

Figure 1. Schematic of the mechanical grips for single fiber tensile loading (a) indirect fiber grip (quasi-static and HSR), (b) direct fiber grip (quasi-static FAVIMAT), and (c) HSR direct fiber grip.

High strain rate tests were employed on the SHTB using the glue tab template to align the specimen in the SHTB and PMMA blocks to grip the fiber consistent with the FAVIMAT approach (see Figure 1c). Poly(p-phenylene terephthalamide) (PPTA, Kevlar 29) fibers, because of their stability and importance to the ballistics industry, are used to test the fidelity of the different gripping methods.

RESULTS AND DISCUSSIONS

Quasi-Static Test Results. PPTA fibers were tested at 2, 5, 10, and 60 mm gauge lengths [4]. Stress-strain curves for the glue-tab specimens exhibit nonlinear behavior starting at ≈ 2 % strain, particularly for the smaller gauge lengths (i.e., 2 mm to 10 mm). The scatter in the curves, are clearly evident from the broader spread of strain-to-failure values for the glue-tab grip specimens (see Figure 2). The increased scatter in the glue-tab method may be associated with inconsistencies in the adhesive bond of the glue to the fiber. In addition, kernel density plots of the fiber strength and plots of the average strain-to-failure values for the two grip methods indicate a consistent progression in the successive values relative to decreasing gauge length only for the direct grip specimen [4].

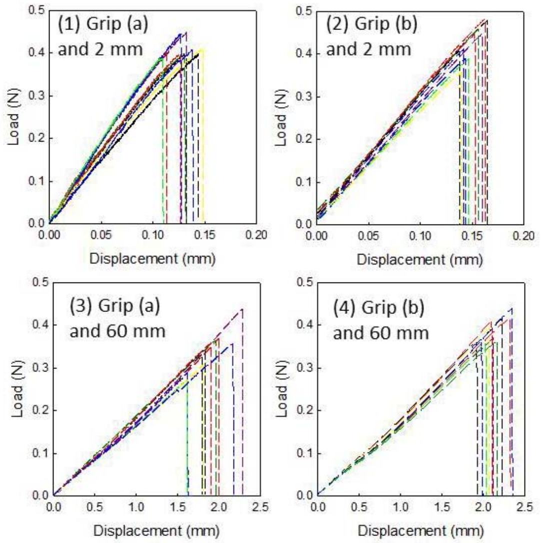

Figure 2. Selected quasi-static stress-strain curves for the 2 mm (1,2) and 60 mm (3,4) gauge length specimens using the glue-tab (1,3) and direct grip (2,4) approaches.

High Strain Rate (HSR) Test Results. Based on the quasi-static analyses the direct grip method was integrated into the SHTB technique. A decrease in the tensile modulus was observed for the 2 mm data relative to the values obtained from 5 mm to 60 mm. Therefore, 5 mm rather than 2 mm gauge length specimens were tested. The HSR test data for this gauge length are plotted relative to quasi-static test data for the 5 mm and 60 mm data in Figure 3.

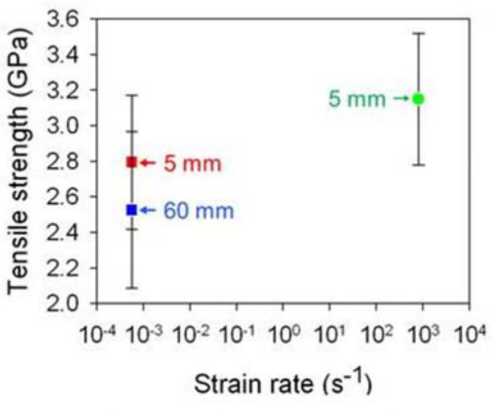

Figure 3. Tensile strengths of PPTA fibers measured under quasi-static loading (5 mm, 60 mm) and HSR loading (5 mm). Error bar indicates standard uncertainty.

The quasi-static data points show the expected increase in average tensile strength (≈ 7 %) when the gauge length of the specimen is decreased from 60 mm to 5 mm. The average tensile strength of the 5 mm HSR specimen is ≈ 14 % higher than its quasi-static data [5]. The percentage strength increase is between values observed by others at 2 mm for Kevlar KM2 and 129 fibers [3].

CONCLUSION

These data and statistical analyses indicate that under quasi-static test conditions the direct gripping of advanced fibers provides data that is more consistent than that obtained from the standard glue tab approach. Integration of this approach into the SHTB technique yields results consistent with those obtained by the slower gluing method. In addition, 10 or more of these samples can routinely be tested in a day, providing enough data to test statistical validity of the often observed increases in tensile strength with increasing strain rate.

FUTURE WORK

The significant tensile strength increase with strain rate indicates that the performance of PPTA fibers may actually be better than expected during ballistic deformations. Because the potential energy absorption of these fibers depends also on their strain-to-failure, direct measure of the failure strain under HSR conditions is needed before a definitive conclusion can be reached. Research is ongoing to verify these initial results.

KEYWORDS

High Strain Rate; Split Hopkinson Tension Bar; Ballistic Fiber; Poly(p-phenylene terephthalamide); Body Armor

REFERENCES

1. NIST Technical Workshop on Research and Metrology of Ballistic Fibers. National Institute of Standards and Technology, 2007.
2. Multiscale Materials Behavior in Ultra-High Loading Rate Environments. U.S. Army Research Laboratory Workshop, 2008.
3. Cheng, M., W. Chen, and T. Weerasooriya. 2005. Mechanical Properties of Kevlar KM2 Single Fiber. *J Eng Mater Technol*, 127(197-203).
4. Kim, J.-H., A. Heckert, S. D. Leigh, H. Kobayashi, W. G. McDonough, K. D. Rice, and G. A. Holmes. 2013. Effects of Fiber Gripping Methods on the Single Fiber Tensile Test: 1. Non-Parametric Statistical Analysis. *J Mater Sci*, DOI 10.1007/s10853-013-7142-y.
5. Kim, J.-H., N. A. Heckert, S. D. Leigh, R. L. Rhorer, H. Kobayashi, W. G. McDonough, K. D. Rice, and G. A. Holmes. 2013. Statistical Analysis of PPTA Fiber Strengths Measured Under High Strain Rate Condition. *Compos Sci Technol*, http://dx.doi.org/10.1016/j.compscitech.2012.03.021.

Surface and Bulk Crystallinity of Polypropylene Filaments

Ali Kilic[1], Eunkyoung Shim[2], Behnam Pourdeyhimi[2]
[1]Istanbul Technical University, Faculty of Textile Technologies and Design, Istanbul, Turkey
[2]The Nonwovens Institute, North Carolina State University, Raleigh, NC
akilic@ncsu.edu

OBJECTIVE

A study on the surface crystallinity of polypropylene (PP) filaments was reported. Results obtained from Attenuated Total Reflection – FTIR were confirmed with analysis via tapping mode (TM) Atomic Force Microscopy.

INTRODUCTION

Morphology over the upper surface of polymer structures are particularly important for effective surface treatment[1,2], wetting ability[3], adhesion[4], paintability[5], cell proliferation[6] and electrostatic charge retention properties[7]. Differential Scanning Calorimetry (DSC), X-ray Diffraction (XRD), and density gradient column are well-known methods for analyzing bulk crystallinity. However a reliable methodology is essential to investigate crystallinity over the surface.

There are several reasons that would be asserted behind the differences in surface and bulk crystallinity of the polymer materials. Differences in thermal history, tendency to oxidative reactions, energetic surface treatment techniques and mechanical stresses will cause significant changes between surface and bulk layers. Interestingly, according to author's knowledge there are few studies on surface crystallinity of fibers, though this property would enlighten important chemical and electrical behaviors. Atomic Force Microscopy(AFM)[8–10], Grazing Angle Incident Xray Diffraction (GIXD) [11,12] and Attenuated Total Reflection IR Spectroscopy (ATR) [13–18] are mentioned techniques to evaluate surface crystallinity of polymeric films.

In spite of the lack of quantitative data, AFM is a reliable, high resolution method to investigate morphology and mechanical properties of polymer surfaces. Tapping mode AFM and nanoindentation are informative for analyzing multiphase systems like copolymer and blends at the highest resolution[19–23]. Tapping mode AFM is based on oscillation of cantilever close to its resonance frequency, thus interaction with the probe and surface results with a shift in the resonance vibration. The height needed to keep the set amplitude constant, provides information about topography, whereas measured phase shift will depend on viscoelastic properties of the surface[23].
GIXRD might be applicable for flat surfaces, which makes test of filaments impossible, however from corresponding GIXRD studies[12] we know that bulk and surface of films will possess almost same crystal structure.

On the other hand it is known that polymer samples with different conformational and configurational properties exhibit distinguishing peaks from each other due to changes in molecular vibrations. Several works have also been done on absorbance characteristics of PP[13,17,18]. Quynn et al[16] have shown that the absorbance ratio at A_{997}/A_{972} is linearly related to polymer density and hence may be used to measure polymer crystallinity.

APPROACH

In this study we analyzed the surface crystallinity of PP filaments via ATR-FTIR spectroscopy. Results were compared with TM-AFM data.
34 MFR iPP resin, having Mn~55,000g/mole, Mw~180,000g/mole molecular weight was used. PP filaments were melt-spun in Hills multifilament spinning line (single screw extruder with an L:D ratio of 24:1). Spinning speed was fixed at 2000m/min and throughput was $0.58\text{ghole}^{-1}\text{min}^{-1}$. Diameters of the filaments were 20µm. To modify surface crystallinity unwounded filaments were annealed at 70 and 110°C for 12h in free-state.

RESULTS AND DISCUSSION

Stiffness analysis was done via patented program in Asylum MFP-3D-SA AFM. Stiffness over the surface for control sample was significantly lower than inner regions. An increase towards inner regions was observed even for untreated sample. Stiffness for heat treated samples were similar for both surface and inner regions. Interestingly up to 0.15µm depth untreated filament had a higher stiffness, which would be due to high shear at spinneret wall resulting with high chain orientation. We observed that crystallinity values continuously increased upon heat treatment (Figure1). However for the case of surface crytallinity annealing at 70 and 110°C resulted with similar crystallinities. This would be due to exclusion of lower molecular weight components and impurities over the surface, which disturbed crystal ordering at high temperatures.

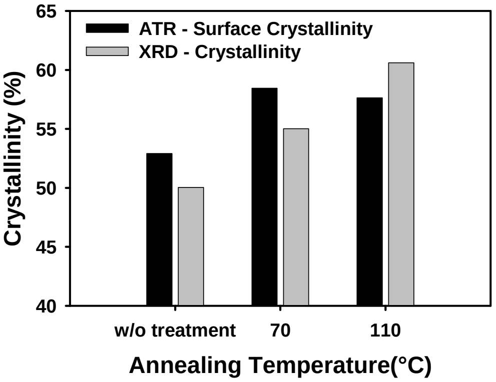

Figure 1. Comparison between ATR-Surface Crystallinity and XRD-crystallinity

CONCLUSION

Differences in the behavior of surface and bulk should be considered particularly for ongoing surface treatment studies. Here using Tapping mode AFM, results obtained from ATR-FTIR technique were confirmed. Overall crystallinity is not same with surface crystallinity as shown after comparing with XRD data. Results would be enlightening for the surface treatment studies on fibrous structures

FUTURE WORK

We are planning to check effect of surface crystalliniy on electrostatic filtration performance.

ACKNOWLEDGMENT

The authors gratefully acknowledge the Nonwovens Cooperative Research Center (NCRC) for financial support of this work. Thanks are also due to Dr Richard Spontak for fruitful discussions, Sunoco Chemicals and Keith Jones at Asylum Research for AFM studies.

REFERENCES

1. Blythe, A. R., Briggs, D., Kendall, C. R., Rance, D. G. and Zichy, V. J. I. Surface modification of polyethylene by electrical discharge treatment and the mechanism of autoadhesion. *Polymer* 19, 1273–1278 (1978).
2. Kim, K. S., Ryu, C. M., Park, C. S., Sur, G. S. and Park, C. E. Investigation of crystallinity effects on the surface of oxygen plasma treated low density polyethylene using X-ray photoelectron spectroscopy. *Polymer* 44, 6287–6295 (2003).
3. Ogita, T., Ponomarev, A. N., Nishimoto, S.-I. & Kagiyat, T. Surface Structure of Low-Density Polyethylene Film Exposed to Air Plasma. *Journal of Macromolecular Science: Part A-Chemistry* 22, 1135–1150 (1985).
4. Nadkarni, P. D., Kildsig, D. O., Kramer, P. A. and Banker, G. S. Effect of surface roughness and coating solvent on film adhesion to tablets. *Journal of Pharmaceutical Sciences* 64, 1554–1557 (1975).
5. Ryntz, R. A. The effects of thermoplastic poly(olefin) (TPO) morphology on subsequent paintability and thermal shock performance. *Progress in Organic Coatings* 27, 241–254 (1996).
6. Washburn, N. R., Yamada, K. M., Simon Jr., C. G., Kennedy, S. B. and Amis, E. J. High-throughput investigation of osteoblast response to polymer crystallinity: influence of nanometer-scale roughness on proliferation. *Biomaterials* 25, 1215–1224 (2004).
7. Arita, Y., Sha Shiratori, S. and Ikezaki, K. A method for detection and visualization of charge trapping sites in amorphous parts in crystalline polymers. *Journal of Electrostatics* 57, 263–271 (2003).
8. De Cupere, V. M. & Rouxhet, P. G. Surface crystallization of poly(ethylene terephtalate) studied by atomic force microscopy. *Polymer* 43, 5571–5576 (2002).
9. Risnes, O. K., Mather, R. R., Neville, A. & Buckman, J. Comparing the surface and internal structure of polypropylene fibres using advanced microscopy techniques. J*ournal of Materials Science* 38, 2161–2165 (2003).
10. De Rovère, A., Shambaugh, R. L. and Edgar, A. Investigation of gravity-spun, melt-spun, and melt-blown polypropylene fibers using atomic force microscopy. *Journal of Applied Polymer Science* 77, 1921–1937 (2000).
11. Kawamoto, N. et al. Microstructural characterization of polypropene surfaces using grazing incidence X-ray diffraction. *Macromolecular Chemistry and Physics* 199, 261–266 (1998).
12. Nishino, T., Matsumoto, T. and Nakamae, K. Surface structure of isotactic polypropylene by X-ray diffraction. *Polymer Engineering & Science* 40, 336–343 (2000).
13. Hobbs, J. P., Sung, C. S. P., Krishnan, K. and Hill, S. Characterization of surface structure and orientation in polypropylene and poly(ethylene terephthalate) films by modified attenuated total reflection IR dichroism studies. *Macromolecules* 16, 193–199 (1983).
14. Yamashita, T. and Ikezaki, K. A method for correlating charge traps of polypropylene to its morphology. *Journal of Electrostatics* 63, 559–564 (2005).
15. Arita, Y., Sha Shiratori, S. and Ikezaki, K. A method for detection and visualization of charge trapping sites in amorphous parts in crystalline polymers. *Journal of Electrostatics* 57, 263–271 (2003).
16. Quynn, R. G., Riley, J. L., Young, D. A. and Noether, H. D. Density, crystallinity, and heptane insolubility in isotactic polypropylene. *Journal of Applied Polymer Science* 2, 166–173 (1959).
17. Bonnerup, C. and Gatenholm, P. Physical modifications of propylene/ethylene-propylen-diene-monomer rubber surfaces. I. Determination of surface composition and surface order by fourier transform infrared-attenuated total reflectance. *Journal of Polymer Science Part B: Polymer Physics* 31, 1487–1494 (1993).
18. Sung, C. S. P. and Hobbs, J. P. Development of Ft Ir Attenuated Total Internal Reflection Dichroism Techniques for Structural - Characterization of Polymer Surfaces. Taylor & Francis. *Chemical Engineering Communications* 30, 229 (1984).
19. Bar, G., Thomann, Y., Brandsch, R., Cantow, H.J. and Whangbo, M.H. Factors Affecting the Height and Phase Images in Tapping Mode Atomic Force Microscopy. Study of Phase-Separated Polymer Blends of Poly(ethene-co-styrene) and Poly(2,6-dimethyl-1,4-phenylene oxide). *Langmuir* 13, 3807–3812 (1997).
20. Bar, G., Ganter, M., Brandsch, R., Delineau, L. and Whangbo, M.H. Examination of Butadiene/Styrene-co-butadiene Rubber Blends by Tapping Mode Atomic Force Microscopy. Importance of the Indentation Depth and Reduced Tip−Sample Energy Dissipation in Tapping Mode Atomic Force Microscopy Study of Elastomers. *Langmuir* 16, 5702–5711 (2000).
21. Jandt, K. D. Developments and perspectives of scanning probe microscopy (SPM) on organic materials systems. *Materials Science and Engineering: R: Reports* 21, 221–295 (1998).
22. Wen, G., Li, X., Liao, Y. and An, L. Surface phase separations of PMMA/SAN blends investigated by atomic force microscopy. *Polymer* 44, 4035–4045 (2003).
23. Konrad, M., Knoll, A., Krausch, G. and Magerle, R. Volume Imaging of an Ultrathin SBS Triblock Copolymer Film. *Macromolecules* 33, 5518–5523 (2000).

Effect of Electrolytic Oxidation and Sizing on the Mechanical Performance of Carbon Fibre Composites

Claudia Creighton, Abdullah Kafi, Bronwyn Fox
Deakin University, Institute for Frontier Materials, Pigdons Road, Waurn Ponds Campus, Geelong, Victoria 3216, Australia
Contact Author: claudia.garschke@deakin.edu.au

ABSTRACT

The mechanical and thermo-dynamical performance of fibre reinforced composites made from carbon fibres selected at different stages of the manufacturing process are experimentally investigated. Untreated, electrolytically oxidized and epoxy sized fiber composites were tested on their interlaminar shear strength (ILSS). Epoxy sized samples provided a significantly higher strength followed by oxidized fiber composites. However, thermo-dynamical analysis (DMTA) showed a shift of storage modulus towards lower temperatures suggesting formation of an interphase between fibre and matrix with different mechanical properties for the sized fibre composites.

INTRODUCTION

The performance of composite laminates is strongly dependent on the adhesion between the fibre reinforcement and resin matrix, with the surface treatment of the fibres playing a key role in determining the level of adhesion achieved. During carbon fibre manufacture, the fibres pass through the electrolytic oxidation process to create oxygen-containing functional groups on the fibre surface, which promote the adhesion of sizing agents applied in another production step. The fibres are coated with a polymer-based sizing agent that will not only protect the fibre but also make the fibre surface more compatible with the resin matrix. The exact role of fibre sizing on fibre-matrix adhesion is the subject of sustained debate in the literature [1]. One of the common failure mechanisms of composites is interplay delamination, which has been shown to be improved with the application of sizing [2]. However, little attention has been paid to the strength of the fibre-matrix interface at elevated temperatures to compare the fibre treatment types. The aim of this work is to investigate the relationship between of fiber surface treatment and fiber-matrix adhesion, as well as to study to what degree the fiber treatment affects subsequent composite strength.

EXPERIMENTAL

Materials

The fibres used in this study were PAN-based carbon fibres Panex 35 (Zoltek, Hungary) with a 50K tow size. The fibres were collected after three stages of production; carbonization, electrolytic oxidation, and epoxy sizing. These are referred to as unoxidised, oxidised, and sized, respectively, throughout this paper. The resin used to prepare composite samples was an automotive grade epoxy resin, Epikote RIMR 935 with hardener Epikure RIMH 937 (Momentive) mixed at a ratio of 100:38 by weight.

Composite Manufacture

Composite laminates of approximately 2.5mm thickness were prepared for mechanical testing. Unidirectional preforms were made from each fibre type, placed on a 5mm thick aluminium plate and vacuum bagged. The dry preform was then infused with resin at 40°C assisted by vacuum. The panels were cured for 5h at 50°C and post cured at 150°C for another 6h. The test specimens were cut using a diamond saw and conditioned as per ASTM D5229 standard prior to testing.

Interlaminar Shear Test (ILSS)

The interlaminar shear strength (ILSS) tests of carbon/epoxy composites were conducted in accordance with ASTM D2344 at a crosshead speed of 1 mm/min following the span to thickness ratio of 4 and length to thickness ratio of 6. The ILSS was calculated from the equation $ILSS = 0.75P_b/b*d$, where P_b represents the breaking load, b the width and d the thickness of specimen. All specimens were supported in a fixture and loaded at mid span. A minimum of 9 specimens per batch were tested.

Dynamic Mechanical Analysis

The thermo-mechanical properties of composite laminates made from untreated, oxidised and sized fibres were compared using DMTA analysis following standard ASTM D7028. Specimens of 12 x 60mm in dimension were tested in dual cantilever mode using a DMA Q800 (TA instruments). The samples were heated from room temperature to 250°C at 5°C/min with a test frequency of 1Hz. The thermo-mechanical characteristics were determined from 5 specimens for each fibre type composite.

Scanning Electron Microscopy (SEM)

The fracture surface of ILSS testes samples was examined using a Joel scanning electron microscope (SEM) and an accelerating voltage of 10kV. The samples were sputter-coated with gold using a Bal-tec SCD50 sputter coater.

RESULTS AND DISCUSSION

Interlaminar Shear Strength

The interlaminar shear strength (ILSS) varied significantly for the materials tested. Composite samples made from epoxy-sized fibres performed best, having strength of 58MPa (Table 1), which is most likely due to better wetting of the fibres by the matrix. Samples containing oxidised fibres showed noticeably lower shear strength of 40MPa followed by unoxidised composite specimens with an average failure load of 34MPa. The better ILSS of the oxidized fibre composites, compared to unoxidised, may be related to the removal of week layers and contaminants from the fibre surface during the electrolytic oxidation process.

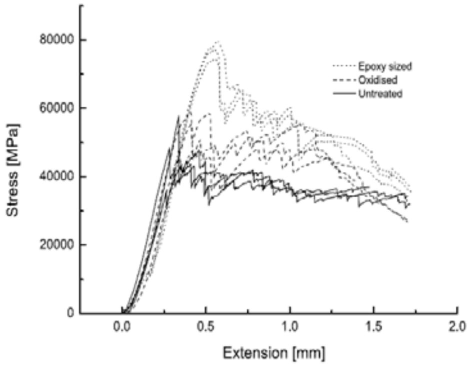

Fig.1 Interlaminar shear strength of unoxidised (line), oxidised (dashed line) and sized fibres (dotted line)

The delamination fracture surface of untreated fibre composites in Fig.1a demonstrates a smooth resin surface, where the fibre appears to be pulled out without resin residuals. The epoxy sized sample Fig.1c in the other hand shows frayed resin sections indicating resin failure rather than failure in the fibre-matrix interface.

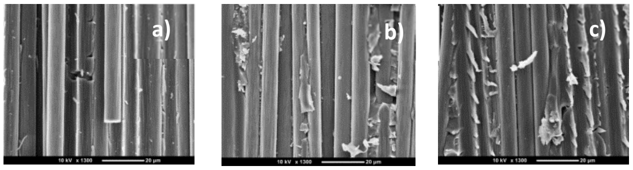

Fig.2. SEM images of carbon fibres: (a) unoxidised, (b) oxidized (c) epoxy sized

Thermal Dynamical Analysis (DMTA)

The tan δ and storage modulus curves of the three different composite types are presented in Fig.3. The storage modulus of the epoxy sized composites shows a loss in strength at lower temperatures when compared to unoxidised and oxidized c indication differences between the samples. The tan δ peak height of DMTA samples was found to vary for the samples tested. This phenomenon has been reported for different sizing and surface treatments with an inverse relationship to the interlaminar shear strength in composites [3, 4]. This observation is also true for the results in this study, the unoxidised fibre composite showing the highest tan δ value (0.49), followed by the oxidised (0.40) and then the sized fibre (0.34) reinforced composite. The temperature at tan δ peak is similar for all cases; however the value is slightly lower for epoxy-sized samples. This small change in the glass transition temperature in the epoxy-sized composite may be due to the existence of an interphase with different mechanical properties compared to the bulk matrix.

Table 1 ILSS and DMTA results for composites made from unoxidised, oxidized and sized fibres

	ILSS	DMTA		
	(MPa)	Storage Modulus (at 30°C) (GPa)	Tan δ_{max}	Tan δ_{peak} (°C)
Unoxidised	34±4.4	38.6±0.7	0.49±0.004	153.4±1.0
Oxidised	40±3.0	41.2±1.1	0.40±0.003	153.8±1.2
Sized	58±2.5	39.7±1.2	0.34±0.019	151.6±0.4

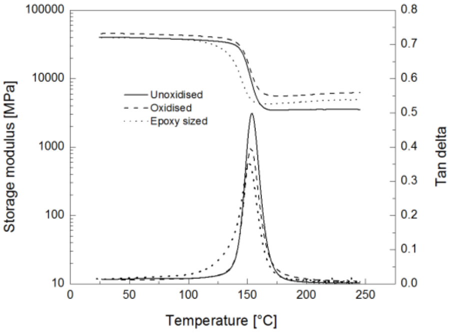

Fig.3 Storage modulus and tan δ of composites made from unoxidised (line), oxidized (dashed line) and epoxy-sized (dotted line) carbon fibres

CONCLUSIONS

Fibre reinforced composites made from untreated, electrolytically oxidized and epoxy sized carbon fibres were tested on their mechanical and thermo-dynamical performance. While sized fibre samples with interlaminar shear strength of 58MPa outperformed the strength of oxidized (40MPa) and unoxidised fibers (34MPa) by ~45%, the thermo-dynamical analysis revealed a loss in strength at temperatures above 100°C. With the sizing applied, SEM images demonstrate fracture in the resin matrix rather than in the fibre-matrix interface predominantly observed with the oxidized and untreated samples. The lower thermo-dynamical resistance suggests a softer interphase between matrix and fibre. Future work will involve nanoscale modulus measurements across the fibre-interphase-matrix region in order to develop further understanding of the observed difference in performance.

ACKNOWLEDGMENT

The authors acknowledge the support of Deakin University and AFFRIC in this research.

REFERENCES

1. Jones, F.R. A Review of Interphase Formation and Design in Fibre-Reinforced Composites. *Journal of Adhesion Science and Technology*, 2010. 24(1): p. 171-202.
2. Zhang, R., et al.. Influence of sizing emulsifier content on the properties of carbon fibers and its composites. *Materials & Design*, 2012. 33(0): p. 367-371.
3. Harris, B., et al.. Study of carbon fibre surface treatments by dynamic mechanical analysis. *Journal of Materials Science*, 1993. 28(12): p. 3353-3366.
4. Afaghi-Khatibi, A. and Y.-W. Mai. Characterisation of fibre/matrix interfacial degradation under cyclic fatigue loading using dynamic mechanical analysis. *Composites Part A: Applied Science and Manufacturing*, 2002. 33(11): p. 1585-1592.

Multifunctional Carbon Nanotube Yarns—Production, Properties, and Applications

Menghe Miao
CSIRO Materials Science & Engineering Division
P.O. Box 21, Belmont, Victoria 3216, Australia
menghe.miao@csiro.au

ABSTRACT

Carbon nanotubes (CNTs) possess very high mechanical strength and are electrically conductive. There have been high expectations that carbon nanotube macrostructures such as fibers or yarns express similar properties. The discovery of drawable carbon nanotube forests opened up the possibility of constructing a wide range of carbon nanotube macrostructures and sparked interests in developing applications from these structures. This presentation covers several aspects of research at CSIRO in recent years on drawable carbon nanotube forests and their resulting macrostructures.

Research on the synthesis of CNT forests has been focused on achieving consistent drawability and increased CNT length. Consistently drawable forests are essential for the production of CNT yarns, in pure or composite, with controlled structure and properties.

The drawn carbon nanotube webs can be spun into continuous pure CNT yarns, by twist insertion, solvent shrinking and rub-densification methods. The yarn strength can be further improved by post spinning treatments. Carbon nanotube yarn production can be scaled up to speeds that are comparable to state-of-the-art conventional extra fine count textile yarn production using specially engineered spinning machinery.

Commonly used methods of manufacturing CNT reinforced polymeric composites generally include dispersing carbon nanotubes in a polymer matrix and then processing the composite material in substantially the same way as for common polymer materials. Carbon nanotubes tend to agglomerate and are thus difficult to disperse and regroup into an aligned structure. Modifications to the CNTs result in damages to the CNT structure and properties. We discovered a new method of improving the alignment of carbon nanotubes in solid-state without dispersing and regrouping them. The use of a lubricant loosens the interconnections between the carbon nanotubes so that they can slide relative to each other and align themselves longitudinally by a series of drawing operations. This method is applied to the production of carbon nanotube/polymer composite fibers via the gel-spinning route and has demonstrated a remarkable reinforcement effect.

Wearable electronics provide a platform for on-body sensing to support people in various situations and activities. They need flexible energy storage devices to ensure high performance, safety and comfortability. Carbon materials are traditionally used for energy storage. We produced threadlike supercapacitors that are much finer but stronger than fine count cotton yarns and are highly resistant to flexing that occurs to clothing all the time. The supercapacitors consist of two CNT yarns infiltrated with polyaniline nanowire arrays that possess large capacitance and can be charged and discharged at very high rates.

Carbon nanotube yarns are multifunctional materials. A wide range of applications have been demonstrated by different laboratories around the world. There is little doubt that this will continue to be a very active area of research.

KEYWORDS

Carbon nanotube; Yarn; Strength; Electrical conductivity; Energy cell.

ACKNOWLEDGMENT

CSIRO colleagues: CP Huyhn, J McDonnell, L Vuckovic, M Redrado Notivoli, D Stewart, F Berthier, N Gibbons, P Smale, J Baum, L Kviz, C Veitch, M Pate, S Barnes, SC Hawkins, JY Cai, TR Gengenbach, K Atkinson, W Humphries, S Lucas.

Collaborators: R Knot (Australian Nuclear Science and Technology Organisation); J Wang, Z Wang, Q Gu (Chinese Academy of Sciences); K Wang, Q Meng, Y Zhang, Z Wei (China National Centre of Nanoscience and Nanotechnology).

REFERENCES

1. K Wang, Q Meng, Y Zhang, Z Wei, M Miao. High Performance Two-Ply Yarn Supercapacitors Based on Carbon Nanotubes and Polyaniline Nanowire Arrays. *Advanced Materials*, DOI: 10.1002/adma.201204598.
2. J Wang, M Miao, Z Wang, W Humphries, Q Gu. A method of mobilizing and aligning carbon nanotubes and its use in gel spinning of composite fibres. *Carbon*. In press.

3. M Miao. Yarn spun from carbon nanotube forests: Production, structure, properties and applications. *Particuology.* In press.
4. M Miao. Production, structure and properties of twistless carbon nanotube yarns with a high density sheath. *Carbon* 50. 2013, (13): pp. 4973-4983.
5. M Miao, SC Hawkins, JY Cai, TR Gengenbach, R Knot, CP Huyhn. Effect of gamma irradiation on the mechanical properties of carbon nanotube yarns. *Carbon* 49. 2011, (14): pp. 4940–4947.
6. M Miao. Electrical conductivity of pure carbon nanotube yarns. *Carbon,* 49. 2011, (12): pp. 3755-3761.
7. M Miao, J McDonnell, L Vuckovic, SC Hawkins. Poisson's ratio and porosity of carbon nanotube dry-spun yarns. *Carbon*, 48. 2010, (10): pp. 2802–2811.

Transverse Modulus of Carbon Fibres

Linda Hillbrick, Jamieson Kaiser, Mickey Huson, Geoff Naylor
CSIRO Materials Science and Engineering, Waurn Ponds, Geelong, Victoria 3216, Australia
mickey.huson@csiro.au

OBJECTIVE

The transverse modulus of carbon fibre is important for modelling the performance of composite materials; however its determination is difficult because of fibre size and geometry. This work explores the two main techniques that are available for determining the transverse modulus of high performance fibres, namely by simple compression and by nano-indentation. In the case of simple compression more than one method of analysis is available hence initial work has been carried out on macro-cylinders in order to shed light on the different methods. A micro-compression tester is being built with the precision needed to cope with the small deformations required for testing a single carbon fibre.

INTRODUCTION

Single fibre transverse compression tests, where a cylindrical fibre is compressed between a pair of plane parallel plates (Figure 1), is a widely reported method for determining the transverse compression properties of highly oriented fibres [1].

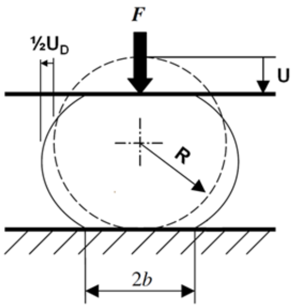

Figure 1. Schematic diagram showing the compression of a fibre between two parallel platens. The fibre has a radius of R, and also shown are the force (F), the diametric expansion (UD), the diametric compression (U) and the contact width (2b).

Several different analytical models have been used to interpret the transverse compressive behaviour of a fibre [2-4], viz. those proposed by Pheonix and Skelton [2], Jawad and Ward [3] and Cheng et al. [4]. This paper evaluates these models by studying the compression of isotropic and anisotropic macro-scale elastic materials.

Nano-indentation techniques based on instrumented indentation (IIT) and atomic force microscopy (AFM) have also been used to study the mechanical properties of samples [5-6].

EXPERIMENTAL

Cylindrical compression

Polyurethane (PU) and poly(methyl methacrylate) (PMMA) cylindrical rods of various diameters and lengths, along with cuboids machined from these rods, were used for compression testing. Samples were initially placed under longitudinal compression followed by transverse compression using a compression rate of 5%/min. In both instances the strain and force were recorded on an Instron 4500. Theoretical transverse compression curves for the three models were generated using the modulus determined from the cuboid experiment on the isotropic PU cylinders. These curves were compared to the experimental transverse compression curves. For the anisotropic PMMA the experimentally determined longitudinal modulus was used in the three models to calculate the transverse modulus. This was compared to the experimental transverse modulus obtained by compressing the cuboids

Nano-indentation

Mechanically polished carbon fibre (M46J) composites were further polished using focussed ion beam (FIB) to produce flat longitudinal cross-sectional fibre surfaces. Ion milling was conducted normal to the surface on a FEI Helios Nanolab 600 Dual-Beam Focused Ion Beam-Scanning Electron Microscope (FIB-SEM). Both the mechanically polished and FIB polished carbon fibre surfaces were nano-indented on a Digital Instruments Dimension 3000 Scanning Probe Microscope using a diamond cube corner probe and a maximum load of 18μN. A Hysitron nano-indenter fitted with a Berkovich diamond indenter was used to indent the mechanically polished surfaces of the carbon fibre with a maximum load of 9000μN.

RESULTS AND DISCUSSION

Cylindrical compression

The Jawad and Ward and the Phoenix and Skelton models were found to be similar and were best at fitting the transverse compression of isotropic PU cylinders as shown in Figure 2.

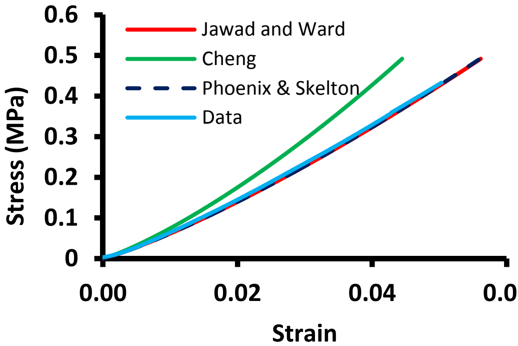

Figure 2. Transverse compression of isotropic PU, E=23 MPa, ν=0.39)

Analysis of the transverse compression curves from the stiffer anisotropic PMMA cylinders showed that the Cheng model yielded results that were closest to the experimental transverse modulus obtained by compressing the cuboids (Table I.)

Table I. Experimental and predicted transverse modulus of PMMA

Sample Length (mm)	PMMA Experimental results		Prediction (ν=0.39)	
			Jawad & Ward's model	Cheng's model
	E_L (GPa)	E_T (GPa)	E_T (GPa)	E_T (GPa)
50	3.3	2.5	2.9	2.5
75	3.3	2.2	3.0	2.6
100	3.4	-	3.0	2.6
Ave.	**3.3**	**2.3**	**3.0**	**2.6**

SPM Nano-indentation

The low force associated with SPM indentation proved to be insufficient to get reliable modulus data. However the SPM indentations did show residual indents on the FIB polished samples (Figure 3A) whilst these indents were not apparent on the mechanically polished surface (Figure 3B).

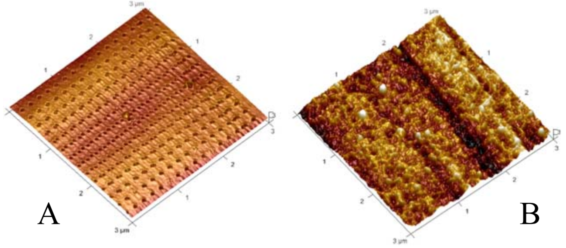

Figure 3. SPM image of M46J composite after indentation by SPM. A) FIB polished and B) mechanically polished

This implies that the surface of the FIB polished fibre was modified during the milling. Raman spectroscopy confirmed this, showing that the surface of the carbon fibre had been converted to an amorphous structure (Figure 4).

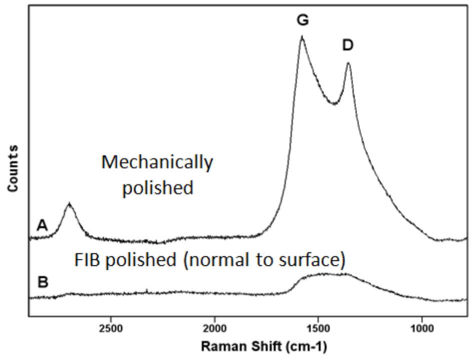

Figure 4. Raman spectra of M46J fibres A) Mechanically polished and B) FIB polished (normal to surface).

In view of this, only the mechanically polished sample was nano-indented by the Hysitron. Indents away from the centre of the fibre gave poor load/penetration curves suggesting the much softer matrix may be influencing the result.

CONCLUSION

Results from the simple compression tests on macro-cylinders are encouraging but clearly show that further is needed to ascertain which of the models is most applicable to the simple compression of carbon fibre. It is clear that sample preparation is very important with regard to obtaining sensible and reproducible nano-indentation data. The role of the matrix in nano-indentation test samples needs to be explored further.

KEYWORDS

Carbon fibre, transverse modulus, compression, nano-indentation.

ACKNOWLEDGMENT

The authors gratefully acknowledge CSIRO Materials Science and Engineering for the funding this study and Dr Jeff Church for conducting the Raman spectroscopy.

REFERENCES

1. Hadley, D.W, et al., Proceedings of the Royal Society of London: Series A, 1965. 285: p. 275-286.
2. Phoenix, S.L. and J. Skelton, *Textile Research Journal*, 1974. 44(12): p. 934-940.
3. Jawad, S.A. and I.M. Ward, *Journal of Materials Science*, 1978. 13(7): p. 1381-1387.
4. Cheng, M. et al., *International Journal of Solids and Structures*, 2004. 41(22-23): p. 6215-6232.
5. Burnham NA. and Colton RJ., *Journal of vacuum science & technology A*, Vacuum, surfaces, and films. 1989;7(4):2906-13.
6. McAllister QP, et al., *Journal of Materials Research*. 2012;27(1):197-213.

Water Effects on Natural Fibers and Its Implications to Shape Memory Polymer Composite Fiber

Jing Lu, Jinlian Hu, Jianping Han
The Hong Kong Polytechnic University
tchujl@polyu.edu.hk

ABSTRACT

Some natural fibers, particularly protein fibers like spider silk and wool show good water sensitive properties. The structures of protein fibers have large quantities of hydrogen bond which is identified as the reason behind the feature. This paper demonstrates the water-sensitive property of wool fiber and shape memory effect by water driven and explores the possibility of water-sensitive shape memory fibers.

INTRODUCTION

Spider silks, as well as many other biomaterials, have a hierarchical structure such as cellulose and wool [1-2]. The primary structure is its amino acid sequence, mainly consisting of highly repetitive glycine and alanine blocks. Large quantities of hydrogen bond exit in these fibers because of the chemical structure of protein molecular. Hydrogen bonds are weak but clusters of weak hydrogen bonds in crystalline domains work cooperatively to resist force and dissipate energy. Clusters of hydrogen bonds in amorphous matrix work as the temporary locks to determine the deformation and shapes of the fiber [3]. Wool fiber shows different tensile curves under different humidity conditions but there have no any report about the shape change and recovery effect driven by water. Water sensitive shape memory polymer was reported by H.M. Huang [4] and Y. Zhu [5]. Hydrogen bonding is used as the switch behind these features. Y. Zhu reported a novel and effective strategy to achieve rapidly switchable shape recovery in a material by a simple wetting process and fixing through an easily applicable programmed drying process. This work also gives a productive method to make the raw materials for water-responsive shape memory fiber spinning.

WATER-SENSITIVE OF NATURAL PROTEIN FIBERS

At high humidity, dragline spider silk can supercontract and the shrinkage up to 50% of its original length[6-7]. Water absorbed during supercontraction is hypothesized to plasticize silk fibers by disrupting hydrogen bonding between proteins, re-orientation and coiling of silk molecules [8]. Figure 1 shows various tensile curves of spider silk and supercontracted silk tested in air and in water. The superontracted spider silk has lower modulus and large elongation in contrast with the naturally spun spider silk.

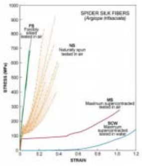

Figure 1 Comparison of stress-strain curves of spider silk[9]

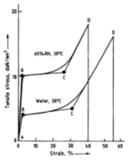

Figure 2 Stress-strain curves of wool tested under various humidity[1]

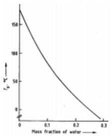

Figure 3 Glass-transition temperature of wool as a function of mass fraction of water[1]

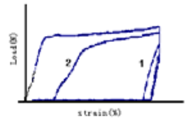

Figure 4 Cyclic tensile curves of wool fiber

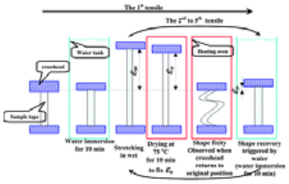

Figure 5 Water-sensitive shape memory effects of shape memory composite

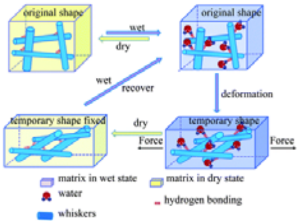

Figure 6 Proposed rapidly switchable water-sensitive shape-memory mechanism for the CNW/TPUs comprising a CNW percolation network in an elastomeric matrix[5]

WATER-DRIVEN SHAPE MEMORY POLYMER AND FIBER SPINNING

A variety of spinning technology is used to make the fiber of such composites, such as wet spinning, dry spinning, dry-wet spinning or electric spinning. A typical wet spinning setup located in the PI's lab is shown in Fig. 10 (Ji et al., 2006). The rheology of such solution will be studied, because the reversible QHB would play a great role on the miscibility of modified celluloses and elastomers. Few literatures can be referred to in this polymer solution. Only the aggregation in film caused by UPy (ureidopyrimidinone) in QHB and the directional lateral aggregation vis the urea and urethane hydrogen bonding motifs was studied by using AFM, DMA, FTIR, DSC (Kautz et al., 2006). Therefore, the composite fibers will be prepared under elevated temperature to avoid the aggregation of QHB units in solution.

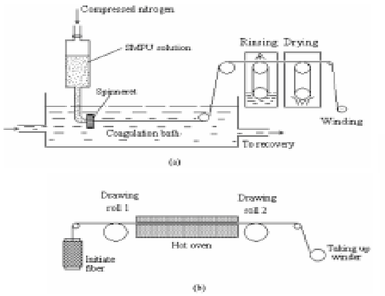

Figure 7 Schematic diagram of (a) the wet spinning equipment and (b) heat setting of fibers

CONCLUSIONS

Water-sensitive protein natural fibers are stressed by virtue of water effects on hydrogen bonding density. Wool fiber also exhibit good water-responsive shape memory effect according to the cyclic tensile testing. The new rapid switchable water-sensitive shape memory polymer composites may open up an avenue for the research and applications of natural/green composites materials in different areas such as textiles, medical, biological and high performance. The wet-spinning of this kind of shape memory polymer composite is feasible. In comparison with shape memory polymer finishing and shape memory polyurethane fibers, the fabric made with cellulose based shape memory fibers will have wrinkle resistance and crease retention and further improve the comfort sensation of textile products such as intimate apparel. It will provide numerous applications for textiles and apparel.

KEYWORDS

Water-sensitive, natural protein fiber, water-responsive shape memory polymer, wet spinning

ACKNOWLEDGMENT

This study was supported by the Hong Kong Government RGC research project (PolyU5182/09E), the Niche Area Fund of the Hong Kong Polytechnic University (J-BB6M) and the Opening Project of State Key Laboratory of Polymer Materials Engineering (Sichuan University) (200803). Authors would like to thank the support from the Materials Research Centre and the team of Shape Memory Textile Centre in the Hong Kong Polytechnic University.

REFERENCES

1. Todd A. Blackledge, Spider silk: a brief review and prospectus on research linking biomechanics and ecology in draglines and orb webs. *Journal of Arachnology*, 2012, 40 (1): 1-12.
2. W. S. Simpson,G. H. Crawshaw , Wool: science and technology, Woodhead Publishing Ltd., England.
3. Denise Brehm, A tangled web: CEE researchers unravel the secrets of spider silk's strength, http://web.mit.edu/newsoffice/2008/rd-spiders-tt0319.html.
4. W. M. Huang, B. Yang, L. An, C. Li, and Y. S. Chan, Water-driven programmable polyurethane shape memory polymer: Demonstration and mechanism, *Appl. Phys. Lett.*, 2005, 86, 11410.
5. Yong Zhu, Jinlian Hu, Hongsheng Luo, Robert J. Young , Libo Deng, Shen Zhang, Ying Fan and Guangdou Ye, Rapidly switchable water-sensitive shape-memory cellulose/elastomer nano-composites, *Soft Matter*, 2012, 8: 2509-2517.
6. Work, R.W., 1981. A comparative study of the supercontraction of major ampullate silk fibers of orb-web-building spiders (Araneae). *J. Arachnol.*, 1981, 9: 299-308.
7. Guinea, G.V., Elices, M., Pe´rez-Rigueiro, J., Plaza, G., Self-tightening of spider silk fibers induced by moisture. *Polymer*, 2003, 44: 5785-5788.
8. Schafer, A., Vehoff, T., Glisovic, A., Salditt, T., Spider silk softening by water uptake: an AFM study. *Eur. Biophys. J. Biophys. Letter*, 2008, 37: 197-204.
9. M. Elices, G.V. Guinea, J. Pérez-Rigueiro, G.R. Plaza, Polymeric fibers with tunable properties: Lessons from spider silk, *Materials Science and Engineering*: *C*, Volume 31, Issue 6, 2011:1184-1188.

Deformation of Dispersed Phase During PS/PP Melt Spinning

Long Chen, Houkang He, Shanshan Sun, Yu Zhang, Zongyi Qin
State Key Laboratory for Modification of Chemical Fibers and Polymer Materials,
College of Materials Science and Engineering, Donghua University, Shanghai 201620, People's Republic of China
happyjack@dhu.edu.cn

STATEMENT OF PURPOSE/OBJECTIVE

Morphology evolution of dispersed phase during the immiscible polymer blends melt-spinning is quiet complex. A radial non-uniform phase morphology has been found in the obtained PP/PS blended fiber, and we believe the radial temperature distribution during fiber solidification mainly contribute to the non-uniformity. The reduced capillary number, Ca^*, is adopted to explain the deformation mechanism of dispersed phase and the radial temperature distribution is calculated from resulted morphology, which provides a new approach to explore the radial distribution of processing conditions over the cross-section of the spin-line.

INTRODUCTION

For the immiscible polymer blends, the properties of its products generally depend on the processing conditions and final morphology. Taylor [1] had developed a basic theory for Newton system which describes the droplet deformation in the matrix under shear flow. Cox [2] generalized this theory to elongational flow. Delaby [3] studied the droplet deformations during an elongational experiment and they found that the droplets deform less than the matrix if the viscosity ratio exceed 1.0. Based on the previous theory, the deformation of a liquid droplet dispersed in a liquid matrix can be described using two dimensionless parameters—capillary number, *Ca*, and viscosity ratio, *p*.

APPROACH

The polypropylene (PP), prepared by our laboratory, and polystyrene (PS), commercial grade of Polystyol 144C from BASF and 951F from Taita Chemical Company, were dried prior to mixing and melt blending at different viscosity ratio of PS to PP (16.6, 9.2, 5.2, and 3.2) and at different PS content(2-16Wt%)) by twin-screw extruder. The PP/PS blended fibers were prepared on a fiber spinning machine at 220°C with take-up velocity from 125m/min to 1000m/min. Obtained fibers were embedding by Spurr [4] epoxy and sliced by ultracryotomy to prepare the samples of extruded fibers, free-falling fibers and take-up fibers in cross sections for SEM. An image analysis software (IPP, image-pro plus) was used to quantify the sizes of dispersed phases and their distribution.

RESULTS AND DISCUSSION

1.1 Influence of take-up velocity on morphology of PS/PP

Take-up velocity is of great importance to the fiber formation and has a deep effect on droplet coalescence. At a steady melt extrusion rate, the influence of take-up velocity on the dispersed phase gradient-structure in blended fibers is shown in Fig. 1.

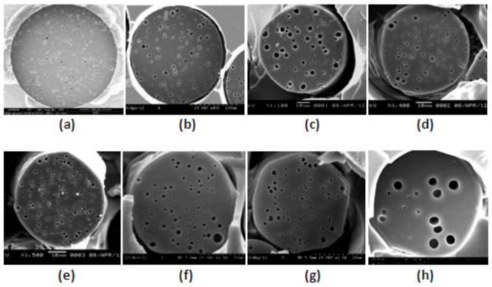

Fig. 1 SEM micrographs of PS/PP blended fibers at different take-up velocity: (a) extruded; (b) free-falling; (c) 125; (d) 250; (e) 375; (f) 500; (g) 750; (h) 1000 m/min

It is found that: (i) the dispersed phases distribute uniformly in the cross section of extruded and free-falling fiber; (ii) the non-uniformity of dispersed phase in PS/PP take-up fibers increases with the take-up velocity; and (iii) the coalescence of dispersed phase plays an important role when take-up velocity increase to 1000m/min which leads to a reduction of droplet number and an increase of average size.

1.2 Influence of viscosity ratio on morphology of PS/PP melt blended fibers

In fact, the viscosity ratio of blends reflects the rheological difference between two components. This paper prepared several PS/PP melt blended fibers under the same processing condition with different viscosity ratio (p=3.2, 5.2, 9.2, 16.6) for morphology investigation. The SEM micrographs are shown in Fig. 2.

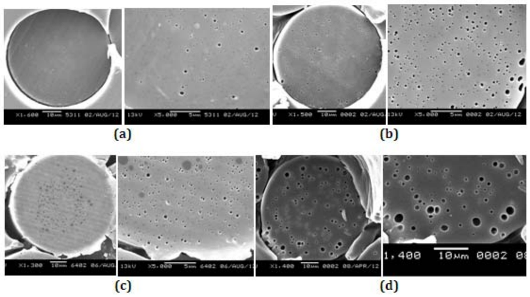

Fig. 2 SEM micrographs of PS/PP blended fibers with different viscosity ratio (take-up velocity is 250m/min): (a) 3.2; (b) 5.2; (c) 9.2; (d) 16.6

Based on statistic analysis, it is found that dispersed phase with high viscosity ratio trends to have relatively more non-uniform in droplet density and size along the cross section, that is, as the viscosity ratio increases, the average size of droplet increases, while the number of droplet decreases from core to surface in PS/PP fibers.

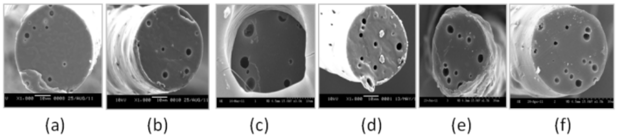

Fig. 3 SEM micrographs of PS/PP blended fibers with different PS content (take-up velocity is 500m/min): (a) 2wt%; (b) 4wt%; (c) 6wt%; (d) 8wt%; (e) 12wt%; (f) 16wt%

The influence of PS content on the dispersed phase gradient-structure in blended fibers is shown in Fig. 3.The number of dispersed phase is basically unchanged while the average size enlarged with the increase of PS content.

1.3 Deformation mechanism of dispersed phase

According to Huneault and et al [5], drop deformation and break-up depend on the reduced capillary number, Ca^*, which is defined as Eq. (1), where Ca is the capillary number and Ca_c is the critical capillary number.

$$Ca^* = \frac{Ca}{Ca_c} \tag{1}$$

Ca depends on strain rate, $\dot{\varepsilon}$, elongational viscosity of matrix, η_m, droplet radius, R, and interfacial tension, σ, expressed as Eq. (2).

$$Ca = \frac{\text{hydrodynamic force}}{\text{interfacial force}} = \frac{\eta_m \dot{\varepsilon} R}{\sigma} \tag{2}$$

Ca_c is only depends on the viscosity ratio, $p=\eta_d/\eta_m$. In the elongational flow, Ca_c is calculated from the Grace's [6] empirical equation. Depending upon the value of Ca^*, the droplets will either deform or break:

for $0.1 > Ca^*$ droplets do not deform,
for $0.1 < Ca^* < 1$ droplets deform, but they do not break,
for $1 < Ca^* < 4$ droplets deform then split into two primary droplets,
for $Ca^* > 4$ droplets deform into stable filaments.

Based on axial-direction consideration, as the temperature of filaments decreases along spin-line, η_d, η_m and p increase, while σ decreases. Ca^* decrease from about 30 at spinneret plate, and droplets deform and extend into long stable filaments. Based on radial-direction consideration, it is found that both Ca^* and Ca are different along the fiber's cross section, which accordingly leads to the non-uniform deformation of the dispersed phase.

1.4 Radial temperature distribution in melt-spinning fiber

Dispersed phase deformation can be calculated by the linear deformation equation as suggested by Taylor [1].

$$D = \frac{L-B}{L+B} = \frac{3}{2} \cdot \frac{\eta_m \dot{\varepsilon} R}{\sigma} \cdot \frac{19p+16}{16(p+1)} = \frac{3}{2} \cdot Ca \cdot \frac{19p+16}{16(p+1)} \tag{3}$$

Through quantification the droplet average size of extruded and take-up fibers along radial zones (from core to surface, denote as i), D_i and Ca_i can be obtained. On the assumption that strain rate is flat on the cross section, Ca is a function of temperature. Fig. 4 shows the calculated temperature along normalized radius (r/R) at solidification point. It is found that the temperature in core is 19.7K higher than that in surface and the radius is 23.35μm. The radial temperature difference around solidification point reaches to 10^5K/m, which is acceptable compared with theoretical value.

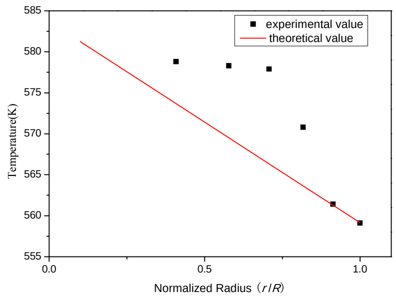

Fig. 4 The radial temperature profile along normalized radius (r/R) in melt-spinning fiber

CONCLUSIONS

The dispersed phase distribute uniformly in the cross section of extruded fiber and the non-uniformity of dispersed phase in PS/PP blended fiber increases not only with the take-up velocity, but also with viscosity ratio. The non-uniform deformation of dispersed phase is attributed to a non-uniform radial temperature distribution, and which leads to non-uniform distribution of Ca, Ca_c and Ca^*. A preliminary exploration of radial temperature distribution has been done, which provide a new approach to study radial dynamics of melt-spinning.

ACKNOWLEDGMENT

- National Natural Science Foundation of China (No.50903013).
- The Fundamental Research Funds for the Central Universities (12D10610).The Fundamental Research Funds for the Central Universities (13D110614).

REFERENCE

[1] Taylor G I. Proceedings of the Royal Society of London Series A, 1932, 138: 41-48.

[2] Cox R G. The Journal of Fluid Mechanics, 1969, 37: 601–623.

[3] Delaby I, Ernst B. Polymer Engineering and Science, 1996, 36 (12): 1627-1635.

[4] Spurr A R. Journal of Ultrasructure Research, 1969, 26 (1-2): 31-43.

[5] Huneault M A, Shi H. Polymer Engeering And Science, 1995, 35 (1): 115-127.

[6] Grace H P. Chemical Engineering Communications, 1982, 14 (3-6): 225-277.

Characterisation of Composite Honeycomb Sandwich Structures Cured Using the Quickstep Process

M. Jennings[1], M. de Souza[1], C. Creighton[1], S. Agius[1], T. Pierlot[2], B. Fox[1]
[1]Institute for Frontier Materials, Deakin University, Waurn Ponds, Australia
[2]CSIRO Materials Science and Engineering, Waurn Ponds, Australia
mjenning@deakin.edu.au

STATEMENT OF OBJECTIVE

This study aims to characterise the skin-core interface of carbon fibre composite honeycomb sandwich structures when cured using the Quickstep process. The effect of adhesive film, skin material and core thickness on mechanical properties and resin fillet geometry will be studied. The results will provide an understanding of the formation of resin fillets when processing honeycomb sandwich structures using the Quickstep process to help improve mechanical performance.

INTRODUCTION

In an effort to sustain natural resources and energy, transport industries are rapidly increasing their use of composites. Key advantages of carbon fibre composites are their high stiffness- and strength-to-weight ratios. If a low density core is added between the layers of carbon fibre lamina, the stiffness and strength of the panel can increase dramatically while the weight increase is insignificant.

Out-of-autoclave curing of lightweight composite sandwich structures is required due to the high pressures of the autoclave that can cause the edges of the core to crush during cure [1]. Extra manufacturing steps or modified materials can be a solution, but out-of-autoclave curing has proved to be the most efficient way to minimise core crush [2]. Most literature studies have focused on using an oven to cure sandwich structures. Ovens are limited by their heating rates and their inability to apply external pressure and cannot provide a full understanding of the effects of processing parameters on resin fillet formation. This study will use the Quickstep process, an out-of-autoclave process that situates the part to be cured between two silicone bladders filled with heat transfer fluid. The Quickstep process is capable of heating rates of up to 20°C/min and can apply pressure up to 100 kPa.

APPROACH

A Design of Experiment approach (DOE, Taguchi) experimental test matrix was designed. The factors and levels used are given in Table I. This results in 18 different trials to be undertaken.

Table I - Factors and levels of materials used in study.

Factors	Level 1	Level 2	Level 3
Adhesive	No Adhesive	FM 300NK	N/A
Skin Material	HexPly M21	HexPly 8552	HexPly M18/1
Core Thickness	15mm	25mm	45mm

The adhesive used was FM 300NK (Cytec Engineered Material) which has high elongation, toughness and ultimate shear strength and a weight of 170 g/m^2. The core material used was para-aramid fibre paper (Kevlar N636) impregnated with a heat resistant phenolic resin in honeycomb form (Shultz, CN2-3.2-48). The density of the core was 48.1 kg/m^3 with a cell size of 3.2 mm. For the skin material pre-impregnated carbon fibre materials were used, all manufactured by Hexcel as part of their HexPly range (Table II). All three skin materials have a resin content above 40%, which enables the prepreg to adhere to the core without the need for additional adhesive [3]. Figure 1 displays the layup schematic typically used for the manufacture of all panels and Table III displays the cure cycles for each skin material.

Table II - Skin material information.

Properties	HexPly M21	HexPly 8552	HexPly M18/1
Fibre form	AS4C 2x2 twill	AS4 UD	G939 4HS
Nom. fibre volume	55.8%	57.42%	55%
Nom. cured ply thickness	0.285 mm	0.130 mm	0.227 mm

Figure 1 - Layup schematic for manufacture of panels.

Table III - Cure cycles used when processing the laminates.

HexPly M21	HexPly 8552	HexPly M18/1
1. Heat at 15°C/min to 125°C. 2. Hold at 125°C for 20 minutes 3. Heat at 1°C/min to 145°C. 4. Hold at 145°C for 30 minutes. 5. Heat at 10°C/min to 170°C. 6. Hold at 170°C for 120 minutes. 7. Cool at maximum rate.	1. Heat at 15°C/min to 115°C. 2. Hold at 115°C for 90 minutes. 3. Heat at 8°C/min to 180°C. 4. Hold at 180°C for 90 minutes. 5. Cool at maximum cooling rate.	1. Heat at 15°C/min to 110°C. 2. Hold at 110°C for 60 minutes. 3. Heat at 15°C/min to 175°C. 4. Hold at 175°C for 120 minutes. 5. Cool at maximum cooling rate.

Samples were cut from panels and mounted in 50 mm diameter cups and the cups were filled and cured for 24 hours with casting epoxy resin EpoFix. Samples were then polished with 240 grit paper, 600 grit and finished with 1200 grit. Final polishing was then performed on the specimens using 9 µm, 3 µm and 1 µm diamond paste.

RESULTS AND DISCUSSION

Initial analysis of images obtained by an optical microscope has indicated that the prepreg resin makes a significant contribution to resin fillet formation and geometry. This occurs even when using adhesive film, as the cross section of a resin fillet in Figure 2 displays, the prepreg resin can cure above the adhesive film. This would indicate that the adhesive film and the prepreg resin are experiencing a low viscosity state at similar times during cure and can therefore interact and combine to form resin fillets. Due to the prepreg resin position on top of the adhesive film, the use of adhesive film when using these particular prepregs as the skin material is unnecessary. The resin content is obviously high enough and therefore there is enough prepreg resin to form resin fillets. Peeling the skin off the core using the Climbing Drum Peel Test (ASTM D1781) can provide further information on the role of adhesive film in the skin-core bond. Analysis of the failure path of the skin debonding can provide further understanding of the adhesive films role, as the boundary between prepreg rein and adhesive film is quite clear and may provide a path for crack propagation.

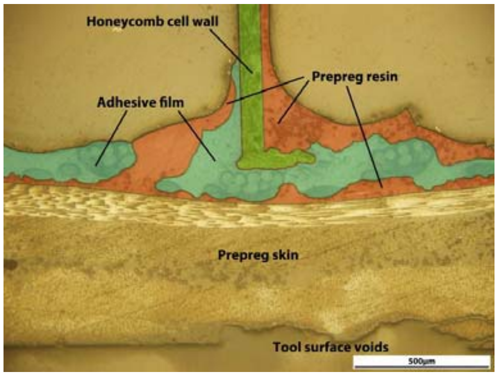

Figure 2 - Prepreg resins combines with the adhesive film to form resin fillets. Skin material shown is HexPly 8552.

Common results found in all panels were inconsistencies in resin fillet size and symmetry around the honeycomb cell walls. An example of these differences can be seen in Figure 3. The resin fillets that have formed on the honeycomb cell wall to the left have a height of approximately 100 µm. The cell walls in the middle and right of the image have one resin fillet at a height of almost 1000 µm, but the fillet on the opposite side of the cell wall is still small. It is thought this is due to pressure difference across cells and will need to be understood and controlled in future manufacturing of experimental panels.

FUTURE WORK

Mechanical testing will be undertaken on the panels to find relationships between the factors and mechanical performance, as well as the relationship between the resin fillet geometry and mechanical performance. To assess the skin-core bond, the skin will be peeled off the core using the Climbing Drum Peel Test. Beams will be loaded in four-point-bending to determine bending strength and stiffness. Compressive strength and stability will be determined by flat wise compressive testing. A computed tomographic (CT) scanner will be used to analyse the resin fillet geometry and failure paths of specimens prior to testing and after testing, respectively.

Future work will build upon the knowledge gained on the effect of material parameters on resin fillet formation and mechanical properties by studying processing parameters. The adjustment of the heating rate and pressure when processing will help provide an understanding of the relationship between minimum resin viscosity, cure pressure and resin fillet size. For both studies, interrupting the cure cycle will provide an understanding of how resin viscosity and pressure affects the rate of fillet formation.

ACKNOWLEDGMENTS

The author would like to thank the Australian Future Fibres Research and Innovation Centre (a collaboration of Deakin University, CSIRO and the Victorian Centre for Advanced Materials Manufacturing) for funding this project. The author would also like to thank Quickstep Technologies Australia for their help in initiating the project collaboration with Quickstep GmbH and Eurocopter, who in turn provided materials and manufacturing knowledge and facilities. Thank you to Carbon Revolution for the use of their CT scanner.

REFERENCES

1. Hsiao, H.M., S.M. Lee, and R.A. Buyny, *Core crush problem in manufacturing of composite sandwich structures: Mechanisms and solutions.* AIAA Journal, 2006. 44(4): p. 901-907.
2. Dulieu-Barton, J.M., D.A. Crump, and D. Griffiths, *Effect of core crush on honeycomb sandwich panels*, in *9th International Conference on Sandwich Structures (ICSS 9)*, G. Ravichandran, Editor. 2010: Pasadena, California.
3. Grove, S.M., E. Popham, and M.E. Miles, *An investigation of the skin/core bond in honeycomb sandwich structures using statistical experimentation techniques.* Composites Part A: Applied Science and Manufacturing, 2006. 37(5): p. 804-812.

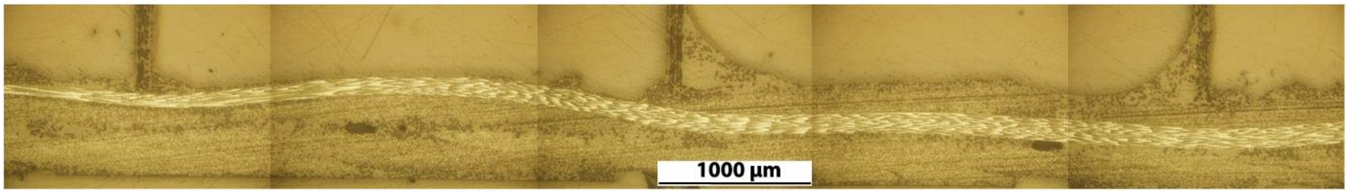

Figure 3 - Panel manufactured with HexPly M21 and without FM 300NK adhesive displaying the inconsistencies in resin fillet geometry that will be investigated further.

Interfacial Improvement of Carbon Fiber/Epoxy Composites by Using Electrospray Carbon Nanotube Deposition

Quanxiang Li[1], Jeffrey Church[2], Abdullah Kafi[1], Minoo Naebe[1], Bronwyn Fox[1]
[1]Deakin University, Institute for Frontier Materials, Pigdons Road, Waurn Ponds Campus, Geelong, Victoria 3216, Australia
[2]CSIRO Materials Science and Engineering, Waurn Ponds, Geelong, Victoria 3216, Australia
bronwyn.fox@deakin.edu.au

ABSTRACT

Carbon nanotubes (CNTs) were coated on unsized carbon fibers using the electrospray deposition method. The overall depositing process resulted in a multi-scale CNT-hybridized structure compared to the original primary carbon fibers. The wetting behavior between fibers and epoxy resin was tested using contact angle measurements for drop-on-fiber systems and indicated good wettability. Single fiber fragmentation tests were conducted on hierarchical fiber/epoxy model composites, demonstrating a significant (~45%) improvement of the apparent interfacial shear strength (IFSS) over the baseline composites. The result is associated with improved stress transfer between the carbon fibers and surrounding matrix through the coated CNT layer.

1. INTRODUCTION

Carbon nanotubes, as nano reinforcement, have previously been introduced onto the surfaces of carbon fibers to increase fiber surface area, create mechanical interlocking, and/or local stiffening at the fiber/matrix interface, all of which may improve stress transfer and interfacial properties [1-3]. However, weaknesses in the manufacturing processes, such as damage to the carbon fibers, are still big issues. Due to its simplicity and cost-effectiveness, electrospray deposition (ESD) is known to be one of the most promising manipulation techniques to deposit nano-materials [4, 5]. The objective of the research is to deposit CNTs onto the carbon fiber surface through ESD, is to improve the interfacial properties, which relate both to the wettability of fibers by the polymer and the interfacial shear strength (IFSS).

2. EXPERIMENTAL

2.1 Preparation of CNT-modified fibers

After mixing CNTs with surfactant (sodium dodecyl sulfonate) in dimethyl formamide, using a combined ultrasonic and centrifugation method, well-dispersed nanotube suspensions were obtained. In order to improve the attachment strength of the CNTs onto the carbon fiber surface, an epoxy resin binder was added to the CNT dispersion. The resulting mixture was electrosprayed onto an array of single carbon fibers.

2.2 Surface morphology measurements

After the CNT-depositing treatment, the carbon fibers were examined in a Supra 55VP scanning electron microscope (SEM).

2.3 Single fiber tensile strength test

Single fiber tensile tests were carried out using a FAVIMAT+AIRobot2 at a crosshead speed of 1 mm/min. A minimum of 40 measurements were conducted for each fiber specimen at a 20 mm gauge length.

2.4 Contact angle measurements

Unsized single carbon fibers and CNT-modified fibers were dipped into an epoxy resin with hardener. After 10 seconds, the specimen was then transferred into an oven (70℃) for curing. Stable polymer droplets were formed on the fibers and images were captured using an Olympus DP70 optical microscope.

2.5 Single fiber fragmentation tests

The method of sample preparation is similar to that used by other researchers [6]. The specimen was fixed to a tensile tester (Instron 5967) and strained up to 6% to ensure crack saturation. A crosshead speed of 0.5 mm/min was used. The fragment measurement is based on the observation under high magnification of debonded areas and fiber cracks or gaps.

3. RESULTS AND DISCUSSION

3.1 Surface characteristics of CNT-deposited carbon fibers

We first examined the morphology of the CNTs on the surface of the carbon fiber after CNT deposition. The surface morphologies of unsized carbon fibers obtained from SEM (Fig. 1a) shows that the fiber surface is rough with many grooves running along the longitudinal direction. After the ESD process, randomly oriented CNTs were deposited uniformly on the fiber surface (Fig. 1b) suggesting that ESD is an effective method to form hybrid materials.

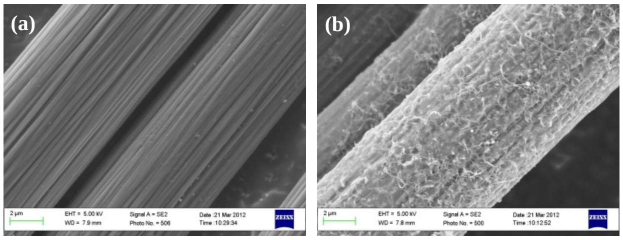

Fig. 1. SEM images of carbon fibers: (a) unsized, (b) CNTs deposited.

3.2 Single fiber tensile tests

The tensile strength of the fibers was evaluated (Fig.2) to see if the mechanical properties of the fiber had been affected by introducing the CNTs and ESD process. A t-test at the 0.05 confidence level showed that the unsized carbon fibers (21.17±3.3 (SD) cN/dtex) were not affected significantly after being coated by the CNTs and binder (21.37±3.5 cN/dtex). Weibull plots also showed that ESD does not lead to more weak points as compared to the untreated fibers.

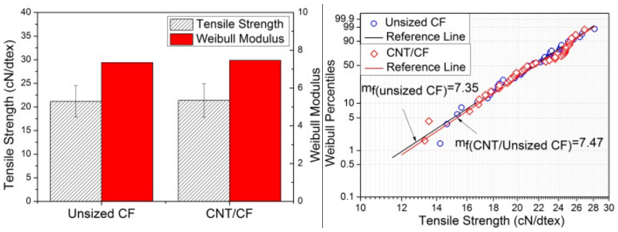

Fig. 2. Mechanical properties (left) and Weibull plots (right) of tensile strength for unsized and CNT deposited CFs.

3.3 Contact angle measurements

Typical micrographs of resin droplets formed on different carbon fibers (Fig. 3) all show barrel-type droplets, which is the preferred configuration when the contact angle is relatively small. The contact angle decreased remarkably after the deposition of the CNTs indicating good wettability by the resin. The reason is that the CNT deposition gave rise to a significant increase in surface area, i.e., the roughness of the pristine carbon fibers surface increased.

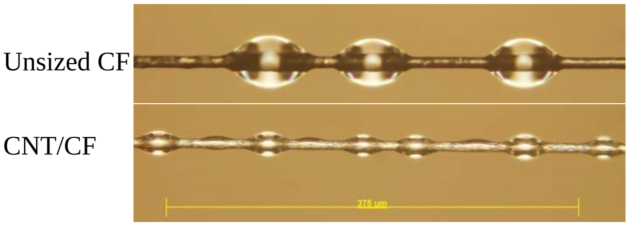

Fig. 3. Resin droplets on CF at a 40x magnification.

3.4 Single fiber fragmentation tests

The interfacial properties of CNT-modified fiber/epoxy resin model composites were investigated further, using single fiber fragmentation tests. The morphology associated with the fiber breaks can offer valuable clues regarding the interface strength [6]. The composite specimens with unsized fibers exhibited apparent debonding at the interface (Fig. 4), implying a relatively weak interface. After coating the fiber surfaces with CNTs, the failure of the composite specimen indicated a moderately strong interface bond, with shorter debonding areas.

The histogram of fragment lengths (Fig. 5) showed that the composite specimens with CNT-modified fibers displayed shorter fragment lengths (478.5±116.1μm) than those with bare carbon fibers (676.1±221.5μm). The T-test at the 0.05 confidence level showed an extremely statistically significant. A quantitative study of the interfacial shear strength was carried out using the Kelly-Tyson model and Weibull fitting to predict the fiber tensile strength at the critical length. It was found that IFSS was improved by (~45% after depositing CNTs onto fiber surface (Fig.5.)

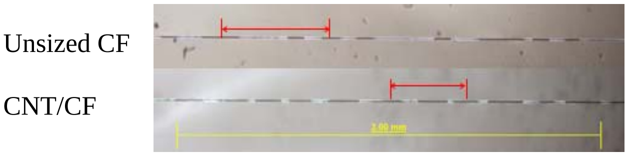

Fig. 4. Birefringence effects of fragmented unsized and CNT deposited CF specimens (Fragment length are shown by red arrows).

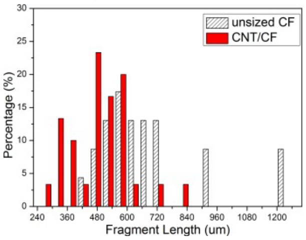

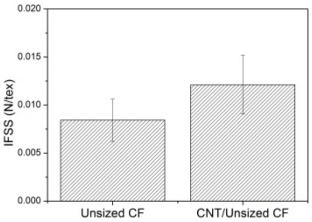

Fig. 5. Histogram of fragment lengths (left) and interfacial shear strength values (right) for unsized and CNT deposited CFs.

4. CONCLUSIONS

CNT-modified carbon fibers were fabricated using an ESD method, which resulted in a multi-scale hybridized structure without any decrease of the fiber tensile strength. The results suggest that ESD is an effective method to form CNT/carbon fiber hybrid multi-scale composites. Contact angle tests demonstrate that the CNT deposition results in good wettability by the resin. The IFSS increased significantly (~45%) after CNT coating. These single fiber level results are encouraging and support further development of this approach. Future work will focus on optimizing preparation parameters, modifying CNT morphology and extending scientific testing.

ACKNOWLEDGMENT

The authors gratefully acknowledge Deakin University, CSIRO Materials Science and Engineering and AFFRIC for the funding to carry out this study.

REFERENCES

[1]E. T. Thostenson, et al. Carbon nanotube/carbon fiber hybrid multiscale composites, *Journal of Applied Physics*, vol. 91, pp. 6034-6037, May 1, 2002.

[2]E. Bekyarova, et al. Multiscale carbon nanotube-carbon fiber reinforcement for advanced epoxy composites. *Langmuir*, vol. 23, pp. 3970-3974, Mar 27, 2007.

[3]A. Laachachi, et al., A chemical method to graft carbon nanotubes onto a carbon fiber. *Materials Letters*, vol. 62, pp. 394-397, Feb 2008.

[4]S. N. Jayasinghe. An advanced jet-based approach to processing nanotubes. *Physica E: Low-dimensional Systems and Nanostructures*, vol. 31, pp. 17-26, 2006.

[5]K. Somroop, et al., Fabrication of Y(2)O(3)-doped BaZrO(3) thin films by electrostatic spray deposition. *Thin Solid Films*, vol. 519, pp. 6408-6412, Jul 29, 2011.

[6]H. Qian, A. Bismarck, E. S. Greenhalgh, and M. S. P. Shaffer. Carbon nanotube grafted carbon fibres: A study of wetting and fibre fragmentation. *Composites Part A-Applied Science and Manufacturing*, vol. 41, pp. 1107-1114, Sep 2010.

Force Shield Textile Composite with Microcapsule System

Rui Wang[1,2], Xing Liu[1,2], Fangli Pang[1,2], Mengxuan Li[1,2], Jiao Huang[1,2], Zhili Zhong[1,2]
[1]Division of Textile, Tianjin Polytechnic University /399, Binshuixi Road, Tianjin, P.R. China, 300387
[2]Key Laboratory of Advanced Textile Composite Materials, Tianjin, P.R. China, 300387
wangrui@tjpu.edu.cn; aibnbpo@hotmail.com

INTRODUCTION

The microcapsule strategy provides a clue to force-sensitive textile. The function layer in this proposal can be applied to various force shield textile composites especially to replace and expand existing body armor. This proposed work seeks to develop a new class of unique performance textile composite materials, which are designed to sense the force and respond in an autonomous fashion to increase the modulus and absorb the energy, protecting the material from damage. To achieve the final goal of the research, the engineered microcapsules which containing diene monomers used for self-healing agent are manufactured and dispersed in the 3-D isotropic nonwoven fabric with catalyst. The mechanism for the releasing and polymerization of core material, incorporate with the model of function layer(nonwoven containing microcapsules and catalyst) changing of modulus(from flexible textile to tough board) are also studied.

APPROACH

Four primary tasks will be discussed in this presentation:

(1) Manufacturing of specification microcapsules.

(2) Function layer is designed and manufactured incorporate with microcapsules well dispersed.

(3) Deformation and modulus changing of function layer are characterized by means of optical microscope (OM), scanning electron microscopic (SEM), high speed camera, and tensile, impact, dynamic mechanical properties are measured.

RESULTS AND DISCUSSION

(1) A mean diameter of 100 μm microcapsules containing norbornene-based monomers (ex, dicyclopentadiene) with a melamine-urea-formaldehyde shell are produced and characterized by differential scanning calorimetry (DSC), thermogravimetric analysis (TGA), scanning electron microscopic (SEM), particle size analyzer(PSA). The presented manufacturing process is appropriate for this purpose.

(2) Function layer showing a sudden change in modulus at certain force applied.

(3) Various mechanical properties will be discussed.

CONCLUSION

The analysis of modulus variation of function layer is directly related to the application situation and functionality as well as the safety of materials. The methodology can be also applied in force shield material like submarine, helmets, and cut resistant gloves etc which require flexibility before certain condition.

FUTURE WORK

Mathematic model of function layer deformation and modulus changing need to be established using finite element for further applications.

REFERENCES

[1] Y. S. Lee, E. D. Wetzel and N. J. Wagner. The ballistic impact characteristics of Kevlar wovenfabrics impregnated with a colloidal shear thickening fluid. *Journal of Materials Science*. 2825-2833 (2003).

[2]. S. R. White, N. R. Sottos, P. H. Geubelle, J. S. Moore, M. R. Kessler, S. R. Sriram, E. N. Brown and S. Viswanathan. Autonomic healing of polymer composites. *Nature*, Vol. 409, 794-797 (2001).

[3] X. Liu, X. Sheng, J. K. Lee, M. R. Kessler. Synthesis and characterization of melamine-urea-fromaldehyde microcapsules containing ENB-based self-healing agents. *Macromol. Mater. Eng.*, Vol. 294, 389-395 (2009).

[4] J.K. Lee and X. Liu, Self-healing microcapsule, and method for preparing the Same. Korea Patent No.10-2012-0024281 (2012).

[5] X. Liu, X. Sheng, J. K. Lee, M. R. Kessler. Rheokinetic evaluation of self-healing agents polymerized by Grubbs catalyst embedded in various thermosetting systems. *Composites Science and Technology*. Vol. 69, 2102-2107 (2009).

[6]S. H. Cho, S. R. White, and P. V. Braun. Self-healing Polymer Coatings. *Adv. Mater*. Vol. 21, 645-649 (2009).

KEYWORDS

Microcapsule, Composite, Force Shield

ACKNOWLEDGMENT

The authors are grateful to Tianjin polytechnic University textile division council for the financial support.

.

Study on Preparation and Properties of Modified Polypropylene Fibers Used in Engineering

Yiren Chen[1], Li He[1], Zhiqiang Fan[2]
[1]Wuhan Textile University,
[2]Changjiang Water Resources Commission of the Minstry of Water Resources
yiren.chen@wtu.edu.cn

INTRODUCTION

The polypropylene fibers have many advantages as excellent engineering fiber, such as good mechanical properties, resistance to chemical attack, moth-eaten and so on, but also there are some fatal weakness: non-absorbent, easy to play group, and cement mixing more difficult, dispersion in the concrete is not conducive to the formation of fiber reinforced concrete collective interface, the cost is relatively high. In order to overcome this shortcoming, we try to polypropylene filled and modified hydrophilic treatment, the preparation of modified polypropylene fibers better than unmodified polypropylene fiber; such as fiber strength increased; Hydrophilic increase; the modified fibers in water also has a certain suspension; reduce the the cost of production.

APPROACH

We selected a heavy calcium carbonate of 1500 items. First of all, the heavy calcium carbonate was wet activatied with surface active agent. Then melt blending the heavy calcium carbonate with polyethylene glycol and polypropylene, spinning.
Two process line of melt blending and spinning:
One-step: Blending polypropylene with the activation heavy calcium carbonate and polyethylene glycol according to the proportion, then spin: At first blending polypropylene with the activation heavy calcium carbonate and granulation according to the proportion, then melt blending the granulation with polyethylene glycol, spinning.

RESULTS AND DISCUSSION

Fiber structure

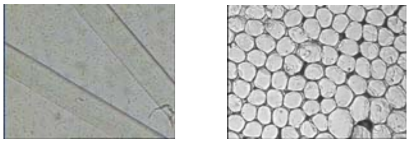

FIGURE 1. The longitudinal and cross-sections of unmodified polypropylene fiber

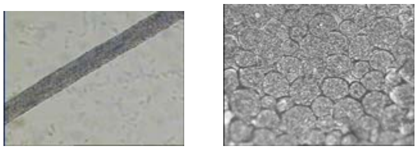

FIGURE 2. The longitudinal and cross-sections of one-step modified polypropylene fiber

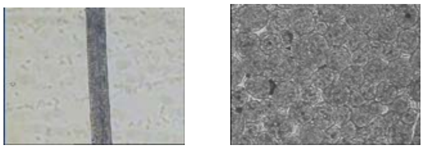

FIGURE 3. The longitudinal and cross-sections of two-step modified polypropylene fiber

The fiber surface of unmodified polypropylene is smooth, the cross section is clear. The fiber surface of modified polypropylene is roughness, the cross section of the fiber surface is covered with tiny holes. The surface rough and porous structure can enhance the hydrophilicity and improve the combined with other materials.

SEM

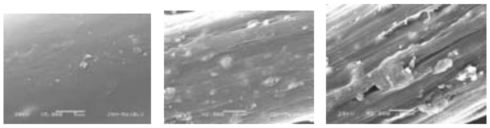

unmodified polypropylene
one-step
two-step

FIGURE 4. The surface SEM images of unmodified olypropylene fiber and modified polypropylene fiber

The fiber surface of the modified polypropylene is obviously different compared with the fiber surface unmodified polypropylene. The fiber surface of unmodified polypropylene is very smooth. The fiber surface of modified polypropylene has many pits appear and the pits uniformly disperse.

Breaking tenacity

unmodified polypropylene: 387.5MPa
One-step modified polypropylene: 481.6 MPa
Two-step modified polypropylene: 462.6 MPa

Alkali resistance rate(%)

The fiber was placed in sodium hydroxide solution of pH=14, at 60 ℃condition for 48 hours, remove and dry, then breaking tenacity test.

unmodified polypropylene: 101.2
One-step modified polypropylene: 99.5
Two-step modified polypropylene: 99.2

Contact angle

unmodified polypropylene: 98.8°
One-step modified polypropylene: 63.0°
Two-step modified polypropylene: 62.1°

Moisture absorption rate

unmodified polypropylene: 0.03
One-step modified polypropylene: 0.50
Two-step modified polypropylene: 0.57

Dispersion in water

The unmodified polypropylene fiber and modified polypropylene fiber were cut to length of 20mm, put the fiber bundle into the water, as shown in Figure 5.

unmodified polypropylene | one-step | two-step

FIGURE 5. The dispersion in water of Unmodified polypropylene fiber and modified polypropylene fiber

Fiber dispersion in water were observated from the vertical and lateral after stir 5 minutes in the glass with a glass rod at the same rate, as shown in Figure 6, 7, 8.

FIGURE 6. Unmodified polypropylene fiber agitated dispersion

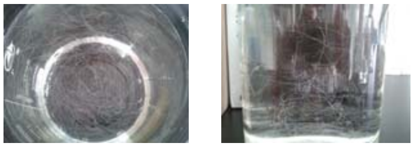

FIGURE 7. Dispersion after agitation of the one-step modified polypropylene fibers

FIGURE 8. Dispersion after agitation of the two-step modified polypropylene fibers

Fiber cement adhesion（g/m^2）

The fibers were mixed into cement for a period of time. The cement contents of fiber surface were tested after dry the water of the fiber surface attached, in order to determine the binding capacity of fiber and cement.

Unmodified polypropylene: 8.10
One-step process modified polypropylene: 55.10
Two-step process modified polypropylene: 66.17

CONCLUSIONS

The modified polypropylene fiber was obviously improved than unmodified polypropylene fiber on mechanical and hydrophilic properties. The breaking tenacity and contact angle of modified polypropylene fiber were different by different preparation process. The mechanical performanc of one-step was better than that of two-step, but the hydrophilic properties of one-step worse than that of two-step.

FUTURE WORK

Only heavy calcium carbonate of 1500 items was selected as filler and polyethylene glycol as the hydrophilic modifier in this paper. We can try modified filler and the hydrophilic reagent more. The processing technology of modified polypropylene fiber can be further explore, such as the processing temperature and soon.

REFERENCES

[1] Hattotuwa G.B. Premalal, H. Ismail, et al. Comparison of the mechanical properities of rice husk powder filled polypropylene composites with talc filled polypropylene composites. *J. Polymer Testing*. 2002, 21 (8): 833-839.
[2] Myriam Saul and Sebastien Navarre. Chemical modification of molten polypropylene by the rmolysis of Peroxidic Compounds. *Macromolecules*. 2003, 6: 7469-7476.

Methacrylate/Hydroxyethyl Methacrylate Fiber for Organic Compounds Absorbent

Yan Feng[1,2], Xiuyang Hao[1], Jian Chen[1]
[1]School of Textiles, Tianjin Polytechnic University
[2]Key Laboratory of Advanced Textile Composite Materials of Ministry of Education,
fengyan@tjpu.edu.cn; fengyan@tjpu.edu.cn

STATEMENT OF PURPOSE

Since oil spill into water resources has recently become one of the greatest causes of water pollution, it is very essential to clean up the spilled oil efficiently at the beginning stage of the pollution to protect water resources. In this paper, the copolymer made from butyl methacylate (BMA), lauryl methacrylate (LMA) and hydroethyl methacylate (HEMA) is synthesized by the method of suspension. Then the organic compounds absorbent polymethacrylate fiber was prepared by gelation-spinning using the copolymer as spinning resin. And the absorptive performance is studied.

INTRODUCTION

As a new type of functional materials, absorptive fiber could provide broad prospects for development with the increasing demands to environment. Absorptive fiber has desirable characteristics such as large absorptive area, easily to be recovered etc. Many chemicals and technologies are applied to make organic oil absorbent fibers with different structures and properties.

APPROACH

The BMA/HEMA or LMA/HEMA copolymers were successfully prepared by suspension polymerization. The dried resin was mixed with a certain volume of dimethylacetamide (DMAc) to be fully swelled. Then the plunger-type spinning machine was used to prepare fiber by gelation-spinning. The fibers were dried for later use after extracting the excessive swelling agent. The absorptive performance, absorbent mechanism and release behavior of BMA/HEMA or LMA/HEMA copolymeric fibers were measured and analyzed.

RESULTS AND DISCUSSION

The FTIR analysis of BMA/HEMA fiber

The FTIR spectrum of BMA / HEMA fiber is shown in Fig. 1.

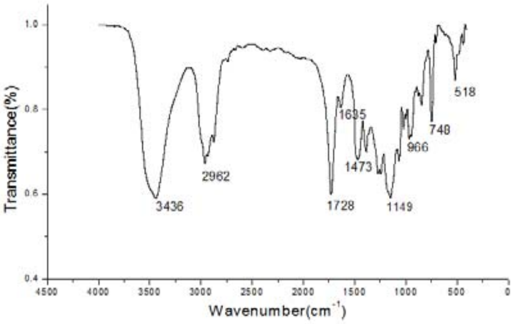

Fig. 1 FTIR spectrum of BMA/HEMA fiber

As shown in Fig.1, the peak at 3436cm^{-1} attributes to hydroxyl absorption peak; the absorption peaks of the methyl and methylene group locate at 2962 and 2852cm^{-1}; the peak at 1728cm-1 attributes to the absorption peak of the carbonyl group; and the peak at 1240 and 1146cm^{-1} are the asymmetric and symmetric stretching vibrations of ester group C-O-C.

The absorptive dynamics of BMA/HEMA fiber to toluene

The saturated absorbency to toluene and trichloroethylene of the fiber is showed in Tab. I.

Tab. I The saturated absorbency of fiber to different organic compounds

Content of LMA(wt%)	trichloroethylene (g/g)	Toluene (g/g)
0	0.1	1.0
5	9.9	4.5

Relationship based on fiber adsorption amount and adsorption time is studied. The absorptive kinetics of BMA/HEMA fiber to toluene is discussed on the basis of first-order kinetic formula and second-order kinetic formula, as shown in Fig.2, where, Qt is the amount of adsorption of the time t; Qe is the maximum amount of adsorption. Fig.2 (a) shows that first-order kinetic equation is y = 1.1412x with correlation coefficient R = 0.8613; Fig.2 (b) shows that the second-order equation is y = 3.241x-1.684 with correlation coefficient R = 0.9595. This indicates that the second-order equation is more suitable to describe fiber adsorption dynamics.

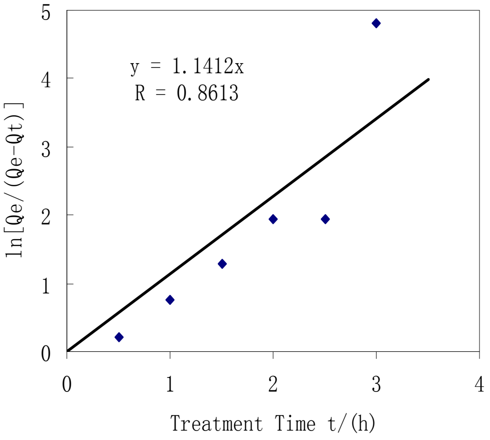

（a）First-order kinetic curve

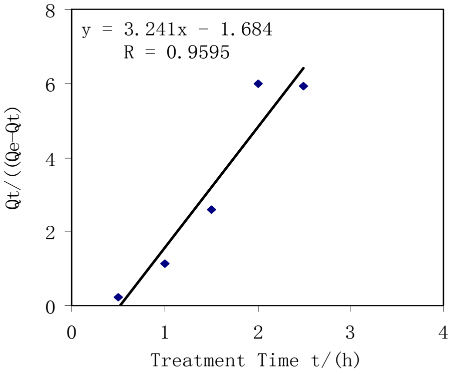

（b）Second-order kinetic curve

Fig. 2 Kinetics curves

The release behavior of the fiber

The effect of LMA content on released behavior of fiber is showed in Fig.3.As shown id Fig.3, the desorptive rate of the fiber with 5wt% LMA is faster than the fiber with no LMA. The reason may be that compared with BMA/HEMA fiber, the concentration gradient between the internal and external of the fiber containing LMA is greater. So the released rate of fiber with 5wt% LMA is higher than the LMA 0wt% fiber.

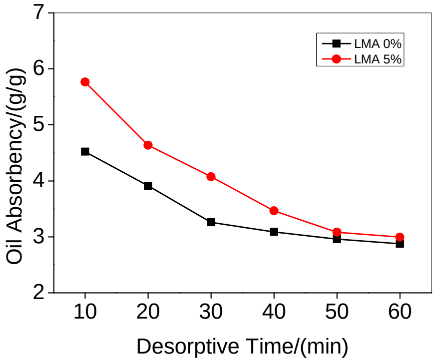

Fig. 3 Effect of LMA content on released behavior of fiber

CONCLUSION

The methacrylate/hydroxyl methacrylate fibers are prepared with BMA or LMA as monomer and HEMA as crosslinker. The absorptive mechanism of the fiber can be described by the second-order kinetic equation.

KEYWORDS

Methacrylate/ Hydroxyethyl Methacrylate Fiber; Absorptive mechanism; Organic Compounds Absorbents

ACKNOWLEDGMENT

The author would like to thank National Natural Science Foundation of China (51103100) for its financial support.

REFERENCES

[1] N. Xu., C. Xiao, Y. Feng, Z. Song, Z. Zhang, S. An. Study on absorptive property and structure of resin copolymerized by butyl methacrylate with hydroxyethyl methacrylate. *Polym. Plast. Technol. Eng.* 2009, 48, 716-722.

[2] Y.Z. Liu, M. Zhou. Electrospun oil sorptive fiber based on EPDM. *J. Polym. Eng.* 2008, 28, 43-53.

[3] A.M. Atta, A.A.H. Abdel-Rahman, N.A. Hamad. Modification and application of poly(ethylene terephethalate) nonwoven fiber using octadecyl acrylate and acrylic acid as oil sorbers. *J. Dispersion Sci. Technol.* 2012, 33, 1492-1502.

[4] Ewa Lobos-Moysa, Michal Bodzek. Application of hybrid biological techniques to the treatment of wastewater containing oil and fat. *Desal. Wat. Treat.* 2012, 46, 32-37.

[5] Y. Feng, C.F. Xiao. Research on butyl methacrylate-lauryl methacrylate copolymeric fibers for oil absorbency. *J. Appl. Polym. Sci.* 2006, 3, 1248–1251.

Characterization and Preparation of Polyamide 66/OV-POSS Nanocomposite Fibre

Lin Xiaoxia[1], Shao Qun[1], Kiptanui Koech Jacob[1], Yimin Wang[2]
[1]College of Materials Science and Engineering, Donghua University
[2]State Key Laboratory for Modification of Chemical Fibers and Polymer Materials, Donghua University
crystalxiaoxia@126.com; ymw@dhu.edu.cn

INTRODUCTION

Poly hexamethylene adipamide (PA66) in our country is mainly used in the production of high performance synthetic fibres and tire-cord fibres for diagonal tire. However, PA66 has some disadvantages. Focusing on the weakness of PA66 fibres, this study employs proper processing technology to incorporate POSS into PA66 with the sole aim of preparing nanocomposite fibre with enhanced thermostability and mechanical properties.

Polyhedral Oligomeric Silsesquioxanc (POSS) is a new type of organic/inorganic hybrid material. It is said that POSS is the third generation of nanometer composite material. The technique, which combined the organic and inorganic phase through covalent bond, can overcome the single organic and inorganic own defects, so as to improve the performance of the material [1-3].

EXPERIMENT

Preparation

The POSS used in this study was eight vinyl POSS and purchased from Shenyang MEICI Fine Chemical Co., Ltd, China. Eight vinyl POSS was converted to OV-POSS as shown in Figure 1. For this reaction 5g eight vinyl POSS, 2.73 g M-chloroperbenzoic acid, and 100 ml dichloromethane were added into a 250ml three neck round-bottomed flask equipped with a mechanical stirrer and a condenser. Solution was stirred for 48 hours under N_2, and the temperature was kept at 45℃. The solution was moved into ice water bath until white solid was precipitated. Then, filter liquor and excess 0.2mol/L $NaHCO_3$ solution were added into the flask and the reaction was carried out in a 45℃ water bath for 2h and separated by a separatory funnel. The subnatant was dried over sodium sulphate to remove the residual water and then transferred to a 50ml flask. Dichloromethane was dislodged by a rotary evaporator. Finally we can obtain white powder OV-POSS.

POSS and PA66 pellets were mixed at high speed for 1 minute, and spin into fibers by twin screw extruder. Because of the sensivity of PA66 towards degradation by moisture and the absorbing moisture capacity of POSS, they needs to be dried in a vacuum before melt spinning process. Blending of PA66 and POSS was done based on weight ratios ranging from 1% to 3% POSS. A master batch was first prepared containing 10% POSS and was then diluted to achieve the required ratios. The PA66-POSS blend was prepared in a twin screw extruder at temperature of 260-265°C and was used for preparing PA66-POSS multyfilament by melt spinning. The screw speed values were calibrated to get the proper dispersion of the materials. Finally, 50 times drawing of PA66/POSS filaments was done in two steps. The first step 10 times drawing was undertaken in the spinning machine. This was achieved by controlling the twin screw speed and the winding (take up) speed. The second and most important 5 times drawing of POSS/PA66 filaments was done on an indigenously built drawing machine. The sole aim of the second drawing is to enhance the molecular orientation and stabilization of the PA66 filament structure for better performance properties. The drawn filament properties were analyzed.

Instruments

Thermal degradation of composites was analyzing using a TA Instruments thermogravimetric analyzer (TGA) The Discovery. Mechanical properties were determined as a function of POSS concentration using XG-1A tensile testing machine.

RESULTS AND DISCUSSION

The effect of POSS on fiber thermal properties

In this study, the Discovery TGA analysis instrument was used to determine the thermal stability of the PA66. Figure 2 shows the TGA for neat PA66 and PA66/POSS nanocomposites with different OV-POSS content. The temperature for 5% weight loss of nanocomposite fiber is about 12℃ higher than that of pure PA66. Above 380°C the neat PA66 decomposes in a single smooth step. And a slight increase in the onset decomposition temperature is observed for PA66/POSS nanocomposite fibres as compared to the pure PA66. It might caused by the adding of POSS will stop the heat and store the thermal energy in POSS.

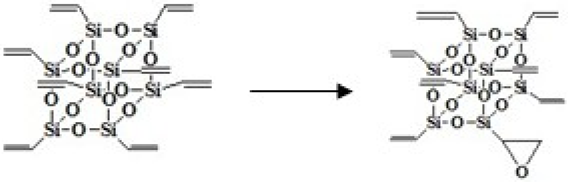

Figure 1 Synthesis route for OV-POSS

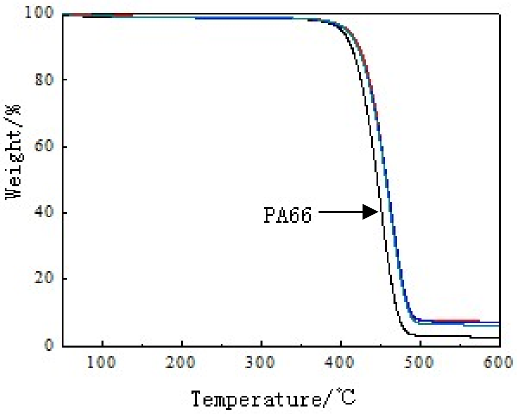

Figure 2 Thermal analysis of PA66 and PA66 with different concentration of OV-POSS

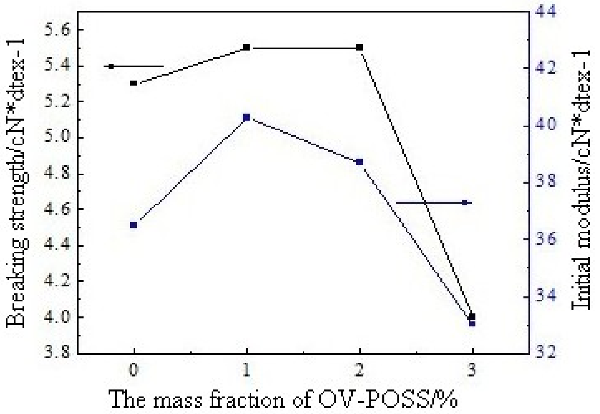

Figure 3 Effect of POSS centent on mechanical properties

The effect of POSS on fiber mechanical properties

The variation of breaking strength and initial modulus of the PA66/POSS nanocomposites with different percentages is shown in Figure 3. It shows that with the increase of OV-POSS, the breaking strength and initial modulus of the nanocomposite fibers were enhanced due to the reinforcement of POSS, and this improvement being more significant at lower OV-POSS content. However, at higher OV-POSS content, less uniformly dispersed and more agglomerats of POSS were formed in the PA66 matrix. As a result, the breaking strength and initial modulus of the PA66/POSS nanocomposites decreased significantly at higher POSS content.

CONCLUSIONS

This study investigated the preparation and characterization of PA66/OV-POSS nanocomposite fibres. As a result, we can find that adding a small amount of OV-POSS can improve the thermal properties of PA66. Moreover, as OV-POSS content increased, fiber thermal properties, the breaking strength and initial modulus of the PA66/POSS nanocomposites were enhanced, but the breaking strength and initial modulus of the PA66/POSS nanocomposites decreased significantly at higher POSS content.

REFERENCES

[1] R Roy, S Komarneni, DM Roy. "Multi-Phasic ceramic composites made by sol-gel technique." *J. Mater. Res. Soc. Symp. Pro*, 1984, 32: 347-359.

[2] DB Drazkowski, A Lee, TA Haddad. "Morphology and phase transitions in styrene-butadiene-styrene triblock copolymer grafted with isobutyl-substituted polyhedral oligomeric silsesquioxanes." *J. Macromolecules*, 2007, 40 (8): 2798-2805.

[3] IA Zucchi, MJ Galante, E Franchini, et al. "Monofunctional epoxy-POSS dispersed in epoxy-amine networks: effect of a prereaction on the morphology and crystallinity of POSS domains." *J. Macromolecules*, 2007, 40 (4): 1274-1282.

Graphene Fibers: A Promising Multifunctional Material

Chao Gao, Zhen Xu, Xiaozhen Hu
MOE Key Laboratory of Macromolecular Synthesis and Functionalization, Department of Polymer Science and Engineering,
Zhejiang University, 38 Zheda Road, Hangzhou 310027, P. R. China
chaogao@zju.edu.cn

INTRODUCTION

Graphene, a single-layer of graphite, possesses exceptional properties such as the strongest mechanical strength (~130 GPa), the fastest carrier mobility (15,000 $cm^2.V^{-1}.s^{-1}$), the highest thermal conductivity (5000 $W.m^{-1}.K^{-1}$), ultrahigh surface area (2630 $m^2.g^{-1}$), high electrical conductivity (~10^6 $S.m^{-1}$), and room-temperature Quantum Hall effect. Such attributes have been widely adopted to fabricate micro-scale devices and macro-scale films. However, it is a great challenge to access continuous fibers due to the poor dispersibility of graphene and the disorder for bulk graphene sheets. Given the graphene characters, such fibers would be versatile and highly useful. Recently, our group and others discovered the liquid crystals of graphene oxide (GO) and pristine graphene, paving the way to macroscopic assembled graphene fibers. Subsequently, we accessed the first continuous graphene fibers by wet-spinning of aqueous solution of liquid crystalline GO followed by chemical reduction. The fabrication process of such novel fibers and their multifunctional performance will be shown in this presentation.

APPROACH

GO was synthesized by chemical oxidation of natural graphite via modified Hummers method. Certain amount of GO was dissolved in water to form concentrated spinning dope by high-speed centrifugation. The spinning dope was injected from the spinneret of a spinning tube into a coagulation bath to form GO fiber. The fiber was collected on a drum to make continuous fiber. The GO fibers were chemically reduced by aqueous HI (40%) to afford neat graphene fibers. Figure 1 schematically shows the wet-spinning apparatus.

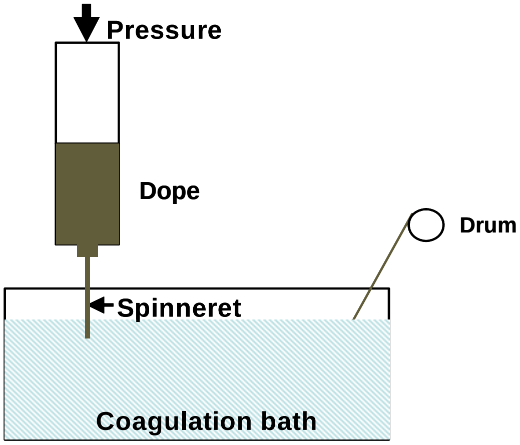

Figure 1. Schematic illustration for the wet-spinning of continuous graphene oxide fibers.

RESULTS AND DISCUSSION

GO liquid crystals. GO can form nematic liquid crystal (LC) phase in either water or organic solvents such as DMF, NMP, and ethanol. The LC structures were confirmed by polarized optical microscopy (POM), small-angle X-ray scattering (SAXS), viscosity measurements, and scanning electron microscopy (SEM). Figure 2 shows GO dispersions after phase separation under polarized light. Narrow dispersed GO sheets can even form chiral LC, as confirmed by POM, SEM, SAXS, and CD measurements. Figure 3 shows the finger-print textures of chiral LC GO observed in POM.

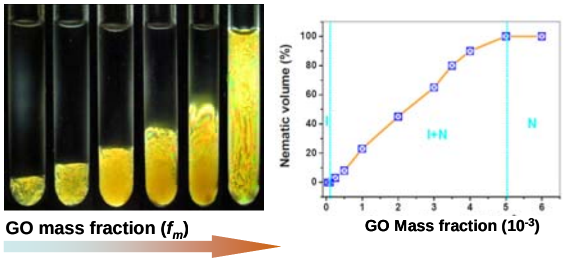

Figure 2. Phase separation between isotropic (I) and nematic (N) phase of GO.

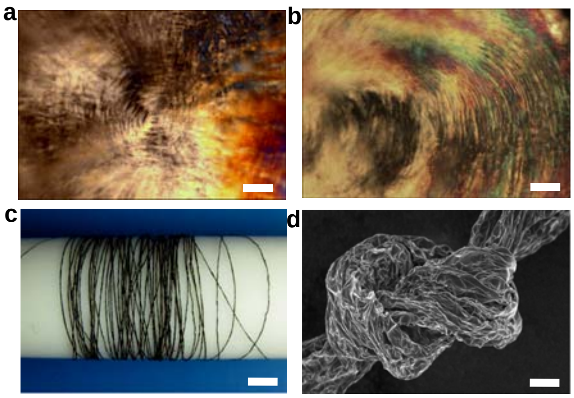

Figure 3. POM images of chiral LC GO (a, b), meters-long graphene fiber (c) and graphene fiber knot (d). Scale bar: 300 µm (a, b), 0.4 cm (c), 40 µm (d).

Neat graphene fibers. Continuous neat graphene fibers up to tens of meters long were made by industrially viable wet-spinning of GO LC, followed by chemical reduction (Figure 3c, d). The fibers showed strong mechanical strength (~0.5 GPa), good flexibility, and excellent electrical conductivity (~10^4 $S.m^{-1}$). Knots were made from graphene fibers without break, and the fibers were used to fabricate meshes with common cotton fibers. Besides, Aerogel-like graphene fibers with giant pores were also produced, which showed strong specific strength and can lift 20,000 times of own weight without deformation.

Graphene-polymer nacre-mimic fibers. Polymer-functionalized graphene was used to prepare continuous fibers. The resulting fibers have perfect "brick and mortar" (B&M) structures, and show good mechanical strength superior to nacre and common artificial nacre composites (Figure 4).

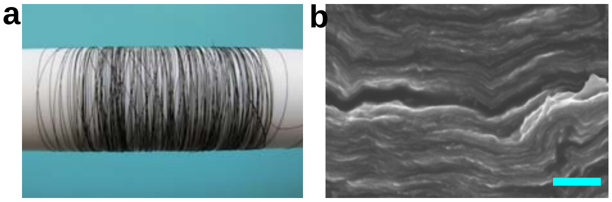

Figure 4. Nacre-mimic fibers of polymer-functionalized graphene. Scale bar: 500 nm.

CONCLUSIONS

GO can form liquid crystals in water and organic solvents, which can be used to make continuous graphene fibers by wet-spinning technology. The graphene fibers showed high mechanical performance and fine electrical conductivity. In addition, nacre-mimic fibers were made from polymer-functionalized graphene. These new fibers promise wide range of applications in fiber supercapacitors, light cables, and sensors.

KEYWORDS

Graphene, liquid crystal, fiber, nacre-mimic

ACKNOWLEDGMENT

This work was supported by the National Natural Science Foundation of China (No. 51173162), Qianjiang Talent Foundation of Zhejiang Province (No. 2010R10021), Fundamental Research Funds for the Central Universities, Research Fund for the Doctoral Program of Higher Education of China (No. 20100101110049), and Zhejiang Provincial Natural Science Foundation of China (No. R4110175).

REFERENCES

1. Z. Xu, C. Gao. *Nat. Commun.* 2011, 2, 571.
2. Z. Xu, C. Gao. *ACS Nano.* 2011, 5, 2908.
3. Z. Xu, Y. Zhang, P. G. Li, C. Gao. *ACS Nano.* 2012, 6, 7103.
4. Z. Xu, C. Gao. *Adv. Mater.* 2013, *25*, 188.
5. X. Z. Hu, Z. Xu, C. Gao. *Sci. Rep.* 2012, 2, 767.

Structure and Property Change of Pre-Drawn Aromatic Copolysulfonamide Fiber During Heat-Drawing Process

Yumei Zhang[1], Jinchao Yu[1], Rui Wang[1], Shenghui Chen[2], Xiaofeng Wang[2], Huaping Wang[1]
[1]State Key Laboratory for Modification of Chemical Fibers and Polymer Materials, Donghua University, Shanghai, 201620, China; [2]Shanghai Tanlon Fiber Co., Ltd, Shanghai, 201419, China
zhangym@dhu.edu.cn

OBJECTIVE

The structure and properties change of pre-drawn aromatic copolysulfonamide fiber during heat-drawing process were studied to indicate the relationship between heat-drawn technology and structure, properties.

INTRODUCTION

Due to their thermal stability, high glass transition, inflaming retarding and low dielectric constant, aromatic polysulfonamide (PSAs) have significant potential application in industrial and aerospace fields. Although the spinning of the some isomerically substituted PSAs had been carried out in a laboratory or pilot scale as early as 1970s[1], the industrialization of the aromatic copolysulfonamide (*co*-PSA) fibers was broken through by Shanghai Tanlon Fiber co. Ltd. till 2008 [2] with the commercial name of Tanlon®. Compared with the poly(4,4'-diphenylsulfonyl terephthalamide) fibers reported by Khudoshev et al [3], the tenacity of the co-PSA fibers Tanlon® increased by introducing m-phenylsulfonyl moieties into the relatively rigid backbone which improved the solubility and spinability of polymers while the thermal stability kept well [4]. However, the knowledge of the basic structure and properties of PSA is still limited. It is interesting to establish relationships between the physical properties and structure of PSA, which is of great practical importance.

EXPERIMENTAL

1) Fiber preparation

The *co*-PSA was synthesized via polycondensation of 4, 4'-diaminodiphenylsulfone, 3, 3'-diaminodiphenylsulfone and terephthaloyl chloridein in DMAc at low temperature. The concentrated solution after polymerization was used as spinning dope directly. The pre-drawn PSA fibers were prepared by wet spinning technique and then heat-drawn at different temperature.

2) Characterization

The cross-sections of a bundle of PSA fibers were cut by slicer and observed using a (Leica DM750P) microscope.
S-S curves were obtained by XQ-1A mechanical tester.
Dynamic mechanical properties were performed on TA Q800 V7.5 instrument in the extension mode with a frequency of 1HZ and heating rate of 10°C /min from 40 to 400°C.
Wide-angle X-ray diffraction (WAXD) experiments were carried out at B14 beam line in shanghai Synchrotron Radiation Facility (SSRF) with a wavelength of 0.124nm. A bundle of PSA fibers were in a sample holder with the fiber direction perpendicular to the X-ray beam. WAXD patterns were recorded using Mar345 imaging plate.
SAXS profiles were obtained at Beamline (16B1) in Shanghai Synchrotron Radiation Facility (SSRF). The wavelength used was 0.124 nm. A CCD X-ray detector (MAR CCD 165) was employed at a distance of 2025 mm from the sample.

RESULTS AND DISCUSSION

1) Properties of *co*-PSA fibers heat-drawn at different temperature

From the DMA curves of the pre-drawn co-PSA fiber in Fig.1, it can be seen that there is a broad peak except the main transition peak corresponding to the glass transition (Tg) at the temperature about 150°C. Therefore, we designed the multiple heat-drawing processes to draw the fiber at the elevated temperature from 140°C to the temperature exceeding Tg.

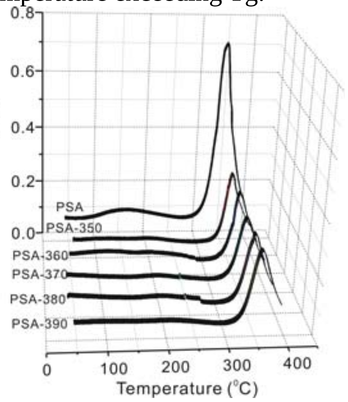

Fig.1 DMA curves of *co*-PSA fibers heat-drawn at different temperatures

From Fig.2, it is shown that the pre-drawn *co*-PSA fiber presented typical stress-strain curves of amorphous polymers. The tenacity and initial modulus of heat drawn fibers increased remarkably while the elongations at break decreased obviously. Especially, as the temperature increased from 350°C to 370°C, the tenacity and initial modulus of the heat-drawn fibers reached the maximum value of 4.6cN/dtex and 39.8cN/dtex, respectively. However, when the temperatures exceeded 380°C, the mechanical properties of heat-drawn fibers worsened with the increase of temperature although the decomposition temperature of the fibers changed little with temperature. As we all known that macroscopic mechanical property change is related to the microstructure of the fibers. How the structures changing during heat-drawing process will be illustrated as following.

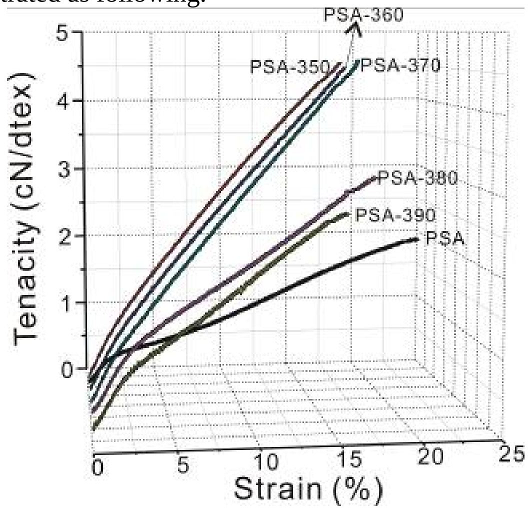

Fig.2 Stress-strain curves of co-PSA fibers heat-drawn at different temperature

2) Morphology and structure change of the co-PSA fibers heat-drawn at different temperature

From Fig.4, the pre-heat-drawn PSA fibers have a weak diffraction ring and a strong diffuse halo, however, the diffraction spots cannot be clearly observed, showing its low crystalline state. When the fiber was heat-drawn, multiple intense diffraction spots can be observed in the figures, indicating the formation of an ordered crystal structure in the fiber. It is obvious that the reflections of heat-drawn PSA fibers located in meridian seem increasingly clear with the rise of temperature, which indicates that the crystalline structure was preferred to orient along the fiber. The crystal orientation fc was given in Table I. Obviously, the crystallinity as well as the degree of crystal orientation of heat-drawn PSA fibers are higher than those of pre-heat-drawn PSA fibers and gradually increase with the rise of temperature. However, the crystal sizes became increasingly larger with the increment of temperature. On the basis of the data of the mechanical properties, there is no doubt that the crystallinity and the degree of crystal orientation contributed significantly to the increase of the strength and decrease of elongation of heat-drawn PSA fibers. It is worth noting that the strength of PSA380 and PSA390 is lower than the other heat-drawn PSA fibers in spite of their higher crystallinity and the degree of crystal orientation. According to the change of the crystal sizes of heat-drawn PSA fibers, it is reasonable for us to deduce that the crystal of greater size could contribute to the total crystallinity of semicrystalline polymers, but is unfavorable for enhancing the strength of heat-drawn PSA fibers when it is over a certain range. Therefore, it is necessary to control the temperature of heat drawing within a proper range in order to improve the mechanical properties of PSA fibers.

Fig.3 WAXD pattern of PSA fibers heat-drawn at different temperature

Table I Parameters of the crystallite structure of PSA fibers from SAXS curves

Temperature/ °C	Pre-drawn fiber	350	360	370	380	390
Crystallinity (%)	18.5	45.1	51.8	56.7	60.3	63.0
Density ($\mathrm{g/cm^3}$)	1.3130	1.3719	1.3824	1.3943	1.4024	1.3925
Hermann factor *fc*	-0.34	0.16	0.24	0.51	0.53	0.67

CONCLUSIONS

The pre-drawn *co*-PSA fiber was heat-drawn with the designed technology of multiple ratios at different temperature varying from 350 to 390℃. It was shown that the decomposition temperature varied little while the glass transition temperature (Tg) increased with the heat-drawn temperature. The tenacity and initial modulus increased when the pre-drawn fiber was heat-drawn although the dependence of mechanical properties on temperature was not linear. From the results of morphology and crystalline structure analysis, it is clear that the crystalline structure formed and the crystallinity, crystal orientation and crystallite size increased of the fibers increased with the heat-drawn temperature. It suggested that the mechanical and thermal properties of pre-drawn fiber improved by heat-drawing due to the formation of order crystalline structure but the exorbitant temperature would lead to thermal oxidation and brittleness for the fibers.

KEYWORDS: aromatic polysulfonamide fiber, structure, properties, heat-drawn

ACKNOWLEDGMENT

This work was financially supported National Natural Science Foundation of China (11079015 and 51273039).

REFERENCES

[1] Banduryan SI, Ivanova NA, Efimova SG, Sokira AN, Shchetinin AM, Frenkel, GG, et al. Fibre Chemisty 1978, 9(5): 484-485.
[2] Wang, J. Huagong Keji Shichang. 2009, 32(2), 6-11. (Chinese)
[3] Kuznetsov G. A., Nikiforov N. I., Lebedev V. P., Zhuravlev V. G., Savinov V. M. Vysokomol. Soyed. 1974, 16, 2711-2716.
[4] Ding X, Chen Y, Chen S, Li J, Wang X, Wang H, et al. J Macromol Sci B 2012, 51:1199–1207.

Thermal Properties of Poly(ethylene terephthalate)/Nanoclay Nanocomposites Fibers

Rustam Hojiyev and Yusuf Ulcay
Department of Textile Engineering, Uludağ University, Bursa, TR, 16059
rustamhodjiyev@gmail.com, yusufulcay@yahoo.com

INTRODUCTION

The potential applications of polymer-clay nanocomposite fiber is improving thermal and fire retardants properties. In our previous study we investigate mechanical properties of PET-clay nanocomposite FDY yarn prepare with melt processing techniques [1]. Several study show that PET-clay nanocomposite fibers have improving thermal properties. Especially in thermal degradation properties, which are directly related with flammability properties of nanocomposite fibers [2,3]. Some of studies is encountered to opposite results, where addition of nanoclay particles are didn't change thermal properties or cause to his reducing [4,5]. In this study thermal property of PET-clay nanocomposite fibers was investigated by thermal gravimetric analysis (TGA). The PET-clay nanocomposite fibers were prepared as in our previous study via masterbatch approach.

EXPERIMENTAL SECTION

Materials

Commercial nanoclay Nanomer I44P and Nanomer I30P was supplied from Desi Kimya ve Maden San Tic A.Ş. which is Amcol's branch company in Turkey. Nanomer I44P is an octadecylamine modified montmorillonite with average particle size 15-20 micron. Nanomer I30P is a dimethyl di(hydroginatedtallow) ammonium modified montmorillonite with average particle size 15-20 micron. Fiber grade PET chips with intrinsic viscosity (IV) 0.635 dL/g and bottle grade poly(buthelene terephthalate) (PBT) chips with IV 0,80 dL/g was used as a carrier polymer. All materials were used in as received form.

Masterbatch Preparation

Masterbatches with different clay contents 5-40% was prepared in contour rotating twin screw extruders (TSE) with special designed screw and length/diameter ratio (L/D) 44. Prior to melt compounding PBT and nanoclay were dry mixed and after that melt compounded in contour rotating TSE at 350 rpm and 240ºC melt temperature.

Spinning of PET/Clay Nanocomposite Fiber

Each mastertbatches was diluted by 5 wt% in fiber spinning procedures. Before dilution procedure moisture was removed by drying masterbatch chips. The spinning of PET/clay nanocomposite yarn with 300 denier and 96 filaments was carried out at 286ºC melt temperature using single screw extruders. The spinning speed was 1300 m/min and simultaneously hot drawn with 2.65 draw ratio in drawing machine for preparation fully drawn yarn (FDY).

Thermal Gravimetric Analysis (TGA)

TGA analysis was done by Seiko Exstar SII 6300 TGA/DTA instruments, between room temperature and 1000ºC, under 30 ml/min N_2 flow and at 10ºC/min heating rate. Approximatly 10 mg was used in TGA analyzing, the FDY yarn was cut and accurately placed to aluminum cell.

RESULTS AND DISCUSSION

In Figure 1 the TGA diagrams of PET-clay nanocomposite fibers prepared from Nanomer I30P are given. It obviously seemed that the thermal properties of nanocomposite yarn are reduced by addition nanoclay. The onset of thermal decomposition temperature is defined as 5% mass loss (T_5) and reducing in T_5 temperature is also seemed, at high clay content the reducing become more pronounced.

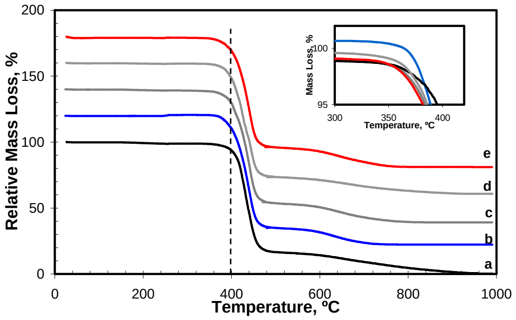

Figure 1: TGA Diagrams of PET-Clay Nanocomposite Fibers Prepared from Nanomer I30P: (a) Pure PET, (b) 0.5% I30P/PET, (c) 1%I30P/PET, 1.5% I30P/PET, 2% I30P/PET.

The TGA diagrams for PET-clay nanocomposite fibers prepared from Nanomer I44P nanoclay is given in Figure 2. The near same results as for I30P/PET nanocomposite yarn are observed for I44P/PET nanocomposite yarn. Its expected addition of nanoclay will improve thermal degradation properties of nanocomposite yarn via barrier properties of clay platelets. However, there are two reasons why such expectation didn't achieve. The main reason related with nano dispersion of clay platelets in PET matrix, its difficult achieve exfoliated nanocomposites via melt preparation techniques and second reason the OH groups in clay edges react as Bronsted acid sites and cause to degradation of PET polymers during melt processing [6].

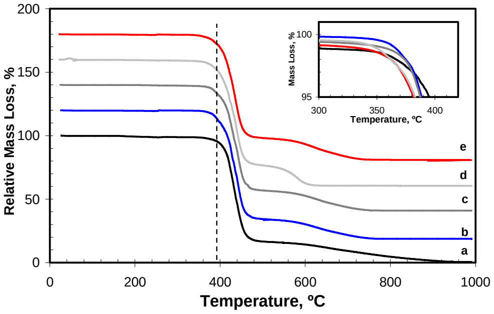

Figure 2: TGA Diagrams of PET-Clay Nanocomposite Fibers Prepared from Nanomer I44P: (a) Pure PET, (b) 0.5% I44P/PET, (c) 1%I44P/PET, 1.5% I44P/PET, 2% I44P/PET.

The T5 temperature is reduced by addition of nanoclay in PET-clay nanocomposite yarns. However the TGA analysis didn't give information about flammability properties of nanocomposite yarn. For example Nazare et al. [7] are also observing reduction in thermal stability of PBT-clay nanocomposites measure by TGA instruments. However, improving in thermal stability was observed beyond 400ºC temperature. Habibi et al. [5] also observe reduction in thermal stability of PET-clay nanocomposites measured by TGA, however from calorimetric measurements addition of nanoclay reduce heat release rate about 25-32% and this pronouncing improvements in flammability of PET-clay nanocomposite.

FUTURE WORK

Future work will investigate flammability of fabrics prepared from PET/clay nanocomposite yarns. Also dyeing properties of PET/clay nanocomposite fibers will be investigated.

ACKNOWLEDGMENT

We acknowledge support from the Turkish Ministry of Science, Industry and Technology through the San-Tez Projects (Project number is 00492.STZ.2009-2).

REFERENCES

[1] Hojiyev, R., Altun, Ş., Ulcay, Y. Fiber Society Conference, Spring 2012.

[2] Jung, M.-H., Chang, J.-H., Kim, J.-C. *Polym. Eng. Sci*., 2007, 47: 1820-1826.

[3] Chang, J.-H., Kim, S.J., Joo, Y.L., Im, S. *Polymer,* 2004, 45: 919-926.

[4] Stoeffler, K., Lafleur, P.G., Denault, J. *Polymer Degradation and Stability*, 93:1332-1350.

[5] Habibi, S., Rashidi, A., Shahvaziyan, M. Proceedings of the 10th Asian Textile Conference, 2009, Ueda, Japan.

[6] Xu, X. et al. *Degradation and Stability*, 2009, Vol. 94, pp. 113-123.

[7] Nazare, S. et al. in *Fire Retardancy of Polymer: New Strategies and Mechanisms*. Edited by Hull, T.R. and Kandolar, 2009, pp. 168-183.

Molecular Orientation Development in Highly Uni- and Bi-axially Stretched ePTFE Filaments

Kyung-Ju Choi
Clean & Science Co., Ltd., 2400 E. Devon Ave., Suite 210, Des Plaines IL 60018, USA

ABSTRACT

The molecular orientation development of the highly uni and bi-axially stretched polytetrafluoroethylene (ePTFE) filaments are analyzed by the wide angle x-ray diffraction (WAXD) flat films and pole figures. The biaxial orientation factors, (f_Z^B , f_y^B) are applied in order to interpret the above data quantitatively. These biaxial orientation factors agree well with the pole figures and the flat film patterns for the corresponding samples.

INTRODUCTION

It is well established that filaments with biaxial molecular orientation posses superior mechanical properties. A considerable number of patents describing the formation of biaxially oriented expanded polytetrafluoroethylene (ePTFE) filaments has been issued . The polytetrafluoroethylene single crystal structure related subjects has been published by E. S. Clark (6 – 9), F. J. Rahl et al., T. W. Bates and W. H. Stockmayer , R. G. Brown , and H. D. Flack. The morphology and structural deformations of polytetrafluoroethylene have been described by H. Okuyama et al., C. J. Speerschneider and C. H. Li, T. Kitamura et al., T. Yamamoto and T. Hara, X. Hao et al. and R. Endo et al. Fiber formation and uniaxial drawing of polytetrafluoroethylene have been investigated by R. Endo et al., H. Yamane et al., T. Morioka et al., R. L. McGee and J. R. Collier and M. Shimizu et al.

The biaxial orientation function was originally developed by R. S. Stein (28). It was further developed by J. L. White and J. E. Spruiell (29). These biaxial orientation functions have been applied to the tubular blown films and blow molded bottles by K. J. Choi et al.

KEYWORDS

Molecular Orientation, Uni-/bi-axially stretched PTFE

EXPERIMENTAL

The material used in the experiment was Daikin F-135. Expansion of the paste-like extruded polymeric material may be accomplished by beginning with a fine PTFE powder by adding a lubricant such as Isopar to form a paste which may then be extruded under high pressure to make PTFE tape. This tape is fed directly from the calendaring processing states to machine direction orienting (MDO) expander. Subsequent expansion stage of the tape occurs in a transverse direction orientation (TDO) stretch in the tenter machine to make ePTFE.

The wide angle x-ray diffraction (WAXD) and pole figure experiments were carried out with highly uni and bi-axially stretched ePTFE filaments at the x-ray laboratory of the University of Tennessee.

Figure 1. PTFE crystal structure at room temperature (Form IV).

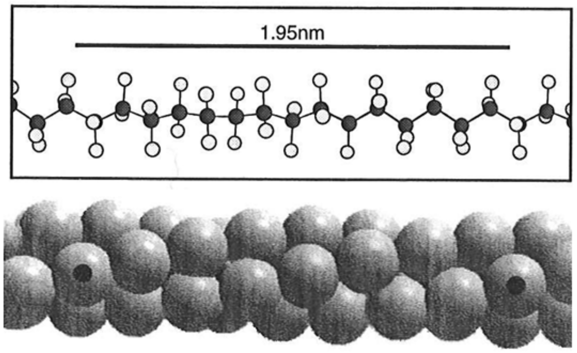

The crystal structure of PTFE at the room temperature is Form IV shown in Figure 1.

The orientation measurement was done with a very strong (100) plane diffracton by utilizing Z. W. Wilchinsky (35) technique.

$$\cos^2\phi_{100,z} = e^2\cos^2\phi_{u,z} + f^2\cos^2\phi_{v,z} + g^2\cos^2\phi_{c,z}$$

$$\cos^2\phi_{u,z} + \cos^2\phi_{v,z} + \cos^2\phi_{c,z} = 1$$

Where ϕ is the angle between Cartesian axis and the normal to a set of (hkl) planes (azimuthal angle). u, v and c are Cartesian coordinate axes of which c is the molecular chain axis and e, f, g be the directional cosines of the normal to a set of hkl planes with respect to the axes u, v and c, respectively. For (100) plane, $e^2 + f^2 = 1$ and $g^2 = 0$. Therefore,

$\cos^2 \phi_{c,z} = 1 - 2\cos^2 \phi_{100,z}$ and

$\cos^2 \phi_{c,y} = 1 - 2\cos^2 \phi_{100,y}$

, and the biaxial orientation factors may be expressed (29) as

$$f^{B}_{c,z} = 2\cos^2\varphi_{c,z} - \cos^2\varphi_{c,y} - 1 =$$

$$2 - 4\cos^2\varphi_{100,z} - 2\cos^2\varphi_{100,y}$$

$$f^{B}_{c,y} = 2\cos^2 \phi_{c,y} - \cos^2 \phi_{c,z} - 1 =$$

$$2 - 4\cos^2 \phi_{100,y} - 2\cos^2 \phi_{100,z}$$

, where z and y are the machine direction (MD) and the transverse direction (TD), respectively.

RESULTS AND DISCUSSION

Figure 2. WAXD flat film patterns of highly uni and bi-axially stretched ePTFE filaments

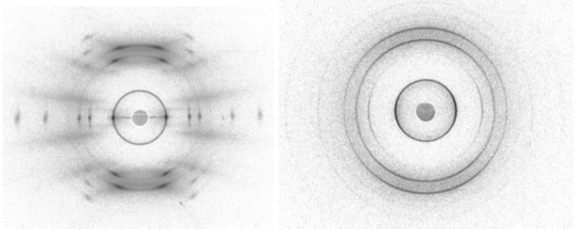

The wide angle x-ray diffraction (WAXD) patterns of highly uni and bi-axially stretched ePTFE filaments are shown in Figure 2.

The highly uni-axially stretched showed distinct symmetric patterns with strong (100), (108), (107), (110), (200) and weak (210), (300), (220), (310), (117) and (118) scattering spots. It is interesting that (100) scattering pattern shows the ring with a strong intensity at the equator. This (100) ring pattern is unusual for a highly uni-axially oriented fiber. Since this is the highly uni-axially drawn thin filaments, it is expected to have slight a-axes molecular orientations toward the other directions. It is a highly oriented pattern.

The highly bi-axially stretched showed rings and an eyebrow patterns. This ring pattern is a good indication of the multi-axial orientation. The (110) eyebrow pattern indicates that some portions of a-axes are 70 to 90 degrees away from the machine direction.

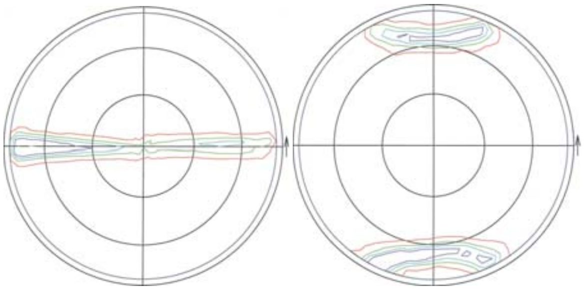

Figure 3 shows (100) and (108) pole figures of the uni-axially stretched film. The a-axes of the uni-axially stretched at the ratio of 48 exhibit almost perpendicular to the machine (stretch) direction (MD) and in the plane of the normal direction (ND) or thickness direction and the transverse direction (TD) similar to the a-axes of the fiber orientation (see (100) pole figure in Figure 3) .

The (108) pole is about 19 degrees away from the MD. Therefore, (108) poles are showing a cone shape in about 15 to 25 degrees far from the MD indicating a strong molecular chain axes align with the MD (see (108) pole figure in Figure 3).

Figure 4 shows (100) and (108) pole figures of the highly bi-axially stretched filaments. The a-axes of the highly bi-axially stretched are almost parallel to the normal (thickness) direction (ND) and perpendicular to the machine (stretch) direction (MD).

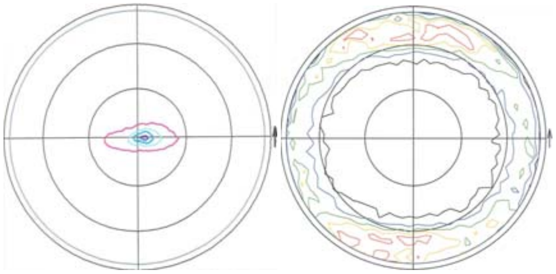

.

The c-crystalline biaxial orientation factors of the highly uni and bi-axially stretched filaments (f^{B}_{Z} , f^{B}_{y}) are (0.75, 0.09) and (0.84, 0.52), respectively.

CONCLUSIONS

The highly uni-axially stretched filaments are not perfectly uni-axially oriented. These biaxial orientation factors agree well with the pole figures and the flat film patterns for the corresponding samples. It appears that there is a room to stretch further even though these samples are highly uni-and bi- axially stretched filaments.

Natural Fibres

Biomimetic Melanin Dyestuffs for Wool Fabric *In Situ* Coloration

Vicky L. L. So, Liang He, John H. Xin
Institute of Textile & Clothing, The Hong Kong Polytechnic University, Hung Hom, Hong Kong, P.R.China
tcxinjh@polyu.edu.hk

ABSTRACT

It was attempted to bio-mimick the natural melanin biosynthetic pathway to dye textile fabric with natural-looking colors. In this method, dopamine was selected as a biomimetic molecule of 3,4-dihydroxyphenylalanine to form melanins-like colorants. It was found that the wool fabric could be dyed to different color hues in a controllable way by adding a second component to the dyeing bath. The dyed wool fabrics had good fastness. SEM analysis showed that the wool fibre surfaces were effectively covered by the polydopamine colorants.

INTRODUCTION

As well-known, melanins are naturally occurred pigments present in human hair, skin and many other animals and plants [1], which are not mutagenic and irritating to the skin. During its formation, melanin colorants don't produce any pollution to the environment. This is a perfect process and really worthy of biomimetically adopting on textile [2]. However, the inability to provide a simple yet effective process for textile coloration in a way of melanin forming has prevented its use in the commercial way. Clearly, there are a number of opportunities to improve it. In our recent research, we have developed a differently effective approach.

With the gradual revealing of the underlying mechanism, we are able to understand the processes to some extent. Two different melanins of eumelanins and pheomelanins are found in human hair. The enzyme tyrosinase [3] first catalyzed the hydroxylation of tyrosine to 3, 4-dihydroxyphenylalanine (DOPA), which was then oxidized to dopachrome and further undergo a series of complex reactions to form eumelanins. On the other hand, dopaquinone could react with nucleophilic cysteine to produce cysdopa, then transformed to pheomelanins in a similar way. Dopamine has the catechol and ethylamino functional group in DOPA, and it is also easily polymerizable under alkali condition or in the presence of oxidants. According to these understandings, dopamine was selected as an ideal molecule of DOPA to biomimetic melanins formation on textile. Several aromatic compounds (Fig. 1) were also incorporated to tune the color hues.

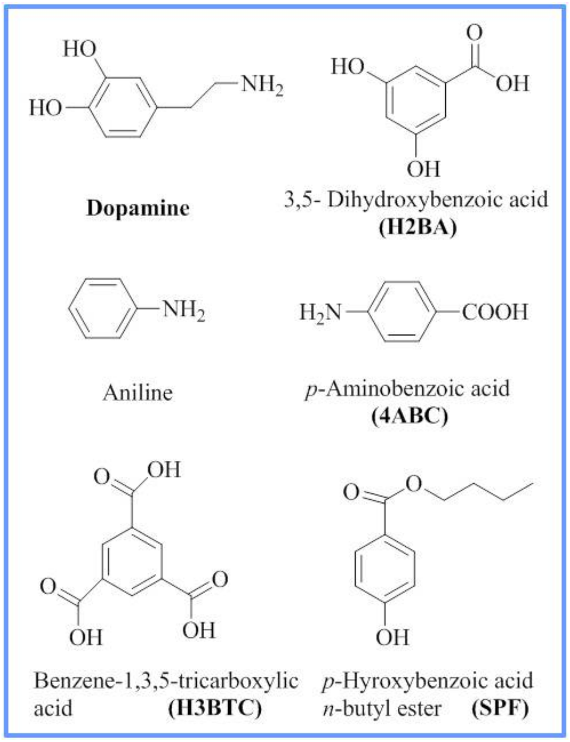

Dopamine

3,5- Dihydroxybenzoic acid **(H2BA)**

Aniline

p-Aminobenzoic acid **(4ABC)**

Benzene-1,3,5-tricarboxylic acid **(H3BTC)**

p-Hyroxybenzoic acid *n*-butyl ester **(SPF)**

Figure 1 Aromatic compounds used in the study.

METHODS

Textile fabric was immersed in an aqueous solution containing 10% of dopamine at room temperature overnight. In this process, the second aromatic component, with the ratio of 5:1 to dopamine, was also added to tune the textile color hues. Subsequently, it was taken out of the bath and sprayed with 1% oxidant solution, and then dried in the air. Finally, the colored fabric was washed in 5‰ sodium dodecyl sulfonate solution at 60 ^{o}C for 10 min and dried in the air for measurements.

RESULTS AND DISCUSSION

Colorimetric analysis

The colorimetric analysis of colored wool samples was shown in Table 1. Dopamine only was first used for biomimetic coloration on wool fabric, which displayed a yellowish color hue with the L*, a*, b* values of 45.82, 7.41 and 21.27, respectively. As shown in the Table 1, the addition of 3,5-Dihydroxybenzoic acid, Benze-1,3,5-tricarboxylic acid and *p*-Hydroxybenzoic acid *n*-butyl ester tuned the obtained color on wool fabric towards less red and less yellow, which showed that the carboxylic group in the components without amino group was favorable to obtain a bluer color hue. The addition of aniline caused the wool color towards redder and less yellow hue, while the presence of *p*-Aminobenzoic acid resulted in the wool fabric towards a little bit redder and yellower color hue. Compared to the wool sample colored by dopamine only, the wool fabric was colored with a deeper brightness in the presence of aniline, while the other four components of 3,5-Dihydroxybenzoic acid, *p*-Aminobenzoic acid, Benze-1,3,5-tricarboxylic acid and *p*-Hydroxybenzoic acid *n*-butyl ester gave the colored wool fabrics a lighter brightness.

Table 1 Colorimetric analysis of colored wool samples

Components	Δ L*	Δa*	Δb*
Dop [a]	45.82	7.41	21.27
Dop +H2BA	18.46	-1.82	-0.44
Dop +Aniline	-8.10	1.56	-2.21
Dop +4ABC	17.39	0.21	7.51
Dop +135BTC	17.81	-2.42	-10.50
Dop +SPF	12.04	-3.35	-2.95

[a] L*, a* and b* values for dopamine use only.

Fastness test

Wash fastness (AATCC Test Method 61-2010) for the colored textile fabrics was also assessed, as listed in Table 2. It was observed that the colored fabrics displayed good ratings of 4-5 or 5 in most cases. The fastness to shade staining was a little bit better than fastness to shade change, and the fastness on wool fabric was better than those on other tested fabrics. Crocking fastness (AATCC Test Method 8-2007) was also assessed. For the dry crocking results, most of the ratings were within the range of 4 to 5 which were close to the rating of the control specimen. For the wet crocking results, the ratings were around 3 to 4/5 in most cases.

Table 2 Wash fastness of the colored textile fabrics

Components	Shade change	Shade staining [a]					
		W	A	P	N	C	A
Dop only	4-5	5	5	5	5	5	5
Dop +H2BA	4-5	5	5	5	5	5	5
Dop +Aniline	4	5	5	5	5	5	5
Dop +4ABC	4	5	5	5	5	5	5
Dop +H3BTC	4-5	5	5	5	5	5	5
Dop +SPF	4-5	5	5	5	5	5	5

[a] W wool, A acrylic, P polyester, N nylon, C cotton, A acetate

Microscopic analysis

As an example, the SEM images for wool fibres before and after coloration were also presented in Figure 2. It can be seen that the blank wool fibres have clear scales on the surfaces, which acts as a barrier to block the dyes to penetrate into the fibre in a conventional coloration process. After the coloration in this study, the surface morphology of the fibres became smoother and the scales disappeared. This result suggested that the fibre surfaces were effectively covered by the polydopamine colorants.

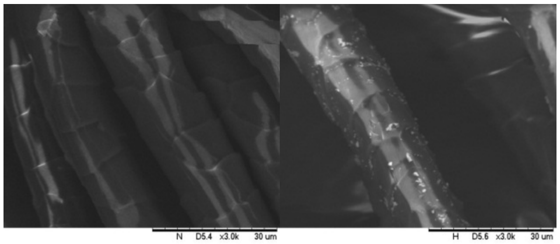

Figure 2 The SEM images of wool fibres before (left) and after (right) coloration.

CONCLUSIONS

It has been developed a biomimetic method to dye textile fabrics. In this method, dopamine was oxidized under the controlled conditions to produce melanin-like colorants. The color hues and brightness on the fabrics could be tuned in a controllable way of adding another aromatic component. The method was also able to be used for other textile fabrics dyeing. It was promising to be an environmental friendly choice compared to the traditional procedure.

ACKNOWLEDGMENTS

The work is financially supported by Research Grants Council of Hong Kong SAR Government project PolyU 5316/10E.

REFERENCES

[1] G. Prota, Med. Res. Rev., 8, 525(1988).
[2] Y. Liu, J. Tang, R. Wang, H. Lu, L. Li, Y. Kong, K. Qi and J. H. Xin, J. Mater. Chem., 17, 1071(2007).
[3] K. C. Brown, E. Marlowe, G. Prota, G. Wenke, *J. Soc. Cosmet. Chem.*, 48, 133 (1997).

Mohair Fibre Quality and Production as Related to Animal Size

Bruce A. McGregor[1] and Kym Butler[2]
[1]Institute for Frontier Materials, Deakin University, Geelong, Australia
[2]Future Farming Systems Research Division, Department of Primary Industries, Werribee, Vic., 3030, Australia

bruce.mcgregor@deakin.edu.au

OBJECTIVE

Mohair is a luxury fibre produced by Angora goats. Mohair has special textile properties and is famed for its lustre. There are many reports of the relationships between mohair attributes and processing[1]. While mohair production can be profitable to farmers there are severe price discounts for faults and poor quality[2]. While genetics is known to affect mohair quality, fundamental relationships between body size and mohair quality have not been determined.

We conducted a series of investigations to quantify the relationships between important mohair quality attributes and live weight and other lifetime factors associated with Angora goats.

INTRODUCTION

The most important mohair quality traits determining price are mean fibre diameter (MFD, μm), which accounts for 60% of the variation in price, staple length (SL, cm) and the incidence of medullated fibres (Med, % by number)[1 ,2]. The quantity of clean fleece (CFW, kg) harvested following shearing is also critical for the economic return of farmers.

Each of these 4 attributes is known to vary substantially during the lifetime of Angora goats. Increase in MFD with age is known and accepted as “micron blowout” and can result in 90% reductions in price. It is unknown to what extent the increase in the proportion of coarser Australian mohair is related to age effects, live weight effects, or genetic effects, and so many mohair producers are not in a position to clearly manage these changes.

There is considerable confusion in the literature about how MFD, SL and Med change over the lifetime of Angora goats. For example, it appears that many previous investigations have been conducted for 2 years or less and have not analyzed the affects of live weight on Med.

This is surprising as allometric relationships are common in animal production, and elsewhere in biology[3].

We report on a series of investigations to examine how MFD, CFW, SL and Med are related to live weight of Angora goats of different genetic origins over their lifetime and how the relationship varies with other lifetime factors.

APPROACH

We used data obtained from a carefully managed flock of Angora goats which had detailed records of pedigree, birth, live weight, fleece production and fibre testing. The goats were progeny of various genetic sources including sires of 100% South African origin, 100% Texan origin, and other interbred admixtures that included sires of South African, Texan and Australian origin. These sires were representative of the genotypes available in Australia.

Mohair was harvested every 6 months for 6 years. Objective fibre tests were conducted using the OFDA100. Live weight (kg) was measured prior to shearing and CFW at shearing. Fleece-free live weights (FFLW) were determined, as was change in FFLW during the shearing interval, and average FFLW during the growing period.

Restricted maximum likelihood (REML) modelling, which allowed the observations of the same animal at different ages to be correlated in an unstructured manner, was developed to relate each fleece attribute to shearing age, AvFFLwt and other lifetime factors [4, 5, 6, 7]. For 2 years the goats were used to study the effects of altering the length of the shearing interval from 3 months to 12 months[8]. The analysis took account of these experimental manipulations.

RESULTS AND DISCUSSION

There was large variation in the main mohair fleece quality attributes (Table I) indicating the difficulty that many farmers have in producing consistent fibre.

Table I. Mean, standard deviation (s.d.) and range in greasy fleece weight (kg), mean fibre diameter (μm), staple length (cm), incidence of medullate fibre (% by number), average live weight (kg) and average liveweight change (kg) for Angora wether goats shorn every 6 months from ages 1 to 6 years (n = 872).

Variable	Mean	s.d.	Range
Greasy fleece weight	2.21	0.64	0.79-4.64
Mean fibre diameter	30.9	5.02	17.6-47.5
Staple length	13.2	1.61	7.2-18.0
Incidence of medullated fibres	1.4	0.72	0.1-4.3
Live weight	38.7	14.26	10.4-73.3
Live weight change	4.0	5.86	-13.8-+22.8

Significant terms in the fixed effects models for CFW, MFD, SL and Med are summarised in Table II. Interactions between terms are not indicated.

Table II. Significant terms in the fixed effects models for clean fleece weight (CFW, kg), mean fibre diameter (MFD, μm), staple length (SL, cm), medullated fibre (Med, % by number).

Fixed effects	CFW	MFD	SL	Med
Shearing frequency and year	✓	✓	✓	✓
Age of goat	✓	✓	✓	✓
Average fleece-free liveweight	✓	✓		✓
Fleece-free liveweight change	✓		✓	
Genetic source		✓		✓
Liveweight at weaning		✓		

Shearing frequency had important effects on mohair, particularly 4 shearings per year compared with the usual practice of 2 shearings per year[8] but altering shearing frequency is not usually economic.

Age of goat was important but not as important as the average FFLW in affecting CFW, MFD and Med. MFD was related to $FFLW^{0.34}$ (Figure 1)[4].

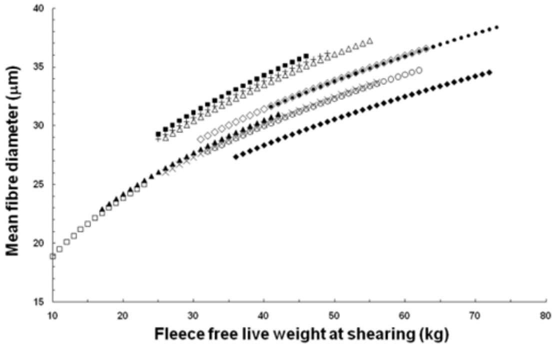

Figure 1. Relationship between mohair mean fibre diameter and fleece-free liveweight at different shearing ages, after adjustment for other terms in the model[4]. Symbols: □, 1-year- old; ▲, 2- year- old; ■, 2.5- year- old; +, 3- year-old; △, 3.5- year- old; ×, 4- year- old; ◇, 4.5- year- old; ○, 5- year- old; ●, 5.5- year- old; ◆, 6- year-old.

CFW was related to $FFLW^{0.67}$, but only when liveweight was lost at the rate of 5–10 kg during a shearing interval of 6 months. The allometric coefficient declined to 0.3 as liveweight change increased from 10 kg loss to 20 kg gain during a shearing interval (Figure 2)[5].

For SL, there was no relationship between size of goat and SL. SL was mainly a function of time between shearing[6].

Generally, within each shearing interval, Med increased with increasing average FFLW. However, the size and shape of the relationship differed greatly between shearing ages[7]. Variation in animal nutrition, as measured by liveweight change during shearing periods, did not affect Med[7].

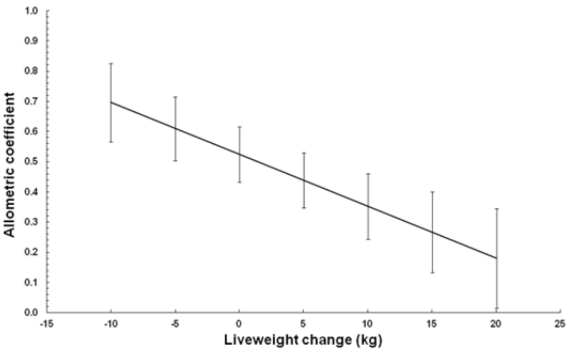

Figure 2. The allometric coefficient relating clean fleece weight to average fleece-free liveweight, and fleece-free liveweight change for Angora goats between 1 and 6 years of age, with 95% confidence limits[5].

There were smaller effects of genetic origin of goats on MFD and Med, providing opportunities to identify and select preferred sires. For MFD, improved liveweight at weaning of one genetic source of young goats was associated with lower MFD.

CONCLUSIONS

Factors which affect liveweight and liveweight at weaning have lifetime effects on mohair MFD.

The advantage of greater CFW in having fewer but larger Angora goats rather than more but smaller goats will come at the detriment of producing lower quality mohair, both in terms of increased MFD and Med and reduced fleece value.

The biological determinants of size of fibres related to cross-sectional area are substantially different to the size determinants of fibre length. Within an age group of Angora goats, the largest animals will be the least efficient in converting improved nutrition to mohair.

ACKNOWLEDGMENT

This work was funded by the Rural Industries Research and Development Corporation, Barton, ACT, and the Victorian Department of Primary Industries. Former colleagues and assisting farmers are gratefully thanked.

REFERENCES

1. Hunter, “Mohair: a review of its properties, processing and applications.” 1993.
2. McGregor and Butler, *Aust. J. Agric. Res.* 55, 1283-1298, 2004.
3. Schmidt-Nielsen, “Scaling: why is animal size so important?.” 1984.
4. McGregor et al., *Anim. Prod. Sci*. 52, 35-43, 2012.
5. McGregor et al., *Anim. Prod. Sci*. 53, 154-162, 2013a.
6. McGregor et al., Anim. Prod. Sci. 53, on line, 2013b.
7. McGregor et al., *Small Rumin. Res*. in press 2013.
8. McGregor and Butler, *J. Agric. Sci*. Camb. 146, 351-361.

Chemical Treatments on Hemp Fibre Composites

Hao Wang[1], Mazed Kabir[1], K.T.Lau[2]
[1]Centre of Excellence in Engineered Fibre Composite, Faculty of Engineering and Surveying, University of Southern Queensland, Toowoomba, Australia
[2]Department of Mechanical Engineering, The Hong Kong Polytechnic University, Hong Kong
Hao.Wang@usq.edu.au

INTRDUCTION

Natural fibres have become an attractive alternative to synthetic fibres in polymer composite structures. This is due to environmental concerns that lead to using more renewable resources in composite structures. Natural fibre constituent contents (cellulose, hemicelluloses and lignin) and hydrophilic nature reduce their compatibility with polymer matrices. Fibre surface modifications using chemical treatments have been successfully used to improve fibre-matrix compatibility. In this study, hemp fibres were treated with alkali and acetyl chemicals. Fibre constituents such as cellulose, hemicelluloses and lignin constituents were separated from treated fibres. The chemical and thermal influences of these constituents on the treated fibres were examined by using scanning electron microscope (SEM) and thermogravimetric analysis (TGA).

EXPERIMENTAL

Chemical treatments

The alkali treatments on hemp fibre used different concentrations of NaOH solutions (0%, 5% and 10%). Hemp fibres were soaked in NaOH solution for 3 hours at room temperature. The fibres were then washed several times with distilled water to allow absorbed alkali to leach from the fibre. The washed fibres were dried at room temperature for 8 hours, and then oven dried at 100°C for another 6 hours. For acetyl treatments, alkali pre-treated hemp fibres were soaked in acetic acid (glacial) and subsequently treated with acetic anhydride at room temperature for 3 hours. Following this treatment, the fibres were washed and then dried in the manner described above.

Chemical analysis

Cellulose, hemicelluloses and lignin constituents from the treated hemp fibre were separated by using sodium chlorite, acetic acid, potassium hydroxide (24% KOH), rectified spirit and sulphuric acid (72% concentration). Treated fibres were crushed into powder and oven dried at 100°C for 2 hours. The dried hemp powder (4 g) was placed in an Erlenmeyer flask and the chemicals were added. The residue from the solution mixture was collected by filtration and washed with distilled water and rectified spirit. The collected residue was oven dried at 105°C for 8 hours before being weighed. The percentage of cellulose, hemicelluloses and lignin were calculated by measuring weight differences.

Microstructure and thermal analysis

SEM micrographs of treated and untreated fibre samples were captured by using scanning electron microscope Model JEOL 6400F. For SEM evaluation, all samples were coated with a layer of gold and 20 kV was used as the accelerating voltage. TGA analysis of fibres was conducted by thermal gravimetric analyser (TGA-Model No. Q500). Between 6 and 10 mg of fibres were taken for analysis. Fibre samples were heated up at a rate of 10°C/min from 10 to 500°C in a helium medium (60 ml/min).

RESULTS AND DISCUSSION

The content of fibre constituents of different treated fibres is presented in Table 1. From Table 1 it can be observed that the hemicelluloses and lignin contents were decreased with NaOH treatment. Removal of hemicelluloses and lignin increased the relative amount of cellulose contents on the treated fibres.

Table I. Fibre constituents before and after chemical treatments.

Fibre treatment	Alkalisation			Alkalisation + acetylation		
%NaOH	Cellul’	HemiC’	Lignin	Cel’	HC	L
0	77.20	5.40	6.67	81.3	4.96	10.3
5	80.03	4.90	4.86	83.2	4.38	4.0
10	88.35	4.67	3.46	92.6	3.85	2.6

Acetyl treatments on the untreated fibres reduced the hemicelluloses content but the measurement of lignin content increased. This was the result of hemicelluloses initially reacting with acetyl groups, then the acetylated hemicelluloses depositing on lignin. Acetyl treatment on alkali pre-treated fibres showed that the amount of cellulose contents were increased with higher concentrations of (5%, 10%) NaOH pre-treatment. This was due to the extraction of more lignin in two consecutive treatment processes as compared to the NaOH treated samples.

Figure 1 shows the hemp fibre before and after chemical treatments. It can be observed that the gummy polysaccharides of lignin, pectin and hemicelluloses are localized on the surfaces of the untreated fibres (Figure 1a). Alkalised fibre surfaces (Figure 1b) appeared as bundles of continuous cellulose elementary fibre. Several patterns of partitions formed among these fibre bundles which could not be seen in the original untreated fibres.

This observation clearly indicated that NaOH treatments could remove the hemicelluloses and lignin coverings from the cellulose surfaces. Similarly, acetylated fibre surfaces (Figure 1c) also exhibited the partitioning of fibre bundle and cleaner surfaces in relation to the untreated fibres.

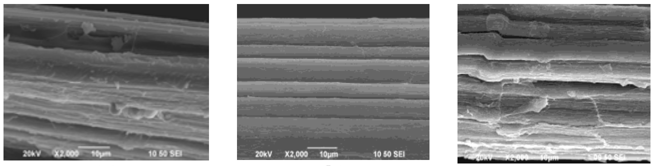
(a) (b) (c)

Figure 1. SEM micrograph of (a) untreated (b) alkalised (c) acetylated fibre surface.

Figure 2 shows the TGA curves of fibre constitutes and the untreated fibre. The thermal degradation process of fibre was divided into four stages: moisture evaporation, hemicelluloses degradation, cellulose degradation and lignin decomposition. Moisture evaporates at lower temperature (25-150°C). After the removal of moisture, between the temperature ranges of 150-500°C, the degradation process begins in the cellulose, hemicellulose, and then lignin constituents [1]. The major fibre decomposition was caused in the second stage where large weight losses were recorded. This was primarily caused by the decomposition of hemicellulose and partly by the lignin degradation. The decomposition temperature of cellulose was much higher than hemicellulose and lignin.

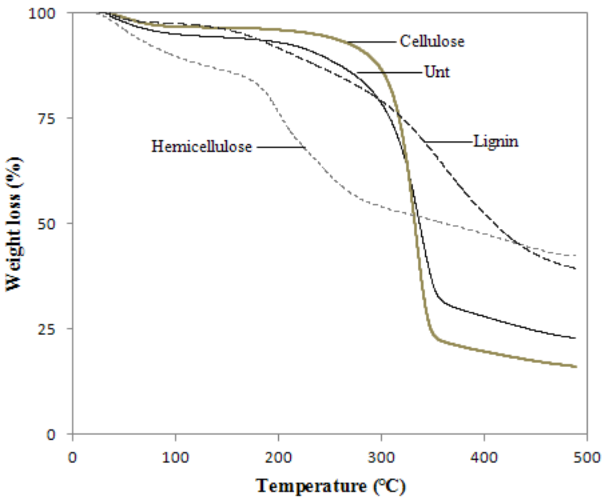

Figure 2. TGA curves of fibre constituents and untreated fibre.

Mechanical properties

The effect of chemical treatments in relation to the interface bonding characteristics between the fibre and matrix can be reflected on their flexural strength properties. Figure 3 shows the bending and shear strengths of untreated and treated composite samples. It is observed that flexural strength of alkali, acetylation and alkali+acetylated fibre composite samples showed 12%, 33% and 17% improvements in strength properties compared to the untreated fibre sample. The improvement in strength can attribute: (1) the increase of cellulose content after treatment; (2) the increase of chemical bonding between fibre and matrix, because the removal of lignin and hemicelluloses expose the more –OH groups to react with matrix [2, 3]. (3) the increase of mechanical bonding because of fibre surface roughness [4].

In the shear test, one side of the V-notched specimen was fixed in the fixture and other side displaced vertically along the fibre direction. It is observed that alkali, acetylation and alkali+acetylated fibre composite samples showed 36.43%, 19.11% and 43.73% higher strength properties compared to the untreated fibre sample. This was presumably due to the higher surface roughness of the treated fibre contributed good bonding with the matrix and provided greater frictional stress transfer along the interface.

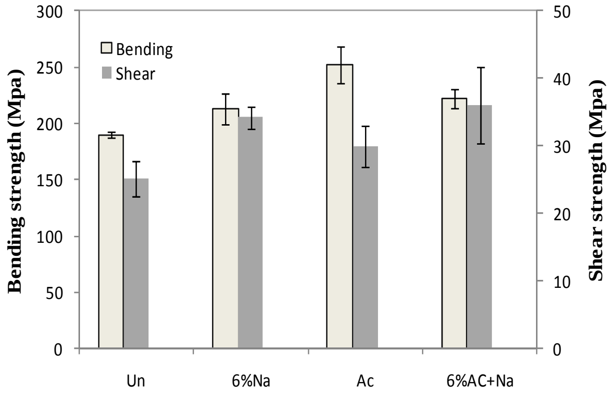

Figure 3. Bending and shear properties of the composites.

CONCLUSION

Chemical treatments change fibre structures by reacting with its constituents. Alkalisation and acetylation reduce the content of hemicellulose and lignin from the fibre. Thermal analysis of fibre revealed that hemicellulose is the most reactive constituent and degraded faster than that of cellulose and lignin. Cellulose exhibited better thermal stability and lignin was degraded in a wide range of temperatures. The hydrophilic nature of the fibres was predominantly caused by the presence of hemicellulose and then lignin constituents.

KEYWORDS: Hemp fibre, natural fibre composites, chemical treatments

REFERENCES

1. H.J. Kim and Y.G. Eom. *Journal of the Korean Wood Science and Technology*, vol. 20, pp. 59-67, 2001.
2. Y.M. Mwaikambo and M.P. Ansell. *Angew Makromol Chem*, Vol 272, pp 108-16, 1999.
3. M. Abdelmouleh, S. Boufi, M.N. Belgacem and A. Dufresne.*Compos Sci Technol*, Vol 67, pp 1627-39, 2007.
4. G.W. Beckermann and K.L. Pickering. *Composites: Part A*, Vol. 39, pp 979-88, 2008.

Water and Soil Resistant Bamboo Fabric by Sol-Gel Nano-Coating

Awais Khatri, Zahir Ahmed, Saiqa Agha, Saqib Munawar, Shahwaiz Khanzada, Saif-ur-Rehman
Mehran University of Engineering and Technology Jamshoro - 76062 Sindh Pakistan
awais.khatri@faculty.muet.edu.pk

SUMMARY

The water repellency and soil release on bamboo fabric was achieved by sol-gel coating using silica and titania nano-particles. The air-permeability and soft handle remained almost unchanged, thus, the inherent wear comfort of the bamboo fabric was maintained. Additionally, the tensile breaking strength of bamboo fabric was increased, thus, increase in durability to mechanical forces such as those during washing may be ensured.

INTRODUCTION

Fabrics made of regenerated bamboo cellulose fiber are popular for their cool, breathable and comfortable characteristics [1-5]. That is mainly due to its highly porous structure [6]. Therefore, they are widely been researched and promoted for the use in clothings. Moreover, the chemical finishing of bamboo textiles using various functional finishes expands the application scope [7-8].

The water and soil resistant finishing of fabrics is a normal demand in today's market specially for baby wears. Hydrocarbon fatty compounds, silicones and fluorochemicals are normally used for water, soil and oil resistance [4, 9]. However, the softness and air-permeability of the fabric are adversely affected resulting reduction in wearing comfort. Application of nano-finishes has recently been promoted for modification of surface characteristics of textile fibers without affecting fiber's inherent properties [10-11].

This study was aimed to produce a water and soil resistant bamboo fabric without affecting the inherent air-permeability and softness, ultimately the wear comfort, of the fabric. The aim was achieved by sol-gel nano-coating of the fabric with silica and titania nano-particles [6, 12-14].

Due to highly porous structure, the fabrics made of bamboo fiber are weaker than other cellulose fibers. Therefore, the tensile breaking strength of the untreated and treated fabrics was also assessed.

EXPERIMENTAL

Single-jersey bamboo fabric (~40 g/m^2) was obtained from Sapphire Textile Mills Pakistan and the fabric was boiled with 2 g/l non-ionic detergent (Ladipur RSK, Clariant Pakistan), for 15min to achieve the water absorbency of 1 sec (AATCC 79).

The solution was prepared in 80ml ethanol containing 20ml tetraethoxysilane (TEOS), 0 – 0.8% silica nano-particles (Aerosil® 200, Evonik Germany), 0 – 0.8% titania nano-particles (Aeroxide® TiO_2 P 25, Evonik Germany), and acetic acid (for solution pH 4-5). The solution was properly mixed through ultrasonic and magnetic stirring to ensure the acidic hydrolysis of TEOS and homogeneous solution. The fabric was padded in the solution on a Rapid laboratory horizontal padder with 80% wet pick-up followed by drying (100^{o}C, 60 sec) then baking (150^{o}C for 60 sec) on a Rapid laboratory stenter. The process recipe and conditions were obtained from our previous works on sol-gel coating of bamboo fabric [6-13].

The treated and untreated fabrics were tested for water repellency (Spray Rating, AATCC 22), soil release (AATCC 130), air-permeability (ASTM D 737), tensile breaking force and elongation (ASTM 5035) and handle (AATCC 5, scale of 1 – 10 was considered as 1 being very stiff and 10 being very soft).

RESULTS AND DISCUSSION

Effectiveness of silica and titania nano-particles concentrations for water and soil repellency: The results of the effect of concentrations on water repellency and soil release are given in Tables I and II. Both, water repellency and soil release increased with increasing concentrations of silica and titania nano-particles. The concentration where maximum effect was obtained was 0.6% silica nano-particles and 0.6% titania nano-particles.

TABLE I Effect of silica nano-particles concentration on water and soil repellency (0.6% titania nano-particles)

Aerosil® 200 concentration [%]	Water repellency [ISO spray rating]	Soil release [1-5 grading]
0	85	1
0.2	85	1.5
0.4	85	1.5
0.6	95	2.5
0.8	95	2

TABLE II Effect of titania nano-particles concentration on water and soil repellency (0.6% silica nano-particles)

Aeroxide® TiO_2 P 25 concentration [%]	Water repellency [ISO spray rating]	Soil release [1-5 grading]
0	80	1
0.2	85	1
0.4	85	2.5
0.6	95	3
0.8	95	3

Effectiveness of the sol-gel process: Table III shows that the bamboo fabric became water and soil resistant after sol-gel treatment, as, very good water repellency and good soil release were achieved. Interestingly, the air-permeability remained unchanged and fabric handle became negligibly stiffer after the treatment, thus ensuring the inherent comfort of the bamboo fabric unaffected. This may be because the nano size of the finishes do not significantly reduce the porosity of the fiber. Further, the TEOS, serving as a bridge between nano-particles and the fiber, has been reported not to alter the properties of the fiber [6, 12-13]. The tensile breaking strength of the fabric increased after the treatment. This may be attributed to the gel network formed within the fiber providing additional bonding among the fiber polymers. A combination of silica and titania nano-particles in sol-gel application resulted a water and soil repellent fabric with unchanged air-permeability, negligibly reduced softness, and improved tensile strength.

TABLE III Water repellency, soil release, air-permeability, handle, and breaking strength and elongation of bamboo knitted fabric before and after sol-gel nano-coating

S. No.	Property	Untreated fabric	Treated fabric
1	Water repellency [ISO spray rating]	0	95
2	Soil release [grading]	0	3
3	Air-Permeability [ml/sec]	> 400	> 400
4	Handle [stiffness-softness scale]	9	8
5	Breaking strength [cN/tex]	13010	14800
6	Elongation [%]	57.9	42.8

CONCLUSION

Sol-gel application of silica and titania nano-particles on bamboo knitted fabric can be done to make the fabric water and soil resistant. This does not change the comfort characteristics of the fabric. Interestingly, the tensile strength is increased, which ultimately increases fabric durability. The finished fabric may be suitable for apparels.

ACKNOWLEDGMENT

We are thankful to Sapphire Textile Mills Pakistan for providing the bamboo knitted fabric.

REFERENCES

[1] Xu Y., Lu Z. Tang R. Structure and thermal properties of bamboo viscose, tencel and conventional viscose fibres. *Journal of Thermal Analysis and Calorimetry*, 89, 1, 197-201, 2007.

[2] Jie F. Bamboo fiber–A new type of textile fiber material. *Tianjin Textile Science and Technology*, 2, 2005.

[3] Sui S., et al. A study of structure and performance of bamboo fibers. *Journal of Textile Research*, 6, 2003.

[4] Heywood D. Textile finishing. *SDC UK* 2003.

[5] Schindler W. D., Hauser P. J. Chemical finishing of textiles. Woodhead Publishing Ltd. Cambridge, 2004.

[6] Khatri A., Shaikh M., Kalhoro A. M., Abbas S. A., Hussain M. Sol-gel Nano-coating of bamboo knitted fabric to improve water repellency and tensile behaviour. *Proceedings: 7th Central European Conference*, 180-183, 2012.

[7] Watanabe I. Development of Sohtake. *Sen'I Gakkaishi*, 60, 7, 2004.

[8] Shen Q. Liu D., Gao Y., Chenc Y. Surface properties of bamboo fiber and a comparison with cotton linter fibers. *Colloids and Surfaces*, 35, 193-195, 2004.

[9] Tomasino C. *Chemistry and Technology of Fabric Preparation and Finishing*. North Carolina State University 1992.

[10] Sawhney A. P. S., Condon B., Singh K. V., Pang S. S., Li G., Hui D. Modern Applications of Nanotechnology in Textiles. *Textile Research Journal*, 78, 8, 731–739, 2008.

[11] Wong Y. W. H., Yuen C. W. M., Leung M. Y. S., S. Ku K. A., Lam H. L. I. Selected applications of nanotechnology in textiles. *AUTEX Research Journal*, 6, 1, 2006.

[12] Tomsic B., Simoncic B., Orel B., Cerne L., Tavcer P. F., Zorko M., Jerman I., Vilcnik A., Kovac J. Sol–gel coating of cellulose fibres with antimicrobial and repellent properties. *Journal of Sol-Gel Science and Technology*, 47, 44-57, 2008.

[13] Textor T., Mahltig B. A sol–gel based surface treatment for preparation of water repellent antistatic textiles. *Applied Surface Science*, 256, 1668–1674, 2010.

[14] Khatri A., Peerzada M. H., Arsalan F. Improvement in tensile strength of bamboo knitted fabric by sol-gel coating. *Mehran University Research Journal of Engineering and Technology*, accepted for publication, 2013.

Silk Cocoon Structure and Its Protective Roles

Jasjeet Kaur[1], Rangam Rajkhowa[1], Takuya Tsuzuki[1], Keith Millington[2], Xungai Wang[1]
[1]Australian Future Fibres Research & Innovation Centre, Institute for Frontier Materials,
Deakin University, Geelong, VIC 3216, Australia
[2]CSIRO Materials Science and Engineering, PO Box 21, Belmont, VIC 3216, Australia
xungai.wang@deakin.edu.au; jkaur@deakin.edu.au

INTRODUCTION

Silk cocoons contain the silk thread (fibroin), silk gum (sericin) and embedded crystals. The cocoon encases the silkworm during its immobile phase and provides defence against external threats. The aim of the study is to investigate the protective roles of the silk cocoon against bacteria and ultraviolet light. This required understanding of the structural components of the cocoon and further isolating these components. Then the cocoon components were tested individually and in combinations for antibacterial properties and UV-absorption properties.

APPROACH

The cocoon structure was studied layer by layer using scanning electron microscopy. Silk fibre was obtained by degumming the silk cocoons using 2% sodium carbonate plus sodium bicarbonate at 98^{0}C for an hour in a laboratory dyeing machine (Ahiba). Silk gum was obtained from the degumming liquor by dialysing it to remove base using a 3.5 KDa dialysis membrane. The concentration of silk sericin was calculated and it was used in the solution form. Silk cocoon crystals were separated by ultrasonicating the cocoon in water and then evaporating the water to obtain a white residue of crystals at 60^{0}C. All the extracted cocoon components were tested for antibacterial properties and UV absorbance properties. AATCC 100-2004 standard test method was used with slight modification to test the antibacterial activity of cocoon components. The UV absorbance of the cocoon components was calculated from the diffuse reflectance values for solid samples and absorbance values for liquid samples.

RESULTS & DISCUSSION

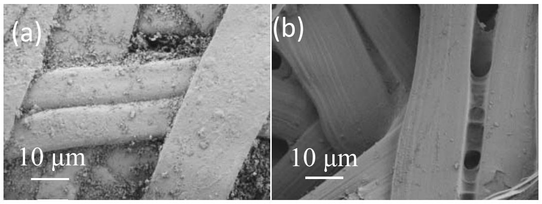

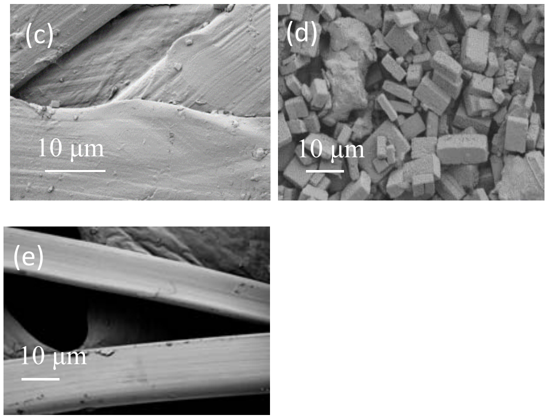

Figure 1: SEM images of (a) outer tasar cocoon layer (b) middle tasar cocoon layer (c) inner tasar cocoon layer, (d) ultrasonicated silk cocoon crystals, and (e) degummed tasar silk fibre

Figure 1 (a-c) shows SEM images of the layer-by-layer cocoon structure. In the outermost layer of the cocoon, a thick layer of sericin on the twin fibres and also a high amount of crystals are evident. In the middle cocoon layer, there is less sericin and fewer crystals than in the outer layer. The innermost layer also contains sericin but less than the outermost layer. The amount of crystals is also least in the innermost layer. Fig 1(d) shows an SEM image of the isolated silk cocoon crystals after ultrasonication. The crystals maintained their original cubic shape even after being exposed to 20 kHz ultrasonication frequency and a high temperature of 75^{0}C. An X-ray diffraction study showed that the separated crystals were composed of calcium oxalate hydrate. Fig. 1(e) shows the SEM image of the degummed fibre. It can be seen that fibres are completely separated from each other after the removal of sericin. After isolation, the cocoon components were tested for their antibacterial and UV-resistance properties.

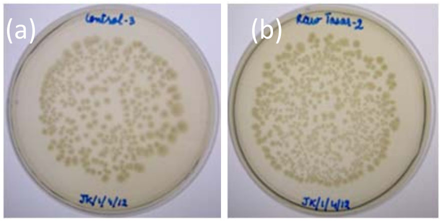

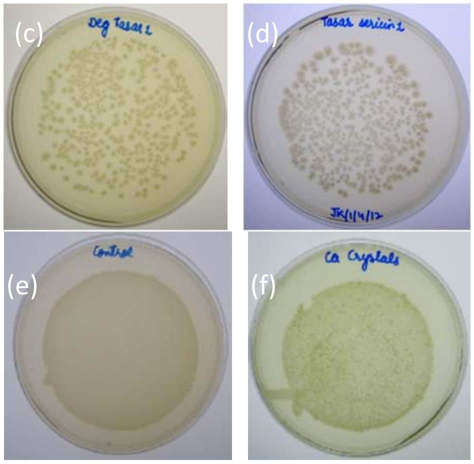

Figure 2: Photographic images showing antibacterial activity of (a) control sample (b) raw cocoon (c) degummed cocoon (d) silk sericin at 10^3 CFU/ml bacterial concentration (e) control sample at 10^8 bacterial conc. (f) silk cocoon crystals at 10^8 bacterial concentration.

Figure 2 (a-d) shows photographic images of the antibacterial activity of the control sample, raw cocoon, degummed cocoon, silk sericin and silk cocoon crystals. It was observed that the number of bacterial colonies in the raw cocoon, degummed cocoon and sericin were similar to that of the control sample. In the images (e-f), the bacterial colonies in the silk cocoon crystals were found similar to the control plate. The results indicate that none of the cocoon components could kill the gram negative bacteria (*E. coli*) partially or completely.

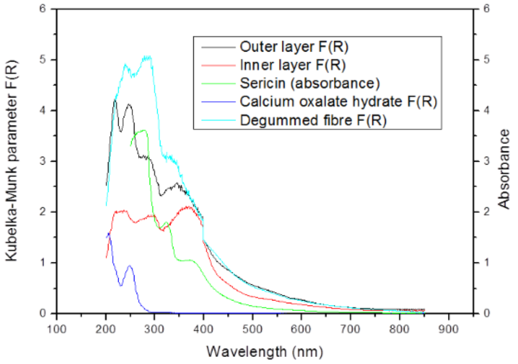

Figure 3: UV absorbance spectra of Tasar cocoon outer side and inner side, Tasar fibre, Tasar sericin and commercial crystals.

Figure 3 shows the UV absorbance spectra of outer and inner side of raw tasar cocoon, degummed tasar silk fibre, tasar sericin and commercial calcium oxalate hydrate powder. It is evident in Figure 3 that commercial calcium oxalate hydrate crystals absorb UV light below 290 nm. Sericin also showed a broad absorption spectrum in the UV range. The spectra of degummed silk showed broad absorption characteristics below 450 nm, indicating that silk protein absorbs UV light.

The outer side of raw tasar cocoon showed UV absorbance peaks at 217 nm, 249 nm, 286 nm and a large peak in the 300-400 nm region. The inner cocoon side showed UV absorbance peaks at 228 nm, 286 nm and a large peak between 300–400 nm. The peak at 249 nm was missing in the inner cocoon region. It is thought that this peak is associated with the presence of the crystals, as the peak intensity is qualitatively in good correlation with the amount of the crystal in the layer: Fig. 1 shows that the amount of the crystals decreases from outer to inner layers, while Fig. 3 shows that the peak at 249 nm weakens from outer to inner layers. Furthermore, the absorbance peaks of commercial calcium oxalate hydrate crystals were found at 210 and 254 nm and the peak at 254 nm could be treated as equivalent to 249 nm.

Therefore it could be concluded that tasar raw silk cocoon absorbs UV radiation in UV-B region (290 – 320 nm) and also in UV-A region (320–400 nm), as it contained fibre and sericin.

CONCLUSIONS

The morphology, antibacterial properties and UV-absorption properties of different cocoon components were studied. It was found that none of the cocoon components had antibacterial activities against gram negative bacteria *E. coli*. Raw tasar cocoon absorbed UV light in both the UV-A and UV-B regions. The optical absorbance in the UV-A region was due to the sericin, whilst the absorbance in the UV-B region was due to the fibre and also sericin.

FUTURE WORK

Our future work will focus on other protective roles of cocoon structures, including looking at the effect of needle penetration on the cocoons. This understanding may help us to design thin, light weight, breathable future garments that serve multiple protective roles.

REFERENCES

1. T. Afrin, T. Tsuzuki, R. K. Kanwar and X. Wang. *Journal of the Textile Institute* 108, 8 (2011).
2. K. R. Millington, *Amino Acids* 43, 1277-1285 (2012).

ACKNOWLEDGMENT

I would like to pay my gratitude to Ms. Tarannum Afrin and Ms. Michelina Del Giudice for their support during my research work.

Wrinkle Resistant Finishing of Cotton Fabric Using HDAS on the Crosslinking Agent

Jianwei Xing, Chengshu Xu, Yan Ren, Wenzhao Shi, Jinshu Liu
Xi’an Polytechnic University, No. 19, Jinhua South Road, Xi’an, Shaanxi, PR China
xjw1123@sina.com

ABSTRACT

The presented investigation is mainly on the development of a new eco-friendly wrinkle resistant cross-linking agent derived from starch. Starch was oxidized to dialdehyde starch (DAS) using periodic acid and the oxidative agent was converted to iodic acid. In the above process the oxidative behavior of periodic acid toward polysaccharides causes the oxidative cleavage of 1,2-glycol structures and so led to the formation of carbonyl groups which can be schematically described in Figure 1.

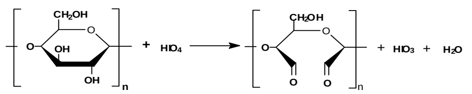

Fig.1. Oxidation of Starch by Periodic Acid to Form Dialdehyde Starch (DAS)

The two carbonyl groups on every repeat unit of DAS resulted from the cleavage of the carbon-carbon bond have the potential to react with the primary hydroxyl groups on cellulose to form the hemiacetals and acetals, which can be shown in Figure 2.

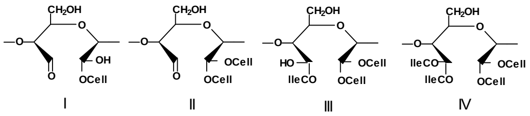

Fig.2. Different Possible Products from the Reaction between DAS and Cellulose

Threfore it was expected that the cross-linking through etherification would impart the crease resistant properties to the cellulose fabrics. According to the well established theory on the wrinkle resistance of cellulose fabrics the covalent cross-linking between the cellulose molecule chains is essential. It is this force that resists the deformation caused by wrinkling or laundering and so the cellulose chains are possible to return to their original position. It is of course of importance that the molecules of any cross-linker should penetrate the fiber to make the cross-linking between cellulose molecule chains possible. DAS, therefore, should be “tailored” to the appropriate sizes and so the degraded segments can reach the amorphous region or penetrate the fiber. In the presented research acid hydrolysis was chosen for the degradation treatment of dialdehyde starch to form the hydrolyzed dialdehyde starch (HDAS). In the DAS acid hydrolysis process the chemical changes as indicated in Fig. 3 would be supposed:

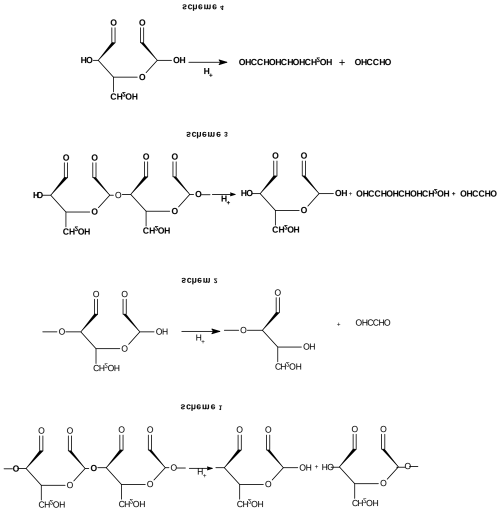

Fig.3. Chemical Changes in DAS Hydrolysis Process

The chain cleavage shown in Scheme 1 can only lead to the decrease in system viscosity. The rupture of C-O bond on the “semi-ring” would be more important in terms of our considerations. It is this bond rupture that results in the formation of glyoxal (Scheme 2-4) and erythrose (Scheme 3-4) and so leads to the increase of carbonyl groups of the system determined. Obviously the product shown in scheme 1 was needed. Hydrazine was employed in the qualitative and quantitative analysis of the carbonyl groups on DAS in the following manner :

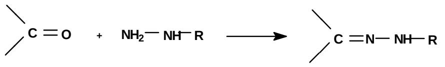

The formed hydrazone, a colored material, was dissolved in an organic solvent and the solution was used for the analysis of HDAS containing carbonyl groups in a spectrophotometric manner. The results confirmed the formation of carbonyl groups on starch molecules by the action of periodi acid. The results also indicated that 2% of hydrochloric acid could only cause the formation of the product shown in scheme 1 and higher concentration of the acid would result in all of products shown in Fig. 3.

As HDAS is a species of aldehyde its activity to cellulose is expected to be somewhat similar to those of glyoxal and other aldehydes. The etherification by means of the formation of hemiacetal and acetal as indicated before is the main force to resist the deformation of the fiber. Taking account of CDRA, CIE whiteness and tensile strength of the treated fabrics a variety of factors such as catalysts, curing temperature, curing time and appropriate additives were evaluated and optimized. In order to suppress the yellow-brown color of the HDAS baths some sodium hypochlorite was added after hydrolysis. A variaty of catalysts were screend and the results showed that the aluminum sulfate behaved much better than the others. The addition of the softener Ultratex FSA, an organopolysiloxane, enhanced the recovery properties to an extraordinary extent. In the process of improving the fabric whiteness zinc chloride was found to suppress the yellowness efficiently and it was used together with sodium sulphate. It should be claimed here that the curing was conducted at 140 ^{o}C for 2 minutes after padding and drying.

The optimized padding bath recipe is shown in Table 1 and the the related results obtained is indicated in Table 2.

Table 1. Recipe of the Optimized Padding Bath

Details	Amounts(%)
HDAS	9.0
$Al_2(SO_4)_3.18H_2O$	1.5
$ZnCl_2$	4.0
Ultratex FSA	2.0

Table 2. Results of the Fabric Treatment

CDRA(^{o})	CIE Whiteness	Tensile Strength (N)
245	55.1	123.60
150*	70.9*	305.50*

*Result for the untreated fabric

According to the results mentioned above the following conclusion are reached:

1. Hydrolyzed dialdehyde starch can be made through the periodic acid oxidation of starch followed by acid hydrolysis.
2. Wrinkle resistant treatment of cotton fabric using HDAS is possible in a conventional pad-dry-cure process.
3. The mixed catalyst system, aluminum sulfate/zinc chloride, was satisfactory in terms of the results based on the recovery properties, the whiteness and the strength retention.
4. The synergistic effect of the softener is significant in the treatment using HDAS as the crosslinker.
5. The yellowness of the fabric occurred during curing still remains a problem for further investigation even though sodium hypochlorite can suppress the fabric discoloration effectively.

Cottonscope Determination of Cotton Fiber Maturity and Fineness Using Small Samples

G.R.S. Naylor[1] and J.E. Rodgers[2]
[1]CSIRO Materials Science and Engineering, Geelong, Vic, Australia; [2]USDA-ARS-SRRC, New Orleans, LA, USA
Geoff.Naylor@csiro.au

INTRODUCTION

Maturity and fiber linear density (sometimes referred to as fineness) are two important fiber quality parameters that have not been routinely measured or used by the industry due to the lack of suitable measurement techniques. Instead the industry has relied on the relatively rapid and inexpensive micronaire measurement. However micronaire is a combination of maturity and linear density and its interpretation can be ambiguous.

Recently a new instrument, The Cottonscope (Cottonscope Ltd, Perth, Australia), has become commercially available and it is provides a user friendly, rapid, accurate and reliable measurements of both fiber maturity and linear density [1-4]. The Cottonscope instrument, illustrated in Figure 1, cleverly incorporates two separate technologies developed by CSIRO (the Siromat™ for measuring fibre maturity and Cottonscan™ for measuring fiber linear density) into one commercial instrument so that the measurements of maturity and fiber linear density are truly independent. Cottonscope is a small and portable instrument weighing approximately six kilograms. It contains a fully automated microscope that captures colour images of cotton snippets in an aqueous suspension. The measurement is completed in approximately 25 seconds, although specimen preparation and weighing currently extends the practical test time to approximately one minute.

Figure 1. Cottonscope system (computer, data collection module unit including. water tank and digital microscope, snippet preparer).

The relatively small sample size used by the Cottonscope (typically 50mg) and the speed of the test makes this technology attractive to cotton breeders[5]. However in some breeding circumstances, even 50mg is not available for testing. This paper explores the opportunity for obtaining useful fiber maturity and linear density information from the Cottonscope when a very limited quantity of material is available.

MATERIALS AND METHODS

The Cottonscope instrument (software version 1.54) was first calibrated using standards and procedures supplied by the manufacturer. Two well blended cotton lint samples representing realistic extremes of fiber maturity and linear density (fineness) values for Upland cottons were chosen for this study. Samples were equilibrated for a minimum of 24 hours in a controlled environment (20°C, 65% RH). A total of 6 replicate Cottonscope measurements (3 loadings/cut samples by 2 replicate measurements per sample) were undertaken for each test.

RESULTS AND DISCUSSION

Cottonscope measurements were undertaken at three different sample mass levels (10mg, 50mg and 90mg). The results are summarized in Figure 2. It can be seen that both the maturity and linear density values show a linear trend with sample mass. The percentage change in values between the largest sample mass (90 mg) and the smallest sample mass (10mg) is approximately 12% for maturity and 42% for linear density. It is interesting that these percentage changes (i.e. the slopes in Figure 2) are similar for both samples, despite their wide difference in fineness and maturity values. This suggests that the ranking of samples for maturity or fineness, which is often more important to a breeder than the absolute values, should be not affected by the sample mass.

As the sample mass decreases, the concentration of fiber snippets in the aqueous suspension in the Cottonscope measurement cell will reduce and so the occurrence of intersecting fibers will also reduce. It is believed that this may be associated with the observed trends apparent in Figure 2.

Note that for the measurements reported in Figure 2, the instrument was calibrated following the normal routine i.e. using a 50mg sample mass for the calibration cotton measurements. A further trial involved recalibrating the instrument at each different sample mass level using that mass for the calibration run. These results are shown in Figure 3. In this case the instrument maturity and linear density values are independent of the sample mass i.e. the recalibration at each mass category adequately compensates for the trend observed in Figure 2, to deliver the correct value, i.e. the same value as in the standard measurement at 50mg.

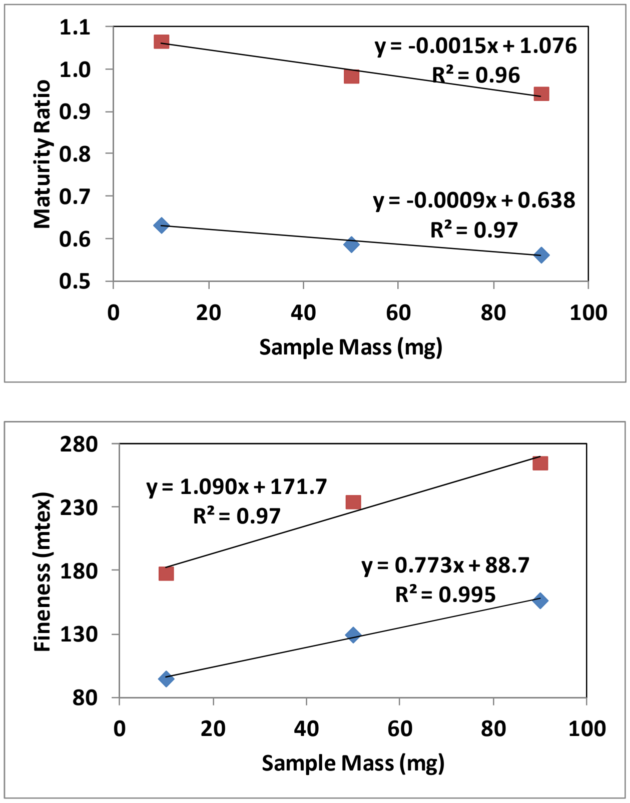

Figure 2. Impact of sample mass on the Cottonscope maturity and linear density (fineness) results.

CONCLUSION

This work demonstrates that the Cottonscope instrument can be usefully used to accurately determine the maturity and linear density (fineness) of cotton fiber samples with sample sizes as small as 10mg.

KEYWORDS

Cotton, fiber, maturity, fineness, linear density, measurement

ACKNOWLEDGMENT

The authors wish to acknowledge Ms. Jeannine Moraitis for her outstanding work in undertaking the experimental measurements.

DISCLAIMER

The use of a company or product name is solely for the purpose of providing specific information and does not imply approval or recommendation by the United States Department of Agriculture to the exclusion of others.

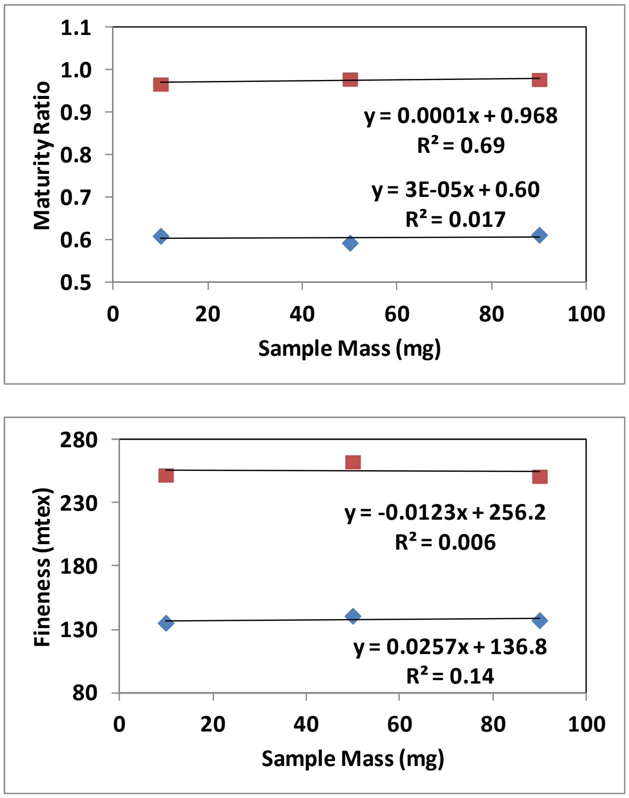

Figure 3. Re-evaluation of the impact of sample mass on the Cottonscope maturity and linear density (fineness) results, after recalibration of the instrument at each sample mass category.

REFERENCES

[1] Naylor G.R.S., Gordon S.G., Hwang H.D., Brims M.A. Cottonscope–Rapid, independent and simultaneous measurement of both cotton fiber linear density (fineness) and maturity. In: *Proc. Beltwide Cotton Conferences*, Atlanta, GA, 2011, pp. 1278-1281.

[2] Gordon S.G. and Naylor G.R.S. Cottonscope: A new instrument for maturity and fineness measurements. (A) Instrument design. In: *Proceedings of the 31st International Cotton Conference*, Bremen, Germany, 2012, pp. 133–142.

[3] Rodgers J. and Thibodeaux D. Cottonscope: A new instrument for maturity and fineness measurements. (B) Experimental results and experiences. In: *Proceedings of the 31st International Cotton Conference*, 2012, Bremen, Germany, 2012, pp. 143–153.

[4] Rodgers J., Delhom C., Fortier C., et al. Rapid measurement of cotton fiber maturity and fineness by image analysis microscopy using the Cottonscope. *Text Res J* 2012; 82: pp. 259–271.

[5] Rodgers J., Delhom C., Hinchcliffe D., et al. A rapid measurement for cotton breeders of maturity and fineness from developing and mature fibers. *Text Res J* 2013; (in press).

Ionic Liquids: Solvents for Protein Polymer Processing

Nolene Byrne and Xungai Wang
Institute for Frontier Materials, Deakin University, Pigdons Road, Waurn Ponds, Victoria 3216, Australia
nolene.byrne@deakin.edu.au

STATEMENT OF PURPOSE

In this abstract, we report on the use of ionic liquids as novel solvents in the processing of protein polymers. We show how ionic liquids (ILs) can be used to dissolve and coagulate silk. We have selected silk as our protein polymer and show how the properties of regenerated silk fibroin (RSF) can be tuned by careful selection of the coagulating ionic liquid solvent.

INTRODUCTION

The processing of protein polymers such as wool and silk remains a challenge due to their poor solubility. While silk is a very attractive material for biomedical and biotechnological applications[1] the regeneration of silk into different formats is a time and energy intensive process. Generally, the processing of silk involves boiling the silk at alkaline pH to remove the sericin. The silk is then dissolved in a solution containing a high concentration of a metal salt, often LiBr. Dialysis is required to remove the salt, finally the amorphous silk is added to either a fluorinated solvent or an acid from which it can then be regenerated into different formats.

A major limitation in the dissolution and regeneration process is that often regenerated silk fibroin (RSF) has poorer material properties when compared with native silk. The coagulation of the RSF is in part responsible for the poorer material properties, and can be greatly impacted by the choice of coagulating solvent.

Recently the use of ionic liquids for biopolymer dissolution has been shown to reduce the total number of dissolution steps as silk cocoons can be directly dissolved. Ionic liquids, often termed designer solvents, are novel solvents, which find application in a diverse range of fields. Ionic liquids consist solely of cations and anions and as such there is a vast number of possible combinations.

In this talk, we show how ionic liquids can be used to both dissolve and regenerate silk. The properties of the regenerated silk can be modified by ionic liquid selection[2].

APPROACH

Silk was dissolved using either traditional methods mentioned above or by directly dissolving the silk cocoons into the ionic liquid 1-butyl-3-methylimidazolium acetate at 100 ° C for several hours.

The silk was regenerated using various protic ionic liquids (pILs) as the coagulating solvent. The pILs investigated were triethylammonium phosphate ($TeaH_2PO_4$), triethylammonium lactate, (TeaLa), triethylammonium triflate, (TeaTf), and triethylammonium mesylate, (TeaMs).

The regenerated silk fibroin was characterized using Fourier transform infrared (FTIR), scanning electron microscope (SEM), differential scanning calorimetry (DSC) and Thermogravimteric analysis (TGA).

RESULTS AND DISCUSSION

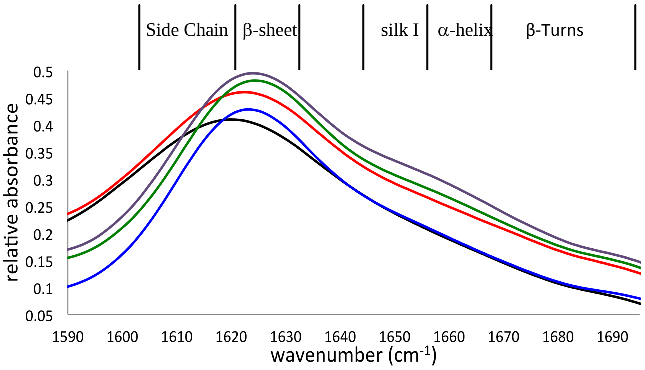

FIGURE 1: FTIR spectra showing the amide I region of the RSF as a function of pIL black native semi domestic fiber, green 80wt%TeaMs, purple 80wt%TeaTf, red 80wt%TeaLa, and blue 80wt%TeaHP

Figure 1 shows the FTIR spectrum of the amide I region of the RSF using different pIL solutions. The amide I region identifies different secondary structures of the silk. When $TeaH_2PO_4$ was used as the coagulation solvent the silk foam shows no α-helix content, which is very similar to native silk fiber. Whereas, when TeaMs was used as the coagulation solvent the structure of the silk foam contains 45% α-helix. The percentage of helical content was shown to be highest in foams coagulated using TeaMs.

Figure 2 shows SEM images of the silk regnerated foams using the different coagulating pIL solutions. Again, the choice of pIL has a considerable impact on the morphology of the silk foams. A porous structure has formed when TeaMs (figure 2a) was used as the coagulation solvent, whereas TeaLA resulted in small spheres. The differences observed in morphology are likely due to a combination of pIL selection and diffusion effects.

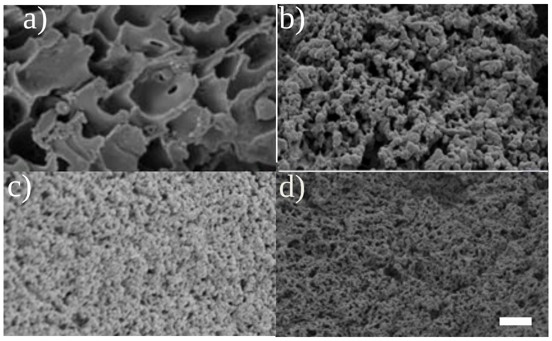

FIGURE 2: SEM images of RSF where the coagulation solvent is (a) 80wt%TeaMs, (b) 80wt%TeaTf, (c) 80wt%TMGLa and (d) 80wt%TeaHP. Scale 10um

CONCLUSION

The use of pILs as the coagulation solvent for silk processing is a novel approach in developing silk scaffolds with tuneable properties. We demonstrated that the choice of pIL can directly impact on both the structure and morphology of the silk foams. The regeneration of silk with highly tuneable properties is a basic requirment if silk, as a material, is to be used in the areas of bio nanotechnology and bio engineering applications. The use of pILs opens up this possibility.

FUTURE WORK

Further studies investigating the structure of the RSF using different pILs and processing conditions are currently underway.

REFERENCES

1. F. Omenetto, D. Kaplan, *Science* 2010, 329, 528.
2. N. Goujon, X. Wang, R. Rajkowa, N. Byrne, *Chemical Communications* 2012. 48, 1278-1280.

KEYWORDS: ionic liquids, regenerated silk fibroin, green processing

Eri Silk: Cocoon, Fibre, and Proteins

Rangam Rajkhowa[1], Ravindeer Rawat[2], Suradip Das[2], Jasjeet Kaur[1], Ben J Allardyce[1]
Utpal Bora[2], Xungai Wang[1]
[1]Australian Future Fibres Research and Innovation Centre, Deakin University, Australia
[2]Department of Biotechnology, Indian Institute of Technology, Guwahati, India
rangam@deakin.edu.au; ubora@iitg.ernet.in

INTRODUCTION

Eri is a commercial silk spun by fully domesticated silkworms *Philosamia Cynthia Ricini*. Widely available host plant (*Ricinus communis*), higher disease resistance and better yield compared to other silkworm silks make eri a highly promising material for textile and biomaterial products. Despite increasing production in a number of countries in recent years, eri silk still remains relatively unknown in the silk industry. Only very limited information is available on eri cocoon structure, fibre properties and its fibre forming protein. This work presents part of our current research in characterizing eri silk and shows that it is distinctly different from other silk species, particularly the popular mulberry silk, in many aspects.

APPROACH

Silk cocoons were harvested at various time points during the cocoon formation process by allowing the silkworm to make the cocoon for a certain period. Cocoon spinning behaviour was observed and early, middle and final part of the cocoons were analysed by scanning electron microscopy. Cocoons were degummed at 98°C using 1% Na_2CO_3, 1% $NaHCO_3$ using a material (cocoon) to liquid (base) ratio of 1:100 to obtain sericin free fibre for further analysis. To characterize molecular weight and secondary structure, silk proteins were isolated from glands of matured 5th instar larva. Protein solutions were also prepared from fibres by dissolving in chaotropic salts followed by dialysis against water. SDS-PAGE was performed on silk solutions to determine molecular weight. Solutions from glands and fibres were subsequently freeze dried to get amorphous silk materials for further characterization. To analyze thermal properties and understand their secondary structure, various silk materials were tested using Instron, DSC and FTIR. Fibre cross section and longitudinal sections were examined. Optical and hydrophilic properties of cast films were measured using visible spectrophotometer and contact angle instruments respectively.

RESULTS AND DISCUSSION

Unlike other type of silk varieties, an eri silkworm does not form a completely closed cocoon and one end remains open. Moreover, a large proportion of cocoon mass is in the form of floss (entangled loose mass) and only the inner portion forms a compact cocoon. Therefore, eri cocoons are not reeled and are only spun to produce yarns.

Figure 1 Some eco races of eri silk worms

Figure 2 Outer, middle and last parts of an eri silk cocoon

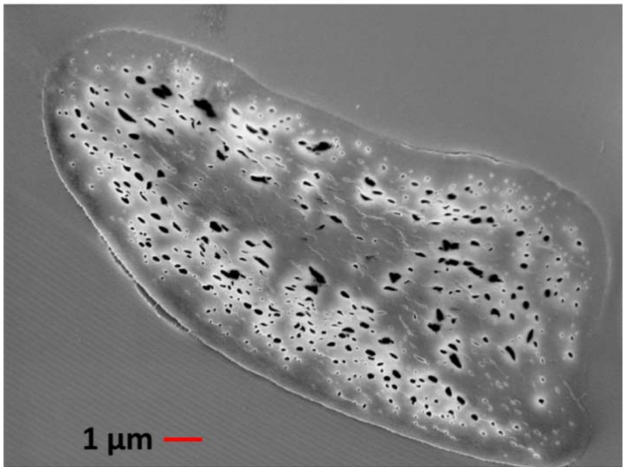

Figure 3 Cross section of eri silk fibre

Unlike mulberry silk which has a triangular cross section, in eri silk, there is a large difference between the major and the minor axis (Fig. 3). Moreover there are a large number of micro pores in eri silk fibre which is a distinct feature in some other non-mulberry silk varieties[1].

Silk fibre forming protein fibroin and gummy protein sericin were derived from middle part of the silk gland. SDS-PAGE of the proteins shows clear bands at around 160 kD and 80 kD, which are likely to be bands from fibroin and sericin respectively.

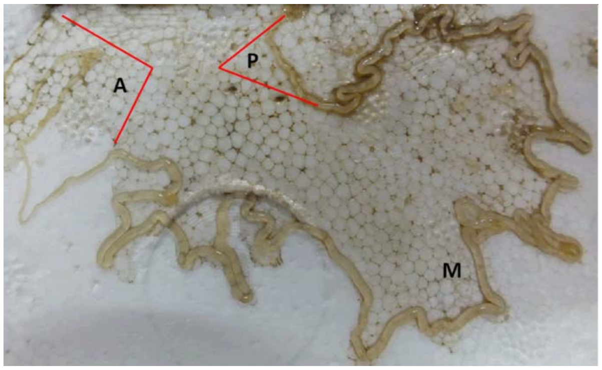

Figure 4 Anterior (A), Middle (M) and Posterior (P) parts of silk gland

On the other hand, fibroin when derived from degummed silk fibre shows a highly smeared pattern in SDS-PAGE. The extent of smearing depends on silk degumming process. In control degumming when only 1% $NaHCO_3$ was used and degumming was performed for 3 times, each of 30 minutes duration, SDS-PAGE showed a less smeared band (lane 1, b in Fig. 5) compared to normal degumming of 2 hrs with Na_2CO_3 and $NaHCO_3$ (lane 2). Thus degumming is responsible for severe degradation of silk protein and developing a standard degumming process is required for maintaining the desired properties of eri silk products.

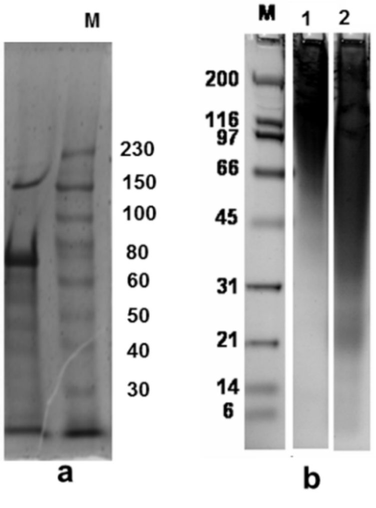

Figure 5 SDS-PAGE of Eri silk (a: from gland; b: from degummed fibre)

Eri fibre has two degradation temperatures. First degradation occurs at 283^0C and the second degradation at 354^0C. This is much higher than the degradation temperature of mulberry silk which degrades at about 300^0C [2]. Glass transition temperature (T_g) was evident at around 222^0C which was confirmed by temperature modulated DSC (Fig.6). Regenerated eri films prepared from silk solution showed T_g between 190^0C-200^0C.

Films prepared from eri silk solution are highly transparent with total transmittance of more than 90% and diffuse transmittance of around 10%. Eri films are also highly hydrophobic. Static contact angle in water of an ethanol stabilized film is about 90^0 compared to about 75^0 found in similarly prepared mulberry silk films.

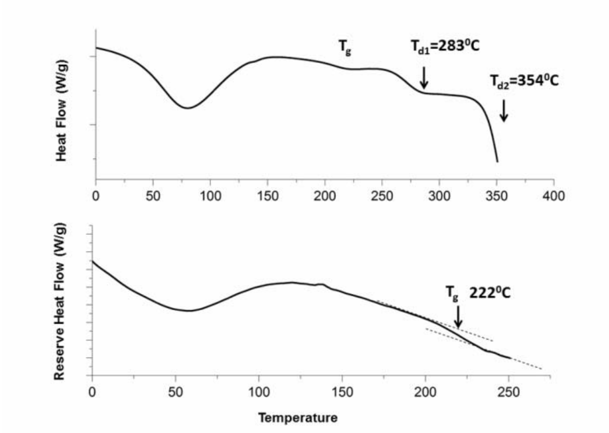

Figure 6 Thermal behaviour of eri silk

CONCLUSIONS

Eri silk is distinctly different than commonly known mulberry silk in many respects. Eri cocoons are open mouthed and loosely structured. Eri silk fibre contains microspores and the fibre cross section has a high major to minor axis ratio. The molecular weight of fibre forming protein is about 160 kD against 390 kD of mulberry silk. Its thermal degradation and glass transition temperatures are higher than that of mulberry silk. Eri silk is more hydrophobic than mulberry silk and films prepared from eri silk are highly transparent.

FUTURE WORK

Future work involves optimization of extraction methods of eri silk fibroin and sericin from silkworm’s gland and cocoons and their further characterization. Biomaterials of eri silk will be developed for a range of applications utilizing its specific properties. The cocoon structure will also be studied and relationship between silk spinning, fibre dimensions and cocoon structure will be examined.

REFERENCES

1. Sen, K. and M. Babu K, Journal of Applied Polymer Science, 2004. 92(2): p. 1080-1097.
2. Rajkhowa, R., et al., Biomacromolecules, 2012. 13(8): p. 2503-2512.

ACKNOWLEDGMENT

We acknowledge the support from Australian Research Council, Australian Academy of Science and Department of Biotechnology, Government of India.

An Assessment of Alternative Cotton Fiber Quality Attributes and Their Influence on Yarn Strength

Robert L. Long[1], Michael P. Bange[2], Christopher D. Delhom[3], Jeffrey S. Church[1], Greg A. Constable[2]

[1]CSIRO Materials Science and Engineering, P.O. Box 21, Belmont, VIC, 3216, Australia
[2]CSIRO Plant Industry, Locked Bag 59, Narrabri, NSW, 2390, [3]USDA-ARS Southern Regional Research Center, 1100 Robert E. Lee Blvd., New Orleans, LA, 70124, United States

robert.long@csiro.au

INTRODUCTION

Knowing the yarn strength performance potential of cotton fiber is advantageous to spinners during mill preparation, and to researchers developing new genotypes and management strategies to produce better fiber. Both micronaire, which is a collective measure of fiber fineness and maturity, and bundle tensile properties, are important standard High Volume Instrument (HVI) fiber quality attributes. Two field experiments over two seasons were conducted to assess the fiber and yarn performance of Australian cotton genotypes. The aim was to assess and compare alternative measures for micronaire, and to compare bundle and single fiber tensile measurements, and assess the relative yarn strength predictive performance of these attributes. Specific fiber measurement comparisons were for linear density [double compression Fineness Maturity Tester (FMT) and gravimetric), maturity ratio (FMT, polarized light, calculated and cross sectional), and tensile properties (HVI bundle and Favimat Robot single fiber).

MATERIALS AND METHODS

Two field experiments were conducted over the 2007 and 2008 harvest seasons to assess the fiber and yarn performance of some Australian cotton genotypes. Genotypes were propagated at the Australian Cotton Research Institute as a randomized complete block design with two replications.

RESULTS AND DISCUSSION

Multiple linear regression models for yarn strength which included yarn manufacturing variables and standard HVI fiber quality parameters performed well but models performed better when alternatives to micronaire were used; e.g. using gravimetric linear density or using laser photometric determined ribbon width (Figure 1). Yarn strength models were also better when single fiber tensile properties were substituted for bundle tensile properties. The substitution of alternative fineness variables for micronaire or single fiber strength for bundle strength in a simple fiber quality index also improved the prediction of yarn strength.

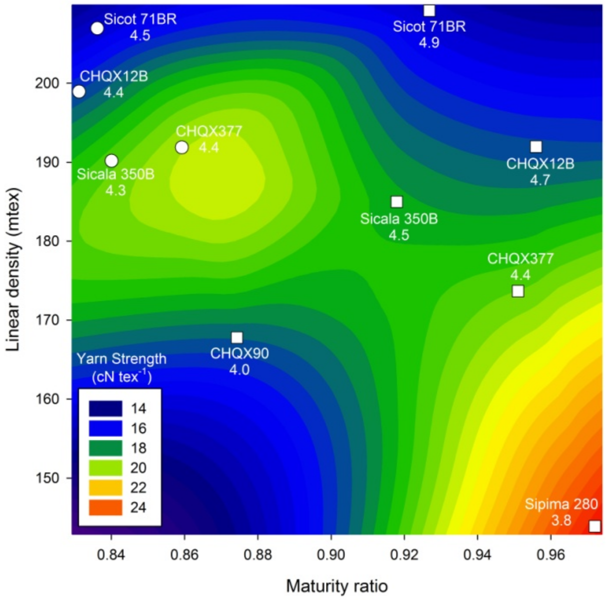

Figure 1. Yarn strength, fiber micronaire, fiber maturity and fiber linear density for some Australian cotton genotypes**.**

CONCLUSION

The work demonstrated that using alternative measures for micronaire, and single fiber tensile properties in replacement for bundle tensile properties, improved the prediction of yarn strength.

KEYWORDS

Cotton, fiber, maturity, fineness, yarn strength.

Photostability of Chemically Modified Silk

Weiguo Chen[1,3], Zongqian Wang[1], Donghui Pan[1], Zhihua Cui[1], Keith Millington[2], Xungai Wang[3]

[1]Engineering Research Center for Eco-Dyeing & Finishing of Textiles, Ministry of Education, Zhejiang Sci-Tech University, Hangzhou 310018, China; [2]Materials Science and Engineering, CSIRO, Geelong 3216, Australia
[3]Institute for Frontier Materials, Deakin University, Geelong 3216, Australia

zhhcui@zstu.edu.cn; wgchen62@126.com

INTRODUCTION

The UV radiation present in sunlight can cause yellowing of silk and wool, tendering, and a decrease in the content of certain amino acids [1]. In early research, certain amino acid residues present in wool keratin and silk fibroin, namely phenylalanine (Phe), tyrosine (Tyr), tryptophan (Trp) and Histidine (His), were proposed as the most likely candidates for producing yellow chromophores [2]. A coupling reaction on the Tyr side group in proteins occurs in the presence of a diazonium salt, as shown Figure 1.

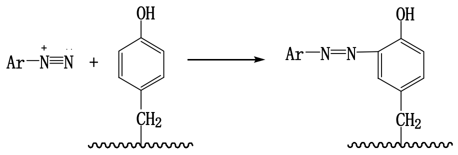

Figure 1. Chemical modification on silk

APPROACH

Modification of silk with o-nitroaniline: A stable solution of the diazonium salt of *o*-nitroaniline was prepared by reaction of *o*-nitroaniline with HCl and then $NaNO_2$ at 0–5℃. Silk fabric was immersed into aqueous NaOH solution (6 g/L) and rapidly padded, then immersed into a solution of the diazonium salt. The treated silk fabric was washed with water several times. A Thermo Nicolet FT-RAMAN 960 Spectrometer was used for characterization. UV-visible transmittance of silk fabric was measured with Lambda 900 spectrophotometer (Perkin-Elmer). The Δ(K/S) of fabrics was measured with a DataColor SF600- PLUS before and after exposing in XENOTEST 150S+. The fabric strength was measured before and after exposing to UVA light of 0.68w/m^2 for 24 hours. Photo induced chemiluminescence (PICL) was measured using a Lumipol 3 instrument previously described [3].

RESULTS AND DISCUSSION

Raman analysis of modified silk fabric

The Raman spectra of modified silk and control fabric are shown in Figure 2.

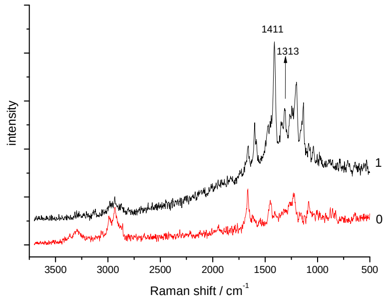

Figure 2. Raman analysis of silk fabric
(0 Original silk; 1 Modified silk)

The spectrum of modified silk shows a peak at 1411 cm^{-1} due to the azo group (-N=N-), demonstrating the successful modification of silk protein. The peak at 1313 cm^{-1} on modified silk is due to the stretching vibration of $-NO_2$ from *o*-nitroaniline.

The UV transmittance of silk fabric

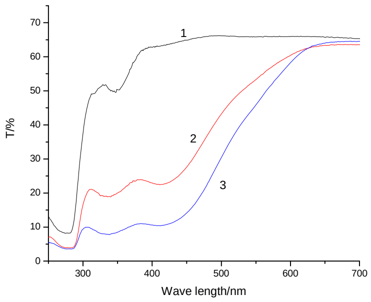

Figure 3. UV-visible transmittance of silk fabric
1 Original, 2 Modified (K/S 7.67), 3 Modified (K/S 14.50)

Figure 3 clearly shows that the transmittance of silk fabric in the 300–500 nm region was greatly reduced after modification.

The Δ(K/S) and strength of silk exposed to light

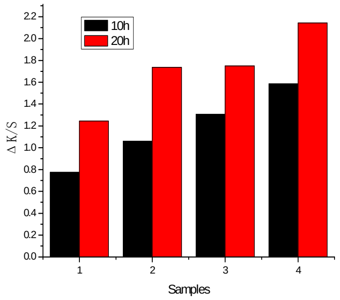

Figure 4 ΔK/S of silk fabrics

1-3 Modified and with K/S 3.24, 7.67, 14.50, respectively; 4 Dyed with acidic dye with K/S 13.13

With the increase of exposing time and the increase of K/S, the ΔK/S before and after exposing increased. However, the ΔK/S on modified silk is lower than that on the silk dyed with acidic dyes. The strength of modified silk fabric with K/S 14.50 was greater than that of original silk after exposure to UV light.

PICL analysis

Figure 5 compares the PICL decay profiles for silk before and after modification.

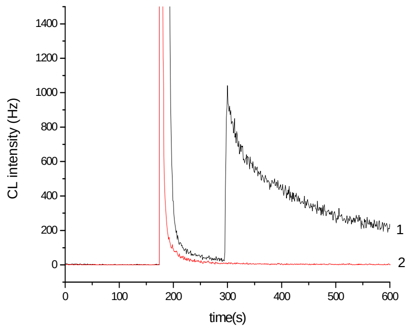

Figure 5 PICL of silk
1-Original, 2-Modified

Before modification, significant numbers of free radicals were formed when oxygen was admitted to the sample, as shown by the large PICL emission. After treatment, no PICL was emitted, suggesting that no free radicals were formed in the modified silk after exposure to UVA (320–400 nm) under the same conditions.

CONCLUSIONS

The modification of the tyrosine residues of silk with the diazonium salt of *o*-nitroaniline eliminates free radical formation following irradiation with UVA light. This suggests that diazotization could be used as a photoprotective treatment for silk.

REFERENCES

[1] Millington KR. The photoyellowing of wool. Part 2: Photoyellowing mechanisms and methods of prevention. *Color Technol* 2006; 122: 301-316.

[2] Asquith RS, Brooke KE. Yellowing of Wool Keratin on Exposure to Ultraviolet Radiation, *J. Soc. Dyers Color*. 1968, 84(3): 159–165.

[3] Millington KR, et al. Photo-induced chemiluminescence from fibrous proteins and polymers. *Polym Degrad Stab* 2008; 93: 640-64.

Assessing Yarns to Predict the Comfort Properties of Fabrics

Maryam Naebe[1], Bruce A. McGregor[1], David Tester[2] and Xungai Wang[1]
CRC for Sheep Industry Innovation and the University of New England, Armidale, NSW 2351
[1]Institute for Frontier Materials, Deakin University, Geelong, Australia
[2]CRC for Sheep Industry Innovation Ltd., CJ Hawkins Homestead, University of New England, Armidale, Australia
maryam.naebe@deakin.edu.au

OBJECTIVE

The feasibility of assessing yarns with the Wool ComfortMeter (WCM) to predict the comfort properties of the corresponding single jersey-knitted fabrics was examined. The relationship between WCM readings of wool knitting yarns and direction and frequency of yarns wound onto a test template were investigated. Using a notched template, yarn winding frequencies of 1, 3, 6, 12, 25 and 50 parallel yarns in two horizontal and vertical directions were tested on the WCM. Vertical windings produced significantly higher readings than horizontal windings. The best predictor of fabric WCM values was using 25 parallel yarns in horizontal direction.

INTRODUCTION

A faster and potentially cheaper method of evaluating the properties of knitted fabrics would be to assess the yarns prior to knitting thus avoiding manufacturing costs and delays.

The WCM instrument was developed as a fast and objective method of predicting the wearer comfort assessment of wool knitwear to replace subjective, lengthy and expensive wearer trials[1, 2].

The instrument uses a measurement wire mounted in a recording head, which scans the surface of the fabric interacting with fibres protruding from the fabric surface. The WCM reading provides a value that is related to the number and density of coarse fibres protruding from the fabric surface[1, 3]. The readings of the WCM have been shown to be strongly correlated with average prickle ratings assigned by wearers of the garments[1] where the changes in comfort affected by different treatments can be detected by the WCM[4].

The objective of this paper is to investigate a reliable predictor of knitted fabric comfort prior to knitting by testing yarns using WCM assessment.

APPROACH

To cover a large range of WCM values, seven pure wool (w) yarns and two 80/20 wool/nylon blends (w/n) with a mean fibre diameter (MFD) range between 16.5 and 24.9 µm were selected. Details are summarized in Table I. Single jersey fabrics were knitted with similar cover factor (CF), knitting gauge, and yarn plies[5].

Yarn testing templates were prepared from acrylic boards to enable the preparation of up to 50 windings of a yarn per test. On each side of the template and located centrally, 50 grooves were incised. For each yarn, six different winding frequencies were tested: 50, 25, 12, 6, 3 and 1per test. For each winding frequency, three separate templates were prepared and measured on the WCM device in a random order[5]. To investigate the effect of vertical direction, only 3 yarns with MFD of 18.5, 19.3 and 21.9 µm were prepared and tested. Yarn and corresponding fabric comfort evaluation was carried out at standard condition whereby each sample was subjected to 10 passes of the measurement device[6].

Table I. Specifications of yarns and their corresponding single jersey knitted fabrics[5]

Yarn ID	Fibre type	MFD (µm)	Fabric ID	Yarn count/ Nm	Gauge	CF
1	w/n	24.9	F1	1/23	14	1.32
2	w/n	22.6	F2	1/23	14	1.20
3	w	17.6	F3	1/40	24	1.28
4	w	18.5	F4	1/40	24	1.20
5	w	22.0	F5	1/40	24	1.20
6	w	19.3	F6	1/40	24	1.20
7	w	21.9	F7	1/40	24	1.28
8	w	24.3	F8	1/40	24	1.20
9	w	16.5	F9	2/72	24	1.28

RESULTS AND DISCUSSION

Effect of direction of winding

Analysis of variance (ANOVA) showed (Table II) a significant effect of yarn winding direction with vertical windings producing higher readings than horizontal windings ($P < 0.001$).

Table II. Effect of yarn winding direction on Wool ComfortMeter values

Winding direction	WCM	s.e.d.[a]	s.d.[b]	s.e.d.[c]
Vertical	842.5	70.28	148.6	18.22
Horizontal	408.7		99.3	

[a] standard error of difference between mean WCM values in different direction
[b] standard deviation
[c] standard error of difference between mean s.d. in different direction

It appeared that there was a mechanical interaction between the testing head and the space between the yarns, or perhaps the sides of the yarns, such that vertical readings were about twice that of horizontal readings. Since testing of yarns presented in the vertical direction is not recommended, further investigation was carried out with the horizontal direction and the corresponding fabrics.

Effect of yarn winding frequency for horizontally wound yarns

The relationship between WCM value, over the range of values observed, and different yarn winding frequencies or yarns and their corresponding fabrics are shown in Figure 1. The logarithmic trend lines fitted to the WCM value vs. yarn winding frequency show the rapid increase in WCM value up to a winding frequency of 25. The WCM values increase proportionally less or remain almost constant between 25 and 50 yarn winding frequency.

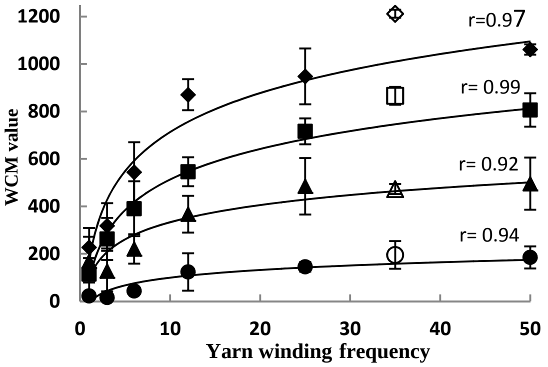

Figure 1. Wool ComfortMeter (WCM) value of selected yarns at different yarn winding frequencies and their corresponding fabrics. Error bars indicate standard deviation. The best line fitted (log) and the corresponding correlation coefficient (r) are shown. Symbols: ♦, yarn 8; ■, yarn 7; ▲, yarn 6; ●, yarn 9. Open symbols referred to the corresponding fabrics.

Yarn winding frequency significantly affected the WCM values ($P = 8.5\times 10^{-17}$, s.e.d.= 1.69, least significant differences; L.S.D.5%=3.35; Table III). There was no difference in WCM values between winding frequencies of 50 and 25, but the values at winding frequencies of 50 and 12 were different These results suggest that a yarn winding frequency of 12 is insufficient to accurately reflect the true WCM values of a yarn but a winding frequency of 50 is probably too many. Therefore, if yarns are to be assessed on the WCM then the 25 windings may provide a compromise between detecting differences between yarns and reducing the time involved in preparing multiple samples with 50 windings[5, 7].

Table III. Effect of yarn winding frequency on Wool ComfortMeter values (WCM). Statistical significance determined after square root transformation. Values with different superscripts differ at $P = 0.05$.

Winding frequency	1	3	6	12	25	50
WCM	141^{d}	185^{d}	333^{c}	480^{b}	$569^{a,b}$	669^{a}

Models for predicting fabric WCM values

To estimate which yarn winding frequency can be used to predict the fabric WCM value, a regression model was applied to fabrics of similar attributes. This regression included all attributes of yarn and fabric along with the comfort value of six different yarn winding frequencies as independent variables. The final general multiple linear model included the WCM value for 25 windings (Yarn 25 WCM) and MFD, both attributes of the yarn (Table IV). No other physical attributes of fabric or yarn was significant in predicting yarn assessed WCM values. This model indicates that a yarn winding frequency of 25 provided a better prediction of fabric WCM values than yarn winding frequencies of 50, 12, 6, 3 or 1. The terms Yarn 25 WCM and its square explained 88.5% of the variation in fabric WCM values.

Table IV. A list of the statistical significance of included terms in the final model for fabric WCM values

Adjustment to final model	β	s.e.	P-value
$(\text{Yarn 25 WCM})^2$	0.0012	0.00029	< 0.001
MFD	84.0	23.6	0.002
Yarn 25 WCM	-0.94	0.459	0.042

CONCLUSIONS

The testing method of winding yarn around a notched template with a yarn frequency of 25 in horizontal direction provided the best precision for the prediction of fabric WCM evaluation. This indicates that evaluation at the yarn stage would be a reliable predictor of knitted fabric comfort, and thus yarn testing would avoid the time and expense of fabric construction.

ACKNOWLEDGMENT

This work was funded by The Cooperative Research Centre for Sheep Industry Innovation Ltd.

REFERENCES

1. Ramsay, et al., *Textile Res. J.*, 82(5), 513-520, 2012.
2. Tester, Anim. Prod Sci., 50, 1077-1081, 2010.
3. McGregor and Naebe, *J. Textile Inst.* in press, 2013.
4. Naebe, et al., *J. Textile Inst.*, published online 7 Jan 2013.
5. Naebe, et al., *J. Textile Inst.*, published online Feb 2013.
6. Naebe, et al., *Textile Res. J.,* 83(1), 83-89, 2013

Naebe, et al., *J. Textile Inst.*, published online 9 Jan 2013.

Sock Fabrics: Measuring the Coefficient of Static and Dynamic Friction to Prevent Blisters

Rebecca Van Amber[1], Raechel Laing[1], Cheryl Wilson[1], Bronwyn Lowe[1], Brian Niven[2]
[1]University of Otago, Department of Applied Sciences, Dunedin, New Zealand
[2]University of Otago, Department of Mathematics and Statistics, Dunedin, New Zealand
raechel.laing@otago.ac.nz; vanre228@student.otago.ac.nz

OBJECTIVE

The objectives of the study were to develop a laboratory test method to measure friction between a simulated 'skin' and sock fabrics that best reflects conditions during use, and to detect differences in frictional forces between simulated skin and fabric, which can be attributed to key controllable variables (fibre type, yarn structure and fabric structure).

INTRODUCTION

Friction blisters have long beleaguered humans, as they are painful, affect locomotion and can provide an opening for infection. Previous studies of socks and sock fabrics have often sought to link fibre type to a lower incidence of blisters. For example, acrylic socks have reported results of fewer and smaller blisters than cotton during wear (Herring and Richie, 1990). Approaches to measure friction or blister incidence differ, sometimes using laboratory methods, but often using human wear trials. To date, no study of sock fabrics has matched experimental fabrics, so the effects of fibre, yarn structure and fabric structure on the frictional behaviour of fabrics have not been clarified.

METHOD

There is no Standard method for measuring friction between fabrics and other surfaces, although several methods have been developed. One common method involves attaching platform to the lower jaw of a tensile tester in order to pull a sled across (the horizontal platform method) Zurek, Jankoiak, and Frydrych (1985); Carr, Posey and Tincher (1988); Ajayi (1992); Jeddi, Shams, Nosraty, and Sarsharzadeh (2003), Hermann, Ramkumar, Seshaiyer and Parameswaran (2004); and Ramkumar, Umrani, Shelly, Tock, Parameswaran, and Smith (2004). A modified version of this method was used in the present work. A small perspex sled (153.52 g) with a contact area of 60 x 50 mm and curved front edge was loaded with 2.25 kg to create pressure equivalent to that applied to a sock when worn by a 70 kg adult (4.01 N/cm^2), and separately 1.25 kg to approximate a youth (38.6 kg). A 60 x 50 mm piece of Lorica Soft® (simulated leather composed of 49% polyurethane, 49% polyamide microfibre, 2% other) was cut lengthwise and attached using double-sided tape to the lower surface of the sled. A new piece of Lorica Soft® was used for each test. The sock fabric specimen (100 x 300 mm, n=5) was attached to the wooden platform (550 x 200 mm) technical rear side up. A 15% pre-extension was applied to each specimen. Once extended, a single piece of double-sided adhesive (100 x 300 mm) was applied to the technical face of the specimen, and the specimen placed adhesive side down on the centre of the platform. The platform was attached horizontally to the lower jaw of a tensile tester fitted with a 100 N load cell. The sled was drawn across the fabric specimen at 250 mm/min using a twisted Kevlar cord attached to the upper jaw. Data collection began after reaching a pre-load of 1N.

A 3 x 3 x 3 factorial experimental design was used [27 experimental fabrics, all combinations of fibre, yarn structure and fabric structure (Table I)].

Table I
Variables and their descriptions

fibre	fine wool, 19 µm
	mid-micron wool, 26 µm
	acrylic, 19 µm
yarn	two-fold conventional, twist 2700
	two-fold low twist, twist 2100
	single conventional, twist 2700
structure	terry
	half-terry*
	single jersey

* Loops on every second course only

The first peak (maximum) was taken as the static friction. The means of peaks and troughs from 5-10 s after the maximum peak were averaged and taken as the dynamic friction.

RESULTS

The coefficient of static and dynamic friction between sock fabrics and synthetic skin were calculated according to:

$$\frac{F_f}{F_N} = \mu$$

Where:
F_f is the force of friction in N
µ is the coefficient of friction
F_N is the normal force in N

Static friction

Weight ($F_{2,216}=298.52$, $p \leq 0.001$), fabric structure ($F_{2,216}=52.09$, $p \leq 0.001$), yarn structure ($F_{2,216}=38.48$, $p \leq 0.001$), and fibre type ($F_{2,216}=16.02$, $p \leq 0.001$) all affected the coefficient of static friction between dry fabrics and the synthetic skin. Fabrics manufactured from acrylic fibres had the highest coefficient of static friction. In these fabric structures, acrylic fibres appear to behave differently than wool fibres when combined with the half-terry structure, resulting in a higher coefficient of static friction ($F_{4,216}=8.68$, $p \leq 0.001$). Higher loads resulted in a higher coefficient of friction regardless of fibre type. Thus, regardless of the weight of the wearer, whether adult or youth, fabric structure, yarn and fibre had a similar effect on frictional characteristics.

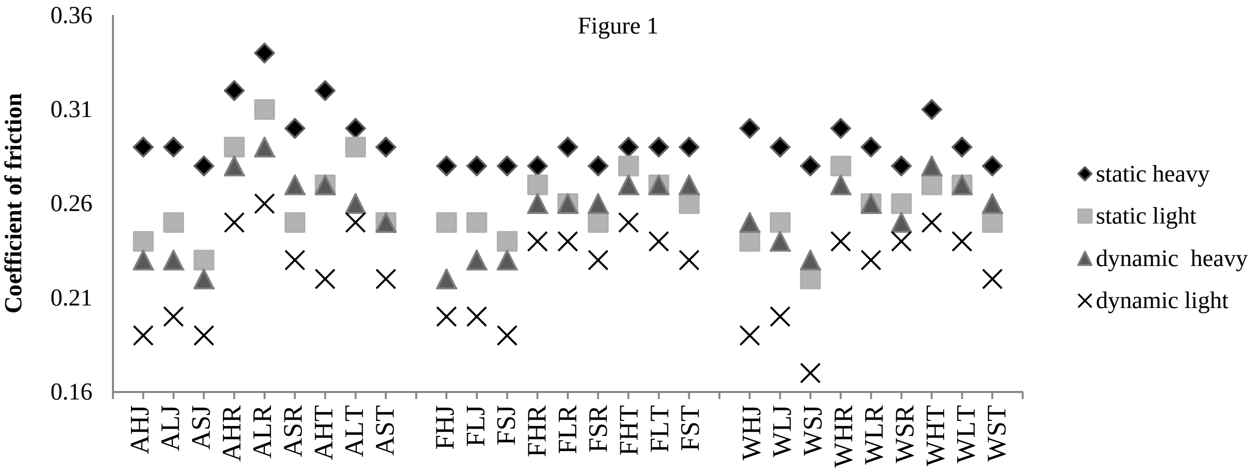

A = acrylic F = fine wool W = mid-micron wool H = high twist yarn L = low twist yarn S = single yarn J = single jersey
R = half-terry T = terry

Dynamic friction

Weight ($F_{2,216}=335.34$, $p\leq0.001$), fabric structure ($F_{2,216}=214.86$, $p\leq0.001$) and yarn structure ($F_{2,216}=14.92$, $p\leq0.001$) all affected the coefficient of dynamic friction. When a heavier load was applied to the fabrics, this resulted in a higher coefficient of dynamic friction than the light weight. Coefficients of dynamic friction observed on the terry and half-terry fabrics were similar and higher than single jersey fabric.

DISCUSSION

Differences between experimental set-ups affect results and make comparisons between the present work and previous work difficult. For example, as pressure between two fabrics increases, a decrease in the coefficient of static and dynamic friction is observed Carr, et al., (1988) Jeddi, et al., (2003). Results from the current study conflict with these findings: instead, as the load increased, so did the coefficient of friction. This was observed for both static and dynamic friction. Although the horizontal platform method was used in both studies, only the frictional properties of *woven* fabrics were examined. It is highly probable that the frictional characteristics of woven and knitted fabrics differ. Neither Carr, et al., (1988) nor Jeddi, et al., (2003) specified the load applied to the sled, and used either self-fabric or an unspecified fabric on the bottom of the sled. Carr's objectives were to investigate friction for an automated fabric separation device, a very different objective to the present work.

Findings of the current work also differ slightly from those of Baussan, Bueno, Rossi and Derler (2012) who reported that terry had the lowest coefficient of dynamic friction when sliding along the orientation of the fabric, but single jersey had the lowest coefficient of dynamic friction when sliding took place in the opposite direction. Making a direct comparison between Baussan, et al., (2012) and the current work is not possible as fabrics in the current work were tested in one direction only and Baussan, et al., (2012) did not examine static friction.

CONCLUSIONS

Fabric structure, yarn structure, fibre and weight affected the coefficient of static friction between the sock fabric and the synthetic skin. Weight and fabric structure in particular affected the parameters analysed. Fibre type had no observable effect on the coefficient of dynamic friction. It is clear that friction between sock fabrics and the skin is a complex just beginning to be understood. Additional work is needed to further understand how different variables affect friction between sock fabrics and relevant surfaces.

REFERENCES

Herring, K. M. and Richie, D. H. 1990. Friction blisters and sock fiber composition: A double-blind study. *Journal of the American Podiatry Association*, 80(2): 63-71.

Zurek, W., Jankoiak, D. and Frydrych, I. 1985. Surface frictional resistance of fabrics woven from filament yarns. *Textile Research Journal*, 55(2): 113-121.

Carr, W. W., Posey, J. E. and Tincher, W. C. 1988. Frictional characteristics of apparel fabrics. *Textile Research Journal*, 58(3): 129-136.

Ajayi, J. O. 1992. Fabric smoothness, friction and handle. *Textile Research Journal*, 62(1): 52-59.

Jeddi, A. A. A., Shams, S., Nosraty, H. and Sarsharzadeh, A. 2003. Relations between fabric structure and friction Part 1: Woven fabrics. *Journal of the Textile Institute*, 94(3): 223-234.

Hermann, D., Ramkumar, S. S., Seshaiyer, P. and Parameswaran, S. 2004. Frictional study of woven fabrics: The relationship between the friction and velocity of testing. *Journal of Applied Polymer Science*, 92(4): 2420-2424.

Ramkumar, S. S., Umrani, A. S., Shelly, D. C., Tock, R. W., Parameswaran, S. and Smith, M. L. 2004. Study of the effect of sliding velocity on the frictional properties of nonwoven fabric substrates. *Wear*, 256(3-4): 221-225.

Baussan, E., Bueno, M. A., Rossi, R. M. and Derler, S. 2012. Analysis of current running sock structures with regard to blister prevention. *Textile Research Journal*.

KEYWORDS

Socks, fabric friction, wool, acrylic

ACKNOWLEDGMENT

Dr. Stewart Collie of AgResearch is gratefully acknowledged for providing experimental fabrics. The Todhunter/Carpenter/ Home Science Alumnae Scholarship for providing tuition fees and living stipend, and a further award was received from the University of Otago Christchurch Earthquake Extension.

Comparative Study of Wool, Cotton, and Ramie Bundle Fibers' Dynamic Mechanical Properties

Zhigang Xia, Weilin Xu, Weigang Cui, JingJing Huang
Key Laboratory of Green Processing and Functional Textiles of New Textile Materials, Ministry of Education, Wuhan Textile University, Wuhan 430073, China
weilin-xu@hotmail.com; zhigang_xia1983@hotmail.com

INTRODUCTION

As fibers are usually processed under different thermal and wet conditions in textile mills [1], it is very crucial to investigate the relation between processing conditions and fiber tensile properties. In specialty, the tension exerted on fibers varies periodically due to ring rail cyclical motion and fiber migration in spinning triangle during the ring spinning. Thus, it is necessary to investigate the fiber dynamic mechanical properties under different thermal conditions.

Dynamic mechanical Analysis (DMA) test methods have been widely employed for investigating the structures and viscoelastic behavior of polymeric materials for determining their relevant stiffness and damping characteristics for various applications [2]. Therefore DMA has been utilized to study properties such fibers such as banana fiber [2], PET fiber [3], and cellulose fibers [4]. Unfortunately, natural fiber bundle DMA properties have not been conducted an extensive and comparative study. In this study, DMA properties of such natural fibers as cotton, ramie and wool were comparatively investigated.

APPROACH

Materials. Cotton fibers were provided by 3542 Textile Co. Ltd., Xiangyang, China. Ramie fibers were provided by Jingyuan Bast Textile Co. Ltd., Xian'ning, China. Wool fibers were provided by Shandong Ruyi worsted spinning mills, Jining, China.

Fiber bundle preparation. Cotton fiber bundles containing different fibers were prepared by the method shown in figure 1.

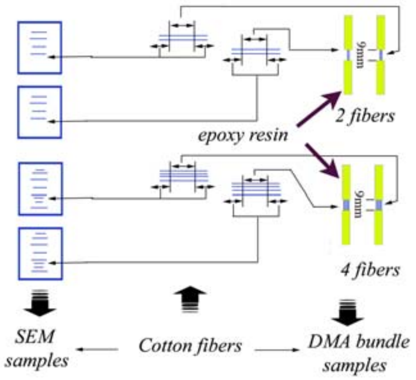

Fig. 1. Cotton fiber bundle preparation

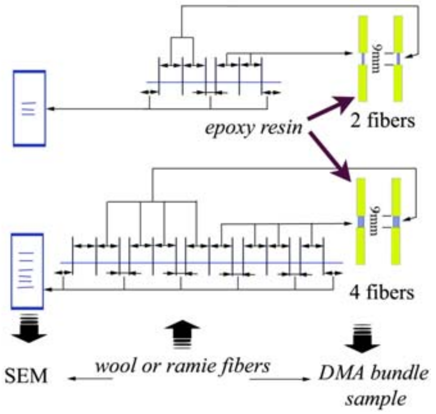

Fig. 2. Wool or ramie fiber bundle preparation

Ramie or wool fiber bundles containing different fibers were prepared by the method shown in figure 2. Each fiber diameter was tested by SEM, and then corresponding fiber bundle diameter was calculated according to equation (1). Cotton D_2 and D_4 are 17715.79 and 20449.66 nm; ramie D_2 and D_4 are 35911.71 and 55310.66 nm; wool D_2 and D_4 are 32239.34 and 49860.40 nm.

$$D_n = \sqrt{d_1^2 + d_2^2 + \cdots + d_n^2} \tag{1}$$

Where D_n represents the fiber bundle diameter; n represents the fiber number; d_n represents the mean diameter of fiber n.

DMA test. Dynamic mechanical property tests were conducted on DMA242 type tester with the following input parameters: dynamic force 0.5 cN; heating ratio 10 ℃/min; temperature range 15-220 ℃. In addition, all the fiber bundles were conditioned at 25 ± 2°C and 60 ± 10% RH for more than 24 hours and exerted 6 twists before testing.

RESULTS AND DISCUSSION

***E'-T* curves comparison for cotton, ramie and wool fiber bundles.** Figures 3, 4 and 5 are the *E'-T* curves for cotton, ramie and wool fiber bundles respectively. Obviously, all the three figures show that the bundle containing 2 fibers (denoted as 2-fiber-bundle) has a higher storage modulus than that containing 4 fibers (denoted as 4-fiber-bundle), which indicates that the bundle containing 2 fibers has a higher rigidity. For cotton and ramie fiber bundles, the drawing stiffness decrease significantly as the heating temperature increases in a range from 25 to 100 °C; this can be seen in figures 3 and 4. Meanwhile, wool fiber bundle show a weak decrease of stiffness as the temperature increases. We ascribe this to the high curvature and strong disulfide linkage structure for wool fibers. Moreover, *E'-T* curves of ramie bundles are more smooth than these of cotton and wool ones, which might be due to escape of ramie from fiber revolution and curvature.

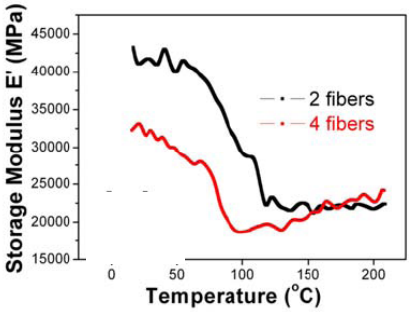

Fig. 3. *E'-T* curves of different cotton bundles

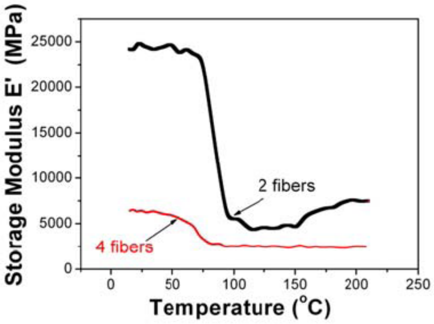

Fig. 4. *E'-T* curves of different ramie bundles

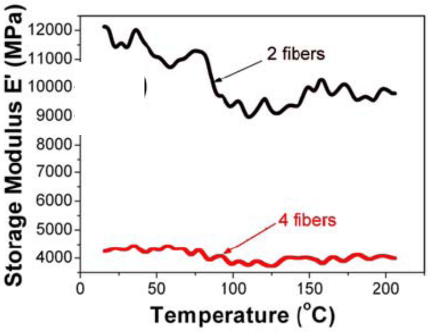

Fig. 5. *E'-T* curves of different wool bundles

Key DMA curve information comparison of different fiber bundles. For an extensive investigation, key DMA curve information were abstract from the *E'-T* and *tanδ-T* curves. $R_{E'}$ index is employed to compare the change of difference between 2-fiber-bundle and 4-fiber-bundle storage modulus with the temperature increase; it can be calculated according to equation (2).

$$R_{E'} = \left(1 - \frac{\left|E_2^{'} - E_4^{'}\right|_{\min}}{\left|E_2^{'} - E_4^{'}\right|_{initial}}\right) \times 100\% \tag{2}$$

According to key DMA curve information in table 1, $R_{E'}$ for cotton and ramie fiber bundles are much higher than that for wool bundles. For each *tanδ-T* curves' information, temperature corresponding to *tanδ* apex for 4-fiber-bundle is lower than that for 2-fiber-bundle. This suggests an easy occurrence of max viscosity during 4-fiber-bundle dynamic drawing. Based on the *tanδ-T* curves information, it can be indicated that ramie fiber bundles are most sensitive to the temperature; while wool fiber bundles are most insensitive to the temperature.

Table I. Key DMA curve information comparison of different fiber bundles

	E'-T curve information				*tanδ-T* curve information		
	Versus temperature (°C)	$\left\|E_2^{'} - E_4^{'}\right\|_{initial}$ (MPa)	$\left\|E_2^{'} - E_4^{'}\right\|_{\min}$ (MPa)	$R_{E'}$ (%)	fiber amount in bundle	*Tanδ* apex	Versus temperature (°C)
cotton	15	10962.86		100.00	2	0.081	107
	152		0.00		4	0.086	74
ramie	15	17775.01		89.39	2	0.159	85
	115		1885.81		4	0.103	71
wool	15	7889.72		33.93	2	0.071	188
	110		5212.78		4	0.087	182

CONCLUSION

The results of this study indicates that cotton and ramie fiber bundles', drawing stiffness decrease more significantly as the heating temperature increases than that for wool fiber bundle in a range from 25 to 100 °C. We ascribe this to the high curvature and strong disulfide linkage structure for wool fibers. According to key DMA curves' information, ramie fiber bundles are most sensitive to the temperature; while wool fiber bundles are most insensitive to the temperature.

ACKNOWLEDGMENT

We greatly acknowledge the support from the National Natural Science Foundation of China (Project No. 51203124) and Major State Basic Research Development Program (973 Program) (Project No. 2012CB722701).

REFERENCES

[1] Vasanthan N. Effect of Heat Setting Temperatures on Tensile Mechanical Properties of Polyamide Fibers. *Textile Res J*, 74, 545-550 (2004).

[2] Laly A.P., Zachariah O., Sabu T. Dynamic mechnical analysis of banana fiber reinforced polyester composites. *Composites Science and Technology*, 63, 283-293 (2003).

[3] Khanna Y.P., Taylor T.J., Kumar R., Dynamic mechanical analysis of fibers. II. Estimation of fiber orientation and characterization of heat set PET yarns. *Journal of Applied Polymer Science*, 42, 693-699 (1991).

[4] Jiang W., Sun L., Hao A., and Chen J.Y. Regenerated cellulose fibers from waste bagasse using ionic liquid. *Textile Res. J.*, 81, 1949-1958 (2011).

The Weft-Knitted Plant-Structured Fabric for Polo Shirt

Qing Chen[1] and Jintu Fan[2]
[1]Institute of Textiles and Clothing, Hong Kong Polytechnic University, Hong Kong
[2]Department of Fiber Science and Apparel Design, Cornell University, New York, USA
jf456@cornell.edu; tccqing@polyu.edu.hk

INTRODUCTION

Under active physical activity or hot and humid environment, evaporation of sweat is essential to release excessive body heat to maintain body temperature. Ideal fabrics for such conditions should remove the sweat from the skin to keep it dry and promote evaporation. For this purpose, a considerable number of moisture management fabrics have been developed. Different techniques, such as special cross-sections of fibers, blending different components of fiber or yarn, novel knitting or weaving structure, chemical treatments were employed. In particular, plant woven structure fabrics mimicking the tree branching network was developed to improve the liquid water absorption and transport properties [1, 2, 3, and 4]. This concept was further extended to weft knitted fabrics [5 and 6]. However, these weft knitting plant structured fabrics are so far too heavy for polo shirt application. In this paper, we report on a new lightweight weft knitted plant structured fabric.

EXPERIMENT

Circular knitting machine (machine gauge E28) was used to develop the fabric. 40 Ne cotton yarn was used to produce the plant structure fabric (171 g/m^2) and compared with the conventional fabric (196 g/m^2) of single pique structure. Figure 1 shows the appearance of the two fabrics.

Vertical wicking test [7], water drop test [8], water vapor permeability [9] as well as air resistance [10] were employed in the project to measure the water transport behavior of two fabrics. Besides, Kawabata evaluation system was applied to demonstrate the handle feeling of fabrics. Skewness change [11], dimensional change [12], and fabric appearance [13] after home laundering were applied to demonstrate the difference between plant structured fabric and commercial fabric.

Finally, the evaluation of the recovery ability after wearing was measured according to AATCC test method 128 [14]. After exposure at 20 ℃ and 65% RH for 24 hours, fabrics were tested in the conditioned room with the air velocity at about 0.2 m/s.

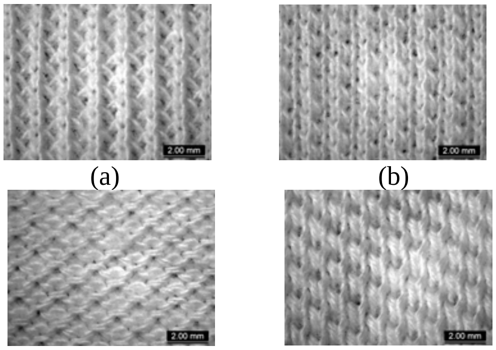

(a) (b)

(b) (d)

(a) backside of plant structured fabric; (b) face side of plant structured fabric; (c) backside of single pique fabric; (d) face side of single pique fabric

Figure 1 fabric appearance

RESULTS AND DISCUSSION

The measurements of various water transport properties, in terms of vertical wicking rate, vertical wicking height (see Figure 2), as well as water absorbency(see Figure 3) demonstrated that plant structured knitted fabric absorbed water faster than the conventional single pique fabric.

The possible explanations of faster water absorption rate of plant-structured knitted fabric are as follows. A branch network was built to reduce the water resistance in this system. The plant-based structure created a greater number of loops at the face side than that at the back side. This promotes faster water evaporation at the face side, creating the cohesion tension force, which forces liquid water to transport from the back side. Loops at the face side with a smaller diameter, and loops at the back side with a larger diameter could create a net capillary force pulling liquid water from the back side to the face side.

Regarding the handle of the fabric as measured in terms of bending, tensile, shearing, surface, and compression properties, the plant structured fabric exhibited softer handle with better recovery (lower hysteresis) than those of the conventional single pique fabric. The plant structured fabric was also found to be dimensionally more stable after home laundering and better in terms of wrinkle recovery as Figure 4 and Figure 5 show.

CONCLUSION

This study demonstrated that the weft knitted plant structured fabric had significantly better water transport property, handle, dimensional stability and wrinkle recovery than the conventional single pique fabric. It is advantageous for polo shirt garments.

FUTURE WORK

Garments made of this weft knitted plant structured fabric have been produced, and manikin tests and wear trials are to be conducted for further evaluation of our new product.

ACKNOWLEDGMENT

The authors would like to acknowledge the funding support from Innovation & Technology Commission of HKSAR and Hong Kong Research Institute of Textiles & Apparel (ITP/039/10TI).

REFERENCES

[1] Fan, J., Sarkar, M., Szeto, Y. and Tao, X., Plant Structured Textile Fabrics, Materials Letters, 61 (2), 561-565 (2007).

[2] Sarkar, M., Fan, J., Szeto, Y. and Tao, X., Biomimetics of Plant Structure in Textile Fabrics for the Improvement of Water Transport Properties, Textile Research Journal, 79(7), 657-668 (2009).

[3] Sarkar, M., Fan, J., Szeto, Y. and Tao, X., Development and Characterization of Light Weight Plant Structured Fabrics, Fibers & polymers, 10(3), 343-350 (2009).

[4] Fan, J., Szeto, Y. and Sarkar, M., Fabric Stimulating the Plant Structure for Moisture Management, US Patent 0220185 (2008).

[5] Chen, Q. Fan, J., Sarkar, M. and Jiang, G., Biomimetics of plant structure in knitted fabrics to improve the liquid water transport properties , Textile Research Journal Vol 80(6): 568-576 (2010).

[6] Chen, Q., Fan, J., Sarkar, M., and Bal, K. Plant Based Biomimetic Branching Structures in Knitted Fabrics for Improved Comfort Related Properties, Textile Research Journal, Vol. 81(10): 1039-1048 (2011).

[7] AATCC Committee RA63, Water Resistance, Absorbency and Wetting Agent: Vertical Wicking of Fabrics.

[8] AATCC Test Method 79-2000, AATCC Committee RA63, Water Resistance, Absorbency, and Wetting Agent Evaluation Test Methods, Absorbency of Textiles.

[9] BS 7209:1990 Water vapor permeable apparel fabrics.

[10] KES-F8-AP1 Air Permeability Tester, Instruction Manual, Kato Tech Co. Ltd., Kyoto, Japan.

[11] AATCC test method 179-2010, Skewness Change in Fabric and Garment Twist Resulting from Automatic Home Laundering.

[12] AATCC test method 135-2010, Dimensional Changes of Fabrics after Home Laundering.

[13] AATCC test method 124-2006, Smoothness Appearance of Fabrics after Repeated Home Laundering.

[14] AATCC test method 128-2009, Wrinkle Recovery of Fabrics: Appearance Method.

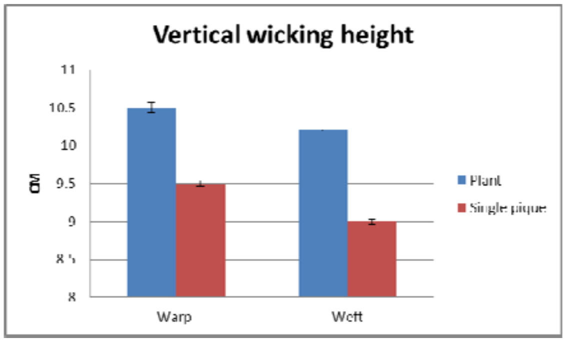

Figure 2 Vertical wicking test

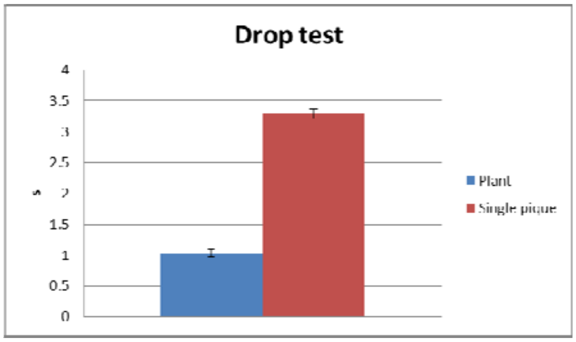

Figure 3 Drop test

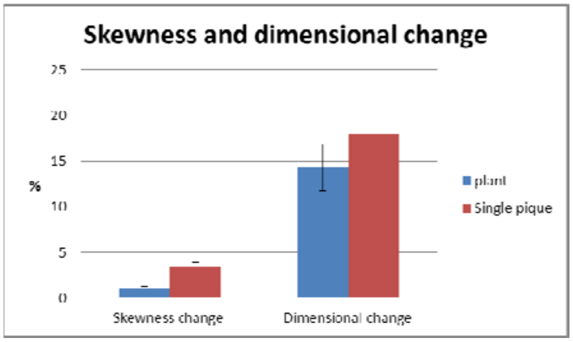

Figure 4 Skewness change and dimensional change test

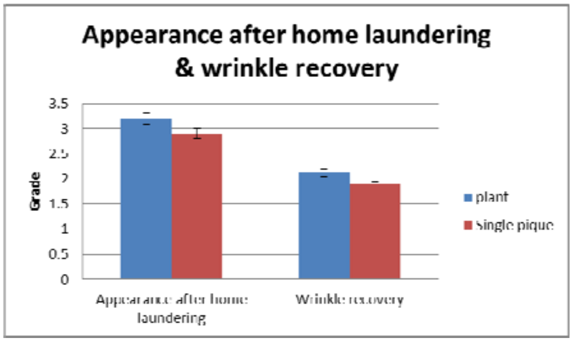

Figure 5 Appearance after home laundering and wrinkle recovery test

Silk Films as Promising Materials for the Repair of Chronic Perforations of the Tympanic Membrane

Ben J. Allardyce[1], Bing Mei Teh[2,3], Rangam Rajkhowa[1], Robert J. Marano[2,3], Sharon L. Redmond[2,3], Yi Shen[2,3,4], Marcus D. Atlas[2,3], Rodney J. Dilley[2,3,5], Xungai Wang[1]

[1]Institute for Frontier Materials, Deakin University, Australia; [2]Ear Science Institute Australia, Australia; [3]Ear Sciences Centre, School of Surgery, The University of Western Australia, Australia; [4]Department of Otolaryngology, Head & Neck, Ningbo Lihuili Hospital (Ningbo Medical Centre), China; [5]Centre for Cell Therapy and Regenerative Medicine, The University of Western Australia, Australia
bena@deakin.edu.au

OBJECTIVE

To assess the suitability of silk as a novel bioscaffold to repair chronic perforations of the tympanic membrane.

INTRODUCTION

Silkworm silks have a long and successful history as a suture material in the body due to their superior mechanical strength and flexibility [1]. In recent times, regenerated silk fibroin has shown great potential as a scaffold material for tissue engineering due to favourable properties such as mechanical strength, biocompatibility and a controllable rate of degradation [2]. The ability to transform native silk into a range of materials such as films, nonwoven mats, porous sponges or hydrogels greatly increases the number of possible biomedical applications [3].

Thin silk films cast from regenerated silk fibroin have recently been identified as a possible graft material to aid in the repair of chronic perforations of the tympanic membrane (TM) [4]. Previous work by our group has shown that films cast from aqueous fibroin and fibroin dissolved in formic acid both show potential in this application as they can support the attachment and growth of human keratinocytes [5, 6].

Although preliminary results are promising, a more detailed investigation of the chemical and mechanical properties of aqueous and formic acid films is required in order to assess which film type is better suited to this application. Also, since the biomechanical properties of silk films vary based on silk species, a comparison between films prepared from different varieties is useful in identifying a material most appropriate for our application.

This study compares some important material properties relevant to TM regeneration such as the transparency, tensile strength, thermal stability and hydrophobicity of silk films. The films were also compared in terms of their ability to allow attachment, growth and migration of human TM keratinocytes.

APPROACH

Cocoons from either *Bombyx mori* (Mulberry silk*)* *Antheraea assamensis* (Muga silk) or *Samia cynthia ricini* (Eri) were degummed and dissolved using a similar method to that described previously (Fig. 1) [7]. Films were cast from these solutions and air dried at room temperature. Formic acid films were prepared by lyophilising aqueous silk and reconstituted using formic acid as previously described [5]. Ethanol annealing was conducted overnight using 70% ethanol.

RESULTS AND DISCUSSION

All films including the ones prepared with formic acid showed excellent transparency and low scattering of light over the visual wavelengths (Fig. 1 shows the results of Mulberry silk films). Transparency is important for clinicians to monitor the condition of the middle ear through the film following TM repair.

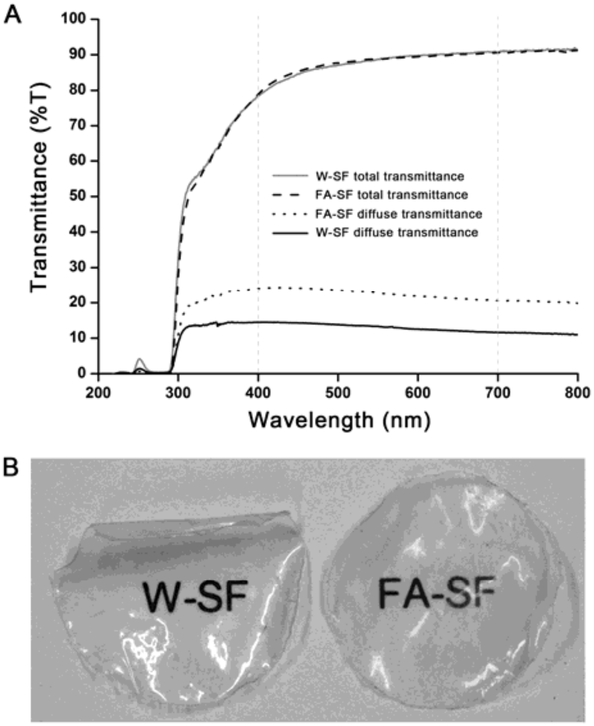

Fig. 1. (A) Transparency of water-based (W-SF) and formic acid-based (F-SF) films between 800 and 200 nm wavelength; (B) Photographs of the films demonstrating their transparency.

Formic acid based films had greater strength and Young's modulus and had higher thermal stability compared with aqueous films, suggesting these films had a more compact molecular structure (Fig. 2).

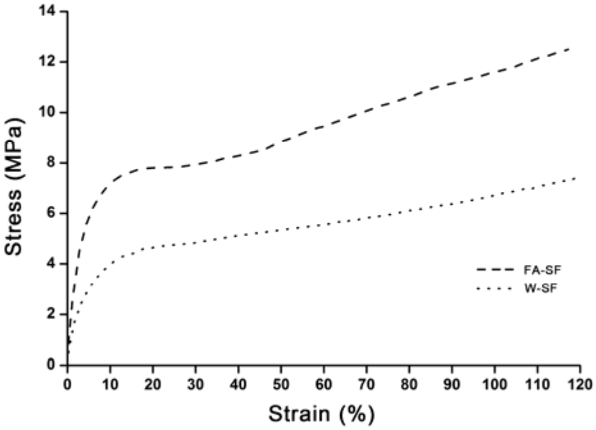

Fig. 2. Stress-strain profile of aqueous (W-SF) and formic acid (FA-SF) films.

In terms of film processing, Mulberry silk has a distinct advantage over other varieties due to better solubility and higher solution stability. Non-Mulberry films on the other hand have higher thermal stability. Cell culture results revealed that all film types were able to support human keratinocytes. The morphological appearance of the cells on the films combined with the results from quantitative gene expression studies indicated normal growth and differentiation on water and formic acid based Mulberry films (Fig. 3).

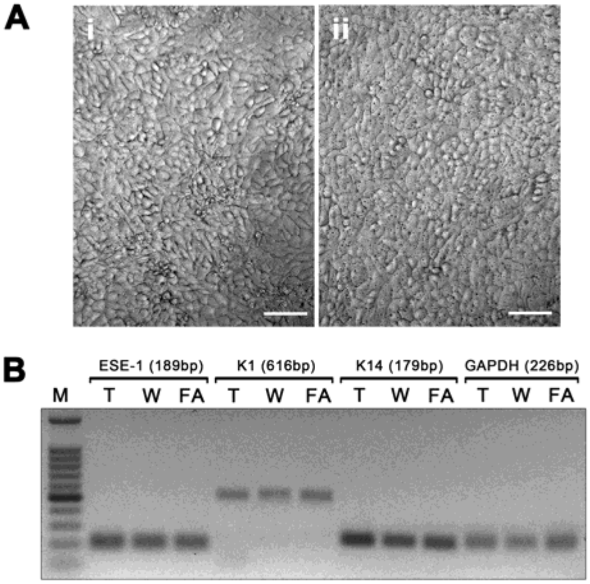

Fig. 3. (A) Photomicrographs of human keratinocytes on aqueous (i) and formic acid films (ii). Scale bar = 500 µm. (B) Gel electrophoresis of PCR products of human keratinocytes cultured directly on TCP culture plates (T), aqueous films (W) and formic acid films (FA). Expression of these epithelial marker (ESE-1, K1 and K14) suggest that cells on all surfaces were growing and differentiating normally as they maintained their normal phenotype.

The formic acid films were also superior in terms of cell adhesion and proliferation (results not shown).

CONCLUSIONS

All film types were deemed to be suitable as a scaffold material for TM regeneration. When comparing the two Mulberry films, formic acid films showed slightly better mechanical and thermal properties as well as cell adhesion and proliferation while aqueous films had a slightly higher cell growth rate.

FUTURE WORK

A more detailed comparison of Mulberry, Muga and Eri films is required in order to identify which silk type provides the best characteristics for this application. The processing steps to make silk films will also be manipulated to provide optimal characteristics.

REFERENCES

[1] Moy RL, Lee A, Zalka A. Commonly used suture materials in skin surgery. *Am Fam Physician*. 1991; 44:2123-8.

[2] Vepari C, Kaplan DL. Silk as a biomaterial. *Prog Polym Sci.* 2007; 32:991-1007.

[3] Rockwood DN, Preda RC, Yucel T, Wang XQ, Lovett ML, Kaplan DL. Materials fabrication from *Bombyx mori* silk fibroin. *Nat Protoc.* 2011; 6:1612-31.

[4] Levin B, Rajkhowa R, Redmond SL, Atlas MD. Grafts in myringoplasty: utilizing a silk fibroin scaffold as a novel device. *Expert Rev Med Devic.* 2009; 6:653-64.

[5] Rajkhowa R, Levin B, Redmond SL, Li LH, Wang LJ, Kanwar JR, et al. Structure and properties of biomedical films prepared from aqueous and acidic silk fibroin solutions. J *Biomed Mater Res* A. 2011; 97A:37-45.

[6] Levin B, Redmond SL, Rajkhowa R, Eikelboom RH, Marano RJ, Atlas MD. Preliminary results of the application of a silk fibroin scaffold to otology. *Otolaryng Head Neck.* 2010; 142:S33-S5.

[7] Rajkhowa R, Wang LJ, Wang XG. Ultra-fine silk powder preparation through rotary and ball milling. *Powder Technol.* 2008; 185:87-95.

Enhanced Moisture Management Properties of Denim Fabrics

Muhammad Bilal Qadir[1], Uzair Hussain[2], Sung Hoon Jeong[1]
[1]Department of Organic and Nano Engineering, Hanyang University, Seoul, Korea
[2]National Textile University, Faisalabad, Pakistan
shjeong@hanyang.ac.kr

STATEMENT OF PURPOSE

This is one part of a comprehensive study of manufacturing of economical denim fabrics having better comfort and mechanical properties. The aim of this part of study was to investigate the effects of different blend ratio of weft cotton/polyester (PC) yarn on the moisture management properties of denim fabrics.

KEYWORDS: moisture management, denim, blend ratio, polyester, cotton

INTRODUCTION

Clothing comfort is one of the basic needs of the wearer. One common definition of human comfort is freedom from pain, a state of physiological, psychological and physical harmony between a human being and the environment [1]. It depends upon the thermo- physiological characteristics of the textile material. In addition to tactile feeling, heat and moisture transfer are key factors, which contribute to clothing comfort perception. Moreover, air and water-vapor permeability properties of clothing also have a significant influence on comfort characteristics [2].

Textile materials may be hydrophobic or hydrophilic in nature. Many complexities are attached with the adsorption and absorption processes. Overall, adsorption and absorption of water in textiles create a big change in their thermal characteristics. This change leads to change in their thermal and moisture sensation and overall comfort properties. There is a strong correlation between moisture management properties of a fabric and its final comfort perception [3-4]. When water is dropped on the surface of any textile material it moves in multi directions. Its movement depends upon the chemical and physical nature of the textile material. The ability to control the movement of moisture is called moisture management of textile material [5].

This study investigated the moisture management properties of denim woven with a constant warp and five different weft yarns having different blend ratio of polyester and cotton. The specific objective of this study was to investigate the effect of different weft yarn materials on the moisture management properties of denim fabrics

APPROACH

Five denim fabrics were manufactured having 100% cotton yarn of linear density of 56.2 tex in warp direction and polyester/cotton blended yarn of linear density of 59.1 tex in weft direction. Polyester to cotton blend ratio in weft yarns were 75:25, 50:50, 35:65, 25:75 and 0:100 for five denim fabrics having different ratio of polyester in weft direction. Desizing of fabric was done by using GSL (0.5% for 4 min) and Faip AM (1% for 15 min) at 55°C. Desizing was followed by rinsing. Bleaching was done by using 50 ml GSL(1%), 500gm caustic soda (10%) at 40°C for 5 min, Hydrogen Per Oxyde (35%) at 90°C for 30 min.

All the fabric samples were tested on an SDL Atlas Moisture Management Tester according to AATCC Test Method 195-2009. The Moisture Management Tester (MMT) was developed by Yi Li, Qing Wen Song and Jun Yan Hu to measure the flow of water when drops of water touch the surface of fabric [6]. The instrument gives different indices, which quantify the movement of water in different directions in a textile material. The fabric side that was used as 'top' during testing in this study refers to that side of the denim fabric on which the weft or filling yarns are predominant. This is the side of denim fabric, which would come into contact with skin when the denim garment is worn. The 'bottom' fabric side had predominantly the cotton warp yarns exposed, which were held constant in the study while the weft yarns were varied from cotton to polyester in different percentages.

RESULTS AND DISCUSSION

All the results of moisture management properties of five denim fabrics are summarized in Table I.

Table I. Summary of results of moisture management properties

Poly. %	WT_T	WT_B	AR_T	AR_B	MWR_T	MWR_B	SS_T	SS_B	R	OMMC
75	4.74	4.47	43.16	55.35	20	20	3.33	3.43	266.072	0.68
50	5.65	5.59	50.07	61.45	20	19	3.14	3.21	241.14	0.6508
35	4.73	4.31	40.47	49.59	16	16	2.69	2.81	197.32	0.536
25	4.26	4.29	41.93	49.94	15	16	2.51	2.64	153.091	0.4739
0	5.05	4.90	37.07	44.78	14	15	2.08	2.21	124.12	0.3907

Table II gives one-way analysis of variance (ANOVA) results for the effect of polyester percentage of weft yarns on fabric moisture management properties. It can be observed from

Table II that the effect of polyester percentage is significant on all the moisture management parameters i.e. wetting time (WT_T & WT_B), absorption rate (AR_T & AR_B), maximum wetted radius (MWR_T & MWR_B), spreading speed (SS_T & SS_B), accumulative one-way transport capability (R) and overall moisture management capability (OMMC) of the fabrics. R-sq (%) give the percentage variation in moisture management parameters that can be explained by changing polyester percentage in weft yarn.

Table II. One-way ANOVA results

Param.	**SS**	**MS**	**F**	**P**	**R-Sq (%)**
WT$_T$	5.257	1.314	4.18	0.013	45.53
WT$_B$	6.011	1.503	4.65	0.008	48.16
AR$_T$	458.7	114.7	5.37	0.004	51.79
AR$_B$	812.0	203.0	6.64	0.001	57.04
MWR$_T$	160.00	40.00	8.89	0.000	64
MWR$_B$	94.00	23.50	7.83	0.001	61.04
SS$_T$	5.007	1.252	9.01	0.000	64.31
SS$_B$	4.637	1.159	8.18	0.000	62.08
R	69785	17446	26.59	0.000	84.17
OMMC	0.29181	0.07295	15.48	0.000	75.59

During moisture management testing, the water drop was allowed to fall first on the ‘top’ surface wherefrom it spread outwards as well as penetrated towards the bottom side of the fabric.

It can be observed from the results that the spreading speed (SS) is higher in case of higher percentage of hydrophobic polyester in weft yarns as compared to hydrophilic cotton. It follows from the results that having hydrophobic yarns on the inner garment side and hydrophilic yarns on the outer garment side will result in higher perspiration spreading on the outer side which will also help in its quicker evaporation because of larger wetted radius (MWR).

Accumulative one-way transport (R) is a measure of the difference between the areas of the liquid moisture content curves of the top and bottom surfaces of a specimen with respect to time. It follows from the results that denim fabrics with higher polyester percentage weft yarns will keep the skin of the wearer dry by transporting the perspiration towards the outer side of the fabric which is away from the skin. This is because in denim, the fabric side which comes in contact with the skin has predominantly exposed weft yarns and the side which is away from the wearer has predominantly exposed warp yarns. Hence a fabric with good accumulative one-way transport from the inner fabric side to the outer side will offer good sweat management to the wearer.

Overall moisture management capability (OMMC) is an index of the overall capability of the fabric to transport moisture and it is calculated by combining three important attributes of performance i.e. AR_B, R and SS_B. So a fabric with good OMMC, will offer good moisture management for the wearer.

Graphical representation of moisture management behavior of denim fabrics having different polyester percentage is shown in Figure 1.

CONCLUSION

Moisture management capacity of denim fabrics is significantly affected by unlike types of weft yarns. Fabrics with pleasurable moisture management capacity can be developed by using a blend of hydrophilic and hydrophobic yarns in the fabric in such a way that the hydrophobic yarns (polyester) are predominantly present on one fabric side, which would come directly in contact with the skin and the hydrophilic yarns (cotton) are predominantly present on the other fabric side.

REFERENCES

1. Slater, K. Human Comfort. Charles C. Thomas Publisher, Springfield Illinois (VS) pp. 4-24, 1985.
2. Li, Y. The Science of Clothing Comfort. *Textile Prog. Ser.* 31(1/2), pp. 22–32, 2001.
3. Amrit, *U. R.AUTEX Res. J.*, 8 (7), 2007.
4. Barker, R. L., *Textile Res. J.*, 76 (1), pp. 27-31, 2006.
5. Hu, J., Y. Li, Yeung, K.W., A.S. Wong., and W. Xu, *Textile Res. J.*, 75 (1), pp. 57-62, 2005.
6. Suleiman, B. M., *J. of Physics D: Applied Physics*, 39, p. 547, 2006.

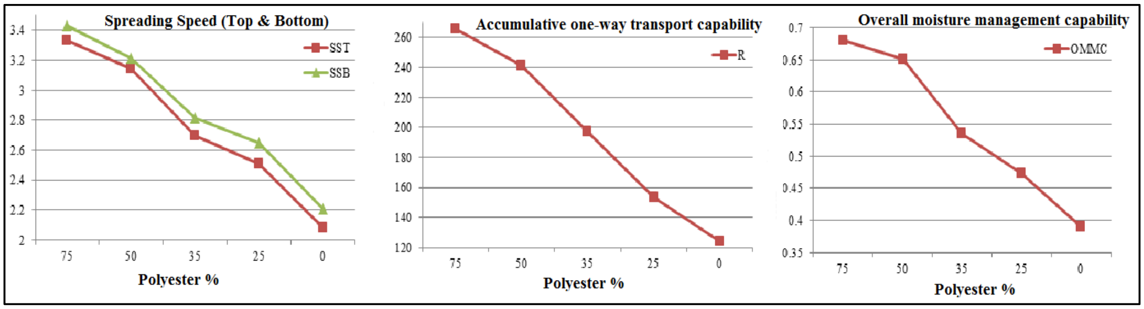

Figure 1. SS, R, OMMC VS Polyester Percentage

Nanofibres

Super-Crystalline Cellulose Nanofibers by Self-Assembling

You-Lo Hsieh
University of California, Davis, CA 95616, USA ylhsieh@ucdavis.edu

Cellulose, nature's most abundant polymer, is a linear syndiotatic homopolymer of β-(1→4)-glycosidic linked D-anhydroglucopyranose. The steric effect in the β-1,4-D(+)-glucopyranose building blocks prevents free rotation along the chains and the extensive inter-molecular and intra-molecular hydrogen bonds from the equatorial primary C6 and secondary C2 and C3 hydroxyls contribute further to the rigid and highly crystalline structure. The challenges for efficient utilization of cellulose are however many. The highly crystalline structure is challenging to dissolve and process for conversion into other forms. The unique chemical and physical structures of cellulose make it the most significant renewable resources for a great variety of high value materials beyond fiber, paper and biofuel. To take full advantage of unique cellulose chemistry and structure, direct utilization based on crystalline cellulose is a superior approach to fulfill their greatest potential. The unique chemical and physical structures of cellulose make it the most significant renewable resources for a great variety of high value materials beyond fiber, paper and biofuel.

Cellulose is part of plant cell walls and requires separation from other substances. Highly crystalline (65%-95%) cellulose nanofibers, commonly referred as nanocellulose, extracted from a broad range of natural sources including tunicate, algae, bacteria and wood have been reported to be 2 to 20 nm wide as aspect ratios varied from 40 (~200 nm long and 5 nm wide) to around 66 (~1 μm long and 15 nm wide) for tunicin whiskers[1]. The bending strength and modulus of these nanocellulose have been estimated by Raman spectroscopy to be ~10 GPa and ~150 GPa,[2] respectively. This impressive bending strength is about one-seventh of 63 GPa for the carbon nanotubes whose tensile strength is predicted to be as high as ~300 GPa at E of ~1 TPa, and much higher than high strength fibers including Kevlar.

This paper presents approaches by which to isolate pure cellulose from biomass, to generate crystalline nanocellulose and to create new nano-materials.

Pure cellulose can be readily obtained from cotton or isolated from other biomass. We have developed streamlined processes to isolate cellulose from under-utilized agricultural and processing byproducts. Crystalline nanocellulose can be derived by chemical and physical methods. Acid hydrolysis (64 wt% H_2SO_4 10 mL/g cellulose, 45°C) of cotton produced cellulose nanocrystals (CNCs) that are <10 nm wide and 200 to 400 nm long.[3]

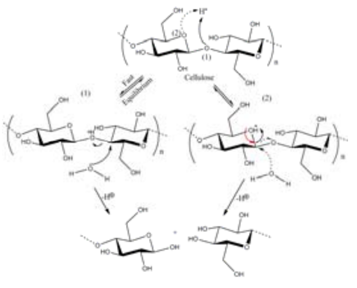

Pure cellulose have also been isolated from rice straw at 36% yield and hydrolyzed into CNCs whose dimensions could be tuned by length of hydrolysis time, i.e., those from 45 min were smaller (11.2 nm wide, 5.06 nm thick and 117 nm long) than those from 30 min (30.7 nm wide, 5.95 nm thick and 270 nm long) (Figure 1).[4]

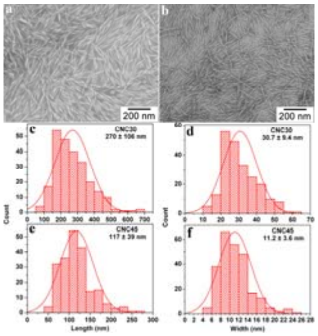

Figure 1. TEM images of CNCs from acid hydrolysis of rice straw cellulose: (a) CNC30; (b) CNC45; and length (c,e) and width (d,f) distributions.

Pure cellulose was isolated from chardonnay grape skins at a 16.4% yield and acid hydrolysis into crystalline (64.3%CrI) CNCs that appeared mostly as spherical nanoparticles with diameters ranging from 10-100 nm and a mean diameter of 48.1 (± 14.6) nm (Figure 2).

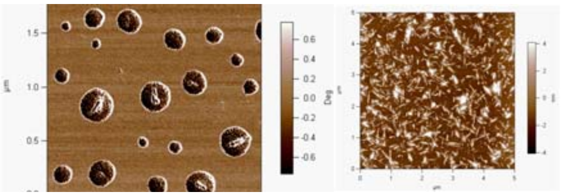

Figure 2. TEM (left) and AFM (right) of Chardonnay grape skin CNCs.

These nanocrystals retained cellulose Iβ crystalline structure and were more crystalline than its source. The sulfate groups introduced on the nanocrystal surfaces enable their swift and stable dispersion in aqueous as well as organic media including ethanol and DMF. The nanocrystals possessed mesoporous structure with an average pore width of 91.99 ± 2.57 Å and a specific surface area of 13.362 m^2/g, about 9 times of the original cellulose (1.547 m^2/g). Moreover, the nanocrystals exhibited significantly improved thermal conductivity and stability, leaving substantially more (30%) carbonaceous residue than the original cellulose. The combined surface charge introduction and fixation of mesoporosity on the cellulose nanocrystals is a highly efficient route to prepare large quantity of high quality cellulose nanocrystals with quick re-dispersion capability for practical applications.

Freeze-drying of diluted CNC suspensions showed both assembled into long fibrous structures: ultra-fine fibers (~400 nm wide) from CNC45 and 1-2 μm wide broad ribbons interspersed with CNC clusters from CNC30. The self-assembled fibers from CNC30 and CNC45 (Figure 3) were more highly crystalline (86.0% and 91.2%, respectively) and contained larger crystallites (7.36 nm and 8.33 nm, respectively) than the original pure rice straw cellulose (61.8%, 4.42 nm).

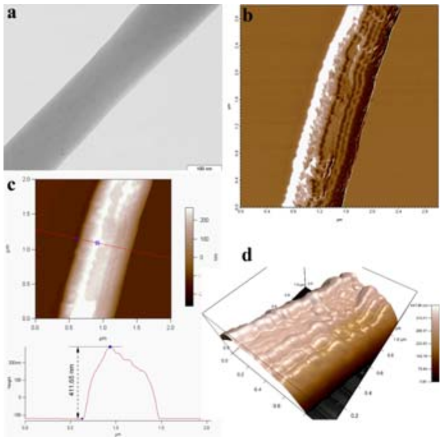

Figure 3. Self-assembled nanofibers from rice straw CNC45 from 0.06%.

The size of assembled fibers varied with CNC concentrations (Figure 4). These self-assembled fibers had essentially nonporous or macroporous structures with the CNCs well aligned along the fiber axis. Furthermore, the self-assembled ultra-fine fibers showed extraordinary structural stability, withstanding vigorous shaking and prolong stirring in water.

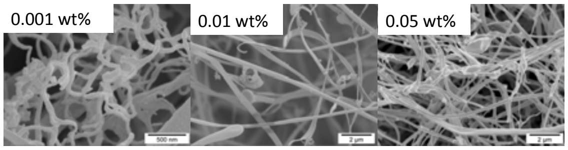

Figure 4. Self-assembled nanofibers from varying concentrations.

Much longer cellulose nanofibrils (CNFs) can be derived by mechanical defibrillation and TEMPO-mediated oxidation (Figure 5). From rice straw cellulose, the mechanical defibrillated CNFs were 82.5% crystalline and bimodally distributed in sizes (2.7 nm wide and 100-200 nm long; 8.5 nm wide and micrometers long). TEMPO mediated oxidation liberated the most uniform, finest (1.7 nm) and micrometer long, but least crystalline (64.4% CrI) CNFs. These fibers also exhibit self-assembling behaviors that depend highly on CNF concentration, media and drying processes. Examples of several self-assembled structures will be presented.

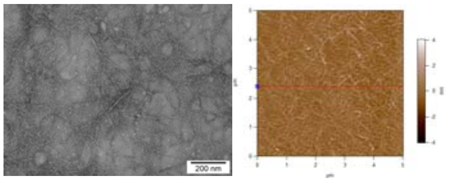

Figure 5. CNF from TEMPO oxidation.

ACKNOWLEDGMENT

Funding from USDA NIFA and California Rice Research Board is greatly appreciated. Research was conducted by P. Lu, F. Jiang and S. Han.

REFERENCES

1. Samir, M. A. S. A., Alloin, F., Dufresne, A. (2005). Review of recent research into cellulosic whiskers, their properties and their application in nanocomposite field. *Biomacromolecules* *6*(2), 612-626.
2. Sturcova, A., Davies, G. R., & Eichhorn, S. J. (2005). Elastic modulus and stress-transfer properties of tunicate cellulose whiskers. *Biomacromolecules, 6*(2), 1055-1061.
3. Lu, P. and Y.-L. Hsieh (2010). Preparation and properties of cellulose nanocrystals. *Carbohydrate Polymers* 82(2): 329–336.
4. Lu, P. and Y.-L. Hsieh (2012). Preparation and characterization of cellulose nanocrystals from rice straw. *Carbohydrate Polymers* 87:564-573.
5. Lu, P. and Y.-L. Hsieh (2009). Cellulose nanocrystal filled poly(acrylic acid) nanocomposite fibrous membranes. *Nanotechnology* 20: 415604-12.
6. Lu, P. and Y.-L. Hsieh (2012). Cellulose isolation and core-shell nanostructures of cellulose nanocrystals from Chardonnay grape skins. *Carbohydrate Polymers* 87(4): 2546-2553.

Mechanical-to-Electrical Energy Conversion of Needleless Electrospun Poly(vinylidene fluoride) Nanofiber Webs

Jian Fang, Haitao Niu, Hongxia Wang, Xungai Wang, Tong Lin
Australian Future Fibres Research and Innovation Centre, Deakin University, VIC 3216, Australia
tong.lin@deakin.edu.au; jian.fang@deakin.edu.au

INTRODUCTION

Inorganic nanowires (e.g. ZnO, InN, GaN, CdS, and ZnS) have recently been reported to show remarkable ability to convert small mechanical energy into electricity and potential applications for self-powered microelectronics and wireless sensor networks [1]. However, inorganic nanowires are brittle and can only work on a very small strain level. It is also hard to integrate inorganic nanowires into a soft material such as plastic film or filament.

In comparison to inorganic nanowires, polymeric nanofibers are much more flexible. Recently, our and other groups' studies have revealed that randomly-oriented electrospun poly(vinylidene fluoride) (PVDF) nanofiber webs have an unusually high mechanical-to-electrical energy conversion effect [2]. However, these PVDF nanofibers were produced by needle-based electrospinning technology. It is known that needle based electrospinning is disadvantageous in narrow operating voltage window, often between 10-25 kV and low fiber production rate.

Needleless electrospinning has emerged as a new electrospinning mode to produce nanofibers on large scales which are operated under a voltage much higher than that for needle electrospinning. In our recent work, we found that needleless electrospun PVDF nanofibers showed much enhanced piezoelectric performance, and the operating voltage for electrospinning indeed had a considerable effect on the piezoelectric properties of the nanofibers. Herein, we report on needleless electrospinning of PVDF nanofibers and their interesting energy harvest properties.

APPROACH

The setup for needleless electrospinning of PVDF nanofibers is illustrated in Figure 1a. 16% and 20% PVDF solutions (solvent: DMF/acetone, 1/1) were used as the materials. For comparison, nanofibers were also prepared by needle electrospinning

RESULTS AND DISCUSSION

Disc electrospinning was carried out by the slow rotation of the disc spinneret and meanwhile applying a high DC voltage on the solution. The applied voltages used in the disc electrospinning were 40, 45, 50, 55 and 60 kV. Figure 1b shows the scanning electron microscopy (SEM) image of the PVDF nanofibers electrospun by the disc at 40 kV. Uniform fibers in the form of randomly-oriented fiber web were obtained, which have a typical fibrous morphology of electrospun nanofibers produced by electrospinning. The needle-electrospun PVDF nanofibers show similar fiber morphology to those electrospun from the disc setup, except that they are finer (Figure 1c).

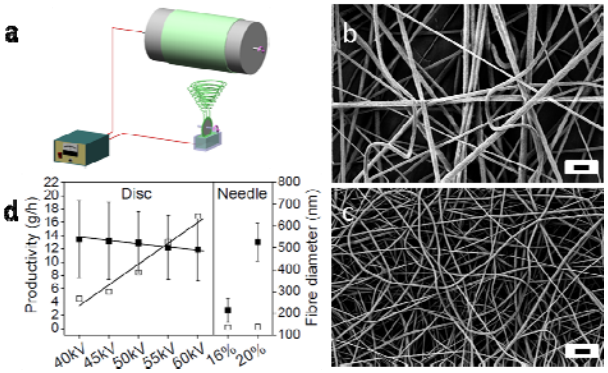

Figure 1 (a) Schematic illustration of the apparatus for disc electrospinning, (b) & (c) SEM images of the PVDF nanofibers electrospun by disc at 40 kV and needle (16% solution) (scale bar: 2 µm), (d) diameter (-■-) and productivity (-□-) of the PVDF nanofibers prepared under different spinning conditions.

It has been found that increasing the applied voltage from 40 kV to 60 kV led to a slight decrease in both average fiber diameter and diameter distribution (Figure 1d). For the needle electrospun PVDF nanofibers using the same polymer solution (16%), the fiber diameter was only 214 ± 54 nm, which was even finer than that of the disc-electrospun nanofibers prepared at 60 kV.

The fiber productivity of two electrospinning techniques is also shown in Figure 1d. For the disc electrospinning, the productivity increased significantly from 4.5 g/h to 16.9 g/h with increasing the applied voltage from 40 kV to 60 kV. However, the needle electrospinning had a much lower productivity than disc electrospinning, only 0.16 g/h for 16% PVDF solution.

Figure 2a shows the structure of the power-generating device. Upon the device receiving a repeated compressive impact, voltage and current signals were generated (Figure 2b). The voltage output was nearly 3 volts while the current output was in the range of 4~5 microamps. When the nanofiber mats were prepared by disc electrospinning using different applied voltages, the electrical outputs of the power-generating devices varied. The fiber mat prepared with a higher applied voltage showed higher voltage and current outputs (Figure 2c & 2d).

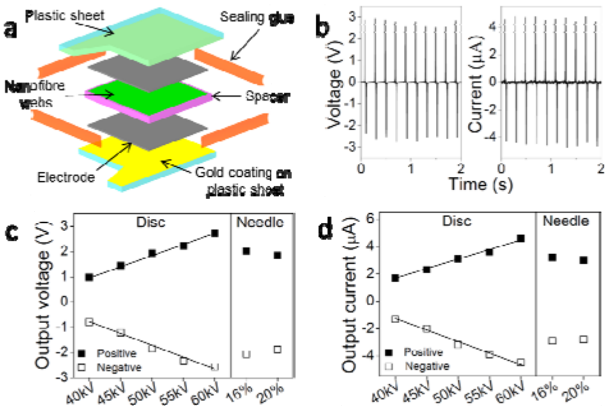

Figure 2 (a) Schematic structure of the nanofiber power generator, (b) typical voltage and current outputs of a nanofiber power generator (nanofiber web was electrospun using disc electrospinning with applied voltage at 60 kV), (c) voltage and (d) current outputs of the power generators made of different nanofiber webs.

When the 16% PVDF solution was used for needle electrospinning, the best performance of the nanofiber device under the optimized applied voltage (16 kV), was 2.05 V and 3.12 µA for voltage and current, respectively. The outputs were equivalent to the disc electrospun nanofiber device made from the same polymer solution at an applied voltage of 50 kV. However, for the 20% PVDF solution, the resultant nanofiber web led to a similar electrical output. This indicates that fiber diameter may have a small effect on the piezoelectric output of nanofiber device. When the nanofiber web was produced by disc electrospinning at an applied voltage greater than 50 kV, the device showed better piezoelectric performance than the nanofiber web produced by needle electrospinning regardless of the fiber diameter.

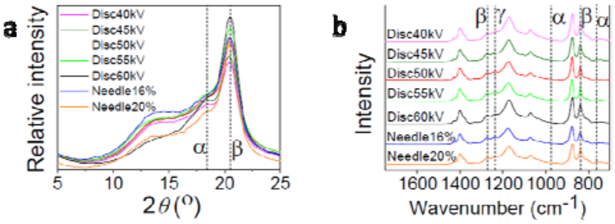

Figure 3 (a) XRD patterns and (b) FTIR spectra of the PVDF nanofibers prepared under different electrospinning conditions.

The crystal phase of the PVDF nanofibers was examined using X-ray diffraction (XRD) and Fourier transform infrared spectroscopy (FTIR). As shown in Figure 3a&b, the intensity of typical β crystal phase peaks increased with increasing the applied voltage in the studied voltage range, meanwhile the α crystal phase peaks had a reverse change. It has been calculated from the FTIR curves that the β crystal phase content of the nanofibers prepared using the disc electrospinning increased from 77.8% to 88.5% when the applied voltage increased from 40 kV to 60 kV. In comparison, the β phase contents were 85.1% and 83.9% for the needle electrospun nanofibers from 16% and 20% solutions, respectively.

To understand the effect of applied voltage on the fiber crystal content, the electric field intensity of the disc and needle electrospinning setups was analysed by a finite element method. For the needle electrospinning, the electric field intensity decreased quickly to zero within a short distance away from the needle tip, while the electric field in the disc electrospinning covered the entire electrospinning zone. When the voltage increased from 40 kV to 60 kV, the electric field intensity along the outmost of the disc edge all increased and the highest electric field intensity on the semicircle increased from 45.53 kV/cm to 68.37 kV/cm. For the needle electrospinning, the intensity at the needle tip was 54.37 kV/cm, when the applied voltage was 16 kV, which was between the electric field intensity of the disc electrospinning at 45 and 50 kV. Higher voltage could lead to higher electric field intensity and stronger mechanical stretching of the polymer solution, resulting in higher β crystal phase content and better macromolecule orientation. At the same time, higher electrostatic and charge repulsive forces facilitate the orientation of chains. As a result, PVDF nanofiber web electrospun under a higher voltage showed better piezoelectric properties with higher electric outputs.

CONCLUSIONS

Disc electrospinning offers a more effective way to produce PVDF nanofibers with better mechanical-to-electrical energy harvesting performance than needle electrospinning.

ACKNOWLEDGMENTS

Funding support from Australian Research Council through the Future Fellowship program is acknowledged.

REFERENCES

[1] Z. L. Wang, J. Song, *Science* 2006, *312*, 243; Z. L. Wang, *Nano Today* 2010, *5*, 512.
[2] J. Fang, X. Wang, T. Lin, *J. Mater. Chem.* 2011, *21*, 11088; D. Mandal, S. Yoon, K. J. Kim, *Macromol. Rapid Commun.* 2011, *32*, 831.

Electrospun Nanofiber Mats with Controlled Microstructures for Nanoparticle Filtration

Negar Ghochaghi, Adetoun Tawio, Gary Tepper
Department of Mechanical and Nuclear Engineering, Virginia Commonwealth University
gctepper@vcu.edu, ghochaghin@vcu.edu

OBJECTIVE

The objective of this study was to demonstrate that electrospinning can be used to produce new fiber filtration media with controlled microstructure. Specific performance parameters including filtration efficiency, pressure drop and Figure of Merit (FOM) were determined and related to microstructure. It is shown that the FOM increases when the electrospun fibers are arranged into alternating layers of aligned course and fine fibers.

Keywords: Fibers, Electrospinning, Air Filtration

INTRODUCTION

Electrospinning is a method to produce ultra fine fibers from various polymers with diameters on the order of submicrons to nanometers [1-6]. Electrospinning normally produces non-woven nanofiber mats, which can be useful for applications such as filtration, implant coatings, tissue scaffolds, drug delivery systems, artificial blood vessels, super hydrophobic surfaces, and wound dressing [4,7-10]. In filtration, pore size is an essential consideration, as it limits particle size. In order to capture nanoparticles in this application, nanoporous mats are needed. In this study we used several different electrospinning techniques to control the morphology and orientation of fibers, and subsequently the pores of the filters. Varying the process, parameters and materials used for electrospinning allows for interesting modifications in fiber morphology. Fabrication and characterization of different fiber orientations such as random, orthogonal, bimodal, unimodal, as well as nanowebs will be presented.

APPROACH

Nylon and polystyrene (PS) solutions (15% nylon, 20% PS, and 25% PS by weight) were used in this study. Different electrospinning setups were used to produce the fibers and control the morphology. DC electrospinning produced random fibers, while the application of high-speed rotation or a gap collector resulted in aligned fibers. Surface morphology was characterized by Scanning Electron Microscopy (SEM). Table I is a summary of electrospinning parameters and Figure 1 shows schematics of the electrospinning systems used.

Electrospinning Method	DC Voltage (kV)	Distance from needle to drum (cm)	Infusion rate (µl/min)
Conventional Method	+7	7	0.8
Rotational Drum	+5.5	7	1.0, 2.0
Gap Method	+7	7	0.8

Table I. Electrospinning parameters.

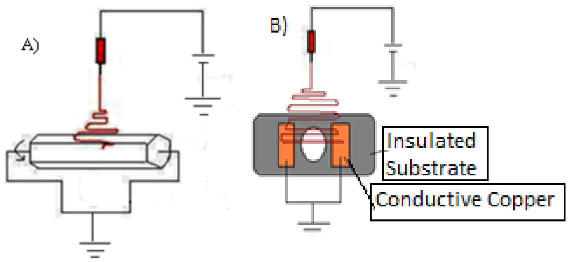

Figure1. Electrospinning system: (A) conventional method (rotation of the drum is optional), (B) gap method.

Figure 2 is a schematic diagram of filter test apparatus used to measure pressure drop and filter efficiency. Table II is a summary of the experimental conditions used for the performance evaluation of the filtration media.

Parameters	Particle Size (µm)	Face Velocity (cm/s)	Filter Diameter (mm)
Values	0.3-0.4	4.8, 14.4	12

Table II. Experimental conditions for filter performance evaluation.

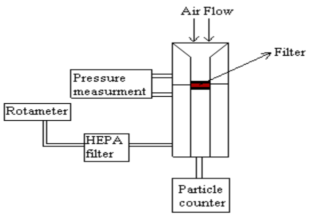

Figure 2. Filter test setup.

RESULTS AND DISCUSSION

In this study three primary morphologies were produced; Orthogonally aligned layers with bimodal fiber diameters, orthogonally aligned layers with unimodal fiber diameters, and aligned fibers with nanowebs. Figure 3 shows representative SEM images of the three different morphologies. Preliminary results of filtration efficiency and pressure drop analysis with respect to layering are shown in the figure 4 for the bimodal orthogonal layers. The overall performance of a filter is usually determined by the Figure of Merit (FOM), which is a measure of filter pressure drop for a given collection efficiency.

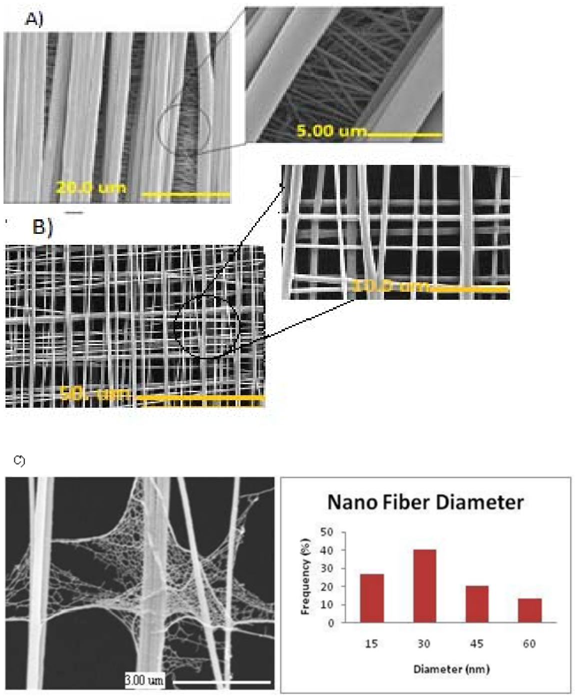

Figure 3. (A) Bimodal Orthogonal Fibers, (B) Unimodal Orthogonal Fibers, (C) Nanoweb and its fiber diameter distribution.

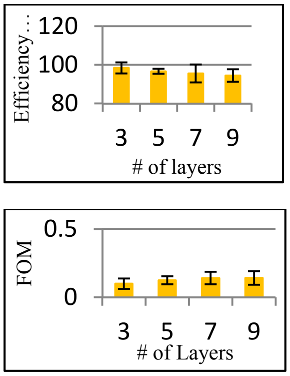

Figure 4. Effect of layering with same mass on filtration efficiency and pressure drop.

CONCLUSION

We were able to use electrospinning to produce filtration media with controlled microstructure. Three different morphologies were produced and characterized. This study is primarily focused on using nano and micro scale fibers for air filtration purposes. By analyzing the FOM we are able to make inferences about the relationship between the morphology of the filter media and the performance. A correlation was observed between overall performance and the number of layers of filters.

ACKNOWLEDGMENT

The authors would like to acknowledge the National Science Foundation and VCU school of Engineering for their financial support.

REFERENCES

1. Formhals. *Patent, U., Ed., US: 1934*, p. 504.
2. Jayesh Doshi, Darrell H. Reneker. *Journal of Electrostatics,* 35, pp. 151, 1995.
3. Darrell H. Reneker, Iksoo Chun. *Nanotechnology,* 7, p. 216, 1996.
4. Zheng-Ming Huang, Y.Z. Zhang, M. Kotaki, S. Ramakrishna. *Composite Science and Technology,* 63, pp. 2223, 2003.
5. Darrell H. Reneker, Alexander L. Yarin. *Polymer,* 49, pp. 2387, 2008.
6. Nandana Bhardwaj, Subhas C. Kundu. *Biotechnology Advances,* 28, pp. 325, 2010.
7. Eugene D. Boland, Gary E. Wnek, David G. Simpson, Kristin J. Pawlowski, And Gary L. Bowlin, *J. Macromol. Sci.–Pure Appl. Chem,.* A38 (12), pp. 1231, 2001.
8. Peter P. Tsai, Heidi Schreuder-Gibson., Phillip Gibson, *Journal of Electrostatics* 54, pp. 333, 2002.
9. Heidi Schreuder-Gibson, Phillip Gibson, Kris Senecal, Michael Sennett, John Walker, Walter Yeomans, David Ziegler, and Peter P. Tsai, *Journal of Advanced Materials* 34, pp. 44, 2002.
10. El-Refaie Kenawy, Gary L. Bowlin, Kevin Mansfield, John Layman, David G. Simpson, Elliot H. Sanders, Gary E. Wnek, *Journal of Controlled Release* 81, pp. 57, 2002.

Induced Negative Viscosity as a Degree of Freedom in the Electrospinning of Polymeric Solutions

Lina M. Sanchez-Botero, Alejandro Garcia, Juan P. Hinestroza
Cornell University, Department of Fiber Science and Apparel Design, Ithaca, NY USA
jh433@cornell.edu

INTRODUCTION

Controlling the viscosity of polymeric materials is one of the most challenging endeavors in fiber manufacturing. The issue becomes more pronunciated in high speed fiber making processes such as electrospinning. In this talk we will discuss diverse strategies developed by our research group aimed at controling the viscosity of polymeric solutions using static and oscillating magnetic fields.

One of the most important scientific contributions of Einstein, although less publicized than his work on the theory of relativity, was the estimation that the viscosity for a suspension of hard spheres will increase as a function of the concentration of the spheres. However, his theoretical work could not consider the possibility that these spheres could be made of magnetic materials as man-made magnetic fluids were only available until 1960s. Recently, several investigations have the demonstrated the presence of anomalous flow behavior in Newtonian solutions of magnetic nanoparticles. One phenomenon in particular, the backward pumping of a ferrofluid in the presence of an alternating/rotating field, has provided evidence that induced negative magnetoviscosities can be achieved. It is expected that by replacing the Newtonian suspending fluid by a viscoleastic fluid such as a polymer solution new and unexpected phenomena may result.

Although the current nanotechnology focus is new, the synthesis, characterization, functionalization, and formulation of magnetic nanoparticle suspensions have been studied during the last four decades. These suspensions, commonly referred to as ferrofluids, are colloidal dispersions of permanently magnetized nanoparticles undergoing rotational and translational Brownian motion in a suspending liquid carrier. The magnetic nanoparticles range between 5-15 nm in diameter and they are usually coated with molecular layers of surfactants or polymers of approximately 1-2 nm in thickness. Since the mechanical and transport properties of these fluids can easily be influenced by an external magnetic field, they have recently attracted scientific and technological interest. Traditional and commercially developed applications of ferrofluids include rotary and exclusion seals which can be found in 60% of the PC's hard drives, stepper motor dampers, and heat transfer fluids in audio speakers and in electrical transformers, where enhanced natural convection occurs in the presence of a magnetic field due to temperature - dependent magnetization.

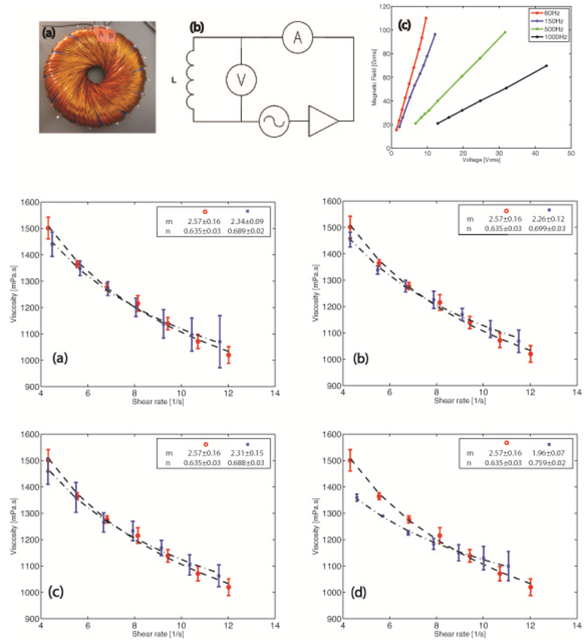

Figure 1. Schematics of the experimental setup used for creating a magnetic field and measuring its effect in the viscosity of the polymer fluid and viscosity measurements as a function of shear rate

Both aqueous and organic carrier-fluid formulations are possible, and due to the capability to design and modify the physical and chemical properties of both the suspending fluid and adsorbed dispersant layer, ferrofluids can be tailored to meet the demands of specific engineering applications. Unusual ferrofluid phenomena in the presence of DC magnetic fields include normal-field and labyrinthine instabilities which have been the subject of numerous theoretical analysis. In the last decade, the attention has been shifted to AC field phenomena, primarily motivated by observations of anomalous ferrofluid flow behavior, such as backward pumping of a ferrofluid in the presence of an alternating or a rotating field. This phenomenon is usually called negative viscosity. One such example arises when a ferrofluid fills the gap between two concentric cylinders, and the inner cylinder (the spindle) is made to rotate while simultaneously applying a rotating magnetic field perpendicular to the cylinder axis. The torque required to rotate the spindle is observed to increase with applied field amplitude and frequency for co-rotation of field and spindle, whereas it is seen to decrease, and indeed even become negative, for counter-rotation of field and spindle. Such observations may be explained phenomenologically by considering that the magnetic torque on the suspended particles is transmitted to the rotating spindle. Similar observations have been made in cylindrical Poiseuille flow of ferrofluids with an applied oscillating field along the cylinder axis. These experimental observations of backward pumping in the presence of an alternating or a rotating magnetic field are the basis for this project.

EXPERIMENTAL APPROACH

Figure 1 represents a schematic of the toroid solenoid used to create an alternating magnetic field used to measure the effect of the field's frequency. A significant decrease of viscosity is noted at higher frequencies of 500 and 1000 Hz (c and d) while the effect of the field is erased at lower frequencies (a and b).

RESULTS AND CONCLUSIONS

In order to validate the results shown in Figure 2 at higher frequencies, a new setup was built as shown in Figure 3. This new setup uses a linear solenoid that can produce higher magnetic fields when coiled around a ferrite hollow bar that works as a field magnifier. The measurements of viscosity show the presence of negative viscosity caused by the rotation of the particles and how this effect is modulated as a function of shear flow.

The experimental results for a solution of polyethylene oxide (Mw=2E6) loaded with magnetite nanoparticles, as shown in Figure 3, present direct evidence of the negative viscosity effect at lower values of shear rate and a recovery and increase in the viscosity values at higher shear rates. It is clear that modulation of the viscosity is possible using alternating magnetic fields and this modulation can tailored the electrospinning characteristics of polymer solutions. It is clearly seen that the viscosity increases and decreases as a function of the shear rate and the frequency. The theoretical approach given by Bacri et al. can somehow explain the observed dependence of viscosity change as a function of the frequency of the applied magnetic field using the following equation:

$$\Delta\eta = \frac{3}{2}\eta\varphi\frac{\Omega - \omega_p}{\Omega} \tag{1}$$

Where ω_p is the mean angular velocity of the particles and Ω is the angular fluid velocity. A fast enough oscillating magnetic field forces the particles to rotate faster than the fluid. As a result the viscosity of the ferrofluid decrease, this phenomena called "negative viscosity effect". However, in the opposite situation the viscosity of the ferrofluid will increase. In our experiments, a statistically significant change in the viscosity is observable at a higher frequency measurements (1000Hz). Nevertheless, the change is higher in both the lowest and higher shear rates. At higher shear rates, the vorticity of the flow, Ω, is expected to have higher values, this means that the angular velocity of the magnetic particles rotation induced by the alternating magnetic field will be smaller than the vorticity. This slow-moving will manifest itself in the increased viscosity. Meanwhile, at smaller values of shear rate, the opposite relation between w_p and Ω might be reached $\omega_p > \Omega$. In this scenario, rotating particles will increase the local vorticity of the flow, inducing decrease in the value of viscosity. In other words, the energy of the magnetic field will be transformed into mechanical energy of the fluid motion.

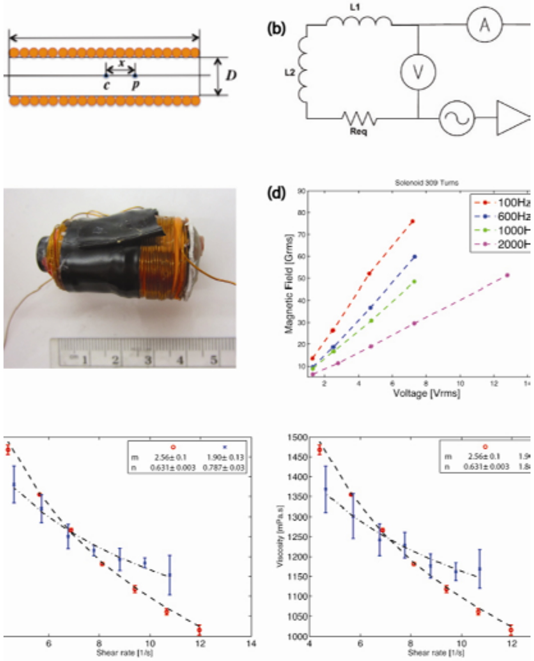

Figure 2. Schematics of the experimental setup used for creating an oscillating magnetic field (using a ferrite bar as a field amplifier) and measuring its effect in the viscosity of the polymer fluid.

KEYWORDS: Negative viscosity, magnetoviscosity, ferrofluids, electrospinning

ACKNOWLEDGMENT

We acknowledge financial support from the National Science Foundation under grant CMMI 0644612

REFERENCES

1. C. Barrera, T. Gould, K. Hyde, G. Montero, J. Hinestroza, C. Rinaldi. "Electrospun Magnetic Nanofibers with Anti-Counterfeiting Applications." Proceedings of 2005 ASME International Mechanical Engineering Congress and Exposition 2005, IMECE2005-82899, 1-9.
2. F. Gazeau, C. Baravian, J.C. Bacri, R. Perzynski, M.I. Shliomis, "Energy conversion in ferrofluids: Magnetic nanoparticles as motors or generators." *Physical Review E* 1997, 56, (1), 614-618.
3. J.C. Bacri, R. Perzynski, M.I. Shliomis, G.I. Burde, "Negative-viscosity effect in a magnetic fluid." *Physical Review Letters* 1995, 75, (11), 2128-2131.
4. M.I. Shliomis, K.I. Morozov. "Negative viscosity of ferrofluid under alternating magnetic-field." *Physics of Fluids* 1994, 6, (8), 2855-2861.
5. G.B. Biddlecombe, Y.K. Gun'ko, J.M. Kelly, S.C. Pillai, J.M.D. Coey, M. Venkatesan, A.P. Douvalis. "Preparation of magnetic nanoparticles and their assemblies using a new Fe(II) alkoxide precursor." *Journal of Materials Chemistry* 2001, 11, (12), 2937-2939.

Characterization of Electrospun Mat Composed of Polymer and Mesoporous Silica Nanoparticles

Slimane Almuhamed[1], Nabyl Khenoussi[1], Magali Bonne[2], Laurence Schacher[1],
Bénédicte Lebeau[2], Dominique C. Adolphe[1], Jocelyne Brendle[2]

[1]Laboratoire de Physique et Mécanique Textiles EAC 7189 CNRS/UHA
ENSISA, 11 rue Alfred Werner F-68093 Mulhouse Cedex France
[2]Equipe Matériaux à Porosité Contrôlée, Institut de Science des Matériaux de Mulhouse, UMR 7361 CNRS/UHA/ENSCMu,
3b rue Alfred Werner - 68093 MULHOUSE CEDEX - FRANCE
laurence.schacher@uha.fr

OBJECTIVE

To enhance performance characteristics of nanofiber materials, introduction of nanomaterials in polymer systems can be envisaged. Among the candidates, ordered mesoporous silica nanomaterials have attracted a wide interest since their discovery in the early 1990's due to their diverse potential applications. A majority of them requiring a high surface area, accessible pores and high pore volume, in addition to other mechanical parameters, optimum and uniform distribution of the filler in the polymer matrix is then desired. The aim of this present work was to prepare polyacrylonitrile (PAN)/SBA-15 nanocomposites by electrospinning. SBA-15 is a type of ordered mesoporous silica nanoparticles. The polymer solution and dispersion process have been optimized and influence of some electrospinning process parameters have been conducted. The properties and the geometry of the electrospun polymer/nanoparticle filament and network with nanoinclusions have been studied to estimate the ratio of accessible pores.

INTRODUCTION

Production of synthetic filaments using electrostatic forces is now extensively studied. A wide variety of polymeric fibers can be electrospun resulting in producing fibers in the nanometer to the submicron scale. Some potential applications include tissue engineering, filtration, sensors, and electronic applications. Ordered mesoporous materials have attracted a great deal of interest in the last years due to their remarkable properties, such as high surface area, narrow pore size distribution and controllable surface chemistry. Electrospun nanofibers with embedded ordered mesoporous silica will present a high potential for various applications in specific areas like catalysis or controlled drug delivery.

MATERIALS & METHODS

Polymer and solvent: The base polymer used for this study is polyacrylonitrile (PAN) with molecular weight Mw = 150000 g.mol^{-1} supplied by Sigma-Aldrich (France). Pure N,N-Dimethylformamide (DMF) (impurities less than 152 ppm in which water is less than 50 ppm) purchased from Fisher Scientific (France) was used as solvent.

Ordered mesopourous silica: SBA-15 was used. It was prepared according to Zhao *et al.* (1) with a specific surface area (S_{BET}) of about 800 m^2.g^{-1} and a mean pore diameter of about 7 nm.

Processing: The preparations were electrospun by means of an electrospinning set-up manufactured at LPMT (France) (2). Obtained materials are collected on a plate of copper covered with a foil of aluminum or a plate of Teflon charged by graphite. Table I gives the electrospinning process parameters.

Table I: Electrospinning conditions

Sample	Voltage (KV)	Gap needle - collector (cm)	Feed-rate (ml/h)	Linear Tension (kV/cm)	Period of Electro-spinning (min)
12wt. %PAN	11.5	20	0.212	0.575	120
	13	20	0.212	0.650	120
	14.5	20	0.212	0.725	120
12wt.%PAN 2wt .%SBA-15	11.5	20	0.212	0.575	120
	13	20	0.212	0.650	120
	14.5	20	0.212	0.725	120
12wt.%PAN 3wt.% SBA-15	11.5	20	0.212	0.575	120
	13	20	0.212	0.650	120
	14.5	20	0.212	0.725	120
12wt.% PAN 5wt.% SBA-15	11.5	20	0.212	0.575	120
	13	20	0.212	0.650	120
	14.5	20	0.212	0.725	120

Three suspensions of SBA-15 particles in DMF with a loading percentage of 2, 3 and 5 wt. %, respectively, were prepared by using a high shear homogenizer operating at 18000 rpm during 30 min followed by an ultra sonication for 30 min at 50°C.

Sample characterization*:* Morphology of the fibers was examined using scanning electron microscopy (SEM). The composition and the texture were characterized using thermogravimetric analysis and nitrogen adsorption, respectively. The specific surface area, the porous volume and the pore size of pristine SBA-15 particles and

(PAN)/SBA-15 nanocomposites) were determined by applying BET (Brunauer-Emmett-Teller), BdB (Broekhof-de Boer) and BJH (Joyner and Halenda) methods (3)(4).

RESULTS AND DISCUSSION

SEM micrographs (Figure 1) show that the SBA-15 particles are not well aligned along the fiber axis and that the applied linear tension induces an increase of the fiber diameter. This might be induced by the size of the aggregates of SBA-15 along with the influence of increased applied voltage.

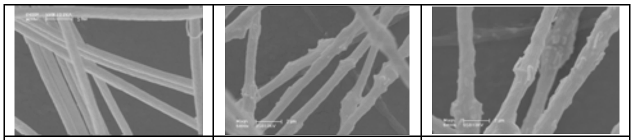
(a) PAN | (b) PAN+2wt.% SAB15 | (c) PAN+5wt.% SBA15

Figure 1: SEM micrographs of nanocomposites

Thermogravimetric analyses reveal that PAN filled with 2, 3 and 5 wt. % of SBA-15 particles in solution yields loading percents of 16, 24 and 30 wt. % of these particles in the solid sub-micron fiber. Data collected from the isotherms of low-temperature adsorption of nitrogen (Figures 2, 3, 4 & 5) demonstrate the presence of two sizes of pores in the sub-micron composites comparing to one mean pore size of SBA-15 particles. In addition, the higher the loading percentage of SBA-15 particles, the closer the mean pore size to that of pristine SBA-15 is.

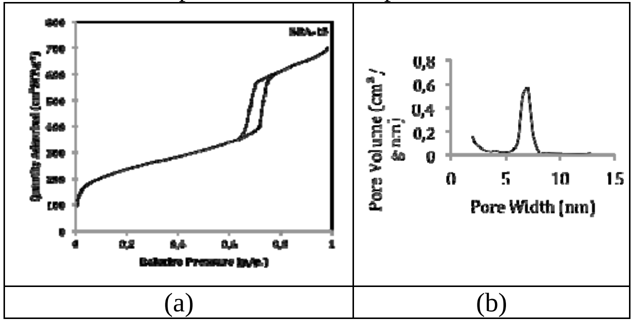

(a) | (b)

Figure 2: Isotherm (a) and pore size distribution (b) for SBA-15

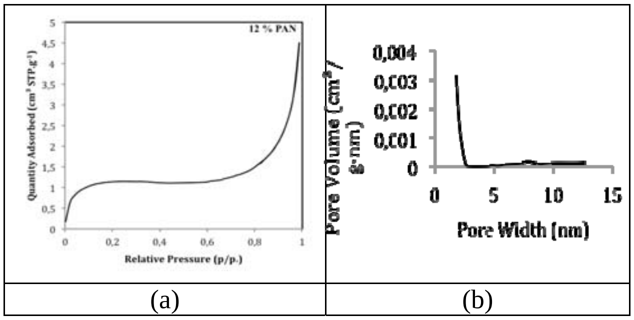

(a) | (b)

Figure 3: Isotherm (a) and pore size distribution (b) for pristine PAN

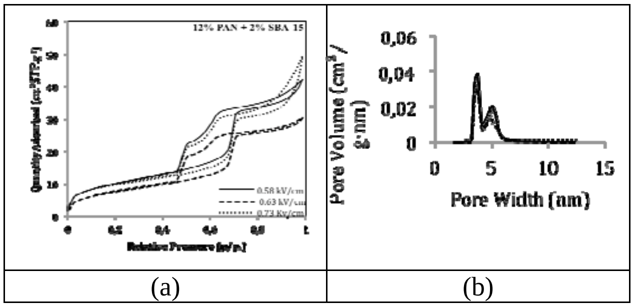

(a) | (b)

Figure 4: Isotherms (a) and pore size distribution (b) for PAN+2 wt.% SBA-15

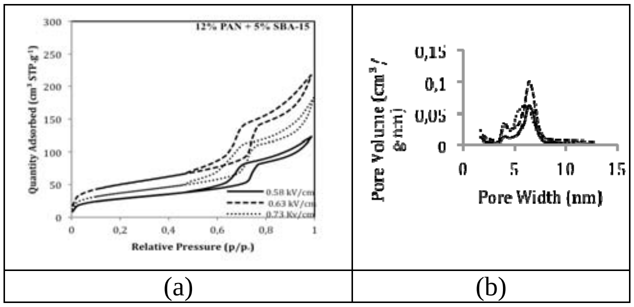

(a) | (b)

Figure 5: Isotherms (a) and pore size distribution (b) for PAN+5 wt.% SBA-15

Calculations made to estimate the ratio of accessible pore of SBA-15 particles located within the produced fibers show that there is a good ratio of accessible pores and that the higher the loading percent of SBA-15, the higher the ratio of accessible pore is.

CONCLUSION

Nanowebs of PAN fibers charged by SBA-15 ordered mesoporous silica particles have been prepared via electrospinning. The addition of SBA-15 has an influence on the diameter and the textural properties of the submicro fibers produced. Thermogravimetric measurement showed that regarding the initial loading percent of SBA-15 particles, 100% of these particles are embedded in the electrospun webs. Collected data from N_2 sorption isotherms reveal that there are a significant percentage of accessible pores of SBA-15 particles in the composite structure. The obtained structure is very promising for further potential applications.

KEYWORDS: nanofibers, nanocomposites, mesoporous SBA-15.

REFERENCES

(1) D. Zhao, J. Feng, Q. Huo, N. Melosh, G. H. Fredrickson, B. F. Chmelka, and G. D. Stucky, Science, 1998, 279, 548-552.
(2) N. Khenoussi, E. Drean, L. Schacher, D. Adolphe and H. Balard Experimental Techniques, first published online: 23 March 2011 DOI: 10.1111/j.1747-1567.2011.00704.x.
(3) S. Brunauer, P. H. Emmett, and E. Teller, J. Am. Chem. Soc., 1938, 60, 309-319.
(4) J. C. P. Broekhoff and J. H. de Boer, Journal of Catalysis, 1967, 9, 8-14.

Encapsulation of Active Agents in Electrospun Nanofibers/Nanowebs

Fatma Kayaci, Zeynep Aytac, Asli Celebioglu, Tamer Uyar
UNAM-Institute of Materials Science & Nanotechnology, Bilkent University, Ankara, 06800, Turkey
tamer@unam.bilkent.edu.tr

ABSTRACT

In this study, we produce functional nanofibers/nanowebs containing active agents such as essential oils, antibacterials, antioxidants, flavors/fragrances via electrospinning technique. The encapsulation of these active agents into electrospun nanofibers/nanowebs was quite possible, however, their stability and/or shelf-life was limited due to their volatile nature. Nevertheless, by forming cyclodextrin inclusion complexes (CD-IC) with these active agents and incorporating CD-IC into electrospun nanofibers/nanowebs, we achieved high temperature stability, slow release and prolonged shelf-life for these active agents. These functional electrospun nanofibers/nanowebs containing active agents can be quite applicable in active food packaging, textiles, biotechnology, etc.

INTRODUCTION

Incorporation of active agents such as essential oils, antibacterials, antioxidants, flavors/fragrances into polymeric matrixes is very appealing for designing multi-functional materials for applications in active food packaging, textile and biotechnology, etc. However, these bioactive agents are mostly volatile and temperature sensitive, therefore, their incorporation into polymeric films are often faces with problems since polymeric films are produced by melt extrusion at high temperatures. Very recently, electrospinning of nanofibers and their nanofibrous webs have received great deal of consideration due to their very large surface area to volume ratio, nanoscale porosity and high encapsulation efficiency of active agents [1-4] Additionally, electrospinning of nanofibers is mostly performed from solution-based systems at room temperature, therefore, homogeneous mixing of additives in the fiber matrix can be easily achieved. It has been shown that functional nanofibers incorporating active compounds such as antibacterials, antioxidants, fragrances and essential oils can be effectively obtained by electrospinning method [1-4]. However, the stability and/or shelf-life of these active agents encapsulated into electrospun nanofibers/nanowebs were again limited due to their volatile nature.

Cyclodextrins (CD) are natural non-toxic cyclic oligosaccharides consisting of α-(1,4)-linked glucopyranose units (Figure 1a). The native CDs are named as α-CD, β-CD and γ-CD having 6, 7 and 8 glucopyranose units, respectively. CD molecules have truncated cone-shaped molecular structure and they have capability of forming non-covalent host-guest inclusion complexes (IC) (Figure 1b) with variety of molecules such as antibacterials, drugs, antioxidants, flavors, essential oils, fragrances, textile additives, etc. By forming CD-IC, the thermal stability and the shelf-life of the volatile active agents can be increased and their release can be controlled or slow down. For this reason, CD and CD-IC are quite applicable in food, pharmaceuticals, cosmetics and textiles, etc [5].

In this study, we have shown that by forming cyclodextrin inclusion complexes (CD-IC) with active agents and incorporating these CD-IC into electrospun nanofibers/nanowebs, we achieved high temperature stability, slow release and prolonged shelf-life for active agents.

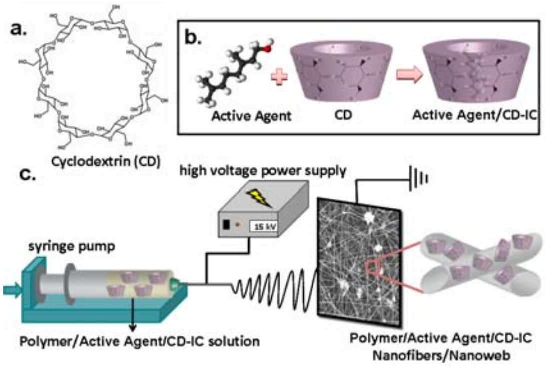

Figure 1. (a) Chemical structure of cyclodextrin (CD). Schematic representations of (b) formation of the active agent/CD-IC, (b) electrospinning of the polymer/active agent/CD-IC nanofibers/nanoweb.

EXPERIMENTAL

We followed two approaches; (1) the solid CD-IC crystals were formed initially and then dispersed in polymeric solution for electrospinning, (2) CD and active agent was complexed in a common solvent of polymer solution for electrospinning. Native CD types (α-CD, β-CD and γ-CD) or chemically-modified CD (hydroxypropyl-beta-cyclodextrin, HPβCD) were used for the CD-IC formation. The active agents used were; essential oils (eugenol, gereniol), antioxidants (vitamin E, quarcetin) antibacterial (allyl isothiocyanate (AITC), triclosan), fragrance/flavor (vanillin). Several types of polymeric matrixes were used; polyvinyl alcohol (PVA), hydroxypropyl cellulose (HPC), polylactic acid (PLA) and polycaprolactone (PCL).

RESULTS AND DISCUSSION

Several different types of polymeric matrixes were chosen such as polyvinyl alcohol (PVA), hydroxypropyl cellulose (HPC), polylactic acid (PLA) and polycaprolactone (PCL) for the electrospinning. Incorporation of active agents such as essential oils (eugenol, gereniol), antioxidants (vitamin E, quarcetin) antibacterial (allyl isothiocyanate (AITC), triclosan), fragrance/flavor (vanillin) was achieved by preparing common solution of polymer/active agent and then electrospun into nanofibers at optimized electrospinning parameters. Additionally, cyclodextrin inclusion complexes (CD-IC) of these active agents were prepared and then these CD-IC were encapsulated into electrospun nanofibers by electrospinning of polymer/CD-IC solutions (Figure 1c). Different types of cyclodextrins (α-CD, β-CD, γ-CD and chemically modified CD) were used for the CD-IC formation to find out the most favorable CD type for the stabilization of active agents.

Uniform and bead-free nanofibers were obtained from polymer/active agent systems (Figure 2a). In the case of polymer/CD-IC systems, the nanofibers were mostly uniform, but, in some cases, it was observed that aggregates of CD-IC crystals were present and distributed in the fiber matrix (Figure 2b). The variations of the fiber diameters were observed for the nanofibers produced from polymer/active agent and polymer /CD-IC systems owing to differences in viscosity and conductivity of the solutions.

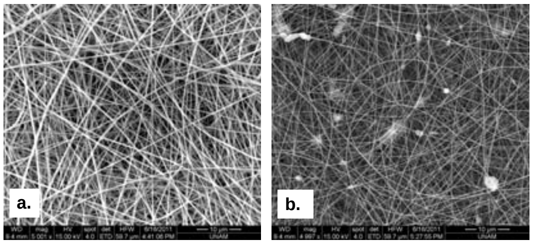

Figure 2. SEM images of (a) PVA/vanillin nanofibers and (b) PVA/vanillin/CD-IC nanofibers.

The presence of the active agents in the nanofibers was investigated by Fourier transform infrared (FTIR) spectroscopy and proton nuclear magnetic resonance (^{1}H-NMR) spectroscopy. We observed that nanofiber matrix without CD-IC could not preserve the active agents due to their volatile nature. However, in the case of polymer/CD-IC, the initial molar ratio was kept after the electrospinning. Moreover, our studies have also shown that high thermal stability, enhanced durability and prolonged shelf-life were achieved for active agents present in polymer/CD-IC nanofibers.

CONCLUSION

In short, the electrospun polymeric nanofibers incorporating CD-IC of active agents have shown high thermal stability and long-term durability which are highly dependent on the CD types used for the complex formation. These functional nanofibers/nanowebs containing active agents and having large surface area and nanoporous structure may be quite useful active food packaging, textiles, biotechnology, etc.

KEYWORDS

cyclodextrin; electrospinning; nanofiber; essential oils; antibacterials; antioxidants; flavors; fragrances; food packaging; textile

ACKNOWLEDGMENTS

Dr. T. Uyar acknowledges TUBITAK (project # 111M459 and 110M612) and EU FP7-PEOPLE-2009-RG Marie Curie-IRG (project # PIRG06-GA-2009-256428) for funding. State Planning Organization (DPT) of Turkey is acknowledged for the support of UNAM-Institute of Materials Science & Nanotechnology. F. Kayaci and A. Celebioglu acknowledge TUBITAK-BIDEB for the national PhD study scholarship.

REFERENCES

1. C. Kriegel, A. Arrechi, K. Kit, D. McClements, J. Weiss, Fabrication, functionalization, and application of electrospun biopolymer nanofibers. *Critical Reviews in Food Science and Nutrition,* 48(8), 775-797, 2008.
2. A.C. Vega-Lugo, L.T. Lim, Controlled release of allyl isothiocyanate using soy protein and poly (lactic acid) electrospun fibers. *Food Research International*, 42(8), 933-940, 2009.
3. T. Uyar, J. Hacaloglu, F. Besenbacher, Electrospun Polyethylene Oxide (PEO) Nanofibers Containing Cyclodextrin Inclusion Complex. *Journal of Nanoscience and Nanotechnology*, 11(5), 3949-3958, 2011.
4. F. Kayaci and T. Uyar, Encapsulation of vanillin/cyclodextrin inclusion complex in electrospun polyvinyl alcohol (PVA) nanowebs: Prolonged shelf-life and high temperature stability of vanillin. *Food Chemistry*, 133(3), 641-649, 2012.
5. A.R. Hedges, Industrial applications of cyclodextrins. *Chem. Rev.*, 98, 2035-2044, 1998.

ZnO Nanorod-Based Solar Textiles for Smart Clothing

Youngjin Chae, Eunae Kim
Department of Clothing and Textiles, Yonsei University
eakim@yonsei.ac.kr

OBJECTIVE

A solar textile for smart clothing was fabricated. Among various type of solar cells, Stainless wire based Dye sensitized solar cell (DSSC) was chosen by considering the optimum physical characteristics (ie: light weight and flexibility) as a clothing material. With the advantage of its wide band-gap, high electronic mobility and reduced recombination, ZnO Nanorod was directly grown on to the flexible stainless steel wire substrate. Several approaches were made to achieve a higher efficiency by considering the practical usage as a power source for the smart clothing.

INTRODUCTION

Presently, various approaches are being made to satisfy the wearing condition and the wear's diverse needs. In the high tech era, the spectrum of these needs is widely expanding beyond the basic needs of garments. Smart clothing can be one of leading needs that promote the new changes in garment to store, interpret or response to the wearing condition. However, to run on smart clothing a compatible, light and effective power source is necessary. Most commercialized power source for smart clothing is heavy, slightly ridge and reveals short life time which can be considered as a crucial limitation to be used as a garment material. The approach of solar cell on flexible materials, such as a fiber type Ti or stainless steel wires, can suitably meet the needs mentioned above with additional advantages of withstanding various physical stresses that may occur in a clothing environment. ZnO nanorod is suggested as the semiconducting layer for flexible solar cell in our present study to meet the property of the bendable wire substrates. Furthermore a solid type electrolyte was prepared by synthesizing a graft copolymer to enhance its physical stability and long term efficiency.

EXPERIMENT

Fabrication of photo electrode

For photo electrode, a ZnO nanorod arrays were prepared onto the Stain less steel wire (0.1mm diameter) template. Wires were sintered at 450 ◦C for 30 min in order to remove the remaining salts and polymers. The prepared electrodes were immersed into ruthenium dye. To prepare a solid-state polymer electrolyte, solid type polymer electrolyte solution was prepared by dissolving PVC-g-POEM was dissolved in THF and MPII, LI and I2 solution in acetonitrile was added

Fabrication of counter electrode

After the ultra-sonication with deionized water, stainless wires were Pt spin coated for 30s and were sintered at 450 ◦C for 30 min.

Fabrication of DSSC

For the cell's textile figure, photo and counter electrodes were fabricated into a satin structure After the weaving process, the ZnO based DSSC was coated with two layers of PET film in a sandwich structure, to maximize its durability.

Measurement of Performance

Short-circuit current density (Jsc, mA), open-circuit voltage (Voc, V) were measured by a solar simulator with an irradiance of 100mW/cm^2 at AM 1.5 by a 50-500 W Xe Lamp (Thermo Oriel, 91193, USA). The Surface of ZnO nanorod arrays on stainless steel wires were examined by Scanning Electron Microscope (SUPRA 55VP, NICEM, Carl Zeiss) images. The dye adsorption was measured by UV-visible spectrophometer (Hewlett-Packard, Hayward, CA) at wavelengths through ranges from 300nm to 800nm.

RESULTS AND DISCUSSION

Table 1. Charactoristics ZnO NRs on SS wire with different growth times

Growth time [h]	NR length [μm]	NR diameter [μm]	BET surface area* [m^2 g^{-1}]
1	3.3	0.20	0.042
3	4.3	0.25	0.097
5	9.7	0.26	0.098
7	3.8	0.23	0.074
8	2.9	0.20	0.078

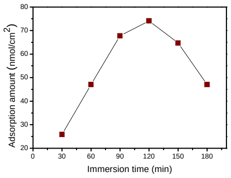

FIGURE 1. Dye adsorption of ZnO nanorod with different immersing time

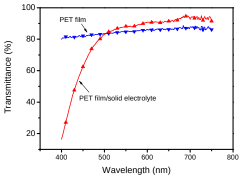

FIGURE 2. Transmittance of PET film

The successful growth of ZnO NRs on the flexible SS wire substrate was examined through SEM images. Also, the growing condition of ZnO nanorod was changed by its growing time (Table 1). Compared to other samples, the sample 5hr growth time has exposed the longest length and largest surface density of the nanorod which is known to be affirmative in increasing the final dye absorption amount that leads to a better performance of the cell. Additionally, while ZnO is known to be vulnerable in most acid dye, an effort to figure the optimized dye loading condition was carried out (Figure 1). The use of solid type electrolyte with PET sealing has not only practically overcome the durability or leaking problem of its similar type but also has increased the final transmittance property of the solar textile (Figure 2). The Performance of our system was compared by the size of the cell or the contact number of photo-counter electrodes. Result has shown a linear increase of the efficiency as the number of the contact has increased.

CONCLUSIONS

A flexible solar textile with a ZnO nanorod as the semiconducting layer of was investigated for smart clothing. To enhance the properties as a garment material, the fiber type DSSC was fabricated into a satin weave structure. Also, for the practical usage and durability of the cell, a solid electrolyte and PET film was selected for the fabrication process. A compatible result that fully explains the advantages of this new type solar textile was shown through our work.

REFERENCES

(1) Koh J H, Koh J K, Seo J A, Shin J S and Kim J H. *Nanotechnology*. 2011, 22 365401.

(2) Zhang Q F, Dandeneau C S, Zhou X Y and Cao G Z. *Adv. Mater*. 2009, 21 4087.

ACKNOWLEDGMENTS

This research was supported by the Ministry of Knowledge Economy (MKE) and Korea Industrial Technology Foundation (KOTEF) through the Human Resource Training Project for Strategic Technology.

Nanocrystal TiO_2 as Scattering Layer for Dye-Sensitized Solar Cells

Xueyang Liu[1], Jian Fang[1], Mei Gao[2], Tong Lin[1]
[1]Institute for Frontier Materials, Deakin University, Geelong, VIC 3216, Australia
[2]CSIRO Materials Science and Engineering, Clayton, VIC 3169, Australia
xueyang@deakin.edu.au; correspondence to: tong.lin@deakin.edu.au

INTRODUCTION

Dye-sensitized solar cells (DSSCs) have attracted enormous interest in both academic and industrial areas because of the low cost, easy fabrication, versatile structure and reasonable conversion efficiency. TiO_2 nanoparticles are often used as the photoactive material in the working electrode. Although an energy conversion efficiency as high as 12.3% has been reported (1), most of the DSSCs have a conversion efficiency far below this value. The low efficiency has been attributed to poor light absorption and photoelectron transfer properties.

Many efforts have been made to improve the performance of working electrode, such as doping TiO_2 with other elements, replacing nanoparticles with one-dimensional TiO_2 and improving light harvesting by using a scattering layer. Introducing an optical scattering layer to enhance the light harvesting capability could be a general solution to improving the solar cell conversion efficiency (2, 3). However, effective scattering materials for DSSCs have not been found yet.

In our recent study, we have successfully synthesized single crystal TiO_2 nanorods (NRs) through a combination of electrospinning and hydrothermal techniques. The unique tetragonal structure of the nanorods made them a promising candidate to improve the solar cell performance as a scattering layer. Herein, we report on the preparation of the TiO_2 nanocrystals, their optical scattering performance and the effect on the photovoltaic properties.

EXPERIMENT

TiO_2 nanofibers were prepared by electrospinning titanium butoxide (TNB)/polyvinylpyrrolidone (PVP) solution in a mixed solvent of ethanol/acetic acid (v/v, 8/2) followed by a calcination treatment at 500 °C to remove all the organic components.

TiO_2 nanorods were grown on the TiO_2 nanofibers using a hydrothermal method. 0.05g TiO_2 nanofibers were added to an aqueous TNB solution containing hydrochloride acid (35%) and water (v/v, 1/1). The hydrothermal reaction was carried out in a sealed Teflon vessel at 150 °C for 4 hours.

To prepare the DSSC device, a slurry paste was prepared by mixing 0.5g commercial TiO_2 nanoparticles with 0.1 ml acetic acid, 3 ml ethanol, 1.5g terpineol and 0.25g ethyl cellulose. Nanoparticle slurry was coated onto a FTO glass by the doctor-blade technique to form bottom layer. After drying at room temperature, the nanoparticle layer was coated with slurry made of nanorods (nanorod 0.5g, acetic acid 0.1ml, ethanol 3ml, terpineol 1.5g and ethyl cellulose 0.25g). The coated FTO was then dried and heated at 500°C for 30 minutes followed by immersing in a 0.3 mM N719 dye solution. After dyeing, the DSSC device was assembled by filling an electrolyte (.0.1M I^-/I_3^- in 3-methoxyproprionitrile) between the working electrode and a counter electrode.

RESULTS AND DISCUSSION

Figure 1a shows the scanning electron microscope (SEM) images of the TiO_2 nanofibers. After removing polymer component from as-electrospun nanofibers, the TiO_2 nanofibers have an average diameter around 83 nm. When TiO_2 nanofibers were subjected to a hydrothermal treatment, lots of tetragonal shaped crystals were grown on the TiO_2 nanofiber surface (Figure 1b).

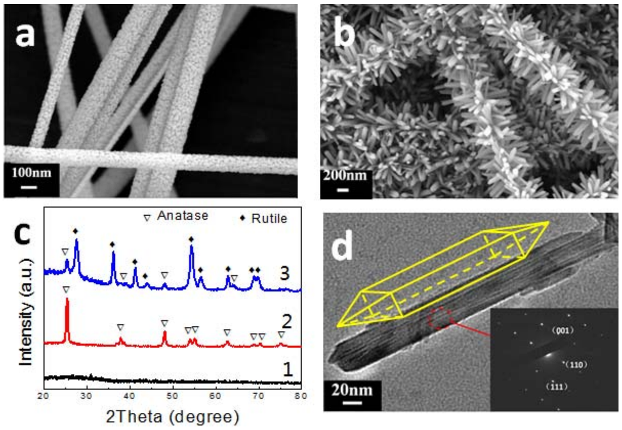

FIGURE 1. SEM images of (a) TiO_2 nanofibers, (b) hydrothermally-formed nanorods on nanofibers (c) XRD patterns of (1) as-spun nanofibers, (2) annealed nanofibers and (3) hierarchical nanofibers (d) TEM image of a single nanorod and selected area electron diffraction pattern (SAED) (insert).

The X-ray diffraction (XRD) measurement indicated that the calcinated nanofibers were almost in a pure anatase state (Figure 1c), while the hierarchical nanofibers contained both anatase and rutile crystal phases with the ratio of 20:80. The transmission electron microscopy (TEM) image and the SAED pattern in Figure 1d confirmed that the TiO_2 nanorods were tetragonal single crystals.

Figure 2a shows the cross-sectional view of TiO_2 working electrode which had a thickness of around 15 microns. It contains a nanoparticle bottom layer and a nanorod top layer. The bottom layer was made of commercial TiO_2 nanoparticles with the size of around 20 nm. The top layer was made of nanorod with width in the range about 30 -40 nm and length 200-250 nm. SEM images also prove that these two layers are tightly bonded together without any gaps between the layers.

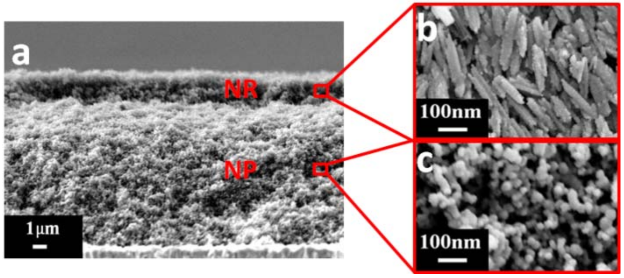

FIGURE 2. SEM images of (a) bilayer TiO_2 electrode made up of a nanoparticle bottom layer and a nanorod top layer, high resolution SEMs of the (b) top and (c) bottom layer.

Figure 3a shows the transmittance spectra of three different working electrodes: FTO glass coated with single layer nanoparticles, FTO glass coated with single layer nanorods, and FTO glass coated with a nanoparticle/nanorod bilayer. The transmittance in the wavelength region of 350-550 nm was low for all three electrodes. In longer wavelengths (550-800 nm), the transmittance for the nanoparticle coated electrode reached up to 82%. However, the transmittance for the nanorod coated electrode was much lower, although it had the same thickness as the nanoparticle layer. For the electrode with a bilayer coating, the transmittance was higher than that of the pure nanorod coated electrode, but far lower than that of the electrode with a nanoparticle layer.

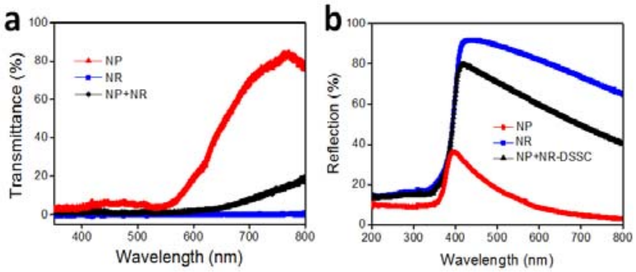

FIGURE 3. (a) Transmission and (b) reflection spectra of working electrodes made of NP (P25) (thickness 15 μm), NR (nanorods, thickness μm), NP/NR (thickness P25 =12μm, NR = 3μm).

The light reflection spectra of the three electrodes are shown in Figure 3b. All TiO_2 electrodes showed a max reflectance at 450 nm. The nanorod coated electrode showed 90% light reflectance, assumedly because of the unique highly-reflective tetragonal nanorod. However, the reflectance for the nanoparticle electrode was only 23%. Although the nanorod in the bilayer electrode was only 3 μm in thickness, it considerable enhanced the reflectance of the electrode, reaching up to 83% at the wavelength of 450 nm.

Figure 4a shows current density-voltage (J-V) curves of the DSSC devices made of those electrodes. For the device made of nanoparticle working electrode (thickness 15μm), the short-circuit current density (J_{sc}) was 10.3 mA/cm^2. Reducing the nanoparticle layer thickness led to a slight decrease in the J_{sc} value (to 9.98 mA/cm^2), but increase in the conversion efficiency from 4.68% to 5.11%, due to the decreased open-circuit voltage (V_{oc}).

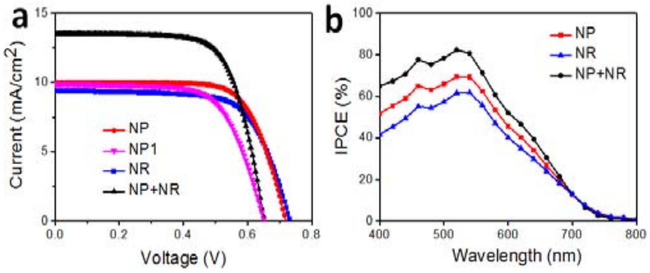

FIGURE 4. (a) *J-V* and (b) IPCE curves of the DSSCs made of NP (thickness, 12μm commercial P25 nanoparticles), NP1 (15μm commercial P25 nanoparticles), NR (15μm TiO_2 nanorods), or NP+NR (12μm P25, 3μm nanorods) working electrodes.

However, when the 12 μm thick nanoparticle layer was covered by a 3 μm nanorod layer, the solar cell efficiency was increased to 6.22%. For the electrode made of only nanorods, the conversion efficiency was only 4.3%, which was lower than the others.

Figure 4b shows the incident photon-to-current conversion efficiency (IPCE) of the DSSC devices. All three devices had a maximum efficiency at the wavelength of 520 nm, representing the maximum absorption wavelength of the N718 dye (4). The nanorod-DSSC device had the lowest IPCE value, while the quantum efficiency for the nanoparticle/nanorod DSSC device was the highest among the three devices. This suggests that the ability to convert incident photons for the DSSC device made of nanoparticles having a thin layer of nanorod scattering layer was better than that of the pure nanoparticle and nanorod devices.

CONCLUSIONS

Crystal TiO_2 nanorods were prepared and used as scattering layer for improvement of DSSC performance. A thin layer of nanorods on nanoparticle working electrode can enhance the conversion efficiency by more than 1%.

KEYWORDS

Hierarchical nanofibers, electrospinning, hydrothermal treatment, TiO_2, dye-sensitized solar cells

REFERENCES

1. M. A. Green, K. Emery, Y. Hishikawa, W. Warta, E. D. Dunlop, *Progress in Photovoltaics: Research and Applications.* 20, 606 (2012).
2. S. Hore, C. Vetter, R. Kern, H. Smit, A. Hinsch, *Solar Energy Materials and Solar Cells.* 90, 1176 (2006).
3. G. Dai, et al. *Journal of Alloys and Compounds.* 539, 264 (2012).
4. Y. Bai, et al. *Advanced Materials.* 24, 5850 (2012).

Process Control of High-Throughput Core-Sheath Electrospinning from a Slit Surface

Xuri Yan, Quynh Pham, John Marini, Robert Mulligan, and Toby Freyman
Arsenal Medical, Inc., Watertown, MA, USA
tfreyman@arsenalmedical.com

OBJECTIVE

Evaluate process parameters and fixture design that control core-sheath electrospinning from a slit-surface.

INTRODUCTION

We have developed a novel electrospinning system capable of producing core-sheath fibers with up to 400-fold increase in volumetric throughput relative to typical needle approaches. This significant improvement in manufacturing rate will help realize the tremendous potential of core-sheath nano and micro fibers for drug delivery/tissue engineering [1], self-healing coatings [2], filters [3], and super-hydrophobic materials [4]. Previously, we have introduced and described this novel technology, demonstrating that control of core-sheath Taylor cone morphology was impacted by the flow velocity and viscosities of the sheath and core solutions. Here, we explore further the capability and functionality of this technology by investigating the impact of applied voltage and fixture design on slit-surface core-sheath electrospinning.

EXPERIMENTAL

The high-throughput electrospinning fixture consists of two triangular shaped troughs that are aligned to a single vertical plane to form a slit-surface (Figure 1). The core slit is set to be slightly below that of the sheath slit. Core and sheath polymer solutions are delivered to the slits through their respective fixtures by applying precise control of pneumatic pressure, ensuring consistent flow rates. The fixture itself is connected to a high voltage source for generation of an electric field. We performed experiments to evaluate the effects of varying the (1) sheath slit width and (2) voltage. The core solution comprised of a 12 wt% polycaprolactone in 6:1 (by volume) chloroform:methanol containing 30% dexamethasone relative to the polymer. For the sheath slit width experiment, the sheath polymer solution was a 3.5 wt% 85/15 poly(lactic-co-glycolic) acid in hexafluoroisopropanol (System A); for the voltage experiment, we used both System A and a 12 wt% polycaprolactone in 6:1 (by volume) in chloroform:methanol (System B) (this system results in a more stable process, allowing for better determination of the impact of voltage). Unless stated otherwise, the sheath and core solution flow rates were set constant to 200 and 20 ml/h, respectively.

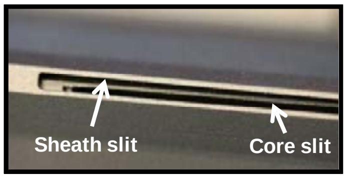

Figure 1. One-dimensional core and sheath slit-surface formed from aligning two fixtures each containing a length-wise slit.

RESULTS AND DISCUSSION

Coaxial electrospinning has garnered a lot of attention within the past decade. While core-sheath electrospun fibers have a tremendous amount of potential, manufacturing challenges limit successful commercialization. We believe that the slit-fixture technology provides an avenue to overcome this challenge by allowing for high throughput processing of core-sheath fibers. However, a comprehensive understanding of the slit-fixture technology is required to maximize its potential. Previously, we demonstrated that formation of distinct core-sheath Taylor cones from the slit-fixture could be manipulated by solution flow velocities and viscosities [5]. Here, we demonstrate that the fixture design and voltage impact process stability and subsequently, core-sheath Taylor cone formation.

Sheath slit width. We investigated the impact of changes in the width of the sheath slit on Taylor cone formation. Specifically, we evaluated electrospinning with three different sheath slit widths (1.5, 2.2 and 3.0mm), while keeping all other parameters constant. For all three designs, the flow rate conditions used satisfy the flow velocity criteria required for core-sheath Taylor cone formation that we established previously (i.e. i.e. $v_{total} > v_{coree}$). Distinct core-sheath Taylor cone formation was not observed from the 3 mm wide slit (Figure 2), while the two smaller slit-width designs

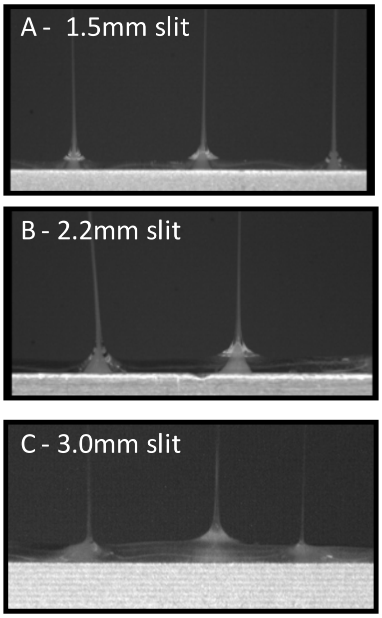

Figure 2. Images depicting distinct (A, B) and non-distinct (C) core-sheath Taylor cones emitted from sheath slits of different widths as indicated.

performed as expected. We believe that at a given voltage, a wider slit results in a lower local electric field that diminishes its ability to overcome the viscous forces and surface tension of the solution; as a result, less stable, non-distinct core-sheath Taylor cones are formed. Interestingly, however, we were able to achieve distinct core-sheath Taylor cones from the 3 mm sheath slit by reducing the core flow rate from 20 ml/h to 10 ml/h. The data to date suggest that multiple, inter-dependent variables (solution flow rates, viscosity, and fixture design) exist that can be leveraged to control core-sheath Taylor cones emitted from a slit-surface.

Voltage. In needle electrospinning, a critical voltage is required for the repulsive electrical forces to overcome the solution surface tension and cause jet initiation; at voltages below this critical voltage, electrospinning does not occur. We performed an experiment to determine the impact of applied voltage on slit-surface electrospinning and found that with System B, increasing the voltage led to an increase in the number of jets emitted per unit length of the slit-fixture (Figure 3A). As the applied voltage increased from 65 to 90 kV, the number of electrospinning jets increased from 8 to 12. Similar results were observed when System A was used (Figure 4). When the applied voltage was set at 55 kV, only 2-3 unevenly spaced jets emitted across the slit-surface and electrospinning performance was poor, evidenced by a lack of good fiber collection; approximately 6 jets were observed at 65 kV; and at 75 kV, a total of 7-8 evenly spaced jets were emitted across the slit surface and electrospinning became more stable, allowing better visualization of core-sheath Taylor cones. These results suggest that a critical voltage is necessary to initiate a requisite number of electrospinning jets across the length of the slit for stable electrospinning to occur. We hypothesize that electrospinning from the slit-fixture becomes compromised, in part, when the number of jets are not in their equilibrium state.

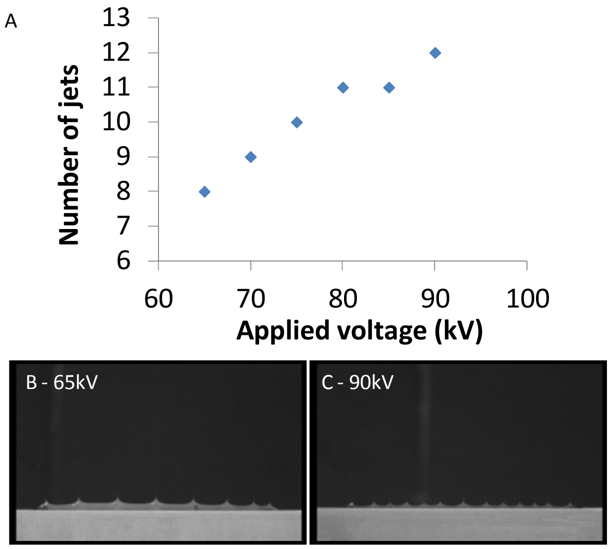

Figure 3. (A) Graph illustrating number of jets along the slit-surface as a function of applied voltage using System B. (B, C) Digital images depicting emitted jets from slit-surface at 65 and 95 kV, respectively.

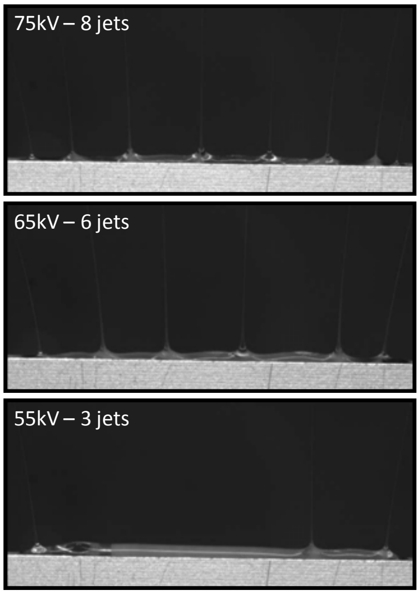

Figure 4. Impact of applied voltage on number of emitted jets from slit-surface using System A.

The data that we have collected on core-sheath slit-surface electrospinning to date indicates that many of the variables (flow rate, viscosity, voltage, etc.) that impact needle electrospinning also influence slit-surface electrospinning. In particular, these multiple variables define and bound specific operating regimes where electrospinning can occur; an understanding of the operating regime and how the multiple variables are inter-related can facilitate process optimization.

CONCLUSION

We have developed a slit-fixture that is capable of producing core-sheath fibers. To date, we have identified solution flow rates, viscosity, voltage, and fixture design as important factors impacting core-sheath electrospinning from a slit-fixture. We expect to utilize these variables to optimize the core-sheath slit-surface electrospinning process for different material systems. Furthermore, a complete understanding of the slit-surface electrospinning technology will help facilitate the successful commercialization of core-sheath fiber across a broad range of applications.

ACKNOWLEDGMENT

This work was performed under the support of the U.S. Department of Commerce, National Institute of Standards and Technology, Technology Innovation Program, Cooperative Agreement #70NANB11H004.

REFERENCES

1. Meinel, A.J., et al. *Eur J Pharm and Eiopharm*. 2012. 81(1): p. 1-3.
2. Park, J.H. and P.V. *Braun. Adv Mater*, 2010. 22(4): p. 496-9.
3. Moghe, A.K. and B.S. Gupta, *Polym Rev*, 2008. 48(2): p. 353-77.
4. Han, D. and A.J. Steckl. *Langmuir*, 2009. 25(16): p. 9454-62.
5. Yan, X., et al. in The Fiber Society. 2012. Boston, MA.

Structure and Properties of Melt Blown Submicron Fiber Nonwoven

Wanli Han[2] and Gajanan Bhat[1]
[1]The University of Tennessee, Knoxville, TN 37996, USA
[2]College of Textiles, Donghua University, Shanghai 201620, People's Republic of China
gbhat@utk.edu

ABSTRACT

Melt blown submicron fibers have been produced by two different multi-holes dies using commercially available polymers on a pilot line. The results showed it was a major step in melt blowing technology to produce nano-scale fibers. Mean fiber diameters (MFD) along with fiber diameter distribution have been studied. Besides, the web structure, properties have been studied in terms of the relationships among pore size and distribution, permeability, fiber diameter and the processing conditions. These results reveal that the air pressures significantly influences the fiber diameter and its distribution. Furthermore, the pore size and pore size distribution are strongly associated with fiber diameter. The current study can provide a general understanding of the nanofiber structure of melt blown webs for commercial production.

INTRODUCTION

Melt blowing continues to be one of the most popular processes to make super fine fibers on the micron or sub-micron scale. In the melt blowing process a thermoplastic polymer is extruded through a die and is rapidly attenuated by the hot air stream to fine diameter fibers [1]. The attenuated fibers are then deposited on a collector screen to form a fine fibered, self-bonded web. The combination of fiber entanglement and fiber-to-fiber bonding provides enough web cohesion so that the web can be used without further bonding. Melt blown fibers generally have diameters in the range of 2 to 5 µm. Due to the large fiber surface area of the meltblown fabrics, they are used in filtration, insulation and liquid absorption applications. Because of the simplicity of the process, any thermoplastic fiber can be melt blown.

Future growth and diversification of the melt blown nonwovens depend on the capability to produce nonwoven fibers with average fiber diameters less than 1 um, commonly referred to as nanofibers [2]. Although true definition of nanofibers requires diameters to be less than 100 nm, in the textile and nonwovens industry, submicron fibers are referred to as nanofibers. The biggest challenge for melt blown nonwoven is to reduce fiber diameters under the commercial melt blowing process conditions. Recently, more and more researchers are focusing on the melt blowing technology, which could be extended to nano-scale fiber sizes, as it would be provide a much easier, faster and cheaper method unlike other technologies to produce nanofibers. Lately, it has been shown that it is possible to produce submicron fibers with minor modifications to the existing meltblowing equipments [3, 4].

In this paper, we studied the nano-scale melt blown fiber diameter and distribution with different multi-hole dies under commercial processing conditions and also evaluated the fabric structure, such as mean pore diameter and air permeability. These studies can provide a general understanding of the nanofiber structure of melt blown webs for commercial production.

EXPERIMENTAL

A commercial grade polypropylene (PP) resin produced by Exxonmobil Chemical Company was melt blown using the six-inch (15.2cm) wide melt blowing line. The process conditions for the melt blowing trials were chosen based on melt temperature and melt flow index of the resin in order to produce submicron fibers. AGR die and Hill die were used to produce submicron fibers. The melt throughput was relatively lower for the nanofiber die. Air rates and die-to-collector distances (DCD) were chosen to produce small fibers and webs with soft hand. The melt and air temperature, throughput and collector speed were held constant.

The samples were characterized for various properties (basis weight, thickness, air permeability, pore size and fiber diameter). Basis weight was recorded by weighing 10 samples of each web at 1/100th of a square meter. The result is expressed in *gsm* (gram per square meter). The thickness was measured using the ASTM standard D5729-97. Air permeability was measured using a TexTest air permeability tester according to ASTM D737-96. The pore size was measured using the PMI porometer (Model CFP- 1100-AEX). From the SEM macrographs, fiber diameters were quantitatively measured using an automated image analysis based software.

RESULTS AND DISCUSSION

The fiber diameter is of great interest. Whereas in the regular meltblowing, the fiber diameters were in the expected range of 3-5 microns, nanofiber die allowed the production of submicron fibers. SEM photographs in figure 1 show that the majority of the fibers are under a micron in diameter.

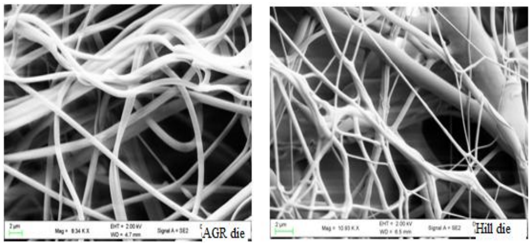

Figure 1. SEM image of melt blown fibers taken at 2.00Kv for AGR and Hill die.

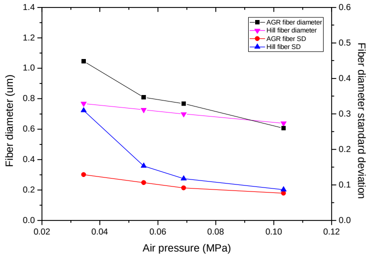

Figure 2. Melt blown fiber diameter and standard deviation.

These data show that the trend is for producing melt blown webs with smaller and more uniform fiber diameters at higher air pressure for the dies. Both experimental and theoretical studies have reported that mean fiber diameter decreases when airflow rate increases [5]. It indicated that it was possible to significantly decrease the average fiber diameter under to 1 um with the multi-hole die using commercially viable processing conditions.

Table I. Properties of melt blown webs.

Sample No.	Air pressure (MPa)	Thickness (mm)	Air permeability (cm^3/s/cm^2)	Pore size (um)
AGR1	0.034	0.61	75.79	13.44
AGR2	0.055	0.70	55.47	11.65
AGR3	0.103	0.57	95.05	10.19
Hill1	0.034	0.45	37.93	14.80
Hill2	0.055	0.44	22.14	11.30
Hill3	0.103	0.40	27.31	10.13

Some of the properties for the samples produced with the nanofiber die are shown in table1. The observation of data has confirmed that the thickness of webs produced from AGR die is higher than those from the Hill's die. The Hill's die had 24 holes per cm while AGR die had 14 holes per cm. With the same throughout and melt blowing processing condition, the initial number of fibers from the die is different. For Hill's die, the finer fibers and coarser bundles can influence the properties. Because of the same mean pore diameter, the higher thickness means that the web is loose and has more pore volume. According to the air permeability test, it shows that the air permeability of webs from AGR die is much higher than that from Hill's die. Air pressure has an important role and influences fiber entanglement, fiber diameter and pore size.

CONCLUSIONS

Submicron fibers were produced by two different multi-hole dies with different processing condition using a melt blown pilot line. The fiber diameter and diameter distribution results demonstrate that the air pressure influences the fiber diameter significantly. The nanofiber web produced using different dies have similar mean pore size but different air permeability. This is due to different fiber movement and entanglement because of different number of holes in the dies and their interaction under various air pressures.

ACKNOWLEDGMENTS

Wanli Han's stay at UTK was supported by DongHua University special PhD International Program. Authors are thankful to Hills, Inc and AG Russell for providing the dies, and ExxonMobil Chemical Company for providing PP resin.

REFERENCES

1. Bhat, G. S. and Malkan, S. R. Extruded Continuous Filament Nonwovens: Advances in Scientific Aspects. *Journal of Applied Polymer Science*, Vol 83, 572-585 (2002).
2. Tan D. H., et al, Meltblown Fibers: Influence of Viscosity and Elasticity on Diameter Distribution. *J Non-Newton Fluid*, Vol 165, 892-900 (2010).
3. Bhat, G. S. and Uppal, R., Nanofiber Nonwovens: Importance, Properties, Productions Technologies and Applications. *Proceedings of the Beltwide Conference,* New Orleans, LA, January 2010.
4. Bhat, G. S., Uppal, R. and Eash, C., Ultrafine Meltblown Fibers for Next Generation Filtration Applications. *Proceedings of the INTC*, Denver, CO, Sept 21-24, 2009.
5. Lee Y. and Wadsworth L. C. Effects of Melt-blowing Process Conditions on Morphological and Mechanical Properties of Polypropylene Webs. *Polymer*, Vol 33, 1200-9 (1992).

Electrospun Nanofibers for Blood Vessel Tissue Engineering

Xiumei Mo, Anlin Yin, Chen Huang
Faculty of Chemistry, Chemical Engineering & Biotechnology, Donghua University, Shanghai, China
xmm@dhu.edu.cn

INTRODUCTION

Electrospinning is a versatile technique, which can generate fibers with diameter ranging from nanometer to microns. The electrospun fibrous structures possess a large surface area to volume ratio, high porosity, and potential for mimicking the structure and function of natural extracellular matrix (ECM). It has been developed for different tissue engineering application, like skin, nerve, blood vessel, bone and cartilage. In this paper electrospinning nanofiber will be used for small diameter blood vessel tissue engineering. Many natural materials (collagen, chitosan and silk) and synthesis polymer (PLA, PCL and P(LLA-CL)) have been electrospun into nanofibers. But the natural materials nanofibers are week in mechanical strength, and the synthesis polymer nanofibers are poor in biocompatibility, here collagen-chitosan-P(LLA-CL) blend nanofibers will be fabricated as blood vessel scaffold to achieve both good biocompatibility and mechanical strength. Coaxial electrospinning was used to spin heparin in the core of the nanofiber to give the tube scaffold anticoagulation properties. The nanofiber tube scaffolds were also implanted into femoral artery of dog for blood vessel tissue regeneration.

APPROACH

Electrospinning nanofibers

Collagen and P(LLA-CL) were dissolved in HFP, while chitosan was dissolved in HFP and TFA (v/v, 9:1) all at weight concentration of 8%. The three solutions were blended at different volume ratios of collagen-chitosan-P(LLA-CL) and used for electrospinning to collect the nanofiber membrane by a aluminum foil or to collect the tubular scaffolds by rotating stainless steel mandrel.

Coaxial electrospinning

The core solution was obtained by adding 0.03, 0.06 and 0.12g heparin in 10 ml distilled water, and the shell solution by resolving 0.6g P(LLA-CL) in 10ml TFE. Through the stainless steel co-axial needles the core solution (heparin) was injected at the flow rate of 0.1 ml/h and the shell solution (P(LLA-CL)) was injected at the rate of 0.8 ml/h to generate the heparin- P(LLA-CL) core-shell nanofibers

Tensile testing

For mechanical testing, five nanofiber specimens (30x10 mm, n=6) were prepared, Mechanical properties were determined by a universal materials testing machine (H5K-S, Hounsfield, England) at ambient temperature and a relative humidity of 65% with an elongation speed of 10 mm min^{-1}. Before testing, all samples were soaked in PBS for 2 h.

Burst pressure

Burst strength testing of electrospun tubes was use the device designed in accordance with section 8.3.3.3 of ANSI/AAMI VP20:1994.31. Tubes, 4 cm in length, hydrated in PBS for 12h were then fixed in the device, pressurized air was introduced into the system, increasing the pressure at a rate of 5mmHgs^{-1} until the tubes ruptured. Results were recorded as the pressure (mmHg) at which the structures ruptured.

Heparin release test

PLLACL nanofibrous mats loaded with different weight ratios of heparin were suspended in PBS (pH 7.4) solution in sealed 6-well plates. Three nanofibrous mats, each weighing 100 ± 5mg, were each soaked in 3.0ml PBS (pH 7.4). Fibrous mats were incubated under static conditions at 37^{o}C in the presence of 5% CO2. At various time points, 1.0 ml supernatant was retrieved from the wells and an equal volume of fresh medium was replaced. The concentration of each retrieved heparin solution was then determined by toluidine blue method. Toluidine blue (3.0 ml) was added into the supernatant which was retrieved from the wells and reacted adequately with heparin for 2 h at 37^{o}C. Hexane (3.0 ml) was then added, and stirred vigorously to separate the heparin-toluidine blue complex formed. The aqueous solution of the samples was tested at 630 nm by an Agilent UV-Vis spectrophotometer (WFH-203B, PerkinElmer, USA).

Implantation

Eight Beagle dogs were anaesthetized by intravenous injection of sodium pentobarbital (30mg/Kg). Segments of the femoral arteries (4cm in length) were removed bilaterally while both sides of the arteries were clamped. The pre-treated 3cm length P(LLA-CL) and heparin-P(LLA-CL) vascular grafts were then separately implanted into the right and left femoral arteries using 7-0 Prolene sutures. The incision was sealed carefully with 4-0 silk sutures. All the dogs were given oral asprin at a dosage of 300 mg/day on the day of surgery and the next 7 days thereafter.

One week, two weeks, one month and three months after graft implantation, DSA and CDFI were performed repeatedly to visualize the patency of the implanted scaffolds. At the end of three months, the animals were killed humanely by overdosed pentobarbital and the implanted grafts were extracted for the histological analyses.

RESULTS AND DISCUSSION

The morphology of different ratios of collagen-chitosan-P(LLA-CL) fibers were observed by SEM as shown in Fig.1A, the nanofibers have the average diameter of 330± 46nm. Fig. 1B showed the P(LLA-CL) nanofiber tube scaffolds with the inner diameter of 3mm, which can be used for implantation in femoral artery of dog.

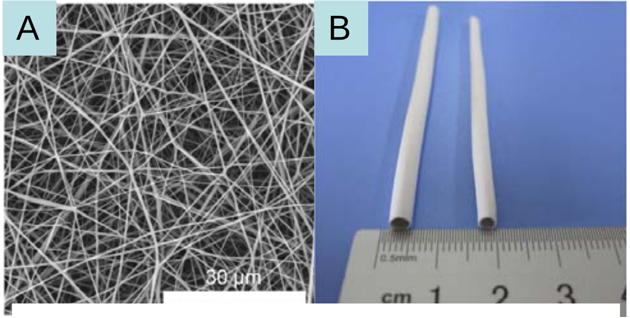

Fig. 1 A.SEM of electrospun collagne-chitosan-P(LLA-CL) nanofibers, B. P(LLA-CL) nanofiber tube scaffolds photo.

Mechanical properties

Fig.2 showed the mechanical properties of collagen-chitosan-P(LLA-CL) nanofibers with different blend ratios. Pure P(LLA-CL) nanofibers is elastic(Fi.2A), with the small amount of natural materials addition the tensile strength of the blend nanofibers increased to 17MPa at collagen:chitosan:P(LLA-CL) ratio of 20:5:75(Fig.2B), the elastic modulus at this blend ratio was also reached the most biggest at 11MPa(Fig.2D), the elongation at break still can keep 110%. But when the natural polymer content exceed the 50% the mechanical properties of the blend nanofibers decreased a lot. So collagen-chitosan-P(LLA-CL) nanofibers (20:5:75) is good for vascular graft fabrication. The burst strength of the nanofiber vascular graft at this blend ratio was also reached the biggest at 3300mmHg(Fig. 3).

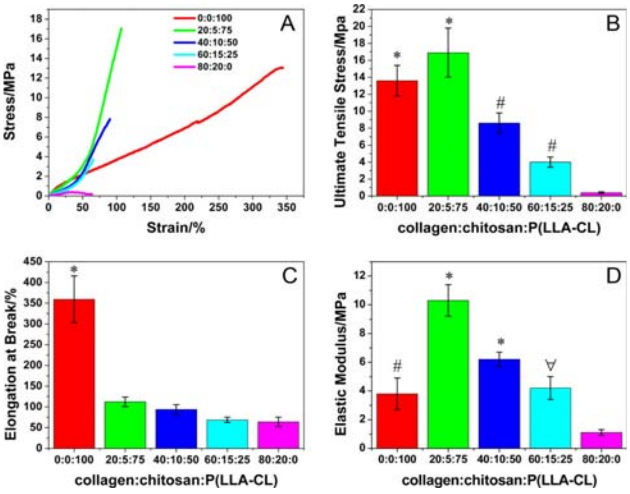

Fig. 2 The mechanical properties of collagen-chitosan-P(LLA-CL) nanofibers with different blend ratios. A.Stress-strain curves, B. Tensile strength, C. Elongation at break, D. Elastic modulus.

Heparin release

Heparin release profiles from coaxially electrospun PLLACL nanofibers with different heparin proportions are shown in Fig.3. The release processes for electrospinning cases can be illustrated by two stages: an initial fast release (stage I) followed by a constant release (stage II). In stage I, there were initial burst releases from electrospun mats and the amount was 20–45%. The whole release process went on for 14 days, until the total amount released was about 70%.

Animal testing

Nanofiber vascular graft implanted in femoral artery as in Fig.5. Fig. 5B showed the Digital Subtraction Angiography (DSA) and Color Doppler Flow Imaging (CDFI) of the blood inflow into the arteries. Blood flow was blocked when passing through the P(LLA-CL) graft, but passed through the heparin loaded graft smoothly with a clear blood flow being traced by CDFI. Based on the DSA results, patency rates at scheduled time points were summarized in Table I.

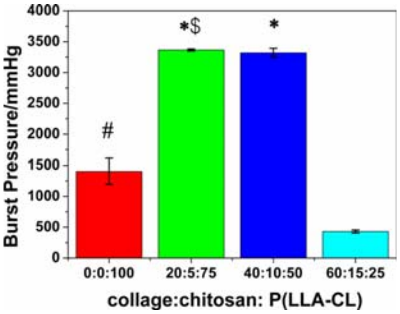

Fig. 3 Burst strength of nanofibers.

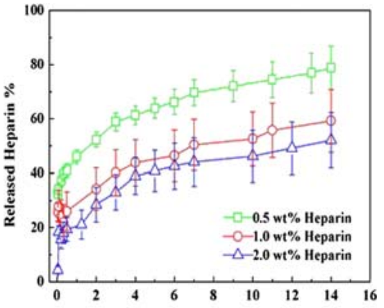

Fig. 4 Heparin release from nanofibers.

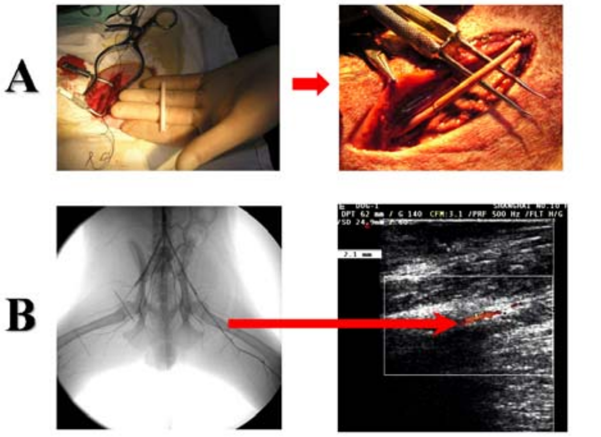

Fig. 5 A. Implantation of the electrospun tubular graft into the femoral artery of dog. B. Typical DSA and CDFI inspection of the implanted grafts after 3 months: the left femoral artery was replaced by heparin-loaded graft and the right one was replaced by P(LLA-CL) graft.

Table I Patency Rate of Vascular Graft

Vascular graft	Patency rate(%)			
	Week 1	Week 2	Month 1	Month 3
P(LLA-CL)	62.5	50.0	25.0	12.5
Heparin-P(LLA-CL)	100	100	75.5	75.5

Discretized Modeling of Whipping Motion During Electrospinning Process

An-Cheng Ruo and Yong Lak Joo
School of Chemical and Biomolecular Engineering, Cornell University, Ithaca, NY, USA
ylj2@cornell.edu

ABSTRACT

The discrete element method (DEM) has been regarded as a potentially efficient approach to the simulation of electrospinning (ES) nanofibers process. By this method, the behaviors such as the whipping motion and the beads-on-string phenomena can be simulated with much higher efficiency than any field-based approach. However, the accuracy and reliability depend on how completely the modeling describes the underlying physics and how high the numerical resolution can be achieved to capture the finer motions. Through comparison with the experimental observations on the initial stable jets, our recent study (2011 JAP) has established the basis for an enhanced modeling of the complete electrospinning process. Now, we further modify the formulas and propose several numerical skills to make the simulation more realistic. We validate the model by comparing with the experiments, especially for the onset of instability and its subsequent growth of disturbances in the nonlinear regime. Then the emergence of beads is predicted and the whipping motions under various operation conditions are also demonstrated by animations. Realistic trajectories imply that DEM can serve as a predictive tool for ES process.

INTRODUCTION

Electrospinning (ES) is a common process that people use to create polymer nanofibers for various industrial or commercial purposes.[1] In the process, a polymeric liquid jet is ejected from a needle nozzle to the air via electrification at a high voltage. Subjected to the electrical force, the liquid is accelerated and a meniscus is formed at the end of the nozzle, in which the charges are transported via electrical conduction and accumulate on the surface due to electrostatic repulsion. The accumulation of surface charges induces the electrical stresses acting on the liquid surface, whereby the jet becomes unstable to small disturbances, which either leads to the axisymmetric varicose instability or develops the bending motion at the downstream. The latter provides an effective process to rapidly elongate the fibers. It is well known that the field-based analysis via continuum mechanics (ex. computational fluid dynamics, CFD) is very difficult to describe such a free surface flow of high aspect ratio. A very large number of spatial grids are required to implement the numerical calculation. Especially when complex polymer rheology is taken into account, the nonlinear constitutive equation usually results in the numerical divergence. While the continuum approach is invalid to ES process, a meshfree particle-based method must be adopted. The discrete element method (DEM) is a particle-based method which was originally developed for the simulation of granular flow system and latter applied to the fracture mechanics for brittle materials under impact loading. Recently, it has become a promising approach for the simulation of rapidly whipping motion in the ES process.[2] In this approach, the liquid jet is considered as a series of discrete charged particles connected by viscoelastic springs. The method allows the 3-D curvilinear path to be predicted by tracking each of the particles in Lagrangian description, which significantly reduces the degree of nonlinearity. Since no geometric grid is required beforehand, DEM is much more efficient and numerically more stable than the field-based methods in the simulation of electrospinning process. In spite of progresses made by the previous works,[2-7] some issues remain unresolved. For example, the poor resolution at the downstream have lost the ability in capturing the finer behaviors, such as the self-similar fractal-like motion.[1,2] To provide a quantitative and reliable prediction, it is necessary to establish a comprehensive modeling and a more robust numerical scheme. In this study, we attempt to improve the modeling by modifying the formulas, such as surface tension, viscoelastic stress, the charge transport, and the aerodynamic drag. Furthermore, we will propose a new skill to improve the numerical resolution so as to make the simulation more realistic. Then, we validate the modeling by investigating the onset of axisymmetric instability to predict the emergence of beads. Finally, results will be compared with experimental observation.

MODELING AND SIMULATION PROCEDURE

The modeling procedure is basically similar to our previous work.[7] The jet ejected from the nozzle is considered as a sequence of viscoelastic dumbbell elements. The mass corresponding to the element is condensed on the particle. Each particle moves according to the Newton's equation of motion. The formulas including viscoelastic force, surface tension, gravity, electrical force, and the aerodynamic drag force resulted from the ambient air are taken into account. the viscoelastic stress is described by using the discretized form of Oldroyd-B or Giesekus model, which consists of two distinct contributions, one from a viscoelastic dumbbell, and the other from a Newtonian solvent in which macromolecules are immersed. Note that the term associated with the upper-convected time derivative was lost by our previous study, but now it is included. The formula for surface tension is also modified by including the capillary force along the axial direction, whereby the axisymmetric instability can be predicted. The aerodynamic drag resulted from the relative motion between the fiber and the ambient air has a significant effect during the electrospinning process especially when the instability takes place. In this study, we employ the formulas proposed by Wang *et al.*[5,6] to account for the drag. To describe the effect of electrification via the discrete model, we assume that each of the particles is carrying a charge which interacts with the electric field to induce an electrical force. The electric field consists of the two parts: (1) the external electric field caused by all electrified environmental facilities; (2) the electrostatic field induced by the other particles. The conservation of free charge is considered to determine the charge carried by each particle. In most experimental setup, a needle-plate configuration of electric field is used. For simplicity, we use the mirror-image method to represent the external field. This approach is to deposit a positive pointwise charge at the nozzle and the other negative charge on the opposite side of the grounded collector plate. The faked charge is then estimated by assuming that the electric field at the plate created by the two faked charges is equal to the uniform field caused by the potential difference between needle and the plate.

The simulation procedure is described as follows. First of all, a single particle is introduced into the system with zero initial velocity. The particle is charged by the applied electric field and then accelerated to move downward. The elongation of element will induce the viscoelastic stress to resist the electrical force. However, there is no upstream particle for the newly-inserted particle to calculate the element length and the strain rate. To describe the elongation, we must fake a imaginary particle following the real particle. The position of faked particle must be updated according to at the velocity calculated by the flow rate. Then, the length of element is determined by calculating the distance between the faked and the real particles. By this method, we can describe the drawing-back effect resulted from the liquid in the nozzle. Furthermore, if no solvent is evaporated in the process, the radius can be determined by using the conservation of mass. Once the particle travels a certain distance away from the nozzle, a new particle is inserted into the system. This process is repeated to create several hundred particles so as to mimic the continuous jetting behavior. For the particles arriving at the collector, we will cancel them out from the computer memory.

To simulate the 3-D bending motion, we must impose a lateral disturbance at the nozzle because the instability cannot occur spontaneously via the discretized modeling. However, as the distance between the particles increases downstream, the resolution will decrease and finally loss the capability of describing finer behaviors. Low resolution may induce numerical instability. Here, we develop a numerical skill to improve the resolution. This method is to separate the elements which are longer than the critical length. When the separation occurs, we insert a new particle into the element (locating at the middle). The new particle must share the mass, charge and momentum of the old particle. Normally, a smaller critical length can capture the finer motion at the further downstream with a higher resolution.

RESULTS AND DISCUSSION

The typical simulations for viscoelastic Boger fluids are shown in Fig. 1, in which we impose a periodic lateral disturbance on the top particle. The charge transport via conduction is found to be the key factor that enhances this kind of whipping motion (because low-conductivity liquid always causes a straight jet). In particular, we also observe some phenomena such as the varicose instability both from the inset of Fig. 1(a) and Fig.1(b). This instability may be caused by the conducting mode induced by electrical conduction.

(a)

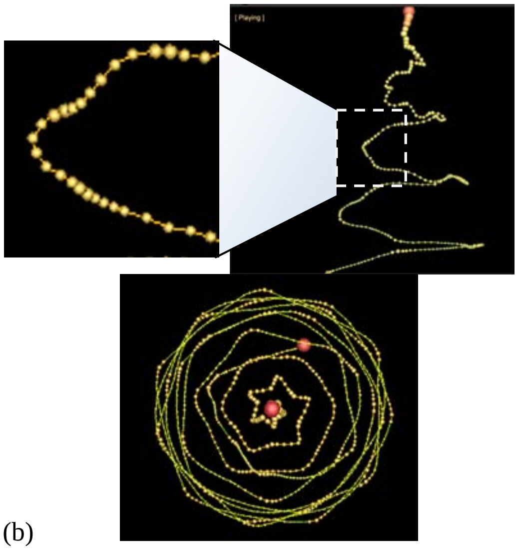

(b)

Fig. 1. Snapshot of the trajectory of a highly conducting liquid jet during electrospinning predicted by discretized modeling: (a) side-view; (b) top view.

CONCLUSIONS

We have improved the method to the simulation of ES process. The unsteady 3-D fiber motion with smoother contour is captured and the finer behaviors are observed. The results inspire us to develop a more comprehensive modeling for other fiber spinning processes.

REFERENCES

[1] D. H. Reneker and A. L. Yarin. Electrospinning jet and polymer nanofibers. *Polymer* 49, pp 2387-2425 (2008).

[2] D. H. Reneker, A. L. Yarin, H. Fong, and S. Koombhongse. Bending instability of electrically charged liquid jets of polymer solutions in electrospinning. *J. App. Phys.* 87, No. 9, pp 4531-4547 (2000).

[3] A. L. Yarin, S. Koombhongse, and D. H. Reneker. Bending instability in electrospinning of nanofibers. *J. App. Phys.* 89, No. 5, pp 3018-3026 (2001).

[4] S. A. Theron, A. L. Yarin, E. Zussman, and E. Kroll. Multiple jets in electrospinning: experiment and modeling. *Polymer* 46, pp 2889-2899 (2005).

[5] Y.-C. Zeng, Y. F. Sun, and X. H. Wang. Numerical approach to modeling fiber motion during melt blowing. *J. App. Polymer Sci.* 119, pp 2112-2123 (2011).

[6] Y. F. Sun, Y.-C. Zeng, and X. H. Wang. Three-dimensional model of whipping motion in the processing of microfibers. *Ins. Eng. Chem. Res.* 50, pp 1099-1109 (2011).

[7] C. P. Carroll and Y. L. Joo. Discretized modeling of electrically driven viscoelastic jets in the initial stage of electrospinning. *J. App. Phys.* 109, 094315 (2011).

Posters

Performance of Flame Retardancy Silk Modified with Water Soluble Vinyl Phosphoamide

Jinping Guan, Guoqiang Chen
College of Textile and Clothing Engineering, Soochow University, Suhzou, Jiangsu, China, 215006
guanjinping@suda,edu.cn; Chenguojiang@suda.edu.cn

INTRODUCTION

Silk is widely used for interior decoration fabrics such as wall coverings, curtains, silk flowers, furniture covers, bedding etc. Such products should be treated with flame retardant to meet requirements of fire regulations in local countries. But now there is lack of effective and durable flame retardant for silk. In previous research, we developed a kind of vinyl phosphate dimethyl-2-(methacryloyloxyethyl) phosphate (DMMEP) for silk and can get durable flame retardancy effect [1]. DMMEP is effective, but the compounds have no commercial products so far. Nitrogen contained compounds have synergism flame retardancy effect with phosphorus based flame retardant [2]. In this paper, element nitrogen was introduced to DMMEP and aimed at producing phosphorus-nitrogen synergism flame retardncy effect. The synthesized new water soluble monomer named dimethyl(methacryloyloxyethyl)phosphoramidate （DMMEPN, seen in scheme 1）. Structures and properties of treated silk fabric were explored in this paper.

MATERIALS

Degummed and bleached silk fabrics (plain woven, 36g/m^2) were purchased from Suzhou HuaSi Silk Printing & Dyeing Co., Ltd. Phosphorusoxychloride, Methacryloyl Chloride, absolute methanol, absolute etheranhydrous, triethylamine(TEA) , methylene dichloride and potassium persulfate were purchased from Shanghai Qiangshun chemical reagent company, China. Monoethanol amine was purchased from Suzhou LianSheng chemical company. TEA was dried by CaH_2 overnight and distilled under reduced pressure before use. Other chemicals was used as received.

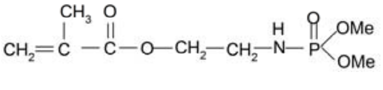

Scheme 1 DMMEPN

APPROACH

Synthesis of DMMEPN

Synthesized as our previous pape^{r}[3].

Fabric treatment procedure

The silk fabric (1g) was immersed into a reaction mixture containing DMMEPN *0.5g, 0.8g, 1g* respectively (the DMMEPN concentration is then 50%, 80% and 100% on the weight of fabric), potassium persulfate (KPS) 3% on the weight of DMMEPN, that is, 0.015g, 0.024g, 0.03g respectively and 30 ml deionized water in a 100 ml erlenmeyer flask, the pH value of the solution was adjusted to 3.5. Then the flask was sealed with a rubber-stopper and put into water bath under oscillating at 90℃ for 60 min. Then the sample was rinsed with methanol in a soxhlet extractor for 3h then followed by water, and finally dried at room temperature under vacuum to a constant weight.

Measurements

Weight gain (%) was calculated as follows:

$$weight\ \ gain(\%) = \frac{W_2 - W_1}{W_1} \times 100 \qquad (1)$$

where w_2 and w_1 are the weight of treated silk fabric and original fabric respectively.Limiting oxygen index (LOI) was measured according to ASTM Standard Method D 2863-97 on a Fire Testing Technology Oxygen Index Instrument. Char length was measured according to ASTM Standard Method D6413-99. Char residue was measured as follows: Weight silk sample W_1 and put into muffin oven at 600 °C for 10 min, and weight the char W_2, Char residue was calculated as follows:

$$char\ residue(\%) = \frac{W_2}{W_1} \times 100 \qquad (2)$$

Char residue morphology was observed by a scanning electron microscopy and the surface of char residues was sputter-coated with gold layer before examination.Thermal gravimetric analysis (TGA) was carried out from 40℃ to 600 ℃ on a 2960 SDT 290 TA instruments with heating rate of 10 ℃/min under the nitrogen atmosphere with flux 100 ml/min, and each sample was controlled to 5~7 mg in primary weight.

RESULTS AND DISCUSSION

Flame retardancy property

The flame retardancy properties of control and FR silk were listed in Table I. When the concentration of DMMEPN was 50%, 80% and 100 % on the weight of silk fabric, the weight gain of silk fabric could reach 8.43%, 13.09% and 24.22% respectively. And the LOI increased with the increasing DMMEPN add on. Only adding 50% DMMEPN, silk fabric could exhibit hard igniting property with a candle like fire with LOI of 29.34% and could pass the vertical flammability test with char length 66 mm. DMMEPN was more effective in flame retardancy for silk fabric than we previously reported . In previous research, silk fabric was treated with only phosphorus contained momomer. When DMMEP concentration is 100%, the LOI of silk fabric is 30.22% , while LOI of 31.75% for 80% DMMEPN treated silk fabric. Less DMMEPN add on could produce better flame retardancy property, which showed that the introduction of nitrogen atom could have synergism flame retardancy effect with phosphorus. Table I also showed that with the increasing weight gain, treated silk was prone to produce more char residue than DMMEP treated silk fabric and control fabric when combustion. This could be explained that P-N bond was more reactive in phosphorylation than P-O bond so that it could decompose more easily and was tend to promote silk produce more char during combustion.

Table I The flammability of control silk and FR silk.

FR	FR add on/%	weight gain/%	LOI/ %	char length/ mm	Char residue/ %
	0	0	23.2	BEL	0.9
DM MEP	50	7.5	26.2	120	1.5
	80	18.8	29.5	68	3.9
	100	27.2	30.2	50	5.2
DM MEP N	50	8.4	29.3	66	5.6
	80	13.1	31.8	44	5.8
	100	24.2	32.4	42	10.9

Note: BEL= Burn Entire Length; FR= Flame retardant

Char residue and its morphology

Figure 1 showed SEM pictures of the char residue formed from control (a) and FR silk (b) after incineration at 600℃ for 10 min.

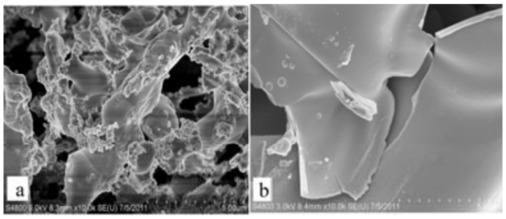

Figure 1Char residue morphology of control silk (a) and FR silk (b, weight gain 24.22%).

From the morphology of char residue, one could see very different appearance of the two pictures. Figure 5(a) showed more porous, loose, and fragile char of control silk, while the char of Figure 5(b) was more solid, rigid and surface intact. It could be inferred that the adding of flame retardant DMMEPN could reduce flammable volatile and prone to form more non-flammable char during combustion. So char of control silk had intumescent phenomenon while FR silk char not.

Thermal gravimetric analysis

Figure 2 showed the TG curves of control silk (a) and FR silk (b, weight gain 24.22%). Corresponding DTG curves could provide the data of decomposition stages and temperatures where maximum weight loss occurred. Thermal decomposition data collected from Figure 2 were listed in Table II. Figure 2 showed that FR silk appeared two significant areas of weight loss. Weight loss at T_{max} =238°C corresponding to the decomposition of flame retardant and 307°C for decomposition of silk itself. Control silk had only one significant weight loss area at T_{max} =327°C. The onset decomposition temperature at weight loss of 11% of FR silk shifted to a lower temperature with 10°C decrease.

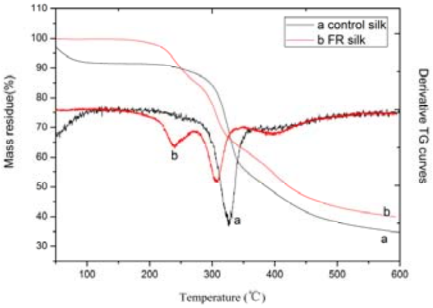

Figure 2 TG curves of control silk (a) and FR silk (b, weight gain 24.22%) in nitrogen atmosphere.

Table II Thermal analysis data collected from Figure 2.

Samples	T_d at weight loss of 11% (°C)	$T_{max}{}^{a}$ (°C)	Char residue at 600°C (%)
Control	263	327	34
FR silk	253	238, 307	40

Note: ^{a} From DTG curves

Decomposed flame retardant interfere with the burning process by catalyzing the dehydration of silk and form more non-flammable char, and the char was more stable than that of control silk, so at the end of decomposition at 600°C showed higher residue char percentage.

CONCLUSIONS

Dimethyl(methacryloyloxyethyl)phosphoramidate（DMMEPN）grafted silk fabric exhibited good flame retardancy with high LOI 32.38%, char length 42mm.TG and char residue morphology showed DMMEPN was more effective than DMMEP previously reported for its P-N synergism effect.

KEYWORDS

Silk; graft copolymerization; flame retardant; phosphoamidate monomer; P-N synergism

ACKNOWLEDGMENT

The authors thank for the funding support of National Nature Science Foundation of China (Grant No. 51003071).

REFERENCES

1. Guan Jinping, Chen Guoqiang. Graft Copolymerization Modification of Silk Fabric with an Organophosphorus Flame Retardant. *Fire and Materials*, 2010, 34(5): 261-270.
2. Hari T. Deo, Nagesh K. Bharat K., Bharat K. Eco-friendly Flame Retardant (FR) Pet Fibers Through P–N Synergism, *Journal of Engineered Fibers and Fabrics*, 2008, 3(4): 23-28.
3. Yang Yumei. A new flame retardant and its application on silk. *Synthesis Chemistry*, 2012, 20(6): 761-763.

The Preparation of Semi-Aromatic Polyamide Fibers

Ai Xin[2], Pingting Wu [2], Yumin Xia[2], Yan Ping Wang[1], and Yimin Wang[1]
[1]State Key Laboratory for Chemical Fiber Modification
[2]College of Material Science and Engineering, DongHua University, Shanghai China,201620
Contact author: 2110250@mail.dhu.edu.cn

Abstract With the rapid development of science and technology, stricter requirements are essential for heat resistance, dimensional stability and precision molding of the organic materials. In this work, appropriate polyamide raw material was selected. And suitable process parameters were adjusted for preparing semi-aromatic polyamide spun fiber by twin-screw extruder. Considering the impact on thermal and mechanical properties, heat treatment under 160□, 60 min was appropriate. And the melting point of post-treat semi-aromatic polyamide fibers was 300□, elongation at break, Young's modulus and tensile strength was 6%, 12.3 GPa and 0.77GPa respectively, which shows that post-processing can greatly improve mechanical properties of semi-aromatic polyamide fibers.

Instruction Because of the characteristics of the structure, semi-aromatic polyamide has excellent property [1]such as outstanding heat resistance, ageing resistance, electrical insulating property and mechanical property. Semi-aromatic polyamide is well appropriate for the production of heat-resistant parts and thin-wall products. It is mainly used in automobile industry and electronic industrials.[2] In this work, the effect of spinning and post heat treatment on fiber properties were discussed.

Results and Discussion

1.1 The property of semi-aromatic polyamide spun fiber

Figure 1(a) shows DSC of the fiber. As is shown, the semi-aromatic polyamide spun fiber began to melt at 260℃ and its melting point was about 292℃. Compared with the raw material, it made no obvious rise. Fiber1 (b) is TG and DTG of the semi-aromatic polyamide spun fiber. It shows that the weightlessness rate reached to the maximum at 490.2℃. Because of the aromatic ring in the chain structure, the fiber had good heat resistance and higher decomposition temperature.[3]

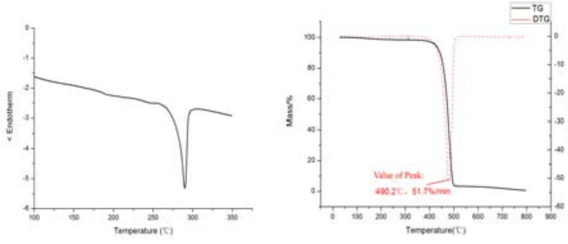

(a) (b)

Figure 1(a) DSC and (b) TG and DTG of the semi-aromatic polyamide spun fiber.

XN-1 fiber tensile tester was used to detect the mechanical properties of the fiber, the results are shown as follows:

Table I Mechanical properties of the fiber.

tensile strength (MPa)	Young modulus (MPa)	elongation at break (%)
357.85	5367.33	63.78

It shows that the tensile strength of the semi-aromatic polyamide spun fiber was 357.85 MPa, Young's modulus 5367.33 MPa, elongation at break 63.78%. However, the fiber's thermal and mechanical properties can't completely meet the need of the production without treatment. So heat treatment was needed to improve the fiber's crystallinity, orientation and its mechanical properties.[4]

1.2 The affect of heat treatment on fiber

1.2.1 The effect of heat treatment on fiber thermal properties

As is seen from Figure 2(a), with the increase of heating time, the melting temperature increased and at the same time, the melting heat enthalpy and the area of the peak grew larger. When the fiber was heated for 60min at 160℃, the melting point reached the highest and the thermal enthalpy and peak area also was the largest. Figure 2(b) shows that at the same heat treatment time, the fiber's melting point rose along with the heat treatment temperature and the melting thermal enthalpy and molten peak area also increased. After 160℃, when the heat treatment temperature continued to increase, instead, it would cause a downward trend to the melting point, melting heat enthalpy and molten peak area.

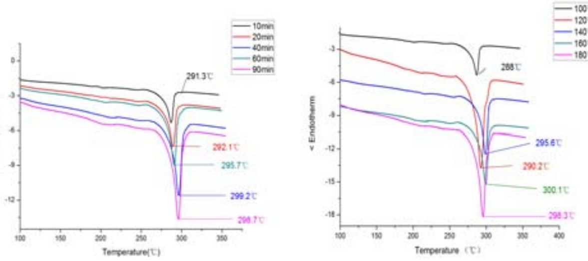

(a) **(b)**

Figure 2(a) DSC of the semi-aromatic polyamide spun fiber under different heating time at 160℃ (b) DSC of the semi-aromatic polyamide spun fiber under different heating temperature.

1.2.2 The effect of heat treatment on fiber mechanical properties

Table II shows that with the heat treatment time going on, the fiber elongation at break declined greatly, but the modulus and tensile strength were greatly improved. The modulus and strength increased to 12.31GPa and 760.03MPa respectively and the elongation at break declined to 6.2% when the fiber was heated for 60 minutes. Table□ shows when the heat treatment temperature reached 160□, the elongation at break was 6.2%, the modulus and strength increased to 12.23GPa and 781.03MPa respectively.

Table II Mechanical properties of the fiber at different time.

Heat treatment time (min)	Tensile strength (MPa)	Young modulus (GPa)	Elongation at break (%)
without treatment	357.8	5.4	63.8
10	622.8	9.5	9.1
20	660.9	10.3	8.7
40	692.7	10.8	7.6
60	760.0	12.3	6.2
90	749.9	11.9	6.6

Table III Mechanical properties of the fiber at different temperature.

Heat treatment temperature (℃)	Tensile strength (MPa)	Young modulus (GPa)	Elongation at break (%)
without treatment	357.85	5.37	63.78
100	525.83	7.57	10.3
120	620.69	9.37	9.2
140	688.8	10.48	7.9
160	781.03	12.23	6.2
180	744.15	11.98	6.4

Conclusion

The elongation at break of semi-aromatic polyamide fibers significantly decreased by heat treatment, while strength and modulus increased. Considering the impact on thermal and mechanical properties, heat treatment under 160℃, 60 min was appropriate. And the melting point of post-treat fiber was 300℃, elongation at break, Young's modulus and tensile strength was 6%, 12.3 GPa and 0.77GPa respectively, which shows that post-processing can greatly improve fiber mechanical properties.

Acknowledgments

This work is supported by Shanghai Leading Academic Discipline Project (No.B603); Innovation Program of Shanghai Municipal Education Commission; the Fundamental Research Funds for the Central Universities and Programmer of Introducing Talents of Discipline to Universities（No. 111-2-04).

Reference

[1]Hongrong Zhang, Yunfang Wei. The Properties of High Performance Semi -Aromatic Nylon Engineering Plastics and Progress in Application. *Fine Chemical Intermediates*, 2002, 32: 1-4.

[2]Siming tan. Grivory HT-Zytel HTN. *New Chemical Materials*, 2002, 30: 52-53.

[3] Saw C K, Collins G, Menczel J, Jaffe M. Thermally induced reorganization in polymer fibers. *Journal of Thermal Analysis and Calorimetry*, 2008, 93(1): 175-182.

[4] Sauer B B, Kampert W G. Thermal and morphological properties of main chain liquid crystalline polymers. *Polymer, 2003*, 44: 2721-2738.

Functionalisation of Carbon Fiber Toward Enhanced Fiber-Matrix Adhesion

Linden Servinis[1], Luke C. Henderson[1], Thomas R Gengenbach[2], Abdullah A. Kafi[1], Mickey G. Huson[3],
Bronwyn L. Fox[1]
[1]Deakin University, Institute for Frontier Materials, Pigdon's Road Waurn Ponds Campus Geelong, 3216, Victoria, Australia; [2] CSIRO Materials Science and Engineering, Bayview Avenue, Clayton, 3168, Victoria, Australia;
[3]CSIRO Materials Science and Engineering, PO Box 21, Geelong, 3216, Victoria, Australia
luke.henderson@deakin.edu.au; lservini@deakin.edu.au

INTRODUCTION

The surface of both oxidized and unoxidized unsized carbon fiber was functionalized using an aziridine linking group derived from reactive nitrenes, attempts were made to install pendant amines using amide chemistry. Surface functionalization using the nitrene approach was supported by X-ray Photoelectron Spectroscopy, in both oxidized and unoxidized carbon fiber. None of the chemical treatment pathways had a significant impact on the tensile strength of the individual fibers, and atomic force microscopy revealed that fibers undergoing these treatment methodologies remained intact, without creating additional surface defects.

APPROACH

Within the last decade, carbon fiber reinforced composites have become regarded as the gold standard of high performance materials. Work toward understanding the roll of interfacial adhesion experienced a boom in the 1970's and 80's [1,2], and is only now experiencing a renaissance, with recent work reigniting the debate about the relative importance of chemical modification and fiber roughness, and their contribution to fiber-matrix adhesion [3,4].
A great deal of research has been centered on the installation of oxygenated species (OH, COOH, C=O), to increase fiber hydrophilicity and enhance non-covalent interactions at the interface, with little focus on covalent interactions[5-7].
Taking inspiration from the vast number of successful functionalisation methods employed in the use of carbon nanomaterials [8,9], a number of synthetic pathways were selected and trialed for application to carbon fiber.

RESULTS AND DISCUSSION

Of the functionalisation methods trialed, two are presented here.

Method 1 involves two treatment stages: treatment 1 (thionyl chloride, acid chloride formation), treatment 2 (acylation with ethylenediamine), taking advantage of the carboxylic acid groups present on the surface of oxidized carbon fiber to introduce a pendant amine moiety.

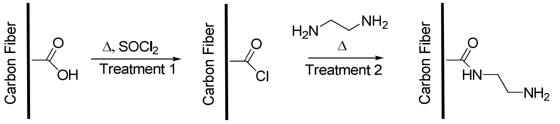

SCHEME 1: functionalisation method 1 (two step treatment)

Method 2 begins with the synthesis of an azide analogue followed by the generation of a reactive nitrene species *in situ* to yield an aziridine product.

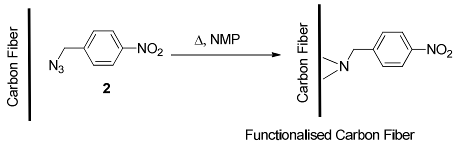

SCHEME 2: functionalisation method 2 (treatment 3)

XPS gave tentative evidence of successful functionalisation by method 2, with a large increase in surface nitrogen at 400 and 406 eV (below).

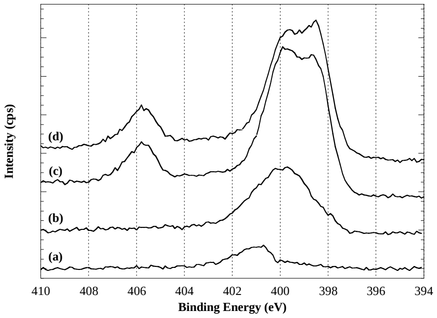

FIGURE 1: High resolution XPS spectra of: (a) unoxidized control, (b) oxidized control, (c) unoxidised treated, (d) oxidized treated fibers (method 2).

All samples then underwent physical characterization by atomic force microscopy, thermogravimetric analysis, and single fiber analyses to obtain linear density, tensile strength, coefficient of friction, and fiber modulus data.

CONCLUSIONS

The nitrene functionalisation method (2) is a viable pathway for introducing pendant surface functional groups to the fiber surface, while there was some evidence which suggested that amide formation (method 1) could also be used to introduce new functionalities. Analysis of the data showed that none of the treatments utilized had a negative effect on the desirable physical properties of the CF.

FUTURE WORK

Investigations using analogues which introduce a new chemical species to the surface, capable of covalent reactions with epoxide based resin systems.

KEYWORDS

Functionalisation, carbon fiber, nitrene

ACKNOWLEDGMENT

This research was made possible with the cooperation of, Zoltek Carbon Fiber Hungary, who kindly supplied unsized carbon fiber for this project. The authors would also like to thank Mr Partrick Brislane of Deakin University for his time and effort in single fiber analyses.

REFERENCES

[1] Piggot MR. The interface in carbon fiber composites. *Carbon*. 27(5), 1989, 657-662.

[2] Ismail IK, Vangsness MD. On the improvement of carbon fiber/matrix adhesion. *Carbon*, 26(5), 1988, 749-751.

[3] Davis DC, et al. A strategy for improving mechanical properties of a fiber reinforced epoxy composite using functionalized carbon nanotubes. *Compos. Sci. Technol.*, 71(8), 2011, 1089-1097

[4] Dai Z, et al. Effect of sizing on carbon fiber surface properties and fibers/epoxy interfacial adhesion. *App. Surf. Sci.*, 257(15), 2011, 6980-6985.

[5] Zeilke U, Hüttinger KJ, Hoffman WP. Surface oxidized carbon fibers: II chemical modification. *Carbon*, 34(8), 1996, 999-1005.

[6] Li L, et al. Surface modification and submicron structure of carbon fibers through high current pulse. *App. Surf. Sci.*, 225(18), 2009, 8030-8035.

[7] Ehlert GJ, Lin Y, Sodano HA. Carboxyl functionalization of carbon fibers through a grafting reaction that preserves fiber tensile strength. *Carbon*, 49(13), 2011, 4246-4255.

[8] Banerjee S, Hemraj-Benny T, Wong SS. Covalent surface chemistry of single walled carbon nanotubes. *Adv. Mater*, 17(1), 2005, 17-29.

[9] Gao C, et al. Scalable functional group engineering of carbon nanotubes by improved one-step nitrene chemistry. *Chem. Mater*, 21(2), 2008, 360-370.

Defect Detection Method on Printed Fabrics

Pengfei Li, Panpan Yang, Junfeng Jing
College of Electronic and Information Xi’an Polytechnic University, Xi’an Shaanxi, 710048, China
jingjun feng0718@sina.com

INTRODUCTION

Flaws on textile fabrics have a great influence on selling price and price reduction ranges from 45% to 65%[1] in the original price of a product. Finding an efficient way to detect defects on printed fabrics is main purpose. This paper proposes an effective method by way of building optimal Gabor filter with selected parameters to solve encountered problems in fabric detection. Gabor filters are coordinated by stainless fabric images in objective function, and genetic algorithm is wielded to arrive the minimum of objective function. The whole proposed method includes training part and defect detection part, whose description could be shown in Figure 1. Likewise, the proposed method has its own disadvantages, and the main disadvantage is that defects caused by destroying the fabric and having the same color as the normal texture could not be perfectly detected on fabrics. We would put much effort into the improvement of implementation on the proposed method and the range of application. The authors gratefully thank the Scientific Research Program Funded by Xi'an Science and Technology Bureau Project (Project Numbers:CX1257③).

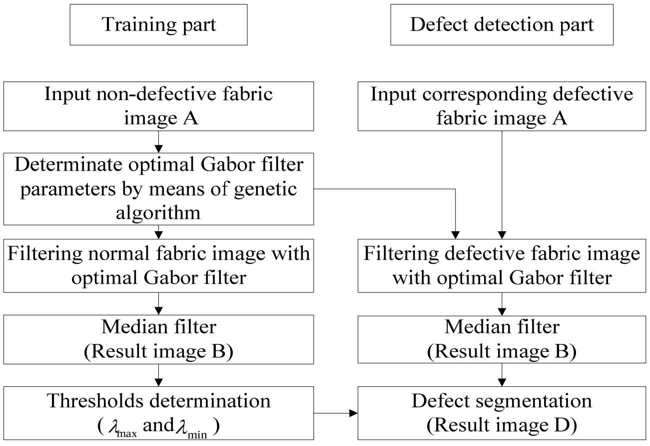

Figure 1. Fabric defect detection method

APPROACH

Gabor function

$$g_e(x, y) = \exp\left\{-\frac{1}{2}\left[\left(\frac{x'}{\sigma_x}\right)^2 + \left(\frac{y'}{\lambda\sigma_x}\right)^2\right]\right\}\cos\left(2\pi u_0 x'\right)$$

among

$$\begin{bmatrix} x' \\ y' \end{bmatrix} = \begin{bmatrix} \cos\theta & -\sin\theta \\ \sin\theta & \cos\theta \end{bmatrix}\begin{bmatrix} x - T_1 \\ y - T_2 \end{bmatrix} \qquad \sigma_y = \lambda\sigma_x$$

ω is a coefficient for controlling the relationship of Gabor function and normal fabric. T_1 is conversion parameter along the x axis. T_2 is conversion parameter along the y axis. λ is variance ratio between x and y axis. θ rotates the value x and y to the corresponding x' and y'. u_0 is sinusoidal wave frequency.

Genetic algorithm

In genetic algorithm, Gabor filter parameters in objective function E constitute the whole parameter group Genetic algorithm searches the minimum of objective function E to obtain the optimal Gabor filter[2]. The whole program of genetic algorithm is detailedly shown in Figure 2. Through the process of genetic algorithm, the most suitable parameters would be obtained to make great contributions to the construction of optimal Gabor filters.

$$E = \min_{\omega, T_x, T_y, \lambda, \theta, u_0}\left[\sum_{x,y}\left(IM(x, y) - \omega g_e(x, y)\right)^2\right]$$

IM is a defect-free fabric image. In the whole algorithm, an individual is binary codes of a parameter in Table I, parameter group means binary codes of all parameters in Table I, population is made of all parameter groups. The parameters obtained by genetic algorithm have to be dealt with the following procedure. Parameters θ_{ga} and u_{0ga} are derived from genetic algorithm.

$$\begin{cases} \theta = \theta_{ga} - \frac{5}{6}\pi \\ u_0 = u_{0ga} - 1.9 \end{cases}$$

Orientation θ and center frequency u_0 captured by parameters θ_{ga} and u_{0ga} would be implemented in optimal

Table I. Exhibition of a maximum and minimum parameter group

ω	τ_1	τ_2	λ	θ	u_0
11111111	11111111	11111111	11111111	11111111	11111111
00000000	00000000	00000000	00000000	00000000	00000000

genetic algorithm are also applied in optimal filters. Contents in Table I display the compositions of each individual and serve expressions of minimum and maximum. The forty-eight ‘ 0 ’ represent minimum in binary codes. The forty-eight ’ 1 ’ mean maximum in binary codes. All parameters appear as a whole in genetic algorithm to realize crossover and mutation

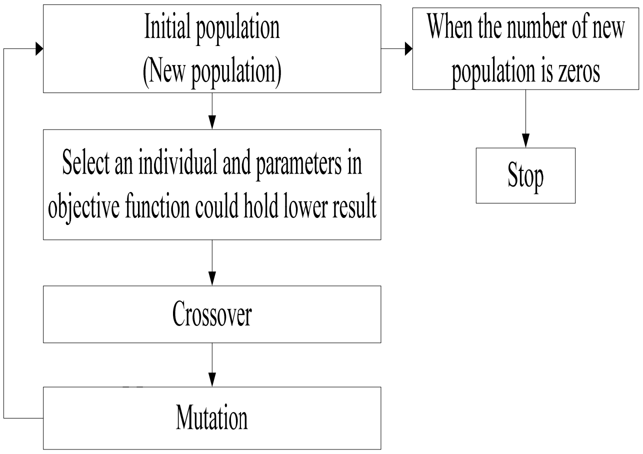

Figure 2. Outline of genetic algorithm

EXPERIMENT RESULTS

Optimal Gabor filters with selected parameters gain from the training step by virtue of genetic algorithm. After filtering fabric images with optimal Gabor filter and binarization in filtered images, various defect inspection results using the optimal Gabor filters are pretty well. Perfect consequences of diversiform flaw detections on patterned fabric images distribute in Figure 3.

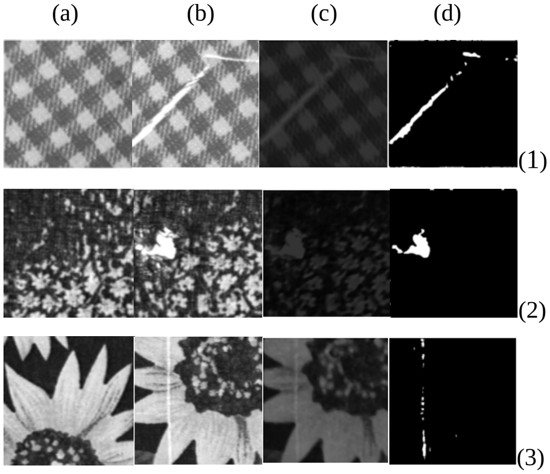

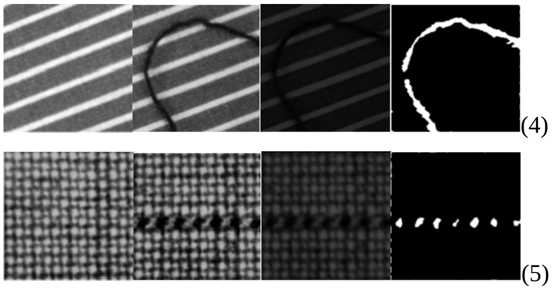

Figure 3. (a) non-defective images, (b) defective images, (c) filtered images, (d) binarization images

CONCLUSIONS

A supervised method is proposed in this paper including training and detection. In the training section, Gabor filter $g_e(x, y)$ could be supervised by a defect-free image IM(x,y) in objective function E. When objective function E reaches the minimum, optimal Gabor filter parameters can be obtained from applied Gabor filter $g_e(x, y)$. An effective way to search the minimum of objective function E is genetic algorithm. In the detection section, selected optimal Gabor filter would be applied in defect detection on corresponding defective fabrics. Perfect detection results can be fulfilled on textile fabrics, especially defect detections on patterned fabric present good results in this work, which are fractionally done in researches.

KEYWORDS: defect detection, Gabor filter, genetic algorithm, textile fabrics.

REFERENCES

[1] K.L.Mak and P.Peng. Detecting defects in textile fabrics with optimal Gabor filters. *International Journal of Computer Science* 2006, 1(4): 274-282.

[2] Kai-Ling Mak and Pai Peng. Fabric defect detection using multi-level tuned-matched Gabor filters. *Journal of Industrial and Management Optimization* 2012, 8(2): 325-341.

Effects of Feeding Modes on the Melt Processability of Acrylonitrile-Methly Acrylate Copolymers and Fibers

Na Han, Xi-yin Gao, Rong Zhang, Xing-xiang Zhang, Wei Li
hannapolyu@163.com, zhangpolyu@yahoo.com.cn

Key Laboratory of Hollow Fiber Membrane Materials and Membrane Process of Ministry of Education; Tianjin Municipal Key Lab of Fiber Modification and Functional Fiber,School of Materials Science and Engineering, Tianjin Polytechnic University, Tianjin 300387, China

ABSTRACT

A series of acrylonitrile-methyl acrylate copolymers with a constant feed molar ratio of 85/15 (85/15 AN/MA) were synthesized by aqueous redox initiated polymerization. Identification of suitable feeding mode and achieving the optimum melt processability of the copolymer were the main objectives of this investigation. PAN copolymer based fibers could be formed by melt spinning at 190~210 °C. The intrinsic viscosities were in the range of 0.30-0.88 dL/g, being affected by the monomer feeding mode. The tensile strengths of as-spun fibers were in the range of 1.2~2.4 cN/dtex. The optimum feeding mode was 1/3 monomers every 60 min.

KEYWORDS: Feeding mode; Acrylonitrile-methyl acrylate copolymer; Melt processability; Fiber

INTRODUCTION

Superior inherent ultraviolet (UV) and chemical resistances of polyacrylonitrile (PAN) make its fibers special in a number of applications [1].Combined with its high resiliency, it is a fiber of choice as a wool substitute. It is also the most important precursor for carbon fibers. Processing of these materials requires solvent based spinning technologies because the polymer decomposes/cyclizes below the crystalline melting point (T_m) which is about 320 °C [2].

Due to this environmentally unfriendly and more expensive technology, the applications of PAN fiber have declined, and are currently well below those possible if they were melt extrudable [3]. Thus we envisioned that efficient utilization of comonomers could disrupt the long range order and allow economical and environmentally attractive melt processing to occur at perhaps 200−220°C, which is more than 100° C above T_g, while still affording strong fibers.

In continuation of the AN-copolymers work from our laboratory [4-6], based on the poor liquidity of the copolymer in our work, in the present study, the feeding ways of monomers were changed to improve the melt flowability. In this study, a series of melt spinnable 85/15 AN/MA copolymers were synthesized with different feeding methods. The copolymer as-spun fibers were fabricated at 190~210 °C. The structures and properties of the copolymers and as-spun fibers were investigated in detail.

APPROACH

The reactor was a 500 mL flask fitted with a stirrer and a condenser.The reactor was charged with 340 mL of de-ionized water. Prior to monomer addition, the flask was purged with nitrogen for 30 min. Then 4.20 g (40.4 mmol) of the SBS dissolved in 10 mL de-ionized water, 4.33 g (16 mmol) of KSP dissolved in 50 mL de-ionized water and 1 mmol DDM were introduced into the reactor. The monomers (327 mmol AN, 57 mmol MA) mixture was added as follows: single feeding: the total monomers were added once. Three feeding: firstly, 1/3 of the monomers were charged to the reactor, and then the remaining thirds of the monomers were added in 60 minute periods. Five feeding: 1/5 of the monomers were added every 30 minute periods. Dropping: the rate of addition of the monomers was continuous throughout the polymerization reaction over 2 hour period. The polymerization was continued for another 1 hour. The obtained polymers were filtered and washed with large amounts of de-ionized water and subsequently dried under vacuum at 70 °C till their weights were constant. The yields of the copolymers were 83-85%.

RESULTS AND DISCUSSION

^{13}C NMR

The ^{13}C NMR spectrum of sample 1 recorded in DMSO-d_6 at room temperature is shown in Fig1. The assignment of different resonance signals has been carried out by comparing the copolymer spectrum with those of homopolymer. For AN units, nitrile carbon (-CN) appeared in the regions δ=120.0–121.5 ppm. For MA units, the resonance signals in the region δ=173.5–175.0 ppm are assigned to carbonyl carbon (-C=O). The –CH, –CN, and -C=O signals are stereospecific [7] and showed splittings, which were due to compositional or configuration sequences.

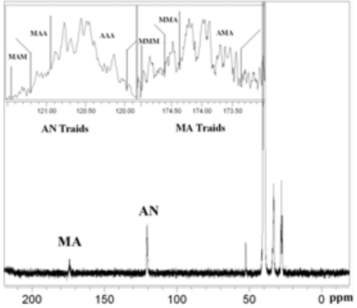

Fig 1. ^{13}C NMR spectrum of the sample 1 85/15 AN/MA copolymer in DMSO-d6 at room temperature

The number average block sequence length (NABSL) of acrylonitrile monomer units was determined from the experimentally observed comonomer triad concentrations[8].

The obtained results show that the NASBL are all significantly lower than that of Amlon® (10.5) in this study. A shorter theoretical sequence length would provide shorter 'crystallizable' AN units and could be expected to exhibit a lower melting point. Table 1 is intrinsic viscosity (IV) and NASBL of AN/MA copolymers. With feeding frequency increasing, it is interesting to note that L_{nA} decreases from 10.53 to 8.00, IV value changes from 0.88 dL/g to 0.31 dL/g ,while that of MA units shows an opposite trend (1.10 - 1.18). The copolymers, with intrinsic viscosity in the range of 0.30-0.60 dL/g, are able to be melt processed. Empirically, an intrinsic viscosity (IV) value of about 0.5 dl/g in NMP at 25 °C proved to be a general target for a melt processable 85/15 copolymer [9]. It is shown that IV of sample 2 is closest to the aim value. It is also demonstrated that the feeding modes of batch splitting can shorten the length of AN units, weaken the interactions between –CN groups indeed and improve the melt flowability of AN/MA copolymers.

Table 1 Intrinsic viscosity and NASBL of AN/MA copolymers

Sample No.	IV (dL/g)	L_{nA}	L_{nB}	L_{nA}/L_{nB}
1	0.88	10.53	1.10	9.57
2	0.56	10.00	1.15	8.70
3	0.43	9.52	1.16	8.21
4	0.31	8.00	1.18	6.78

Morphologies of the fibers

Fig. 2 presents the SEM micrographs of the fibers synthesized by the three feeding methods. The side surface of the fibers was very smooth and had no bubbles. The cross-section was compact. This shows that the copolymers can be melted completely and the melt processability was excellent.

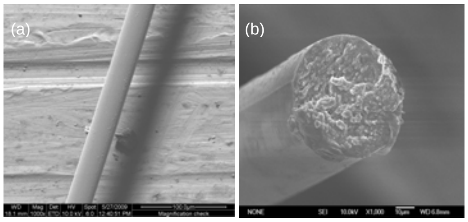

Fig 2 SEM micrographs of fibers prepared with three feeding modes

Physical mechanical properties

Physical mechanical properties of the fibers from the copolymers could be tailored by choosing the desired melt-processing conditions. The melt-spinning AN/MA fibers prepared through sample 1-4 were remarked as F1, F2, F3 and F4 respectively. Attempts were made to obtain oriented fibers at a maximum winding speed without breakage in thread line. The tensile stress–strain plots for the fibers are displayed in Fig.3.

The tensile strength and elongation of the as-spun fibers decreased with increasing in feeding times. The as-spun fiber F4 synthesized by dropping shows a lowest tensile strength of 1.2 cN/dtex. The tensile strengths of F3 and F2 were 1.8 and 2.4 cN/dtex, respectively. In contrast to the other samples, F2 copolymer fiber had the best mechanical properties. It is reconfirmed that the optimum feeding mode was 1/3 monomers every 60 min. Further investigations of the properties of the fibers from these melt processible copolymers are in progress and will be reported later.

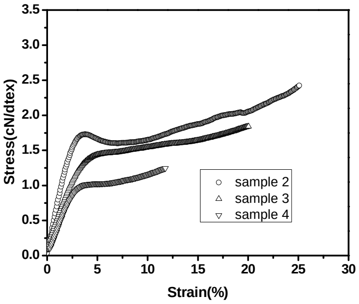

Fig. 3. Stress–strain curves of the fibers

CONCLUSIONS

A series of acrylonitrile-methyl acrylate copolymers with a constant mole ratio (AN/MA 85/15) were synthesized by aqueous redox initiated polymerization with different feeding methods. The intrinsic viscosity was in the range of 0.3-0.88 dL/g with the different feeding methods. The number average sequence length of AN units decreased from 10.53 to 8.0 when the feeding mode was changed from flood feeding to dropping. The copolymers, with intrinsic viscosity in the range of 0.30-0.60 dL/g, are able to be melt processed. In contrast, the copolymer with an intrinsic viscosity of 0.88 dL/g was unable to be melt-spun. The tensile strengths of the as-spun fibers were in the range of 1.2–2.4 cN/dtex. The melt processability of PAN was improved dramatically by the batch splitting mode. Moreover, the optimum feeding mode is 1/3 monomer every 60 min.

ACKNOWLEDGMENT

The authors are thankful to the National Natural Science Fund of China (No. 21206123), Research Fund for the Doctoral Program of Higher Education of China (No. 20111201120001) and Aviation Science Funds (201229Q2002) for financial support.

REFERENCES

[1] Tirrell, D.A. *Copolymerization*. In *Encyclopedia of Polymer Science and Engineering.* H.F. Mark, N.M. Bikales, C.G. Overberger, G. Menges, Eds., New York: Wiley-Interscience, 1986, p. 192.
[2] Clarke, A. J.; Bailey, J. E. *Nature*, 1973, 243, 146.
[3] Hutchinson, S.R., Tonelli, A. E., Gupta B. S., et al. *A J. Mater. Sci*., 2008, 43, 5143.
[4] Han, N., Zhang, X.X., Wang, X.C., et al.. *Macromol. Res.,* 2010, 18, 144.
[5] Han, N., Zhang, X.X., Yu, W.Y., et al. *Macromol. Res*., 2010, 18, 1060.
[6] Gao, X.Y., Han, N., Zhang, X.X., et al. *J. Mater. Sci*., 2009, 44, 5877.
[7] Kapur, G.S., Brar, A.S. *J Polym Sci Part A: Polym. Chem*., 1991, 29, 479.
[8] Minagawa, M., Taira, T., Yabuta, Y., et al. *Macromolecules*, 2001, 34, 3679.
[9] Bhanu, V.A., Rangarajan, P., Wiles, K., et al. *Polymer*, 2002, 43, 4841.

Dyeing and UV Protection Properties of Chrysophanol on Polylactic Acid Fiber

Jiawei Wang[1], Xiangrong Wang[1,2]
[1]College of Textile and Clothing Engineering, Soochow University, Suzhou, 215021, China
[2]National Engineering Laboratory for Modern Silk, Soochow University, Suzhou, 215123, China
jxlwjw_2003@sina.com; wangxiangrong@suda.edu.cn

STATEMENT OF PURPOSE

Polylactic acid (PLA) fiber is a biodegradable synthetic fiber, that is, it could be decomposed into carbon dioxide and water through the action of microorganisms. We investigated the dyeing of PLA fiber with chrysophanol and UV protection properties of dyed fabrics, hoping to explore the possibility of natural dyes dyeing on PLA fiber.

INTRODUCTION

PLA fiber has been widely applied to the textile industry because of its good features [1]. Disperse dyes are widely used in PLA fiber dyeing, however, recent studies have discovered that some synthetic dyes are irritant to skin, even lead to skin disease and cancer[2-3]. Natural dyes seem to be less harmful to humans and environment, and nowadays they could be considered as a better alternative to synthetic dyes [4-5]. Chrysophanol is the active ingredient of rhubarb, also is one of the traditional Chinese herbal medicine. Fig. 1 shows the structure of chrysophanol, it belongs to the anthraquinone derivatives and has good molecule planarity. There are no hydrophilic groups in its molecule, such as carboxyl group. Chrysophanol is almost insoluble in water. It's similar to the ordinary disperse dyes in structure and solubility. Chrysophanol has a strong anti-bacterial and anti-inflamatory effect, so textiles dyed with chrysophanol may have some healing and health-care effect on the wearers [6].

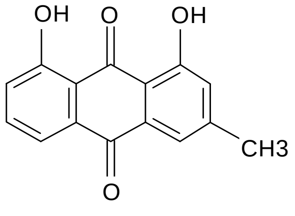

Fig. 1. Structure of chrysophanol.

APPROACH

Adsorption isotherm

The PLA fabrics were dipped into the dyebath at a liquor ratio 1000:1. In each initial dyebath containing various concentration chrysophanol, pH 5.0 acetate buffer, 0.5 g·dm^{-3} Paregal O (polyoxyethylene alkyl ether surfactant). Dyeing was carried out at 90℃ and 100℃ for 240 min. The amount of chrysophanol absorbed by the PLA fiber was measured by extraction with N,N -Dimethylformamide (DMF) at 95℃, leading to the determination of the sorption isotherms.

Effect of initial chrysophanol concentration

The dyebath containing various concentration chrysophanol and 0.5 g·dm-3 of Paregal O were prepared, while the pH value was controlled to 5.0, and the liquor ratio was 100:1. Dyeing was started at 40℃ and the temperature was raised by 3℃/min to 110℃, continued for 90 min at the final temperature. The K/S values of dyed fibers were tested with the UltraScanXE Computer Color Matching System.

UV protection properties test

Ultraviolet transmittance and UV-protection factor (UPF) of undyed and dyed fabric were tested with the UV-1000F Ultraviolet Transmittance Analyzer, transmission measurements were made in the 250-400 nm range with a 1 nm step.

RESULTS AND DISCUSSION

Adsorption isotherms of chrysophanol on PLA fiber

Fig. 2 showed the adsorption isotherms of chrysophanol on PLA fiber at 90℃ and 100℃.

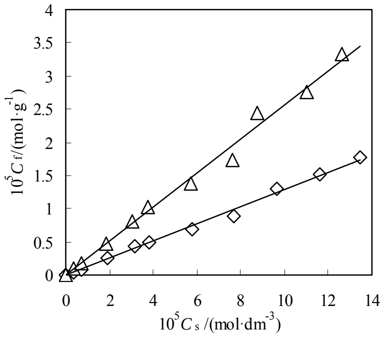

Fig. 2. Adsorption isotherms of chrysophanol dyeing on PLA fiber: -◇-90℃; -△-100℃.

As can be seen, the adsorption of chrysophanol on PLA fiber increased linearly with the concentration of chrysophanol increasing. So the adsorption of chrysophanol on PLA fiber accorded with Nerst

Partition Relation. This was similar to the adsorption of disperse dyes on PLA fiber [7].

Table I listed the thermodynamic parameters. The results revealed that the apparent partition coefficient and the affinity increased with the temperature increasing, in other words more chrysophanol could be adsorbed at higher temperature.

Table I. The thermodynamic parameters of chrysophanol dyeing on PLA fiber.

Temperature /℃	Partition coefficient /dm^3·kg^{-1}	Standard affinity /kJ·mol^{-1}
90	129.69	14.68
100	256.6	17.20

Effect of initial dye concentration

In Fig. 3, the K/S value of the dyed fiber significantly increased with the increasing chrysophanol concentration below 1% o.w.f.. When the chrysophanol concentration exceeded 2% o.w.f., the K/S value of the dyed fiber changed very little. This result suggested that the maximum dye uptake of chrysophanol on PLA fiber is relatively small.

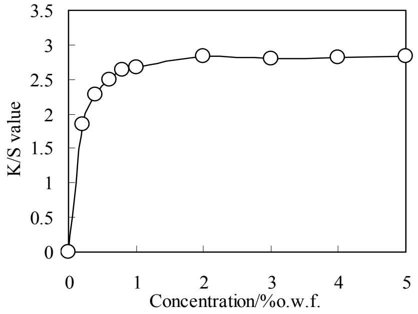

Fig. 3. Building-up property of chrysophanol dyeing on PLA fiber.

UV protection properties

Table Ⅱ listed the UV-protection factor value of undyed and dyed PLA fabrics. The results revealed that the ultraviolet protection factor (UPF) value of the dyed PLA fabrics enhances from 13.64 to 129.44, so the dyed PLA fabrics with chrysophanol exhibited good UV protection function.

Table II. The UPF value of undyed and dyed fabrics.

Undyed fabric	Dyed fabric
13.64	129.44

The Ultraviolet transmittance curves of undyed and dyed fabrics were showed in Fig. 4. The results indicated that the dyed PLA fabric with chrysophanol reached the good protection level and the UV transmittance were all below 5% at wavelength from 250 to 400, which refered to the European standard for Sun Protective Clothing and the Chinese National standard GB/T18830-2002.

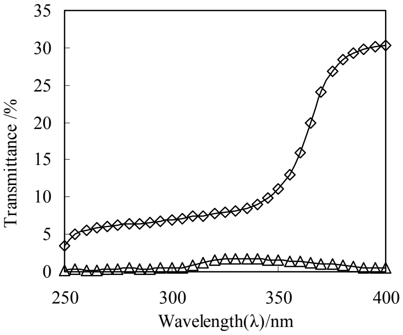

Fig. 4. Ultraviolet transmittance curves: -◇- undyed fabrics; -△- dyed fabrics.

CONCLUSIONS

The sorption isotherms of the chrysophanol on PLA fiber fitted Nerst Partition Relation. The partition coefficient and affinity increased with increasing temperature, it indicated more chrysophanol could be adsorbed at higher temperature. The PLA fabric dyed with chrysophanol exhibited good UV protection function.

KEYWORDS

PLA fiber; chrysophanol; natural dyes; dyeing; UV protection

ACKNOWLEDGMENT

Financial support for this work was provided by A Project Funded by the Priority Academic Program Development of Jiangsu Higher Education Institutions.

REFERENCES

[1] Oksman K., Skrifvars M., Selin J. F. *Composites Science and Technology*, 2003, 63: 1317-1324.

[2] Fu K. J., Min J., Li Z. R., et al.. *Journal of Donghua University* (Eng. Ed.), 2008, 25 (5): 601-606.

[3] Qian H. F., Zhang F. *Journal of Textile Research*, 2005, 26 (1): 13-16.

[4] Cristea D., Vilarem G. *Dyes and Pigments*, 2006, 70: 238-245.

[5] Montazer M., Parvinzadeh M. *Fibers and Polymers*, 2007, 8 (2): 181-185.

[6] Wang C. Z., Cheng H. J., Guan Y. *Chinese Journal of Microecology,* 2008, 20 (6), 570-572.

[7] Fu Z. J., Zheng H., Guo S., etal. *Dyeing & Finishing*, 2007, 33 (10): 6-9.

Verification of Color Prediction Models for Yarn-Dyed Woven Fabrics

Youngjoo Chae, H. John Xin, and Tao Hua
The Institute of Textiles and Clothing, Faculty of Applied Science and Textiles, The Hong Kong Polytechnic University
fchae@hanmail.net; john.xin@polyu.edu.hk; tao.hua@polyu.edu.hk

Keywords: yarn-dyed woven fabric; color prediction; color mixing model; geometric model; model verification

INTRODUCTION

The color design and expression is the most important aspect of woven fabric design. Unlike printed or piece-dyed fabrics, the final visualized color of yarn-dyed woven fabrics comes from the yarn color but in the form of weave structure. In the past, before the introduction of computers in the fabric production process, multiple trials were required for successful color reproduction.

These days, however, automated accurate digital color methodology is available to match the final fabric to the original design. Especially, in color recipe prediction for yarn-dyed woven fabrics, the geometric properties of the fabric are considered as well as the colors of each yarn used. The geometric properties affect the color contribution of each yarn on the fabric surface, so with this information, the prediction of the final color for a given design is possible.

Numerous color prediction models for clothing materials have been developed on the basis of different color formulation theories and techniques. However, only three combined geometric–color mixing models, i.e. simple K/S, log K/S, and DG models, have been tested for yarn-dyed woven fabrics[1,2]. Therefore, this study is aimed at verifying the effectiveness of various color models developed and determine the most appropriate model to predict the final color attributes of woven fabrics.

METHODOLOGY

Specimens

10 woven fabrics of different color combinations of warp and weft yarns and weave structures were constructed using a LX3202 Staubli jacquard machine. As the color combination, white yarns were equally used for warp, and red and blue yarns were used respectively for weft. As the weave structure, five different weaves, i.e. 1/1 plain, 1/2 twill, 2/1 twill, 1/4 sateen and 4/1 satin, were used. The yarn material (polyester), yarn diameter (0.125mm), and fabric density (47x30/cm), were equally controlled.

Instrumental color measurement

The spectral reflectance of three yarns and 10 fabrics was measured using a Macbeth Color-Eye 7000A spectrophotometer with the following specifications: diffuse/8° geometry, specular component excluded, UV excluded, and large area view. The measured reflectance data were converted into K/S, L*, a*, b*, C*, and h° values using CIE 10° standard observer and illuminant D65.

Color prediction

The final color prediction for each fabric was conducted in two steps. Firstly, each color proportion on the fabric surface was calculated using a developed geometric model[1] [Eqs. (1)-(3)] with the assumption that woven structures have a two-dimensional flat surface which is divided into three color portions: warp, weft, and background (Fig. 1).

$$C_1 = \frac{WFN(d_1 \times p_2) + [(WN \times FN) - WFN]d_1(p_2 - d_2)}{WNp_1 \times FNp_2} \quad (1)$$

$$C_2 = \frac{FFN(d_2 \times p_1) + [(WN \times FN) - FFN]d_2(p_1 - d_1)}{WNp_1 \times FNp_2} \quad (2)$$

$$C_b = 1 - (C_1 + C_2) \quad (3)$$

Where:

C_1, C_2, C_b = the proportion of warp yarn color, weft yarn color, and background color, respectively

WN, *FN* = the number of warp yarns and weft yarns in a repeat, respectively

WFN, *FFN* = the number of warp floats and weft floats in a repeat, respectively

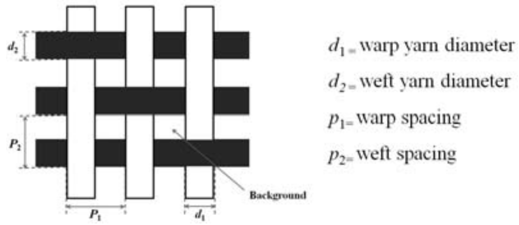

FIG. 1. Two-dimensional fabric surface.

In the second step, based on each color proportion obtained in the first step, the final color attributes of fabrics were predicted by six color mixing models: simple K/S model (Eq. (4)), log K/S model[3] (Eq. (5)), Dimitrovski-Gabrijelcic model [4] (Eqs. (6)-(8)), Noechel model-1944[5] (Eq. (9)), Stearns–Noechel model-2002[6] (Eq. (11)), and Warburton–Oliver model[7] (Eq. (13)).

$$(K/S)_{\lambda,\mathrm{mix}} = (K/S)_{\lambda,s} + \sum_{i=1}^{n} c_i (K/S)_{\lambda,i} \quad (4)$$

$$\log(K/S)_{\lambda,\mathrm{mix}} = \sum_{i=1}^{n} c_i \log(K/S)_{\lambda,i} \quad (5)$$

Where:

$(K/S)_{\mathrm{mix}}$, $(K/S)_{\mathrm{s}}$, $(K/S)_{\mathrm{i}}$ = the (K/S) value of mixture, undyed substrate, and *i*th color at unit concentration, respectively

c_i = the proportion of *i*th color in the mixture

$$L^* = (L^*_w c_w) + (L^*_f c_f) + (L^*_b c_b) \quad (6)$$

$$a^* = (a^*_w c_w) + (a^*_f c_f) + (a^*_b c_b) \quad (7)$$

$$b^* = (b^*_w c_w) + (b^*_f c_f) + (b^*_b c_b) \quad (8)$$

Where:

c_w, c_f, c_b = the proportion of warp yarn color, weft yarn color, and background color, respectively

L^*_w, L^*_f, L^*_b = the lightness value of warp yarn, weft yarn, and background, respectively

a^*_w, a^*_f, a^*_b = the redness-greenness value of warp yarn, weft yarn, and background, respectively

b^*_w, b^*_f, b^*_b = the blueness-yellowness value of warp yarn, weft yarn, and background, respectively

$$f[R_{\text{blend}}(\lambda)] = \sum_i x_i \cdot f[R_i(\lambda)] \qquad (9)$$

Where:

$R_{\text{blend}}(\lambda)$, $R_i(\lambda)$ = the reflectance value of blend and *i*th component at wavelength λ, respectively

x_i = the proportion of *i*th component in the blend

f = the additive function provided by the authors as follows:

$$f[R(\lambda)] = \frac{1 - R(\lambda)}{b \cdot [R(\lambda) - 0.01] + 0.01} \qquad (10)$$

Where:

b = the dimensionless constant determined experimentally (mean value of published and unpublished values = 0.12[6])

$$\varphi[R_{\text{blend}}(\lambda)] = \sum_i x_i \cdot \varphi[R_i(\lambda)] \qquad (11)$$

Where:

$R_{\text{blend}}(\lambda)$, $R_i(\lambda)$ = the reflectance value of blend and *i*th component at wavelength λ, respectively

x_i = the proportion of *i*th component in the blend

φ = the additive function newly provided by the authors as follows:

$$\varphi[R(\lambda)] = \frac{1000 \cdot [1 - R(\lambda)]}{(0.12 \cdot \lambda + 42.75) \cdot [R(\lambda) - 0.01] + 0.01} \qquad (12)$$

$$R = R_1^{x} R_2^{1-x} \qquad (13)$$

Where:

R, R_i = the reflectance value of blend and *i*th component, respectively

x, $1-x$ = the proportion of each component

The predicted color attributes of each fabric were then compared to measured color attributes by calculating the color difference, ΔE.

RESULTS

The calculated color proportions for each weave structure, combined to six color mixing models, are shown in Table I. The color differences between measured and predicted values are presented in Fig. 2.

Among six color mixing models, log K/S model, DG model, and WO model were generally found to be potentially useful to predict final colors of yarn-dyed woven fabrics. In particular, differently from the result of previous study[1] on the verification of color models for woven fabrics, combined geometric DG colour mixing model was found to perform best with the least average error. In addition, WO model, which had never been tested for woven fabrics, was newly found to be useful as much as log K/S model.

TABLE I. Predicted color proportions of warp and weft yarns and background.

Weave structure	Color proportions (%)		
	Warp	Weft	Background
Plain	47.29	26.47	26.24
1/2 twill	44	30.19	25.81
2/1 twill	51.34	22.85	25.81
1/4 sateen	41.31	33.01	25.68
4/1 satin	54.55	19.77	25.68

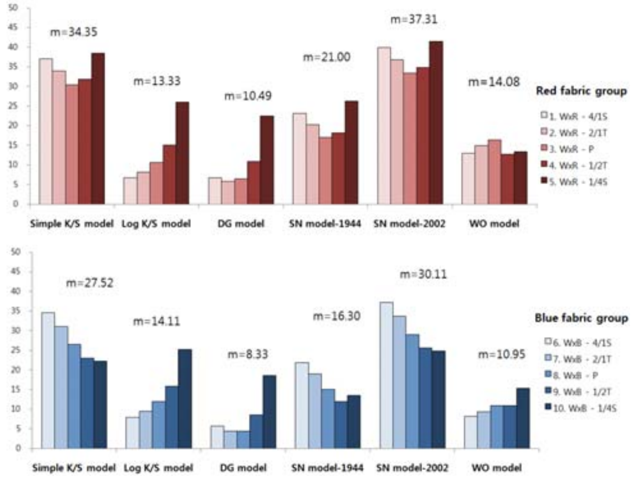

FIG. 2. CIELAB ΔE of predicted and measured values for six colour mixing models.

ACKNOWLEDGMENT

This research was supported by a Hong Kong PhD Fellowship Scheme offered by Research Grants Council (RGC), University Grants Committee (UGC).

REFERENCES

1. Mathur, K., Hinks, D., Seyam, A. M., Donaldson, R. A. (2009). *Color Research and Application*, 34(3), 225-232.
2. Mathur, K. (2007). *PhD thesis, North Carolina: North Carolina State University*.
3. Reed, J., Jasper, W., Hinks, D. (2004). *AATCC International Conference and Exhibition, Greenville, SC.*
4. Dimitrovski, K., Gabrijelcic, H. (2004). *AUTEX Research Journal*, 4(4), 187-193.
5. Stearns, E. I., Noechel, F. (1944). *American Dyestuff Reporter*, 33(9), 177-180.
6. Philips-Invernizzi, B., Dupont, D., Jolly-Desodt, A. M., Cazé, C. (2002). *Color Research and Application*, 27(2), 100-107.
7. Warburton, P., Oliver, P. (1954). *Textile Institute*, 361-373.

Rheological of OV-POSS/PA66 Nanocomposites

Lin Xiaoxia[1], Qun Shao[1], Yimin Wang[2]
[1]College of Materials Science and Engineering, Donghua University
[2]State Key Laboratory for Modification of Chemical Fibers and Polymer Materials
crystalxiaoxia@126.com; ymw@dhu.edu.cn

INTRODUCTION

Poly hexamethylene adipamide (PA66) has been widely used in our country, especially as diagonal tire-cord fibres for its comprehensive properties. However, fiber thermal and mechanical properties can’t meet high demand for heavy vehicles. Focusing on this issue, this study employs chemical grafting method to introduce the eight vinyl POSS epoxy into the PA66 to form strong chemical bonds[1-2]. Since the polymer rheology will significantly influence spinning process, the flowing properties of the nanocomposite system must be studied before fiber spinning in order to achieve good results.

EXPERIMENT

The POSS used in this study was eight vinyl POSS .It was purchased from Shenyang MEICI Fine Chemical Co., Ltd, China, and converted to OV-POSS in our laboratory. Then, OV-POSS/PA66 nanocomposite fibres were prepared by melt extrusion, and the flowing behavior of the nanocomposite system was studied in our laboratory.

RESULTS AND DISCUSSION

Melt index

The melt index of the PA66/POSS composites is shown in Table I. Melt index of the PA66/POSS nanocomposites increases with increasing OV-POSS content, indicating that the flowing properties of the PA66/POSS nanocomposites become better. This is because that the adding of OV-POSS reduces the intermolecular force in PA66, thus increasing the flowing properties of the PA66. But the flowing properties of the composites with higher percentage of OV-POSS tend to be unchanged. This is because that only part of OP-POSS can improve the flow, and most of OV-POSS plays the role of filler. So we can find that adding a small amount of OV-POSS can improve the flow properties, and it will influence the spinning performance of PA66 as discribed with.

Dynamic viscosity

The relationship of dynamic viscosity of OV-POSS/PA66 melt and oscillation frequency with different percentages is shown in Figure 1. As the frequency increases, the dynamic viscosity is decreased. The shear thinning behavior shows that both pure PA66 and OV-POSS/PA66 composite system are typical pseudoplastic fluids. Dramatic decline of dynamic viscocity is observed for PA66/POSS nanocomposite system as compared to the pure PA66. However, at higher OV-POSS content(3%), less uniformly dispersed and more agglomerated bundles of POSS were formed in the PA66 matrix. As a result, the viscosity of the composite system does not decrease any more at higher POSS content. This kind of phenomenon is not obvious for the case of low frequency, and four curves are close. But curves reduce significantly at the high frequency.

Modulus

The relationship of storage modulus and loss modulus of composite system and oscillation frequency with different percentages of OPSS are shown in Figures 2 and 3. From figure 2, we can find the storage modulus of OV-POSS/PA66 increases as compared to the pure PA66, and this phenomenon is more obvious in the low frequency region. From figure 3, we can find the adding amount of OV-POSS does not impact the loss modulus of nanocomposites obviously. This is because the adding of OV-POSS lead to the increase of interface and the enhance of interaction force. Thus the modulus of system presents a gradually increasing trend.

Loss tangent

When the polymer melt is under alternating stress, the smaller the loss tangent is, the faster the melt elasticity responses, and it indicates that the melt elasticity becomes larger. The relationship of loss tangent of composite

Table I. Melt index of PA66 with different percentages of OV-POSS

OP-POSS / wt %	**MFR / g/10min**
0	14.2
1	16.6
2	17.8
3	18.2

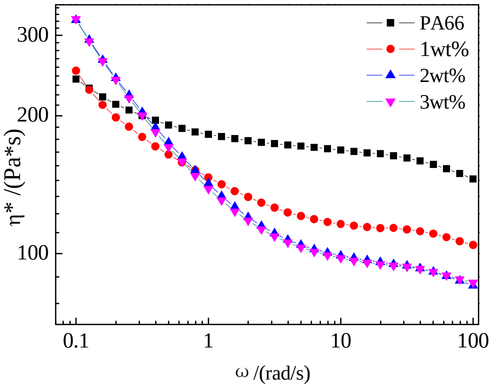

Figure 1. Complex viscosity-frequency curves of OV-POSS/PA66 with varying POSS concentration(275℃)

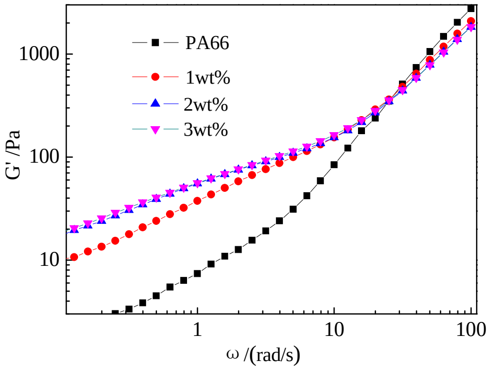

Figure 2. Storage modulus-frequency curves of OV-POSS/PA66 with varying POSS concentration

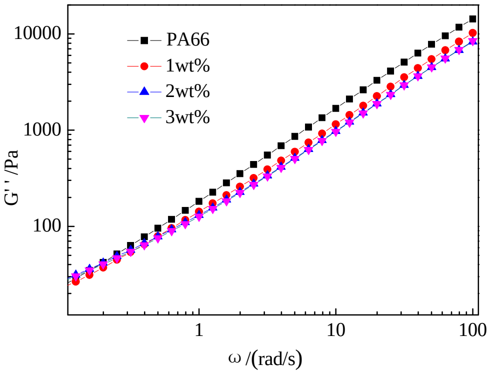

Figure 3. Loss modulus-frequency curves of OV-POSS/PA66 with different concentration of POSS

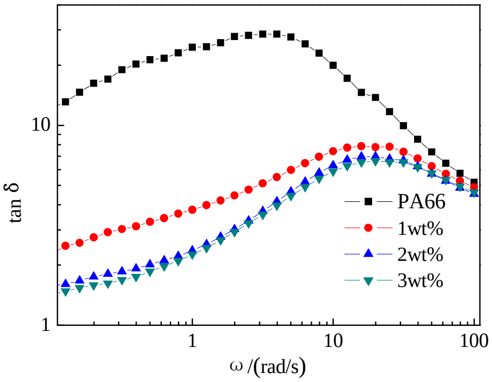

Figure 4. Loss factor-frequency curves of OV-POSS/PA66 with different concentration of POSS

system and frequency with different percentages of OPSS is shown in Figure 4. In this figure, there is a internal friction peak on each curve. With the increase of OV-POSS content, the internal friction peak position is shifted to the high frequency direction. And the loss tangent of OV-POSS/PA66 decreases as compared to the pure PA66. So we can find that adding a small amount of OV-POSS can improve the elasticity of melt.

CONCLUSIONS

This study investigated the rheological of OV-POSS/PA66 nanocomposites. As a result, we can find that adding a small amount of OV-POSS can improve the flowing properties and the elasticity of PA66. Moreover, the OV-POSS content influences the viscosity of the system significantly in the high shear rate.

REFERENCES

[1] Wang Z B, Leng S W, Wang Z G, et a1. Nano-structured organic-inorganic copolymer networks based on polymethaerylate-functionalized octaphenylsilsesquioxane and methylmethacrylate: Synthesis and characterization. *Macromolecules*, 2011, 44(3): 565-567.

[2] Choi J, Harcup J, Yee A F, et al. Organic/inorganic hybrid composites from cubic silsesquioxanes. *Joural of the American Chemical Society*, 2001, 123(46): 11420-11430.

Preparation and Photoluminescence of $LaBO_3$: Eu^{3+} Nanofibres

Chuanxiang Qin[1,2], Tong Lin[1]
[1]Institute for Frontier Materials, Deakin University, Geelong, VIC 3217, Australia
[2]Soochow University, Suzhou 215123, China
Contact author: tong.lin@deakin.edu.au

INTRODUCTION

Rare earth orthoborate luminescent materials have attracted much attention owing to the low toxicity, strong luminescence, high chemical stability, and exceptional optical damage threshold[1,2]. They show great potential to be used in areas such as fluorescent lighting systems, display devices, X-ray screen detectors and phosphor marking scintillators. Among which the Eu^{3+} doped $LaBO_3$ phosphor with aragonite structure exhibits better chromaticity than that of vaterite-type $LnBO_3$:Eu^{3+} (Ln=Y, Gd, and Lu) systems [2,3]. $LaBO_3$ crystallizes into acentric space group possessing trigonal borate coordination and has been proved to be good host lattices for rare earth ions, such as Er^{3+}, Eu^{3+} and Tb^{3+}, to prepare luminescent materials[1,2,4].

One-dimensional (1D) nanostructured luminescent rare earth orthoborates are of particular interest because of the shape-specific, quantum confinement effects and the applications as electrically, magnetically, or optically functional host materials [5,6]. 1D nano-materials fabricated by electrospinning have become important for their exceptionally long length, uniform diameter, diverse composition and high surface to volume ratio[5].

In this study, we prepare aragonite type $LaBO_3$: Eu^{3+} nanofibres through electrospinning of a precursor solution that was prepared by a Pechini process, and subsequent calcination treatment.

APPROACH

The stoichiometric La_2O_3, Eu_2O_3 and H_3BO_3 were dissolved in aqueous solution of nitric acid containing citric acid. The molar ratio of metal ions to citric acid was controlled at 1:2. Poly (vinyl pyrrolidone) (PVP) in dimethylformamide/ethanol solution was then added to the metal/nitric/citric solution and mixed to form a homogeneous solution which was subjected to electrospinning under applied voltage of 15 kV, spinning distance of 15 cm and flow rate of 0.5 mL/h. The as-electrospun fibre mat was dried in an oven at 120 °C for 5 hours, and then heated at 600~800 °C for 6 hours in air.

RESULTS AND DISCUSSION

Fig. 1 shows the SEM images of the fibre mat before and after the calcination treatment. Before calcination, the as-electrospun fibres looked uniform with an average diameter about 200 nm. The fibres became curvy after the calcination treatment, with the diameter reduced to less than 100 nm. The reduction in fibre diameter during calcination was attributed to the removal of PVP from the fibres, and the crystallization of borate.

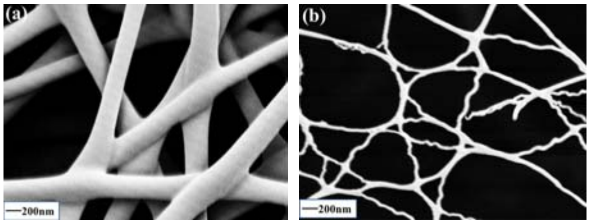

Fig. 1 SEM images of electrospun fibre mat (a) before and (b) after calcination treatment.

The crystal structure and phase purity, was measured by the powder XRD using a Philips X'Pert diffractometer with Ni-filtered Cu Kα radiation (λ=1.54056 Å). For the as-electrospun fibre sample, no diffraction peak was observed except for the broad band at 2θ=21°, which was ascribed to the semi-crystalline PVP. When the precursor fibres was calcined at 600 °C, the broad peak disappeared and diffraction peaks showing the crystal phase characteristic of H-$LaBO_3$ (JCPDS 13-0571[7]) occurred. When the annealing temperature was 750 °C or 800 °C, the sample showed well-defined diffraction peaks, which showed the typical characteristic of the orthorhombic aragonite-type $LaBO_3$ crystal (JCPDS 12-076 [1]).

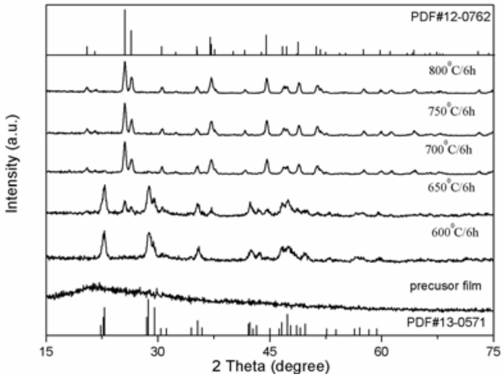

Fig. 2 XRD patterns of electrospun fibres before and after calcination at different temperatures.

The excitation and emission spectra were recorded at room temperature on a luminescence spectrometer (Perkin-Elmer, LS-50B) with a 150 W Xe lamp as an excitation source.

Fig. 3a shows the excitation spectra of the $LaBO_3$:Eu^{3+} fibre samples by monitoring the $^5D_0$-$^7F_2$ transition of Eu^{3+} at 614 nm. A broad band (230-330 nm) was assigned to Eu^{3+}-O^{2-} charge transfer (CT) bands along with sharp line peaks of Eu^{3+} between 360 and 470nm, corresponding to the transitions of ${}^7F_0$-${}^5D_4$, ${}^7F_0$-${}^5L_7$, ${}^7F_0$-${}^5L_6$ and ${}^7F_0$-${}^5D_2$, respectively. The inset spectra show that all the f-f transitions increase with increasing the heat-treatment temperature, attributable to the improvement of crystallinity.

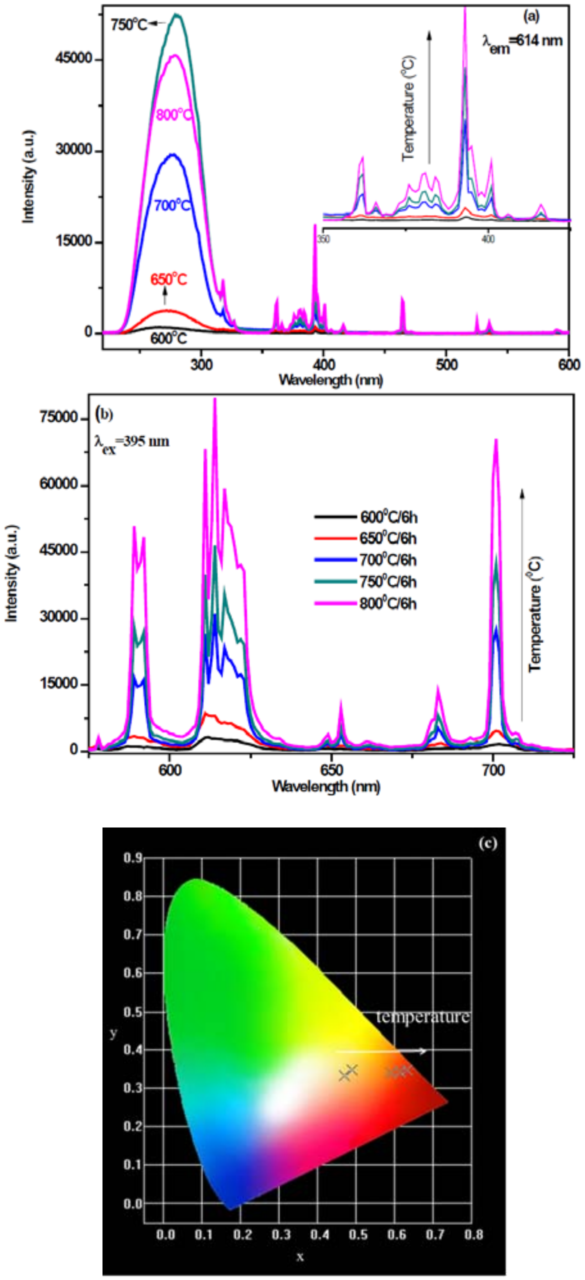

Fig. 3 (a) Photoluminescence excitation spectra, (b) emission spectra and (c) CIE chromaticity diagram of the $LaBO_3$:Eu^{3+} fibres annealed at different temperatures for 6 hours.

Fig. 3b shows the emission spectra of $LaBO_3$:Eu^{3+} fibres excited at 395 nm. Peaks correspond to the transitions from ${}^5D_0$ to ${}^7F_0$, ${}^7F_1$, ${}^7F_2$, ${}^7F_3$ and ${}^7F_4$ of Eu^{3+} were found in the spectra. The emission peak from ${}^5D_0$–${}^7F_2$ transition, which is an electric-dipole allowed and hypersensitive to the environment, dominated the emission spectra. In comparison with other Eu^{3+} doped materials in which the characteristic emissions often comprise equal contributions from ${}^5D_0$-${}^7F_1$ and ${}^5D_0$-${}^7F_2$ transitions[3], such fluorescent fibre has better colour chromaticity.

The CIE (Commission Internationale de l'Eclairage) chromaticity coordinates of electrospun fibres were calculated based on the emission spectra and shown in Fig. 3c. With increasing the annealing temperature during the fibre preparation, their CIE chromaticity coordinates shifted from orange-red to deep red.

CONCLUSION

Aragonite type $LaBO_3$: Eu^{3+} nanofibres prepared by electrospinning and subsequent calcination treatment show luminescent characteristics corresponding to Eu^{3+}. Upon excitation with UV light, the emission is dominated by the ${}^5D_0$–${}^7F_2$ transition of Eu^{3+} which has red fluorescence with good colour chromaticity. The $LaBO_3$: Eu^{3+} nanofibres may find applications as a red luminescence material.

ACKNOWLEDGMENT

The authors thank the financial support from National Natural Science Foundation of China (No. 50903057, 51273134) and Jiangsu Provincial Natural Science Foundation of China (No. BK2012635). Alfred Deakin Postdoctoral Fellowship Grant funded to the 1st author is also acknowledged.

REFERENCES

1. Jia G, Zhang C, Wang C, et al., CrystEngComm, 2012. 14(2): 579-584.
2. Tukia M, Hölsä J, Lastusaari M, et al., *Optical Materials*, 2005. 27(9): 1516-1522.
3. LiY, Zhang J, Zhang X, et al., *Chemistry of Materials*, 2009. 21(3): 468-475.
4. Giesber H, Ballato J, Chumanov G, et al., Journal of Applied Physics, 2003. 93(11): 8987-8994.
5. Hou Z, Li C, Yang J, et al., *Journal of Materials Chemistry*, 2009. 19(18): 2737-2746.
6. Shen H, Feng S, Wang Y, et al., *Journal of Alloys and Compounds,* 2013. 550(0): 531-535.
7. Lemanceau S, Bertrand-Chadeyron G, Mahiou R, et al., *Journal of Solid State Chemistry*, 1999. 148(2): 229-235.

The Study of Compatible Performance Between β-Cyclodextrin/Lavender Spices and Regenerated Cellulose

Baijun Xi[1], Die Wang[1,2], Lanping Shen [2], Gang Song[2]
[1]College of Textiles & Fashion, Shaoxing University, 508 West Huancheng Road, Shaoxing 312000, P. R. China
[2]School of Textile and materials, Xi'an Polytechnic University, 19 Jinhua South Road, Xi'an 710048, China
xbj@usx.edu.cn

STATEMENT OF PURPOSE/OBJECTIVE

This paper mainly uses the β-cyclodextrin wrapping lavender flavor molecules to improve the compatible performance between spices and regenerated cellulose. Therefore we will observe the chance of the micro-capsule under different conditions under Nikon video Microscope and scanning electron microscope to analyze the compatible performance between spices and regenerated cellulose.

INTRODUCTION

The fragrant regenerated cellulose fiber is made by fusing the regenerated cellulose with the fragrance oils or spices to spinning solution for spinning. Making the fabric being fragrant can improve the production added value and satisfy the market requirement. Spices micro-capsule made by β-cyclodextrin, being at the molecular level, can improve the release rates of spices and compatible performance between spices and regenerated cellulose [1]. In this paper, β-cyclodextrin/ lavender spices micro-capsule can be made by the β-cyclodextrin wrapping flavor molecules, then the compatible performance between spices and regenerated cellulose was discussed.

APPROACH

First we should prepare the β-cyclodextrin/lavender spices micro-capsule. The details can be got as following steps. The β-cyclodextrin saturated solution and spices solution should be prepared. The spices solution was prepared at a volume concentration of 1 to 1 with ethanol solution. Extracting the spices solution by a syringe slowly injected into the β-cyclodextrin saturated solution, and stirred the mixed solution for 2 hours at 45℃, then placed 24 hours for refrigeration. The resulted solution was filtrated in order to get the filter cake. The filter cake was washed with anhydrous ethanol until there is no oil stains for getting the β-cyclodextrin/spices micro-capsule [2-3]. Secondly the size of β-cyclodextrin/spices micro-capsule was observed by SEM SNG-3000. Lastly the compatible performance between β-cyclodextrin/spices and regenerated cellulose under different conditions was analyzed by Nikon video Microscope and SEM SNG-3000.

RESULTS AND DISCUSSION

Particle Size Observing

Particle sizes of β-cyclodextrin/spices micro-capsule was observed by SEM SNG-3000, as shown in Figure 1. Its appearance is diamond. Its minimum size is about 2 μm and the maximum size is about 13 μm, which is fit for producing the fragrant regenerated cellulose fiber.

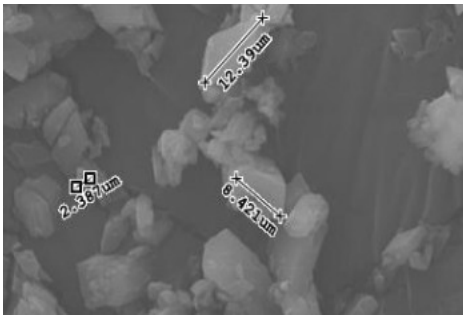

Fig. 1. Particle sizes of β-cyclodextrin/spices micro-capsule (×1000)

Stability Analysis of β-cyclodextrin/ lavender spices Micro-capsule

Thermal, acid, alkali stabilities of β-cyclodextrin/spices micro-capsule can be shown in Figures 2-4 respectively. Thermal stability of β-cyclodextrin/spices micro-capsule was observed in boiling water at 100 ℃. The β-cyclodextrin/spices micro-capsule in boiling water dissolves hardly and its particle dispersibility and sizes does not change obviously. The β-cyclodextrin/spices micro-capsule was put in to the sulfuric acid solution with pH 1 and sodium hydroxide solution with pH 14 in order to discuss the acid and alkali stability respectively. The β-cyclodextrin/spices micro-capsule does not involve chemical reaction and dissolution in acid and alkali solution. The particle size and appearance are also affected by the acid and alkali environment. These facts show that the β-cyclodextrin/spices micro-capsule can be used in the wet spinning process.

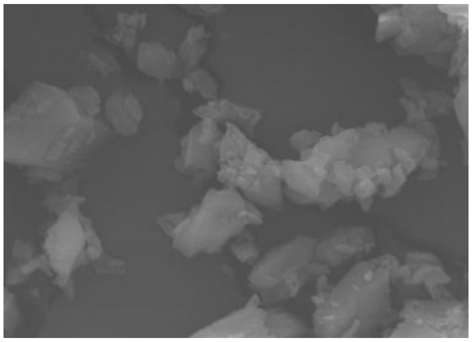

Fig. 2. Thermal stability of β-cyclodextrin/spices micro-capsule (×1000)

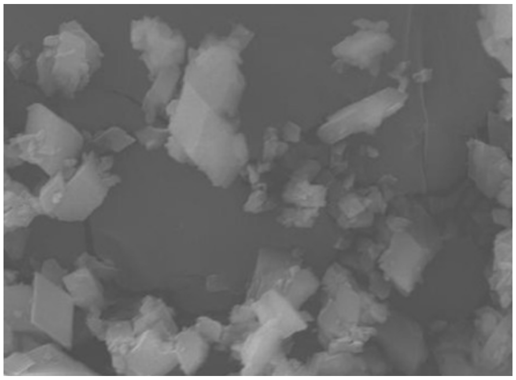

Fig. 3. Acid resistance of β-cyclodextrin/spices micro-capsule (×1000)

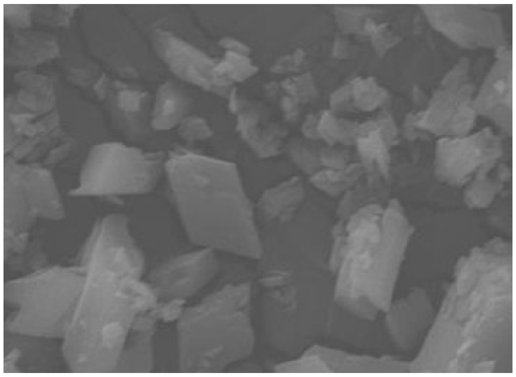

Fig. 4. Alkali resistance of β-cyclodextrin/spices micro-capsule (×1000)

Spinnability Analysis

The β-cyclodextrin/lavender spices micro-capsule was added into the spinning solution and was conducted out deaeration processing for 4 hours, and then it was spun into the fragrant regenerated cellulose fiber, as shown in Figure 5. The fiber surface with groove stripe shape is smooth and good light reflection. The fiber has not only good luster performance but also fragrance after slight friction. Therefore this method can be used to produce the fragrant regenerated cellulose fiber.

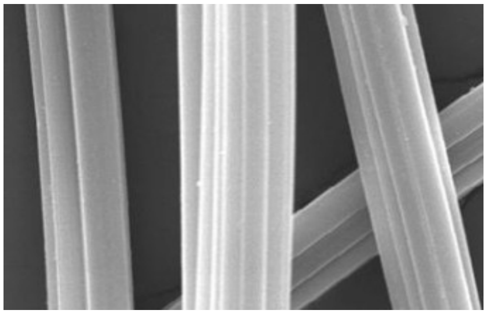

Fig. 5. The fragrant regenerated cellulose fiber (×1000)

CONCLUSION

The β-cyclodextrin/lavender spices micro-capsule has good thermal stability, acid resistance and alkali resistance. The β-cyclodextrin as wall materials, warp the lavender spices molecules, which can decrease slow-release rate effectively and prevent the high temperature and sunrays damage. Therefore the β-cyclodextrin/lavender spices micro-capsule is fit for producing the regenerated cellulose. The fragrant regenerated cellulose fiber made by adding β-cyclodextrin/lavender spices micro-capsule into spinning solution has good performance. The differential fragrant regenerated cellulose fiber will be developed in the future.

REFERENCES

[1] Wang C.X., Chen S. L. Micro morphology and inclusion mechanism of the fragrance microcapsule of β-cyclodextrin. *Journal of Textile Research*, 2005, 26(6): 22-24.

[2] Xiao Z.B., Lv C.C., Feng T. Research review of β-cyclodextrin/flavor encapsulation. *Cereals and Oils*, 2010, 3: 1-6.

[3] Yan M.C., Xu Y.M., an X.W., et al. Study on the preparation of β-cyclodextrin micro-capsules of perfume, *Detergent amd Cosmetics*, 2006, 29(4): 19-21.

Preparation and Mechanical Properties of Thermoplastic Films from Superfine Down Powder

Wenbin Li[1, 2], Weigang Cui[2], Xin Wang[2], Weilin Xu[2], Xin Liu[2]
[1]College of Textiles, Donghua University, Shanghai 201620, P. R. China
[2]Key Laboratory of Green Processing and Functional Textiles of New Textile Materials, Ministry of Education, Wuhan University of Science and Engineering, Wuhan 430073, China
Liuxin0111184@hotmail.com

INTRODUCTION

In recent years there are great interests in protein fibers to produce new biomaterials and reuse waste protein materials [1-3]. Compared to synthetic polymer, these protein materials are usually biocompatible, degradable and environmentally friendly. One important method of reusing protein fibers is to extract keratin from these protein fibers using complex chemical methods, the keratin was then blended with synthetic polymer to produce protein biomaterials. However, keratin solution is instable in the process of extruding and hot-pressing under high temperature due to the destruction of its super-molecular structure. It is necessary to find a new way to promote the usage of protein fiber for functional applications under high temperature. Down fiber is usually of lower density and much cheaper than wool fiber and silk fiber. Furthermore, superfine down powder may be one of the best available additives for producing thermoplastic films under high temperature. A variety of thermally proceeded protein films have been prepared and the convenient plasticizing agents are glycerol and soybean oil [4, 5]. However, the film modified by glycerol showed higher weight loss of glycerol which limited its application. Formamide is one of the most important biochemical models has two C=O and one N-H corresponding to the receptor and donor of hydrogen bond proton respectively. So there are many N-H······O=C bonds in the backbone of formamide, and can react with H_2O by forming various hydrogen bonds. Moreover, fomamide has the similar group and bonds with that of superfine down powder. Superfine down powder has a large amount of the amino acid, of which the cysteine is a sulfur-containing amino acid and can form sulfur-sulfur (S-S) cystine bonds with other intra- or intermolecular cysteine molecules. Therefore, this indicates that the formamide is an excellent plasticizing agent to prepare superfine down powder films. In this paper, superfine down powder was blended with various amounts of formamide and then the blends were hot-pressed into thermoplastic films, which showed semitransparent and toughness properties.

APPROACH

Materials. Superfine down powder (SDP) was produced from duck feather on a purpose-built machine, and the average diameter of the powder was 1.546 μm. Acetone was supplied from Kedi Co. Ltd., Tianjin, China. Formamide (A. R.) was supplied from Kedi Co. Ltd., Tianjin, China.

Film preparation. Thermoplastic films with different contents of formamide were prepared according to the following procedures: superfine down powder was added into a beaker and then formamide was slowly added into the beaker. To avoid some aggregates of superfine down powder, the blend powder was mixed in an All-Purpose High-speed Smashing Machines. Then, the blend was sandwiched between two Teflon-coated compression molder and hot-pressed into thin films on a plate vulcanization machine (XLB-D350×350, china). After pressing, the film was removed from the molder and cooled until its temperature reached room temperature. This resulted in circular films with around 1.5 mm in thickness and different diameter. Amount of formamide were changed in experimental by 20 %, 25 %, 30 %, 35 %, 40 %, 45 % and 50 % to the weight of superfine down powder.

Mechanical properties. Mechanical properties were tested on an Instron 5566 Universal Testing Machine, at a gauge length of 50 mm and strain rate of 50 mm/min. The length and width of samples respective was 60 mm and 20mm. Each sample was tested 5 times and the results were averaged. The weight of the film was tested immediately after the film was cooled down, after that, the samples were weight every three days at room temperature.

Weight loss. Weight loss was calculated according to the equation:

$$Weight\ loss(\%) = (W_1 - W_2)/W_1$$

Where, W_1 is the original weight of the film, W_2 is the weight of film after different storage time.

RESULTS AND DISCUSSION

Loss of formamide of thermoplastic films from superfine down powder. The weight loss percentages of the thermoplastic films (pressed at 130 °C and 5 Mpa for 5min) under different storage time are shown in Figure 1. The curves of weight loss showed a sharp slop within 9days, and this showed the removal of formamide from the films. After 12 days the weight of films became stable comparatively suggesting that formamide is a good plaster compared with glycerol, which could be also observed in Figure 2. It could be seen clearly that after 1 day and 2 days there were a few amount of glycerol on the surface of glycerol thermoplastic films, but on the contrary the formamide could not be found on the surface of formamide thermoplastic films even if the films were exposed to atmosphere for 2 days. This indicates that formamide is a good plasticizer and can form more chemical bond with superfine down powder.

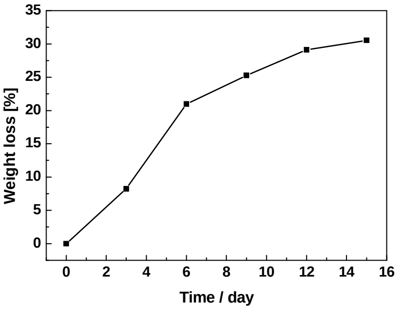

Fig. 1. The weight loss of thermoplastic films exposed to atmosphere with different times.

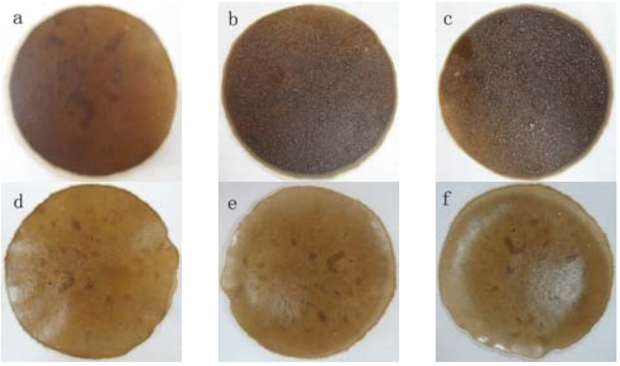

Fig. 2. Superfine down powder thermoplastic films: a. glycerol (0 day); b. glycerol (1day later); c. glycerol (2 days later); d. formamide (0 day); e. formamide (1 day later) f. formamide (2 days later).

Mechanical properties of thermoplastic films from superfine down powder. The tensile strength, elongation at break and elongation at break of thermoplastic films with different formamide contents are shown in Figure 3. It was apparent that with the increase in formamide content, the tensile strength and Young's modulus of thermoplastic films decreased steadily, but the elongation at break reached an maximum value when formamide content was around 35%. It is obvious that the superfine down powder films became more ductile with the increase in formamide content. With the increase in formamide content, the diameter of films increased and the thickness decreased at the same time. When the formamide content was lower than 20% the pressed films were too brittle to obtain good mechanical properties, and films with greater than 50% formamide were incomplete after hot-pressing. It is evidently that adding of formamide made the down powder film ductile and deformable.

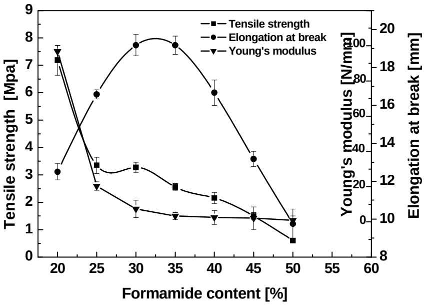

Fig. 3. Tensile strength and elongation at break of superfine down powder thermoplastic films with different formamide content.

CONCLUSIONS

The results of this study indicates that the formamide is a good plasticizer, which not only improves the mechanical properties of superfine down powder thermoplastic films largely, but also sustains the excellent protein properties of down powder. With the increase in formamide content, the tensile strength and Young's modulus decreased steadily. However, the elongation at break reached a maximum value when fromamide content was around 35%. This suggests the more formamide content, the more ductile thermoplastic films we can obtained.

ACKNOWLEDGMENT

We greatly acknowledge the support from the National Natural Science Foundation of China (Project No. 51203124) and Major State Basic Research Development Program (973 Program) (Project No. 2012CB722701).

REFERENCES

[1] Bullions T. A., Hoffman D., Gillespie R. A., Price-O'Brien J., Loos A. C. Contributions of feather fibers and various cellulose fibers to the mechanical properties of polypropylene matrix composites. *Composites Science and Technology*, 66, 102-114 (2006).

[2] Martínez-Hernández A. L., Velasco-Santos C., Icaza M. D., Castañño V. M. Mechanical properties evaluation of new composites with protein biofibers reinforcing poly(methyl methacrylate). *Polymer*, 46, 8233-8238 (2005).

[3] Barone J. R., Schmidt W. F., Liebner C. F. E. Compounding and molding of polyethylene composites reinforced with keratin feather fiber. *Composites Science and Technology*, 65, 683-692 (2005).

[4] Barone J. R., Schmidt W. F., Liebner C. F. E. Thermally processed keratin films. *Journal of Applied Polymer Science*, 97, 1644-1651 (2005).

[5] Barone J. R., Schmidt W. F., Gregoire N. T. Extrusion of feather keratin. *Journal of Applied Polymer Science*, 100, 1432-1442 (2006).

Mechanical Properties of Polypropylene Composites Reinforced with Down Feather Whisker

Xin Liu, Yuanjia Cheng, Fengxiang Chen, Hongjun Yang, Weilin Xu
State Key Laboratory of New Textile Materials and Advanced Technology, Wuhan Textile University, Wuhan 430073,
People's Republic of China
weilin-xu@hotmail.com

STATEMENT OF PURPOSE

Polypropylene composites reinforced with down feather whisker with and without surface modification were prepared and characterized through a series of tensile tests.

INTRODUCTION

In this study, down feather was cut into down feather whisker (DFW), which has the length to diameter ratio of 20-50. DFW sustains the excellent properties of protein materials and has stable structure against high temperature. Therefore application of DFW to thermoplastics resin industry is available under high temperature, and the polypropylene/DFW composites are expected to have the following properties: low density, degradability, good design and manufacture flexibility and hydrophilic property, which could be used in breathable plastic, hydrophilic fiber, agricultural sheet and even biomedical materials industries. But DFW has hydrophilic surfaces that make it incompatible with polypropylene. The interfacial adhesion between whisker and polymer is one of the major factors determining the ultimate mechanical properties of composites. The surface of several fillers, such as mesoporous, plate-like talc (T), needle-like wollastonite (W), SiO_2, Al_2O_3, ZrO_2, TiO_2 (anatase), TiO_2 (rutile), Fe_2O_3, and Fe_3O_4, modified by titanate coupling agent reagent, showed better interfacial adhesion between fillers and synthetic polymer matrix [14-19]. Q. H. Fang and coworkers have proved the chemical reaction between soy protein isolate and NDZ-201[20]. DFW contains much hydrophilic groups such as hydroxyl, carboxyl and amino group. Hydroxyl groups present in DFW can react with isopropyl tri(dioctylpyrophosphate) titanate (NDZ-201) to Ti-O bonds, respectively. Moreover, long chain hydrocarbon segments of NDZ-201 are compatible with polypropylene. Therefore, this suggests that NDZ-201 is an excellent modifying agent to improve both the dispersion of DFW in PP matrix and the interfacial adhesion between DFW and polypropylene. In present work the effects of NDZ-201 on the interfacial adhesion, mechanical properties of PP/DFW composites were studied.

APPROACH

Materials. Isotactic Polypropylene (MFR = 36 g/10 min) was obtained from Panjin Co. Ltd., China. Down feather of duck was purchased from Maolong-wuzhong Down Co. Ltd., Shaoxing, China. Acetone was supplied from Kedi Co. Ltd., Tianjin, China. Titanate coupling reagent used, Isopropyl tri(dioctylpyrophosphate) titanate (NDZ-201, $C_{51}H_{112}O_{22}P_6Ti$) was purchased from Nanjing Shuguang Chemical Group Co. Ltd., Nanjing, China.

Surface Modification of Superfine Down Powder. Down feather was cut into down feather whisker (DFW) on the self-made machine. DFW was cleaned from acetone for 2 hours and then dried at 105 ºC for 2 hours. A certain amount of NDZ-201 (5 % by weight of DFW) was dissolved in acetone under room temperature for 5 min, and then DFW was put into the solution and dispersed by ultrasonic at 80 ºC for 3 h. The modified down feather whisker (MDFW) was filtered by filter paper and dried at 105 ºC for 5 h to remove residual NDZ-201.

Composites Preparation. Composite pellets at various composition ratios were prepared in a twin-screw extruder (SHJ-18, china) using different routes: (a) varying amounts of DFW (10 %, 20 %, 30 %, 50%, 60 % by weight of PP) were compounded with PP; (b) a certain mount of MDFW (20 % by weight of PP) was compounded with PP. After dried at 105 ºC for 2 h, these pellets were respectively sandwiched between Teflon-coated compression molder and hot-pressed into thin sheets at 190 ºC and 5 MPa for 5 min on the plate vulcanization machine (XLB-D350×350, china). After pressing, the sheets were removed from the molder and cooled until they reached room temperature. This resulted in foursquare sheets with around 0.5 mm in thickness and sides of 100 mm × 100 mm.

Scanning electron microscopy (SEM). Morphologies of DFW and cross-section of composites were examined on a Scanning Electron Microscope (JSM-5610LV), at 25 kV after gold coating.

Tensile properties of composites. Relation between stress and strain was performed on an Instron 5566 Universal Testing Machine, at a gauge length of 50 mm and strain rate of 50 mm/min. The width and thickness of samples respective was 20 mm and 0.5mm. Each sample was tested 5 times and the results were averaged.

RESULTS AND DISCUSSION

SEM analysis of composites. The cross-section morphologies of pure PP, PP/DFW composites and PP/MDFW composites were shown in Figure 5. Based on Figure 5(a), the cross-section of pure PP was smooth. As the amount of DFW was 20 % and 50 %, DFW was separated from PP matrix and not uniformly distributed in PP matrix. But the cross-section of PP/MDFW composites (Figure 1(d)) showed that MDFW was uniformly distributed in PP matrix and mostly linked with PP matrix. Furthermore, based on Figure 1(e-f), it could be seen clearly that there were gaps between DFW and PP matrix, but the gaps between MDFW and PP matrix could not be found in PP/MDFW composites. This indicated that NDZ-201 was an excellent coupling agent, which efficiently improved both the dispersion of powder in PP matrix and the interfacial adhesion between MDFW and PP matrix.

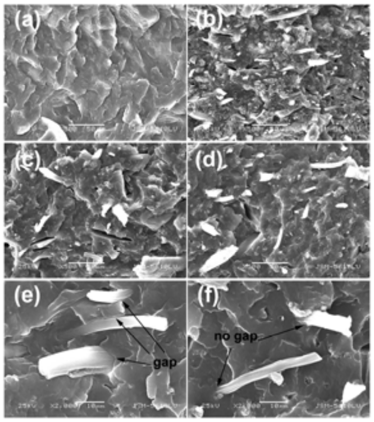

Figure 1. SEM microphotographs of cross-section: (a) pure PP, (b) PP/DFW composite (50:50), (c) and (e) PP/DFW composite (80:20), and (d) and (f) PP/MDFW composite (80:20).

Mechanical properties of composites. Average values of tensile strength, elongation at break and Young's modulus for pure PP, PP/DFW composites and PP/MDFW composites were summarized in Table 1. It was obvious that the tensile strength and the elongation at break of PP/DFW composites decreased as the increase in the content of DFW due to the poor compatibility between DFW and PP matrix. For higher content of DFW, polymer matrix formed did not cover them completely, producing voids that weaken the interface and obstruct the load transfer between DFW and matrix. For PP/DFW composites (80:20), the tensile strength and the elongation at break decreased to 26.80 MPa and 2.100 mm respectively. It was worth noting that the maximum tensile strength of 31.25 MPa achieved with the PP/MDFW composites (80:20) revealed an important contribution from the MDFW to the tensile strength of composites. This is result of the even dispersion of MDFW and good interfacial adhesion between MDFW and PP matrix. All the composites had a Young's modulus larger than pure PP as observed in Table 2. As the amount of DFW was 50 %, the Young's modulus of PP/DFW composites could reach an increase by 35.0 %. In addition, the Young's modulus of PP/MDFW composites was larger than that of PP/DFW composites. Young's modulus of all the composites increased due to the stiffening effect of DFW, which was stiffer than pure PP and diminished the matrix's flexibility. Moreover, for PP/MDFW composites, improved interfacial adhesion between two phases was another important fact to increase Young's modulus. Therefore, in order to use completely the DFW's potential as reinforcement, an even dispersion of DFW and strong chemical or physical bonds between DFW and PP matrix were necessary, to transfer the load between both phases. This indicated that that NDZ-201 was an excellent modifying agent to improve both the dispersion of DFW in PP matrix and the interfacial adhesion between both phases.

TABLE 1. Tensile strength, elongation at break and Young's modulus for different composites.

Composites (content of whisker)	Tensile strength	Elongation at break	Young' modulus
	(MPa)	(mm)	(N/mm)
Pure PP	28.89 ± 1.95	4.264 ± 0.372	252.1 ± 12.1
PP/DFW (90:10)	27.24 ± 2.60	2.354 ± 0.251	214.3 ± 18.5
PP/DFW (80:20)	25.80 ± 2.28	1.921 ± 0.187	292.1 ± 21.7
PP/DFW (70:30)	24.27 ± 2.09	1.518 ± 0.213	287.2 ± 32.6
PP/DFW (50:50)	19.87 ± 1.06	0.923 ± 0.072	321.1 ± 28.6
PP/MDFW (80:20)	31.25 ± 1.53	2.550 ± 0.138	305.8 ± 28.6

CONCLUSIONS

The result of this study indicated that the addition of DFW leaded to an increase in the tensile strength of PP/DFW composites, and NDZ-201 acted as an effective modification agent to improve the weak interfacial adhesion between DFW and PP matrix.

ACKNOWLEDGMENT

We greatly acknowledge the support from the National Natural Science Foundation of China (Project No. 51203124) and Major State Basic Research Development Program (973 Program) (Project No. 2012CB722701).

REFERENCES

[1] Wang Z.W., Wang T.J., Wang Z.W., Jin Y. The adsorption and reaction of a titanate coupling reagent on the surfaces of different nanoparticles in supercritical CO2. *Journal of Colloid and Interface Science*, 2006, 304(1): 152-159.

[2] Wang N., Fang Q.H., Zhang J., Chen E.F., Zhang X.B. Incorporation of nano-sized mesoporous MCM-41 material used as fillers in natural rubber composite. *Materials Science and Engineering: A*, 2011, 528(9): 3321-3325.

[3] Cho Y.S., Yi G.R., Hong J.J., Jang S.H., Yang S.M. Colloidal indium tin oxide nanoparticles for transparent and conductive films. *Thin Solid Films*, 2006, 515(4): 1864-1871.

[4] Zhang Y., Yu J.R., Chen L., Zhu J., Hu Z.M. Surface Modification of Ultrahigh-molecular-weight Polyethylene Fibers with Coupling Agent during Extraction Process. *Journal of Macromolecular Science, Part B: Physics*, 2009, 48(2): 391-404.

[5] Li T.Y., Wang N., Fang Q.H. Incorporation of modified soy protein isolate as filier in BR/SBR blends. *Journal of Materials Science,* 2010, 45(7): 1904-1911.

Study on a New Type of Hot-Melting Polyester Sea-Island

Haihua Zhan, Xiaodong Shang, Huaqiang Li, Xingxing Ye, Xisi Jiang
College of Textiles & Fashion, Shaoxing University, 508 West Huancheng Road, Shaoxing 312000, P. R. China
Contact author: zhh21080@163.com

STATEMENT OF PURPOSE/OBJECTIVE

By researching the property of hot-melting polyester sea-island filament, tentatively probing into the character of the filaments produced in different technological conditions to find out which can meet the needs of the market best. We hope the filament produced by the refitted double twister has better physical property, appearance and the section than the one manufactured by the polyester spring machine KF6-800, and is more suitable for the industrialization applications.

INTRODUCTION

The new type of hot-melting polyester filament, adopting the core-sheath com-pound filature with the cortex of low melting point new type of hot melting polyester constituents and the sandwich layer of normal polyester, first make the multifilament of monofilament in fine fibrousness and then make the core-sheath compound filatures bond into a monofilament through a special post-processing technology ; thus it produces the new type of hot-melting polyester sea-island filament, overcoming the challenge of spinning low melting point coarse-denier polyester filament and attaining the goal of reducing the cost of the fiber while improving its property.

APPROACH

This experimental material adopts 83dtex/24f core-sheath compound filaments.

Preparing method 1: made from common two-for-one twister machine by increasing hot boxes and yarn ducts. T-he twisting process of the silk thread is mainly divided in-to two phases: 1) The twisting process: the same operating principle with normal two for one twister machines, namely to inflict couple of forces in the cross section of the silk thread to make the cross section twist some angle to the neighboring cross section around its central axis. 2) The setting process: temporarily closed the displacement restoring capacity aroused by twisting and adopt the temperature of about 200℃ to carry out the dry heat setting.

Taking full advantage of the property of the equipment after transformation, adopting the raw material of the 83dtex/24F core-sheath compound filature whose cortex melting point is 167℃ and being under the process conditions, of which the processing speed is 250m/min, the twist is 100twists/m,the winding angle is 30 degree, the down-feeding rate is -1%,the up-feeding rate is 3.6% and the hot-box's temperatures are respectively 180℃ ,190℃,200℃ and 210℃, products are made in the representation of A1,A2,A3 and A4.

Preparing method 2 adopted ordinary texturing machine as following steps. Model KF6-800, made by Wuxi Textile machinery manufacturing limited company. Technological conditions: processing speed: 280m/min, temperature of the first heating cabinet: 130℃, ratio: 1.5, drawing ratio: 1.003, the second overfeeding: 1.0%, the third overfeeding: 11%. On the circumstance of stable conditions above, we set the temperature of the second heating cabinet respectively as 150℃、170℃、190℃、210℃, products shown as B1、B2、B3、B4.

RESULTS AND DISCUSSION

Density of monofilament

The size of monofilament textured from common texturing machine is thicker than that form a one-step two-for-one twister, for during the process of texturing, filament is extended by the drafting axis, thus thinner than multifilament. Stretch yarn machine KF6-800 doesn't stretch filament, however, to have a better shape, it is necessary for a second and third feed, and thus the size of monofilament will be thicker and shorter.

Stretchability

That breaking tenacity and breaking length of sample A is bigger than sample B, stretch ability of monofilament from improved two-for-one twister is bigger than the sample form stretch yarn machine KF6-800. That is, for one reason, fiber is more abrasion-proof for a better roundness when passed through false twister. Monofilament from stretch yarn machine has a much poorer in breaking tenacity and breaking length.

When other conditions remain the same, fiber made by two-for-one twister may be different due to variation of drying machine temperature tenacity of filament improves with the rising of temperature and stretch ability falls down after a climbing-up, that's because the incomplete agglutination at a relative low temperature and part of the multifilament are squeezed out, but when the temperature is too high, the molecular chain of the low-melting-point constituent are broken. The breaking tenacity and breaking length of filament made by KF6-800 are inversely proportional to the temperature of the second heater. The sample used in this experiment is low-melting-point composited filament, the melting point of the cortex is 167℃, and the same as the former one high temperature will speed up the damage of the macromolecular structure of low-temperature polyester. Hence the strength and elongation will be lower at a higher modular temperature.

Shrinkage rate in boiling water

The shrinkage ratio of monofilament A made by the modification of the double twisting mechanism is less than of monofilament B made by the KF6-800 stretch yarn mechanism.

According to the mechanism of shrinking, the shrinkage super polymer depends on the orientation of amorphous region, as high polymers for synthetic fiber are crystalline polymer with two-phase structure, the shrinkage of it depends on the orientation and crystallization of fiber and it's more depend on crystallization factors, that's because the orientation and network knot and increases with the rising of crystallization rate, therefore shrinkage declines. Higher crystallization leads to lower shrinkage. During the process of texturing on twister, multifilament were stretched at a high modular temperature and a low processing speed, the shrinkage hence decreases due to the high crystallization rate. And crystallization rate is in proportion to the increasing of modular temperature, shrinkage of it in boiling water has a linear relationship with the crystallization rate, the shrinkage of monofilament textured by both machine all decreases when modular temperature rises.

Unifilar section morphology

Use SNG-300 type scanning electron microscope magnified 500 times to observe the vertical and horizontal section of monofilaments A and B, as shown in Figure 1. The results indicate:

Longitudinal section: A1 is not well agglutinated for low temperature, while the section of A2-A4 is very smooth than the first one. For sample B, the indenture on its section suggests a poor agglutination of the sample. When put into production, A2-A4 will perform better sample B.

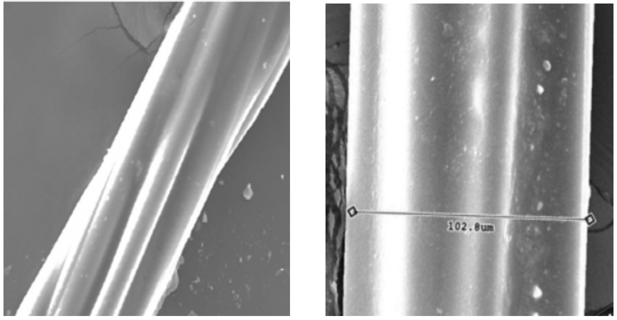

(a) A1 (b) A2-A4

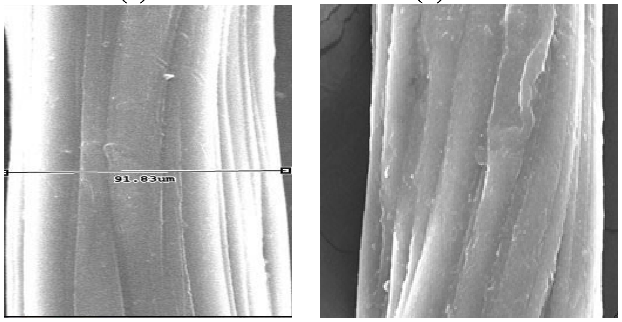

(c) B1,B2 (d) B3-B4

Fig.1 SEM of monofilaments A and B

Cross section: The appearance as well as agglutination of sample A is better than the other two samples. It is a sea-island filament. Furthermore, it shows that improved two-for-one twister can better adapt to the industry and has a profound potential market, the filament made by it performs well both in tenacity and perfect roundness.

DSC plot

A sample because of its own two-component mutual infiltration of integration in the DSC curve test process, there is no obvious absorption heat melting phenomenon, and when the quantity of heat of absorption than B sample is less; And B sample in the test process of 158.6 ℃ place has obvious endothermic phenomenon, in the melt when the quantity of heat of A need to compare, based on the above two points that B sample in their own the hot melt process have deficiencies, double component does not meet the perfect fusion. In the industrial way, a clear can achieve more people use requirement.

CONCLUSIONS

A. skin-cored polymeric multifilament can be produced by improved twister and texturing machine, the product can have a good mechanism and appearance.

B. with the increasing of temperature of the second heater, the breaking tenacity and breaking length of monofilament declines during the process on the common texturing machine, and its strength and elongation are not as good as that textured by two-for-one twister.

C. the results of DSC plot, the transverse and longitudinal section, shrinkage in boiling water and stretch ability shows that improved two-for-one twister is better than the common texturing machine, and performs perfect at the modular temperature of 190 ℃ when other conditions remain the same .

REFERENCES

[1] Wu Ting. Relationship between Processing Parameters and Effect of One-step Two-for-one Twister [J]. Zhejiang Province. *Silk*, 2002, (2): pp. 33-35.

[2] Li Ruqin, Song Juncai. Techniques of Test and Measurement for Fiber and Textile [M]. Shanghai. Donghua University Press, 2009.

[3] Zeng Xin, Yang Ruiling, Yang Xin. Research on Spinning Process of Low Melting-point Polymeric Fiber [J]. Shanghai. *Synthetic Fiber*, 2004, (1).

[4] Wang Xianlou. Basic Knowledge of polyester production [M]. Beijing. Textile Industry Press, 1993, pp. 61, 96.

[5] Matthias Wagner, Lu Liming. Foundation of Thermal Analysis Apllication [M]. Shanghai. Donghua University Press, 2011.

[6] Xiao Ru, Yang Weizhong, Gu Lixia. Influence on Strecthability of CDP-FDY Fiber Stretching Temperature [J]. Shanghai. *Synthetic Fiber*, 2002, 31 (4): pp. 12-15.

Research on Mechanical Properties of 100% Cotton Anti-Creasing Yarns

Yunli Wang[1], Jun Chen[2], Shan Cheng[2], Zongli Mao[1], Mingmin Dong[1], Weilin Xu[2]
[1]College of Chemistry and Chemical Engineering, Wuhan Textile University, Wuhan 430073, P. R. China
[2]Key Laboratory of Green Processing and Functional Textiles of New Textile Materials, Ministry of Education, Wuhan Textile University, Wuhan 430073, P. R. China
wangyunli002@163.com; weilin-xu@hotmail.com

STATEMENT OF PURPOSE

The traditional pad-dry-cure (PDC) Anti-creasing finishing process always results in severe decline of the fabrics in mechanical properties. When the proportion of anti-creasing fibers lessened in the fabrics, the mechanical properties and the overall qualities of the finished fabrics would be sustained in a higher level. In this study, the cotton yarns were treated with anti-creasing resin. The relationship between the process parameters and mechanical properties of the treated fibers was analyzed and discussed. This work provides primary results for researchers to understand the effect of anti-creasing yarns on the whole fabric.

INTRODUCTION

Cotton fiber possesses some outstanding properties, including good hydrophilicity and permeability, soft handle, and wearability, etc. So it is widely used in textile industry for many years [1]. Unfortunately, cotton fiber goods very easily wrinkle during using and washing, and seriously affect their fashion and appearance [2]. Thus, the anti-creasing finishing is vital to maintain their appearance style [3]. The conventional finishing method is PDC process, which the fabric is regarded as a whole, and every cotton fiber acquires uniform treating effect [4]. However, the fatal problem is that the process will lead to a sharp drop in the fiber strength [5]. In addition, the other properties of fabric are also worse after finished [6].

If the partial fibers in the fabric were modified to anti-crease, and the proportion of crosslinking fibers reduced, which kept the mechanical properties of fabrics in a higher degree. At the same time, the wearability and comfortability would be improved than the traditional PDC process. Therefore, the contradiction between anti-creasing properties and strength loss can be effectively solved though still has a long way to go to industrialize.

In our previous study, we tested the yarn WRA, and discussed the relationship between the treating process and anti-creasing properties of cotton yarns [7]. In this work, the tensile strength of yarn was measured and used to study the effects of the process parameter on mechanical properties of cotton yarns. The results provided the primary data for people knowing and using anti-creasing yarns to produce the easy care textiles and improve the fabric overall quality.

APPROACH

Materials

19.4 tex 100% cotton yarn was spun in laboratory. Anti-creasing finishing agent PS-14 (N-methylol type resin) and catalyst C-5 were provided by Dymatic Investment Co., Ltd., Wuhan, China. Penetrating agent JFC was the present of Yinhe Chemical Co., Ltd., Wuhan, China.

Yarn anti-creasing treatment

500mL anti-creasing finishing solution containing a certain concentration of PS-14, C-5 and 1g/L JFC was prepared. A bundle of 80 meters cotton yarn was steeped and rolled two times in treating solution, respectively. Subsequently, it was dried at 80 ˚C in oven, and then cured at elevated temperature for a certain time in another oven. Next, the properties of yarn before and after treatment were analyzed and evaluated.

Measurements

A FTIR instrument (BRUKER TENSOR 27, Germany) was used to measure the infrared spectra of the yarns.

The yarn tensile strength was measured according to GB/T 3916-1997 standard.

RESULTS AND DISCUSSION

FTIR analysis of yarn before and after treatment

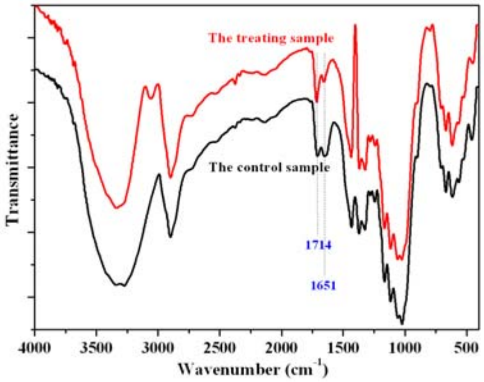

FIG. 1 FTIR spectra of samples before and after treatment.

The FTIR spectra of the yarns before and after crosslinking treatment are shown in Fig. 1. The FTIR spectrum of the control sample has a strong absorption peak at 1651 cm^{-1}, which is assigned as characteristic peak of cotton fiber. After treating, the intensity of absorbance peak at 1714 cm^{-1} is strengthened compared with the control. This is typically characteristic absorption peak of carbonyl group, indicating crosslinking reaction between fiber macromolecules. Consequently, it endues the anti-creasing property of material accompanying the loss of tensile strength.

Effect of curing temperature on yarn tensile strength

Fig. 2 shows the change of yarn tensile strength with elevated curing temperature. The yarn tensile strength gradually descended when the temperature heightened. Temperature was crucial in urging the crosslinking reaction of cotton fiber with finishing agent. With higher temperature, the etherification arose between cellulose macromolecules, restricting the movement and slippage of cellulosic macromolecules, and reducing the yarn tensile strength. On the other hand, the acid degradation at higher temperature was also an important reason.

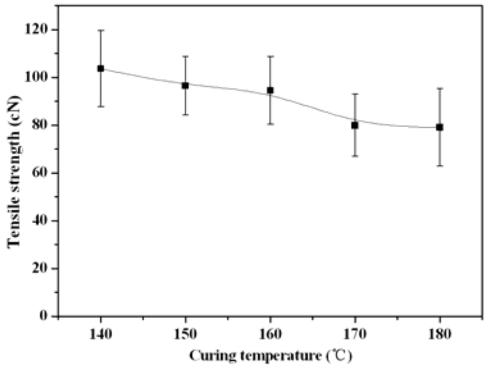

FIG. 2 Effect of curing temperature on yarn tensile strength.

Effect of curing time on yarn tensile strength

As shown in Fig. 3, there is a similar change law of the yarn tensile strength with the curing temperature effect. This is typical time temperature equivalence at yarn anti-creasing treatment. With prolonged curing time, it increasingly fully reacted between fiber macromolecules through crosslinking. Certainly, the acid degradation was also sharper here. So, there is the graphic trend.

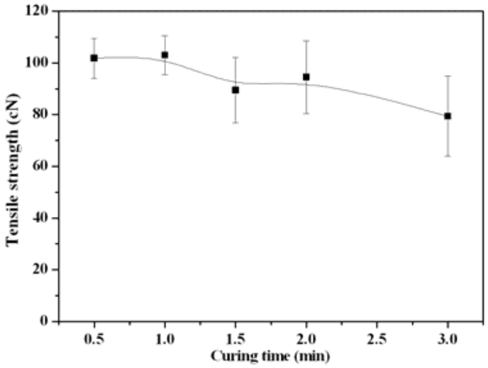

FIG. 3 Effect of curing time on yarn tensile strength.

Effect of finishing agent concentration on yarn tensile strength

The relationship between yarn tensile strength and finishing agent concentration is shown in Fig. 4. The yarn tensile strength basically decreased with enhanced finishing agent concentration. This was mainly because that there were more hydroxyl groups in cotton fiber reacting with increasing finishing agent concentration.

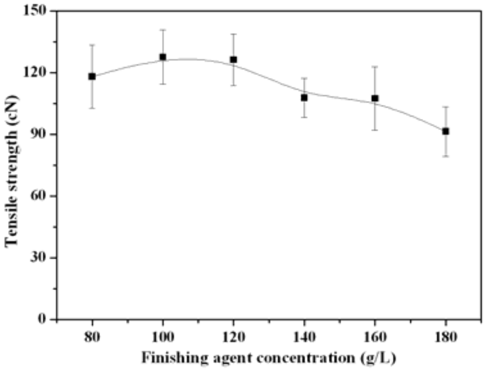

FIG. 4 Effect of finishing agent concentration on yarn tensile strength.

Effect of catalyst concentration on yarn tensile strength

Fig. 5 shows the graph of yarn tensile strength with catalyst concentration change. The change of yarn tensile strength was flat during increasing the catalyst concentration. This indicated that the effect of catalyst on yarn tensile strength was small.

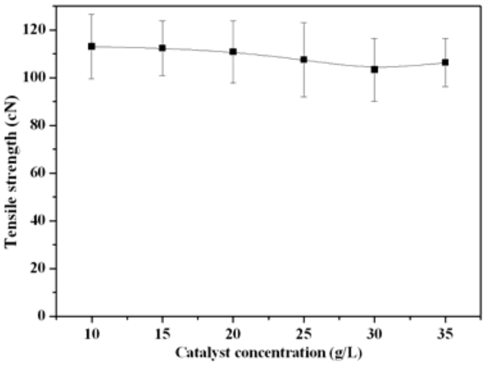

FIG. 5 Effect of catalyst concentration on yarn tensile strength.

CONCLUSION

The cotton yarn was anti-creased, and the influence factor on yarn tensile strength was analyzed and discussed.

ACKNOWLEDGMENT

We greatly acknowledge the support from the Major State Basic Research Development Program (973 Program) (Project No. 2012CB722701).

REFERENCES

[1] Karmakar S. R. *Textile Science and Technology*, Elsevier: New York, 1999.

[2] Hassan M. S. Crease recovery properties of cotton fabrics modified by urea resins under the effect of gamma irradiation. *Radiat. Phys. Chem.*, 2009, 78, 333-337.

[3] Lo L. Y., et al. Understanding wrinkle resistance (Part I). *AATCC Review*, 2007, 7, 28-31.

[4] Chang H.-L., Chen C.-C. Crosslinking of cotton with DMDMDHEU in the presence of sodium chloride. *Textile Research Journal*, 1996, 66, 803-809.

[5] Xu W., Li Y. Cotton fabric strength loss from treatment with polycarboxylic acids for durable press performance. *Textile Research Journal*, 2000, 70, 957-961.

[6] Steele R., Giddings L. E. Jr. The mechanical properties of cellulose fabrics treated with monomethylol and dimethylol ureas. *Textile Research Journal*, 1956, 26, 116-123.

[7] Wang Y., et al. Research on anti-creasing properties of 100% cotton yarns. *Advanced Materials Research*, 2013, 602-604, 2291-2294.

Coloration of Silk Fibers with Gold Nanoparticles

Bin Tang, Lu Sun, and Xungai Wang
Australian Future Fibres Research and Innovation Centre, Institute for Frontier Materials,
Deakin University, Geelong, Victoria 3216, Australia.
xwang@deakin.edu.au; bin.tang@deakin.edu.au

INTRODUCTION

Noble metal (gold and silver) nanoparticles (NPs) have attracted special attention in modern materials science because of their promising applications in various fields such as biological catalysis, detection, electronics and optics. The localized surface plasmon resonance (LSPR) property of noble metal NPs is important for applications in surface enhanced spectroscopy, sensing, and nanophotonic devices. Light interacts with metal NPs, causing conduction electrons to locally oscillate around NPs at a certain frequency. The excitation of surface plasmons by light is known as LSPR [1]. This optical property results in brilliant and fascinating colors.

Textile products with functionalities have generated great interest in recent years. Many attempts have been made to enhance functionalities of textiles, such as antibacterial, antistatic, stain resistant, and UV protection. Silk as a natural protein fiber is widely used in the textile industry due to its inherently elegant sheen, excellent flexibility, environmental friendliness and good comfort. Modification of silk with nanoparticles can improve the function of silk.

In the present study, we employ an assembly approach and an in-situ synthesis method to achieve coloration of silk fibers with gold NPs. Morphology and optical features of silk fibers with gold NPs were characterized. Moreover, the other properties of in-situ synthesized gold NP modified silk including color, washing colorfastness and light colorfastness were investigated as well.

EXPERIMENT SECTION

Preparation of gold NPs.

Gold NPs were prepared by reduction of tetrachloroauric acid ($HAuCl_4$) with citrate through thermal chemistry. A solution of $HAuCl_4$ (0.2 mM) in the presence of citrate (1.0 mM) was used for both the heating and photochemical experiments. Heating experiments were performed at 95 ^oC in the water bath for up to 30 min.

Coloration of silk fibers through assembly of gold NPs.

Silk fibers were colored with the synthesized gold NPs by an exhaustion coloring process [2]. The pH value of gold NP solution was adjusted to 4.0 with acetic acid. The fibers were added to the gold NP solutions at a certain ratio. The dyeing temperature and time were 20 ^oC and 120 min, respectively. After dyeing the fibers were rinsed with running deionized water to remove unfixed gold NPs from the fiber surface.

In-situ synthesis of gold NPs on silk fibers.

The silk fibers were immersed in $HAuCl_4$ solution and placed for 15 min. Color of silk changed to light yellow due to absorption of gold ions. Subsequently, the $HAuCl_4$ solution with silk fibers was heated at 85 ^oC in water bath for 30 min. The silk fibers in solution turn to red after heating treatment. The fibers were rinsed with deionized water before dyeing at room temperature.

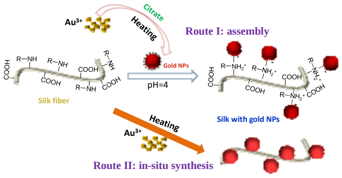

Scheme 1. Illustration of two routes for coloration of silk with gold NPs.

RESULTS AND DISCUSSION

Scheme 1 presents strategy for coloration of silk with gold NPs, including two routes. One is an assembly approach [2]. The gold NPs were synthesized in solution under heating in the presence of citrate. The as-synthesized gold NPs were used to color the silk fibers through an assembled method. The other one is in-situ synthesis method. The $HAuCl_4$ solution with silk fibers was heated and gold NPs were produced through in-situ reduction of gold ions on silk fibers.

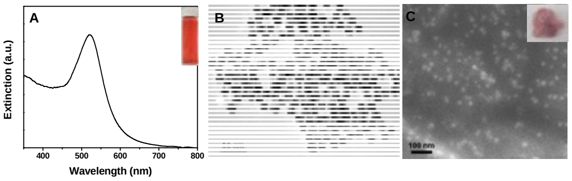

Figure 1. (A) Extinction spectrum and photo of gold NP solution by heating. (B) TEM image corresponding to gold NPs. (C) SEM image of silk fiber treated with assembled gold NPs.

The LSPR extinction band of the gold NPs from heating is centred around 519 nm, which gives rise to the wine red color of gold NP solution (Figure 1A). Transmission electron microscopy (TEM) characterization demonstrates that most of the gold NPs are spherical in shape and have good monodispersity (Figure 1B). The as-synthesized gold NPs were assembled on the surface of silk fibers through electrostatic interaction between fiber and nanoparticles at suitable pH value (Rout I in Scheme 1) [2]. The wine red color of gold NPs solution faded gradually during the process of coloration and finally the solution was colorless, indicating that almost all the gold NPs were assembled onto the silk fibers. Comparing the extinction spectra (not shown) of gold NP solution before and after coloration, it is noted that LSPR bands of the gold NPs disappeared, revealing that the assembling of gold NPs onto the silk fibers was quite complete, with virtually no gold NPs left in the final solution. Silk fibers inherited the LSPR optical properties to exhibit red color. Nevertheless, the colors of the modified silk fibers were slightly different from that of gold NP solutions due to the environment changes around gold NPs, which is consistent with the previous report about coloration of wool with silver NPs [3]. Scanning electron microscopy (SEM) image of the silk fibers colored with gold NPs is depicted in Figure 1C. It can be seen that most of the gold NPs are distributed evenly on the fiber surface.

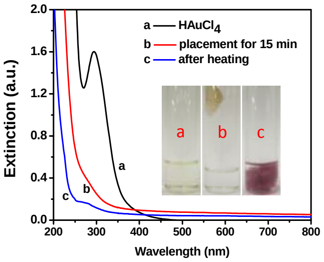

Figure 2. Extinction spectra of (a) $HAuCl_4$ aqueous solution, (b) $HAuCl_4$ solution with silk fibers after placement for 15 min and (c) $HAuCl_4$ solution with silk fibers after heating.

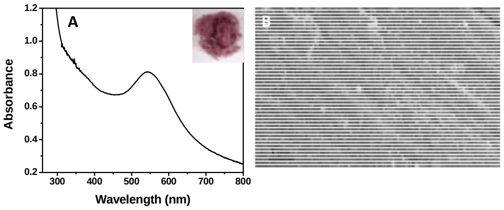

Figure 3. (A) Absorbance spectrum and photo of silk fibers treated with in-situ synthesized gold NPs. (B) SEM image of in-situ synthesized gold NPs on silk fiber.

In addition to the assembly approach, the in-situ synthesis method was developed to accomplish the coloration of silk fibers with gold NPs (Rout II in Scheme 1). Figure 2 shows the absorbance spectra of $HAuCl_4$ solution during the coloration of silk. The absorbance band of initial $HAuCl_4$ solution around 290 nm due to charge transfer between the metal and chloro ligands decreased dramatically after silk fibers was immersed in the $HAuCl_4$ solution and almost disappeared within 15 min, which implies that the Au ions in solution were absorbed by silk fibers (Figure 2). The silk fibers in solution changed to red after heating, indicating the producing of gold NPs on silk fibers (photo in Figure 2). The intensity of absorbance band of solution after heating decreased further (curve c in Figure 2), revealing that nearly no Au ions remained in the solution. Figure 3A depicts the absorbance spectrum of silk fibers treated with in-situ synthesized gold NPs. A single absorbance band located at 543 nm presents in the absorbance spectrum, which is attributed to LSPR of gold NPs on the silk fibers. The silk fibers with in-situ synthesized gold NPs also exhibit red in color (insert in Figure 3A). SEM further demonstrated that the gold NPs were in-situ synthesized on surface of silk fiber through heating (Figure 3B).

Colorfastness of dyed fabrics is very important property in industry. The silk fabrics with in-situ synthesized gold NPs were washed for 45 min at 50 ºC in the presence of ECE reference detergent. Color change (ΔE) before and after washing was obtained. ΔE did not vary obviously after the first washing cycle; even after the silk fabrics was washing for six cycles. The results indicate that the silk fabrics colored with in-situ synthesized gold NPs have a good washing colorfastness. In addition, the silk fabrics with gold NPs were irradiated for 60 h under simulated sunlight to inspect the colorfastness to light. Color of silk fabrics with gold NPs after irradiation changed slightly ($\Delta E=1.00 \pm 0.28$), which reveals that the silk fabrics with in-situ synthesized gold NPs possess a good colorfastness to light.

CONCLUSIONS

Two routes including assembly approach and in-situ synthesis method were used to realize coloration of silk fibers and fabrics with gold NPs. The assembly process of gold NPs on silk fibers can be completed at room temperature much lower than the typical dyeing temperature (close to boil). The assembly of gold NPs on silk fibers was suggested to be completed through the electrostatic interaction between metal NPs and fibers. The in-situ synthesis method provides a simple route to achieve the coloration of silk fibers with gold NPs. The modified silk fibers inherited the LSPR properties of gold NPs and showed red color. The in-situ synthesized gold NPs treated silk fabrics have good washing colorfastness and light colorfastness, which is significant for application of silk with gold NPs in industry. The combination of plasmon materials and different fibers has the potential in functionalizing a range of conventional textile materials.

KEYWORDS: Coloration, Silk, Gold nanoparticles, Self-assembly, In-situ synthesis.

ACKNOWLEDGMENT

This research was supported by the Central Research Grants Scheme and Alfred Deakin Postdoctoral Research Fellowship scheme at Deakin University.

REFERENCES

[1] Kelly KL, Coronado E, Zhao LL and Schatz GC. *J. Phys. Chem. B* 2003; 107 (3): 668-677.
[2] Tang B, Tao J, Xu S, Wang J, Hurren C, Xu W, Sun L and Wang X. *Chem. Eng. J.* 2011; 172(1): 601-607.
[3] Tang B, Wang J, Xu S, Afrin T, Xu W, Sun L and Wang X. *J. Colloid Interface Sci.* 2011; 356(2): 513-518.

Hydrophilicity of the Hydrophilic Copolyester

Xiangling Chen, Chaosheng Wang, Huaping Wang, Qiong Wang, Jianwu Li
State Key Laboratory for Modification of Chemical Fibers and Polymer Materials, College of Materials Science and Engineering, Donghua University, Shanghai 201620, P. R. China
chenxiangling@mail.dhu.edu.cn

OBJECTIVE

A series of hydrophilic copolyesters were prepared via copolymerization method by PTA, EG, SIPE as the third monomer, polyols (FMA01) as the fourth monomer. The hydrophilicity of the hydrophilic copolyester were described by contact angle (CA), moisture regain and moisture absorption rate, wet rate.

INTRODUCTION

Poly (ethylene terephthalate) (PET) is widely used in ordinary life for fibers, films, bottles, and plastics because of its unique performance.[1-2] The physical properties of PET fiber, such as fiber strength, wear resistance, recovery and size stability can meet various uses. Whereas the moisture absorption property of PET fiber is quite lowly.[3] As intimate apparel, the comfort of PET clothes is very poor, it is difficult to eject sweat especially when the human body is sweating, thus gives the unpleasant feeling of body.[4] To overcome these disadvantages, various research methods have been applied to PET modifications.[5] Such as copolymerization method which introduces water hydrophilic groups or flexible groups into macromolecular chain, including carboxyl, amides and amino groups. Among the abovementioned wide variety of hydrophilic groups, polyols are one of the most suitable monomers for copolymerization. It can raise the hydrophilic property of PET, improves the comfort feelings and expand application scope of PET fiber.

EXPERIMENTS

Materials

Purified Terephthalic Acid was supplied by Zhejiang Jiabao New Fiber Group Co., Ltd,Shaoxing, China; Ethylene Glycol, Ethylene Glycol Antimony and FMA01 were supplied by Jiangsu Hengli Chemical Fiber Co., Ltd, Wujiang, China; 5-sodium Suflo Bis-(hydroxyethyl) Isophthalate wassupplied by Jiangyin Huahong Chemical Fiber Co.,Ltd, Jiangyin, China; Triphenyl Phosphate and Titanium dioxide were supplied by Enterprise Group Pharmaceutical Co., Ltd, Shanghai, China.

Preparation Procedure

The feedings of PTA, EG (130 mol % of PTA), SIPE (3 mol % of PTA), $Sb(EG)_3$ (0.04 wt% of PTA), TPP (0.03 wt% of PTA) and TiO_2 (0.5 wt% of PTA), and various mol ratio of FMA01 shown in Table 1 were set. The reaction was carried out in a 5L stainless steel vessel equipped with a nitrogen inlet, a mechanical stirrer and temperature control system. So the viscosity could be judged from the variation of stirring motor power. The temperature circumstance of esterification reaction was 230-250 °C, and reaction pressure was 0.3-0.4 MPa. The esterification reaction finished when the water received to a certain value. The reaction mixture was stirred at 250-260°C for 50min while the pressure was carefully reduced to 600 Pa. The pressure was further reduced to less than 30Pa, and temperature condition of the polymerization was 260-275°C. The reaction completed when the stirring motor power reached to a certain value.

RESULTS AND DISCUSSION

Characteristic Viscosity: The results were listed in Table I. The characteristic viscosity of hydrophilic copolyesters reduced with the increase of FMA01. Characteristic viscosity of hydrophilic copolyesters met the spin ability requirements when the adding amount of FMA01 was below 0.8%. Due to the structure of polyhydroxyl, this could introduce hydroxyl active point to polymerization when adding more than 0.8%amount of FMA01. In addition, excess active point occurred in polymerization process and could cause local cross-linking effect, which led to the difficulties of forming linear molecular structure and resulted in the reduce of characteristic viscosity.

Table I Materials and properties of the hydrophilic copolyesters

Sample	HCDP-1	HCDP-2	HCDP-3	HCDP-4	HCDP-5
FMA01(mol% of PTA)	0.1	0.25	0.5	0.8	1.0
[η](dL/g)	0.682	0.672	0.655	0.594	0.437
Contact Angle(°)	80.2	69.2	62.8	54.5	42.6

Contact Angle: Surface hydrophilic property of copolyester could be analyzed by CA measurement, which was an important parameter to study wetting phenomenon.[6] And CA values got smaller, thehydrophilic property of copolyester were better. The contact angle value shown in Fig.1 and Table I, decreased gradually with the increase of the FMA01 content, the wetting property increased. The CA value was between 42.6° and 80.2°. The polyhydroxy structure took part in copolymerization, and some of them could still exposure to the surface. Water molecules and hydroxyl formed hydrogen bond when water droplet contacted the copolyester film, increased the hydrophilic property

It has been shown in Fig.1, the speed of water absorption of hydrophilic copolyester was rapider than PER. After 15 minutes, the CA value of hydrophilic copolyester was became 0°, which means all the water has been absorbed.

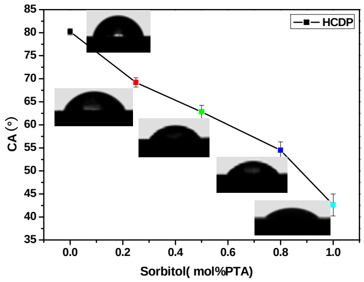

Fig. 1 Contact angle of hydrophilic copolyester

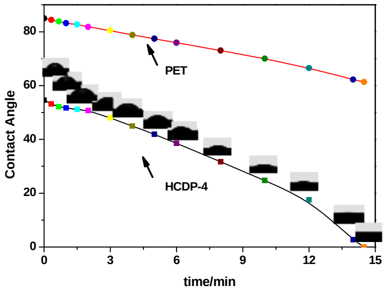

Fig. 2 the relationships between CA value and time

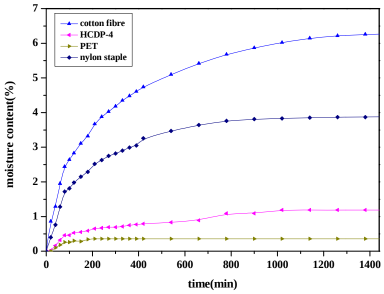

Fig. 3 gaseous water absorbent curve

Form the Fig.3; we can see the water absorption rate was rapid at an initial stage. This is due to the lower water content of the fiber at the initial stage, hydrophilic groups in the fiber has good conjunction ability with the gaseous water molecules. Cotton fibers have a large number of hydroxyl groups, means strong affinity strength with water molecules and combining with the water molecules easily. However, as time increases, the moisture absorption rate is gradually slow down, and the fiber absorbent wet and release exothermic, so that the temperature of the fibers elevate. The vapor pressure increases in the fiber, leading to the partial water vapor pressure gradient decreases in the fiber, and the gap between the fibers is filling of water gas, reducing the speed of the water molecules comes into the fiber, the fiber absorb water slowly. Generally speaking, the modified polyester fiber (copolyester) of HCDP-4 can achieve faster balance than that of cotton fibers.

The gaseous water desorption curve （fig.4）shows that at the beginning stage, the water release rate is quick in the fiber. With the increase of time, changes in the moisture regain gradually slow down, at the constant weight after 50min.

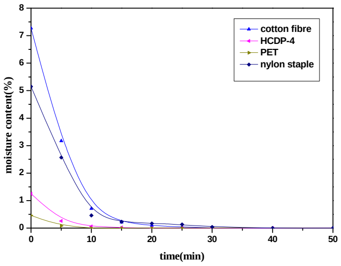

Fig. 4 the gaseous water desorption curve

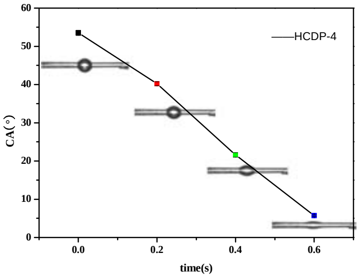

Fig.5 CA-time of modified fiber of HCDP-4

Fig.5 shows that the hydrophilic fibers have good moisture ability; the momentary contact angle of liquid water with the fiber is 55 °. With time increasing, t = 0.6s, the contact angle is reduced to 5 °, the fibers have absorbed moisture completely.

CONCLUSIONS

Results showed that such modified copolymers had excellent hydrophilic properties. With the increase of polyols (FMA01), characteristic viscosity decreased with the increase of polyols (FMA01).When SIPE was 3mol% and FMA01 reached 0.8mol%, the wetting property of copolyester film turned to hydrophilic with water contact angle of 54.5°.The modified polyester has better moisture absorbent, the moisture regain, the desorption rate, the absorption rate is higher than that of conventional polyester fibers.

KEYWORDS: hydrophilicity, contact angle, moisture regain, absorption rate, desorption rate

REFERENCES

[1] F. Seto, A. Kishida and Y. Muraoka: Appl. Polym. Sci. Vol. 74 (1999), p. 1524.

[2] D. PR Kint and S. Munoz-Guerra: Polym. Int. Vol. 52 (2003), p. 321.

[3] I. Donelli, P. Taddei and P.F. Smet: Biotechnol. Bioeng. Vol. 103 (2009), p. 845.

[4] X. Wang, G. Cao and W. Xu: Appl. Polym. Sci. Vol. 112 (2009), p. 1959.

[5] A.C. Ijzer, A. Arun and S.R. Reijerkerk: Appl. Polym. Sci. Vol. 117 (2010), p. 1394.

[6] K.J. Townsend, K. Busse and J. Kressler: Biotechnol. Prog. Vol. 21 (2005), p. 959.

Understanding the Interactions in Acrylic Copolymer/1-Butyl-3-Methylimidazolium Chloride from Solution Rheology

Xinjun Zhu, Yumei Zhang, Huaping Wang
State Key Laboratory for Modification of Chemical Fibers and Polymer Materials, Donghua University, Shanghai 201620, China
wanghp@dhu.edu.cn

OBJECTIVE

The rheological behavior of acrylic copolymer/1-Butyl-3-Methylimidazolium Chloride ([BMIM]Cl) solutions was investigated to understand the mechanism of interactions between acrylic copolymers and [BMIM]Cl.

INTRODUCTION

Besides the common solvents such as dimethylformamide (DMF), dimethylacetamide (DMAc) and dimethyl sulfoxide (DMSO)[1] which are usually used as spinning solvents for PAN, ionic liquids (ILs) also have been proved to be effective solvents for PAN homo- and copolymers.[2, 3] A clear picture can be visualized from the literature concerning the interactions between acrylic polymers and the common solvents.[4] However, the interactions between acrylic copolymers and ionic liquid solvents have not yet been clear. Although some measurements such as nuclear magnetic resonance (NMR) and infrared spectroscopy (IR) have always proved to be the effective ways to characterize the interactions between macromolecule and solvent,[5] it is not easy to carry out the analogous experiments for the polymer solutions in ILs owing to high viscosities of ionic liquids[6] and polymer/ILs solutions. The method of rheology can provide a useful tool to investigate the properties of solutions.

EXPERIMENTAL

1) Materials

PAN homopolymer and copolymers with methyl acrylate (MA) and acrylamide (AM) as comonomer respectively, were synthesized in water by conventional free-radical polymerization.

2) Solution preparation

The polymers were dried and dissolved in [BMIM]Cl at 90 °C to produce a viscous solution.

3) Rheological measurements

The rheological measurements were conducted using an advanced rotational rheometer (Physica MCR 301, Anton Paar) equipped with two concentric parallel plates (diameter: 25 mm).

RESULTS AND DISCUSSION

The apparent viscosity as a function of shear rate for all the solutions of various concentrations were examined at 80 °C. An example of PAN homo-polymer solutions is shown in Fig.1.

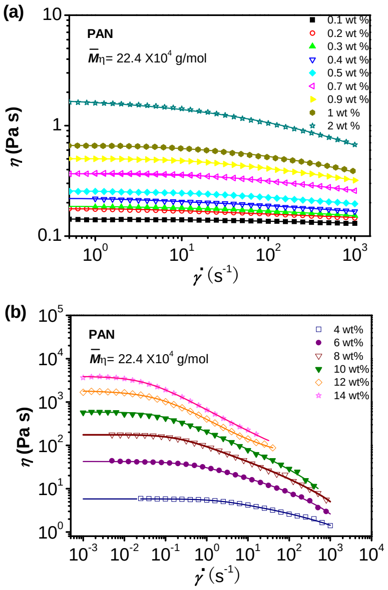

Fig.1. Shear rate dependence of apparent viscosity for selected PAN/[BMIM]Cl solutions at 80°C

The concentration dependence of specific viscosity η_{sp} of acrylic polymer solutions was investigated, as illustrated in Fig. 2. The data of PAN/[BMIM]Cl solutions and poly(AN-co-MA)/[BMIM]Cl mounted on the lines in both semidilute and entangled regimes with slopes of 1.78 and 4.74, respectively. Taking experimental error into consideration, these scaling exponents were found in agreement with scaling predictions by Colby and Rubinstein[7] for neutral polymer in θ-solvent. However, the concentration dependence of η_{sp} for poly(AN-co-AM) (AN/AM = 97/3) in [BMIM]Cl display different power law: between c^* and c_e, $\eta_{sp} \sim (c[\eta])^{1.19}$ and above c_e, $\eta_{sp} \sim (c[\eta])^{3.88}$. The consistency between theory prediction and experimental data suggests that [BMIM]Cl is a good solvent for poly(AN-co-AM) (AN/AM = 97/3) at 80°C. However, MA as a comonomer incorporated into PAN

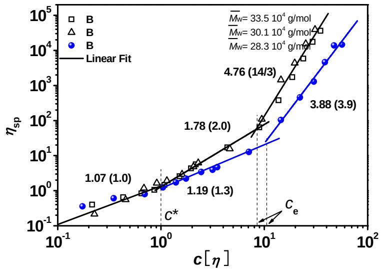

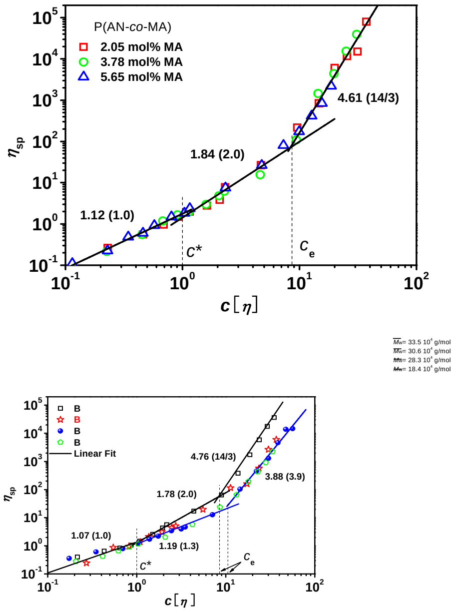

Fig.2. Plot of specific viscosity η_{sp} against overlap parameter c[η] for acrylic polymer solutions at 80°C

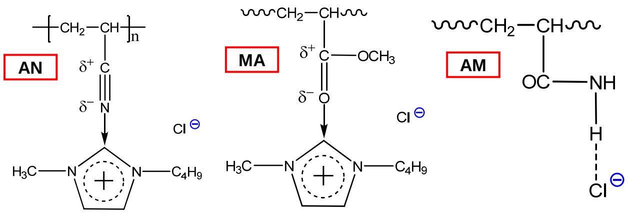

Fig.3. Proposed schematic diagram for the interactions between PAN copolymers and [BMIM]Cl backbone cannot change the θ-behavior of [BMIM]Cl

So in current studies an attempt has been made in order to explain the role of the interactions between nitrile group and cations in the dissolution of PAN homopolymer in [BMIM]Cl. This dissolution should be caused by the interruption and breaking of the dipolar-dipolar interactions of PAN and the formation of interactions between −C≡N group and 1-butyl-3-methylimidazolium cation [BMIM]$^+$. The schematic diagram of the interaction between −C≡N and [BMIM]$^+$ ion is proposed in Fig. 3. Due to the relatively large cation size of [BMIM]$^+$, [BMIM]Cl could not form such strong complex with PAN backbone as it has not the same strong solvation power as Na$^+$ and Zn^{2+}.[8] This weaker interactions result in [BMIM]Cl as θ-solvent for PAN homo-polymer. For poly(AN-co-MA), owing to the nature of electron donating, polar group of carbonyl group (C=O) in poly(AN-co-MA) could coordinate to [BMIM]$^+$ ion. However, due to pendant shaped ester group of MA, the solvating ability of the polymer is dominated by the −C≡N group. The interactions between poly(AN-co-AM) and [BMIM]Cl could be different from that for PAN and poly(AN-co-AM) with [BMIM]Cl. Poly(AN-co-AM) consists of repeating monomer units acrylonitrile AN and acrylamide AM. In addition to carbonyl group, the latter comonomer also contains amino group ($-NH_2$) with two protons as electron acceptor sites which may take part in hydrogen bonding. Thereby, the interactions between poly(AN-co-AM) with [BMIM]Cl include not only the interactions mentioned above but also the new hydrogen bond formed between $-NH_2$ and Cl$^-$. The solvating ability of poly(AN-co-AM) copolymer could be significantly improved with increasing the content of AM.

CONCLUSIONS

Scaling analysis of the specific viscosity and relaxation time-concentration power law indicated that both PAN homo-polymer and copolymer poly(acrylonitrile-*co*-methyl acrylate) (poly(AN-*co*-MA)) in [BMIM]Cl behave as neutral polymer in a θ-solvent. However, [BMIM]Cl acts as a good solvent for poly(acrylonitrile-*co*-acrylamide) (poly(AN-*co*-AM)). It was suggested that the interaction between −C ≡ N and [BMIM]+ should interrupt and break the dipolar-dipolar interaction of PAN resulting in the dissolution of PAN in [BMIM]Cl. Such interaction between −C≡N and [BMIM]$^+$ ion is still dominated the solvating ability of poly(AN-*co*-MA) in [BMIM]Cl, even though C=O in MA repeat unit could coordinate to [BMIM]$^+$. The dissolution capacity of [BMIM]Cl for poly(AN-co-AM) can be evidently improved due to the extra hydrogen bond interaction between $-NH_2$ group of AM and Cl$^-$ of [BMIM]Cl.

KEYWORDS: polyacrylonitrile, ionic liquids, rheology, interaction, copolymer

ACKNOWLEDGMENT

This work is supported by a grant from Shanghai Municipal Education Commission (10ZZ44 and 08GG11) and PhD Innovation Foundation of Donghua University (9D10622).

REFERENCES

[1] J. Brandrup, E. Immergut, E. Grulke, *Polymer handbook*, Wiley Interscience, New York, 1999.
[2] W. Liu, L. Cheng, H. Zhang, Y. Zhang, H. Wang, M. Yu, *Int. J. Mol. Sci.* 2007, 8(3), 180-188.
[3] S. X. Wan, Y. M. Zhang, H. P. Wang, *Polym. Advan. Technol.* 2008, 20(11), 857-862.
[4] J. Du, X. Zhang, *J. Appl. Polym. Sci.* 2008, 109(5), 2935-2941.
[5] A. T. Fafarman, P. A. Sigala, D. Herschlag, S. G. Boxer, *J. Am. Chem. Soc.* 2010, 132(37), 12811-12813.
[6] H. Jin, B. O'Hare, J. Dong, S. Arzhantsev, G. A. Baker, J. F. Wishart, A. J. Benesi, M. Maroncelli, *J. Phys. Chem. B* 2008, 112(1), 81-92.
[7] R. H. Colby, Rheol. *Acta 2010*, 49(5), 425-442.
[8] A. R. Hoskins, H. G. M. Edwards, A. F. Johnson, *J. Mol. Struct.* 1991, 263(C), 1-10.

Reducing Noise Level in Vehicles by Spunbonded Nonwovens Made from Bicomponent Filaments

Fatih Suvari[1], Yusuf Ulcay[1,2], Benoit Maze[3], Behnam Pourdeyhimi[3]
[1]Uludag University, Faculty of Engineering and Architecture, Textile Engineering Dept., Bursa, Turkey
[2]Bursa Technical University, Bursa, Turkey
[3]The Nonwovens Institute, North Carolina State University, Raleigh, NC, USA
suvari@uludag.edu.tr; ulcay@uludag.edu.tr

INTRODUCTION

Driver and passengers inside of a vehicle are influenced by various noise sources such as engine, exhaust system, gears, tires, and wind [1]. The schematic of the primary noise sources are shown in Figure 1. Noise level has to be reduced in passenger vehicles for comfort concerns. There are several methods exist to reduce noise level. One of them is using sound absorber materials to dissipate sound.

Sound absorber materials are effective in a variety of locations inside the vehicle. They can be placed above the headliner, behind the door panel and pillar trim, and under the carpet [2].

Nonwovens are known to have useful acoustical properties and are used as sound absorbers because of their fiber network geometry, bulk and low density. Nonwovens are rather complex porous structures and often have very low solidity (solid volume fraction). The pores (voids) are rather complex also as they are in the form of a bundle of capillaries. Most nonwovens would have a solid volume fraction of 20% or less. These structures inherently have pores with tortuous paths and pores filled with air. This makes nonwovens ideal for sound absorption. It is important to note that most sound absorbers are based on rather thick fibrous structures or foams.

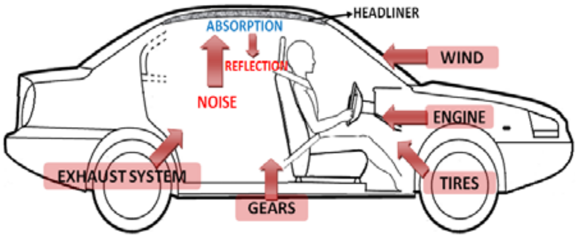

Figure 1 Primary Noise Sources for Cars

Previous studies showed that a decrease in fiber diameter leads to an improvement in acoustical properties of nonwovens. We believe more small pores can be constituted in a fiber network by using thinner fibers inside of a nonwoven. There will be more frictional loses due to expansion and contraction of the air within the small pores, while sound wave passes through.

The aim of this study is to discuss potential use of spunbonded nonwovens that contain bicomponent islands-in-the-sea filaments as a sound absorptive material inside of passenger vehicles.

MATERIALS

All the nonwoven webs made from islands-in-the-sea bicomponent filaments used in this study were produced at the Nonwovens Institute's Partners' Pilot facilities located at North Carolina State University. Bicomponent spunbonded webs were produced by using Nylon-6 (PA6) as the 'Island' polymer and Polyethylene (PE) as the 'Sea' polymer. Basic properties of these polymers are summarized in Table I.

FABRIC FORMATION

All the filaments in nonwovens had a polymer ratio of 75% for the 'Island' polymer and 25% for the 'Sea' polymer. The basis weight of the spunbonded bicomponent nonwoven webs prior to the hydroentangling was kept at ~ 100 g/m^2. Nonwoven fabrics were produced by the spunbond process and bonded (and fibrillated) by hydroentangling as specified in US patent 7,981,226 by Pourdeyhimi, et al.

The hydroentangling unit at the pilot facilities at the Nonwovens Institute comprises 5 manifolds or injectors. The first is used for wetting and pre-entangling the web and is normally at a low pressure of 30 to 50 bar. The other 4 manifolds entangle the web on the face on a belt (2 manifolds) and the back on a drum (2 manifolds). A single pass through the machine is not normally sufficient to cause fibrillation and also entangling and consolidation. Therefore, the webs were passed through the machine for multiple passes; each pass with a pre-wet and two manifolds on the belt and two on the drum. The spunbonded webs were passed three times though the hydroentangling unit at 10 m/min and at a pressure of 25, 150, 220, 220, 220 bar, respectively.

Table I Properties of Polymers Used

Polymer	Trade Name	Supplier	Melting TemperatureT_m (^oC)	Density(g/cm^3)
PA6	Ultramid BS 700	BASF	220	1.14
PE	ASPUN 6811A	Dow Chemical Co.	125	0.94

In hydroentangling, the fibers/filaments are split/ fibrillated and bonded mechanically by subjecting the web to high-pressure hydroentangling water jets. The islands can also be released by dissolving sea, but it is not environmentally friendly and increases the final cost of the product.

RESULTS AND DISCUSSION

Classic spunbonding process can produce nonwoven fabrics with a diameter of 10 – 80 μm. On the other hand, spunbonding process using bicomponent technology is one of the available processes that can produce nonwovens with submicron filaments. Islands-in-the-sea spunbond structures can form superior structures in terms of strength, durability and porosity.

Nonwoven cross sections were examined by using Scanning Electron Microscopy (SEM). Scanning electron micrographs were obtained on a Tescan VEGA3 SBU microscope. Prior to scanning, the specimens were coated with a layer of AuPd using a Denton Vacuum Sputter Coater.

It should be noted that average diameter of the island filaments in 108 I/S nonwoven is less than one micrometer (Figure 2).

Spunbonded nonwovens that contain filaments with islands-in-the-sea cross section can be good structures for sound absorption because they can be custom-designed with specific fiber size and solid volume fraction (solidity).

Note that it is remarkable that the hydroentangling of a islands-in-the-sea nonwoven resulted in a smooth (Figure 3) porous surface. Since this property is an advantage in terms of aesthetic aspect, islands-in-the-sea nonwovens has a potential to be used in vehicles.

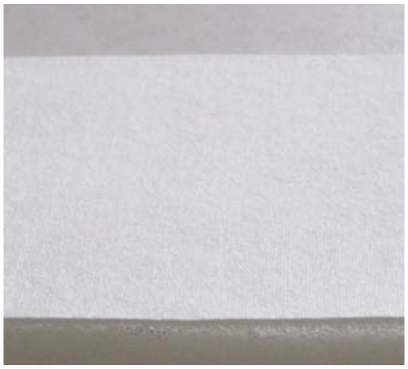

Figure 3 Smooth Surface of I/S Nonwoven

CONCLUSION

- Sound absorption properties of islands-in-the-sea nonwovens can be adjusted for a specific frequency range by changing fabric structure.
- Comfort for passengers inside a vehicle can be improved by reducing noise level with an application of islands-in-the-sea nonwovens.
- They can be used in automobiles especially as a headliner, where their low thickness, low weight, and pleasant look are advantage.

FUTURE WORK

Future work will be investigation of acoustical behavior of composite structures containing islands-in-the-sea nonwovens.

KEYWORDS

Spunbonding, sound absorption, bicomponent filaments, islands-in-the-sea.

ACKNOWLEDGMENT

This work was supported by a grant from the Nonwovens Institute at North Carolina State University.

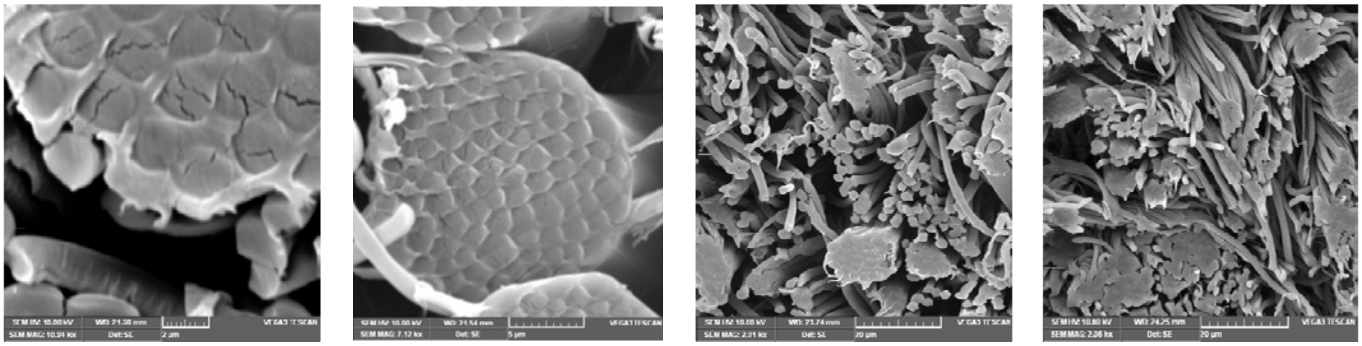

(a) 37 Islands-in-the-sea filament

(b) 108 Islands-in-the-sea filament

(c) Nonwoven with 37 islands

(d) Nonwoven with 108 islands

Figure 2 Cross Section Images of Islands-in-the-sea Bicomponent Filaments (left) and I/S Nonwovens (right)

REFERENCES

[1] Nick, A., Becker, U., Thoma, W. 2002. Improved Acoustic Behavior of Interior Parts of Renewable Resources in the Automotive Industry. *Journal of Polymers and the Environment*, July, 10(3), pp. 115-118.

[2] Zent, A., Long, J. T. 2007. Automotive Sound Absorbing Material Survey Results. *SAE International.*

Optimizing Spindle Speed of Ring Spun Yarn

Sahito Iftikhar Ali, Arbab Alvira Ayoub, Sung Hoon Jeong
Department of Organic and Nano Engineering, Hanyang University, Seoul, Korea
shjeong@hanyang.ac.kr

STATEMENT OF PURPOSE

This study aims to investigate effect of spindle speed of ring spinning machine on hairiness index and structure of single yarn and to investigate optimized spindle speed for short staple cotton yarn spinning for producing lesser hairiness.

INTRODUCTION

Yarn structure has always been given principal significance when determining the end use and performance characteristics of a yarn. In other words the structure of yarn governs its use. In the structure of yarn, hairiness has always been a problem and many experiments have been undertaken in the past to reduce yarn hairiness in mandate to make the outer edges of yarn smoother. Newer technologies, like compact spinning have gained a lot of commercial prominence in the recent years, to reduce yarn hairiness [1, 2]. It is said that the yarn structure is dependent primarily upon the raw material, spinning process, spinning unit, machine, machine settings, twist, etc [3]. Many of these have been investigated in the past and optimized already for particular end used. However increase of spindle speed has been a focus of machine manufacturers which can be increased with compromise of yarn quality. All important yarn properties are known to depend on yarn structure. Differences in the properties of yarns spun with different technologies can be attributed to the differences in their structures. Hence optimizing process parameters and machine settings on ring spinning machine is of inordinate deal of importance.

APPROACH

Many yarn and fabric properties are dependent on the structure of yarn. Therefore a possible variation in the structure of yarn was investigated through varying spindle speed or drafting speed of ring spinning machine. Yarn structural changes were examined at six different spindle speeds from 11000 rpm to 21000 rpm with a 2000 rpm interval. Three yarn counts were prepared in the same manner, 20’s, 25’s and 30’s Ne. A total of eighteen yarn types were made to investigate Hairiness index and structure of yarn. Raw material used for the work was cotton fibers in the form of bale, trade name MNH-93 which is a Pakistani cotton variety. The raw fiber properties are given in the following table 1.1.

Table 1.1 Cotton fiber properties

Fiber Properties	Values
50% Span Length	14.30
2.5% Span Length	30.37
Uniformity Ratio	47.11
Mic value	4.6
Bundle Fiber Strength	7gf/tex
Short Fiber Index (SFI)	4.68

RESULTS AND DISCUSSION

Effect of spindle speed on hairiness index

Yarn hairiness was found to have variation with respect to the variation in the drafting speed. These results are compared in fig. 1.1 for 20’s, 25’s and 30’s Ne yarns respectively.

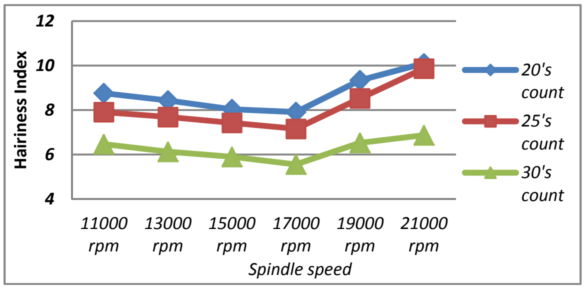

Fig: 1.1 Hairiness Index of 20’s, 25’s and 30’s yarns at different spindle speeds

It is noticeable in the figures above that the hairiness kept on decreasing as the drafting speed is increased from 11000 rpm to 17000 rpm. This may be due to the increase in spindle speed which makes the twist flow closer to front roller nip and spinning triangle will be smaller and fibers in selvedge will be integrated better into yarn. It again starts to increase after 17000 rpm. It should also be added here that at higher spindle speeds, i-e above 17000 rpm, air drag and heat generation due to frictional contact of the fibers increases, which causes the fibers to slip out of the yarn body to become hairiness. Thus it can be said that at 17000 rpm we can produce a yarn that is optimum in terms of hairiness.

Effect of spindle speed on structure of yarn

An observable effect of variation in spindle speed was observed on the structure of yarn. Video Microscope was used to view and analyze the structure of yarn and investigate the type of variation. Below are video microscope images of the three counts of yarn spun at 11000, 13000, 15000, 17000, 19000 and 21000 rpm spindle speed.

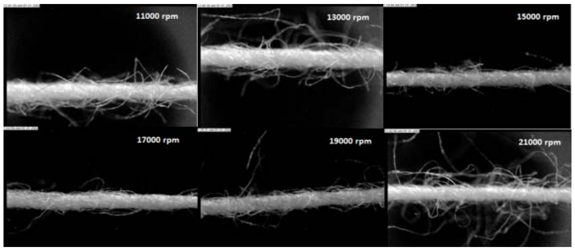

Fig 1.3 Yarn structure of 20's yarn spun at different spindle speeds

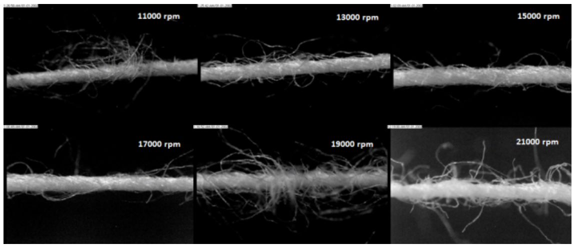

Fig 1.4 Yarn structure of 25's yarn spun at different spindle speeds

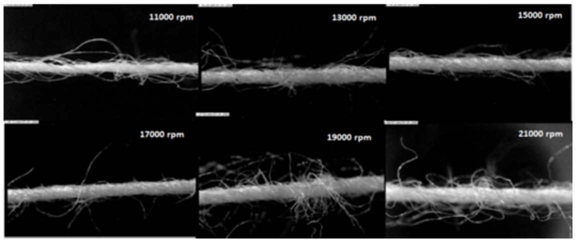

Fig 1.5 Yarn structure of 30's yarn spun at different spindle speeds

Starting from Fig. 1.3 at 11000 rpm, we see that the fibers in the yarn are not very much aligned and therefore they are not readily twisted. The fibers are seen as in a random position within the yarn structure and axis. As the spindle speed is increased, the fibers are seen to develop a parallel alignment and due to that they are caught in the twist, this phenomenon can be seen increasing from 13000 rpm up to 17000 rpm. Increase in the spindle speed gets the fibers more parallel and yarn structure seems to be regular (up to 17000 rpm). It is seen that at 17000 rpm spindle speed the yarn structure is more regular which causes less hairy yarn. After 17000 rpm spindle speed the structure is seen to get hairy and very hairy at 21000 rpm spindle speed and can go beyond if spindle speed is increased further.

CONCLUSIONS

Most of the manufacturers run their machines at higher speeds to get higher productivity but at the cost of yarn quality. From the experiments it is seen that the hairiness of yarns produce of MNH-93 can be kept lowest at spindle speed of around 17000 rpm. Also the structure of yarn was found to be more regular at 17000 rpm spindle speed which gives yarn more strength an carry these advantages when being woven or knitted for fabric.

REFERENCES

[1] Stahlecker, H. RoCoS Rotorcraft Compact Spinning: Magnetic Compacting. 2005: www.oerotorcraft.com.

[2] Wang, X., Miao, M., How, Y. Studies of JetRing Spinning Part I: Reducing Yarn Hairiness with the Jet Ring. *Textile Research Journal*, Vol. 67, No. 4, 1997: pp. 253-258.

[3] G K Tyagi, Manik Bhowmick, S Bhattacharyya and R Kumar. Effect of Spinning conditions on mechanical and performance characteristics of cotton ring and compact spun yarn. *Indian Journal of Fibers and Textile Research*, Vol. 35, March 2010: pp. 21-30.

[4] Ismail Usta. Effect of Balloon Angle on the Hairiness and other Yarn Properties of Polyester Ring Spun Yarn. *FIBRES & TEXTILES in Eastern Europe*. January / December / A 2008, Vol. 16, No. 5 (70): pp. 40-47.

[5] Md. Osman Ghani Miazi, A. K. M. Mahabubuzzaman, Md. Mazedul Kabir. Effect of Spindle Speed on Textile Properties and Productivity of Fine Jute Yarn. *Daffodil International University Journal of Science and Technology*, Volume 4, Issue 2, July 2009.

Thermal Properties of Mattress Protectors for the Prevention of Pressure Ulcers

Liliana Fontes[1,2], Maria José Abreu[1,2], Miguel Ângelo Carvalho[1,2] & Jorge Almeida Santos[3,4,5]
[1]Department of Textile Engineering, University of Minho, Portugal, [2]Center for Textile Science and Technology, University of Minho, Portugal, [3]Algoritmi Center, University of Minho, Portugal, [4]Department of Basic Psychology, University of Minho, Portugal, [5]Center of Graphic Computation
liliana_magalhaes@hotmail.com

OBJECTIVE

Our goal is to compare the thermal properties of six mattress protectors by testing with a thermal manikin and with the equipment Alambeta.

INTRODUCTION

Pressure Ulcers develop when there is excessive pressure on a bony prominence for a long period of time, which may compress the tissue and blood vessels between the bone and the support surface (Theaker, 2003). Temperature plays an important role in their development. Therefore, it is crucial to evaluate materials used for their prevention in terms of their thermal properties. Moreover, these properties are pivotal in the comfort perceived by the end-user.

APPROACH

The characteristics of the six tested mattress protectors are summarized in Table I.

Table I– Characteristics of all samples

Code	Fabric	Filling	Base
A001	70% bamboo; 30% polyester	70% polyester; 30% bamboo	100% cotton
A002	100% cotton	100% polyester	100% polyurethane
A003	100% cotton	-	100% polyurethane
A004	80% cotton; 20% polyester	-	100% polyurethane
A005	100% polyester	100% cotton	100% cotton
A006	75% cotton; 25% polyester	100% polyester	100% PVC

All six samples were tested on a thermal dry-manikin with a human adult female figure divided into 20 segments. The program used maintains temperature at the skin level constant at 33 ºC. The results are given as the heat power (in Watts) needed to maintain this temperature on each segment. The manikin was laid down in a prone position with its back on a mattress covered with each of the samples. A control trial was carried out with the manikin naked and without materials.

Table II summarizes the parameters measured on the other equipment used for this project.

Table II – Alambeta parameters

Symbol	Parameter	Unit
q_{max}	Maximum heat flux	W/m^2K
r	Thermal resistance	m^2K/W
b	Thermal absorptivity	$W.s^{1/2}/m^2K$

RESULTS AND DISCUSSION

Results from the thermal manikin will be presented as the average heating power (W) needed to maintain a constant temperature (33º C) in each body segment. Only the relevant segments are presented – areas such as the face, for example, were excluded from analysis (cf. Figure 1).

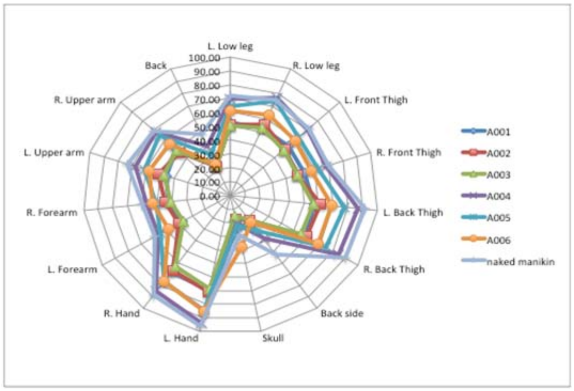

Figure 1 – Average heating power (W) for each segment for all samples

Because the manikin was naked when the mattress protectors were tested, the results shown do not differ much from the control (naked manikin). Sample A004 shows the worse thermal performance – it consistently needs more heating power to keep the temperature constant on all body parts. Samples A005 and A006 appear quite similar, and are only marginally more thermally efficient than sample A004. On the other hand, the remaining samples

A001, A002 and A003 show the best thermal performance and are practically indistinguishable.

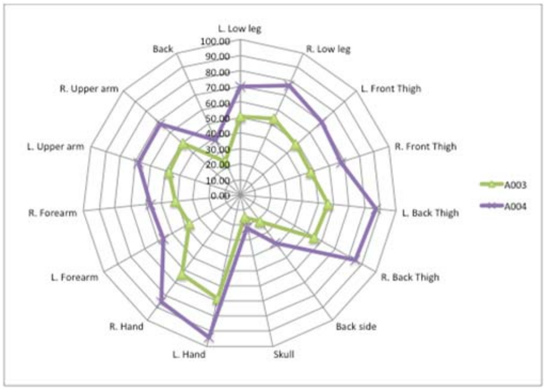

Figure 2 – Average heating power (W) for each segment for samples A003 and A004

Figure 2 provides an easier visual comparison between the best and worst samples tested, respectively samples A003 and A004, with the former requiring more heating power in order to maintain temperature at 33º C. Differences between the two average of 20W are quite noticeable in areas such as the back of the thighs, which present a difference of approximately 30W.

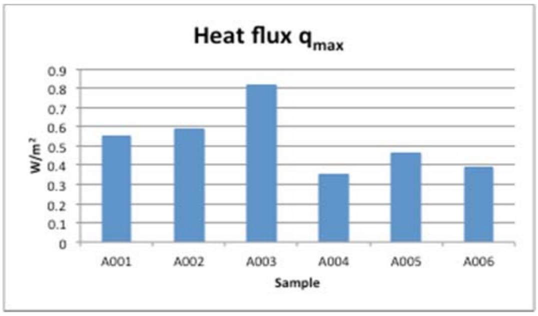

Figure 3 – Thermal heat flux and for all samples

Figure 3 presents maximum heat flux for all samples, which characterizes the instant thermal feeling provided by the material. The graph clearly shows that sample A003 was by far the one with the highest heat flux, thus making it the best-performing material. On the other hand, sample A004 showed the worst performance, with a heat flux more than 2.5 times lower than sample A003. These results resemble the ones from the manikin, in that they show that the best-performing samples are A001, A002 and A003, but further refine them – whereas with the manikin the three best samples were practically indistinguishable from each other, maximum heat flux reveals notable differences. Finally, samples A004, A005 and A006 show worse performance.

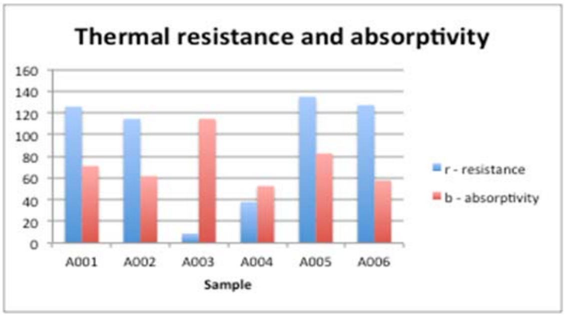

Figure 4 – Thermal resistance and absorptivity

Figure 4 shows thermal resistance and absorptivity. Materials with low absorptivity and high resistance are insulating – users maintain their temperature constant. On the other hand, textiles with high absorptivity and low resistance allow more exchange of heat flux. For preventing Pressure Ulcers, an insulating material is desirable, since it prevents temperature fluctuation. Hence, sample A002 appears to perform best, with one of the highest values of resistance and relatively low values of absorptivity. Still, when fluctuations in skin temperature are a concern, a cover with no insulating properties may be beneficial, allowing the skin to cool when in contact with the material. In this case, sample A003 again shows the best results – lowest resistance and highest absorptivity.

CONCLUSION

The results presented here suggest that, for thermal comfort and management purposes, sample A003 is the best choice, especially if the objective is to allow for heat to be exchanged between the user and the material. However, to reduce temperature variation, sample A002 should be considered – it showed excellent performance on both equipment, and its extreme thickness (8mm) allow a better capacity to distribute pressure.

ACKNOWLEDGMENT

This work is financed by FEDER funds through the Competitive Factors Operational Program (COMPETE) and by national funds through FCT (Portuguese Foundation for Science and Technology) with the grant SFRH/BD/79762/2011 and the project PEst-C/CTM/U10264/2011.

REFERENCE

Theaker, C. (2003). Pressure sore prevention in he critically ill: what you don’t know, what you should know and why it’s important. *Intensive and Critical Care Nursing*, 19, 163–168.

Factors Affecting UV Protection of Textiles at the Fiber Level

Yao Yu[1], Christopher Hurren[1], Lu Sun[1], Keith R. Millington[2], Xungai Wang[1]
[1]Australian Future Fibers Research and Innovation Centre, Institute for Frontier Materials, Deakin University, Geelong, 3216 Australia
[2]CSIRO Materials Science and Engineering, Geelong Technology Precinct, Deakin University, Geelong 3216, Australia
yaoy@deakin.edu.au

ABSTRACT

UV (ultraviolet) protective clothing (textiles) is important for the public. This study focused on the impact of fiber parameters on UV protection of textiles. It sought to understand how the light goes through different fibers. Significant effects of fiber parameters on UV protection of textiles were shown by statistical analysis. Fabric-evoked prickle was also included in this study to reach the aim of achieving textiles with both high UV protection and good tactile comfort.

KEYWORDS

UV protection, fiber, prickle

INTRODUCTION

Excessive UV exposure is harmful to human health, so UV protection is necessary for the general public. Wearing UV protective clothing is an effective way for limiting UV exposure, particularly if the clothing items are comfortable and fit for outdoor activities.

Wool can provide a higher UV protection when compared with other fiber types, such as cotton, nylon, silk and viscose rayon [1-4]. Fabric-evoked prickle is perceived to be common in wool fabrics when the fabrics are worn next to skin. Studies have shown that prickle is not caused by an allergenic response, but by the mechanical stimulation from the protruding fiber ends to nerves close to the skin surface, although there are individual differences in human population [5-8]. The proportion of fiber ends greater than 32 μm in diameter, protruding from the surface, is the key factor to predict the extent of fabric-evoked prickle [9], and guides both subjective and objective measurement [10].

This study combines the fiber parameters affecting UV protection of textiles and the factor that governs fabric prickle, to help optimize fiber parameters while designing fabrics with both high levels of UV protection and good tactile comfort.

APPROACH

Sample preparing: Fiber samples of a mass of 600 mg were put into a black container, which was used as the sample holder. The circular sample holder had a diameter of 23 mm and a thickness of 10 mm. Fibers in each sample were placed in a random orientation across the open area. This container was used to maintain a constant volume and density for each sample.

Fiber tests: With constant density of fiber samples, the experiments were designed by varying only the fiber type, so the effect of fiber type on UV absorption could be examined. For the same fiber type, the fiber diameter was varied to see whether it had any effect on UV absorption. Fibers of different types but with the same mass and similar average diameters or width, including cotton, hemp, bamboo viscose, wool, eri silk, viscose, nylon 66 and polyester, were used in the tests. Cotton and wool fibers with different fiber diameters/widths but the same mass were also analyzed.

Measurement method: Diffuse reflectance (DR) spectra on loose fibers were measured using a CARY 300 Bio UV-VIS spectrophotometer (VARIAN INC., USA) at a wavelength between 250 nm and 400 nm. UV diffuse transmittance is the best way to measure penetration of UV through materials, but this requires the specimens to be thin and even, like a fine fabric. Using loose fiber, it was undesirable to prepare the samples that thin for diffuse transmittance; otherwise the fiber density uniformity cannot be ensured for the experiments. Hence DR spectra was undertaken as sample preparation was more reliable and was measured using the re-emission function F(R), which is proportional to the absorption of the sample.

Mean fiber diameter, comfort factor, spin fineness, coefficient of variation (CV %) of fiber diameter, and the percentages of fiber ends greater than 32 μm in diameter were measured using an OFDA 2000 (BSC Electronics, Australia), with the fiber samples cut into 2 mm snippets and spread on a 70 mm glass slide. Yellowness was measured with a GretagMacbethTM Colour-Eye® 7000A (Colourspec Pty. Ltd, Australia).

Statistical analysis: Univariate analysis was applied to analyze the data to identify whether the effects of fiber parameters on UV absorption of samples were significant. Principal factor analysis was used to get the primary components. The factors analyzed were mean fiber diameter, comfort factor, spin fineness, CV % of fiber diameter, the percentage of fiber ends greater than 25-32 μm in diameter, fiber type and yellowness. Since there were some differences in samples' colors, yellowness was considered. The prediction model with principal components was achieved.

RESULTS AND DISCUSSION

Test results: Different fiber types gave different UV absorption, and wool fibers provided the highest UV absorption amongst the fiber types examined in this study, followed by hemp and polyester. This may be related to the chemical components (protein) of wool and the benzene rings in polyester. Natural impurities, lignin, and σ-π valence bonds all could make hemp (17.41 μm) have a relatively high UV absorption. The cellulose based fibers had the lowest UV absorption among the fibers measured. The average diameters of viscose (14.13 µm), cotton5 (14.59 µm) and polyester (13.35 µm) were similar, but polyester gave higher UV absorption than the other fiber types (see FIGURE 2).

Data analysis: UV absorption was analyzed as the dependent variable. Fiber type and fiber diameter were fixed factors, and yellowness was as a covariate during the univariate analysis. For cotton and wool data, mean fiber diameter was a fixed factor. Univariate analysis results showed that in the UV wavelengths range, fiber type and mean fiber diameter have significant effects on UV absorption.

TABLE I shows the analysis result of cotton fibers with different fiber diameters. The effect of mean fiber diameter on UV absorption is significant ($P<0.05$). Yellowness as covariant is a secondary variable that can affect the dependent variable (UV absorption); however it is not a principle component as shown by the factor analysis results.

TABLE I. Tests of Between-Subjects Effects
Dependent Variable: UV absorption

Source	Type I Sum of Squares	df	Mean Square	F	Sig.
Model	99.627[a]	5	19.925	355.237	0.000
yellowness	98.282	1	98.282	1752.206	0.000
diameter	1.345	4	0.336	5.994	0.000
Error	42.068	750	0.056		
Total	141.695	755			

a. R Squared=0.703 (Adjusted R Squared=0.701)

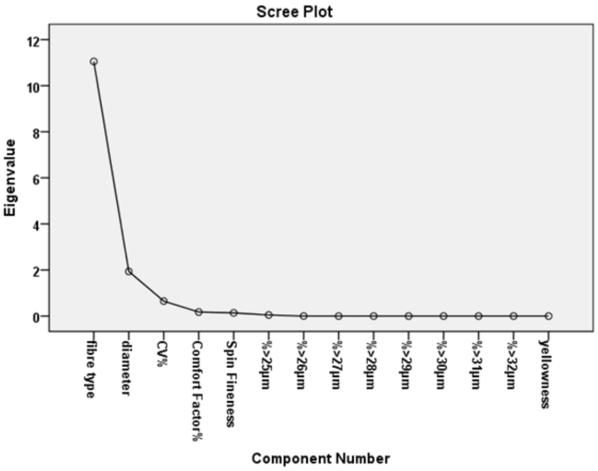

FIGURE 1 Scree plot of components

From FIGURE 1, the result of principal factor analysis shows that fiber type and mean fiber diameter are two principle components in all the factors analyzed, which means they play the main roles for influencing UV absorption.

Optimized diameter:

The samples were ordered by increasing UV absorption (integrated area in the range of UV wavelength 250-400 nm) in FIGURE 2. Samples No.7 (bamboo viscose 21.75 µm), No.12 (hemp 17.41 µm), No.14 (wool 30.68 µm) and No.18 (wool 44.02 µm) had a high proportion of coarse fibers (%>32 µm), which would be expected to cause fabric-evoked prickle if the fabric is worn next to skin.

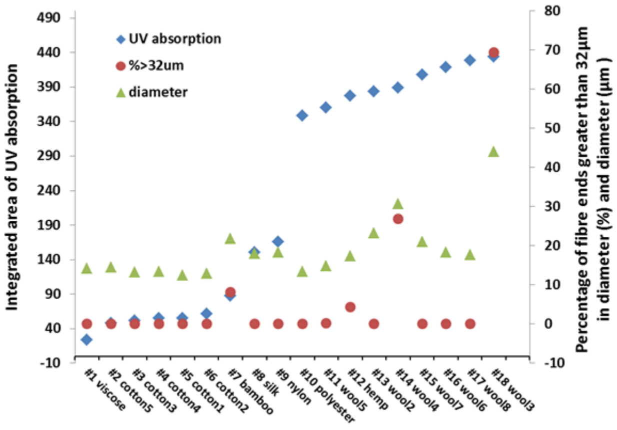

FIGURE 2 UV absorption in increasing trend and diameter distribution (%>32µm)

Wool sample No.17 (wool 17.62 µm) is a good choice for next-to-skin fabrics as it has no fibers coarser than 32 µm (0%) and a relatively high UV absorption (UV protection).

CONCLUSIONS

Fiber type and mean fiber diameter have significant effects on UV absorption. Wool fibers have relatively high UV absorption. For next-to-skin wear, the fabric-evoked prickle should be considered as well as UV protection. Among the fiber examined in this study, fine wool fibers offer both good next-to-skin comfort and high UV protection.

REFERENCES

[1] H. Harvilicz, Chemical Market Reporter, 256 (1999) 45.
[2] R. Hilfiker, W. Kaufmann, G. Reinert, E. Schmdt, Textile Research Journal, 66 (1996) 61-70.
[3] C.V.d. Keybus, J. Laperre, R. Roelandts, Journal Of The American Academy Of Dermatology, 54 (2006) 86-93.
[4] G. Reinert, F. Fuso, R. Hilfiker, E. Schmidt, Textile chemist and colorist, 29 (1997) 36-43.
[5] R.K. Garnsworthy, Australasian Textiles, 8 (1988) 26-29.
[6] R.K. Garnsworthy, R.L. Gully, P. Kenins, R.J. Mayfield, R.A. Westerman, Journal of Neurophysiology, 59 (1988) 1083-1097.
[7] G.R.S. Naylor, C.J. Veitch, R.J. Mayfield, Textile Research Journal, 62 (1992) 487-493.
[8] G.R.S. Naylor, Textile Research Journal, 80 (2010) 537-547.
[9] G.R.S. Naylor, Proceedings ofthe Combined (NZ and AUS) Conference of The Textile Institute, (2009) 31-34.
[10] M. Naebe, Y. Yu, B. McGregor, D. Tester, X. Wang, Textile Research Journal, (2012).

Preparation of SiO_2/TiO_2 with Eliminated Photocatalytic Activity

Mingwen Zhang, Lu Sun, Xungai Wang
Australian Future Fibres Research & Innovation Centre, Institute for Frontier Materials, Deakin University,
Geelong, Victoria 3216, Australia.
lu.sun@deakin.edu.au; mingwen@deakin.edu.au

ABSTRACT

To improve the photostability of wool fiber which is sensitive to photocatalytic activity of TiO_2, core-shell structured TiO_2@SiO_2 nanoparticles (NPs) were fabricated. Crystal types of TiO_2 were characterized by XRD. TEM images were taken to reveal the structures of TiO_2 before and after silica coating. UV-Vis spectra and phtocatalytic activity properties of TiO_2 before and after silica coating showed the core-shell structure endowed TiO_2 NPs with high transmittance, strong UV-shielding, and low photocatalysis properties, which are ideal for protecting wool against photoyellowing from sunlight.

INTRODUCTION

Wool fiber is well known as a superior natural textile material due to its resilience and softness. However the photodegradation caused by sunlight, particularly from UV rays, makes the fiber weak and yellow [1-4], which is a critical problem for the wool industry. The most widely used protective method is application of UV absorbers to wool [5-7]. Compared with the organic UV absorbers, inorganic UV absorbers, such as ZnO and TiO_2, are generally non-toxic, more stable and effective. Development of nano-science and nano-technology provides new approaches to a better application of these inorganic UV absorbers [8-12]. However, wool is so highly sensitive and delicate that the process of photoyellowing can be greatly accelerated by reactive radicals generated by the photosensitized inorganic UV absorbers due to their strong photocatalysis [13, 14].

In this study, core-shell structured TiO_2@SiO_2 NPs were fabricated with solid silica shells around rutile-type TiO_2 core particles. These core-shell structured TiO_2 NPs have high UV absorbance and low photocatalytic activity, which will reduce the photoyellowing of wool fabrics significantly.

APPROACH

The detailed preparation procedure is described in Fig. 1. Firstly, an acidic hydrothermal treatment was employed to synthesize the rutile type TiO_2 nano-grains from Degussa P25 NPs [15]. And then SiO_2 shells were coated onto the surfaces of synthesized particles by stöber method [16].

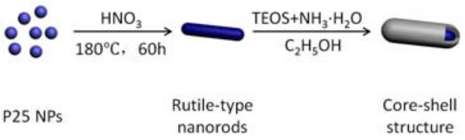

Fig. 1 Procedure for the fabrication of TiO_2@SiO_2 NPs.

RESULTS AND DISCUSSION

From the XRD spectrum of Degussa P25 NPs before and after acidic hydrothermal treatment which is shown as Fig. 2, a crystal type transformation was observed by noting the disappeared peaks of anatase (101) and generated peaks of rutile (110) phases.

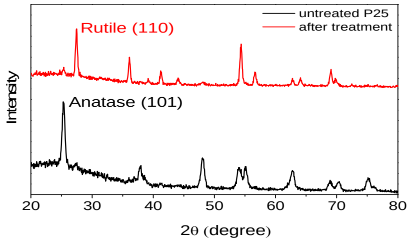

Fig. 2 XRD spectra of Degussa P25 NPs before and after acidic hydrothermal treatment.

A crystal transformation of Degussa P25 NPs from anatase to rutile type and the change of external layer of particles after silica coating can be seen from TEM images (Fig. 3). The average width and length of synthesized rutile nanorods are around 33 and 102 nm respectively. And the thickness of outmost silica layer is about 1 nm.

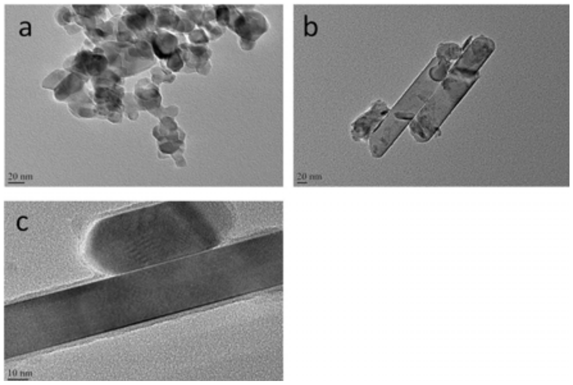

Fig. 3 TEM images of a) Degussa P25 NPs, b) rutile type TiO_2 nano-grains and c) $TiO_2@SiO_2$ NPs.

The UV absorbing ability of Degussa P25 NPs before and after crystal type transformation as well as the subsequent silica coating is demonstrated in Fig. 4(a). Their photocatalytic activity was evaluated by the photodegradation of Rhodamine B under simulated sunlight. The changes of dye concentration under different time UV irradiation are indicated in Fig. 4(b).

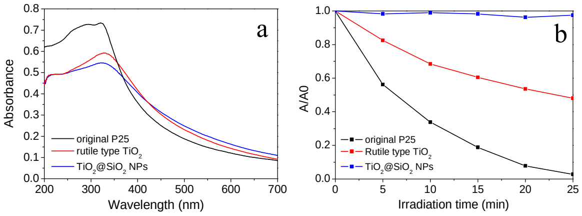

Fig. 4 a) UV-Vis spectra and b) photocatalytic activity of Degussa P25 NPs before and after crystal transformation as well as the subsequent silica coating.

Compared with the original P25 NPs, the UV-absorption of fabricated $TiO_2@SiO_2$ NPs is decreased about 24%, whilst the photocatalytic activity is almost blocked completely. In addition, a slightly increase of absorbance is observed in the visible region, which indicates that the dispersibility of the nanoparticles after modification is maintained.

CONCLUSIONS

Core-shell structured $TiO_2@SiO_2$ NPs have been prepared successfully. These structured nanoparticles had high UV absorbing ability and low photocatalytic activity, as well as good transparence. These nanoparticles may have applications in UV protection of organic substrates such as wool fabrics.

FUTURE WORK

Further work is on-going to modify the surface of synthesized $TiO_2@SiO_2$ NPs with functional groups by silica grafting as well as apply these particles to wool for protection against photoyellowing.

REFERENCES

[1] Launer, H. F. *Textile Research Journal*, (1965) 35, 395.

[2] Launer, H. F. *Textile Research Journal*, (1965) 35, 813.

[3] Millington, K. R. *Coloration Technology*, (2006) 122, 169.

[4] Millington, K. R. *Coloration Technology*, (2006) 122, 301.

[5] Evans, N. A., Waters, P. J. *Textile Research Journal*, (1981) 51, 432.

[6] Evans, N. A., Waters, P. J., Wilshire, J. F. K. *Textile Research Journal*, (1986) 56, 203.

[7] Carr, C. M., Leaver, I. H. *Journal of Applied Polymer Science*, (1987) 33, 2087.

[8] Sun, L., Rippon, J. A., Cookson, P. G., Wang, X.., King, K., Koulaeva, O., Beltrame, R. *International Journal of Technology Transfer and Commercialisation*, (2008) 7, 224.

[9] Becheri, A., Dürr, M., Lo Nostro, P., Baglioni, P. *Journal of Nanoparticle Research*, (2008) 10, 679.

[10] Mosimann, W., Benisek, L., Burdeska, K., Leaver, I., Myers, P., Reinert, G., Wilshire, J. A. New Commercial UV Absorber for the Protection of Wool and Wool Dyeings, In *Proceedings of the 8th International Wool Textile Research Conference*, Christchurch, NZ. IV (1990).

[11] Montazer, M., Pakdel, E., Moghadam, M. *Fibers and Polymers*, (2010) 11, 967.

[12] Xianqiong Chen, Yuyang Liu, Haifeng Shi, Xiaowen Wang, Kaihong Qi, Xiang Zhou, Xin, J. H. *Textile Research Journal*, (2010) 80, 2214.

[13] Sun, L., Rippon, J. A., Cookson, P. G., Koulaeva, O., Wang, X. *Chemical engineering journal*, (2009) 147, 391.

[14] Zhang, H., Millington, K. R., Wang, X. *Polymer Degradation and Stability*, (2009) 94, 278.

[15] Li, X., Leng, Y., Li, J. G., Xiu, Z., Huo, D., Sun, X., Ishigaki, T. *Current Nanoscience*, (2010) 6, 110.

[16] Stöber, W., Fink, A., Bohn, E. *Journal of Colloid and Interface Science*, (1968) 26, 62.

Influence of He/O_2 Atmospheric Pressure Plasma Jet Treatment on Desizing of Starch Phosphate and Poly(vinyl alcohol)

Xuming Li[1], Yiping Qiu[2]
[1] College of Textile and Clothing, Shaoxing University, Shaoxing 312000, China
[2]College of Textiles, Donghua University, Shanghai 201620, China
lixm@usx.edu.cn

INTRODUCTION

The sizing process is necessary in the textile industry to prevent abrasion, fluffiness, and break of the warp during the weaving process [1-3]. In practice, the blends of starches or modified starches [4-6] and polyvinyl alcohol (PVA) [7] are widely used as sizing agents for cotton fabric. However, sizing agents inhibit the processes of bleaching, dyeing and treatment with surfactants and hence the sizes have to be removed through desizing.

The methods of desizing, which reduce energy and water consumptions, are very attractive. Plasma treatment is an environmentally friendly technique[9]. Peng et al. [16] studied the solubility of PVA film after atmospheric plasma treatment under different conditions. Cai et al. used low-pressure plasma and atmospheric pressure plasma treatment to remove PVA size on cotton and viscose fabrics [12]. All these research results show that plasma treatment is an effective technique for improving the solubility of PVA size in cold and hot water.

However, so far, little has been reported about the influence of atmospheric pressure plasma treatment on desizing of blends of starch phosphate and PVA. Thus, the objective of this study was to examine how helium/oxygen (He/O_2) atmospheric pressure plasma jet (APPJ) treatment influences the solubility of the blends of starch phosphate and PVA on cotton fabric.

EXPERIMENTAL

Materials

A plain weave cotton fabric is used in this study with fabric counts of 38/30 (warp/weft)/cm and yarn counts of 40s. The sizes used in present study are phosphate modified starch and PVA, which were provided by Zhejiang Yuelong Holding Group Co., Ltd (Shaoxing City, China). Hydrogen peroxide is 30% solution, supplied by Jinlu Chemical Company (Shanghai City, China). The percent sizing ratio throughout the experiment was 5.45%.

Plasma treatment

The sized samples were plasma treated by the atmospheric pressure plasma jet (APPJ) (Atomflo-R, Surfx Company, USA) with 30 L/min of pure helium+0.3 L/min of oxygen (He/O_2) gas. The distance between the nozzle and the substrate was 2mm and output power was 60 W. Treatment time were 5s, 20s, 35s and 50s, respectively.

H_2O_2 desizing

The untreated sized fabrics were treated in a desizing bath containing 2g/l H_2O_2 (30%) at 85℃ for 20min. Then the samples were subjected to a hot wash. All samples were dried then placed into standard condition for 24 h for weight measurement.

Washing

The control and plasma treated fabrics were subjected to a cold wash and a hot wash, then dried and placed into standard condition for 24h for weight measurement. In the cold wash, the fabrics were immersed in deionzed water at 30℃ and stirred for 20min with a liquor: fabric ratio of 50:1. The hot wash was performed in the same way except that the temperature of water was 85℃. Here, the original mass of size on the fabric was 5.2% of the sized fabric mass.

Surface morphology analysis (SEM)

The SEM facility (JSM-5600LV model. Japan) was used to reveal the change of the surface morphology of the sized cotton fabric after plasma treatment and desizing.

Surface chemical composition analysis (XPS)

To investigate the surface chemical composition changes of the sized fabric before and after plasma treatment, the X-ray photoelectron spectrometer (XPS) (ESCALAB 250 model, Thermo Electron VG Scientific, USA) was employed.

RESULTS AND DISCUSSION

XPS analysis

Relative chemical composition for sized cotton fabrics untreated and treated with APPJ is presented in Table Ⅰ. The O/C ratios were 0.35, 0.72 and 0.86, respectively for the control, the samples with treatment time of 20s and 50s. The oxygen content increase indicated that higher levels of oxygen-containing polar groups were formed on the sized fabric surface after plasma treatment.

Table Ⅱ presents the results of C1s peak deconvolution analysis, showing a distinctive change of functional groups on the sized fabric surface after plasma treatment. The C-C/C-H component decreased significantly even after a short exposure of 20s, but it showed little change for further increases in exposure time up to 50s. Meanwhile, the components of C-O-H/C-O-C, C=O and O-C=O increased greatly after plasma treatment. Increase of hydrophilic groups may improve the water solubility of the blended sizes.

Table I. Relative chemical composition for sized cotton fabrics untreated and treated with APPJ.

Sample	Chemical composition (%)			Atomic ratio O/C
	C1s	O1s	N1s	
Control	72.6	25.7	1.7	0.35
Plasma treated, 20s	57.6	41.6	0.8	0.72
Plasma treated, 50s	53.4	45.9	0.7	0.86

Table. II. Results of deconvolution of C1s peak of sized cotton fabrics untreated and treated with APPJ.

Sample	Relative area of different chemical bonds (%)			
	C-C/C-H	C-O-H/C-O-C	C=O	O-C=O
Control	61.0	30.1	7.7	1.2
Plasma treated, 20s	25.3	50.8	18.9	5.0
Plasma treated, 50s	23.7	51.2	14.3	10.8

SEM analysis

Fig.2 shows the SEM images of fabrics after desizing under different conditions. After plasma treated 35s and subsequent hot washing, almost all sizes on cotton was removed. In comparison, although some size was removed by only hot washing, a substantial amount of size remaining on the fiber surfaces.

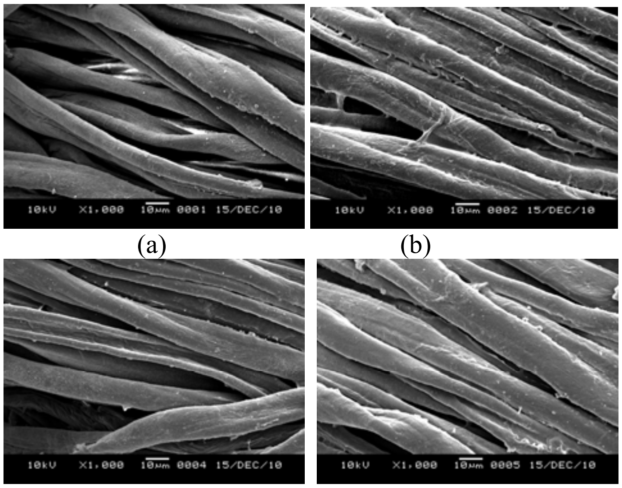

(a) (b)

(c) (d)

Fig. 2. The surface morphology of fabrics after desizing under different conditions: (a) control (no sized), (b) sized, (c) plasma treated 35s followed by hot washing, (d) only hot washing.

Influence of plasma treatment on desizing

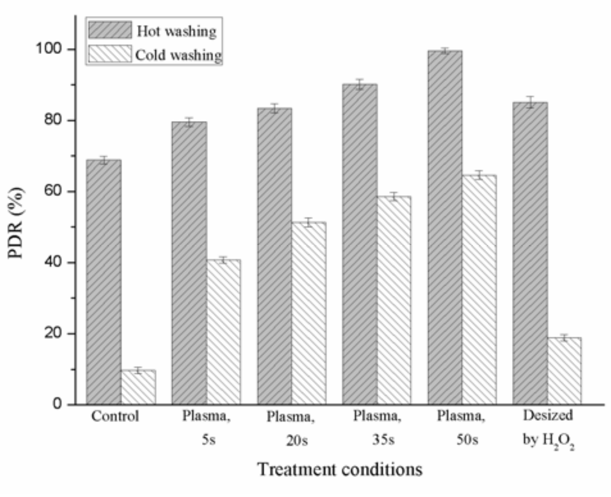

Fig. 3. Percent desizing ratio (PDR) at different treatment conditions.

The percent dsizing ratio (PDR) under various treatment conditions are shown in Fig.3. The PDR significantly increased with an increase of plasma treatment time followed by hot washing. More than 90% PDR achieved after 35s treatment. Although the desizing efficiency was just slightly enhanced for plasma treated fabrics followed by cold washing, it was interesting that 64% PDR was achieved by plasma treatment plus a cold wash, which was much higher than the PDR of 19% by the H_20_2 desizing treatment under low temperature.

CONCLUSION

The influence of He/O_2 APPJ treatment on removal of blends of starch phosphate and PVA on cotton fabrics was investigated. Plasma treatment resulted in significant increase of removal of the blended size followed by hot washing, but it was less effective in cold washing. The biggest PDR was achieved after 50s plasma treatment. Therefore, the use of the APPJ has shown effectiveness in desizing and provides an alternative approach that decreases the water, energy and chemicals consumption.

Keywords: Atmospheric pressure plasma jet (APPJ), Starch phosphate, Poly (vinyl alcohol) (PVA), Desizing, XPS, SEM

ACKNOWLEDGMENT

This work was supported by Natural Science Foundation for the Youth (Nos. 50803010 and 60904056).

REFERENCES

1. Takeshi Fukuda, Michiko Kato-Murai. *Appl. Microbiol. Biotechnol.* 77 (2008): 1225–1232.
2. C.D. Livengood, C. Tomasion, *Tex. Chem*. Col. 12 (1980): 67-70.
3. J.P. Moreau, Tex. *Chem. Col.* 13 (1981): 22-27.
4. Pervin Aniş, Asim Davulcu, Hüseyin Aksel Eren. *Fibres and Textiles in Eastern Europe* 16 (2008): 100-103.
5. Lange N. K. *Textile Chemist and Colorist* 29 (1997): 23-26.
6. K. Opwis, D. Knittel, A. Kele., E. Schollmeyer. *Starch/Starke* 51 (1999) 348-353.
7. Tatsuma Mori, Michio Sakimoto. *J. Chem. Tech. Biotechnol.* 68 (1997): 151-156.
8. J.R. Chen, X.Y. Wang, W. Tomiji, J. *Appl. Polym. Sci*. 72 (1999): 1327–1333.
9. Z.S. Cai, Y.P. Qiu, J. *Appl. Polym. Sci*. 109 (2008): 1257–1261.
10. Shujing Peng, Zhiqiang Gao, Jie Sun, Lan Yao, Yiping Qiu. *Appl. Surf. Sci*. 255 (2009): 9458–9462.

Heat and Moisture Transfer Through Hydrophilic and Hydrophobic Multilayered Fabric System

Duck Weon Lee, Eun Gyeong Han, Eunae Kim
Department of Clothing & Textiles, Yonsei University, Seoul 120-749, Korea
eakim@yonsei.ac.kr

OBJECTIVE

Various combinations of hydrophilic and hydrophobic fabric layers are expected to result in different microclimate temperature and humidity as their transport mechanisms are different. Three different layers of fabrics with or without air layers were compared to determine the relative effect of the hydrophilicity/hydrophobicity of the fabrics and the air layer. The obtained results will provide us the information to design comfortable garment layering system.

INTRODUCTION

There have been studies for the heat and moisture transport of hydrophilic and hydrophobic fabrics and their combinations. Their studies are mostly for the single layers of woven fabrics [1,2] or for the double knit structure[3]. The effect of hydrophilicity is relatively well defined but the combined effects with the air layer on the comfort properties are not sufficiently investigated. The heat conductivity of air is low (0.024 W/K·m) [4] and play a role as a barrier for the heat and moisture transfer in the fabric layers. Rayon is most widely used for the linings of wool suits not only as it is slippery but also as its moisture regain is high and transfers vapor state sweat to the wool very effectively and keep the wearer comfortable. In this context, study on the layering system is meaningful in terms of hydrophilicity and air layer between fabrics.

APPROACH

Material

Two types of fabrics, cotton and polyester, which were representative hydrophilic and hydrophobic fibers were chosen. Table I describes their characteristics. Moisture regain of cotton is largely different from polyester because of the hydroxyl groups. Air resistance of polyester was five times bigger than cotton fabric.

Table I. Characteristics of the sample fabrics

Fabric Type	Cotton	Polyester
Structure	Plain weave	Plain weave
Thickness (mm)	0.23	0.12
Weight (g/m^2)	96	68
Heat conductivity	0.03	0.05
Air resistance (Kpa s/m)	0.21	1.20
Moisture regain (20°C & 65%)	7 - 8%	0 - 0.4%

Experimental Methods

Human-Clothing-Environment (HCE) simulator [5] was used to measure microclimate temperature and humidity. Temperature of the hot plate, which is skin part, was 34± 0.1°C, and micro pump (ISM 907, Ismatec, Switzerland) provided the sweat-distributed layer with 8ml of distilled water. Environmental temperature and relative humidity in the chamber were 21 ± 1°C and 55 ± 5%. The wind speed was 0.2–0.7 m/s. Figure 1 shows the HCE simulator and its test rig.

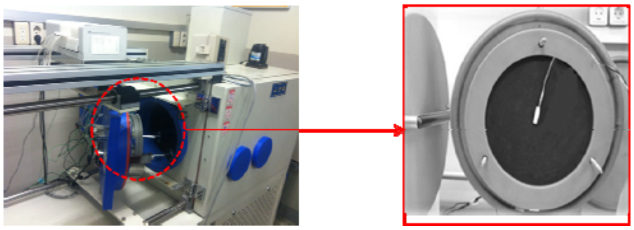

Figure 1. Human-clothing-environment simulator and its test rig

After completing the combinations of sample fabrics on the test rig, the whole fabric system was exposed to the chamber. As shown in Table II, three layers were sequentially assigned in a test rig in HCE.

Table II. Combination of fabric layers

	1st Layer	2nd Layer	3rd Layer
1	Cotton (C)	Cotton (C)	Cotton (C)
2	Polyester (P)	Polyester (P)	Polyester (P)
3	Cotton (C)	Cotton (C)	Polyester (P)
4	Polyester (P)	Polyester (P)	Cotton (C)
5	Cotton (C)	Polyester (P)	Cotton (C)
6	Polyester (P)	Cotton (C)	Polyester (P)
7	Polyester (P)	Cotton (C)	Cotton (C)
8	Cotton (C)	Polyester (P)	Polyester (P)

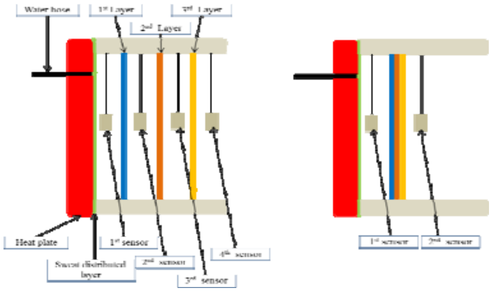

Figure 2. Schematic of two types of the multilayered fabric systems with microclimates and without microclimates in the test rig of HCE

Figure 2 demonstrates schematic of two types of the fabric assembly with and without having air layer between fabric layers in the test rig of HCE. The CHS-APS temperature and relative humidity sensors (TDK, Japan; high polymer sensors) were located between layers and external environment. Microclimate temperature and humidity were recorded every minute by the data logger.

RESULTS AND DISCUSSION

Hydrohilicity

The average temperatures in the multilayered systems, consisting of polyester layers, were higher than the other multilayered systems, composed of cotton layers as shown in Figure 3 (eg., PPP vs. CCC, CCP vs. PPC, CPC vs. PCP, CPP vs. PCC). When PPP compared with CCC individually, their average temperature were similar to each other as shown in Figure 3. It demonstrated that the average temperature in PPP was basically higher than that in CCC. In addition, the temperature difference as well, as the rate of temperature in PCP and CPC which were sequentially arrayed by a different type of the layer were relatively smaller than the other types of the multilayered systems. On the other hand, in the total temperature difference, CCC, PPP, CCP, and PPC were relatively higher than that of the remained multilayered systems from the first microclimate to the third one.

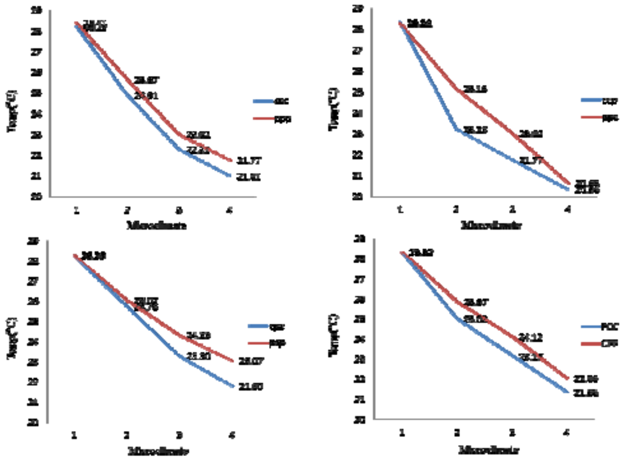

Figure 3. Change in temperature in the multilayered systems

Furthermore, the research presumed that the last layer of PPP and CCC was governed by the external environment because the average temperature in both of PPP and CCC are curved at the same time during heat and mass passed the third layer.

Air Layer

Figure 4 shows a temperature difference in the multilayered systems which had air layer and no air layer. In case of PCP, a temperature difference was the smallest, while in the case of CCP, it was the biggest. When cotton layer is dominant the difference was larger than when polyester was dominant.

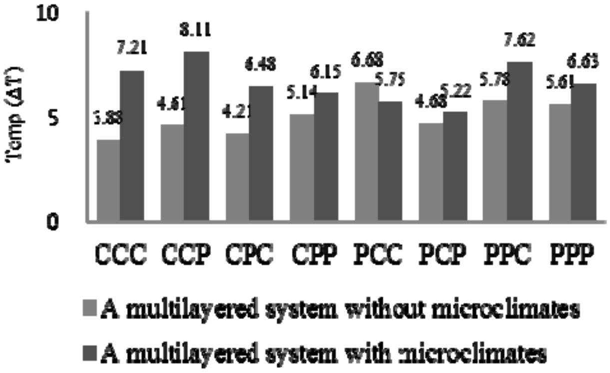

Figure 4. Temperature difference in a multilayered system with and without air layers.

CONCLUSION

From the results, heat transfer could be differed based on properties of the multilayered fabric systems consisting of hydrophobic and hydrophilic materials. Hence, the average temperatures in each multilayered fabric system were different in accordance with a order of combinations the fabrics' properties. In addition, effects of the microclimates in the multilayered system can be changed according to a type of multilayered garment system. Therefore, this research demonstrated that heat transfer affecting comfort of the human could be adjusted by properties of each layer and microclimate's distance forming a multilayered garment system

REFERENCES

[1] M.J. Moran, H.N. Shapiro. *Fundamentals of Engineering Thermodynamics*, John Wiley & Sons, Inc., Hoboken, NJ, 2008.

[2] K. Min, Y. Son, C. Kim, Y. Lee, K. Hong. Heat and moisture transfer from skin to environment through fabrics: A mathematical model. *International Journal of Heat and Mass Transfer* 50 (2007), pp. 5292-5304.

[3] D. Mitchell, L.C. Senay. Acclimatization in a hot, humid environment: energy exchange, body temperature, and sweating. *Journal of Applied Physiology* 40 (5) (1976), pp. 768-778.

[4] K. Eunae. Performance of selected clothing system under subzero conditions: Determination of performance by a human-clothing-environment simulator. *Textile Research Journal* 7 (301) (2006).

Intuitional and Quantitative Evaluation Technique of Polyvinyl Alcohol (PVA) Fiber Dispersion in Concrete via X-ray Imaging

Yumin Xia[1], Yanping Wang[1], Yimin Wang[1,2]
[1]College of Materials Science and Engineering, Donghua University,
[2]State Key Laboratory for Modification of Chemical Fibers and Polymer Materials
japuming@gmail.com; ymw@dhu.edu.cn

INTRODUCTION

With the development of textile fibers, fiber-reinforced concrete (FRC) has become possible and turned into a typical composite that consists of a brittle matrix and ductile fibers. Research have shown that compared with plain concrete FRC has higher energy absorption, and impact resistance can be increased substantially with addition of synthetic fibers randomly distributing in the concrete. The effectiveness of the fiber added depends on the degree of fiber dispersion and a certain of works were to improve the fiber dispersion. Several methods have been employed such as the fresh mixture method, the scanning electron microscope method and the simulation experiment. However, these method are indirect and designed for small range evaluation. It is urgent to find an intuitional and detectable technique to analyze fiber dispersion in the matrix.

Poly(vinyl alcohol) is a polyhydroxylated polymer and can be fabricated into high performance PVA fiber with excellent mechanical properties, and it was introduced into the FRC in recent year and exhibited excellent reinforcement in flexural strength and toughness, tensile performance, impact resistance and durability of cementitious materials. Barium sulphate ($BaSO_4$) is a shading material widely used in X-ray photography because of its no harm to human and strong shielding capability. In this paper we presents a direct detection method via fabricate $BaSO_4$/PVA composite fibers by gel-spinning with varying $BaSO_4$ content and were dispersed in the concrete matrix forming FRC. X-ray photography was taken to show the dispersion of PVA/$BaSO_4$ fiber in the matrix. Furthermore, a fractal model was established to evaluate the degree of dispersion.

EXPERIMENTAL

Materials and preparation

PVA (Mn about 80,000) and Barium sulphate were purchased locally. According to a certain proportion, PVA slice, DMSO, $BaSO_4$ water and titanate coupling agent were mixed in dissolution kettle. The mixture was heated to 60 °C and stirred for 2 h, and then at 90 °C for 4 h. After deaeration, the solution was immitted into spinning machine, measured and pumped by the metering pump, while the spinning temperature was kept at 90±2 °C. The spinneret, with orifice of 0.6 mm diameter, was maintained 0.5 cm away from the ethanol coagulation bath which is at -10 °C, while the winding velocity was at 20 m/min. Fibers were extracted by ethanol for 2 h and drawn for 3, 2, 1.5 times at 120, 150, 180 °C successively and respectively.

The fibers was cut into 3 cm. The matrix used was a cement based slurry with type I cement. The water-to-cement ratio was 0.35. Fibers were used at proportion of 3 wt% and 5 wt%. The resulting concrete slab was photographed by a X-ray machine with tube voltage of 100 kV, tube current of 100 mA and exposure time of 0.2 s.

Characterization

The mechanical properties of $BaSO_4$/PVA fibers were measured with a universal testing machine in our laboratory. The hybrid fibers were analyzed by scanning electron microscopy (SEM) to show the dispersion of $BaSO_4$ particle in the polymer matrix.

Fractal model for evaluation of fiber dispersion

The X-ray photos were digitalized and fibers was captured. And the position of each fiber was located and transfered into digital coordinates. A fractal model was established to evaluate the dispersion of fibers.

RESULTS AND DISCUSSION

SEM Analysis

$BaSO_4$ used is fine inorganic particle, and insoluble in organic solvent, so the dispersion of $BaSO_4$ particles has an enormous influence on the mechanical performance of the hybrid fibers. The cross sections of $BaSO_4$/PVA fibers with different $BaSO_4$ content were scanned with SEM (Figure 1). In the figure, the size of $BaSO_4$ particle is 100 nm to

1μm and these particles dispersed uniformly in the PVA matrix.

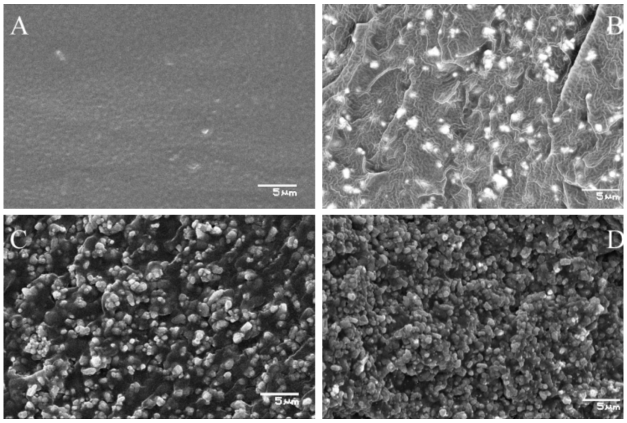

Figure 1. SEM for cross sections of pure PVA fiber and $BaSO_4$/PVA fibers: (A) Pure PVA fiber; (B) 20 wt% $BaSO_4$/PVA fiber; (C) 50 wt% $BaSO_4$/PVA fiber; (D) 70 wt% $BaSO_4$/PVA fiber. (White bar: 5 μm)

Mechanical properties

Form the SEM we found the fine $BaSO_4$ particles and the PVA matrix were blended well and there is no obvious interface defect. However, the hybrid fibers' mechanical performance decreased significantly compared with the PVA fiber (Table 1). The strength and modulus decreased as the $BaSO_4$ content increasing, but still meet the requirements for the reinforcement application.

Table 1. Mechanical properties of $BaSO_4$/PVA fibers.

Sample	Strength (cN/dtex)	Elongation at break (%)	Modulus (cN/dtex)
Pure PVA fiber	4.43	19.28	82.71
20 wt% $BaSO_4$	4.05	14.82	56.39
40 wt% $BaSO_4$	2.47	12.36	34.26
50 wt% $BaSO_4$	2.35	9.55	27.25
60 wt% $BaSO_4$	2.17	7.30	21.90
70 wt% $BaSO_4$	1.79	6.78	18.31

Fractal model for evaluation of fiber dispersion

Figure2A is the X-ray image of the $BaSO_4$/PVA fiber-reinforced concrete, and the dispersion of fibers was clearly visible. After digitalization, the dispersion of each fiber was converted into coordinate. Distribution factors (f_D) for each coordinate were calculated from a fractal model. In this model, f_D presents uniformity of surrounding fibers. When f_D is close to 2, the uniformity is good. f_D bigger than 2, indicates the fibers disperse sparsely; oppositely, the fibers disperse densely.

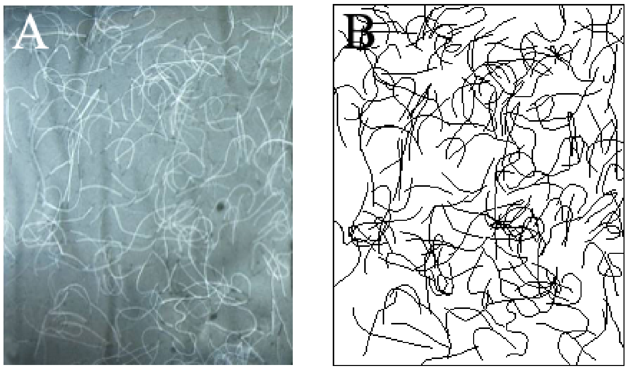

Figure 2. (A) X-ray image of 70 wt% $BaSO_4$/PVA fiber-reinforced concrete; (B) Image of digitalized fiber dispersion in FRC.

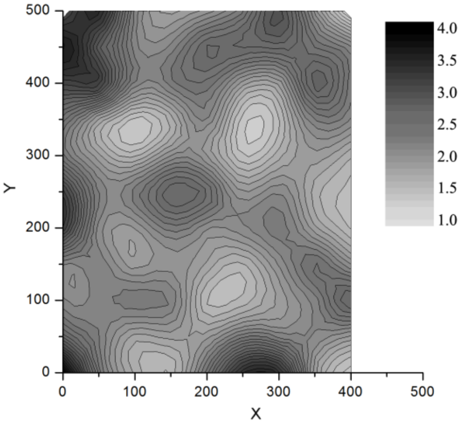

Figure 3. Dispersion of the distribution factors calculated from fractal model.

CONCLUSIONS

This paper proposes a new technique to evaluate the fiber dispersion in fiber-reinforced concrete. Owe to the X-ray shading characteristic of the $BaSO_4$/PVA fibers, the fiber dispersion is visualized and can be analyzed numerically through a fractal model. This technique is expected to be useful in assessing the influence of the fiber dispersion on the mechanical properties of fiber-reinforced concrete.

REFERENCES

[1] Najm H, Naaman A E et al. *Advn. Cem. Bas. Mat.* 1994, 1:115-121.
[2] Lee B Y, Kim J K et al. *Cement & Concrete Composites*. 2009, 31:408-417.

Emulsion Electrospinning of Sodium Alginate and Polylactic Acid Fiber with Skin-Core Structure

Yurong Yan[1], Jinyi Zhao[1], Jianfei Xie[2], Shuhan Hong[1], Chunyan Li[1]
[1]Department of Polymer Materials and Engineering, South China University of Technology, Guangzhou, China, 510640
[2]Guangzhou Fiber Product Testing Institure, Guangzhou China, 510220
yryan@scut.edu.cn

INTRODUCTION

Sodium alginate is a kind of widely used dressing materials because they tend to dissolve or gel in the wound bed and form a kind of swelled calcium alginates after the ion-change reaction between sodium alginate and calcium in blood or tissue fluid, and block the further bleeding of wound. Sodium alginate fiber can be used in knit or woven products in dressing, and the performance will be improved if the fiber with the diameter in nano scale because it is small diameter, high surface, and a kind of breathable dressing environment can be provide. Electrospinning is a useful way to prepare nanofiber, but sodium alginate is not easy to formation in electrospinning process and the sole sodium alginate is so weak in application, so blending systems were used for some special purpose. Some time, a kind of compound sodium alginate fibers can be got by using co-axial electrospinning. But for actual application, co-axial ecetrospinning is not easy to carry out in mass production.

Compared to co-axial electrospinning, emulsion electrospinning process is better controllable, and can be used more widely. Emulsion electrospinning has very special significance in making nanofibers with active substance, special drugs and wound dressing. During emulsion electrospinning, a kind of skin-core structure can be formed because the drawing tendency of electrostatic force and the evaporation of solvents in w/o and o/w systems.

In our research, nanofibers with sodium alginate as skin and polylactic acid as core was designed by using w/o emulsion electrospinning. Here, sodium alginate can gel and block the pore of the dressing then provide a micro-environment for the wound bed, and PLA can provide the tensile strength for the whole dressing. But how to control the special structure during the electrospinning process is the key part of our research here.

EXPERIMENT

Emulsion solution was carried out in two steps. First sodium alginate solution was prepared and then it was added into $CHCl_3$ with or without Span80, after a strong string, PLA was adding and formed an unique emulsion solution. Electrospinning setup was shown in Figure 1. Conductivity, surface tension and viscosity of solutions were tested and the final fiber mats were characterized by using FTIR, SEM, DSC and CLSM respectively.

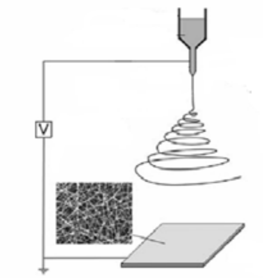

Figure 1. Electrospinning set-up

RESULTS AND DISCUSSION

The ratio of dispersed phase influences the final skin-core structure in fiber. We found that, the surface tension of emulsion will increase with the content of dispersed (Figure 2), that means, the higher the sodium alginate content is, the higher the electrospinning voltage is used.

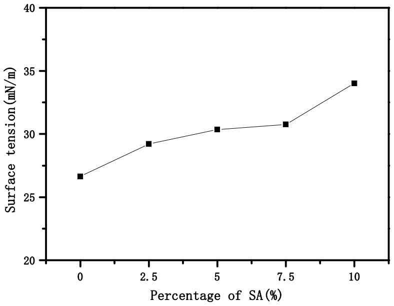

Figure 2. The influence of dispersed content on the surface tension of emulsion

Span 80 is very important during the emulsion elecrospinning (as shown in Figure 3). We can only get some beads instead of fiber mat if we did not use Span 80, which means no stable emulsion solution can be prepared without Span 80. The content of Span 80 will determined the phase size in emulsion system at the same time.

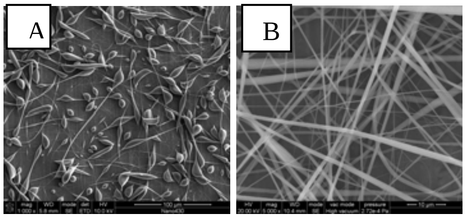

Figure 3. Images of 6.5%PLA solution with and without Span80

In order to identify the sodium alginate forming the skin part of the fiber, we dyed fiber with Rhodamine B, and tested it on Leica TCS SPE Confocal Laser Scanning Microscope. The result was shown in Figure 4. It was shown that the bright red color was covered all around fibers, that mean the dyed sodium alginate formed the skin part of fibers. In the component fibers, only sodium alginate can be dyed by Rhodamine B.

Figure 4. CLSM image of nanofibers with sodium alginate content of 10% comparing to PLA content

Why the fiber can form in skin-core structure and the skin part composed mostly by sodium alginate, we illustrate the possible mechanism in Figure 5.

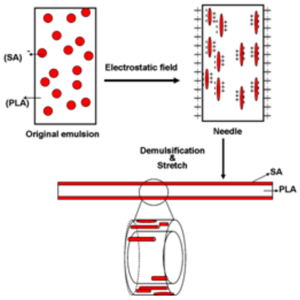

Figure 5. The possible theory of emulsion electrospinning of SA-PLA emulsion

CONCLUSIONS

Ultrafine sodium alginate/PLA fibers can be obtained by emulsion electrospinning. The minimum voltage used in electrospinning was increased with increasing the percentage of alginate sodium solution in emulsion, and the appropriate Span 80 is important for the fiber formation. From the CLSM images, SA was found all around the fibers, which indicated that some SA was dispersed on the surface of fiber.

KEYWORDS

Emulsion electrospinning, Sodium alginate, PLA, Skin-core

ACKNOWLEDGMENT

This work was supported by National Nature Science Funds for Young Scholar of China (Grant No. 51003033), the fundamental research Funds for the Central Universities of South China University of Technology(Grant No. 2009ZM0225), and by the Opening Project of the Key Laboratory of Polymer Processing Engineering, Ministry of Education, China (No.20111006).

REFERENCES

1. Jeong S. I., Krebs M. D., Bonino C. A., et al. *Macromolecular Bioscience*, 2010, 10(8): 934-943.
2. Young Jae Lee, Won Seok Lyoo. *Journal of Polymer Science, Part B: Polymer Physics*, 2009: 1916-26.
3. Li X. Q., Su Y., Liu S. P., et al. *Colloids and Surfaces B-Biointerfaces*, 2010, 75(2): 418-424.
4. Xie J. W., Ng W. J., Lee L. Y., et al. *Journal of Colloid and Interface Science*, 2008, 317(2): 469-476.
5. Angeles M., Cheng H. L., Velankar S. S. *Polymers for Advanced Technologies*, 2008, 19(7): 728-733.
6. Lamprecht A., Schafer U. F., Lehr C. M. C. *European Journal of Pharmaceutics and Biopharmaceutics*, 2000, 49(1): 1-9.
7. Nie H. R., He A. H., Zheng J. F., et al. *Biomacromolecules*, 2008, 9(5): 1362-1365.
8. Bhattarai N., Miqin Zhang. *Nanotechnology*, 2007: 455601-1-10.

Smart Fibrous Materials for Water Harvesting

Yee-yee Kong[1], J. H. Xin[1], Xiaowen Wang[1], Yu-yang Liu[2]
[1]The Hong Kong Polytechnic University, Hong Kong; [2]3M
john.xin@polyu.edu.hk

STATEMENT OF PURPOSE/OBJECTIVE

This paper presents the development of a special kind of smart fibrous materials with the ability to capture mist from atmosphere. It was achieved through building the system with hierarchical micro/macro-porous fibrous network and utilizes the switchable hydrophobic and hydrophilic properties of smart nanomaterials. The layer of nano titania coating on fiber surface offers a novel type of functional materials that display a high level of hydrophilicity upon light illumination. The combination of hydrophobic and hydrophilic characteristics formed within fibrous matrix in desired pattern gives rise to an attractive property for collecting moisture from air.

INTRODUCTION

Harvesting water from atmosphere is vital for the living organisms especially in areas that water resources are scarce. In remote areas such as Peru, Chile, Nepal, Guatemala and Eritrea, residents suffer from water scarcity. They collect water from fog by "water harvesting nets" in which dew would be trapped on the threads of giant polyethylene nets and drips into gutters leading to cistern [1]. This method, however, cannot stand windy weather as water droplets would be blown off from the nets.

Scientists designed materials with moisture collecting property by advanced surface engineering of topographic feature that mimicking surface pattern of Namib Desert beetle [2-4]. Parkner and Lawrence fabricated a hydrophobic wax coating embedded in arrays of hydrophilic glass spheres [4]. Rubner and Cohen's team produced textured surface that combining alternating hydrophobic polymer and hydrophilic silica beads [2]. Cho and co-workers follow the similar strategy, attached azobenzene on top of multilayers of polymer and silica beads [3] with extreme wetting properties controlled by UV/Vis irradiation. These studies allow the control of fluid transport confined in micro or nano-scale and promote the development of many nano-devices, yet facing the challenges of scalable fabrication and cost effectiveness. Besides, these patterned surfaces are utilized on 2-D surfaces of rigid substrates and usually involved complicated synthesis procedure. Using fibrous material assemblies have many advantages in water harvesting. This is because that there exist numerous capillary channels in a fibrous assembly that if the materials are carefully designed would allow more efficient water harvesting. Another advantage of using fibrous materials is that those materials are widely available and very economic to use.

APPROACH

In this paper, we present a facile way for fabricating smart fibrous materials with unique light-triggered properties of fog collecting. Our core strategy to create these properties is to utilize stimuli responsive materials with switchable hydrophobicity and hydrophilicity and incorporate them into the fibrous materials. Among various stimuli responsive materials, titanium dioxide is the material of choice due to its benign properties and chemical stabilities. Nanoscale titanium dioxide was synthesis by sol-gel route and incorporated within fibrous cotton by simple pad-dry-cure process. The materials exhibit light-induced superhydrophilic property. By creating the surface with desired hydrophobic-hydrophilic pattern, the materials demonstrate water harvesting property to collect the water from atmosphere. This study could pave the way for new material designs for fog-collecting materials in fogbound areas and water harvesting materials in arid regions.

RESULTS AND DISCUSSION

Structure and Surface morphology analysis

Fig. 1(a) shows the TEM bright field micrograph of titania nanosol, revealing the grain sizes ranging from 5 to 10nm. Debye-Scherrer ring was observed in the corresponding selected area electron diffraction (SAED) pattern of the inserted micrograph. HRTEM image in Fig. 1(b) indicates the crystalline characteristic of titania that the lattice fringes with d-spacing of 0.352nm which corresponding to (101) planes, suggesting that the crystalline nature is anatase phase [5]. Fig. 1(c) shows the untreated cotton fiber, indicating that the surface is smooth with natural striations. Fig. 1(d) shows the cotton fiber coated with titania nanosol. In contrast to smooth cotton fiber surface, the TiO_2 coated surface is rough with microporous structure.

Mist capturing test

We exploited the hydrophilic-hydrophobic character of TiO_2-cotton to create a material that with the ability to collect water from mist. The cotton fabric after the titania treatment became hydrophobic. The fabric was irradiated with solar light simulator through a mask to transform the irradiated region of substrate from hydrophobic to hydrophilic. To create a surface with anisotropic wettability, we constructed a patterning surface consisted an array of hydrophilic spots on the hydrophobic background. The hydrophilic spots were approximately 1 to 1.5 mm apart and ~0.5mm in diameter. This design was referenced from the exoskeleton of *Stenocara beetle* in Namib desert [4].

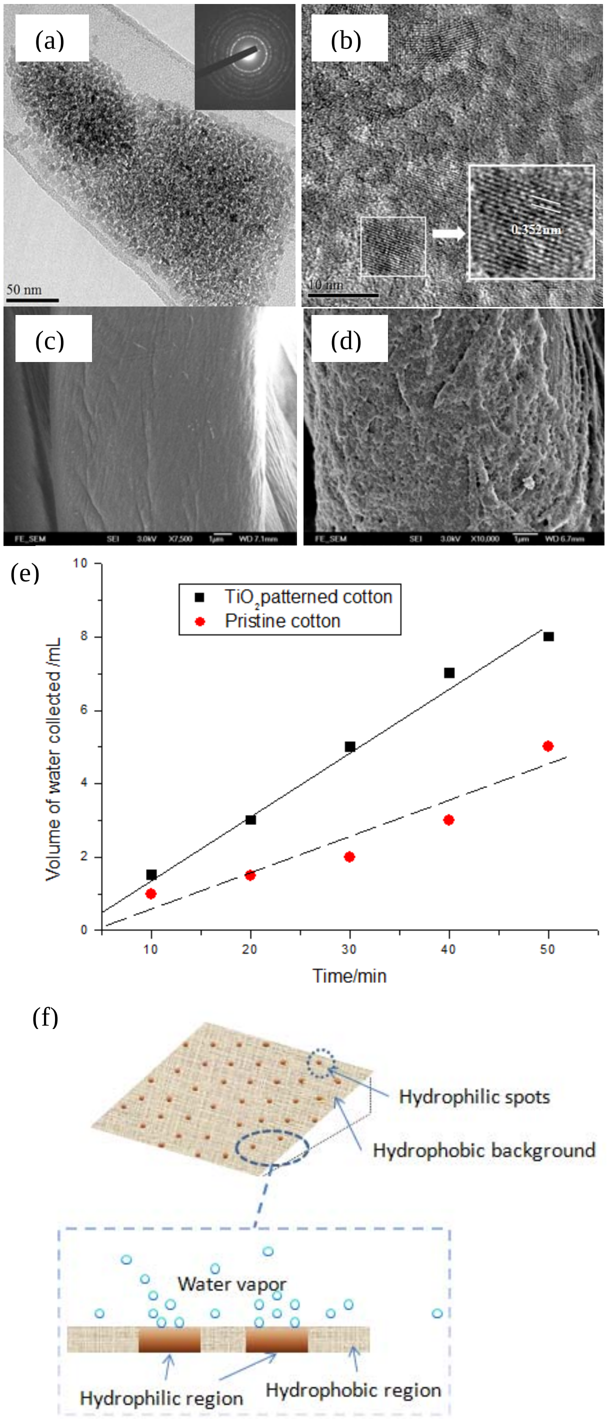

Fig. 1 TEM micrographs of titania sol at (a) bright field image, inset is the corresponding selected area electron diffraction (SAED); (b) HRTEM image. Electron microscopy images of (c) cellulosic fibrous substrate and (d) titania coated fibrous substrates. (e) Amount of water collected (mL) as a function of time. (f) Schematic of fog collecting fibrous substrate and the cross section image indicating how water is collected.

We tested the water harvesting property of the TiO_2-cotton with patterned surface under a stream of humidified air. Fig. 1(e) shows the amount of water collected as function of time. As seen from the figure, there was an improvement in the amount of water collected on the TiO_2-cotton with patterned surface relative to pristine cotton that without patterned surface. When TiO_2-cotton with patterned substrate was placed in fog (Fig 1(f)), tiny water drops started to condense on fabric surface. Since the hydrophobic and hydrophilic regions possess heterogeneous vapour-to-liquid nucleation [6], the hydrophilic regions have greater droplet nucleation rate than that in the hydrophobic regions. Water vapor tend to gather on the hydrophilic regions and grows large enough, then detached from the hydrophilic regions to the hydrophobic background and then be collected to cistern.

CONCLUSION

To conclude, smart fibrous materials with unique light-triggered water harvesting properties were achieved by single one-step fabric treatment of nanotitania. Nano-crystalline titania was formed on fibers surface as revealed by TEM and SEM. With the hydrophobic and hydrophilic pattern, preliminary results showed that smart fibrous materials displayed the ability to collect water from mist. Future work will be conducted towards the investigation of the water capturing mechanism and the improvement of water capture capacity. The proposed method is simple, economic and has high potential for scalable fabrication. The creation of this new kind material should make a contribution to the sustainability of arid areas with water shortage.

ACKNOWLEDGMENT

The authors acknowledge the financial support of the Hong Kong Polytechnic University.

REFERENCES

[1] Information on http:biomechanics.bio.uci.edu /_html/nh_biomech/namib/beetle.htm.

[2] L. Zhai, M. C. Berg, F. C. Cebeci, Y. Kim, J. M. Milwid, M. F. Rubner, R.E. Cohen. *Nano Lett.* 6 (2006): pp. 1213-1217.

[3] H. S.Lim, J. T.Han, D.Kwak, M. Jin, K. Cho. *J. Am. Chem. Soc.* 128 (2006): pp. 14458-14459.

[4] Andrew R. Parker and Chris R. Lawrence. *Nature*, Vol. 414 (2001): pp. 33-34.

[5] A. D. Walid. and J.H. Xin. *Chem. Commun. (*2005): pp. 2110-2112.

[6] K.K. Varanasi, M. Hsu, N. Bhate, W. Yang, T. Deng. *Appl. Phys. Lett*., 95 (2009): 094101.

Evaluation of Two Cooling Systems Under a Fire Fighter Coverall

LPJ Teunissen[1], Li-Chu Wang[2], Chin-hsien Huang[2], Shih-nung Chou[2], Gwo-tsuen Jou[2], Daanen Ham[1],
[1]TNO, [2]Taiwan Textile Research Institute
lawang.0269@ttri.org.tw

INTRODUCTION

Firemen are exposed to extreme heat. In combination with heavy physical exercise and protective equipment, this may lead to heat strain (Cheung, Petersen, & McLellan, 2010). Several attempts were made to reduce heat strain by active cooling. Feeding the exhaust gases from the breathing apparatus back into the suit to enhance evaporative cooling, was not effective (Williams et al., 2011). The combination of an ice vest with forearm cooling seemed very effective in reducing heat strain (Barr, Gregson, Sutton, & Reilly, 2009).

This study investigated two chest cooling techniques under fire protective garments: a cooling vest with cooling pads (TTRI system- made by Taiwan Textile Research Institute) and a vest with cold perfusing water.

APPROACH

Nine male subjects, participated in three identical experimental sessions, involving 30 min rest, 30 min treadmill walking (at a speed of 6 km/h) and 10 min recovery in hot conditions (30°C, 50% relative humidity). In all conditions, the under layer consisted of 100% cotton underwear (underpants and T-shirt) and the outer layer was a European style firefighter's coverall. The three conditions were defined by the different middle layers:

1. Control condition: no middle layer;
2. TTRI condition: cooling vest based on cooling pads;
3. Water perfusion condition: cooling vest perfused with cold water.

The measurements included rectal temperature, skin temperature (4 locations), heart rate, sweat loss, thermal sensation, thermal comfort, humidity sensation and rate of perceived exertion (RPE).

RESULTS

Rectal temperature is shown in Fig. 1. No differences were observed between conditions and conditions over time.

Mean skin temperature is shown in Fig. 2. Statistical analysis showed that the mean skin temperature was significantly lower in the water perfused suit ($p<0.001$). This is mainly due to the temperature drop of the iButton sensor at the scapula, which was located under the perfused suit.

Thermal sensation is shown in Fig. 3. Statistical analysis showed that the thermal sensation ratings were higher for control than for both cooling systems and higher for the TTRI system than for the water perfused system.

Thermal comfort is shown in Fig. 4. No differences were observed between conditions and conditions over time.

The weight differences are shown in Fig. 5. The T-shirt weighted significantly less at the end for the water perfused system and the body weight loss was also less.

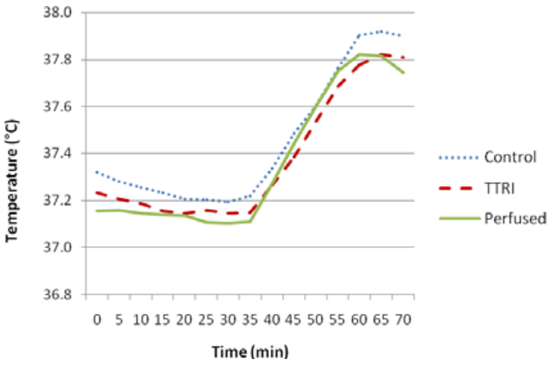

Fig. 1. Rectal temperature (°C) against time for the 3 experimental conditions.

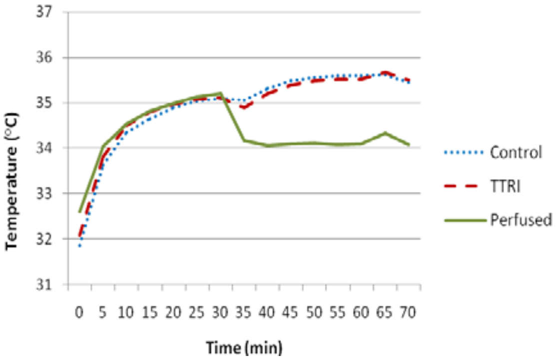

Fig. 2. Mean skin temperature averaged over 4 locations for the 3 experimental conditions.

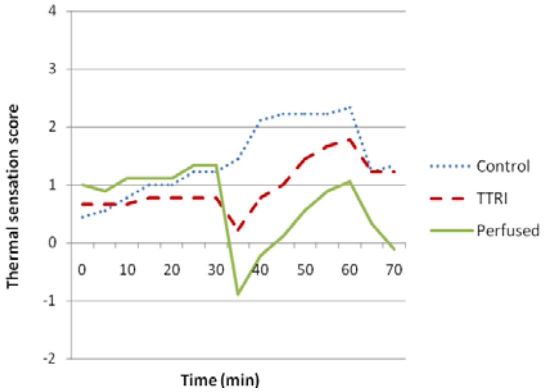

Fig. 3. Thermal sensation for the three experimental conditions.

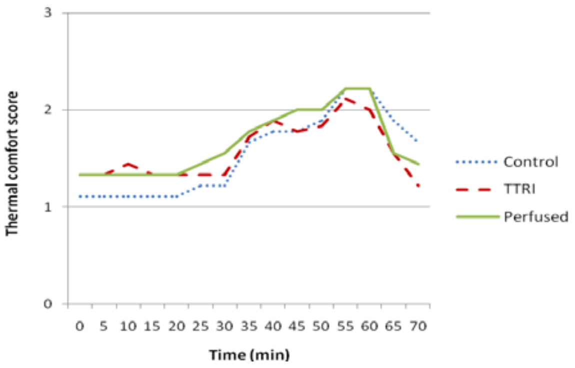

Fig. 4. Thermal comfort for the three experimental conditions.

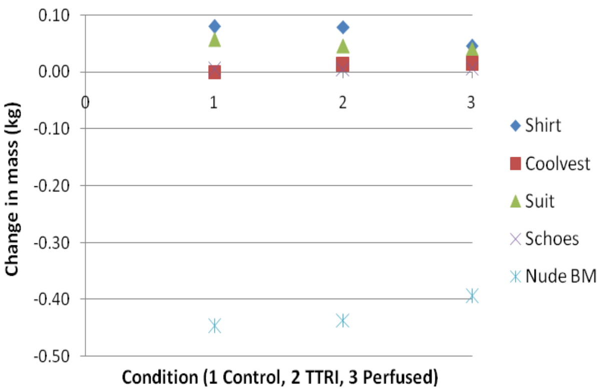

Fig. 5. Body weight loss (Nude BM) and weight gain of the equipment (shirt, cool vest, suit and shoes).

DISCUSSION

The results clearly show that both cooling systems give a better thermal sensation, in particular the perfused system. The mean skin temperature is lower for the perfused vest only. This is mainly due to the fact that one of the iButtons sensor was positioned exactly under the perfused vest (scapula iButton), which was not the case for the TTRI system. If an iButton would have been directly under the TTRI system, a lower mean skin temperature may have been shown as well.

It is striking that the lower thermal sensation for the cooling systems is not translated into better comfort. It has been shown before that comfort is not only related to what people feel, but also what they appreciate (Helander & Zhang, 1997), while thermal sensation is more related to skin temperature. In our study the lowest mean skin temperature is indeed associated with the lowest thermal sensation. It may be that thermal comfort has a closer link to core temperature than thermal sensation (Kato et al., 2001).

All other variables were not significantly different between control, TTRI system and water perfused vest.
The subjects indicated that they liked the initial cooling of the TTRI system, but that later in the experiment they could not feel the cooling any more. In some cases the pads were deformed in the pockets.

It has to be noticed that using water in the space between skin and personal protective equipment may lead to increased risk for steam formation during firefighting and thus for skin burns. It has to be established if this is the case for the systems under investigation.

The water perfused vest was related to about 40 to 60 g less sweat loss. Sweat loss is mainly driven by core temperature and to a lesser extent by skin temperature. The visible reduction in core temperature at the end of the session with the perfused vest may have caused the reduction in sweat loss and the reduced weight gain of the T-shirt.

CONCLUSION

We conclude that wearing the water perfused vest improves thermal sensation, lowers mean skin temperature and reduces body weight loss and T-shirt weight gain while exercising in the heat, but has no effect on core temperature, heart rate, thermal comfort and humidity sensation. Wearing a vest with water soaked pads also improves thermal sensation, but has no effect on thermal strain, heart rate, thermal comfort and weight loss.

KEYWORDS

Cooling vest; Thermal sensation; Fire fighter

ACKNOWLEDGMENT

The authors would like to acknowledge the financial support for this study by Department of Industrial Technology, Ministry of Economic, Taiwan, R.O.C., and also the researchers in TNO and TTRI who helped in the research.

REFERENCES

Cheung, S. S., Petersen, S. R., McLellan, T. M. (2010). Physiological strain and countermeasures with firefighting. *Scandinavian Journal of Medicine and Science in Sports*, 20(SUPPL. 3): 103-116. doi: 10.1111/j.1600-0838.2010.01215.

Williams, W. J., Coca, A., Roberge, R., Shepherd, A., Powell, J., Shaffer, R. E. Physiological responses to wearing a prototype firefighter ensemble compared with a standard ensemble. *Journal of Occupational and Environmental Hygiene*, 2001, 8(1): 49-57.

Barr, D., Gregson, W., Sutton, L., & Reilly, T. (2009). A practical cooling strategy for reducing the physiological strain associated with firefighting activity in the heat. *Ergonomics*, 52(4): 413-420. doi: 10.1080/00140130802707675.

Helander, M. G., Zhang, L. (1997). Field studies of comfort and discomfort in sitting. *Ergonomics*, 40: 895-915.

Kato, M., Sugenoya, J., Matsumoto, T., Nishiyama, T., Nishimura, N., Inukai, Y., Yonezawa, H. (2001). The effects of facial fanning on thermal comfort sensation during hyperthermia. *Pflugers Archive European Journal of Physiology*, 443(2): 175-179. doi: 10.1007/s004240100681.

Preparation of a Novel Hydrophilic Copolyester

Jianwu Li, Peng Ji, Huan Wang, Qiong Wang, Huaping Wang
State Key Laboratory for Modification of Chemical Fibers and Polymer Materials, College of Materials Science and Engineering, Donghua University, Shanghai 201620, China
dh1132026@163.com

ABSTRACT

The paper mainly focused on the preparation of a novel hydrophilic copolyester via different modified monomers. The mechanism of copolymerization was investigated using DSC and FTIR spectrum analysis. Furthermore, the hydrophilic property of prepared hydrophilic copolyester and fiber was tested by CA(Contact angle) and moisture regain. The hydrophilic copolyester exhibited better hydrophilic efficiency compared blank polyester.

INTRODUCTION

Polyester has been widely used due to its outstanding combination properties, such as excellent wash and wearable, good dimensional stability, anti-wrinkle, and quick drying properties. However, 100% polyester has an extremely poor moisture management property, as compared to natural fibers, such as cotton. Polyester has a moisture regain of only 0.4% (measured at a relative humidity of 65% and 20°Cfor 24h), while cotton has a moisture regain of about 8.0%. The poor wear comfortness of PET fiber limited its application in the field of sportswear, under garment etc.

A novel of hydrophilic copolyester was prepared via copolymerization method with purified terephthalic acid (PTA), ethylene glycol (EG), 5-sodium suflo bis-(hydroxyethyl) isophthalate (SIPE) as the third monomer, polyethylene glycol (PEG) as fourth monomer and polyols as the fifth monomer.

APPROACH

A novel of hydrophilic copolyester was prepared via PTA direct esterification route with the incorporation of polyols (0~1mol% of PTA) at the first esterification stage shown as scheme 1 and scheme 2. The reaction conditions were controlled at 230-250°C, 0.2~0.4 MPa. When the amount of the esterification water reached 87-90% of its theoretical volume, the first esterification stage was considered to be finished. The third monomer SIPE and the fourth monomer PEG (Mn=6000) were added into the polymerization reactor at the end of Esterification I. Esterification II was finished until the esterification water reached 95-97% of its theoretical value. Constant agitation was begun after the esterification and then vacuum was slowly carried at stage of Polycondensation I. The temperature was increased from 250°C to 275°C, and the pressure was reduced to less than 60 kPa in 50min. The end of Polycondensation II stage was determined when the stirring power was increased to the set value. Blank sample of polyester without adding the third, fourth and fifth monomer was also prepared. The polyester and hydrophilic copolyester fibers were prepared by means of melt spinning.

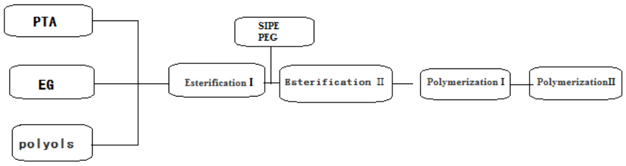

Scheme 1. Preparation process of hydrophilic copolyester

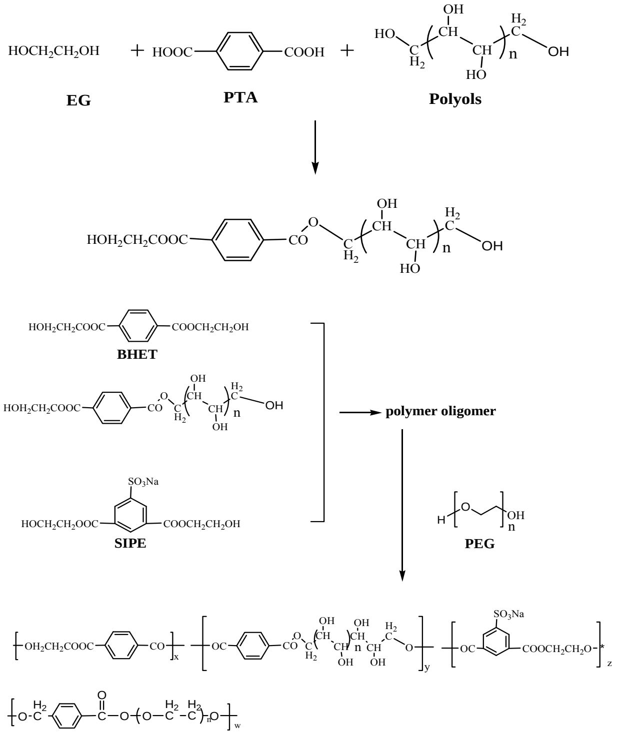

Scheme 2. The mechanism of prepared hydrophilic copolyester

RESULTS AND DISCUSSION

The intrinsic viscosity [η] of prepared hydrophilic copolyester and polyester was 0.62dl/g, 0.64dl/g respectively. The thermal property of polyester and hydrophilic copolyester was characterized by DSC as shown in Figure 1. The stereoregularity of the copolyester structure was destroyed because of the addition of the third monomer SIPE. The segment of copolyester at a lower temperature was difficult to assemble into the lattice due to the polarity of the sulfonic acid group and sterically hindered effect, resulting in the decreased speed of copolyester crystallization. It made the cold crystallization temperature T_c of copolyester higher than polyester (shown in Table 1).

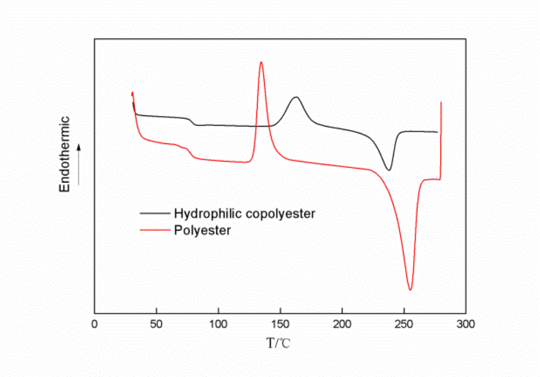

Figure 1. DSC curves of hydrophilic copolyester and polyester samples

According to $T_m = \Delta H_m / \Delta S_m$, the melting point T_m of copolyester was determined by the melting enthalpy (ΔH_m) and the molten entropy (ΔS_m). The value of ΔS_m increased and the value of ΔH_m decreased with the addition of the fourth monomer PEG and the fifth monomer polyols, resulting in the T_m of hydrophilic copolyester less than the polyester.

Table I. Testing results for copolyester and polyester samples(A--Polyester B--Hydrophilic copolyester)

Sample	T_m (°C)	T_c(°C)	W(%)	CA(°)	
A	256	135	0.4	85.0	
B	240	160	1.2	58.2	

The CA (Contact Angle) of hydrophilic copolyester was 58.2° less than polyester. Hydrophilic copolyester fiber has a moisture regain of 1.2% (measured at a relative humidity of 65% and 20°C for 24h), while polyester fiber has a moisture regain of about 0.4%. It illustrated that the hydrophilic property of prepared copolyester was much better that polyester.

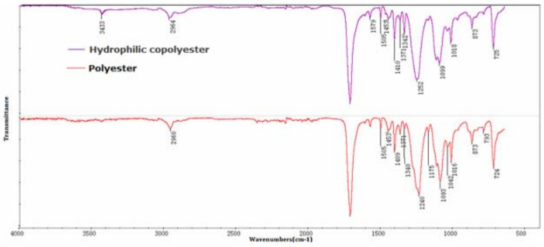

Figure 2. FT-IR spectrum of polyester and hydrophilic copolyester

The hydrophilic copolyester was analyzed by FT-IR spectroscopy. The carbonyl group (-OH) found in the region of 3433 cm^{-1} because of adding polyols into copolymerization. The characteristic peak of prepared hydrophilic copolyester was consistent with the target product.

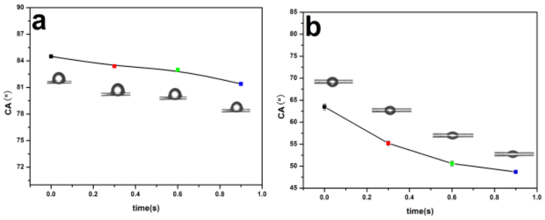

Figure 3. Relationship between CA and wetting time (a--Polyester fiber b--Hydrophilic copolyester fiber)

The relationship between CA and wetting time was also analyzed as shown in Figure 3. The wetting behavior of the polyester fiber and hydrophilic copolyester fiber was a dynamic process. The CA of the polyester fiber was almost no change with wetting time while the CA of hydrophilic copolyester fiber was a tremendous change in short time, illustrating the hydrophilic property of prepared copolyester was better.

CONCLUSIONS

Hydrophilic copolyester was prepared via copolymerization method with SIPE as the third monomer, PEG(Mn=6000) as the fourth monomer and polyols as the fifth monomer. The cold crystallization temperature of copolyester higher than polyester and the Tm of hydrophilic copolyester less than the polyester. The characteristic peak of prepared hydrophilic copolyester was consistent with the target product. The hydrophilic property of prepared copolyester was better.

FUTURE WORK

Further studies will focused on the relationship between each modified monomer and the hydrophilic properties of the copolyester and optimization of the polymerization recipe.

REFERENCES

[1] Zaman Masuduz , Liu Hongbin, Xiao Huning, et al. Hydrophilic modification of polyester fabric by applying nanocrystalline cellulose containing surface finish. *Carbohydrate Polymers*， 2013, 91: 560-567.

[2] Gu S Y, Xiao R, Gu L X. Crystallization Behavior of Copolymer Poly (ethylene terephthalate/isophthalate) (IPET). *Journal of Donghua University (Eng. Ed.)*, 2001, 18: 1-5.

[3] Lee J H, Park S H, et al. Effect of pretreatment conditions on the hydrolysis and water absorption behavior of poly(ethylene terephthalate) fibrous assembly. *Polymer International*, 2012, 61: 657-663.

[4] Gao G, Zhang L, et al. Crystalline and Thermal Behavior of Poly(ethylene terephthalate)/Polyphenoxy Blends. *Journal of Applied Polymer Science*, 2005, 97: 878-885.

Ambulatory Monitoring of ECG Signals Using Textile Electrodes

Thamizhisai Periyaswamt and Daniela P. Agnello
Central Michigan University, Mt Pleasant, Michigan, USA
periy1t@cmich.edu

RESEARCH OBJECTIVES

Continuous monitoring of physiological signals under ambulatory conditions is essential under the paradigm of remote medical monitoring and telemedicine, especially among the aging population. Several products have been tested under laboratory conditions using wearable health monitoring devices, either augmented or embedded within the clothing systems. Nevertheless, the challenge of devising a reliable and robust system that is immune to artifacts, caused by relative motion between the sensors and the physical body landmarks, still remains under research investigations. Furthermore, these sensor-embedded clothing systems are limited in their prolonged wearability, making them restrictive for continuous ambulatory monitoring. This research attempts to address the signal reliability and wearability problems associated with the embedded clothing systems from the perspectives of fabric construction properties, sensor integration and garment design. We propose (i) a novel system of garment construction using an approach called componentized maximum stretchable orientation (MSO), and (ii) an embedded electrode with conductive fabric to monitor human ECG signals. Results show that the system is capable of obtaining reliable signal under conditions of walking, with high signal-to-noise ratio.

INTRODUCTION

Continuous health monitoring is becoming a necessity among different population groups including sports personnel, aged and rehabilitating people. In order to better monitor short and long term changes in the vital signals, a more reliable ready-to-wear monitoring system that would serve as an interface to the human electrophysiological system needs to be developed. Several classes of wearable health monitoring systems (WHMS) exist based on the degree of sensor invasiveness (either surface mounted or implanted), application (sports, ambulatory, etc.) and their degree of integration with clothing systems. The latter class of clothing based WHMSs remains promising and versatile in continuous health monitoring. They often adopt textiles and apparels as their medium of housing to embed the sensors and other electronics needed for signal acquisition. The long-standing issues of signal instability, compromised reliability and robustness, however, are still persistent.

The advent of miniaturized electronics and advanced functional materials has expanded the horizons of clothing based WHMSs. Often a set of vital signals are to be monitored to assess the health conditions. Systems such as *LifeShirt* measures 30 vital signals of the wearer where the sensors are woven into fabric structure to monitor the physiological signals[1]. Similarly, integration of sensor networks in a clothing system has been demonstrated by *MagIC* [2]. However, extending the applicability of these systems either under clinical of telemedicine setup is limited by the reliability of signals. Essentially, these signals are corrupted by motion artifacts and sensor noises.

It was reported that fabric properties, cut positioning of sensors and garment adherence factors play a significant role in acquired signal quality and to achieve freedom of movement and comfort [3, 4]. Hence, continuous real-time monitoring mandates reengineering of clothing design and sensor integration techniques to achieve robust and reliable systems.

The present work is aimed towards reengineering the clothing based WHMSs to minimize the above-mentioned issues. A stretch-to-fit garment system employing the principles of MSO was developed for continuous ECG monitoring. The system uses conductive fabrics as the medium of interface for physiological signal acquisition. The system was tested under walking conditions and was further analyzed for signal reliability and quality.

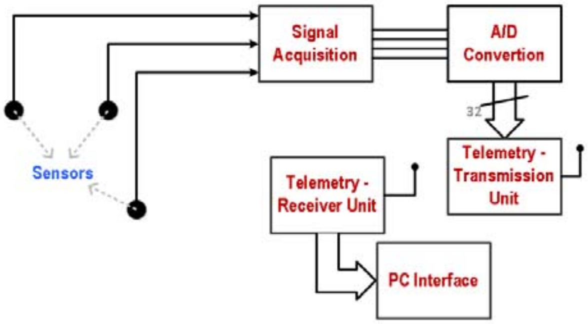

Figure 1. System level architecture of the ECG monitoring setup.

SYSTEM DESIGN AND IMPLEMENTATION

Signal Acquisition and Transmission

A system level architecture is shown in Figure-1. Electrical potential signals measured via conductive fabric sensor were telemetered to a PC after filtering and digitization. . Signals sampled at 256 samples per second were filtered using a low-pass IIR filter. The conductive fabric that served as an interface between the skin and the electrical conductors was comprised of yarns coated with metallic conductor particles. The size and weight of the unit was significantly reduced by thin solid-state batteries. Similarly, the size and contact resistance of sensors were reduced by using a dry contact capacitive coupling sensor of size 10x10mm with 3.5mm thickness interfaced with conductive fabric.

Design Principles using MSO

Maximum stretchable orientation uses the methodology of aligning the fabric components in multiple orientations such that they are in cohesion with the uniaxial extension of muscles. Figure-2 shows a schematic of the clothing panel arrangements in relation to the muscle expansion. With this methodology, the relative motion between the skin surface and the sensor mount is minimized. Whenever the MSO is orthogonal to the direction of muscle extension, which generally occurs as a result of bending, stretching or movement, the rigidity of the fabric would induce a relative movement with the skin surface causing severe motion artifacts [see Figure-2 (panel)].

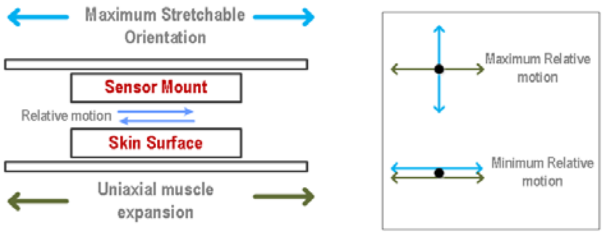

Figure 2. Schematic of the MSO approach. (Right) Panel depicts the relative orientation between the panels and the muscle under two conditions.

RESULTS AND DISCUSSIONS

The developed clothing system is shown in Figure-3. Colored striations on the panels [see Figure-3 (right)] show the gradient of the MSO directions. The system was developed using a stretch-to-fit material to ensure adequate pressure between the sensor and the point of skin contact.

Figure 3. ECG monitoring garment with the componentized fabric panels. Striations show the gradient of the stretch orientation.

A sample plot of the acquired signal is shown in Figure-4. Compared to the classic ECG system using a gel-based electrode, the textile-based sensor produced high-frequency jitter noise. Nevertheless, the low-frequency parametric characteristics of an ECG signal are retained sufficiently for further analysis.

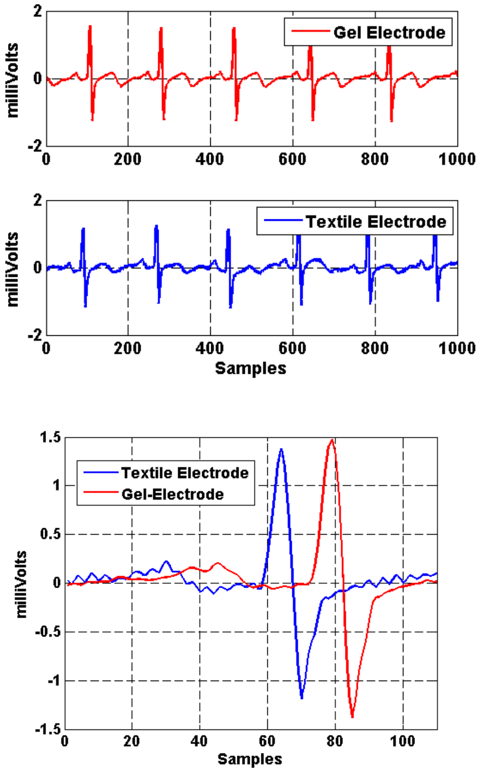

Figure 4. Comparison of ECG signals from classical gel-based and textile-based electrodes.

CONCLUSION

The MSO approach for garment design shows promise in terms of minimizing the relative motion of the skin and the sensor under ambulatory conditions. Furthermore, the electrical characteristic of the conductive fabric based dry electrode is capable of generating comparable signal quality with the gel-based electrodes. With additional signal monitoring setup and stackable light-weight thin-film batteries, prolonged usage of the system is possible. The proposed system would offer unprecedented opportunities for telemedicine and remote health monitoring.

REFERENCES

[1]. Kyle A.M., Rogers P.I., Seongwook Han, Peng-Sheng Chen, March K.L. LifeShirt® acquisition system to monitor ECG from ambulatory swine and the implementation of an arrhythmia detection algorithm. *EMBC*: pp. 4820-4823, Sept. 2009

[2]. Di Rienzo M., Meriggi P., Rizzo F., Castiglioni P., Lombardi C., Ferratini M., Parati G. Textile Technology for the Vital Signs Monitoring in Telemedicine and Extreme Environments. *Information Technology in Biomedicine*, IEEE Transactions. Vol. 14, No. 3, pp. 711-717, May 2010.

[3]. Di Rienzo M., Rizzo F., Meriggi P., Castiglioni P., Mazzoleni P., Ferrarin M., Ferratini M. MagIC: a Textile System for Vital Signs Monitoring. Advancement in Design and Embedded Intelligence for Daily Life Applications. *EMBS* 2007. Vol., No., pp. 3958-3961, 22-26 Aug. 2007.

[4]. Chan M., Estève D., Fourniols J., Escriba C., Campo E. Smart wearable systems: Current status and future challenges. *Artificial Intelligence in Medicine*. Vol. 56, Issue 3, pp. 137-156, November 2012.

Non-Isothermal Crystallization Kinetics of Bio-Based Polyester

Chaosheng Wang, Huan Wang, Peng Ji, Huaping Wang
State Key Laboratory for Modification of Chemical Fibers and Polymer Materials, College of Materials Science
and Engineering, Donghua University, Shanghai 201620, China
cswang@dhu.edu.cn

ABSTRACT

The non-isothermal equation was extended to describe non-isothermal cold crystallization kinetics of oriented polyer[1].Comparison with the petroleum based polyester, the non-isothermal crystallization kinetics of bio-based polyester was studied by DSC in this paper. The validity of the Jeziorny and Mo equation was examined by using a DSC crystallization curve of bio-based polyester and petroleum based polyester. The results show the crystallization ability of bio-based polyester is lower than that of petroleum base polyester.

INTRODUCTION

With the reducing of petroleum resource, environmentally friendly bio-based polyester becomes a promising material in replace of petroleum based polyester. Bio-based polyester is prepared from PTA and bio-EG, where the bio-EG was obtained from the crops fermentation. The Bio-EG has content of ~95% EG and ~5% other polyols, such as 1,2-PDO, 1,4-butyl glycol etc. The existence of polyols in bio-based polyester brings the bio-based polyester fiber new features, such as softer handling, higher dye uptake, etc. The crystallization ability of the polymer has a great influence on the fiber formation process and performance. It is essential to study the crystallization kinetics of bio-based polyester.

APPROACH

Direct esterification method was adopted to was prepare the bio-based polyester. The PTA and bio-EG with the molar ratio 1:1.3 were mixed, and then catalyst (0.04 wt% of PTA), stabilizer (0.04 wt% of PTA) and delustering agent TiO_2 (1.2 wt% of PTA) were added. The esterification was operated under 0-0.3 MPa, for 4-5 hours, and the polycondensation was occurred at 270-280 ºC for 3-4 hours..For comparison, the blank sample of PET was also prepared.

The samples were dried in a vacuum oven at 105 ºC for 12h. The non-isothermal crystallization process was carried by DSC method. The weights of all samples were about 7.0 mg. Samples were heated to 280 ºC at 100ºC/min under nitrogen atmosphere and held for 5 min and then cooled to 30ºC at a constant cooling rate of 2.5ºC /min, 5 ºC /min, 10 ºC /min and 20ºC /min respectively.

RESULTS AND DISCUSSION

The DSC cooling curve was shown in Figure 1(a) and Figure 1(b) for petroleum based polyester and bio-based polyester respectively. From Figure 1, the crystallization peak width of bio-based polyester was wider than that of petroleum based polyester, which means that the crystal lattice of bio-based polyester was less perfect than that of petroleum base polyester.

Table 1 shows that with the increase of cooling rate, the crystallization peak temperature tends to reduce, The crystallization process was controlled by nucleation[2]. The half-time of crystallization ($t_{1/2}$) is defined as the time taken from the onset of the relative crystallization until 50% completion in the non-isothermal crystallization process. Bio-based polyester's $t_{1/2}$ is longer than that of petroleum based polyester, which indicates that the bio-based polyester's crystallization is tougher than that of petroleum based polyester.

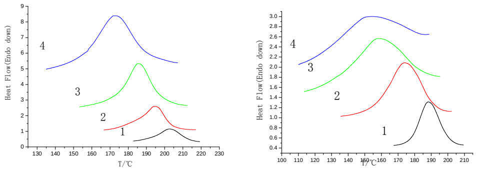

(a) (b)

Figure 1. crystallization peak of (a) petroleum based polyester, (b) bio-based polyester

Table 1. Crystallization parameters of samples at different cooling rate

Samples	R (ºC /min)	2.5	5	10	20
(a)	Tp(ºC)	202.65	194.16	185.41	172.73
	$t_{1/2}$(min)	7.219	4.656	2.754	1.603
(b)	Tp(ºC)	188.56	174.16	158.72	154.88
	$t_{1/2}$(min)	7.713	4.730	3.230	1.603

Jeziorny method Figure2 shows curves for polyester crystallization kinetics with Jeziorny method. From Figure 2, the two kinds of polyester have a good linear relationship in their main crystallization process, which indicates that the main crystallization process of two kinds of polyester is well agree with Avrami model[3].

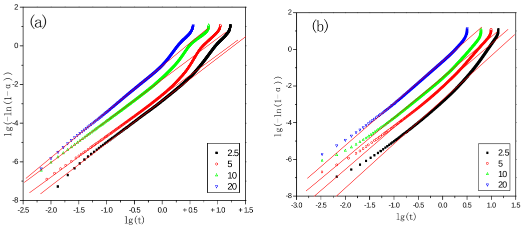

(a) (b)

Figure 2. Jeziorny plots of (a) petroleum based polyester, (b) bio-based polyester for non-isothermal melt-crystallization.

The crystallization rate constant K_c and Avrami index n of the two kinds of polyester are shown in Table 2. It is clear that with increase in cooling rate, K_c increased, It suggests that the crystallization rate will increase with increase in the cooling rate. The n value of the two kinds of polyester was greater than 2 at cooling rate of 2.5 ºC /min, which shows that the crystal model in the crystallization of polyester in their main process is three-dimensional growth. However, when the degree of supercooling was higher, the n value reduced to less than 2 which means the crystal is insufficient and the crystal region may tend to two-dimensional growth.

Table 2. Non-isothermal crystallization kinetics parameters for Jeziorny method at different cooling rate

R(ºC /min）	（a）		（b）	
	n	K_c	n	K_c
2.5	2.833	0.131	2.748	0.109
5	2.575	0.379	1.979	0.349
10	1.746	0.610	1.517	0.601
20	1.038	0.761	0.637	0.767

Mo Method From Figure 3, the two kinds of polyester have a good linear relationship in their main crystallization process. From the data displayed in Table 3, it is apparent that *F(T)* increases along with the increase in the degree of C_t, thus it becomes more and more difficult for the system to achieve a certain degree of crystallinity [4]. For the same degree of crystallinity, the *F(T)* of bio-based polyester is higher than that of petroleum based polyester, which shows that the crystallization ability of bio-based polyester is lower than that of petroleum based polyester. The main reason is that bio-based glycol contains other polyols which may lead to lower molecular chain regularity. The rigidity of molecular chain segment was reduced, which hindered the crystallization.

Table 3.Non-isothermal crystallization kinetics parameters for Mo method

C_t/%		20	40	60	80
（a）	α	1.439	1.558	1.643	1.741
	F(T)	13.14	13.22	13.36	13.56
（b）	α	1.238	1.394	1.511	1.632
	F(T)	14.50	14.99	15.31	15.52

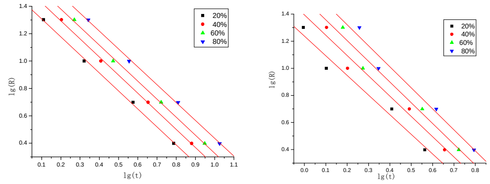

(a) (b)

Figure 3. Mo method plots of (a) petroleum based polyester, (b) bio-based polyester for non-isothermal cooling crystallization.

CONCLUSIONS

(1) Non-isothermal crystallization kinetics studies show that bio-based polyester's crystallization peak temperature decreased with the increase of cooling rate. At the same cooling rate, bio-based polyester's crystallization peak temperature was slightly lower than petroleum based polyester's crystallization peak temperature. This suggests that the existence of polyols in bio-based polyester makes the molecular chain flexible. This makes it more difficult to realize stable arrangement of the molecular chain in the lattice thus higher degree of supercooling is needed to realize crystallization.

(2) Bio-based polyester's $t_{1/2}$ is longer than that of petroleum based polyester, which means bio-based polyester's crystal is tougher than that of petroleum based polyester due to the molecular chain irregularity caused by the existence of other polyols.

(3) In the Mo model, at the same degree of crystallinity, bio-based polyester's *F(T)* was higher than that of petroleum based polyester's *F(T)*, which indicates that bio-based polyester's crystallization ability is lower than that of petroleum based polyester.

REFERENCES

[1] Z.Zhang, M.Ren, J.Zhao, S.Wu, H.Sun. Kinetics of non-isothermal cold crystallization of uniaxially oriented poly(ethylene terephthalate);*Polyme*,2003 44:2547–2551

[2] D. Wu , J.L Zhou, et al.Study on Non-isothermal Crystallization Behavior of PET/PBT Blends. *China Plastics Industry*, 38(5), 2010:55-57.

[3] S.D Tang, X. Zhong. Structural effects of ionomers on the morphology, isothermal crystallization kinetics and melting behaviors of PET/ionomers. *Polymer*, 50, 2008: 1054-1061.

[4] N. Dangseeyun, P. Srimoaon, et al. Isothermal melt-crystallization and melting behavior for three linear aromatic polyesters. *Thermochimica Acta*, 409, 2004:63-77.

Biosorption of Phenol by Cashmere Guard Hair Powder

Kiran Patil, Xungai Wang, Tong Lin
Institute for Frontier Materials, Deakin University, Geelong, VIC 3217, Australia
kapat@deakin.edu.au; xungai.wang@deakin.edu.au; tong.lin@deakin.edu.au

INTRODUCTION

Phenol is an industrial material widely used in manufacturing commercial substances such as epoxy resins, drugs, explosives, polymers, detergents, perfumes, dyes, cosmetics, and preservatives. It is a toxic organic compound and often found in the industrial waste water. Phenol is also a main organic constituent in the condensate streams of coal gasification and liquefaction processes.

Phenol pollution of aquatic ecosystems poses a great threat to the indigenous biota, including algae, protozoa, invertebrates and vertebrates. It causes reduced fertility, decreased survival of the young and inhibition of growth. The absorption of phenol by the human skin promotes tumour formation, and also affects kidneys, lungs, lever and vascular systems. Over exposure to phenol can cause comas, convulsions, cyanosis and death [1].

Due to its toxic nature, the Environmental Protection Agency of USA has set a water purification standard of less than 1 part per billion (ppb) of phenol in water.

Methods used to remove phenol from aqueous systems have been classified into destructive (oxidation) and recuperative (adsorption) methods [2]. Although activated carbon is the most widely used adsorbent, the high cost has led researches to finding cost effective materials as phenol adsorbents [3, 4].

In the present study, we found that cashmere guard hair powder could be a potential candidate for phenol removal. Cashmere guard hair - a stiff, coarse, low value counterpart of niche cashmere fibres that gets separated as a waste during the industrial processing of cashmere fleece has been milled into ultrafine powder particles.

APPROACH

Cashmere guard hair was milled into fine particles using the processing sequence: Chopping → Attritor milling → Spray Drying. The cleaned cashmere guard hairs were initially chopped into 1-2 mm snippets by processing through a rotary blade cutter (*Pulverisette 19*, from *Fritsch, Germany*). 200 g of cashmere guard hair snippets were further wet milled in a batch process, using an attritor (*IS, Union Process, USA*) with yttrium doped zirconium oxide milling media and teflon coated milling tank. The hair snippets were milled in the attritor for 6 h at 280 rpm stirrer speed, using 20 kg milling media (5 mm in diameter) and deionised water to achieve a 1:10 material (kg) to liquor (L) ratio. The wet milled slurry was finally spray dried using a laboratory spray drier (*B-290, Buchi Labortechnik AG*) to get dry powder particles.

The potential of cashmere guard hair powder in the absorption of phenol from its aqueous solution was examined in a batch process with a colorimetric method [5], using UV-VIS absorption spectroscopy. All the samples under investigation were separately weighed to approx. 400 mg in a 50 ml centrifuge reaction tube. The sample containing reaction tubes were poured with 40 ml of 50 ppm phenol solution in Milli-Q water. The pH of phenol solution was adjusted either with 0.1 N HCl or 0.1N NaOH, as desired. The reaction tubes were quickly agitated on a vibrator and consequently kept shaking on a rotating disk. At certain time intervals, 200 µl of sample solution was taken in a 50 ml glass vial from each sample tube. Each sample solution was further diluted to 2500 µl with Milli-Q water. 15 µl of 2% 4-aminoantipyrine and 50 µl of 2N ammonium hydroxide solutions were added to each sample solution after shaking. Finally, 50 µl of 2% potassium ferricyanide was added. The sample vials were mixed well on a vibrator, before and after the addition of potassium ferricyanide. The phenol concentration in each of the sample solution was calculated by measuring its absorbance at 505 nm wavelength on a UV-VIS spectrometer, which was priorly calibrated with standard phenol solutions. The percentage change in phenol concentration based on its initial concentration was reported as % absorption yield.

RESULTS AND DISCUSSION

Figure 1 shows the morphology of cashmere guard hair fibres before and after the milling treatment. Cashmere guard hair fibres had a cylindrical shape and scales on its surface (Figure 1a). They appeared to be distinctly larger in diameter (approx. 80 µm) compared to other animal hair fibres such as wool and silk which are typically around 20 µm. After milling and spray-drying, cashmere guard hair powder showed a globular mushroom like morphology (Figure 1b). The volume-based d(0.5) value measured by the optical diffraction method for the cashmere guard hair powder was 4.63 µm (Figure 1c).

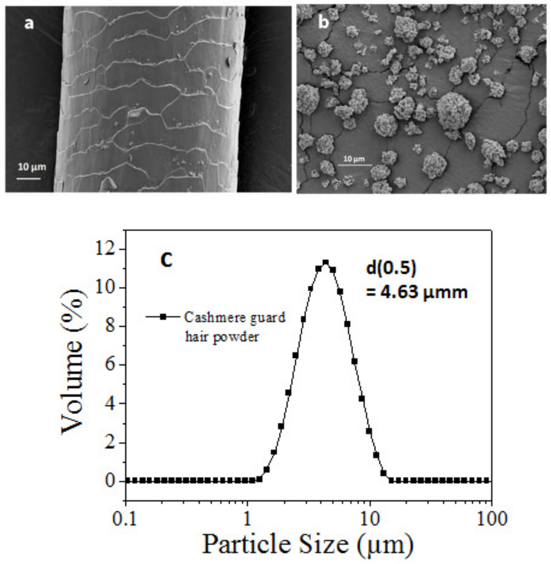

Figure 1: (a) SEM image of cashmere guard hair (b). SEM image of cashmere guard hair powder, and (c). Particle size distribution of cashmere guard hair powder.

Figure 2a shows the absorption yield of the cashmere guard hair powder to phenol in water. Phenol is effectively absorbed by cashmere guard hair powder under acidic conditions. The absorption yield of cashmere guard hair powder superseded its parent hair at all studied pH conditions, except at pH 8.6. Furthermore, the cashmere guard hair powder absorbed 100% of the available phenol in the solution in 48 hours at pH 4, when the parent hair fibre almost reached its equilibrium with approx. 10% absorption only.

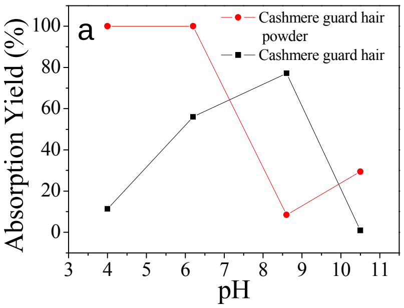

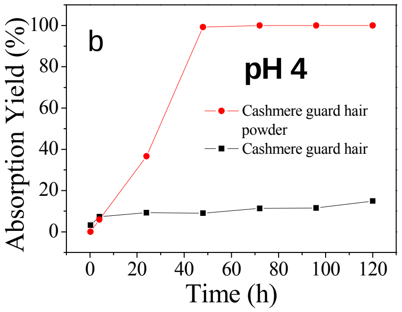

Figure 2: Effect of (a) pH and (b) time on phenol absorption yield of cashmere guard hair powder from 50 ppm solution at 30 °C with 1:100 MLR in 120 h.

CONCLUSION

The milled powder particles of cashmere guard hair, a waste product from cashmere industry, can effectively absorb toxic phenolic substances from their aqueous solutions.

REFERENCES

1. Bruce, R.M., J. Santodonato, and M.W. Neal. Summary review of the health effects associated with phenol. *Toxicology and Industrial Health*, 1987. 3(4): p. 535-568.
2. Dutta, N.N., S. Borthakur, and R. Baruah. A novel process for recovery of phenol from alkaline wastewater: Laboratory study and predesign cost estimate. *Water Environment Research*, 1998. 70(1): p. 4-9.
3. Banat, F.A. and S. Al-Asheh. The use of human hair waste as a phenol biosorbent. *Adsorption Science and Technology*, 2001. 19(7): p. 599-608.
4. Banat, F.A. and S. Al-Asheh. Biosorption of phenol by chicken feathers. *Environmental Engineering and Policy*, 2000. 2(2): p. 85-90.
5. Martin, R. Rapid colorimetric estimation of phenol. Analytical Chemistry, 1949. 21(11): p. 1419-1420.

Tri-Component Bio-Composite Materials from 'Green Processing'

Rasike De Silva, Xungai Wang, and Nolene Byrne
Institute for Frontier Materials, Deakin University, Pigdons Road, Waurn Ponds, Victoria 3216, Australia
nolene.byrne@deakin.edu.au, rdesil@deakin.edu.au

KEYWORDS: Bio-polymer, ionic liquid, green processing

STATEMENT OF PURPOSE

In this abstract, we report on the successful development of a range of novel green tri-composite bio-films. We have blended the natural polymers cotton, silk and wool using an environmentally friendly processing route. The new bio-films showed enhanced thermal stability and comparative mechanical properties.

INTRODUCTION

Cotton, silk and wool are three widely used natural polymer fibres. Each year, significant amounts of these polymers are discarded as unprocessable fibre waste in the textile industry as well as in our daily life[1]. This, combined with the need to develop alternatives to current fossil fuel derived polymers[2], means more attention should be given to reusing these renewable resources.

Room temperature ionic liquids (RTILs) are considered as green solvents which could replace organic solvents in bio-polymer processing[3]. Dissolution of the bio-polymers in RTILs is attributed to their ability in disrupting and breaking the intramolecular hydrogen bonding network of the polymer[4]. 1-allyl-3-methylimidazolium chloride (AMIMCl) is a powerful RTIL used previously to regenerate cellulose[3, 5]. In this work, AMIMCl was used as the dissolution solvent and water was used as the coagulating solvent for the bio-films. The films were characterized using Fourier transform infrared (FTIR) spectroscopy to investigate the hydrogen bonding of the new bio-films, scanning electron microscope (SEM) to reveal the morphology of the bio-films, Thermogravimteric analysis (TGA) to examine thermal stability and dynamic mechanical analysis (DMA) to examine mechanical properties.

APPROACH

Single and multi-bio-polymer solutions were made by dissolving a total of 10wt% raw cotton lint, wild type silk and wool in AMIMCl at varying concentrations as listed in Table I. The films were obtained by coagulating in distilled water. Films were rinsed several times to remove excess AMIMCl. The AMIMCl was recycled by evaporating water as described[5].

TABLE I: Composites prepared in this study.

Sample name	*Bio-polymer composition*
C100	100%cotton
S100	100%silk
W100	100%wool
C90	90%cotton,5%silk,5% wool
C80	80%cotton,10%silk,10%wool
C70	70%cotton,15%silk,15%wool
C50	50%cotton,25%silk,25%wool

RESULTS AND DISCUSSION

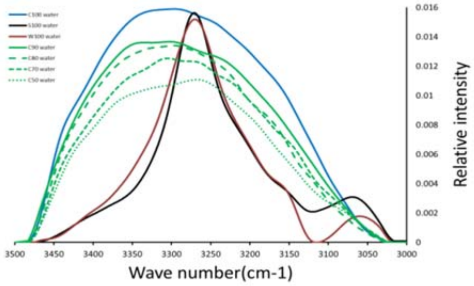

FIGURE 1: FTIR spectrum of regenerated bio-films.

Figure 1 shows the FTIR spectra of the various bio-films in the 3000-3500cm-1 region. Two peaks were obtained for S100 and W100at3275cm^{-1} and 3060cm^{-1}, which are attributed to O-H and C-H stretching vibrations[1], whereas C100 shows a single broad OH stretch band at 3300cm^{-1}

Hydrogen bond interactions between the three components of the new composite bio-films is observed by a shift in the OH band of the C100 film to lower wavelengths as the silk and wool content increases.

Figure 2 shows the TGA curves of the bio-films. The thermal degradation temperature for C100, S100 and W100 was 233°C, 278°C, and 227°C, respectively, while C90, C80, C70, and C50 composites degradation temperatures were 238^{o}C, 259°C, 286°C, and 290°C, respectively. The thermal degradation temperature of the new bio-films was enhanced with the addition of the protein component, with the T_d of C70 and C50 being greater than the single component films. This could be attributed to the formation of hydrogen bonding within cotton and protein fibres as revealed from FTIR results.

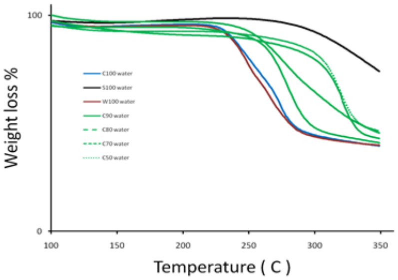

FIGURE 2: TGA curves of regenerated bio films.

Table II shows the mechanical properties of the bio-films. C100 has the highest stress, strain at breakage and Young's modulus. The addition of the protein fibres reduces the mechanical properties gradually.

TABLE II: Mechanical properties of bio-films.

Sample name	*Stress at breakage(MPa)*	*Strain at breakage(%)*	*Young's modulus(GPa)*
C100	57.98	4.48	1.88
C90	47.53	3.31	1.79
C80	45.87	2.98	1.77
C70	30.42	1.48	1.76
C50	28.94	1.6	1.70

Figure 4 shows SEM images of the bio-films. It reveals a continuous morphology which verifies complete dissolution of bio-polymers in the ionic liquid.

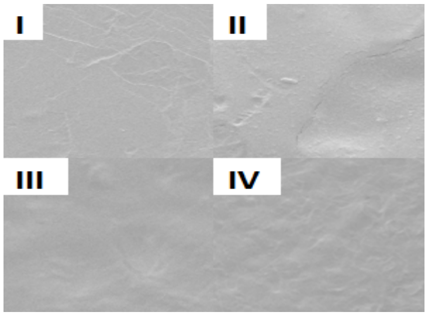

FIGURE 4: SEM images of C100 (I), C90 (II), C70 (III) and C50 (IV).

CONCLUSION

We successfully developed tri-composite bio-films using environmentally friendly processing methods. The new bio-films showed enhanced thermal stability compared with the single component films.

FUTURE WORK

Bio films will be made using different coagulating solvents such as methanol and isopropanol to study the impact of coagulating solvent.

REFERENCES

[1] R. Li and D. Wang. Preparation of regenerated wool keratin films from wool keratin–ionic liquid solutions. *Journal of Applied Polymer Science*, 2012.

[2] A. Mohanty, M. Misra, and L. Drzal. Sustainable bio-composites from renewable resources: opportunities and challenges in the green materials world. *Journal of Polymers and the Environment*, vol. 10, pp. 19-26, 2002.

[3] Y. Cao, J. Wu, J. Zhang, H. Li, Y. Zhang, and J. He. Room temperature ionic liquids (RTILs): A new and versatile platform for cellulose processing and derivatization. *Chemical Engineering Journal*, vol. 147, pp. 13-21, 2009.

[4] R. P. Swatloski, S. K. Spear, J. D. Holbrey, and R. D. Rogers. Dissolution of cellose with ionic liquids. *Journal of the American Chemical Society*, vol. 124, pp. 4974-4975, 2002.

[5] H. Zhang, J. Wu, J. Zhang, and J. He. 1-Allyl-3-methylimidazolium chloride room temperature ionic liquid: A new and powerful nonderivatizing solvent for cellulose. *Macromolecules*, vol. 38, pp. 8272-8277, 2005.

Creative Shading Effect in Digital Jacquard Textiles

Ken Ri Kim and Frankie Ng
Institute of Textiles and Clothing, The Hong Kong Polytechnic University, Hung Hom, Kowloon, Hong Kong
frankie.ng@polyu.edu.hk, kenri.kim@connect.polyu.hk

PURPOSE/OBJECTIVES OF STUDY

This study aims at optimising the structural design method of creative shading effect in digital jacquard textiles. Based on appropriate weaving structure design, diverse shading effects are developed for woven fabrics. Reference was made to the full-colour compound structures [1] [2], of which the optimal conditions in jacquard weaving structures was proposed for representing shading colour effects on the fabric surface against a given gradated image. The principles of structural designs are adopted while the size of single weaves is expended and created with different increases of interweaving points. It was to testify the appropriateness toward an improvement of colour appearance and stability through modification of weaving structures by an extra weft figuring method with one end of white ground [3]. Since primary colours are defined as the ‘first’ or ‘principle’ colours which cannot be achieved by mixing any other colours [4], primary coloured yarns are thus considered as the first selections for the fillings to reproduce a wide scope of weave colours. The detailed objectives of this study are 1) to identify optimised structure formats and size scopes for natural colour representation via deployment of an electronic weave machine and jacquard CAD system and 2) to testify the possibility of enlarging weave colour ranges through mixing primary colour groups of filling yarns and 3) to expand and originate new design concepts of jacquards.

INTRODUCTION

Jacquard textiles in rich colours are created by intricate weave structures. Computerised weaving technology such as jacquard CAD systems and electronic weaving looms today have made design process exceptionally convenient and also reduced considerable time in production. Yet, production of highly intricate design patterns with a great number of colours still proves difficult. It is so due to the limits on yarn number in filling yarns and the inconvenience on warp yarn replacements. So far, creation and reproduction of jacquard fabrics of picturesque designs have been relying on weft yarn colour assortments rather than warp yarns. In a prior study, achievement has been made on the shaded weave structures [1] [2]. The formation enables different degrees of lights and shades to obtain in graduated manner, so that a natural form of motif can be represented in a natural way [5]. A great number of weave colours were possible to be achieved by the deployment of full-colour compound structures and the layer combination mode in the previous development. However, the applied sizes of weave structures as well as the varieties in derivatives were limited. Either twill or sateen weave structures are commonly used for shading effects to vary the floats of weft and warp [5].Yet, in this study, sateen weave formations are preferred for achieving smooth texture of surface and were investigated to identify optimised weave sizes in terms of fabric firmness as well as to generate natural colour ways on face of fabrics.

APPROACH

The technology of colourful jacquard fabric lies in two core aspects: structure and image design. With the support of advanced electronic weaving machines and textile CAD systems, diverse applications in both sides can be created and applied. Based on the full-colour compound structures and layered-combination mode, a wide scope of weave colour reproduction was attempted. The framework was first designed to establish theoretical foundation in both structure and colour aspects and further evaluated through empirical experiments. As jacquard design and fabrication become more flexible with technical assistance of jacquard CADs and electronic weaving machines, any prerequisite condition was investigated to fulfil the requirements in the course of building a design environment for weaving. Background researches focused on colourful jacquard textile designs to attain the depth of research to originate new knowledge. Traditional ways of sateen weaves from 12 to 40 sizes are modified and enhanced to achieve different degrees of light effects in weaving forms. As rich-coloured artworks for jacquard fabrication broadly adopts CMYK scheme, this study is developed based on the subtractive colour system as well as the four primary colours [6]. The experiments were planned to commence with a spectrum image to examine levels of technical comprehension. Design concepts are being expanded and explored toward innovative ends.

EXPRIMENTS AND RESULTS

Weave databases from 12- to 40-thread were created and experimented with different increasing values of interlacements so as to discover the correlation between weave structures and image designs. The inter-relationship between them was further analysed in relation with the colour appearance. The experiments were designed in a way that all the weave sizes were applied to the invited spectrum image to classify the appropriateness for fabric firmness and colour presentation. The spectrum image was consisted of a large number of colour shads, thus, the image was an ideal choice to prove technical comprehension and capability to fulfil the study goals. Primary colour threads were selected for extra wefts as they can reproduce a wider scope in weaving.

CONCLUSIONS

It was crucial in an initial stage of the study to comprehend the depth of the weaving technologies, e.g., full-compound structures and layered-combination mode, in order to create further applications in woven structures. So far, the majority of the intended aim and objectives were successfully fulfilled via experiments by which optimised conditions of weave sizes and image management are proposed and suggested.

FUTURE WORK

This study advances the full-colour compound structure and the layered-combination mode. Digitalised jacquard textiles and primary colours have been explored in this study. Certain limitations and problems are identified, further investigations are proposed as the followings: 1) Different methodological approaches on layered-combination modes are required for further improvement on jacquard colour reproducibility, 2) different applications on digitalised jacquard textiles are essential to enhance colour reproduction, and 3) the expansion on materials for innovative jacquard effects and techniques.

KEYWORDS

Shading effect, CMYK colour scheme, colourful jacquard

ACKNOWLEDGMENT

The authors would like to acknowledge the financial support provided by The Hong Kong Polytechnic University in the form of a postgraduate scholarship.

REFERENCES

[1] Ng, M.C.F., and Zhou. J., Full-colour compound structure for digital jacquard fabric design, *Journal of the Textile Institute*, Vol.101, 2010, pp. 52-57.
[2] Zhou, J. Research and creation of printing-like effect digital jacquard fabric, *Advanced Materials Research*, Vol. 295-297, 2011, pp. 2568-2571.
[3] Watson, W., and Grosicki, Z. *Watson's Advanced Textile Design: Compound Woven Structures*, 4th ed., 1977, pp. 13-14.
[4] Zollinger, H. *Colour: A Multidisciplinary Approach*, 1999, pp. 17-18.
[5] Watson, W., and Grosicki, Z. *Watson's Textile Design and Colour: Elementary Weaves and Figured Fabrics*, 7th ed., 1975, pp. 130.
[6] Xin, J.H. *Total Colour Management in Textiles*, 2006, pp. 180.

Structure and Composition Research of Lotus Petiole Fiber and Ramie Fiber

Genyang Cao[1,2], Haona Wang[3], Weilin Xu[1]
[1]Ministry of Education Key Laboratory of New Textile Materials Green Processing and Functionalization, Wuhan Textile University, Wuhan, Hubei, 430073, China
[2]Textile Materials and Technology Lab, Donghua University, Shanghai, 201620, China
[3]Textile Clothing College, Wuhan Institute of Technology, Wuhan, 430074, China
genyang.cao@wtu.edu.cn

STATEMENT OF PURPOSE

In this paper, ramie fiber and lotus petiole fiber were compared in structure and composition. The structure and composition of the two fibers were probed with SEM, TG and FT-IR.

INTRODUCTION

Nowadays, with the increasing awareness of environment issues and the demand of natural fabrics, more and more attentions were paid to natural fibers, such as ramie fiber [1], bamboo fiber [2] and flax fiber [3]. It has been an important research area and many more natural fibers were found. Most of the fibers were applied in clothing and composites. Ramie fiber and lotus petiole fiber were very popular in Asia, especially in India

.

Lotus is very useful in Chinese Medicine, and it grows in North America and many parts of China [4], with lotus leaf and lotus nuts being used as herbal medicine in China. Lotus is also used in tea for reducing pathogenic fire [5]. Lotus fiber can be obtained from lotus root and petiole. It is easier to get fiber in petiole than in root, because the the petiole contains more fibers [6]. Two methods of preparing lotus fiber have been reported: one method is fiber extraction from lotus petiole [4], and the other is retting for degumming [6]. The ramie fiber is the oldest vegetable and textile fiber [7]. It has been used in textile, composite and Chinese medicine. In this paper, we compared the ramie and lotus petiole fiber with SEM, TG and FT-IR.

APPROACH

Lotus petioles were supplied by Donghua University. Lotus petioles were dipped into a degumming solution, which was composed with 15g/L sodium hydroxide and 6g/L soap flakes, and then kept the solution in 100°C for two hours. After the treatment, lotus petiole fibers were obtained. The fibers were neutralized with 1g/L H_2SO_4 solution, and then washed in deionized water. The ramie fiber was purchased from the market.

The SEM images of the samples were examined using a Quanta 200 (FEI in Holland). The samples were coated with gold to avoid sample charging under the electron beam.

The thermal stabilities of lotus petiole fiber and ramie fiber were characterized using a TG 209F1 instrument. Dynamic TG scans were performed under a nitrogen atmosphere and heated up to 700°C and the rate of heating was 10°C/min.

The FT-IR spectra were recorded in the range of 400-4000cm^{-1}. The samples were sheared into powder and then blended with KBr followed by pressing the mixture into ultra–thin pellets.

RESULTS AND DISCUSSION

Surface morphology analysis

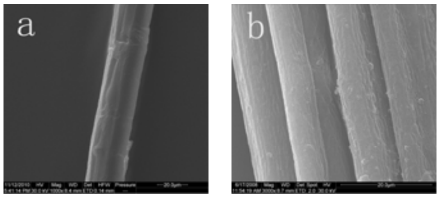

Fig. 1. SEM images of the longitudinal shape of ramie fiber and lotus petiole fiber: (a) ramie fiber (b) lotus petiole fiber

Ramie fiber is white and very soft. The fiber surface in Fig. 1a is smooth. The fineness of ramie fiber is about 25 µm, but the lotus petiole fiber is about 20 µm. Lotus petiole fiber prepared with the method of degumming is much longer than other natural fibers, such as cotton. The lotus petiole fiber layer is adhered to the internal surface of the petiole wall. Fig. 1b shows the longitudinal morphology of lotus petiole fiber. There was some gelatine covering on the surface of the fiber, and the lotus petiole fibers are bundled together with gelatine. The surface of lotus petiole fiber is not as smooth as the ramie fiber.

Thermo gravimetric analysis (TGA)

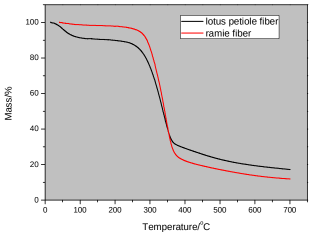

Fig. 2 TG curves of lotus petiole fiber and ramie fiber

The TG curve of ramie fiber shows weight loss of 3.8% up to 257°C in Fig.2, due to loss of adsorbed moisture in fiber. The TG curve of lotus petiole fiber shows obvious weight loss of 13% at the same temperature. This phenomenon indicates that the commercial moisture regain of lotus petiole fiber is higher than ramie fiber. The degradation temperature of lotus petiole fiber and ramie fiber are in the same area. It is in the range of 230-260°C. The weight losses in the ranges of 260-373°C for lotus petiole fiber and ramie fiber are 55.52% and 70.97%, respectively.

FT-IR spectroscopy

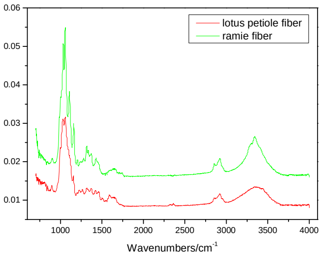

Fig. 3 The FT-IR spectra of lotus petiole fiber and ramie fiber

The FT-IR spectra of lotus petiole fiber and ramie fiber are shown in Fig. 3. In the contrast with the curve of ramie fiber, the characteristic peaks of lotus petiole fiber are almost the same, such as the absorption peaks at 3361 cm^{-1} and 2900 cm^{-1}, which can be considered as O-H bond stretching vibrations or CH bond and CH_2 bond stretching vibrations [8]. The strong absorption peak of 1033 cm^{-1} also can be found in both ramie fiber and lotus petiole fiber spectrum. FT-IR can confirm that the composition of the two fibers is similar.

CONCLUSIONS

The results indicate ramie fiber is much smoother than lotus petiole fiber. The TG curves show the commercial moisture regains of lotus petiole fiber is higher than that of ramie fiber. FTIR results show that the composition of the two fiber types is similar.

FUTURE WORK

We will investigate the fiber crystal structures with X-ray diffraction.

ACKNOWLEDGMENT

We greatly acknowledge the support from the Major State Basic Research Development Program (973 Program) (Project No. 2012CB722701).

REFERENCES

[1] M. Rutkowska1, H. Janik, et al. *Polish Journal of Environmental Studies*. Vol. 9 (2010), p. 937.
[2] K. M. M. Rao, K. M. Rao. *Composite Structures*. Vol. 77 (2007), p. 288.
[3] H. Cheung, M. Ho, et al. *Composites: Part B*. Vol. 40 (2009), p. 655.
[4] D. Chen, Y. Gan, et al. *Journal of Textile Research*. Vol. 30 (2009), p. 18.
[5] Y. Ono, E. Hattori and Y. Fukaya. *Journal of Ethnopharmacology*, Vol. 106 (2006), p. 238.
[6] D. Liu, G. Han, J. Huang, Y. Zhang. *Carbohydrate Polymers*. Vol. 75 (2009), p. 39.
[7] G. Consultants: Colourage. Vol. 57 (2010), p. 85
[8] R. M. Silverstin, F. X. Webster. *Spectrometric Identification of Organic Compounds* (Wiley, N.Y., 1998).

A Comparative Study on UV-Absorbing Titanium Dioxide Sol Gel Treatments for Wool

Hu Zhang, Santanu Deb-Choudhury, Jeffrey Plowman, Duane Harland, and Jolon Dyer
AgResearch Limited, Lincoln Research Centre, Christchurch, New Zealand, 8140
hu.zhang@agresearch.co.nz

ABSTRACT

Many studies have reported that TiO_2 sol gel treatment can effectively impart new function to textile substrates, which includes UV shielding, self-cleaning, anti-bacteria, odour control and insect resistance amongst other properties [1, 2].

As a protein fibre, wool inherently absorbs UV light relatively well and can largely reduce the transmission of harmful UV light passing through the fibre, albeit with associated degradation of the proteins [3]. By applying transparent and colourless UV-absorbing TiO_2 sol gel to wool, it could be anticipated that the UV shielding property of treated wool would be further enhanced, with appearance retention also being improved.

The formation of a metal oxide sol solution involves the hydrolysis of the precursor materials and subsequent condensation reactions. The condensation reactions lead to the formation of colloidal particles with sizes in the nanometre range (1 nm -1μm) [4]. However, few studies have examined the effect of the precursor concentration i.e. the metal oxide content in the prepared sol solution on the intrinsic properties of treated wool.

In our study, TiO_2 nanosols were synthesized by hydrolyzing different amounts of titanium tetraisopropoxide (TTIP) in acidic ethanol media. The prepared TiO_2 nanosols were characterized by transmission electron microscopy (TEM) (Fig.1) and UV/vis spectroscopy. Wool fabrics were coated by prepared TiO_2 sol solutions via the dip-dry-cure method. The optical, morphological features (Fig. 2) and tensile properties of three types of TiO_2 sol gel treated wool fabrics were then compared to one another.

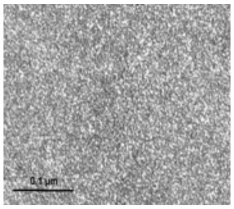

Fig. 1 TEM image of TiO_2 sol solution derived film

The results manifest that the original appearance of the treated wool fabrics was well retained after the TiO_2 sol gel treatment. In the meanwhile, when a relatively higher precursor concentration was selected, a thicker coating and a better UV shielding property were obtained on the TiO_2 sol gel treated wool fabrics. Also, the tensile strength and elongation at break of the treated wool fabrics were largely improved by the treatment but the degree of improvement seemed to be less dependent on the TiO_2 concentration of the sol gel applied to the wool. Thus, this study has demonstrated the practicality of the further development, application and commercialization of TiO_2 sol gel-based treatments for high value wool products

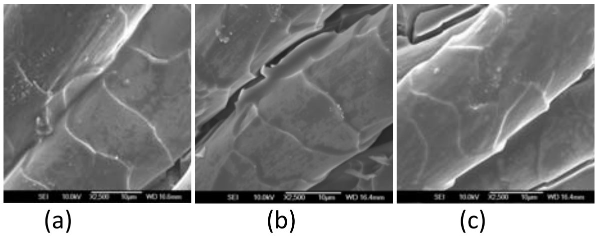

Fig. 2 SEM images of wool coated by TiO_2 sol solutions prepared at (a) low, (b) medium and (c) high precursor concentrations

ACKNOWLEDGMENT

This work is financially supported by a Wool Research Organization of New Zealand Inc and New Zealand Wool Industry Charitable Trust Postdoctoral Fellowship.

REFERENCES

1. Daoud, W.A., et al. *Chemistry of Materials*, 2008. 20(4): p. 1242-1244.
2. Ibrahim, N., R. Refaie, and A. Ahmed. *Journal of Industrial Textiles*, 2010. 40(1): p. 65-83.
3. Nicholls, C.H. and M.T. Pailthore. *Journal of Textile Institute*, 1976. 67(11): p. 397-403.
4. Wright, J.D. and N.A.J.M. Sommerdijk. *Sol-Gel Materials: Chemistry and Applications,* 2001. London: Taylor & Francis Book Ltd.

Study on the Clothing Pressure of Elastic Weft-Knitted Fabrics

Shangmei Wu, Peng Zhou, Lei Wang, Wan Li, Jihong Wu
Key Laboratory of New Textile Materials Green Processing and Functionalisation, Ministry of Education
Wuhan Textile University, Wuhan, China
Jihong_wu@wtu.edu.cn

ABSTRACT

In this paper, the relationships between clothing pressure and tensile elongation and organizational structure are discussed. The tensile elongation and relationship between clothing pressure and spandex content were researched. The results show that the content of spandex, fabric density and weight per square meter are important factors affecting the elasticity and clothing pressure of fabrics. Elastic yarn has negative contribution to the fabric in horizontal direction, the negative contribution rate is inversely proportional to spandex content, and the overall effect is not significant. Influence of structure on clothing pressure not only in absolute terms, but also affects the direction of pressure.

INTRODUCTION

In 1990, a number of Asian scholars studied clothing pressure comfort, especially in Japan. Toyonori Nishimatsu [1] made a pressure tester by using the elastic optical fiber to evaluate the pressure comfort of men's socks. Harumi-M and Miyuki-N [2] pointed out the bad influences to human body caused by inappropriate clothing pressure.

In China, the study on clothing pressure began in recent ten years. Li Y. [3] in the Hong Kong Polytechnic University developed a biomechanical model to describe and simulate the clothing pressure and stress-strain curve after wearing the bra. Wong and Zhang [4] analyzed the influence of fabric mechanical property on clothing dynamic pressure distribution and pressure comfort on tight-fit sportswear. Fan J T [5] developed a soft mannequin for predicting pressure on human body.

The focus of this investigation was to study the clothing pressure and the effect of the spandex content and fabric structure. The tensile property of elastic fabrics is also examined in this study. The conclusions of the study could supply some references to design and development of elastic knitted fabrics.

APPROACH

In this study, six fabrics of different spandex content that are commonly used for clothing pressure were studied. A summery of fabric specification is presented in Table 1 and Table 2.

Table 1 The specimen sewing perimeter at different elongation

Elongation %	0	20%	40%	60%	80%	100%
Sample length (mm)	314	261	224	196	174	157

Table 2 The structural parameters of samples

	W(g/m^2)	composition	Content（%）
1	216	viscouse	0
2	220	cotton/spandex	89/11
3	180	cotton/spandex	89.63/10.37
4	185	cotton/spandex	92.12/7.98
5	170	cotton/spandex	94.75/5.25
6	160	cotton/spandex	95.41/4.59

The pressure management tester consists of pressure sensor, cylinder and monitor. The test system used pressure sensors to measure pressure index of the clothing, and the pressure signal is then converted into an electrical signal, through the data acquisition system. Figure 1 shows the pressure tester used in this study.

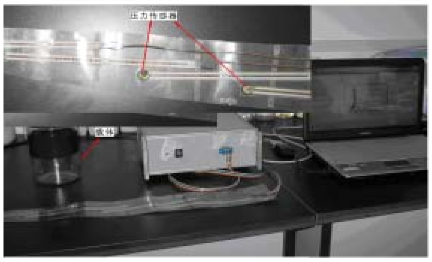

Figure 1 Pressure management tester

RESULTS AND DISCUSSION

The relationship between clothing pressure and elongation Figure 2 and Figure 3 show the effect of elongation on clothing pressure. The clothing pressure of fabric in longitudinal direction increases with the increase of fabric elongation. When the elongation was between 0 and about 20%, the clothing pressure increased rapidly. The clothing pressure showed a slow increase at about 20% to 40%. When the elongation was above 40%, there is a rapid increase in clothing pressure.

Figure 3 shows the relationship between weft clothing pressure and elongation. Obviously, it has a positive correlation between the weft clothing pressure and elongation of the fabric.

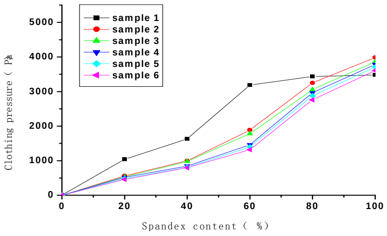

Figure 2 The clothing pressure curves of samples in longitudinal

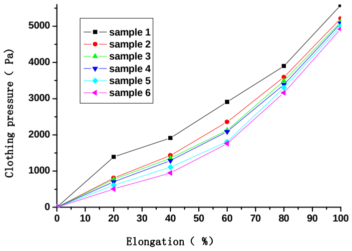

Figure 3 The clothing pressure curves of samples in crosswise

The relationship between clothing pressure and spandex content In longitudinal and crosswise directions, the more spandex the fabric contains, the greater the clothing pressure is. It is shown that the clothing pressure of knitted fabric without spandex is higher than spandex fabric in different elongation from figure 2 and figure 3. The spandex elastic knitted fabric not only has good elastic stretch, but also low clothing pressure in the elongated state than the fabric without spandex.

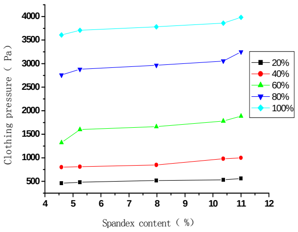

Figure 4 The relationship curve between clothing pressure and spandex content in Longitudinal

Figure 4 and Figure 5 show the test of clothing pressure and spandex content. In a variety of elongation, the clothing pressure increases while the elongation increases, but it is not obvious. So spandex content is not a crucial factor affecting the clothing pressure of elastic knitted fabrics. As long as the spandex exists, fabric has elasticity and elastic recovery that will produce a certain clothing pressure.

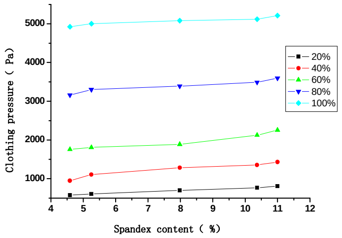

Figure 5 The relationship curve between clothing pressure and PU content in crosswise

CONCLUSION

The content of spandex, fabric density and weight per square meter are important factors affecting the elasticity and clothing pressure of fabrics. Elastic yarn has negative contribution to the fabric in horizontal direction, the negative contribution rate is inversely proportional to spandex content, and the overall effect is not significant. Influence of structure on garment pressure is not only in absolute terms, the structure also affects the direction of pressure.

REFERENCES

[1] Toyonori Nishimatsu. Fabric stiffness. *J. Textile Inst*, 1998, (75): 307-313.

[2] Harumi-M, Miyuki, Hideo-M, et al. Effects of Clothing Pressure Exerted on a Trunk on Heart Rate, Blood Pressure, Skin Blood Flow and Respiratory Function. *Journal of the Textile Machinery Society of Japan*. 2001, 54(20): 57-62.

[3] Li Yi. Sensory Engineering Design of Textile and Apparel Products. *J. 82nd World Conference*. The Textile Institute. Egypt. 2002. 23-27.

[4] Wong A.S. W. Li. Y. Influence of fabric mechanical property on clothing dynamic pressure comfort on tight-fit sportswear. *Journal of Textile Institue*. 1998, (68): 211-224.

[5] Yu W, Fan J T, Qian X M et al. A soft mannequin for predicting girdle pressure on human body. *J. Sen' I Gakkaishi*. 2004 (2): 57-64.

Coating of Carbon Fibres Using a Novel Three-Step Plasma Treatment

Zhiqiang Chen[1], Xiujuan J. Dai[1], Peter R. Lamb[1], Johan du Plessis[2], David Rubin de Celis Leal[1], Luhua Li[1], Kevin Magniez[1], Bronwyn L. Fox[1], Xungai Wang[1]
[1]Institute for Frontier Materials, Deakin University, Geelong Waurn Ponds, Victoria 3216, Australia
[2]School of Applied Sciences, RMIT University, GPO Box 2476V, Melbourne, Victoria 3001, Australia
zhiqianc@deakin.edu.au

INTRODUCTION

The interfacial adhesion between the fibres and a matrix is a crucial factor in determining the mechanical properties of carbon fibre-reinforced composites. Therefore, a variety of techniques for the surface treatment of CFs have been developed to improve fibre-matrix adhesion. Plasma polymerization has been utilized to deposit a thin polymeric film on the fibre surface for improving the adhesion between the CFs and the matrix [1]. However, the current methods of continuous wave plasma polymerization hardly retain the functional groups from the monomer, which may lead to weak interfacial adhesion between the deposited plasma polymer and the CF.

A three-step plasma treatment was therefore developed to strongly attach a plasma polymer to the fibre surface [2]. This method has been further developed to apply to functionalization of CFs. Firstly, the CFs were treated by Ar plasma (Step I) for activating and cleaning the CF surface. This was followed by O_2 plasma treatment (Step II) for incorporation of oxygen-containing functional groups. Finally, a HA film was deposited on the CF surface by a combination of continuous wave and pulsed (CW + P) plasma polymerization (Step III).

RESULTS AND DISCUSSION

XPS results

The untreated carbon fibres (u-CFs) had about 95% C and 5% O (Table I) and their C1s spectra (Figure 1a) can be decomposed into three components at 284.6 eV, 286.2 eV, and 288.9 eV, which correspond to graphite (C=C), hydroxyl (C-OH/C-O-C) and carboxyl groups (O-C=C) [3], respectively. The oxygen might come from air contamination during the production process. No nitrogen atoms were detected on the u-CF surface as shown in Table I. At the Step I, Ar plasma treatment increased slightly the O content on the CF surface. This is because the oxygen from air is incorporated onto the activated surface of CFs by Ar plasma treatment. The O concentration on the O_2-Ar-CF surface (Step II) was increased by about 170% in comparison to the u-CFs. This is because the activated surface of CFs after Ar plasma treatment can easily react with oxygen species during the oxygen pulsed plasma to form oxygen functional groups.

After the plasma polymerization of HA (Step III), N atoms were introduced on the CF surface. They constitute about 8% of the atoms (Table I). The O content decreased from nearly 13% before, to 3.2% after, the plasma polymerization. This is because the CF is covered by a polymeric film after HA plasma polymerization, which is confirmed by SEM observations (Figure 2d). The C1s peak for the HAPP-O_2-Ar-CFs (Figure 1b) has components at 284.6eV and 285.8eV. The peak at 285.8 eV corresponds to amine groups (C-NH_2 or C-NH-C) [3].

Table I Atomic concentrations of C, O and N on the surface of untreated and treated CFs.

	Sample	C at.%	O at.%	N at.%
	u-CF	95.3	4.7	—
Step I	Ar-CF	94.8	5.2	—
Step II	O_2-Ar-CF	87.5	12.5	—
Step III	HAPP-O_2-Ar-CF	88.6	3.2	8.2

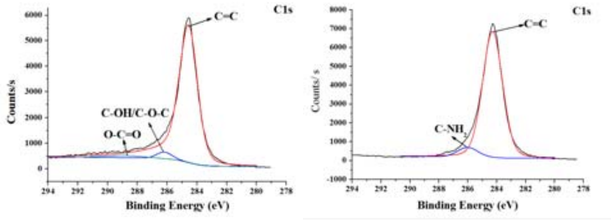

(a) (b)

Figure 1. XPS C1s spectra of CFs: (a) u-CFs; (b) HAPP-O_2-Ar-CFs.

SEM and AFM

The surface morphology of the CFs before and after the different plasma treatments is shown in Figure 2. The surface of the u-CF seems to be relatively smooth (Figure 2a). After the gaseous plasma treatments (Figures 2b and c), there is no significant visible change in the surface. Both samples of the Ar-CF and O_2-Ar-CF show a smooth surface. Figure 2d shows a SEM image of the CF after HA plasma polymerization. It can be seen that the CF is coated with the HA plasma polymer. From the enlarged image in Figure 2e, the CF surface is fairly uniformly and tightly covered by the HA film.

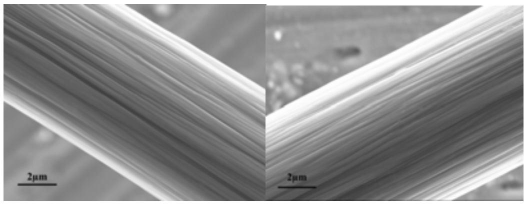

(a) (b)

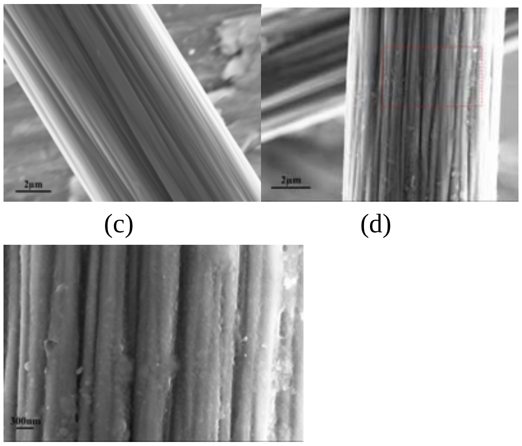

(c) (d)

(e)

Figure 2. SEM images of CFs: (a) u-CF; (b) Ar-CF; (c) O2-Ar-CF; (d) HAPP-O_2-Ar-CF; (e) the enlargement of the region indicated by the red rectangle in (d).

The topography of the CFs before and after plasma treatment was examined by AFM (Figure 3). The surface of u-CFs is smooth with a number of grooves along the fibre (Figure 3a). The grooves on the surface of both Ar-CFs (Figure 3b) and O_2-Ar-CFs (Figure 3c) are slightly deeper, which may be due to plasma etching. After the HA plasma polymerization, the grooves on the HAPP-O_2-Ar-CFs surface are nearly invisible (Figure 3d), because the surface of the CFs is covered by a thin polymeric film. This is in good agreement with the SEM observations.

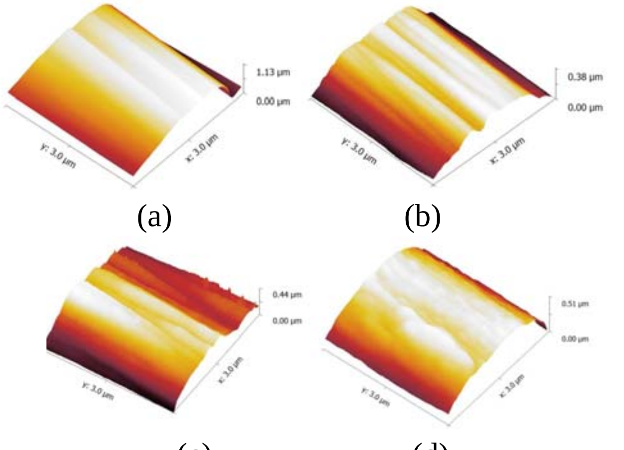

(a) (b)

(c) (d)

Figure 3. AFM images of the CF surface: (a) u-CF; (b) Ar-CF; (c) O_2-Ar-CF; (d) HAPP-O_2-Ar-CF.

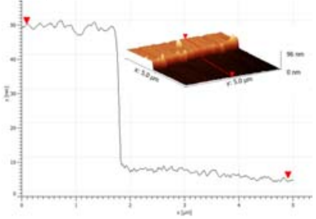

Figure 4. An individual AFM scan line of a HAPP step on a Si wafer; the inset is the three-dimensional AFM image of the HAPP step.

The thickness of HA plasma polymer on the CF surface was measured by AFM using the surface masking technique [4].

A representative AFM image of the HA plasma polymer step on a Si wafer, with a section analysis on an individual scan line in the image is presented in Figure 4. The plasma polymer step is clearly shown in a three-dimensional AFM image in the inset of Figure 4. From Figure 4, the thickness of the HA film can be calculated by subtracting the lower peak value from the upper, which is about 40 nm.

Single fibre tensile strength

Single fibre tensile tests were carried out using a FAVIMAT+ automatic linear density, crimp and tensile tester (Textechno H.Stein GmbH &Co. KG, Germany). The tensile strength of the CFs was measured at a gauge length of 20 mm and the fibre was extended to failure at a downward speed of 1 mm/min. At least 50 fibres for each sample were tested. From Figure 5, the three-step plasma treatment slightly increased the single carbon fibre tensile strength; and the inset SEM image of the fractured cross-section of HA-O_2-CF, showed good adhesion between the fibre and the plasma polymer.

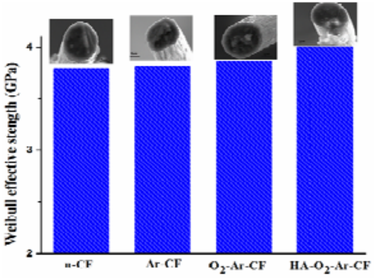

Figure 5. Weibull analysis of single CF fibre tensile tests; the insets are their corresponding SEM images of the fracture cross-section.

CONCLUSIONS

The three-step plasma treatment has produced a plasma polymer with amine groups and adhesion to the CF surface, without damaging the mechanical properties of CFs. It presents a potential way for replacing sizing carbon fibres or reducing the amount of sizing agent needed.

KEYWORDS: carbon fibre, plasma polymerization, tensile strength

ACKNOWLEDGMENT

We very much appreciate the technical assistance from R. Lovett, M. Wright and thank RMIT University for access to their XPS facility.

REFERENCES

[1] Dilsiz N, Ebert E, Weisweiler W, Akovali G. *J Colloid Interface Sci.* 1995; 170(1): 241-8.
[2] Wan A, Dai XJ, Magniez K, du Plessis J, Yu W, Wang X. *Textile Research Journal*. 2013, in press.
[3] Felten A, Bittencourt C, Pireaux JJ, Van Lier G, Charlier JC. *J Appl Phys*. 2005; 98(7):1-9.
[4] Hartley PG, Thissen H, Vaithianathan T, Griesser HJ. *Plasmas Polym*. 2000; 5(1) :47-6.

The Feasibility Study on the Grille Application of Basalt Continuous Filament

Zhili Zhong and Hongjie Zhang
School of Textiles, Tianjin Polytechnic University, 300160, P.R. China
zhjie827@163.com

PURPOSE

Grilles play an important role in water conservancy, transportation, garden and so on. They help to buffer external shocks and improve the durability of structures supported by the grille. The paper summarizes the grille specifications and analyzes their advantages and disadvantages. It is known that the basalt continuous filaments (BCF) have high tensile strength and are relatively cheap. This paper focuses on the acid and basic resistant capability of basalt grille.

INTRODUCTION

With the rapid economic development, established roads cannot satisfy the increasing traffic, which makes the road crack, dent, and even break. This not only greatly affects the traffic flow, but also poses a threat to the peoples' lives [1].

The application of grille, particularly those with high tensile strength and modulus, helps to ensure that the road receives uniform loading stress. Some literatures have reported that if grille are used the bending strength of road layer can be markedly improved [2,3]. There are several types of grilles, including plastic grille, steel grille, glass fiber grille and polyester fiber grille. The two main forming processes for grille are extrusion-drawing process (E-D process) and knitting process, with the former more suitable for plastic (Figure. 1) and the latter for fibers mainly (Figure. 2).

Figure 1. Grille by E-D process

Basalt continuous filament (BCF) is typically made from basalt ore after melt-spinning process. Compared with many other fibers, basalt fibers are known to have better mechanical performance, such as strength and fatigue-resistance, over a wide temperature range (-267-700℃), and good affinity with concrete and soil [4, 5].

Figure 2. Grille by knitting process

These characteristics exactly match the current selection criteria for grille, but the acid and basic resistance of basalt grille has not been studied, which is the subject of this study.

APPROACH

The BCFs were immersed into 2 mol/L NaOH and HCl solution for 0.5 h, 1 h, 1.5 h, 2 h and 2.5 h respectively. In order to compare the weight loss rate of the basalt continuous filament, boiling distilled water was used as the control.

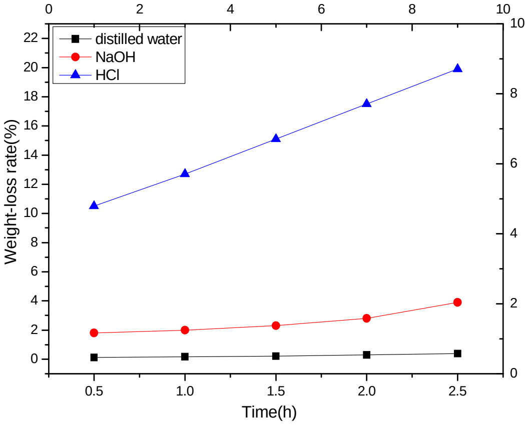

Figure 3. Weight loss rate in different solution

RESULTS AND DISCUSSION

The analysis shown in Figure 3 reveals that the weight-loss rate of basalt fibers under alkali, acid condition and boiling distilled water. Compared with glass fibers, the weight loss rate of basalt fibers was far below the E-glass fiber, the latter can reach 2.1%, 6.0% and 38.9% respectively. Basalt fiber grille exhibited better performance stability under the same condition [6].

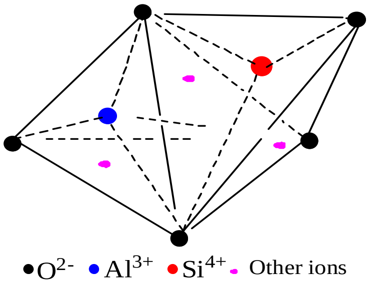

Figure 4. Distribution of internal ions

The main chemical compositions of basalt fibers are as follows: SiO_2, Al_2O_3, CaO, Fe_2O_3, TiO_2 and other ions, in which SiO_2 accounts for about 50%. BCFs have a skeleton microstructure mainly consisted of SiO_2 and Al_2O_3 chains. Other ions like Mg^{2+}, Na^+, K^+ were dispersed in the internal structure (Figure4) to balance stable structure and special properties [7].

As shown in Figure 5, continuous linear lattice was another feature of the oxygen atoms, which can maintain the stability of the internal structure and reduce the stress by the external forces, to minimize the damage of the main structure.

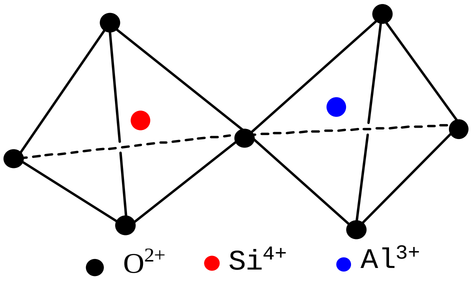

Figure 5. Linear connection of the internal structure

CONCLUSION

Basalt continuous filament has been studied mainly in terms of its mechanical properties, especially in the aspect of reinforced materials. Yet little is known about it chemical properties, only some researches on the surface modification. So there were some existences of security risks under acid and alkali condition.

Studies have been to relate acid and alkali resistance of basalt fiber, it has been shown that the properties of the BCF was significantly lower than the glass fiber under the same conditions. The weight loss rate of the BCF was less than half of glass fiber, it was only 0.3%, 2.8% and 17.5%, respectively in distilled water, 2M NaOH and 2M HCl.

Basalt continuous filament (BCF) is superior to existing raw grille materials in terms of acid-basic resistance. So basalt continuous filament may be used as a new grille reinforcing material for its excellent chemical stability and chemical properties.

FUTURE WORK

Future work will focus on in-situ performance of BCF grille.

REFERENCES

[1] Z.Q. Li, R.L. Hu, W. Fu, G.R. Tan, Y.X. Zhou and R.Q. Yue. Study on using geogrids to reinforce embankment of expressway. *Rock and Soil Mechanics*, China, Vol. 29, pp. 795-799, March 2008.

[2] C.Zhang and B.F.Pan. Analysis of mixture for skin coat of asphalt pavement on freeway. *Northern Communications*, China, Vol. 8, pp. 6-8, 2007.

[3] M. Xue. Advance in production of plastics geogrids. *Modern Plastics Processing and Applications*, China, Vol. 16, pp. 58-60, December 2004.

[4] Y.L. Shi and J.H. Bai. Application of glass grid in preventing the reflecting crack in bituminous concrete pavement. *Forestry Science and Technology Information*, China, Vol. 41, pp.112-114, December 2008.

[5] B. Wei, H.L. Cao and S.H. Song. Environmental resistance and mechanical and performance of basalt and glass fibers. Materials Sciences and Engineering A, China, Vol. 527, pp. 4708-4715, April 2010.

[6] J.H. Lee, K.Y. Rhee and S.J. Park. The tensile and thermal properties of modified CNT-reinforced basalt/ epoxy composites. *Materials Sciences and Engineering A*, Republic of Korea, Vol. 527, pp. 6838-6843, July 2010.

[7] H.L. Cao, H.J. Lang and S.H. Meng. Experimental research on the basic structure and properties of the continuous basalt fiber. *Hi-Tech Fiber & Application*, China, Vol. 32, pp. 8-13, October 2010.

A Multiscale Approach to Quantify Friction Properties of Carbon Fibres

Abdullah Kafi[1], Claudia Creighton[1], Mickey Huson[2], Bronwyn Fox[1]
[1]Deakin University, Institute for Frontier Materials, Pigdons Road, Waurn Ponds Campus, Geelong, Victoria 3216, Australia; [2]CSIRO Materials Science and Engineering, Waurn Ponds, Geelong, Victoria 3216, Australia
Contact Author: abdullah.kafi@deakin.edu.au

ABSTRACT

A detailed physical and chemical characterisation was conducted on carbon fibres collected after three stages of the manufacturing process, viz. carbonisation, electrolytic oxidation, and epoxy sizing. Surface topography measured by Scanning Probe Microscopy (SPM) revealed longitudinal ridges and striations along the fibre axis for the three fibre types. The SPM surface roughness did not show any difference, the coefficient of friction however, as measured by an automated single fibre tester, proved to be a sensitive measure of surface functionality, showed 98% increase in friction for sized fibre compared to the unsized one. As there is no significant difference in surface roughness, the frictional differences are most likely due to the changed surface chemistry.

INTRODUCTION

In the process of manufacturing carbon fibres, fibres are coated with a polymer based sizing agent that will not only protect the fibre but also make the fibre surface more compatible with the desired polymer matrix. Before sizing, fibres are electrolytically oxidised to create oxygen-containing functional groups on the fibre surface, which promotes the adhesion of sizing formulations. In order to develop a realistic understanding, not only of the adhesion between the fibre and the matrix material, but also of the adhesion between the fibre and the sizing formulations, it is necessary to develop a systematic procedure to quantify the surface functionality of the carbon fibre surface. Even though there have been plenty of efforts devoted to modify the carbon fibre surface using various treatments and sizing methods [1], there are relatively few articles [2] which have suggested reliable methods, and discussed systematic ways, to measure the surface properties of carbon fibre. This work employs a range of techniques to characterise the physical properties of carbon fibres collected after different stages of production.

EXPERIMENTAL

Materials

The carbon fibres used in this study were PAN-based 50K automotive grade fibres (Panex 35), supplied by Zoltek Hungary, with a Young's modulus of 242 GPa and tensile strength of 4.1 GPa

Scanning Electron Microscopy (SEM)

SEM secondary electron images were obtained using a Hitachi model S4300 SE/N Schottky Scanning Electron Microscope using a 1.2 kV accelerating voltage and a 6.5 mm working distance. SEM images were captured without any coating.

Scanning Probe Microscopy (SPM)

SPM analysis was conducted on a Digital Instruments Dimension 3000 SPM which was operated in contact mode using silicon nitride probes with pyramidal tips (nominal radius of 40 nm) on cantilevers having a nominal spring constant of 0.12 N/m. The surface roughness calculations were based on the full 3 µm x 3 µm height image after applying a 3rd order flattening routine using the V5.31 NanoScope software.

The relative coefficient of friction between the silicon nitride tip and carbon fibres was determined by simultaneously collecting lateral force images, at a range of different applied forces, for both forward and reverse (trace and retrace) movement of the tip from at least 8 random spots on three filaments from each fibre type. A single standard Si_3N_4 probe was used for all the coefficient of friction experiments.

Coefficient of Friction from Automated Single Fibre Tester

An Automated Single Fibre Tester (FAVIMAT+ Robot 2, Textechno H. Stein) was used to measure the coefficient of friction of single carbon fibres over a length of 25mm at a speed of 20 mm/min using a pretension of 0.08 cN/tex.

RESULTS AND DISCUSSION

Surface Topography

SEM images revealed longitudinal ridges and striations along the fibre axis for the three fibre types (Fig. 1). The observed surface morphology is believed to be a consequence of the solution spinning process. There were no obvious differences between the fibre types other than some irregular patches on the surface of sized fibre suggesting that the surface was not uniformly coated with epoxy sizing**.**

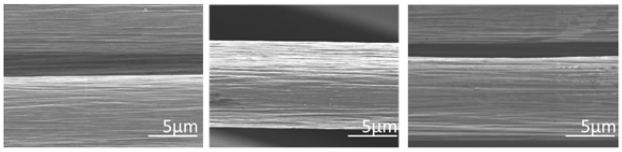

Fig. 1 SEM images of unoxidised, oxidised, and sized carbon fibres.

Fig. 2 showed surface topography of the sized fibres are relatively smooth surfaces and differed from other two samples in that axial striations were partially covered by epoxy coating on the surface.

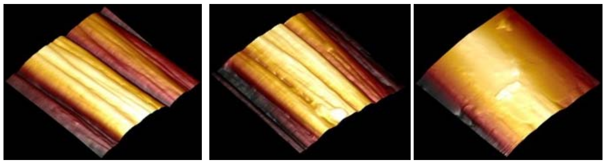

Fig. 2 Three representative SPM 3D height images of each of the unoxidised, oxidised, and sized carbon fibres.

Surface Roughness and Friction

Surface roughness analysis was based on SPM height images taken over a 3x3 μm area. It can be seen from Table 1 that the roughness values are highest for oxidised fibres with no difference between unoxidised and sized fibres. An increase of surface roughness of carbon fibres after oxidative treatment was also reported by Bekyarova et al. [3], however, Servinis et al. [4] working on the same unoxidised and oxidised fibres as in this paper, reported no increase in roughness as a consequence of oxidation. The increase in roughness presented in Table 1 is most likely due to the inadvertent selection, from mass produced 50K tow, of individual oxidised fibres with unusually high levels of surface contaminants**.**

Table 1 SPM Roughness and friction properties of carbon fibres. Results are reported as mean (± standard deviation). Different letters within each column imply results that are statistically different at $p<0.05$.

Fibres	Surface Roughness (nm)	Relative Coefficient of Friction from SPM	Coefficient of Friction from FAVIMAT
Unoxidised	37±17^{a}	0.017±0.007^{a}	0.143±0.05^{a}
Oxidised	50±10^{b}	0.017±0.005^{a}	0.216±0.04^{b}
Sized	33±13^{a}	0.022±0.01^{a}	0.283±0.05^{c}

Average values of the relative coefficient of friction, determined by SPM, for the three fibre types are shown in Table 1 and show a slight, but statistically insignificant, increase in friction for the sized fibre.

Whilst no variation in nano-scale friction was found between samples, the macro-scale fibre-to-metal friction values measured by the FAVIMAT instrument indicated a clear difference between the three samples (Table 1 and Fig. 3). The measurement in this case was carried out over a 25 mm long fibre surface as compared to 3μm in the case of the SPM measurement and also uses much higher normal forces (0.7 cN vs 70 nN). The results indicate that the force required to pull a single filament through three metal bars was the highest for sized fibre followed by oxidised and unoxidised fibres.

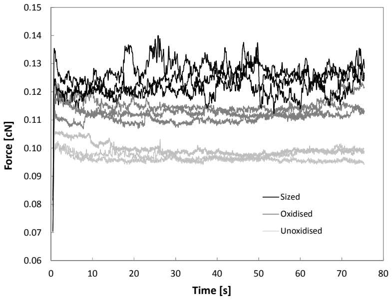

Fig. 3 Single fibre friction measurement comparing unoxidised, oxidised, and sized carbon fibres.

The coefficient of friction for the three fibre types is listed in Table 1. The sized fibre would also have a softer surface, potentially leading to greater contact between the fibre surface and the metal bars. Further studies on surface chemistry are currently underway based on surface energy analyzer.

CONCLUSION

The study has successfully adopted a multi-scale approach to quantify friction properties of carbon fibres collected after carbonisation, electrolytic oxidation, and epoxy sizing. SEM and SPM analysis showed very little difference between the morphologies and roughness of the three fibre types. The relative coefficient of friction as measured by SPM was also unchanged across the three fibre types, however friction measured on a macro-scale was shown to be a sensitive measure of surface chemistry. The coefficient of friction, measured by an automated single fibre tester, increased from 0.14 for the unoxidised fibre to 0.22 upon oxidation and then 0.28 after sizing. Since the topography is not varying, this is most likely due to the changed surface chemistry of the carbon fibre.

REFERENCES

1. Zhang X, Fan X, Yan C, Li H, Zhu Y, Li X, et al. Interfacial microstructure and properties of carbon fiber composites modified with graphene oxide. *ACS Applied Materials & Interfaces*. 2012, 4(3): 1543-52
2. Dai Z, Shi F, Zhang B, Li M, Zhang Z. Effect of sizing on carbon fiber surface properties and fibers/epoxy interfacial adhesion. *Applied Surface Science*. 2011, 257(15): 6980-5
3. Bekyarova E, Thostenson E, Yu A, Kim H, Gao J, Tang J, et al. Multiscale carbon nanotube-carbon fiber reinforcement for advanced epoxy composites. *Langmuir*. 2007, 23(7): 3970-4.
4. Servinis L, Henderson LC, Gengenbach TR, Kafi AA, Huson MG, Fox BL. Surface functionalization of unsized carbon fiber using nitrenes derived from organic azides. *Carbon.* 2012, 54: 378-88.

Evolutionary Engineering of Bacillus Strain for Biofunctionalization of PET Fabrics

Jixian Gong[1,2], Zheng Li [1,2],Huiqin Li[1,2], Qiujin Li[1,2], Jianfei Zhang[1,2]
[1]School of Textiles, Tianjin Polytechnic University, Tianjin 300160, China
[2]Key Laboratory of Advanced Textile Composites, Ministry of Education of China, Tianjin 300160, China
gongjixian@126.com; zhangjianfei@tjpu.edu.cn

ABSTRACT

Polyethylene terephthalate (PET) shows excellent properties for textile applications. However, textiles made of PET are uncomfortable to wear for its poor water absorption and adsorption due to the hydrophobic surface. Bioprocess methods are potential tools for fabric modification. However, high crystallinity negatively affects the ability of the enzymes to hydrolyse PET. Although several kinds of hydrolyzing enzymes, such as cutinases, lipase and esterases, have been reported to applied in modification of PET fabric, new microorganism strains remain need to be developed for obtaining more powerful biocatalyst in the modification of PET fabric.

Evolutionary engineering is a novel whole-genome wide engineering strategy inspired by natural evolution for strain improvement. This method exploits natural design principles and can be vary effective in phenotype improvement. There have been many recent examples in which satisfactory performance of rationally designed strains was achieved only through evolutionary engineering.

In our previous study, a kind of bacilli strain was isolated from the waste water of PET processing factory and has been employed to treat the PET fabrics for improving the comfortable property. In this investigation, the strategy of evolutionary engineering was applied to improve the utilization of PET polymer as carbon source for bacilli strain in the processing of surface biofunctionalization of PET materials. A selection procedure was developed for adaptive evolution of bacilli strain to improve the ability of conversion of PET to small molecular substance in a bacillus strain metabolizes pathways.

To increase genetic variability, the initial strain was mutagenesised with ultraviolet radiation to acquire the initial strain population. Evolution of bacilli strain capable of growth on PET as the sole carbon source was started with the initial strain population. The nano- particle of PET was prepared as substrate. In the process of adaptive evolution, the concentration of PET nano- particle was increased slowly until it became the sole carbon source. After a total of 200 generations of selective cultivation, the populations can growth stably on PET nano- particle. The evolved strain was selected and isolated from the populations. The result shows that the evolved strain have the improved capability in surface modification of PET fabrics. The approach of strain improvement presented in this investigation may provide an attractive promising alternative for the application of biotechnology in textile engineering.

KEYWORDS

Biocatalysis, Evolutionary engineering, Strain improvement, Polyethylene terephthalate, Biofunctionalization

Electrospinning of Nanofibre Yarns Using a Novel Ring Collector

Muhammad Nadeem Shuakat, Xungai Wang, Tong Lin
Australian Future Fibres Research & Innovation Centre, Deakin University, VIC 3216, Australia
tong.lin@deakin.edu.au

INTRODUCTION

Nanofibres produced by electrospinning technique have shown enormous potential for applications in filtration, bio-technology, composites, energy generation, and energy storage. However, nanofibre products are mostly restricted to randomly-orientated nonwoven webs/mats.

Converting nanofibres into yarns would considerably improve their strength, handling, storage and subsequent processing ability. Nanofibre yarns have been prepared by several methods. For example, non-solvent liquid [1] has been utilized as collector to convert a nanofibre web into yarns. However, such yarns have problems with fused and beaded nanofibres, and they also require an additional drying process. Solid collector [2] can produce properly dried nanofibres with effective control over twist, but nanofibres are affixed to solid collector, inflicting damage to nanofibres, thus reducing the overall yarn production.

In our lab, a modified needle electrospinning setup has been developed to prepare highly-twisted nanofibre yarns using an intermediate rotating collector [3] . This method substantially reduced fibre damage and improved yarn quality. Nevertheless, the yarns are collected from the same zone as that of electrospinning, which resulted in deposition of some un-stretched and hooked nanofibres on already twisted yarn and winder. These hooked and un-stretched nanofibres deteriorated overall yarn strength and quality.

In this work, nanofibre yarns were electrospun using a novel ring collector which separated fibre spinning and yarn winding in two regions.

APPROACH

A purpose built cylindrical ring was used to whirlpool nanofibres and twist them into a continuous nanofibre yarn, as shown in the Figure 1. 16% PVDF-HPF solution in a mixture of Acetone and DMF (volume ratio, 1:1) was electrospun by two needle-based electrospinning nozzles near the inner edge of the ring collector. Fast rotating ring collector pulled the nanofibres to pass through the ring collector, which were transferred and twisted into nanofibre yarn on the other side of the ring.

RESULTS AND DISCUSSION

The needle nozzles were placed along the ring collector in such a way that nanofibres generated by the two nozzles deposited on ring collector. When ring collector was stationery the fibres got deposited on its inner surface. As soon as the ring collector started rotating, no further deposition occurred on the ring, instead nanofibres started whirling inside the ring collector. These fast rotating nanofibres passed through the ring collector under the influence of air flow which was generated by an exhaust fan installed at top of electrospinning setup.

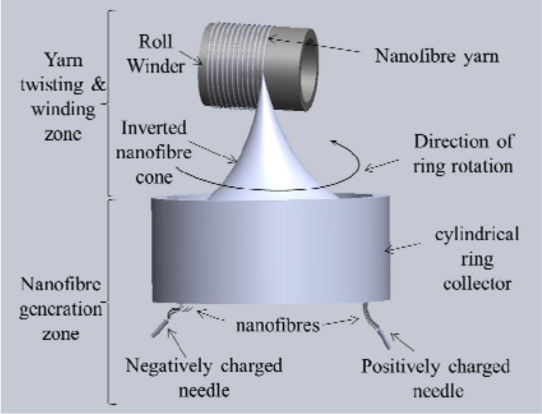

Figure 1 Setup for production of nanofibre yarns.

On reaching other side, nanofibres slowly lost momentum and converged as nanofibre cone on the top of the ring. The top edge of cone was rotating slowly with reference to the bottom edge attached to ring. This relative movement introduced twists to the fibre bundle. The twisted yarn was taken by the winder while lower part of cone was still connected to the ring collector. In this way, nanofibre yarn was produced continuously.

As the newly generated nanofibres were deposited inside the fibre cone, no astray fibres were found on the yarn surface. It was worth noting that as nanofibres were produced in the lower zone and they were drafted while coming through the ring collector, almost all of the fibres were aligned along the yarn axis at an angle of 6^o as shown in the Figure 3 (c). Only few fibres could be seen going out of the alignment. These nanofibres were broken from the fibre cone and went out on surface.

The average diameter of the nanofibre yarn was 99.94 μm, and the average diameter of the nanofibres was 239 nm. The diameter distribution in yarn was mostly concentrated, between 98 to 104 μm, whereas the diameter distribution of the nanofibres was in the range between 180 nm to 270 nm as shown in the histogram in Figure 3 (a) and 3 (b).

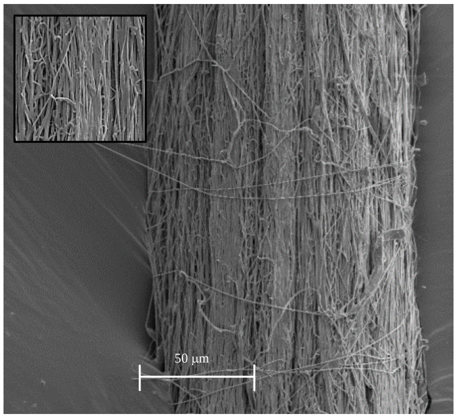

Figure 2 Electrospun nanofibre yarn produced by novel ring collector, inset magnified view of same yarn.

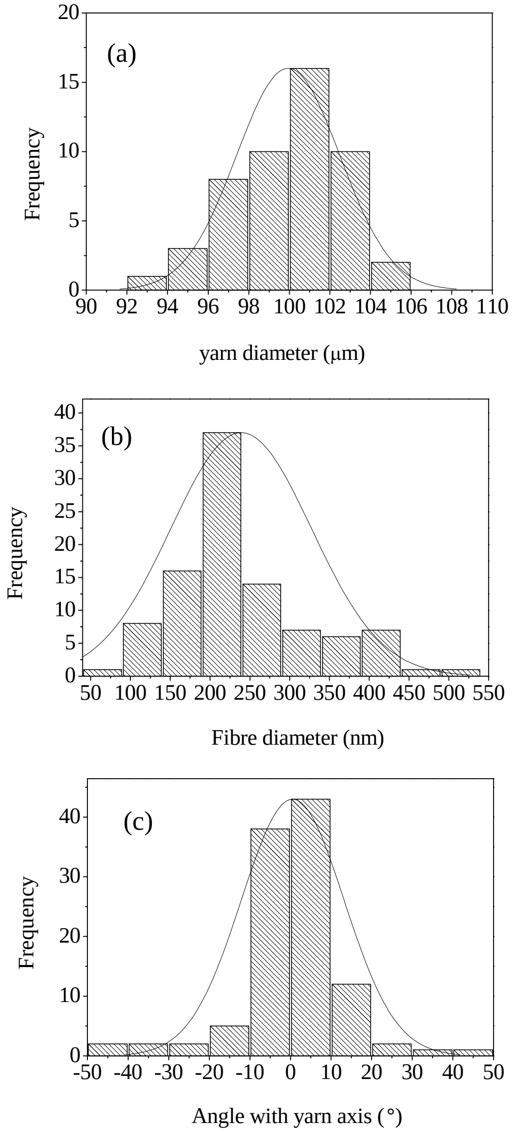

Figure 3 Histograms showing the diameter distribution of (a) nanofibre yarns, (b) nanofibres and (c) deviation angle of nanofibre from yarn axis.

It was found that nanofibres produced by this method were fully dried and had very good fibre alignment in final nanofibre yarn.

The tensile properties of the nanofibre yarn produced by the novel ring collector were determined. As shown in Figure 4, the tensile strength of the nanofibre yarn was 51.40 MPa and the elongation at break was 257.6%. Both the tensile strength and elongation at break exceeded the maximum value of aligned PVDF-HPF nanofibre-web-strip produced by needle electrospinning using the same solution, approximately, 38 MPa and 198% respectively [3].

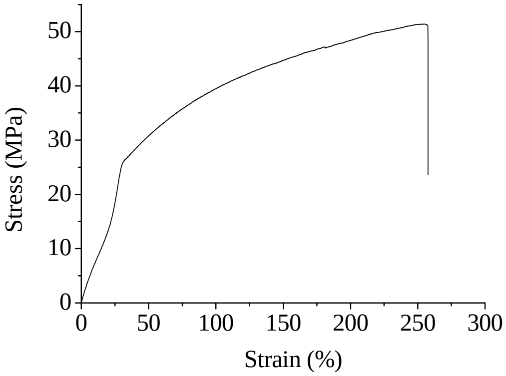

Figure 4 Stress-strain curve of the nanofibre yarn produced.

CONCLUSION

A novel nanofibre yarn spinner has been developed using two needle-based electrospinning nozzles and a ring collector. Our work indicated that PVDF-HFP nanofibre yarns produced from 16% PVDF-HFP solution had an average diameter of 99.94 μm and the nanofibres inside the yarn had an average diameter of 239 nm. The nanofibres in the yarn were well aligned with a surface twist angle of 6^{o} along yarn axis. The yarn showed improved mechanical properties compared to the nanofibre web electrospun from the same polymer solution.

REFERENCES

1. Teo, W.E., et al. A dynamic liquid support system for continuous electrospun yarn fabrication. *Polymer,* 2007. 48(12): p. 3400-3405.
2. Dabirian, F., et al. Manufacturing of twisted continuous PAN nanofiber yarn by electrospinning process. *Fibers and Polymers,* 2011. 12(5): p. 610-615.
3. Ali, U., et al. Direct electrospinning of highly twisted, continuous nanofiber yarns. *Journal of the Textile Institute,* 2012. 103(1): p. 1-9.

Thermo-Responsive PNIPAM Hydrogel Nanofibres Photocrosslinked by Azido-POSS

Jing Wang, Alessandra Sutti, Tong Lin, Xungai Wang
Institute for Frontier Materials, Deakin University, Waurn Ponds, VIC 3216, Australia
asutti@deakin.edu.au; jing.wang@deakin.edu.au

ABSTRACT

Photocrosslinkable thermo-responsive nanofibres were prepared by electrospinning poly(N-isopropylacrylamide) (PNIPAM) in the presence of an Azido-polyhedral oligomeric silsesquioxane (Azido-POSS). ultraviolet light (UV) irradiation yielded a highly-crosslinked hydrogel network within 2 min. The treated nanofibres showed outstanding stability in water, excellent hydrogel characteristics, fast response to temperature changes with fast swelling and de-swelling .

INTRODUCTION

Hydrogels capable of responding to surrounding temperature variations by swelling and de-swelling, also called thermo-responsive hydrogels [1], are some of the most studied "smart" polymeric gels. In this field, arguably the most significant challenge is to achieve both fast response and structural hydrogel integrity during the repeated volume changes [2]. Nanomaterials have been shown promising results in these regards. For example, Wang et al. [3] have recently reported a simple methodto obtain electrospun PNIPAM nanofibres via thermal treatment, using OpePOSS as a crosslinker. However, heat-treatment has many disadvantages, such as fibre shrinkage during processing[4]. Heat treatments also become a major limitation in some areas of application (such as tissue engineering) where potential cargoes (proteins, or other biomolecules of interest, for instance) could deteriorate during heat curing[5]. A different way to crosslink PNIPAM is thus sought, ideally allowing room temperature treatments and minor morphological variations.

In this study, a new photocrosslinkable PNIPAM-based formulation was used to produce nanofibres: linear PNIPAM was electrospun in the presence of an Azido-POSS as a photocrosslinker, followed by a UV treatment at room temperature. The as-prepared hydrogel nanofibres showed fast swelling/de-swelling responses triggered by temperature changes.

EXPERIMENTAL

The polymer solution for electrospinning was prepared by dissolving PNIPAM and Azido-POSS (synthesized in our lab) in a DMF/THF (1:1, vol/vol) solution at room temperature. The solutions were electrospun using a conventional electrospinning setup[6] to yield nanofibre mats. During electrospinning, the solution flow rate, the applied voltage and the electrospinning distance were set at 0.8 mL/hr, 12 kV and 17 cm, respectively.

To obtain a highly-crosslinked PNIPAM network, the as-electrospun nanofibres were subjected to UV irradiation (Hg medium pressure, 450 W, 6 cm lamp-sample distance) at room temperature for 2 min, 5 min, 10 min, 15 min, and 20 min, respectively.

RESULTS AND DISCUSSION

Synthesis and structure of photocrosslinker Azido-POSS.

Fig. 1 shows the synthetic path to Azido-POSS, which has eight photo-active azido groups.

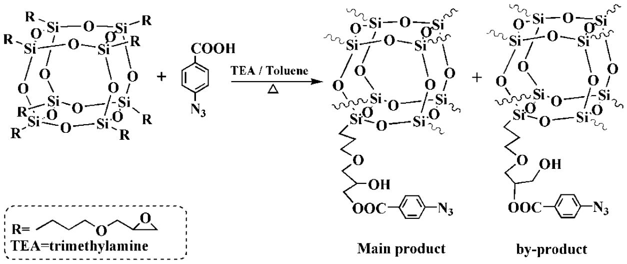

Fig. 1 Synthetic route of Azido-POSS via esterification between azidobenzoic acid and OpePOSS.

Photocrosslinking mechanism.

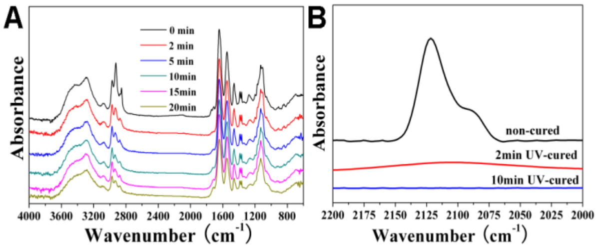

Fig. 2 (A) FT-IR spectra of UV-treated Azido-POSS/PNIPAM nanofibres at different treating time. (B) FT-IR spectra of selected UV-treated samples at wavenumber between 2000~2200 cm^{-1}.

FTIR analysis. The pre-prepared PNIPAM nanofibres were UV-cured for 2 min, 5 min, 10 min, 15 min, and 20 min, respectively. The FTIR spectra of non-cured PNIPAM/Azido-POSS and UV photo-crosslinked PNIPAM/Azido-POSS nanofibres at different UV-exposure time are presented in Fig. 2A. The FTIR bands were assigned as follows: 1366-1386 cm^{-1} deformation of the two methyls in $–C(CH_3)_2$; 1458 cm^{-1} $–CH_3$ and $–CH_2$(deformation); 1545-1645 cm^{-1} amide II band (stretching); 1710-1735 cm^{-1} –O–C=O stretching; ~2125 cm^{-1} $–N_3$ asymmetric stretching; 2854 cm^{-1} $–CH_2$ symmetric stretching; 2873 cm^{-1} $–CH_3$ symmetric stretching; 2925 cm^{-1} $–CH_2$ asymmetric stretching; 2970 cm^{-1} $–CH_3$ asymmetric stretching; 3070 cm^{-1} amide II overtone; wide band around 3300 cm^{-1} secondary amide –NH stretching. A peak ascribed to the azide group is visible in the untreated sample as a shoulder at about ~2125 cm^{-1}. The intensity of the aryl-azide peak was observed to decrease as a function of time. Importantly, after just two minutes of treatment, the peak was barely measurable, as shown in Fig. 2B, suggesting that the crosslinking reaction was nearly complete after 2 min.

DSC analysis. DSC curves for photo-crosslinked PNIPAM/Azido-POSS nanofibres are shown in Fig. 3. For the non-cured nanofibres, the DSC curve showed a strong and exothermic peak at around 210 °C. This peak has been related to the decomposition of the azido-group, $–N_3$, in arylazide-contaning molecules[7]. However, no similar peak was found for the UV-treated samples, inferring that such decomposition could not take place after the photo-crosslinking treatment. All samples showed a glass transition (Tg) peak at around 120~140ºC. These results also suggest that the activation and decomposition of the azide upon exposure to UV light had high yield and rate.

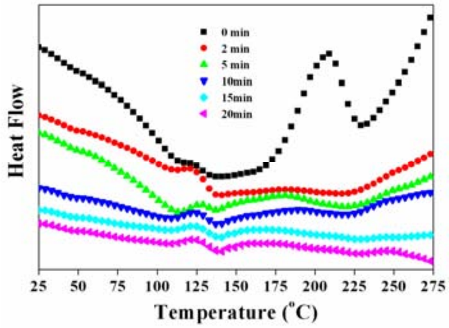

Fig. 3 DSC curves for the non-treated and UV-treated PNIPAM/AzidoPOSS nanofibres.

Thermo-responsive properties of photocrosslinked PNIPAM nanofibres.

When untreated nanofibre mats were immersed in water at 20 °C, the fibre mats gradually dissolved (Fig. 4A1). Even one single drop of water was enough to dissolve the 2 cm^2 non-cured mat, as shown in Fig. 4C1~3. When the water in which the first mat was dissolved (Fig. 4A1) was heated to 40 °C, no fibrous structure was recovered and the solution became cloudy (Fig. 4A2). In contrast, the nanofibre mat treated for 2 min under UV light became swollen and transparent upon immersion in water at 20 °C(Fig. 4B1), showing no sign of dissolution, degradation or weight change after several weeks' immersing in water. It was observed that the projected size of the photo-crosslinked nanofibre mats (Fig. 4D1) decreased upon wetting with cold water (Fig. 4D2), while the thickness of the mat increased (Fig. 4E2). This phenomenon, commonly observed in nanofibre swelling, was not observed when using thermally crosslinked nanofibre mats,[3] and can be ascribed to molecular relaxation taking place in presence of solvent. When the swollen nanofibre mats were immersed into hot water, both projected size (Fig. 4D3) and thickness (Fig. 4E3) decreased due to the de-swelling process characteristic of PNIPAM, taking place above LCST. The macroscopic shrinking was quantified by measuring the area of a nanofibre mat above and below LCST. Based on Fig. 4D1~D3 and Fig. 4E1~E3 the volumetric values of dry, swollen (below LCST) and de-swollen (above LCST) samples were calculated as 46.3, 106.7 and 14.7 mm^3, respectively, indicating that the increased volume of the nanofibre mat can be related to the absorption of water. Additionally, the nanofibre mat above LCST (de-swollen state) showed a reduced volume, when compared to the same sample below LCST. This suggests that the volume transition of PNIPAM affects the size of the nanofibre mat in the three dimensions.

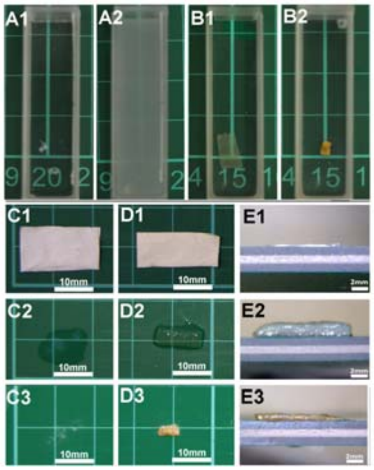

Fig. 4 Digital images of: (A1) non-cured nanofibre mat dissolving in cold water (20 °C) and (A2) followed by hot water (40 °C); (B1) UV-cured Azido-POSS/PNIPAM nanofibres in cold water (20 °C) and (B2) followed by hot water (40 °C); Non-cured and UV-cured PNIPAM nanofibres in: (C1, D1)dry state, (C2, D2) cold water and (C3, D3)hot water; Thickness changes of UV-cured PNIPAM nanofibre mats: (E1)dry sample, (E2) swollen state below LCST and (E3) shrunk state above LCST.

CONCLUSIONS

A novel strategy was used to produce stable and re-usable thermo-responsive PNIPAM hydrogel nanofibres by photo-crosslinking PNIPAM with Azido-POSS. Insoluble nanofibres composed of a highly-crosslinked PNIPAM polymer network were produced after electrospinning and subsequent UV photo-crosslinking. The UV-crosslinker Azido-POSS played a crucial role in the formation of a highly-crosslinked polymer network. The UV-cured nanofibre mats quickly became swollen and transparent upon contact with water at a temperature below their lower critical solution temperature (LCST) and showed fast and repeatable response to temperature.

REFERENCES

1. A. K. Bajpai, S. K. Shukla, S. Bhanu and S. Kankane. *Progress in Polymer Science*, 2008, 33, 1088-1118.
2. J. L. Drury and D. J. Mooney. *Biomaterials*, 2003, 24, 4337-4351.
3. J. Wang, A. Sutti, X. Wang and T. Lin, *Soft Matter*, 2011, 7, 4364-4369.
4. H. Hou, J. J. Ge, J. Zeng, Q. Li, D. H. Reneker, A. Greiner and S. Z. D. Cheng. *Chem. Mater*, 2005, 17, 967-973.
5. R. Cavaliere, E. C. Ciocatto, B. C. Giovanella, C. Heidelberger, R. O. Johnson, M. Margottini, B. Mondovi, G. Moricca and A. Rossi-Fanelli. *Cancer*, 1967, 20, 1351-1381.
6. T. Lin, H. Wang and X. Wang. *Nanotechnology*, 2004, 15, 1375.
7. G. L'Abbe, *Chemical Reviews*, 1969, 69, 345-363.

The Effect of Composites Thickness on the Performance of Footwear Insole Used for Diabetic Patients

W.T. Lo[1], K.L. Yick[1], S.P. Ng[2], J. Yip[1], H.H. Kwan[3], Y.Y. Kwong[3], and C.F. Cheng[3]
[1]Institute of Textiles and Clothing, The Hong Kong Polytechnic University, Hong Kong
[2]Hong Kong Community College, The Hong Kong Polytechnic University, Hong Kong
[3]Prosthetics and Orthotics Services, Hospital Authority, Hong Kong
cathylwt.lo@connect.polyu.hk

INTRODUCTION

Diabetic foot ulcers are highly associated with elevated pressure and foot deformity [1]. Custom-made orthotic footwear and insoles are cost effective and used as practical means to treat patients with diabetics so that plantar pressure is reduced by increasing the contact area [2]. To accommodate foot dimension changes and provide cushioning and sustainable control of the foot structure, a combination of several types of insole materials with varying thicknesses is often prescribed for orthotic insoles. Past literatures however mainly focused on evaluating the properties and performance of single materials [3, 4, 5]. Information on the effect of differences in thickness on the performance of composited insoles and thermal comfort properties is somewhat limited. The performance and efficacy of insoles therefore greatly depend on the experience of individual practitioners. A systematic evaluation of the properties of insole composites and the effect of insole thickness on the key performance of orthotic insoles are to be investigated in this study. Since footwear hygiene is also one of the concerns for patients with diabetes, higher temperatures and moisture content in footwear will encourage the growth and different types of bacteria found on feet, which will further result in sores and wound infections, the thermal comfort properties of composite insoles are also studied.

METHODOLOGY

Test materials A total of 3 types of orthotic insole materials with different thicknesses, which are frequently used in applications that accommodate, cushion and control, were sourced for the production of diabetic foot insoles. A total of 6 composites (A to G) were fabricated based on the 3 types of insole materials. To compare the property performance of the composites, Samples R1, R2 and R3 are taken as the control, which are made of single fabrication pilings with a pre-determined thickness up to 18 mm.

Test methods By using a new approach of property evaluation for orthotic insole materials, the energy absorption percentage and water vapor permeability properties of insoles composed of multiple layers of materials were measured. The energy absorption performance of insole materials is measured by using a dynamic load cell at the bottom of the purposed-made instrument. The energy absorption capacity of the insole material is presented as Equation 1. For the water vapor permeability, a composite sample attached to a dish filled with distilled water, was weighed before and after 24 hours. The weight change of the dish assembly represented the ability of water to transmit through the materials as shown in Equation 2. A higher weight loss value means greater water vapor permeability of the test materials, which results in reducing the moisture content of the in-shoe environment.

$$\mathrm{EA}_x(\%) = (1 - \mathrm{E}_x/\mathrm{E}_o) * 100\% \quad \text{(Equation 1)}$$

$$\text{Water Vapor Transmission rate} = G/(t * A)$$

(Equation 2)

RESULTS AND DISCUSSION

Results revealed that the composited material samples display increases in energy absorption when there is an increase in thickness in each layer and exhibit considerable differences in impact patterns in comparison to the control samples. Of these, the effect of material thickness on energy absorption in the accommodation layer is more noticeable (Samples A and D), and this may be related to Sample R1 in that Nora® Lunairflex, which is made of a single material, has outstanding energy absorption at 60.68% in comparison to the cushioning layer made of Nora® Lunalastike in Sample R2. In considering the effectiveness of softer insole materials in peak pressure reduction [6], slight increases in thickness in the accommodation and the cushioning layers could contribute to the majority of energy reduction without any changes in the hardness. It can also be observed that the changes in the energy absorption of the composite insoles could be predicted from the properties of the accommodation and the cushioning layers.

The force-time graph reveals that insoles made of composite materials may form a new pattern of energy absorption behavior and change the reacting time. It can be seen from the force-time graph in Figure 2 that all composited samples display similar curve patterns whilst they are noticeably different from the reference samples. Apparently, the composited samples which have lower energy absorption show higher peak force, which respond differently as opposed to the reference samples because lower energy absorption may result in the low peak force displayed in the graph.

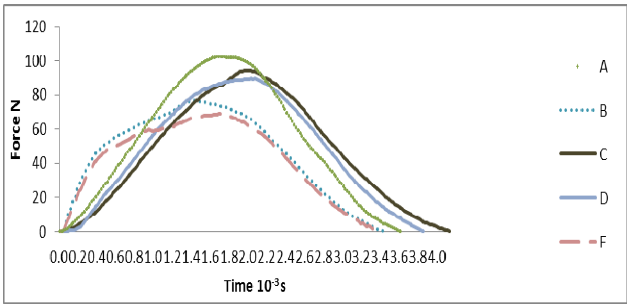

Figure 1a. Force-time graph for force absorption behavior of composited insoles A-E

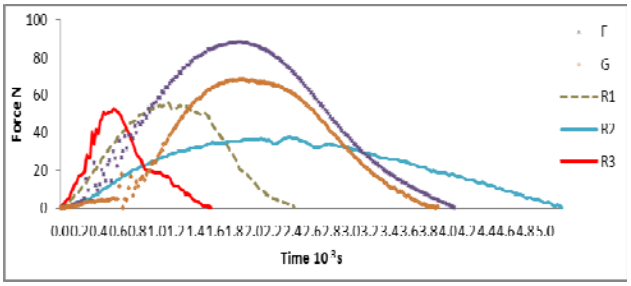

Figure 2b. Force-time graph for force absorption behavior of composited insoles F-R3

It was observed that insole thickness has an adverse relationship with water vapor permeability. The composited insoles that have a thinner structure (Sample A: 14 mm) may contain fewer barriers thus allowing effective heat dissipation and moisture transfer, which is the key to enhancing overall comfort inside orthotic footwear. In terms of the effect of the thicker perforated material, Nora® Lunairflex, on water vapor permeability, Sample D showed a lower water vapor permeability value in comparison to Sample A because the overall thickness is apparently more important for water vapor transmission, even though Sample D has a thicker perforated material.

CONCLUSIONS

This study suggests that material thickness could affect the performance of insoles made of composite materials. A new approach which uses energy absorption and compressive stress can effectively evaluate the performance of insole composites made of multiple layers of materials on the basis of their fabrication material. The thermal comfort data in terms of water vapor permeability indicate that thickness is comfort-related. In considering the development of composited insoles in practice, the overall insole performance could be optimized by modifying the thickness of corresponding samples made of a single material that having pronounceable characteristics. Hence, to improve the energy absorption properties of composited insoles without changing the hardness, thicker accommodation and cushioning layers are recommended. On the other hand, it is not advisable to increase the thickness of the control layer as this may adversely affect the overall comfort of the insole composite.

ACKNOWLEDGMENT

The material in this article is based on work supported by the Department of Prosthetics and Orthotics at the Kowloon and Queen Elizabeth Hospitals in Hong Kong. We would like to thank the Research Grant Council for funding this research, RGC No. PolyU 5308/11E, and the Departmental Grant of the Institute of Textiles and Clothing, The Hong Kong Polytechnic University, for funding this research project (PolyU RTD6).

KEYWORDS

Orthotic insoles, insole materials, diabetic foot, thermal comfort properties

REFERENCES

1. Bus, S.A. Foot structure and footwear prescription in diabetes mellitus. *Diabetes Metabolism Research and Reviews*, 24 (Suppl 1) 2008, S90-S95.
2. Foto, J.G. Compact and portable digitally controlled device for testing footwear materials: technical note. *Journal of Rehabilitation Research and Development*, 45 (6) 2008, 893-900.
3. Foto, J.G., Birke, J.A. Evaluation of multidensity orthotic materials used in footwear for patients with diabetes. *Foot & Ankle International*, 19 (12) 1998, 836-841.
4. Brodsky, J.W., Pollo, F.E., Cheleuitte, D., Baum, B.S. Physical properties, durability and energy-dissipation function of dual-density orthotic materials used in insoles for diabetic patients. *Foot & Ankle International*, 28 (8) 2007, 880-889.
5. Paton, J., Jones, R.B., Stenhouse, E., Bruce, G. The physical characteristics of materials used in the manufacture of orthoses for patients with diabetes. *Foot & Ankle International*, 28 (10) 2007, 1057-1063.
6. Cheung, J.T., Zhang, M. Parametric design of pressure-relieving foot orthosis using statistics-based finite element method. *Medical Engineering and Physics*, 30(3) 2008, 269-277.

Multifunctional Conducting Polymer Fibres for Drug Delivery Applications

Dorna Esrafilzadeh, Simon E. Moulton, Joselito M. Razal, Elise M. Stewart, Gordon G. Wallace
Intelligent Polymer Research Institute and the Australian Research Council Centre of Excellence for Electromaterials Science, AIIM Facility, University of Wollongong Innovation Campus, North Wollongong NSW Australia 2522
gwallace@uow.edu.au; smoulton@uow.edu.au

INTRODUCTION

Advances in the fabrication of neuroprosthetic electrodes have attracted considerable interest from biomedical researchers. These electrodes are incorporated into a neuroprosthetic device capable of, electrically stimulating and recording of neuron activity. Critical to the successful application of these electrodes is their biocompatibility, stable conductivity, lower impedance and flexibility whilst maintaining appropriate mechanical properties [1] . A relatively new conducting material, namely organic conducting polymers (OCPs), is being utilized in the fabrication of electrode structures capable of electrically stimulating cells as well as recording cellular activity The unique characteristics of OCPs such as biocompatibility with higher surface area, compare to traditional conductors such as metals, make them an appropriate choice to apply in biomedical research [2]. Two types of OCPs namely poly(3,4-ethylenedioxythiophene) (PEDOT) and polypyrrole (Ppy) have been shown to be biocompatible conductors with lower impedance and have been employed to coat metal electrode surfaces, resulting in an enhancement of electrode/cellular communication [3]. Moreover, these structures have widely been used for controlled release of a range of biomolecules such as anti-inflammatory and antibiotic drugs. Fabrication of conducting fibers has previously been achieved by us and applied to a biomedical application [4]. In the work presented here, we discuss the fabrication of OCP wetspun fibers (PEDOT:PSS-CHI/Ppy) incorporating the antibiotic drug ciprofloxacin hydrochloride (cipro). These conducting fibers were tested for their mechanical, electrical and drug deliver properties using a range of techniques and were shown to possess good electrical and mechanical properties. We also show that it is possible to control the release of cipro from the conducting fiber and that the incorporated and released cipro is still active against gram positive and gram negative bacteria.

APPROACH

Poly(3,4-ethylenedioxythiophene) poly(styrenesulfonate) (PEDOT: PSS) pellets were obtained from Agfa (Orgacon dryTM, Lot A6 0000 AC) with water content of 9.8m/m% H_2O and used as supplied. High molecular weight Chitosan (CHI) was purchased from Sigma (>75% deacetylation) and Ciprofloxacin Hydrochloride was obtained from MP Biomedical Inc. (Lot No. of 8460H) with $M_W = 367.84$. Pyrrole monomer was purchased from Merck and distilled prior to use and stored at -20°C when not in use. Deionised Milli-Q water (18 MΩ cm^{-1}) was used to prepare all aqueous solutions. The release of Ciprofloxacin hydrochloride was measured in Phosphate Buffer Saline (PBS) solution with pH≈ 7.4 prepared by dissolving standard PBS tablet (Merck, Germany) in 1 L Milli-Q water (18MΩcm^{-1}). Concentrated acetic acid was purchased from Sigma and diluted using Milli-Q water. The wetspinning method was used to fabricate PEDOT:PSS-CHI fibres by injecting PEDOT:PSS with concentration of 25 mg/ml into the 1.0 wt% chitosan solution. The feeding rate of wetspinning pump was 15 mL/hr using a 5.0 mL syringe with a detachable needle (20 gauge) used as a spinneret. The PEDOT:PSS-CHI fibers were washed and dried under tension after wetspinning. The second layer (Ppy) was polymerised electrochemically onto the PEDOT:PSS-CHI fibre, from a 0.2 M pyrrole monomer containing 5.0 mM Ciprofloxacin hydrochloride in MilliQ water. The electrochemical polymerisation was performed under galvanostatic mode utilizing a platinum mesh (counter electrode), Ag/AgCl (reference electrode) and the PEDOT:PSS-CHI fiber as the working electrode. The release of ciprofloxacin was measured by UV.vis spectroscopy at a wavelength of 270nm. For electrically stimulated release, the cell contained a platinum mesh auxiliary, Ag/AgCl reference and the PEDOT:PSS-CHI/Ppy.Cipro fiber. Samples of release mediums were collected over three days with each aliquot being collected and replaced with fresh PBS. The aliquots were kept at 2 °C until drug measurements were performed.

RESULTS AND DISCUSSION

The PEDOT:PSS-CHI fibres were wetspun by the injection of a PEDOT:PSS solution into a solution of chitosan (1 wt%) and the fiber formation occurring by the reaction between negatively charge of PSS and positively charge of amine group in chitosan. The morphology of fibers was analyzed using scanning electron microscopy (SEM) and show a compact and dense structure with average diameter of 56 ± 7 μm (Fig. 1A – white arrow).

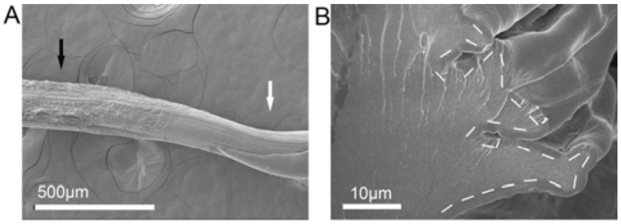

Fig 1. (A) Scanning electron microscopy (SEM) image of PEDOT:PSS-CHI fibre without (white arrow) and with (black arrow) the Ppy.Cipro layer. (B) SEM image of cross-section of fibre. (The white lines show the Ppy.Cipro layer) [5].

The electrochemistry and conductivity of these fibres was analyzed (Fig 2A and B) and was shown to be suitable to allow a second conducting polymer layer to be electrochemically deposited onto. The second layer was composed of polypyrrole doped with the antibiotic ciprofloxacin (Ppy.Cipro). The SEM in Fig 1A and 1B shows a change in morphology of fibres before and after polymerisation of second layer.

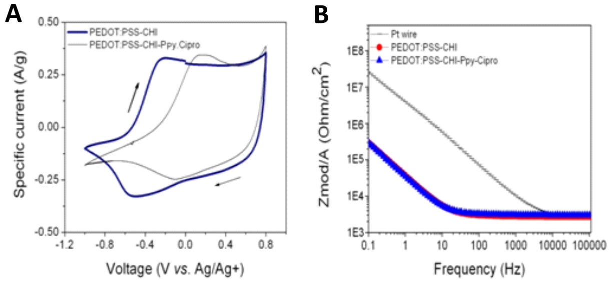

The release of ciprofloxacin hydrochloride from Ppy.Cipro under passive and electrically stimulated conditions was measured by UV.vis over 3 days (Fig. 3). The non-stimulated (passive) release showed most of ciprofloxacin was released during first 9 hours followed by a plateau. While, the release of ciprofloxacin increased in higher concentration and longer time points by electrical stimulation.

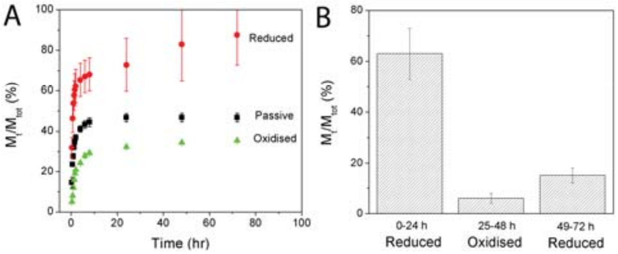

Fig 3. (A) release profile of Cipro release during oxidized, reduced and passive state of conducting polymer within 72h. B) Release profile of Cipro with switching between oxidized and reduced state of Ppy layer.

CONCLUSION

Conducting polymer fibres have been fabricated via wet-spinning method and represents solid and promising structures to incorporate antibiotic drug. The release of ciprofloxacin has been investigated under passive and stimulated conditions. The results showed the capability of these novel fibres to control drug release in specific timeframe required and demonstrated promises in drug delivery applications.

ACKNOWLEDGMENT

The authors gratefully acknowledge the Australian Research Council and the ARC Centre of Excellence for Electromaterials Science (ACES) for their continued financial support. The authors also wish to thank the Australian Research Council for the Federation Fellowship (Wallace), Queen Elizabeth II Fellowship (Moulton) and Australian Post-doctoral Fellowship (Razal).

REFERENCES

1. Abidian, M.R. and D.C. Martin. Experimental and theoretical characterization of implantable neural microelectrodes modified with conducting polymer nanotubes. *Biomaterials*, 2008. 29(9): p. 1273-1283.
2. Green, R.A., et al. Conducting polymers for neural interfaces: Challenges in developing an effective long-term implant. *Biomaterials*. 29(24-25): p. 3393-3399.
3. Abidian, M.R. and D.C. Martin Multifunctional Nanobiomaterials for Neural Interfaces. *Advanced Functional Materials*, 2009. 19(4): p. 573-585.
4. Razal, J.M., K.J. Gilmore, and G.G. Wallace Carbon Nanotube Biofiber Formation in a Polymer-Free Coagulation Bath. *Advanced Functional Material*s, 2008. 18(1): p. 61-66.
5. Esrafilzadeh, D., et al. Multifunctional conducting fibres with electrically controlled release of ciprofloxacin. *Journal of Controlled Release*, DOI: 10.1016/j.jconrel.2013.01.022

Precision Wet-Spinning of Cell-Impregnated Alginate Fibres for Tissue Engineering

R. Cornock[1, 2], M. Kita[1, 2], A. Quigley[1, 2], G. G. Wallace[1, 2], R. M. I. Kapsa[1, 2],
[1]AIntelligent Polymer Research Institute, ARC Centre of Excellence for Electromaterials Science, University of Wollongong
[2]Centre for Clinical Neurosciences and Neurological Research, St. Vincent's Hospital Melbourne
rmik@unimelb.edu.au; rcornock@uow.edu.au

INTRODUCTION

The selective assembly of functionalised fibres produced by wet-spinning into implantable three dimensional contructs presents attractive prospects for the field of medical bionics[1]. In particular, the incorporation of biological factors and large numbers of cells within biocompatible and macroporous fibres is expected to deliver improvements to drug delivery platforms as well as to tissue engineering biotechnology[2, 3].

Hydrogel class materials, in particular chitosan and sodium alginate, are suitable for soft tissue engineering applications due to their compliance with the physical properties of target tissues and permissive degradation profile that elicits minimal inflammatory response [4, 5]. The wet-spinning process allows for these materials to be deposited, woven or knitted into defined structures [6]. Thorough optimisation of novel processes for biomaterial fabrication is paramount, as the resulting devices and conduits become both more effective and reproducible with precision assembly[7].

OBJECTIVE

This study assessed wet-spinning technology as a method for generating three dimensional soft gel fiber geometries biologically functionalized by incorporation of live cells. This was achieved through the analysis of process parameters, fibre dimension, as well as cell-loading, viability, position and alignment.

Sodium alginate of varying concentrations was selected as a matrix material for the fibres. Primary myoblasts from C57BL10-ROSA mice were used for fabrication of regenerative muscle constructs, exploiting geometric compatibility between muscle structure linearity and wet-spun fiber output. This process was developed into a an optimised methodology for reproducible production of fibres using this model, and a three dimensional myo-regenerative conduit developed.

APPROACH

Materials. A buffer solution of 4-(2-hydroxyethyl)-1-piperazineethanesulfonic acid (HEPES, Biochemical, #L505388) was made up to a concentration of 20mM in a 308mM sodium chloride (NaCl) solution. Alginic acid with sodium salt (Sigma, #035K0205) was made to concentrations of 2% and 4% (wt/v) at 60°C under stirring. A ROSA mouse myoblast cell line was grown to 80% confluence in a series of thirty T-75 flasks in 20mL of Dulbecco's Modified Eagle's Medium (DMEM) at 37°C. The cells were then trypsinised and centrifuged at 280g for 2 minutes to pellet the cells. The cells were then resuspended in HEPES solution to concentrations of 20, 40 and 60 millions cells/mL. Mixing with corresponding alginate solutions resulted in cell concentrations of 10, 20 and 30 million cells/mL for both 1% and 2% (wt/v) alginate concentration.

Wet Spinning. A wet spinning arrangement as described in Figure 1, was used to fabricate cell-impregnated alginate fibres. An aqueous coagulation bath (L=1m) of 2% calcium chloride (Sigma, #48H0106) was utilised in cross-linking the fibres. Solutions were extruded into a coagulation bath using a high precision KD Scientific KDS-410 constant volume syringe pump at a rate of 0.03mL/min (32G nozzle - EFD Nordson). A rotating drum was operated at a fixed velocity of 2cm/s for the collection of fibres following coagulation.

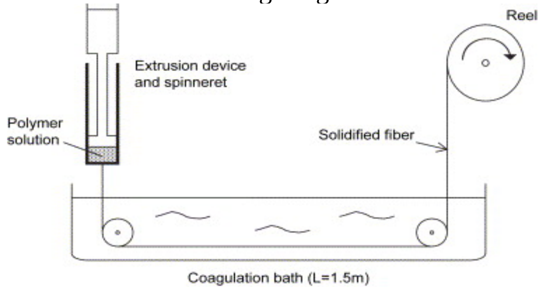

Figure 1: Basis of the wet-spinning process, adapted from Ruijter et al.[8]

Analysis. For viability , fibres were collected into HEPES containing 1µM calcein AM in DMSO and 1µg/mL of propidium iodide (PI). An Olympus IX70 fluorescence microscope was used at 10x to observe cell viability and fibre dimension (n>3). For cryoslicing, fibres were embedded into Tissue-Tek Optimal Cutting Temperature Compound and placed into a slurry of dry ice and ethanol. These were stored at -70°C before being sliced using a LEICA CM1900 Rapid Sectioning Cryostat. Four independent experiments were carried out to ensure the repeatability of the fabrication process. Finally, several fibres were collected into both proliferation and differentiation media for observation.

RESULTS AND DISCUSSION

Each of the cell loadings tested were successfully fabricated repeatedly into fibres of both 1% and 2% alginate matrices (Figure 2). Through optimisation of the material feed rate and handling methods, large quantities of cell laden fibres could be manufactured. While there were minor differences in the fibre diameters observed (~130-150µm), the alginate concentration and cell loadings demonstrate no correlation to any significant differences in diameter (Figure 3).

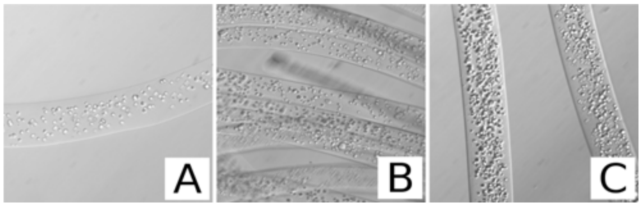

Figure 2: Alginate fibres (2% wt/v) impregnated with A) 10M cells/mL, B) 20M cells/mL, C) 30M cells/mL.

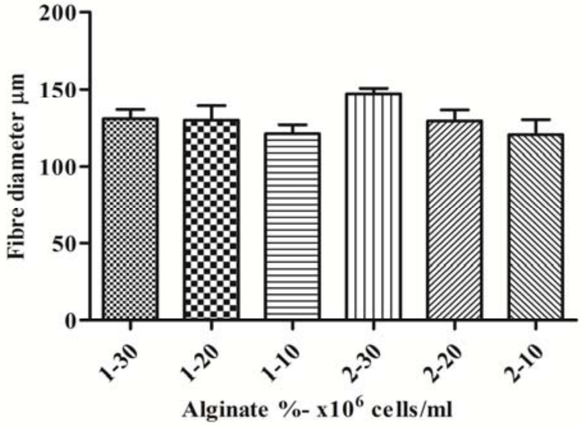

Figure 3: Average fibre dimension with respect to cell and alginate concentration.

Samples produced with 1% alginate and 20 million cells/mL showed the highest cell viability over the four experiements of 96 ± 1% (**Figure 4**).

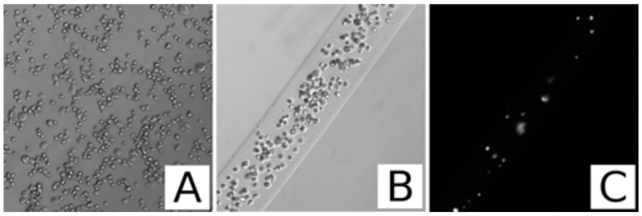

Figure 4: A) Cell formulation prespin. B) 1% alginate fibre containing 20M cells/mL. C) Same fibre under fluorescence, showing cell death through PI staining.

Fibres produced using 2% alginate as a matrix material, while displaying similar fibre diameters, demonstrated a lowered cell viability and consistency when compared to the 1% alginate fibres (Figure 5). Finally, in a preliminary attempt to produce a wet-spun, cell-laden three-dimensional construct, a 5-layer, 1% alginate, 20M cells/mL mesh was produced through the continual 90° reorientation of the mounted collection substrate (Figure 6).

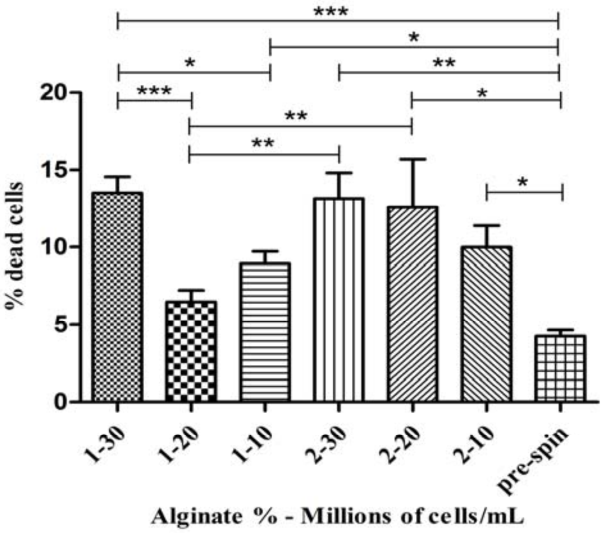

Figure 5: Comparison of cell viability for each tested subgroup over four independent experiments (n=4). A one-way ANOVA was applied to the data (*** for $p<0.05$, ** for $p<0.01$, * for $p<0.001$).

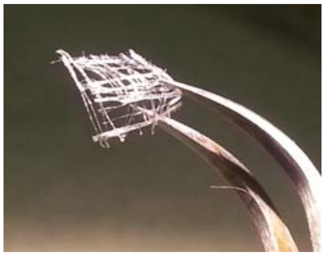

Figure 6: Multi-layered, wet-spun mesh of 1% wt/v alginate containing 20M cells/mL.

CONCLUSION

This work communicates the successful fabrication of cell-laden fibres at high cell concentrations. The cells remain viable post-fabrication and it was determined that the most efficient subgroup consisted of a 1% wt/v alginate matrix incorporating a cell concentration of 20M cells/mL. A cell-loaded, three dimensional wet-spun scaffold was successfully produced.

FUTURE WORK

Future experimentation will integrate slow release growth factors and other biologically relevant agents such as anti-inflammatory therapeutics into these systems. Cells of varying description should be fabricated into multi-layered structures to meet specific three-dimensional tissue engineering requirements, and *in vivo* studies be carried out in animal models to observe cell migration and engraftment in target tissues such as muscle and nerve.

KEYWORDS: Alginate, hydrogel, wet-spinning, fibre, fiber, microfiber, cell encapsulation, tissue engineering, additive fabrication.

ACKNOWLEDGEMENT

The authors wish to acknowledge the Australian Research Council (ARC:- CE0561616; ARC Centre of Excellence for Electromaterials Science (ACES)) and National Health and Medical Research Council (NHMRC:- 573430) for funding this work.

REFERENCES

[1] Gordon G.Wallace, Simon E. Moulton, Michael J. Higgins, and Robert M. I. Kapsa. *Organic Bionics*. Wiley-VCH, 2012.

[2] Yi. Hong, Haiqing Song, Zhengwei Mao, Changyou Gao, and Jiacong Shen. Covalently crosslinked chitosan hydrogel: Properties of in vitro degradation and chondrocyte encapsulation. *Acta Biomater*., 3:23-31, 2006.

[3] Bo Ram Lee, Kwang Ho Lee, Edward Kang, Dong-Sik Kim, and Sang-Hoon Lee. Microfluidic wet spinning of chitosan-alginate microfibers and encapsulation of hepg2 cells in fibers. *Biomicrofluidics*, 5:022208, 2011.

[4] Yimin Qin. A comparison of alginate and chitosan bres. *Med. Device Technol.*, pp. 34-37, 2004.

[5] F. M. Berthiaume. *Methods in Bioengineering*: *3D Tissue Engineering*. Artech House, 2010.

[6] Y. Y. Chen, C. T. Chiu, Y. P. Chang, and Y. J. Wang. Fabrication of porous gelatin microfibers using an aqueous wet-spinning process. *Artif. Cell. Blood Sub*., 37:173-176, 2009.

[7] V. Mironov, T. Trusk, V. Kasyanov, S. Little, R. Swaja, and R. Markwald. Biofabrication: a 21st century manufacturing paradigm. *Biofabrication*, 1:022001, 2009.

[8] Christiaan Ruijter, Eduardo Mendes, Hanneke Boerstoel, and Stephen J.Picken. Orientational order and mechanical properties of poly(amide-blockaramid) alternating block copolymer films and fibres. *Polymer*, 47:8517-8526, 2006.

Wet-Spinning of Multifunctional Graphene Fibers Using Graphene Oxide Liquid Crystals

Rouhollah Jalili[1], Seyed Hamed Aboutalebi[2], Dorna Esrafilzadeh[1], Roderick L. Shepherd[1], Jun Chen [1], Sima Aminorroaya-Yamini[2], Konstantin Konstantinov[2], Andrew I. Minett[3], Joselito M. Razal[1], and Gordon G. Wallace[1]

[1]Intelligent Polymer Research Institute and ARC Centre of Excellence for Electromaterials Science; [2]Institute for Superconducting and Electronic Materials, AIIM Facility, Innovation Campus, University of Wollongong, North Wollongong, NSW 2522; [3]Laboratory for Sustainable Technology School of Chemical and Biomolecular Engineering, University of Sydney, Sydney NSW 2006 Australia

gwallace@uow.edu.au; rjalili@uow.edu.au

INTRODUCTION

The recent discovery of liquid crystalline (LC) behavior of graphene oxide (GO) dispersions in various organic, and aqueous media brings added control to the assembly of larger structures using the chemical process approach.[1-3] The LC state can be used to direct the ordered assembly of nanocomponents in macroscopic structures via simple methods like wet-spinning. [3]

Here, we developed a scaleable fabrication route to produce graphene fibers via a facile continuoes wet-spinning methode. We develop solid understanding in the required criteria to correlate processability with LC behavior, aspect ratio and the dispersion concentration to provide a viable platform for spinning of LC GO. We demonstrate a striking result that highlits the importance of GO sheet size and polydispersity in generating wet-spinnable LC GO dispersions from very low spinning dope concentrations (as low as 0.075 wt. %). The new knowledge gained through rheological investigations provides a sound explanation as to why continuous spinning of binder-free GO fibers is enabled by the LC behavior at this very low concentration.

EXPERIMENTAL

Wet-spinning experiment was involved injecting LC GO dispersion into a coagulation bath to produce the gel-state GO fiber. Dried GO fibers were obtained by washing the gel-state GO fibers with water, then 25 vol. % ethanol or acetone and then air-drying the fiber under tension at room temperature. Reduction of GO fibers (rGO) was carried out by overnight annealing at 220 °C under vacuum.

RESULTS AND DISCUSSION

Based on our previously described GO synthesis protocols [2] and completely eliminating the sonication previously deemed necessary in the complete exfoliation of GO sheets, we have produced ultra-large GO sheets with lateral size of up to ~100 µm (Figure. 1). SEM survey of GO sheets confirmed that the majority of the lateral GO sheet sizes are in the tens of micrometers domain with an average lateral sheet size of 37 µm.

Aqueous GO dispersions at concentrations ranging from 0.10 to 5.00 mg ml^{-1} were examined using polarized optical microscopy and displayed that nematic phase start to form at GO concentrations close to 0.25 mg ml^{-1}.

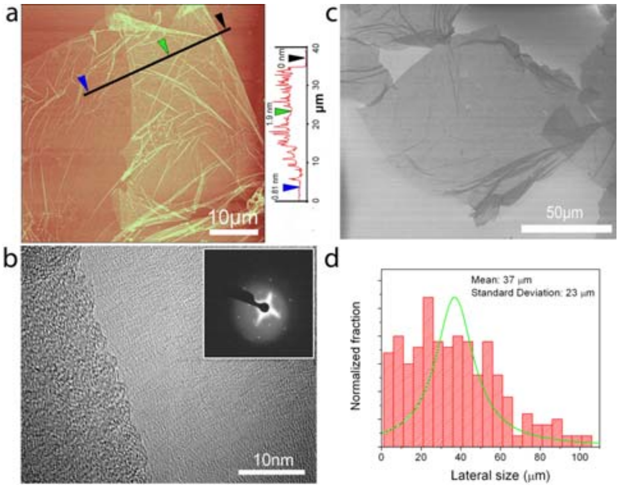

Figure 1. As-prepared GO dispersions predominantly contain giant monolayer GO sheets. (a) AFM image of a large GO sheet with lateral size >75 µm. Inset shows the height profile derived from the marked line in the AFM image showing monolayer GO sheet thickness of ~0.81 nm. (b) High-resolution TEM image of monolayer GO sheet and the corresponding electron diffraction pattern (inset). (c) Representative SEM images of GO sheets present in as-prepared GO dispersions contain GO sheets with lateral size as large as 100 µm, (d) The corresponding lateral size distribution of GO sheets (the diameter of an equal-area circle).

Below 0.25 mg ml^{-1}, GO dispersions were completely isotropic and un-spinnable (i.e. GO sheets simply spread into the coagulation bath). At higher concentration (between 0.25 to 0.75 mg ml^{-1}), transition of biphasic to fully nematic phase is observed (i.e. when isotropic and nematic phases co-exist). This biphasic concentration range only demonstrated partial spinnability in fiber spinning processes. This partial spinnability is characterized by the weak cohesion of the GO dispersion upon injecting in the coagulation bath, which resulted in short lengths of gel-state GO fibers. Also observed in this concentration range is that the nematic phase volume fraction (φ_{nem}) increased with GO concentration. Using GO concentration of ≥ 0.75 mg ml^{-1}, when fully nematic phase forms, in fiber wet-spinning resulted in long lengths of robust gel-state fibers. GO concentrations of 0.75 mg ml^{-1} to 5 mg ml^{-1} showed similar ease of spinnability by following coagulation methods: non-solvent precipitation, dispersion destabilization using acid, base or salt solutions, ionic cross-linking using divalent cations, and coagulation by amphiphilic or oppositely charged polymers.

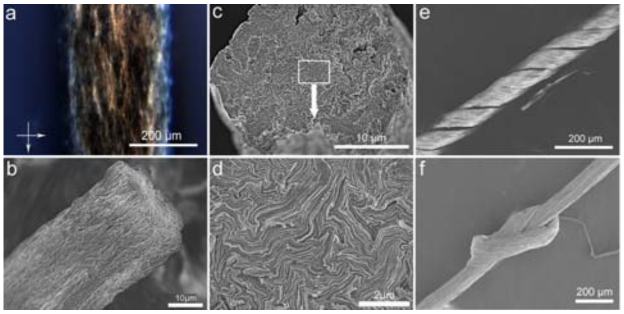

Figure 5. (a) Polarized optical micrograph of as-spun gel-state GO fiber showing birefringence. Birefringence properties confirmed ordered LC domains were formed and preserved during spinning process (arrows show polarizers direction). SEM images of an as-spun GO fiber showing (b) Corrugated surface and (c) Near-circular cross-section. (d) Close-up SEM image of the cross-section of GO fiber shown in b revealing GO sheet planes that are oriented along the fiber axis. (e-f) SEM images of crumpled and knotted rGO yarns showing their flexibility.

As-spun GO fibers prepared by ionic cross-linking and polyionic complexation (using the positively charged polymer, chitosan) displayed the highest mechanical properties with Young's modulus (E), ultimate strength (δ) and toughness (T) of 22.6±1.9 GPa, 442±18 MPa and 4.8 J g^{-1}, respectively. Apart from chitosan, coagulation in $CaCl_2$ which exploits ionic cross-linking using divalent cations (Ca^{2+}) also resulted in fibers with extraordinary mechanical properties (E = 20.1±2.1 GPa, δ = 412±30 MPa and T = 4.8 J g^{-1}). The best as-spun GO fiber strength (~442 MPa) is higher than previously reported GO and rGO -based materials such as GO papers (~120 MPa), [4] RGOF/PVA fibers (~120 MPa), [5] LC GO fibers (~102 MPa), [6] stretched "ultrastrong" GO fibers (364 MPa), [7] fibers produced from graphene nanoribbons (378 MPa), [8] hydrothermally converted rGO fibers (~180 MPa) and thermally reduced rGO fibers (420 MPa). [9] In terms of modulus, the GO fiber (22.6 GPa) is inferior to the highest modulus of GO paper (42 GPa) [4] and fibers produced from graphene nanoribbons (36.2 GPa), [8] but the difference in breaking strain is substantial (3.2 % for GO fiber *vs.* ~0.4 % for GO paper and 1.1% for fibers produced from graphene nanoribbons) resulting in toughness (4.8 J g^{-1}) considerably higher than both. [4, 8] The strength of as-spun GO fiber is also much higher than single yarns of pure multi-walled CNTs (~250 MPa). [10] It should be noted that the GO used in this study is much larger compared to "giant GO" [7] (37μm in this study *vs* 18μm), which is the basis of the enhanced improvement in mechanical properties attained in the current study. Although this reduction method was effective as evidenced by increase in the electrical conductivity (~250 S m^{-1}), the mechanical properties were found to be lower compared to the parent GO fiber.

CONCLUSION

The promising properties of GO and rGO fibers presented here are potentially applicable in many specialized technical applications. Fundamental understanding of the GO dispersion chemistry and rheology, the associated fiber spinning processes, and the resultant material properties, presented here along with one-step production of rGO fibers will provide scope for the development of next generation advanced GO/rGO-based fiber architectures and associated technologies. The simplicity and the scalability of the processes described here will enable safe and cost-effective large-scale production of GO/rGO fiber to find a place in the smart fiber industry (i.e. fibers that integrate applications in energy, environmental monitoring and biomedical engineering).

KEYWORDS

Graphene oxide, liquid crystal, fiber, multifunctional textiles

REFERENCES

[1] R. Jalili, S. H. Aboutalebi, D. Esrafilzadeh, K. Konstantinov, S. E. Moulton, J. M. Razal, G. G. Wallace. *ACS Nano* 2013.
[2] S. H. Aboutalebi, M. M. Gudarzi, Q. B. Zheng, J.-K. Kim. *Adv. Funct. Mater.* 2011, 21, 2978.
[3] R. Jalili, S. H. Aboutalebi, D. Esrafilzadeh, S. R. L., C. Jun, A.-Y. Sima, K. Konstantinov, M. A. I., J. M. Razal, G. G. Wallace. *Adv. Funct. Mater*. 2013.
[4] D. A. Dikin, S. Stankovich, E. J. Zimney, R. D. Piner, G. H. B. Dommett, G. Evmenenko, S. T. Nguyen, R. S. Ruoff. *Nature* 2007, 448, 457.
[5] M. K. Shin, B. Lee, S. H. Kim, J. A. Lee, G. M. Spinks, S. Gambhir, G. G. Wallace, M. E. Kozlov, R. H. Baughman, S. J. Kim. *Nat Commun*. 2012, 3, 650.
[6] Z. Xu, C. Gao. *Nat Commun.* 2011, 2, 571.
[7] J. Yan, T. Wei, B. Shao, Z. Fan, W. Qian, M. Zhang, F. Wei. *Carbon* 2010, 48, 487.
[8] C. Xiang, N. Behabtu, Y. Liu, H. G. Chae, C. C. Young, B. Genorio, D. E. Tsentalovich, C. Zhang, D. V. Kosynkin, J. R. Lomeda, C.-C. Hwang, S. Kumar, M. Pasquali, J. M. Tour. *ACS Nano* 2013, 7, 1628.
[9] Z. Dong, C. Jiang, H. Cheng, Y. Zhao, G. Shi, L. Jiang, L. Qu. *Adv. Mater.* 2012, 24, 1856.
[10] M. Zhang, K. R. Atkinson, R. H. Baughman. *Science* 2004, 306, 1358.

Combined Wet-Spinning and Electrospinning: Novel and Facile Method to Fabricate Micro-Nano Scale Conducting Fibres

Dorna Esrafilzadeh, Rouhollah Jalili, Kerry J. Gilmore, Joselito M. Razal, Simon L. Moulton, Gordon G. Wallace

ARC Centre of Excellence for Electromaterials Science and Intelligent Polymer Research Institute, University of Wollongong, Wollongong, NSW 2522, Australia

de256@uowmail.edu.au; gwallace@uow.edu.au

INTRODUCTION

One of the main challenges in tissue engineering is to design and fabricate an appropriate 3D extra cellular matrix (ECM) with capability to tune the *in vivo* environment in conjugation with additional requirements for cells enhancement. The composition, topology and artichectures of ECM are critical to achieve the desirable functionality of tissue or organ to be regenerated [1].

ECM fabricated from conducting polymer can offer intriguing platforms for tissue regeneration due to their capability to enhance cellular growth via electrical stimuli as well as controlling the release of biological molecules [2]. Topological design and biocompatibility of the conducting ECM are critical factors in order to have appropriate *in vivo* environment for cells, their attachment to ECM and ability to transfer the electrical signals to the cells. Recent increasing attention for utilising conducting polymers in regenerative medicine have turn them into highly demanding materials to fabricate into complex 3D structures by scalable methods such as wet-spinning. In addition, electro-spinning is a well-established, versatile technique to produce ultra-fine fibres in different artichectures including random oriented mats, aligned, twisted and untwisted yarns with high surface area to volume ratio. Since the dimension of nanofibres is a few orders of magnitude smaller than cells, cells posses promising interaction against the nanofibers [1].

In this study, we introduce a novel and facile method to integrate wet-spinning and electro-spinning to fabricate continues multifunctional fibres. In this method Poly(3,4-ethylenedioxythiophene) poly(styrenesulfonate) (PEDOT: PSS) is being injected into a chitosan coagulation bath to form a hybrid fiber [2] followed by washing process in an ethanol bath. At the same time, PLA-PLGA nanofibers are being electro-spun on the top of the ethanol washing bath. When PEDOT:PSS-Chitosan hybrid fibers taking up from the washing bath, it being covered by electrospun PLA-PLGA nanofibers to form PEDOT:PSS-Chitosan/PLA-PLGA yarn.

APPROACH

Poly(3,4-ethylenedioxythiophene) poly(styrenesulfonate) (PEDOT: PSS) pellets were obtained from Agfa (Orgacon dryTM, Lot A6 0000 AC) with water content of 9.8m/m% H_2O and used as supplied. High molecular weight Chitosan (CHI) was purchased from Sigma (>75% deacetylation). Poly lactic-co-glycolic acid (PLGA) (75:25) was purchase from Purac (Singapore).

The wet-spinning method was used to fabricate PEDOT:PSS-CHI fibres by injecting PEDOT:PSS with concentration of 25 mg/ml into the 1.0 wt% chitosan solution. The feeding rate of wet-spinning pump was 15 mL/hr using a 5.0 mL syringe with a detachable needle (20 gauge) used as a spinneret. The electro-spinning set up has been modified to receive the wet-spun fibre into ethanol bath while 25 mg/ml PLGA in DMF was electro-spun on top of fibre with feeding ratio of 15 ml/h. Finally, the fibres were collected on spool.

RESULTS AND DISCUSSION

Novel mico-nano dimensional fibres were fabricated using combination of wet and electro spinning. The scanning electron microscopy (SEM) of fibres presented unique, new structure with micro fibres underneath of electro-spun layer. Fig 1 shows the SEM images of fibres with different magnifications.

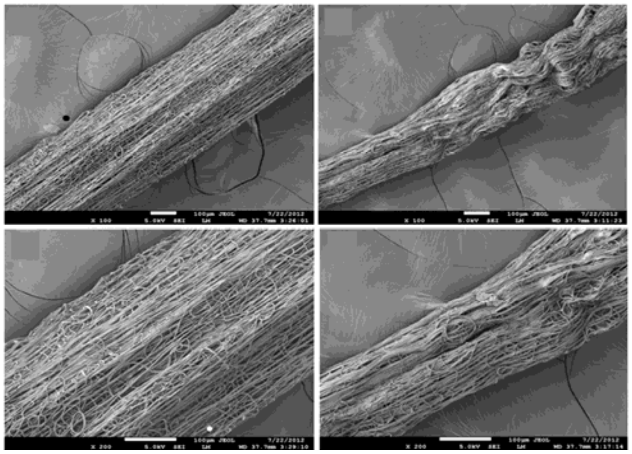

Fig 1. SEM images of fibres with different magnifications.

The size distribution of fibres carried our by SEM demonstrated sub-micron dimension of fibres (Fig. 2) however, the nano dimension of electro-spun layer can be achieved by modifying electro-spinning feeding ratio and polymer concentration.

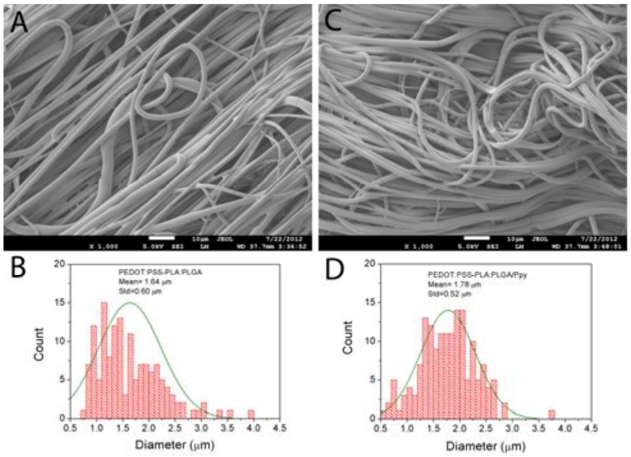

Fig 2. SEM of electro-spun layer with 1000X magnification (A and C). Size distribution of electro-spun layer (B and D).

CONCLUSION

Novel three-dimensional structure was delivered by combination of electro and wet-spinning systems. The morphology of the fibres was characterised using scanning electron microscopy. The presence of sub-micron electro-spun layer open lots of doors in biomedical engineering whilst, the electrochemical property of fibres can facilitate cells development using electrical stimulation.

ACKNOWLEDMENTS

The authors gratefully acknowledge the Australian Research Council and the ARC Centre of Excellence for Electromaterials Science (ACES) for their continued financial support. The authors also wish to thank the Australian Research Council for the Federation Fellowship (Wallace), Queen Elizabeth II Fellowship (Moulton) and Australian Post-doctoral Fellowship (Razal).

REFERENCES

1. Ku, S.H. and C.B. Park. Combined Effect of Mussel Inspired Surface Modification and Topographical Cues on the Behavior of Skeletal Myoblasts. *Advanced Healthcare Materials*, 2013: p. doi: 10.1002/adhm.201300067

2. Esrafilzadeh, D., et al. Multifunctional conducting fibres with electrically controlled release of ciprofloxacin. *Journal of Controlled Release*, DOI: 10.1016/j.jconrel.2013.01.022

Living Fibres: 3D Hydrogel Fibres for Tissue Engineering

Anita Quigley[1,2], Magdalena Kita[1,2], Rhys Cornock[1,2], Tharun Mysore[1,2], Javad Foroughi[1],
Gordon G Wallace[1], Robert MI Kapsa[1,2]
[1]Intelligent Polymer Research Institute, AIIM Facility, Innovation Campus, University of Wollongong, Wollongong, NSW 2500, New South Wales, Australia
[2]Centre for Neuroscience and Neurological Research, St Vincent's Hospital, Fitzroy, Melbourne, Victoria 3065, Australia.
anitaq@uow.edu.au; rmik@unimelb.edu.au

PURPOSE

To use rapid fibre spinning technologies for the creation of 3D constructs for cell delivery, tissue engineering and the study of 3D cellular interactions. This study describes the fabrication of biosynthetic soft gel fibers containing myoblasts and myogenic growth factors and their use for restoration of dystrophin expression in dystrophic *mdx* mouse muscle.

INTRODUCTION

Tissue engineering approaches generally involve cell seeding onto biological or synthetically based scaffolds, prior to implantation or analysis *in vitro*.[1] We have combined the synthesis of hydrogel biomaterials with cell seeding in one process to create cell laden hydrogel fibres, amenable to transplantation as well as for study of cellular interactions and behaviour in 3D.

Cell transplantation for replacement of lost muscle tissue has shown limited potential to date and we propose that this can be improved by controlled pre-engineering of proliferative differentiation-resistant muscle cellular constructs *ex vivo* prior to their implantation as biosynthetic myoregenerative scaffolds.[2,3]

This study shows that use of alginate rods as delivery vehicles for myoblasts may improve the transplantation potential and remodelling of dystrophic muscle.

APPROACH

Wet Spinning of myogenic cell-laden fibres

Primary myoblasts (muscle precursor cells) were prepared from transgenic 129S4Gt(ROSA)26 mice, backcrossed to a C57Bl10 background (St Vincent's Hospital Melbourne #013/11), using methods previously described by our laboratories.[4] Purified myoblasts were resuspended in Alginate (1-2%) (NovaMatrix) containing a cocktail of defined cytokines, prior to wet spinning. Myoblasts were seeded into alginate solution (2%) at a density of approximately 3 x 10^6 cells/ml. Non crosslinked alginate-cell preparations were then spun through a syringe into a coagulation bath (1M length) containing 150mM NaCl, 10mM HEPES, 110mM $CaCl_2$. Fibres were deposited on a rotating collection drum and immediately placed in cell media or buffer for analysis of cell viability and/or transplantation.

In Vitro and *In Vivo* analysis of Cell Laden Fibres

Immediately after wet spinning, cell laden fibres were stained with Calcein AM (Life Technologies) and Propidium Iodide (Sigma) to identify viable and non-viable cells. For *in vivo* transplantation, alginate fibres were prepared containing a cytokine cocktail designed to improve cell survival. Fibres (approximately 500µm in diameter) were prepared as described above and washed briefly in PBS, before transplantation into the gastrocnemius muscle of *mdx* mice. Fibres were left for 4, 8 and 12 weeks before analysis. Gastrocnemius muscles were notexin treated, to induce a regenerative environment, prior to fibre implantation.

Muscles were harvested and snap frozen in liquid nitrogen-cooled isopentane and cryosectioned for analysis. Hematoxylin and Eosin staining was performed to determine tissue reaction to the fibres. Sections were stained for ROSA transgene activity, as well as dystrophin expression to identify donor cells.

RESULTS AND DISCUSSION

Myoblast laden alginate fibres could be spun at diameters ranging from 100µm to 800µm, depending on the spinning method and parameters employed. Analysis of cell viability in alginate fibres demonstrated at least 92% cell survival *in vitro* (Fig. 1) after the spinning process.

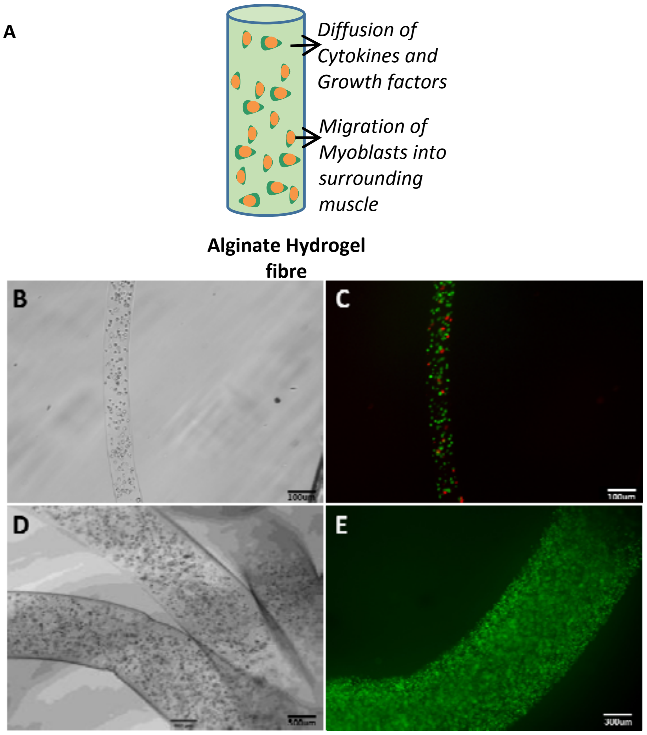

Fig. 1: Primary myoblasts wet spun into Alginate hydrogel fibres loaded with cytokines (A, B), were assessed for survival (C:- calcein, green, alive and propidium iodide; red, dead) showed a survival rate of > 92% (C & E). Fibre diameter ranged between 100µm (B & C) and 800µm (D & E). These fibres were implanted into the dystrophic muscles of *mdx* mice (Fig 2)

In vivo analysis of cell delivery to muscle demonstrated survival of cells within alginate rods at 2, and 4 weeks with migration of donor cells from alginate fibres to surrounding muscle seen at 4, 8 and 12 weeks (Fig. 2). Inclusion of cytokines into alginate fibres showed some improvement in myoblast survival in a number of animals, and a decline in donor cell number seen over time in the treated animals, was proposed to be due to a lack of innervation of the newly-formed muscle.

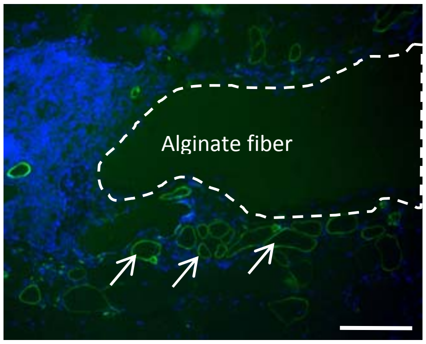

Fig. 2: Fluorescent image showing newly formed dystrophin expressing muscle fibres (arrows) at 12 weeks post-transplant of LIF and myoblast containing alginate rods. Cell nuclei are shown in blue. Arrows indicate donor cells. Scale bar is 100□m.

CONCLUSIONS

Cell laden hydrogel fibres can be used for cell delivery as well as for the delivery of cytokines and biofactors to tissues. In addition, these fibers can be used to expand cell numbers prior to and post transplantation.

FUTURE WORK

An ongoing study is currently underway to expand upon the results observed in this study. Ongoing experiments involve the construction of 3D scaffolds using fiber spinning technologies as well as other fabrication methods including printing and electrospinning that incorporate biofactors to promote innervation of the newly formed muscle *in vivo*. Future experiments will utilize these fabrication methods for cell transplantation and delivery of biofactors to muscle and nerve tissues.

ACKNOWLEDGEMENTS

The authors would like to thank the Australian Research Council (CE0561616) the National Health and Medical Research Council (573430) and the Australian Nano-Fabrication Facility (ANFF) for supporting this work.

REFERENCES

[1] Gordon G. Wallace, Simon E. Moulton, Michael J. Higgins, and Robert M.I. Kapsa. *Organic Bionics*., Wiley-VCH, 2012.

[2] Yi. Hong, Haiqing Song, Zhengwei Mao, Changyou Gao, and Jiacong Shen. Covalently crosslinked chitosan hydrogel: Properties of in vitro degradation and chondrocyte encapsulation. *Acta Biomater*., 3:23-31, 2006.

[3] Bo Ram Lee, Kwang Ho Lee, Edward Kang, Dong-Sik Kim, and Sang-Hoon Lee. Microfluidic wet spinning of chitosan-alginate microfibers and encapsulation of hepg2 cells in fibers. *Biomicrofluidics*, 5:022208, 2011.

[4] Marian Todaro, Anita F. Quigley, Magdalena Kita, Judy Chin, Kym Lowes, Andrew J. Kornberg, Mark J. Cook, Robert M.I. Kapsa, *Hum. Mutat*., 2007, 28, 816.

Production of Silk Nanoparticles

Mehdi Kazemimostaghim[1], Rangam Rajkhowa[1], Takuya Tsuzuki[1,2], Xungai Wang[1, 3]
[1]Australian Future Fibres Research and Innovation Centre, Deakin University, Geelong, VIC 3217, Australia
[2] Research School of Engineering, Australian National University, Canberra, ACT 0200, Australia
[3]School of Textile Science and Engineering, Wuhan Textile University, Wuhan, China
mkazemim@deakin.edu.au

INTRODUCTION

As a textile fibre, silk has outstanding properties such as good lustre, dye and moisture absorption as well as high toughness, which differentiate it from other natural and synthetic fibres used in the textile industry [1]. Raw silk consists of two fibroin protein filaments which are surrounded by a glue-like protein named sericin [1]. Due to its good mechanical strength and biocompatibility, silk fibre has been used as sutures for many years. High wet strength, good resistance to enzymatic breakdown, good oxygen permeability and drug binding also make silk a suitable biomaterial [2]. Silk fibroin has been used for bone regeneration [1], blood vessels [3], tissue scaffold, drug delivery, enzyme immobilization, wound healing, and cosmetics [1]. For these applications, various silk morphologies including powders, films, foams, nanofibres, and composites have been used.

It is relatively difficult to convert silk fibre directly into fine powders, as silk is flexible and has a high mechanical strength. Therefore, silk powder is commonly made using chemical processes (bottom-up). In the chemical methods, silk particles are regenerated from silk dissolved in solvents that have the ability to break down the strong intermolecular forces between β-sheets [4]. The drawback of chemical methods is that the regenerated silk protein is de-natured since the chemicals used change the native structures of silk. Furthermore, the chemicals should be removed from the silk particles by dialysis, which is a lengthy process.

In the past, some attempts have been made to use mechanical methods to produce silk powders. In these top-down methods, silk fibres were broken to small pieces by crushing or milling. However, production of submicron silk particles with a narrow size distribution has been difficult. In this work, we produced such silk particles using a combination of attritor milling and bead milling processes.

APPROACH

Eri silk was selected as the raw material, as it has lower mechanical strength than the common Mulberry silk. Degummed fibres were chopped by a cutter mill until the snippets could pass through a 1 mm grid. Wet milling of the snippets was carried out in an attritor mill in deionized water with yttrium-doped zirconium oxide balls of 5 mm in diameter as the grinding media, until volume median particle size, d(0.5), of around 7µ was achieved. Then, a bead mill was used with cerium-doped zirconium oxide grinding beads (0.5-0.6 mm) having a volume of 55-60 mL at pHs 10, 7, and 3. Milling speed was adjusted between 1500 to 4000 rpm. After removing the base ($NaOH+NaHCO_3$ buffer), the bead-milled slurry was processed with a laboratory spray dryer (B-290 from Buchi) to produce dry powders. Malvern Mastersizer 2000 was used for determining particle sizes. Scanning electron microscope (SEM), X-ray diffraction (XRD), Fourier transform infrared (FTIR) spectroscopy, differential scanning calorimetry (DSC), and thermogravimetric analysis (TGA) were utilized to explore the morphology and structure of silk particles.

RESULTS AND DISCUSSION

One method to prevent particles from aggregation during milling is by utilizing electrostatic repulsive force between the particles. This can be achieved by inducing positive or negative charge to the particles [5]. Silk is an amphoteric protein with the isoelectric pH of 3.8-4.5. In the pH ranges below the isoelectric point, silk is positively charged, and above that it is negatively charged. In general, above the isoelectric point, a higher pH value gives a larger negative zeta potential and hence stronger electrostatic repulsion between particles. On the other hand, increasing the pH causes degradation of silk fibre due to hydrolysis of the polypeptide chain [6]. Therefore, in this study, to have a maximum electrostatic repulsion effect with less chemical damage to silk fibre, the pH value was restricted to below 10. Processing parameters for bead milling such as bead load, milling speed, silk concentration, and milling time, and pH were optimized in terms of milling efficiency.

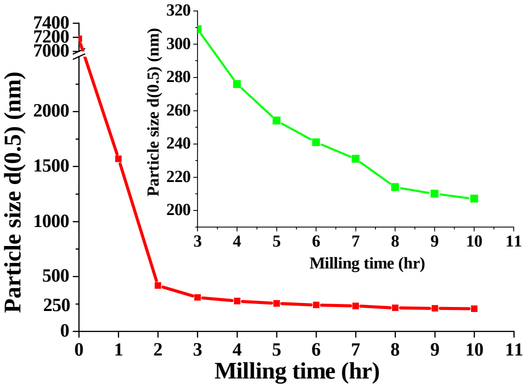

Figure 1. Volume median particle size d(0.5) as a function of milling time at 2% slurry, 2000 rpm speed, 60 mL bead load, and pH 10.

It was found that silk concentration of 2% (w/w), milling speed of 2000 rpm, bead load of 60 g and pH 10 gave the highest efficiency in the size reduction of silk particles with high reproducibility. Figure 1 shows d(0.5) as a function of milling time. The y-axis is expanded in the inset graph for the data above 3 hours. After 10 hours of milling, d(0.5) decreased from 7,180 nm to 207 nm. The d(0.5) was reduced rapidly during the first 2 hours of milling and subsequently decreased gradually until it reached a steady state. The particle size can be controlled by adjusting the milling time (Fig. 1).

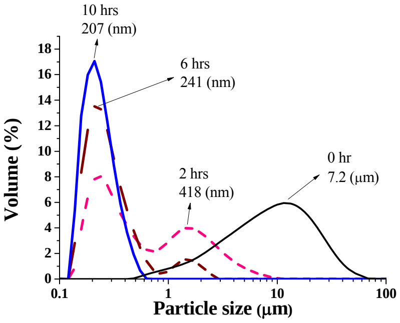

Figure 2. Particle size distribution and d(0.5) of silk particles after attritor milling (0 hr), and after bead milling for 2, 6, and 10 hrs at 2% slurry, 2000 rpm speed, 60 mL bead load, and pH 10.

Figure 2 shows the particle size distribution of primary silk particles after attritor milling down to 7.2 μm in d(0.5), followed by bead milling for 2, 6, and 10 hours. During the initial phase of bead milling, the particle size had a bimodal distribution. After two hours of milling, the two peaks were almost equal in size, but while the process was continued up to 10 hours, the left side peak increased in size until the two peaks converged into a single peak.

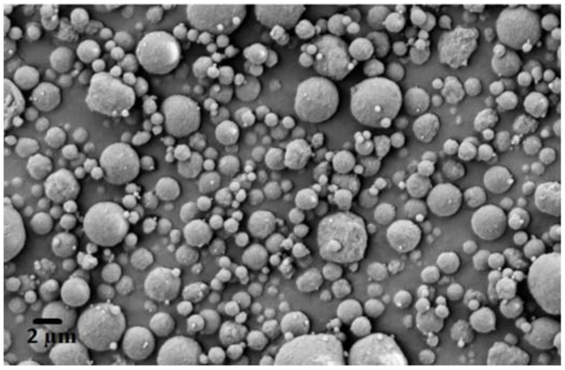

Figure 3. SEM image of silk particles after spray drying.

Figure 3 shows an SEM image of spray-dried particles after bead milling. It illustrates the spherical shape of particles of 0.2 - 4 μm in diameter. The spherical shape is typical of spray dried particles caused by the surface tension of water.

The observation of amide I-V vibration spectra is a useful method for understanding the secondary structure of polypeptides and proteins. The amide III region (1200 to 1300 cm^{-1}) is an area highly sensitive to the structural changes of Eri silk. Comparing the FTIR spectra (a) and (b) in Figure 4, it is evident that 207 nm particles had a β structure similar to that of original Eri silk fibres. However, XRD results indicated no crystallinity in the 207 nm particles. This discrepancy was due to the sensitivity of FTIR to short-range order, and XRD to long-range order [7]. DSC and TGA results were similar for original fibre and submicron particles, especially in their decomposition temperature, indicating minimal damage to the short range order of silk particles by using high pH.

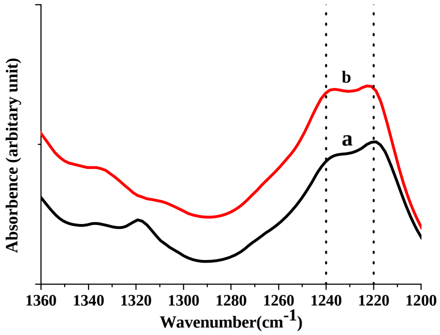

Figure 4. FTIR spectra of Eri silk: (a) fibre, (b) 207 nm powder.

CONCLUSION

Bead milling was used to produce silk nanoparticles from silk fibres. Silk fibres were first milled to d(0.5) of 7 μm using an attritor mill, followed by bead milling for further size reduction. It was found that d(0.5) of the silk particles could be reduced down to ~200 nm with a narrow particle size distribution. FTIR results indicated that 200 nm particles had the same β protein structure as silk fibre while XRD study revealed that the long range order between the β structures was lost during milling.

REFERENCES

[1] J.G. Hardy, L.M. Römer, T.R. Scheibel. Polymeric materials based on silk proteins. *Polymer*, 49 (2008) 4309-4327.

[2] N. Minoura, S.I. Aiba, M. Higuchi, Y. Gotoh, M. Tsukada, Y. Imai. Attachment and Growth of Fibroblast Cells on Silk Fibroin. *Biochemical and Biophysical Research Communications,* 208 (1995) 511-516.

[3] M. Lovett, C. Cannizzaro, L. Daheron, B. Messmer, G. Vunjak-Novakovic, D.L. Kaplan. Silk fibroin microtubes for blood vessel engineering. *Biomaterials*, 28 (2007) 5271-5279.

[4] A.S. Lammel, X. Hu, S.-H. Park, D.L. Kaplan, T.R. Scheibel. Controlling silk fibroin particle features for drug delivery. *Biomaterials*, 31 (2010) 4583-4591.

[5] W. Peukert, H.-C. Schwarzer, F. Stenger. Control of aggregation in production and handling of nanoparticles. *Chemical Engineering and Processing: Process Intensification*, 44 (2005) 245-252.

[6] M. Gulrajani. Degumming of silk. *Review of Progress in Coloration and Related Topics*, 22 (1992) 79-89.

[7] I.C. Um, H. Kweon, Y.H. Park, S. Hudson. Structural characteristics and properties of the regenerated silk fibroin prepared from formic acid. *International Journal of Biological Macromolecules*, 29 (2001) 91-97.

Keynote Speakers

Applications of Electrospun Nonwoven Fiber Membranes for Sensing and Separations

Gregory C. Rutledge
Department of Chemical Engineering, Massachusetts Institute of Technology, Cambridge, MA 02139 USA
rutledge@mit.edu

SUMMARY

Ultrafine polymer fibers, with diameters less than 1 micron, represent a field of growing importance for fiber science and technology worldwide, with explosive growth in the technical and patent literature over the past decade. Nonwoven sheets of these novel fibers offer unique combinations of high specific surface area, high porosity, and small inter-fiber distances. Electrospinning technology provides a remarkably simple and inexpensive means to develop materials for applications that take advantage of some of these unique qualities. This talk will offer an overview of selected applications of these novel materials as membranes for sensing and separations.

In the sensing arena, we discuss materials that operate as chemiresistive sensors. Due to their high specific surface area, electrospun fibers offer a particularly high level of sensitivity and large dynamic range. With their small diameters, they also present relatively fast response times. In this work, we demonstrate the high individual fiber conductivities that can be realized with electrospun fibers of intrinsically conducting polymers like polyaniline (PAni), optionally doped to varying degrees with (+)-camphor-10-sulfonic acid (HCSA). We show that the measured resistance of the nonwoven mats can be explained entirely in terms of the individual fiber conductivity and the structure of the nonwoven membranes.[1] Exposure to gases like ammonia or nitrogen dioxide that are electron-donating or electron-withdrawing, respectively, alter the conductivity of the fiber, so that the exposure can be measured as a change in sheet resistance of the membrane. A reaction-diffusion model is developed to extract important parameters that characterize the diffusion and reaction of gaseous species within the fiber. Time permitting, we may also discuss the development of carbon nanofibers derived from electrospun poly(acrylonitrile) fibers as chemiresistive biosensors.[2]

In the area of separations, we have studied the selective wetting and transport of aqueous and organic liquids through electrospun membranes. Nanofiber membranes are uniquely suited to applications requiring super-phobic or super-philic character, through the combined effects of fiber size, in-plane fiber orientation and high porosity.[3] However, they are also relatively compressible, and subject to deformation under typical membrane separation operating conditions. Such deformation can compromise performance. We discuss the measurement of compressibility of electronspun fiber membranes and how this compressibility can be taken into account when analyzing for hydraulic permeabilities of the membranes. [4]

REFERENCES

1. Zhang, Y., Rutledge, G.C. “Electrical conductivity of elecrtrospun polyaniline and polyaniline-blend fiber mats”, Macromolecules 2012, 45, 4238.
2. Mao, X., Simeon, F., Rutledge, G.C., Hatton, T.A., “Electrospun carbon nanofiber webs with controlled density of states for sensor applications”, Adv. Mater. 2013, 25(9), 1309.
3. Ma, M., Hill, R.M., Rutledge, G.C. “A review of recent results on superhydrophobic materials based on micro- and nano-fibers”, J. Adh. Sci. Technol. 2008, 22, 1799.
4. Choong, L.T., Mannarino, M.M., Basu, S., Rutledge, G.C., “Compressibility of Electrospun Fiber Mats”, J. Mater. Sci. (submitted).

ACKNOWLEDGMENT

Portions of this work have been funded by the King Fahd University of Petroleum and Minerals (KFUPM)through the Center for Clean Water and Clean Energy at MIT, the US Department of Energy, the US Army through the Institute for Soldier Nanotechnologies at MIT.

Highly Functional Fibres for Bionics

Gordon G. Wallace
ARC Centre of Excellence for Electromaterials Science (ACES)
Intelligent Polymer Research Institute
AIIM Facility, Innovation Campus, Wollongong, NSW 2522, Australia
E-mail: gwallace@uow.edu.au

The use of organic conductors to provide a more effective communications channel between the world of biology and electronics has attracted considerable attention recently www.youtube.com/watch?v=FDa3QuEIYXw*

The fact that electrical stimulation of such conductors provides a conduit for direct electrical communication with living cells as well as enabling controlled release of bioactive molecules has enabled effective communication with nerve cells www.youtube.com/watch?v=Xl8xAo2aROw*

Nanostructured organic conducting polymer platforms have also been used to provide directional growth to muscle cells and a highly effective platform for electrical stimulation www.youtube.com/watch?v=rpYVn8MVK2k*

There is a need therefore to continue to evolve innovative protocols that enable fabrication of organic conducting polymers containing structures with spatial control in the micro to nanodomain. Fibre spinning provides us with a versatile strategy. Both wet-spinning and electrospinning have been used by us to create long lengths of highly functional fibres for Bionics. We have used wet-spinning to provide micron dimensional topographical cues on a conducting polymer platform to control the direction of neurite outgrowth or to ensure the alignment of muscle cells. In subsequent studies we have shown that nanodimensional fibres created by electrospinning also, surprisingly, act as topographical cues to provide directional growth.

We have also utilized spinning techniques to produce fibres containing bioactive molecules to provide controlled delivery of drugs or other growth factors. Co-axial spinning techniques have proven highly effective in producing such structures, these approaches provide a pragmatic approach to tailoring release profiles through manipulation of structure rather than material composition.

Besides the ability to build in bioactivity there are two physical properties of fibres destined for use in medical bionics that are critical: mechanical and electronic properties. We have produced a number of conducting structures with tuneable mechanical properties achieved through the formation of composites. Host materials include biocompatible polyurethanes or naturally occurring chitosan. Biodegradable polymers such as PLA-PLGA have also been employed. The conducting components investigated here included organic conducting polymers, carbon nanotubes and graphene.

Applications: Working with clinical collaborators at St Vincent's Hospital in Melbourne we have identified some area of application.

Conduits for nerve and muscle regeneration

In these studies the ultimate structure will provide sites for cell adhesion and proliferation, as well as alignment and conduits for electrical stimulation. Recently we demonstrated that the conduit shown in Figure 1 is highly effective in supporting peripheral nerve regeneration over a 1 cm defect. Current studies are aimed at introducing electrical stimulation conduits.

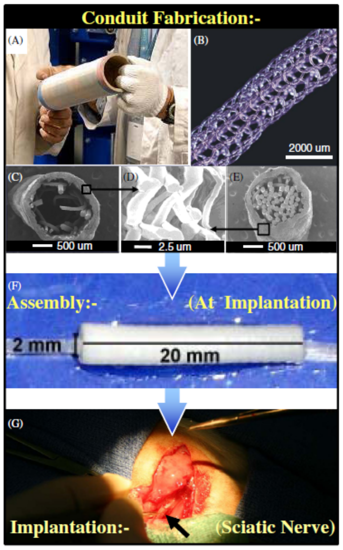

Figure 1. (From Reference 5) The process of the nerve repair conduit engineering consisted of fiber extrusion (A), knitting of the conduit infrastructure using PLA (B), electrospinning a PLA membrane on the outside of the knitted sheath (C) with controlled pore size of approximately 2 μm (D). The full conduit contained fiber components selective for nerve growth guidance

and Schwann cell growth over the proliferation of fibroblasts (E), with the internal guidance fibers provided separately to the conduit to allow the assembly with a fresh multimodal hydrogel containing growth factors (final configuration with MGF-1, LIF, NT-3 and SMDF) (F) immediately prior to surgical implantation (conduit indicated by the black arrow) into rats with axotomized sciatic nerves (G).

Devices for implantation into the brain for epilepsy, detection and control

In these studies our ultimate implant will be capable of detecting signals arising from the brain that provide a warning of an impending seizure. The signals will be used to trigger release of anti epileptic drugs from a nanofibrous network. Our current work involves animal studies to determine the compatibility of such networks in the brain and the effect of localised drug delivery from the structures.

Here we will review our progress in each of these areas.

Key Recent Publications

(1) Wallace, G.G., Moulton, S.E., Higgins, M.J., Kapsa, R.M.I. Organic Bionics. *Wiley-VCH Verlag & Co. KGaA*, Boschstr. 12, 69469 Weinheim, Germany 2012.

(2) Moulton, S.E., Higgins, M., Kapsa, R.M.I., Wallace, G.G. Organic Bionics: A New Dimension in Neural Communications. *Advanced Functional Materials* 2012, 22, 2003-2014.

(3) Yue, Z., Moulton, S.E., Cook, M., O'Leary, S., Wallace, G.G. Controlled Delivery for Neuro-Bionic Devices. *Advanced Drug Delivery Reviews* (Accepted)

(4) Wallace, G.G., Higgins, M.J., Moulton S.E., Wang, C. Nanobionics: The Impact of Nanotechnology on Implantable Medical Bionic Devices. *Nanoscale* 2012, 4, 4327-4347.

(5) Quigley, A.F., Bulluss, K.J., Kyratzis, I.L.B., Gilmore, K., Mysore, T., Schirmer, K.S.U., Kennedy, E.L., O'Shea, M., Truong, Y.B., Edwards, S.L., Peeters, G., Herwig, P., Razal, J.M., Campbell, T.E., Lowes, K.N., Higgins, M.J., Moulton S.E., Murphy, M.A., Cook, M.J., Clark, G.M., Wallace, G.G., Kapsa, R.M.I. Engineering a multimodal nerve conduit for repair of injured peripheral nerve. *Journal of Neural Engineering* 2013 10 (1), 016008.

*All links are animated DVDs with voiceover.